Lecture Notes in Electrical Engineering 814

Manohar Mishra · Renu Sharma ·
Akshay Kumar Rathore ·
Janmenjoy Nayak ·
Bighnaraj Naik *Editors*

Innovation in Electrical Power Engineering, Communication, and Computing Technology

Proceedings of Second IEPCCT 2021

Springer

Lecture Notes in Electrical Engineering

Volume 814

The book series *Lecture Notes in Electrical Engineering* (LNEE) publishes the latest developments in Electrical Engineering - quickly, informally and in high quality. While original research reported in proceedings and monographs has traditionally formed the core of LNEE, we also encourage authors to submit books devoted to supporting student education and professional training in the various fields and applications areas of electrical engineering. The series cover classical and emerging topics concerning:

- Communication Engineering, Information Theory and Networks
- Electronics Engineering and Microelectronics
- Signal, Image and Speech Processing
- Wireless and Mobile Communication
- Circuits and Systems
- Energy Systems, Power Electronics and Electrical Machines
- Electro-optical Engineering
- Instrumentation Engineering
- Avionics Engineering
- Control Systems
- Internet-of-Things and Cybersecurity
- Biomedical Devices, MEMS and NEMS

For general information about this book series, comments or suggestions, please contact leontina.dicecco@springer.com.

To submit a proposal or request further information, please contact the Publishing Editor in your country:

China

Jasmine Dou, Editor (jasmine.dou@springer.com)

India, Japan, Rest of Asia

Swati Meherishi, Editorial Director (Swati.Meherishi@springer.com)

Southeast Asia, Australia, New Zealand

Ramesh Nath Premnath, Editor (ramesh.premnath@springernature.com)

USA, Canada:

Michael Luby, Senior Editor (michael.luby@springer.com)

All other Countries:

Leontina Di Cecco, Senior Editor (leontina.dicecco@springer.com)

**** This series is indexed by EI Compendex and Scopus databases. ****

More information about this series at https://link.springer.com/bookseries/7818

Manohar Mishra · Renu Sharma ·
Akshay Kumar Rathore · Janmenjoy Nayak ·
Bighnaraj Naik
Editors

Innovation in Electrical Power Engineering, Communication, and Computing Technology

Proceedings of Second IEPCCT 2021

Springer

Editors
Manohar Mishra
Department of Electrical and Electronics Engineering
Institute of Technical Education and Research
Siksha 'O' Anusandhan (Deemed to be University)
Bhubaneswar, India

Akshay Kumar Rathore
Concordia University
Montreal, QC, Canada

Bighnaraj Naik
Department of Computer Application
Veer Surendra Sai University of Technology
Burla, India

Renu Sharma
Department of Electrical Engineering
Institute of Technical Education and Research
Siksha 'O' Anusandhan (Deemed to be University)
Bhubaneswar, India

Janmenjoy Nayak
Department of Computer Science Engineering
Aditya Institute of Technology and Management
K Kotturu, India

ISSN 1876-1100 ISSN 1876-1119 (electronic)
Lecture Notes in Electrical Engineering
ISBN 978-981-16-7075-6 ISBN 978-981-16-7076-3 (eBook)
https://doi.org/10.1007/978-981-16-7076-3

This Springer imprint is published by the registered company Springer Nature Singapore Pte Ltd.
The registered company address is: 152 Beach Road, #21-01/04 Gateway East, Singapore 189721, Singapore

IEPCCT Committee

Chief Patron

Prof. Manoj Ranjan Nayak, President, Siksha 'O' Anusandhan (Deemed to be University), Bhubaneswar, Odisha, India

Patron

Prof. Ashok Kumar Mohapatra, Vice-Chancellor, Siksha 'O' Anusandhan (Deemed to be University), Bhubaneswar, Odisha, India

Honorary General Chair

Prof. Pradipta Kishore Dash, Director, Multi-disciplinary Research Center (MDRC), Siksha 'O' Anusandhan (Deemed to be University), Bhubaneswar, Odisha, India

General Chairs

Prof. Bijaya Ketan Panigrahi, Professor, Department of Electrical Engineering, IIT Delhi, India
Prof. Pradipta Kumar Nanda, Dean (Research), Siksha 'O' Anusandhan (Deemed to be University), Bhubaneswar, Odisha, India
Prof. Akshay Kumar Rathore, Professor, Department of Electrical Engineering, Concordia University, Canada

Prof. Renu Sharma, Professor, Department of Electrical Engineering, Siksha 'O' Anusandhan (Deemed to be University), Bhubaneswar, Odisha, India

General Co-chairs

Prof. Sanjeeb Kumar Kar, Siksha 'O' Anusandhan (Deemed to be University), Bhubaneswar, Odisha, India
Dr. Danilo Pelusi, University of Teramo, Italy
Prof. Pravat Kumar Rout, Siksha 'O' Anusandhan (Deemed to be University), Bhubaneswar, Odisha, India
Prof. Binod Kumar Sahu, Siksha 'O' Anusandhan (Deemed to be University), Bhubaneswar, Odisha, India
Prof. Niranjan Nayak, Siksha 'O' Anusandhan (Deemed to be University), Bhubaneswar, Odisha, India

Program Chairs

Prof. Janmenjoy Nayak, Associate Professor, Department of Computer Science and Engineering, Sri Sivani College of Engineering, Srikakulam, Andhra Pradesh, India
Prof. Bighnaraj Naik, Assistant Professor, Department of Computer Application, Veer Surendra Sai University of Technology, Burla, Odisha, India
Dr. Kumari Kasturi, Siksha 'O' Anusandhan (Deemed to be University), Bhubaneswar, Odisha, India
Dr. Satish Choudhury, Siksha 'O' Anusandhan (Deemed to be University), Bhubaneswar, Odisha, India

Organizing Chairs

Prof. Manohar Mishra, Associate Professor, Department of Electrical and Electronics Engineering, Siksha 'O' Anusandhan (Deemed to be University), Bhubaneswar, Odisha, India
Prof. Manoj Kumar Debnath, Assistant Professor, Department of Electrical Engineering, Siksha 'O' Anusandhan (Deemed to be University), Bhubaneswar, Odisha, India

International Advisory Committee

Prof. Damodar Acharya (Chair), Siksha 'O' Anusandhan (Deemed to be University), Bhubaneswar, Odisha, India
Prof. Sanjib Kumar Panda, NUS, Singapore
Prof. Bayoumi, Ehab H. E., Abu Dhabi Men's College, UAE
Prof. A. Abraham, Machine Intelligence Research Labs, USA
Prof. Sanjeevikumar Padmanaban, Aalborg University, Denmark
Prof. Akshay Kumar Rathore, Concordia University, Chicago
Prof. Ramazan Bayindir, Gazi University, Turkey
Dr. Danilo Pelusi, University of Teramo, Italy
Prof. Akhtar Kalam, Melbourne, Australia
Prof. Prasanta Mohapatra, University of California
Dr. Ahamed Zobaa, Brunel University, UK
Prof. R. C. Bansal, College of Engineering, University of Sharjah
Prof. Mamta Agiwal, Sejong University, Seoul, South Korea

National Advisory Committee

Prof. Damodar Acharya (Chair), Siksha 'O' Anusandhan (Deemed to be University), Bhubaneswar, Odisha, India
Prof. Bidyadhar Subudhi, IIT Goa, India
Prof. S. R. Samantray, IIT Bhubaneswar, India
Prof. S. K. Kulkarni, AGU, Shimla, India
Prof. Niva Das, Siksha 'O' Anusandhan (Deemed to be University), Bhubaneswar, Odisha, India
Dr. Swagatam Das, Indian Statistical Institute, Kolkata, India
Prof. Trilochan Panigrahi, NIT Goa, India
Prof. C. N. Bhende, IIT Bhubaneswar, India
Prof. S. K. Bharadwaj, MNNIT, Madhya Pradesh, India
Prof. Srikanta Pattnaik, Siksha 'O' Anusandhan (Deemed to be University), Bhubaneswar, Odisha, India
Prof. P. K. Sahu, Siksha 'O' Anusandhan (Deemed to be University), Bhubaneswar, Odisha, India

Technical Committee

Dr. Danilo Pelusi, University of Teramo, Italy
Dr. Sazia Hasan, BITS-Pilani, Dubai Campus
Dr. Abhisek Rajan, NIT, Sikkim

Dr. Mohit Ranjan Panda, CVRCE, Bhubaneswar
Dr. Shahed Mohammadi, Yandegan University, Tonekabon, Iran
Dr. Sukanta Kishore Bisoyi, CVRCE, Bhubaneswar
Dr. G. T. Chandrasekhar, SSCE, Andhra Pradesh
Dr. Soumya Ranjan Mishra, MVJ College of Engineering, Bengaluru
Dr. Prakash Kumar Ray, CET Bhubaneswar, BPUT, Bhubaneswar, India
Dr. Malaya Kumar Nath, NIT, Puducherry
Prof. Sumit Kushwaha, Kamla Nehru Institute of Technology, Uttar Pradesh
Dr. Trupti Swanakar, SOA, Bhubaneswar
Prof. Jyotir Moy Chatterjee, Asia Pacific University of Technology and Innovation, Nepal
Dr. Joymala Moirangthen, NUS, Singapore
Dr. Krishnanand K. R., NUS, Singapore
Dr. Sidhartha Panda, VSSUT Engineering College, Burla
Dr. N. P. Padhy, IIT Roorkee
Prof. M. Nageswara Rao, KL University, Vijayawada
Prof. P. S. Kulkarni, VNIT, Nagpur
Dr. Ahmed Faheem Zobaa, BU, UK
Dr. Akhtar Kalam, VU, Australia
Dr. Rajesh Kumar Patnaik, GMR, Andhra Pradesh
Dr. Krushna Keshab Mohapatra, SOA, Bhubaneswar
Dr. Kolla Bhanu Prakash, KL University, Vijayawada

Publicity Chairs

Prof. Amar Bijaya Nanda, Siksha 'O' Anusandhan, Bhubaneswar, India
Dr. Basanta Kumar Panigrahi, Siksha 'O' Anusandhan, Bhubaneswar, India
Dr. Tapas Kumar Mohapatra, Siksha 'O' Anusandhan, Bhubaneswar, India
Dr. Tanmoya Parida, Siksha 'O' Anusandhan, Bhubaneswar, India

Website Chairs

Dr. Nakul Charan Sahu, Siksha 'O' Anusandhan, Bhubaneswar, India
Mr. P. Suresh Kumar, DLBCE, Visakhapatnam
Dr. Shubhranshu Mohan Parida, Siksha 'O' Anusandhan, Bhubaneswar, India

Registration Chairs

Prof. Pradeep Kumar Mohanty, Siksha 'O' Anusandhan, Bhubaneswar, India
Dr. Satish Choudhury, Siksha 'O' Anusandhan, Bhubaneswar, India
Dr. Amiya Kumar Naik, Siksha 'O' Anusandhan, Bhubaneswar, India
Mr. Rasmi Ranjan Panigrahi, GEC, Bhubaneswar, India

Publication Chairs

Dr. Binod Kumar Sahu, Siksha 'O' Anusandhan, Bhubaneswar, India
Dr. Manohar Mishra, Siksha 'O' Anusandhan, Bhubaneswar, India
Prof. Renu Sharma, Siksha 'O' Anusandhan, Bhubaneswar, India

Finance Chair

Prof. Manas Kumar Malik, Siksha 'O' Anusandhan, Bhubaneswar, India
Dr. Priyabrata Pattanaik, Siksha 'O' Anusandhan, Bhubaneswar, India

Sponsorship Chairs

Prof. Ranjan Kumar Mallick, Siksha 'O' Anusandhan, Bhubaneswar, India
Dr. Sujit Kumar Dash, Siksha 'O' Anusandhan, Bhubaneswar, India
Dr. Subhendu Pati, Siksha 'O' Anusandhan, Bhubaneswar, India
Dr. Sasank Choudhury, Siksha 'O' Anusandhan, Bhubaneswar, India

IEPCCT Reviewers

Dr. Santosh Ku Sahoo, CVR College of Engineering
Dr. Kola Bhanu Prakash, KL University, Vijayawada
Dr. Sarat Ch. Nayak, Department of CSE, CMR College of Engineering and Technology (Autonomous), Hyderabad, India
Dr. G. T. Chandra Sekhar, SSCE, Srikakulam
Mr. Ch. Jagan Mohan Rao, AITAM, Andhra Pradesh
Dr. Swagat Kumar Pati, SOA, Bhubaneswar
Dr. Pradeep Kumar Mohanty, SOA, Bhubaneswar
Dr. Kaushik Paul, NIT Jamshedpur

Mr. Nimai Patel, Government College of Engineering, Keonjhar
Dr. Bhagyalaxmi Jena, SOA, Bhubaneswar
Ms. Kumari Kasturi, SOA, Bhubaneswar
Mr. Tapas Mohapatra, SOA, Bhubaneswar
Mr. Abhisek Parida, NIT Rourkela
Dr. Prakash Chandra Sahoo, SIT, Sambalpur
Dr. P. Vittal, AITAM, Andhra Pradesh
Mr. P. Suresh Kumar, Dr. Lankapalli Bullayya College
Mr. Suresh Chandra Moharana, Kalinga Institute of Industrial Technology (KIIT), Bhubaneswar
Dr. P. M. K. Prasad, GVP College of Engineering for Women, Visakhapatnam, Andhra Pradesh, India
Mr. Debasis Mohapatra, PMEC, Berhampur
Dr. A. Abdul Rasheed, CMR Institute of Technology, Bengaluru
P. Raman, GMR Institute of Technology, Andhra Pradesh
Dr. B. Naik, VSSUT, Burla
Dr. J. Nayak, AITAM, Andhra Pradesh
Dr. Abhisek Rajan, NIT Sikkim
Dr. B. Surendiran, Associate Dean (Academic), Department of CSE, NIT Puducherry
Dr. Renu Sharma, ITER, SOA, Bhubaneswar
Dr. Sonali Goel, ITER, SOA, Bhubaneswar
Dr. Debadatta Amaresh Gadanayak, ITER, SOA, Bhubaneswar
Dr. Manoj Kumar Debnath, ITER, SOA, Bhubaneswar
Dr. Binod Kumar Sahu, ITER, SOA, Bhubaneswar
Dr. Sanjeeb Kumar Kar, ITER, SOA, Bhubaneswar
Mr. Priya Ranjan Satpathy, ITER, SOA, Bhubaneswar
Miss. Sasmita Jena, ITER, SOA, Bhubaneswar
Mr. Rasmi Ranjan Panigrahi, ITER, SOA, Bhubaneswar
Dr. Satish Choudhury, ITER, SOA, Bhubaneswar
Prof. S. S. Dash, GEC Keonjhor
Swapna Rekha, SSCE, Srikakulam
Dukka Karun Kumar Reddy, Dr. L. Bullayya College of Engineering
Sarat Nayak, CMR College of Engineering and Technology, Hyderabad
Benudhar Sahu, ITER, SOA, Bhubaneswar
Meryleen Mohapatra, ITER, SOA, Bhubaneswar
Dr. Kanthi Andhavarapu, SSCE, Srikakulam
L. V. Sureshkumar, GMR Institute of Technology, Andhra Pradesh
Bhanja Kishore Swain, ITER, SOA, Bhubaneswar
Mihir Narayan Mohanty, ITER, SOA, Bhubaneswar
Manoj Kumar Swain, GEC, Bhubaneswar
Dr. Subhashree Choudhury, ITER, SOA, Bhubaneswar
Pritam Bhowmik, Budge Budge Institute of Technology
Manohar Mishra, ITER, SOA, Bhubaneswar
Buddhadeva Sahoo, ITER, SOA, Bhubaneswar
Pandit Byomakesha Dash, Aditya Institute of Technology and Management

Bhaskar Patnaik, BPUT, Rourkela
Sheetal Chandak, ITER, SOA, Bhubaneswar
Sesha Sai Brundavanam, LIET, Andhra Pradesh, India
Subhashree Mohapatra, ITER, SOA, Bhubaneswar
Shazia Hasan, BITS-Pilani, Dubai

Preface

The current industrial revolution (Fourth Industrial Revolution or Industy 4.0) is the fusion of several key technologies such as artificial intelligence (AI), robotics, cybersecurity, the Internet of Things (IoT), genetic engineering, quantum computing, and more. Application of these key technologies in electrical, electronics, and computer engineering domain may lead to future development of our society. The innovation in any technology and their approach of application in diverse domain can make the system become smarter. The innovation in electrical, communication, and computing technology is always interrelated to each other. A continuous research in all these domains as well as proper disseminating the work is highly important for the development of the global society.

The second international conference entitled 'Innovation in Electrical Power Engineering, Communication, and Computing Technology,' (IEPCCT-2021) is organized by the Department of Electrical Engineering, Institute of Technical Education and Research, Siksha 'O' Anusandhan (Deemed to be University), Bhubaneswar, Odisha, India, on September, 24–26, 2021. The conference is focused in the direction of numerous advanced concepts or cutting-edge tools applied for electrical, electronics, and computer science domain. More than 122 numbers of articles have been received through online related to the scope of the conference area. Out of these submissions, the editors have chosen only 47 high-quality articles after a thorough rigorous peer review process. In the peer review process, several highly knowledgeable researchers/professors with expertise in single/multi-domain are assisted the editors in unbiased decision making of the acceptance of the selected articles. Moreover, valuable suggestions of the advisory, program, and technical committee also help the editors for smoothing the peer review process. The complete review process is based on several criteria, such as major contribution, technicality, clarity, and originality of some latest findings. The whole process starting from initial submission to the acceptances notification to authors is done electronically.

The 2nd international conference 'IEPCCT-2021' focuses on sharing research and ideas among different academicians, researches, and scientists from throughout the world with an intention to global development. Therefore, the conference includes various keynotes address particular to the scope of IEPCCT research topics. The

sessions including (presentation of author's contribution and keynotes address) are principally organized in accordance with the significance and interdependency of the articles with reference to the basic concept and motivation of the conference.

The accepted manuscripts (original research and survey articles) have been well-organized to emphasize the cutting-edge technologies applied in electrical, electronics, and computer science domains. We appreciate the authors' contribution and value the choice that is 'IEPCCT' for disseminating the output of their research findings. We are also grateful for the help received from the each individual reviewer and the program committee members regarding peer review process.

We are highly thankful to the management of SOA (Deemed to be University) and each faculty member of the Department of Electrical Engineering, ITER, for their constant support and motivation for making the conference successful. The editors would also like to thank Springer editorial members for their constant help and for publishing the proceedings in 'Lecture Notes in Electrical Engineering' series.

Bhubaneswar, India — Manohar Mishra
Bhubaneswar, India — Renu Sharma
Montreal, Canada — Akshay Kumar Rathore
K Kotturu, India — Janmenjoy Nayak
Burla, India — Bighnaraj Naik

Acknowledgements

The editors are opportune to put forward key proposal and significance of IEPCCT conference. This conference has attracted more than 200 academicians, professionals, and researchers all over the globe. The conference showed the gamut of original research findings. We could able to have communes in diversified fields of electrical, electronics, and computation engineering.

We would like to thank all the authors for their contributions. We sincerely show our gratitude to the authors who contributed their time and expertise.

We would like to convey our heartfelt thanks to national and international advisory committee to be supportive and guiding us throughout the pre- and post-conference. We have been opportune to have strong eminent academician reviewer team who holistically did the reviewing and gave the critical and strong remarks on the manuscripts.

We profusely thank the organizing committee who has shown the level of eagerness by well organizing and managing throughout the conference.

Before finalization and accepting the manuscripts for oral presentation at conference, submitted manuscripts have been double-blind peer re-evaluated. We appreciate the responsibility shouldered by reviewers for putting effort to re-evaluate the manuscripts in time bound frame to enhance the quality of the proceedings.

Our profound and authentic gratitude to the editorial members of Springer Publishing team. The proceeding sees the day of light in the graceful, innovative, and intelligent ways.

The IEPCCT conference and proceedings ensured the acknowledgments to a huge congregation of people.

About the Conference

The conference **"2nd International Conference on Innovation in Electrical Power Engineering, Communication, and Computing Technology" (IEPCCT-2021)** is focused in the direction of numerous advanced concepts or cutting-edge tools applied for electrical, electronics, and computer science domain. IEPCCT is a multidisciplinary conference organized with an intention of sharing knowledge and views among each other by the different background of peoples, such as academicians, scientists, research scholars, and students working in the areas of electrical, electronics, advanced computing, and intelligent engineering. By this process, the authors/listeners (national or international levels) have got an opportunity to collaborate theirs thoughts in the direction of global development. The major objective of IEPCCT is to provide a useful platform for the global researchers to present their recent inventions in fronts of well-known professors and researcher's working on similar research fields. It also helps to create awareness about the status of basic scientific study compared to current developments in distinct research domain.

The conference IEPCCT-2021 is directed in the direction of the knowledge and structure of positive research in different applications of electrical power engineering, communication, and computing technology those are leading and governing the technological domain. The proceedings of IEPCCT-2021 will be aiming the postgraduate students and researchers working in the discipline of electrical, electronics, and computer science. Nowadays, the multidisciplinary researches have gained a huge attention to fulfill the necessities of smart cities/countries/worlds. Therefore, this book may assist the future development/researches by providing several recent innovations on electrical, computing, and communication engineering.

Contents

About the Editors

Dr. Manohar Mishra is an Associate Professor in the Department of Electronics and Electrical Engineering Department, under the Faculty of Engineering and Technology, Siksha 'O' Anusandhan University, Bhubaneswar. He received his Ph.D. in Electrical Engineering, M.Tech. in Power Electronics and Drives and B.Tech. in Electrical engineering in 2017, 2012 and 2008, respectively. He has published more than 40 research papers in various reputed peer reviewed International Journals, Conferences and Book Chapters. He has served as reviewers for various reputed Journal publishers such as Springer, IEEE, Elsevier and Inderscience. At present, he has more than 10 years of teaching experience in the field of Electrical Engineering. He is a Senior Member of IEEE. He is currently guiding 4 Ph.D. and Master scholar. His area of interest includes power system analysis, power system protection, signal processing, power quality, distribution generation system, Micro-grid. He has served as Convener and Volume Editor of International Conference on Innovation in Electrical Power Engineering, Communication and Computing Technology (IEPCCT-2019) and International Conference on Green Technology for Smart City and Society (GTSCS-2020). Currently, he is serving as Guest editor in different journals such as *International Journal of Power Electronics* (Inderscience Publisher) and *International Journal of Innovative Computing and Application* (Inderscience Publisher), *Nural Computing and Application* (Springer).

Dr. Renu Sharma is working as a Professor and Head of the Department Electrical Engineering under the Faculty of Engineering and Technology, Siksha 'O' Anusandhan University, Bhubaneswar. She received her Ph.D. in Electrical Engineering from Siksha 'O' Anusandhan University, Bhubaneswar in 2014 and M.Tech. in Electrical Engineering from Jadavpur University in 2006. At present, she has more than 20 years of teaching experience in the field of Electrical Engineering. She is Life Member IE (India), Member IET, Senior Member IEEE, Life member ISTE, Life member ISSE. Her research areas are Smart Grid, Soft Computing, Solar Photovoltaic systems, Power system Scheduling, Evolutionary Algorithms and Wireless Sensor Networks. She has published more than 80 research papers in various reputed peer reviewed International Journals, Conferences and Book Chapters. She has served

as reviewers from various reputed Journal publishers such as Springer, IEEE, Elsevier and Inderscience. She is currently guiding 8 Ph.D. scholar and 1 Postdoctoral fellow. She has organized several FDP and workshops sponsored by Typhoon HIL, AICTE, DST etc. She has served as General Chair and Volume Editor of International Conference on Innovation in Electrical Power Engineering, Communication and Computing Technology (IEPCCT-2019) and International Conference on Green Technology for Smart City and Society (GTSCS-2020).

Prof. Akshay Kumar Rathore received the M.Tech. degree in Electrical Machines and Drives from the Indian Institute of Technology (BHU), Varanasi, India, in 2003 and Ph.D. degree in Power Electronics from University of Victoria, Victoria, BC, Canada, in 2008. He had two Postdoctoral Research Appointments with the University of Wuppertal, Germany, and University of Illinois at Chicago, IL, USA. He was an Assistant Professor in Electrical and Computer Engineering, National University of Singapore. He is currently an Associate Professor at in Electrical and Computer Engineering, Concordia University, Canada. He has published more than 200 research papers in international journals and conferences including 73 IEEE Transactions. His research is mainly focused on current-fed converters and multilevel inverters. He received the Gold Medal during his M.Tech. degree for securing highest academic standing among all electrical engineering specializations. He received the 2013 IEEE IAS Andrew W. Smith Outstanding Young Member Achievement Award, 2014 Isao Takahashi Power Electronics Award, and 2017 IEEE IES Davin Irwin Early Career Award. He is an Associate Editor of *IEEE Transactions on Industrial Electronics*, *IEEE Transactions on Industry Applications*, *IEEE Transactions on Transportation Electrification*, *IEEE Journal of Emerging Selected Topics in Power Electronics* and an Editor of *IEEE Transactions on Sustainable Energy* and *IEEE Transactions on Vehicular Technology*. He served as paper review chair for *Industrial Automation and Control in IEEE Transactions on Industry Applications*. He is currently Prominent Lecturer and Executive Board Member at-Large of IEEE Industry Applications Society and was Distinguished Lecturer for 2017–18. He has served and has been serving several technical committees and conference organizing committees in various roles.

Dr. Janmenjoy Nayak is working as an Associate Professor, Department of Computer Science and Engineering, Aditya Institute of Technology and Management (AITAM), Tekkali, K. Kotturu, Andhra Pradesh-532201, India. He has published more than 80 research papers in various reputed peer reviewed Referred Journals, International Conferences and Book Chapters. He is the recipient of Best researcher award from Jawaharlal Nehru University of Technology, Kakinada, Andhra Pradesh for the AY: 2018–2019, Young Faculty in Engineering-2017 Award by Venus International Foundation, Chennai and Best Young Researcher in Computer Science Engineering, by Institute of Technical and Scientific Research ITSR Foundation Award-2017, Jaipur Rajasthan. Moreover, he is the recipient of Outstanding Reviewer for the Journal *Engineering Applications of Artificial Intelligence* for 2017, by Elsevier Publications. His area of interest includes data mining, nature inspired algorithms

and soft computing. He is the regular member of IEEE and life member of some of the reputed societies like CSI India, etc. He has edited four books from various publishers such as Elsevier, Springer and IGI Global. He has been serving as Guest Editor of various journal special issue from Elsevier, Springer and Inderscience. He has served as Volume Editor of International Conference on Computational Intelligence in Data Mining (ICCIDM-2017, ICCIDM-2018), International Conference on Computational Intelligence in Pattern Recognition (CIPR-2019), International Conference on Application of Robotics in Industry using Advanced Mechanisms (ARIAM-2019) and International Conference on Soft Computing in Data Analytics (SCDA-2018).

Dr. Bighnaraj Naik is an Assistant Professor in the Department of Computer Application, Veer Surendra Sai University of Technology (Formerly UCE Burla), Odisha, India. He received his Ph.D. in Computer Science and Engineering, M.Tech. in Computer Science and Engineering and B.E. in information technology in 2016, 2009 and 2006, respectively. He has published more than 90 research papers in various reputed peer reviewed International Journals, Conferences and Book Chapters. He has edited 4 books from various publishers such as Elsevier, Springer and IGI Global. At present, he has more than 10 years of teaching experience in the field of Computer Science and IT. He is a member of IEEE. His area of interest includes Data Mining, Computational Intelligence, Soft Computing and its applications. He has served as Convener and Volume Editor of International Conference on Computational Intelligence in Data Mining (ICCIDM-2017, ICCIDM-2018) and International Conference on Computational Intelligence in Pattern Recognition-2019, IIEST, Shibpur, West Bengal. He has been serving as Guest Editor of various journal special issues from Elsevier, Springer and Inderscience.

Congestion Management in the Deregulated Market: A Brief Survey

Bijaya Kumar Mohapatra, Deepak Kumar Gupta, Chinmoy Kumar Panigrahi, and Subash Ranjan Kabat

Abstract The development of deregulated power systems has resulted in the overloading of transmission grids or network interference. Congestion happens when the transmission lines are not adequate to transfer power as per load requirement even required power is available. In congestion management, the power is utilized proficiently without ignoring system constraints. Congestion has severe effects, including severe system damage on power systems. The problems of the power system are managed by methods of congestion management in deregulated power systems. Various methods for handling system congestion have been reported. This paper examines the different works reported by the researchers for the management of congestion, which also show the importance of the management of congestion.

Keywords Congestion management · Deregulated power system · Generation rescheduling · Optimal power flow available transmission capacity · Unit commitment

1 Introduction

Congestion happens when the transmission lines are not adequate to transfer power as per load requirement even required power is available. In congestion management, the power is utilized proficiently without ignoring system constraints. In Ref. [1] recommends a structure to control the power flows of the transmission lines within the specified limit in a deregulated electricity market situation by curtailing the congestion cost with and without adding renewable energy sources. In the reported work, the problem of relieving congestion in a competitive power market, to minimize the network power loss and enhance the voltage profile and network security during the transactions, is described.

The restructuring of power in congestion management is based on organizational and operational improvements. The commodity-based power market has been

B. K. Mohapatra (✉) · D. K. Gupta · C. K. Panigrahi · S. R. Kabat
School of Electrical Engineering, KIIT Deemed To Be University, Bhubaneswar, India

M. Mishra et al. (eds.), *Innovation in Electrical Power Engineering, Communication, and Computing Technology*, Lecture Notes in Electrical Engineering 814,
https://doi.org/10.1007/978-981-16-7076-3_1

replaced by price-based liberalized power markets. To ensure optimal pricing in a competitive environment, the number of market participants and sellers will determine the cost per unit. Overloading and congestion in the system result in frequent voltage outages, violations of transmission capacity thermal restrictions, and a threat to the power system's security and operability. In Ref. [2] describe OPF approaches based on system structures which provide a systematic overview of the supplying solution. Various strategies have been examined to assure congestion management in a competitive market structure, such as counter trading and redispatching, bidding, auctioning methods, nodal or zonal pricing model [3]. In a deregulated power system, congestion management is critical. The work done in the field of congestion management has shown that the traditional regulated power system is becoming more popular in the competitive power market. In a real-time scenario, the electric power supply system was altered. In its current state, transmission congestion requires adequate transfer capacity. In Ref. [4] describes congestion management as concerned with one or more operational limitations that affect the gird's ability to function. In comparison to traditional electric power systems, unrestricted competition power market limitations are more prevalent because; unlike traditional systems, each seller requires maximum benefits. Congestion management oversees both technical and financial issues, implying that it provides action solutions as well as a pricing allocation method. In Ref. [5] under unbalanced or congested systems, the goal of congestion management would be to share the ISO-determined MW schedules based on loading forecasting with system security and dependable operations to maximize benefits to market participants and power markets. To relieve congested lines, sufficient power is provided to interruptible loads with the help of ISO. The power system can also be curtailed to relieve the congested condition system.

This article is dedicated to reviewing various solution methodologies to eliminate congestion in deregulated systems in a reorganized system environment along with issues and challenges. In addition to that, many studies have been conducted to determine the best congestion management method to prevent transmission line congestion despite the increase in power demand. Certain methods used are generation rescheduling (GR) optimal power flow (OPF), available transfer capability (ATC), flexible AC transmission system (FACTS) equipment, price control scheme, and load curtailment. Each of these technologies has advantages and disadvantages.

2 Congestion Management Major Issues

The reforming of the electric supply is a complex task since national energy policies and regulations have a variety of effects on congestion management. The issue of line overloading in traditional power sectors can be readily remedied by redistributing the outputs of generator units, either as corrective or preventive actions, resulting in the reallocation of economic benefits of numerous generations participating in commodities.

Congested lines have a direct influence on GENCOs in an aggressive market, and optimal bidding techniques are significantly affected for effective bidding techniques in the competitive electricity market; a new technology introduction is required [6]. Congestion management has conflicted with the goals of different GENCOs due to their marketing techniques according to a review of the literature on congestion management; they have extensively employed techniques such as the neuro-fuzzy pricing forecasting approach to anticipate LMP values at a node or in an area.

Every individual participant expects to enhance their advantages through the redistribution of generated energy, which results in the manipulation of the benefits of others, but in the case of a bilateral transaction, both parties require rapid and equal decrease. In Ref. [7] with all of these factors in play, congestion management becomes a critical role. When the system is overloaded, the cost increases rapidly. Because of the rise in congestion prices, the regulating bids for electric power providers and customers have grown. The lack of alignment between the regulating authority (owner) and market participants (customer) is the major issue with congestion management. The deregulated power system becomes more stable than the regulated conventional power system in this case. As a result, managing the system without congestion control is challenging. As a result, many strategies have been used to implement preventive congestion management procedures to make the system congestion-free. Then, utilizing corrective congestion management strategies, implement generation rescheduling, which is cost-effective. Congestion management is used in this situation to impose limitations on the energy market and competitive environment, consequently reducing the subject of deregulation.

3 In a Congested Power System, a Real-Time Scenario

Different players, such as generator owners, transmission network owners, and load suppliers, are involved in congestion control in the power system operating environment. Each market has its independent grid operator, known as the independent system operator (ISO), who is in charge of hourly (time to time), daily, and weekly load ability forecasting calculations, as well as the system's long-term operation [8]. The congestion management players can assess the power system concerns based on the foregoing explanation. Apart from that, many internal players play important roles in the restructured industry's power system operation.

They are:

- Increasing power demand and unbalances in power system operation and control.
- Increasing the power of market corporations so that they are held accountable for their judgments.
- Increased demand for power exchange data from a variety of market participants.
- Issues with renewable energy are becoming more prevalent.
- The economic impact of various generating sources and the environment.

- Requirement analysis for numerous participants to fulfill the value of energy sources.
- Introduction to software technology and numerical methods analysis for power industry problems.

Electric energy can be stored in batteries, which are energy storage devices. Because storing significant amounts of energy is uneconomical, it can be generated and consumed instantaneously. The power consumption fluctuates dramatically on a daily, weekly, seasonal, and random component basis [9]. Energy is important in the purchase and sale of energy, but other services such as reactive power, automatic generator management, and reverse power are also necessary to supply stable power. The ancillary power service can be constructed and used to make these services easier to trade. According to Kirchhoff's laws, which govern the ISO's network routes, the supply and consumer have a well-distributed power. As a result, the system becomes congested, affecting generator outputs and customer consumption. Adjustments are made to energy units, auxiliary power services, and transmission network lines that are interconnected, and this, along with real-time demand mechanisms, results in an efficient electricity market [10].

4 Congestion Management Methodologies

Due to the open transmission system, congestion management (CM) is one of the most difficult tasks in energy liberalization. As the number of energy transactions between marketplace participants increases, the transmission grid cannot transfer energy under market agreements. In this case, the assignment of the independent system operator (ISO) is to establish a bunch of rules and regulations to make sure full control of marketplace operators to maintain the standard rank of system consistency and safety. ISO usually monitors transactions and checks system status, part of which is to manage network congestion. In the liberalized energy market, ISO plays a vital role in maintaining the safety and reliability of the system without violating the constraints of the energy system.

The complete set of operations or processes is called congestion management and mainly includes available transmission capacity (ATC), power generation reprogramming, load reduction, and demand response. ISO can divide the grid into multiple areas based on price to manage congestion. Congestion costs also play an important role in congestion management. Recent CM methods are mainly based on power generation reprogramming, demand response, electric vehicles, and hybrid methods. Renewable energy and battery vehicles are played an important role in CM by the application of smart technology in refurbished electrical systems. The CM methodology is closely related to the complete market design. The main goal of CM technology is to organize the exchange of network functions among the required market participants. The following summarizes several CM technologies considered in this review document.

4.1 Congestion Management by Generation Rescheduling (GR)

Generation rescheduling (GR) is a technology widely used to manage congestion in retrofit energy systems. GR approaches to regulate congestion in power plants were presented in the literature [11, 12]. Both types of research focused on reducing operating expenses and minimizing generation. The GR approach is a typical way of handling congestion but is slow and ineffectual [13]. Using artificial intelligence, algorithms like GA [14–16] and PSO [17] have been used to improve the reprogramming of generating techniques. GR also was based on real and reactive power reprogramming by virtual power flow via the overloaded line [18]. The virtual flow concept is based on the principle of superposition and DC load flow which has made rearrangement processes easier and faster. Active power generators based on the sensitivity of their generators were reprogrammed optimally in the literature [19]. The redispatch generators are picked according to the high magnitude of the sensitivity of a generator, which required a good mathematical analysis iteration to avoid errors while preserving the GR method's efficiency.

4.2 Congestion Management by Optimal Power Flow (OPF)

The purpose of the optimal power flow technique is to lower generation costs while also benefiting consumers in terms of power system parameters. When the system is overloaded, the OPF can be used to help analyze overloading problems. For power balancing situations and curtailment tactics, a full matrix for congestion management includes a pool market environment, bilateral markets, and multilateral markets. Curtailment rules have the primary goal of reducing deviations from scheduled transactions. In multilateral transactions, the system's reliability is measured through congestion management, which leads to fewer curtailments and congestion penalties than in bilateral transactions. Decentralized risk-based congestion management is an optimization approach that may be utilized to determine thermal overloads. In most congested systems, a soft technique termed optimal power flow control is commonly employed in scheduling and lowering congestion costs.

4.3 Congestion Management by Available Transfer Capability (ATC)

The report of the hour to hour and day to day is uploaded in the website named Open Access Same Time Information System (OASIS) using the available transfer capabilities. To allocate any transaction, go to the OASIS website and get a report

on the details of the transaction. OASIS develops automated scheduling, which has the potential to help with data exchange in the energy market and congestion control in the future.

4.4 Congestion Management by Flexible AC Transmission Systems (FACTS) Devices

Deregulation of power markets, i.e., supplying power inexpensively and efficiently, is the fundamental restriction in congestion management. In addition to the excess congestion charges, line congestion raises the cost of the supply unit. The primary goal of FACTS devices is to boost the transmission line's transfer capacity. By executing voltage management, power system stability limits, and reactive power compensation also lowers congestion costs. Some FACTS devices, such as the SSSC and UPFC, have been recommended as the best reactive power balancing devices. Under challenging conditions, a closed-loop controller with DC link and UPFC in conjunction provides advocate pricing for operating systems.

4.5 Congestion Management by Price Control

This price system is separated into many pricing units in this topology. Excessive generating unit costs will result in reduced pricing, whereas excessive power demand would result in a higher price. In this case, spot market tenders must submit separate bids for different areas. In addition, the network is used to calculate area prices and control market congestion.

4.6 Congestion Management by Load Curtailment

Another strategy for congestion management is used in this transaction-based curtailment approach. The ISO monitors the system in real time for security threats. In the case that such violations occur are imminent, the transmission loading relief (TLR) method of transaction curtailment is used. Transactions are chosen to be restricted by parameters such as transaction size, relative impact on congested line flows, and the firmness level before dispatch. In this strategy, the price and the true value of the transmission are not important issues. This can therefore lead to economic difficulties while this strategy improves reliability.

5 Congestion Management Case Studies

This paper discusses and reviews congestion management cases from nations such as Switzerland (Entras), Japan, Thailand, Australia, and the Nordic countries. One example is the management of congestion in Switzerland. The Swiss TSOs have decided to use the power management by congestion management concept due to recent increases in line loads resulting in congestion [20]. This approach encompasses three processes: congestion forecasting, system elimination determination, system methodology, and implementation. Congestion can be eliminated using optimal power flow methods that combine topological measures such as network element operational status variations, transformer tapping adjustments, and substation reconfiguration management, as well as redispatching congested lines using globally optimal power flow solutions.

6 Congestion Management Issues and Challenges

Congestion management is a difficult problem to guarantee system safety and stability [21]. The management of efficiency, uncontrolled loads, and climate change issues is one of the main concerns in demand management, because of an insufficient structure, lack of incentives, and infrastructure [22]. The following are some of the problems and challenges with congestion management:

- While the most effective technique is widely accepted for congestion reduction, the real power schedule alters reactive power flows and can cause additional power system problems. As a result, reactive power reprogramming is often advocated, in addition to active power reprogramming, complicating the dispatch problem further. The load shedding is carried out within the timeframe based on available contracts and reprogramming.
- The availability of DG sources can be used in the existing smart grid plans, although its scale and location are crucial. Congestion must be handled immediately, which means that a rapid and reliable solution must be deployed to prevent safety and stability problems. CM problems are solved using a variety of conventional and non-conventional techniques of optimizing, but proper computer intelligence techniques are still required which are robust for system changes.
- Modeling is important because the CM is in practice a multifarious challenge task. Several policies have been proposed in the literature that uses approximate techniques to resolve the problem, but all of them suffer from the optimal local problem. However, the accuracy of these methods is important during the stress situation, and various sensitivity factors and power transfer distribution factors (PTDF) have been present. Since exact problem modeling increases the computing load, it is essential that the problem modeling is properly balanced and accurate.
- FACTS devices can be present in the system and can be used to reduce congestion. However, it is essential to take into account operational costs and other financial

considerations. The primary objective of the installation of these devices is to improve system stability, safety, and other factors so that congestion may be a secondary objective.
- Many systems can be used to regulate congestion of the system; however, control cost measures can be a problem, so the best measure and coordination measures must be assessed.
- Control of congestion can be performed in several ways, including market-based methods. The creation of a transmission network and transmission rights can be appropriately exploited during congestion management.
- The majority of the solutions use static congestion management approaches based on the static rating of the device. It can also assess the dynamic rate of the transmission cables.

7 Critical Discussion on Research Gaps

The most difficult difficulties encountered in the deregulated power market are operational characteristics of power systems. In open access transmission systems, OPF is increasingly being used for transmission costs and transaction evaluation. It is also possible to do research on different dispatch and curtailment tactics. In a deregulated environment, the sensitivity approach for selecting optimal locations of FACTS devices can only provide an approximate understanding of the optimal location for those devices. In a deregulated market, more dependable solutions for optimal electricity flow must be created. Some research gaps have been identified after summarizing this review effort, and they are listed below.

- Distributed energy resources, such as EVs and variable demands, solar and wind energy, and so on, are increasingly being integrated into smart grids. As a result, forecasting and developing appropriate energy plans for the system's smooth functioning have grown more difficult for aggregators.
- Local control is the most important consideration in FACTS-based CM system control techniques. For modern DPMs and smart grids to adjust line power flow as desired while avoiding congestion, this is insufficient.
- System operators face a significant problem in effectively utilizing solar and wind energy in congested transmission lines.
- Due to less realistic limits and uncertainty in client behavior, the distributed system operator faces a decision challenge in maximizing demand-side flexibility.
- Congestion management will be employed in the future with complicated real-world applications in domains like as dynamic congestion management with integrated ramp rate constraint, and probabilistic optimization with wind or PV systems.

8 Conclusion

The paper discusses the various problems and their solutions for congestion management under a deregulated environment. Solution methodologies for different problems such as generation section, transmission section, and distribution section. In these sections, various solution methodologies like generation rescheduling, optimal power flow, ATC, FACTS devices, price control, and load curtailment, etc. have been discussed in detail. From this study, we got to know many techniques which are used for congestion management. Possible future work and existing problems in the deregulated system are also discussed in this thrust area. The work reported in this paper mainly contributes to the extensive literature survey along with the solution methodologies and future scope.

References

1. Farzana DF, Mahadevan K (2020) Performance comparison using firefly and PSO algorithms on congestion management of deregulated power market involving renewable energy sources. Soft Comput 24(2):1473–1482
2. Purchala K, Meeus L, Belmans R (2003) Implementation aspects of coordinated auctioning for congestion management. In: 2003 IEEE Bologna power tech conference proceedings, vol 4, p 5
3. Yamin HY, Shahidehpour SM (2003) Transmission congestion and voltage profile management coordination in competitive electricity markets. Int J Electr Power Energy Syst 25(10):849–861
4. Yamina HY, Shahidehpour SM (2003) Congestion management coordination in the deregulated power market. Electr Power Syst Res 65(2):119–127
5. Nayak AS (2001) Congestion management in restructured power systems using optimal power flow framework
6. Bompard E, Correia P, Gross G, Amelin M (2003) Congestion-management schemes: a comparative analysis under a unified framework. IEEE Trans Power Syst 18(1):346–352
7. Tuan LA, Bhattacharya K, Daalder J (2004) A review on congestion management methods in deregulated electricity markets. Power 4:6
8. Iba K (2005) Identification of transmission line user and congestion management by loop flow controllers. In International symposium CIGRE/IEEE PES, 2005. IEEE, pp 307–314
9. Sinha AK, Talukdar BK, Mukhopadhyay S, Bose A (2004) Pool dispatch strategies and congestion management in deregulated power systems. In 2004 International conference on power system technology, 2004. PowerCon 2004, vol 2. IEEE, pp 1851–1856
10. Bhattacharya K, Daalder J (2005) Transmission congestion management in bilateral markets: an interruptible load auction solution. Electr Power Syst Res 74(3):379–389
11. Reddy SS (2016) Multi-objective based congestion management using generation rescheduling and load shedding. IEEE Trans Power Syst 32(2):852–863
12. Kumari CR, Anitha M (2013) Re-dispatch approach for congestion relief in deregulated power systems. J Eng Trends Technol (IJETT) 4(5):1776–1780
13. Retnamony R, Raglend IJ (2015) Congestion management is to enhance the transient stability in a deregulated power system using FACTS devices. In 2015 International conference on control, instrumentation, communication and computational technologies (ICCICCT). IEEE, pp 744–752
14. Sivakumar S, Devaraj D (2014) Congestion management in deregulated power system by rescheduling of generators using genetic algorithm. In: 2014 International conference on power signals control and computations (EPSCICON). IEEE, pp 1–5

15. Pal S, Sen S, Sengupta S (2015) Power network reconfiguration for congestion management and loss minimization using genetic algorithm
16. Rajesh R, Mutharasan A, Rameshkumar T, Senthilkumaran B (2015) Congestion management in deregulated environment using generation rescheduling with an intelligent approach. Int J Appl Eng Res 10(20):41665–41668
17. Mahala H, Kumar Y (2016) Active & reactive power rescheduling for congestion management using new PSO strategy. In: 2016 IEEE students' conference on electrical, electronics and computer science (SCEECS). IEEE, pp 1–4
18. Thukaram D (2016) Congestion management based on virtual real power flows. In: 2016 Biennial International conference on power and energy systems: towards sustainable energy (PESTSE). IEEE, pp 1–5
19. Kumaravelan G, Chidambararaj N, Chitra K (2015) Optimal active power rescheduling of generators for congestion management using new definition of sensitivity. Int J Emerg Technol Comput Sci Electron (IJETCSE) 13(1):111–115
20. Kumar A, Srivastava SC, Singh SN (2005) Congestion management in competitive power market: a bibliographical survey. Electr Power Syst Res 76(1–3):153–164
21. Afkousi-Paqaleh M, Fard AAT, Rashidinejad M (2010) Distributed generation placement for congestion management considering economic and financial issues. Electr Eng 92(6):193–201
22. Pandey SN, Tapaswi S, Srivastava L (2010) Integrated evolutionary neural network approach with distributed computing for congestion management. Appl Soft Comput 10(1):251–260

Design and Analysis of RF Optimization in 2G GSM and 4G LTE Network

Deepak Kumar Barik, Sabita Mali, Farida A. Ali, and Arun Agarwal

Abstract Measurement and optimization of the quality, coverage and capacity of a wireless network system is one of the mandate conditions for today's mobile technology. For that, numerous radio frequency (RF) drive test tools are used for wireless technologies like global system for mobile communication (GSM), code division multiple access (CDMA), global package radio services (GPRS), third generation (3G), evolution data optimized (EVDO), etc. In this work, two such tools like telecom expense management software (TEMS) and X-CAL are used to collect reasonable data accurately in real time for two different mobile networks like GSM and long-term evolution (LTE). Basically, the drive testing technique is nothing but an automobile that carries a wireless network system making set up for drive test and at the same time RF engineers keep records of various parameters (physical and virtual) of mobile cellular service for report making for a particular geographical area. The drive testing technique is categorized into three broad headings as: network benchmarking, optimization and troubleshooting and finally service quality monitoring. The objective of these types of drive tests is to collect datasets like signal level, signal quality, dropped calls, blocked calls, call statistics, Global Position System (GPS) location co-ordinates, etc. In this process, drive testing files are used to diagnose the root sources of dropped calls or omitted neighbour cell assignments due to specific disputes, typically confined disputes or network disputes. Objective of drive test and electromagnetic field wave (EMF) survey is to optimize RF in the mobile wireless

D. K. Barik
National Institute of Technology Manipur, Imphal, Manipur, India

S. Mali (✉) · F. A. Ali · A. Agarwal
Department of Electronics and Communication Engineering, Faculty of Engineering and Technology, Institute of Technical Education and Research, Siksha 'O' Anusandhan (Deemed To Be University), Bhubaneswar, Odisha 751030, India
e-mail: sabitamali@soa.ac.in

F. A. Ali
e-mail: faridaali@soa.ac.in

A. Agarwal
e-mail: arunagarwal@soa.ac.in

M. Mishra et al. (eds.), *Innovation in Electrical Power Engineering, Communication, and Computing Technology*, Lecture Notes in Electrical Engineering 814,
https://doi.org/10.1007/978-981-16-7076-3_2

network. In this process, one network can optimize its throughput power by using less spectrum by proper regulation work of RF engineer.

Keywords Capacity · Drive test · Optimization · TEMS · 2G GSM · 3G · 4G LTE · RF · Wireless network

1 Introduction

The introduction starts with the different generation of mobile network, its drive tests and electromagnetic field wave (EMF) survey. The mobile wireless networks have evolved from first generation (1G) to presently fifth generation (5G) networks offering high-speed data transfer in the range of gigabits/sec along with multimedia applications. Communication technology working at such a high speed needs special attention and infrastructure so as to keep track of the real-time signal strength. Therefore, adaptive modulation techniques had been employed in the physical layer, which allowed the wireless systems to choose the modulation of highest order. Due to this, the GSM and LTE network's drive test results showed improved system throughput because of reliable transmission. For the 2G and 3G drive tests, TEMS software is used, which also contains the procedure of the 4G drive test and its parameters. TEMS is a network lifecycle automation tool which allows to optimize the quality of mobile network, and it delivers the ability to drive test and dynamically analyze the performance by measuring end user experience. In this paper, the use of X-CAL software in 4G is also included. X-CAL is world's leading drive test tool which is designed to monitor, maintain, troubleshoot and optimize wireless voice and data network performance [1–5]. It contains the procedure for EMF survey. TEMS investigation is main tool of drive testing, and it consists of both hardware and software. EMF survey is performed to collect the effective isotropic radiated power (EIRP) ratio to know about the strength of electromagnetic field (EMF) signal across base system substation. So the survey performed by the companies to provide automation tools which allows to optimize Telecom regularity authority of India (TRAI) is called as EMF survey. This survey is needed to check the harmful effects arise because of high-power radiation of electromagnetic wave from the towers. Similarly, RF survey is a collection of data from site or in field for installing a new site. RF survey is used for checking practicality of cell site, for making determination for coverage region of cell site and for deciding the link with another cell site. This task can results in physical changes in the network by adding or modifying new sites and/or equipment. Day by day, many issues arise in wireless network which can restricts the signal from reaching all parts. So this survey is used to find and eliminate the problems occur in site and also helps to find the place where multipath distortion can occur [6–10].

As per the concept of RF design, it is desired that before any new or existing RF planning, there must be drive test to check real signal strength and its coverage. That means as per biological population, what must be the signal strength that has to be imagined by the RF engineer. The layout should be determined by experience keeping

in mind where the signal strength will be more or less. Therefore, RF optimization is primary aspect of a proper drive test and EMF survey [11–14].

2 Measurement of Radio Resources

A set of basic physical transmission parameters which is needed to support a signal waveform carrying end user information corresponding to a reference service is known as radio resources. These physical transmission parameters depend on different multiple access technique which is being used. In this section, the performance results of radio resources on live network are analyzed using the test Ericsson mobile system (TEMS) Cell Planner software.

2.1 Measurement of Radio Parameters Using TEMS

Wireless access and mobile support are the two features for the measurement of radio parameters. TEMS allows to test every new function and feature in the network and allows to verify, optimize and troubleshoot the mobile network. TEMS simulation results are used to determine the accuracy of coverage predictions and the amount of traffic that each system could support. Figure 1 shows a sample report generated by TEMS showing important measurements.

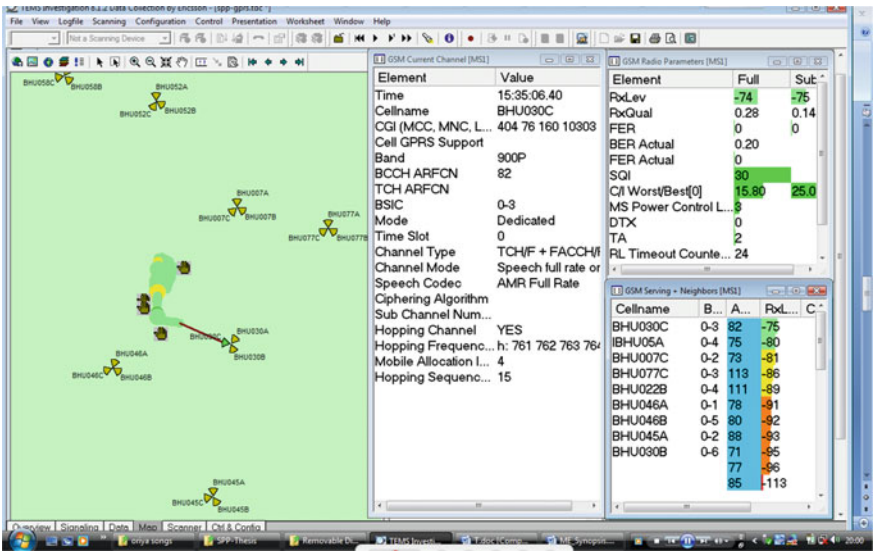

Fig. 1 Sample report generated

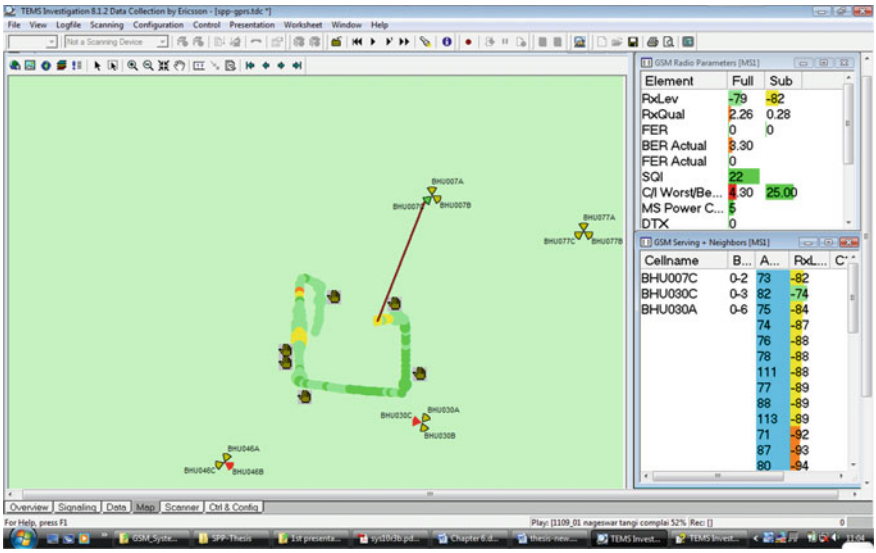

Fig. 2 Received signal power measurement

2.2 *Received Signal Power*

Now the value of received signal power ranges between −10 dbm and −110 dbm, but normally it should be less than −90 dbm. Along with received signal power, other factors which are measured are the signal quality and the bit error rate, and it is shown in Fig. 2.

2.3 *Interference*

Interference is recognized here by carrier to noise ratio (C/I) during the drive. By which, in a given path, it can be known that effect interference, which is shown in Fig. 3.

2.4 *Speech Quality*

To analyze the measurements, data obtained from a test drive for about 80 s at 10 s interval are depicted in Fig. 4.

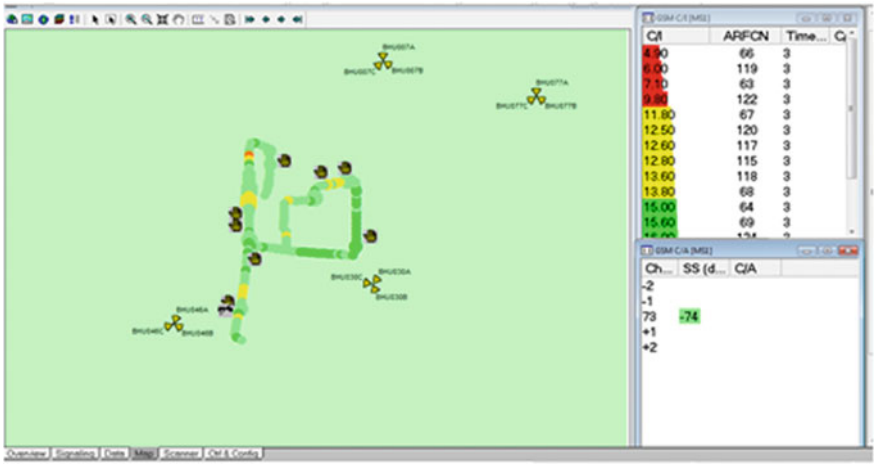

Fig. 3 C/I measurements report

Fig. 4 Measurement of speech quality

3 Analysis of Measurements

3.1 Measurement of Radio Parameters

To analyze the measurements, data obtained from a test drive for about 80 s at 10 s interval are depicted in Table 1.

Table 1 Measurement of some important radio parameters

Time (s)	RxLev (receiver level) (dbm)	Speech quality index (SQI)	C/I (carrier-to-interference ratio)	Receiver quality
0	−76	30	14.6	0.57
10	−80	29	9	2.26
20	−85	29	13.9	0.57
30	−76	11	11.6	1.13
40	−74	29	16.3	6.1
50	−63	30	18.7	4.53
60	−78	27	18.8	0.14
70	−65	22	19.1	2.26
80	−68	30	17.6	1.13

3.2 Handover

Decisions about handovers are made for the phone by the network (normally in the BSC) and not by the phone itself. The phone contributes in the decision-making process by reporting the signal strength of neighboring cells, but the network bases the final handover decision on other information as well (independent measurements of signal strength and also estimates of radio quality and timing advance). Now, the TEMS log file only contains the phone's own "advisory" measurements, whereas the uplink file includes the final decision arrived at by the BSC. Therefore, the uplink data shows more clearly how the phone interacts with the network. The measurements taken just before and after the handover are mentioned in a tabular form in Table 2. The following observation can be made from the readings. In all cases, there is successful handover between sectors. In BHU030C with −69 dbm, also handover has taken place because still stronger signal is received from same cell sector A.

Table 2 Radio resources measured during handover

Existing cell	Parameters				New cell	Parameters				Remarks
	RxLev	RxQual	TA	C/I		RxLev	RxQual	TA	C/I	
BHU030C	−85	0.57	2	9.9	BHU007C	−75	0.57	2	12.6	Handover success
BHU007C	−76	4.53	2	7.4	BHU030C	−74	0.57	2	24	-do-
BHU030C	−77	0.28	1	19	BHU046A	−72	1.13	1	8.4	-do-
BHU046A	−74	0.57	1	14.5	BHU030C	−74	0.14	1	17.7	-do-
BHU030C	−69	0.14	2	16.6	BHU030A	−56	0.14	0	19.5	-do-

Table 3 Radio parameters measured during drive test

Observation	Time of observation	Measured parameters			Remarks
		RxLev (dbm)	RxQual	C/I	
Limited service mode	8:46:55.62	−106	17.1	2.1	Poor signal
Location area update failure	8:48:44.32	−69	0.61	4.78	Malfunction in software/HLR showing illegal MS
Call end	8:53:53.73	−97			MS initiated release
Call dropped	8:54:12.55	−111	18.1	−1.9	Poor signal
Call dropped	8:55:07.33	−110	18.1	−1.3	– do–
Data link failure	9:05:14.04	−83	0.53	14	Poor signal strength
Limited service mode	9:17:21.68	−95	18.1	2.5	Low signal strength
Handover failure	9:17:26.85	−98	4.53	−1.1	– do–
Blocked call	9:20:28.23	−97	18.1	3.9	No traffic channel assignment
RACH error	9:20:43.01	−77	0.66	11	Channel assignment error
Call dropped	9:32:35.07	−100	18.1	0.6	Poor signal

3.3 Other Observations During Drive Test

Some other features recorded during a drive test are mentioned in Table 3.

It can be noted that with good RxLev and other parameters location update failure happens. That may be due to IMSI unknown in HLR, illegal MS, illegal ME, PLMN not allowed, location identification not allowed or roaming not allowed.

4 Conclusion

The telecommunication network faces numerous problems due to increasing number of subscribers, mobility capacity of users and complexity of the radio network. To measure the RF quality, RF optimization is required as the network expands. The network performance can be improved by repeating RF optimization. The service quality and resource can be improved in network by optimization. Drive testing in GSM RF optimization is performed both manually and automatically (automatic network management system) for the improvement of performance of the network. Drive testing equipment (DTE) can be attached to moving vehicle to serve in GSM test area, and it can be monitored by the server. By using the Internet, real-time drive data of all time can be simultaneously collected.

In this paper, the detailed procedure of GSM and LTE drive test is learned along with its different parameters are studied and presented. Procedure of log file processing in TEMS software is taken and noted for GSM. A comparison of performance is traced from drive test, and their different parameters are analyzed. To minimize the cost of operation, optimizing the RF for a wireless network is a basic requirement. By doing so, it can be found out that signal power and signal quality, C/I measurement ratio and speech quality will be so clear that a RF engineer can easily detect any faults if present.

References

1. Zander J (2001) Radio resource management for wireless networks. Artech House Inc.
2. Kyriazakos S, Karetsos G, Gkroustiotis E, Kechagias C, Fournogerakis P (2001) Congestion study and resource management in cellular networks of present and future generation. In: IST mobile summit 2001. Barcelona, Spain, 9–12 September 2001
3. Kechagias, Papaoulakis S, Nikitopoulos N, Karambalis D (2002) A comprehensive study on performance evaluation of operational GSM and GPRS systems under varying traffic conditions. In: IST mobile and wireless telecommunications summit. Greece
4. Rappaport TS (2003) Wireless communications, principles and practice, 2nd edn. Pearson Publications
5. Ekström H, Furuskär A, Karlsson J, Meyer M, Parkvall S, Torsner J, Wahlqvist M (2006) Technical solutions for the 3G long-term evolution. IEEE Commun Mag 44(3):38–45
6. Parkvall ED, Furuskär A, Ericsson RS (2008) ITU global standard for IMT-advanced; LTE advanced—evolving LTE. In: Vehicular technology conference, 2008. VTC 2008-Fall, 21–24 Sept 2008. IEEE, pp 1–5
7. Haider B, Zafrullah M, Islam MK (2009) Radio frequency optimization & QoS evaluation in operational GSM. In: Proceedings of the world congress on engineering and computer science 2009, vol I WCECS 2009, October 20–22, 2009. San Francisco, USA
8. Ronai A (2009) LTE ready mobile backhaul. Cargon Networks Report
9. Gunawan A (2010) LTE technology, challenge, and business. Technical Seminar, Sharjah, 18 Jan 2010
10. Chitranshi R, Kushwaha J, Pancholy P (2012) Intelligent optimization of GSM network. Int J Eng Sci Innov Technol (IJESIT) 1(2)
11. Durga Prasad YVS (2017) RF optimization in GSM. IJASTEMS 3(6)
12. Seytnazarov SO (2010) RF optimization issues in GSM networks. In: 2010 4th International conference on application of information and communication technologies, pp 1–5. https://doi.org/10.1109/ICAICT.2010.5611802
13. Balis P, Tanhatalab MR (2019) LTE practical optimization achievements on throughput in live cellular networks. In: 2019 1st International conference on cybernetics and intelligent system (ICORIS), pp 51–56. https://doi.org/10.1109/ICORIS.2019.8874877
14. Angadi AV, Yashaswini SD, Balaji K, Padma U (2019) RF planning and optimization practices applied to improve the KPI's of 4G LTE network. In: 2019 3rd International conference on electronics, communication and aerospace technology (ICECA), pp 848–851. https://doi.org/10.1109/ICECA.2019.8821937

Artificial Pancreas (AP) Based on the Fractional-Order PID Controller (FOPIDC) with JAYA Optimization Technique

Akshaya Kumar Patra, Anuja Nanda, Bidyadhar Rout, Dillip Kumar Subudhi, and Saswata Pani

Abstract This chapter presents the design of JAYA-FOPIDC to inject the optimal dose of insulin through the MID for blood glucose (BG) regulation in Type-I diabetes mellitus (TIDM) patients. In this strategy, the controller parameters are tuned based on the JAYA optimization technique for better control execution. The capability of the JAYA-FOPIDC as to accuracy, robustness and stability is tested by use of MATLAB and SIMULINK. The procured outputs reveal the better implementation of JAYA-FOPIDC to regulate the BG level within the range of *normoglycemia* (70–120 mg/dl). The justification of improved control execution of the JAYA-FOPIDC is revealed by the relative result examination with different prominent control techniques.

Keywords Type-I diabetes · Pancreas · Arterial glucose · FOPIDC · JAYA

1 Introduction

In view of the WHO report, one among the most far-reaching illnesses is diabetes and it appears due to inactiveness of the pancreas. It diminishes insulin affectability

A. K. Patra (✉) · A. Nanda
Department of Electrical and Electronics Engineering, ITER, S'O'A University, Bhubaneswar 751030, India

B. Rout
Department of Electrical Engineering, VSSUT, Burla 768017, India

D. K. Subudhi
Department of Computer Science and Information Technology, ITER, S'O'A University, Bhubaneswar 751030, India

S. Pani
Department of Electronics and Telecommunication, IIIT Bhubaneswar, Bhubaneswar 751003, India
e-mail: b218065@iiit-bh.ac.in

M. Mishra et al. (eds.), *Innovation in Electrical Power Engineering, Communication, and Computing Technology*, Lecture Notes in Electrical Engineering 814,
https://doi.org/10.1007/978-981-16-7076-3_3

impacting normal range of BG level in a healthy body. As of now, the various examination projects are attempted by some scientists to organize this type of difficulties by conceiving progressed clinical hardware like MID. Till date, BG is physically controlled to embrace the open circle control system. Diabetic conditions may develop due to troubles in dealing with the inward framework changes and outside aggravations by actualizing the control circle procedure. The improvement of implanted AP allowing the adequate amount of insulin infusion proportionate to the sensor assessment in the patient's model can give the way to join closed-loop control algorithm. Figure 1a shows an overall structure of a TIDM patient along with AP. AP comprises (i) glucose sensor, (ii) controller and (iii) MID. Sensor counts the

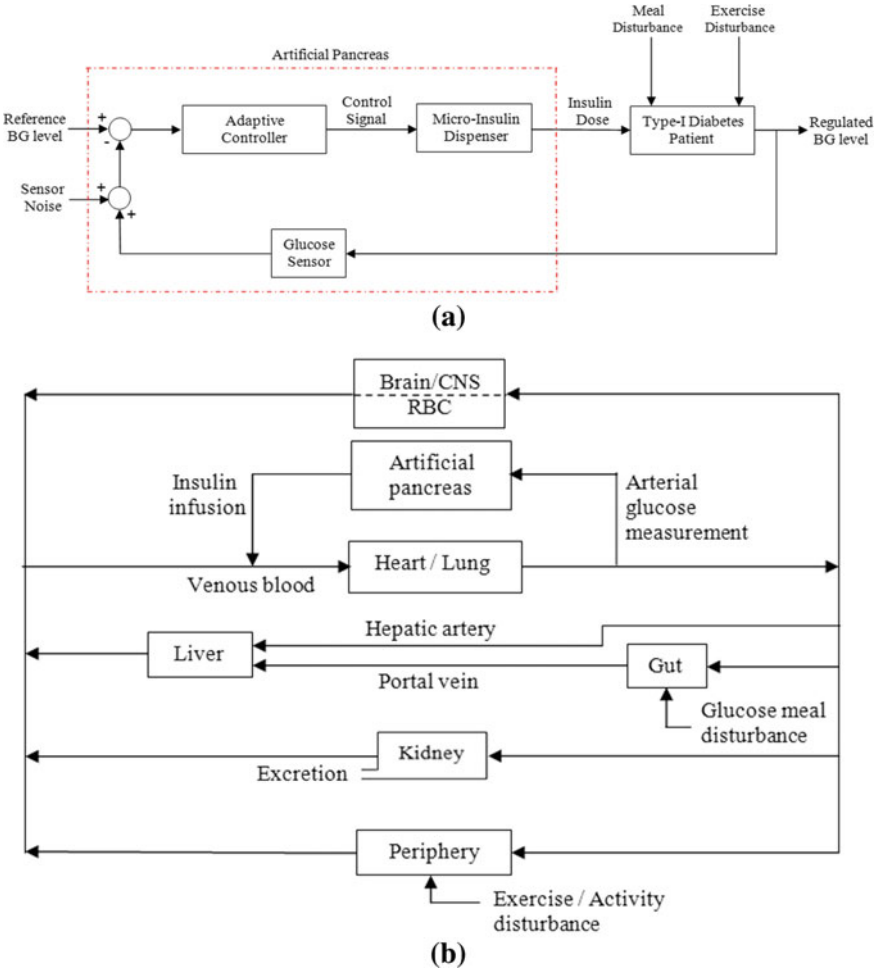

Fig. 1 **a** Integration of JAYA-FOPIDC in the patient; **b** patient in form of compartmental structure; **c** patient numerical structure; **d** MID numerical structure

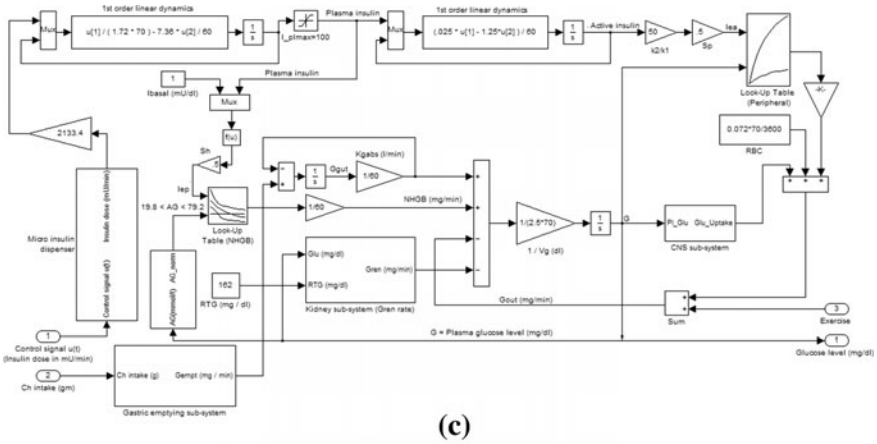

(c)

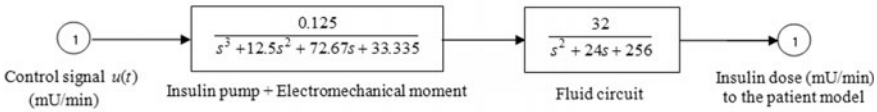

(d)

Fig. 1 (continued)

level of BG in the patient and communicates data to the controller. Then, it produces a control signal concerning the data of glucose sensor. The MID supplies the desired amount of insulin into VB to balance the glucose level, as indicated by the control signal.

An estimated 422 million people worldwide suffer from fluctuating blood glucose levels out of which at least 77 million are in India. The feedback control of insulin distribution is needed to keep up careful planning and portion of the medication to counter the glucose level [1]. The wide investigation is going on in the area of biomaterials for fine element transport applied to drug distribution and biocompatible equipment and sensors; development of control algorithms giving adaptive and robust response along with disturbances and model uncertainties is also important [1]. Many such control techniques for automated drug distribution have been deliberated in different articles [1–3]. The closed-loop insulin therapy includes the interaction among the dynamics of the GM process, model uncertainties and effects of control inputs. Based on this approach, numerous researchers recommended very familiar control algorithms such as PID [4], fuzzy [5], LQG [6–8], H-infinity [9–11] and SM [12, 13] to deal the BG regulation problems. However, the above approaches are not insensitive to uncertainty in spite of good action. Accordingly, actual control factors setting for better implementation and getting away from moderate activity, the current work proposes another new mechanism utilizing the improved feedback loop.

In this suggested approach (JAYA-FOPIDC), the controller parameters are tuned based on the JAYA optimization technique for better control execution. This JAYA optimization technique is clearly described in the literature [14]. The JAYA-FOPIDC gives a high degree of freedom in controlling of system parameters. The main objective of JAYA-FOPIDC is to provide improved feedback loop in appraisal to other well-acknowledged control schemes.

The rest part of this chapter is organized as follows. Section 2 demonstrates the numerical descriptions of the GM process. Section 3 represents the design procedure of JAYA-FOPIDC to regulate level of BG within the suitable range. Numerical and simulation outputs of the JAYA-FOPIDC are represented in Sect. 4. Final observations are demonstrated in Sect. 5.

2 Problem Formulations

In this section, the numerical descriptions of the GM process are clearly described.

2.1 Clinical Support

Diabetes is a gathering of clinical problems categorized by chronic high level of BG more than 144 mg/dl, named as *hyperglycemia.* It is initiated either by the lack of insulin, or its action or both [15–21]. Diabetes arises when the body can't utilize glucose successfully. It is delegated as Type I & II, as per the rate of insulin infusion in the body. In Type 1, the patient's system is totally unfit to create insulin. In Type II, insulin is delivered at a lesser rate and its activity is also inhibited. Despite the varying demands of food, fasting and exercise, BG levels are very tightly regulated in the VB.

Carbohydrate is the original source of energy. Human body needs glucose for the any type of activities of the life. VB receives glucose from the gut compartment. Gut compartment gets glucose from the carbohydrate food. It is the 'external' source of glucose in circulation. VB absorbs glucose from the gut, and then that glucose is transferred to the liver. That glucose is deposited in the liver as a form of glycogen and delivered again into VB, when the level of BG becomes too low. It is the 'internal' source of glucose. Glucose is metabolized along with O_2 inside the cell producing energy, CO_2 and H_2O [15–21].

Insulin is the one type of hormone and acts as a key. It is synthesized in the β cells of the pancreas. It can control the discharge of chemical energy from the glucose. Insulin encourages the liver to absorb the glucose from the VB and stores as a form of glycogen, when BG level is high. When BG level drops too low, stored glycogen is again converted to glucose and delivered into VB. The muscles and peripheral cells also utilize glucose to produce energy with help of insulin. It has second function to turn off the release of 'internal' glucose into the VB by the liver during the meal

ingestion. Both functions of insulin are absent in the case of diabetes patients. Cells do not utilize glucose appropriately and liver produces 'internal' glucose, as a result uncontrolled rise of BG level [15–21]. Subsequently, as the BG exceeds the RTG value, some quantity of plasma glucose is drain out through kidney.

2.2 Simulation Structure of Patient

In the past few decades, different authors have proposed a number of models representing the process of glucose–insulin (GI) interaction for the BG level control as depicted by the GI dynamics. Among these, Lehmann et al. [18, 19] suggested a model, which is widely adopted in simulation and testing of several control methods owing to its structural simplicity and a good resemblance to human metabolism dynamics. In the current study, the effectiveness verification of the suggested controller to regulate the blood glucose level has been carried out using this model. Figure 1b shows a GI interaction process model attached with the inbuilt insulin dosage controller, and this patient model consists of six segments like periphery, liver, kidney, gut, heart and brain.

The aforementioned model is based on the assumptions as: (1) The patient lacks in the natural insulin secretion completely; (2) an extra cellular glucose is like a single glucose pool; (3) the segment of gut cares the combined effect of intestine and stomach. Both the production of hepatic glucose and intestinal absorption cause glucose to enter into the blood stream. A continuous measurement of the regulated arterial glucose is required to input the controller as a feedback. At 5-min interval, the input to the controller is computed like the insulin infused into the VB by the implanted insulin pump. But, the sampling interval is calculated based on the sensor technology and the support device involved. Meal and exercise are added as the disturbances to the gut and periphery, respectively. Synthesis of the whole process of GM in a diabetic patient is accomplished after the analysis of insulin, glucose flow and their characteristics. Based on the action of insulin, a reduced model of the patient is presented in Fig. 1c.

2.3 MID

In this study, one type of MID is considered, which is recommended by Cochin [21]. It works on variable pumping rate principle. Elementary component of MID is the storage capsule, the micropump, the accumulator, the pump return valve and necessary electronic control. Other sensing and controlling blocks are a chromatograph to determine BG level, an accelerometer to determine the patient is active or resting and a pulse monitor to keep track of the heart rate. A microprocessor is used to collect all these information from the patient and take decision to deliver proper doses of insulin into the VB. The simulation structure of the MID is exposed in the Fig. 1d.

2.4 *Investigation of Patient Activities*

In this section, the response variation of several parameters linked to BG metabolic phenomena is verified with the intake of 60.00 gm meal at 600 and 1300 min exercise under the noise of the Gaussian activities. In the present study, a fixed insulin dose named as basal dose of insulin is considered. Figure 2a indicates the plasma glucose-level transient variations in VB and the rate of insulin infusion in the blood. The deviations in NHGB rate, gut produced glucose and its rate of excretion via kidney including the uptake rate of sugar by some organs are shown in Fig. 2b.

Liver and peripheral cells are organs that depend on insulin will underutilize glucose owing to insulin lack resulting in uncontrolled BG level increment and subsequently glucose level surpasses 144 mg/dl that causes *hyperglycemia.* Now, the partial VB glucose extraction by the kidney with the glucose-level rise matching to RTG value is represented by Fig. 2c. The results in Fig. 2a–c reflect the patient model with wide varying transient responses, and the level of glucose in patient under all conditions is below the normal BG level. This depicts the patient dynamics sensitiveness to

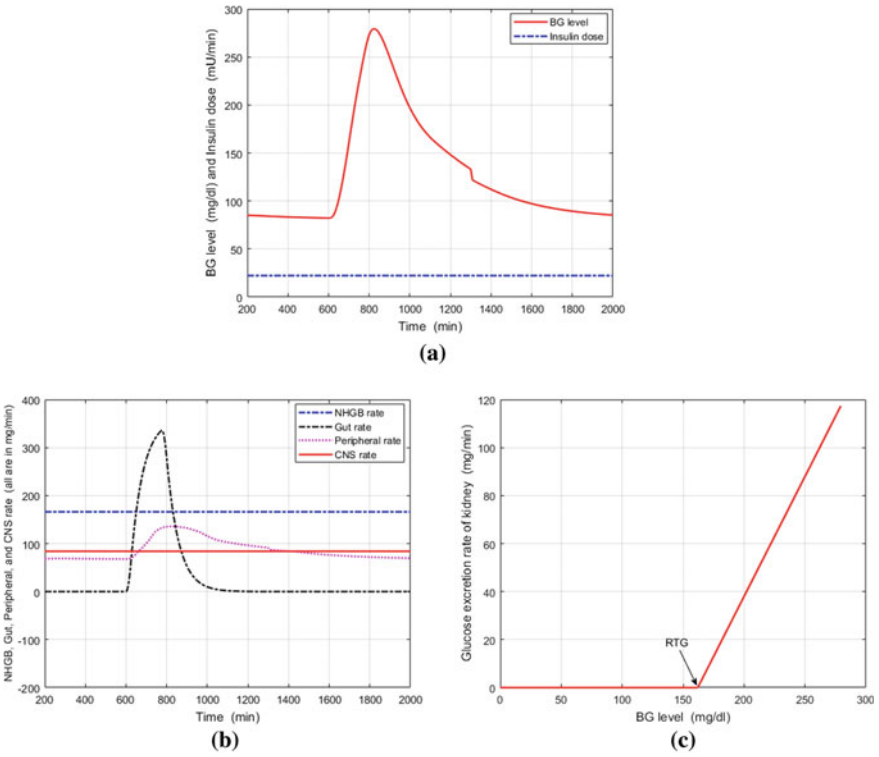

Fig. 2 Characteristics of patient structure: **a** relationship between the BG level and insulin secretion; **b** production and utilization of glucose by the organs; **c** relationship between the glucose excretion rate of kidney and BG level

the presence of the uncertainty and disturbances. So, to overcome these uncertainties and disturbances present in patient model, adaptive control technique-based AP is to be designed.

3 Control Algorithms

The JAYA-FOPIDC control mechanism is clearly established in Sect. 3.1. The patient performance with JAYA-FOPIDC as far as stability, accuracy and robustness is deliberated. The control phenomena like settling time t_s, steady-state error e_{ss} (%), peak overshoot O_{Peak} and peak undershoot U_{Peak} are also estimated and synthetized with suitable justification of the JAYA-FOPIDC control activities.

3.1 Development of JAYA-FOPIDC

The JAYA-FOPIDC is integrated with patient structure as shown in Fig. 1a. In this strategy, $e(t)$ is input variable, and $u(t)$ is output variable. TF of JAYA-FOPIDC is framed [22]:

$$\mathrm{TF} = K_p + \frac{K_i}{s^{\alpha}} + K_d s^{\beta} \tag{1}$$

where K_p, K_i, K_d, α and β are controller variables. These variables are assessed based on patient activity for the smallest value of the objective function j as characterized in Eq. (2).

$$j = \int_0^{\infty} |e(t)| t \mathrm{d}t \tag{2}$$

where absolute value of error signal is significant by $|e(t)|$. For regulating of plasma glucose concentration, the control variables are estimated through the JAYA optimization technique. It has a tendency to get struck on local minima's JAYA algorithm provides better computational accuracy, and it has a tendency to avoid local minima's and maxima's provide a perfect match. In this study, the JAYA algorithm variables are population size (100); number of design variables (6); termination criteria (iterations) (100). The optimized control variables are signified in Table 1. Optimized

Table 1 Optimized JAYA-FOPIDC variables

K_p	K_d	K_i	α	β
10	8	0.05	0.7	0.9

values of control variables are adopted based on JAYA optimization algorithm. The structure and working principle of JAYA algorithm are signified in the Fig. 3a, b.

4 Results

Patient activities with JAYA-FOPIDC are properly investigated in this section.

4.1 Patient Activities with JAYA-FOPID Control

Here, JAYA-FOPIDC for the patient model examined all profiles along with the allied disturbances and uncertainties as varied exercise, random glucose intake in the form of carbohydrates, sensor and actuator noise, etc. The insulin dose and BG-level response variation are verified with the intake of 60.00 gm meal at 600 and 1300 min exercise as described in Fig. 4a. Under identical conditions, other profiles of human organs are represented in Fig. 4b.

Figure 4a–c depicts the responses indicating the reduction of BG level to 83.3 mg/dl owing to more intake of glucose by peripheral muscles and liver which depend on insulin as compared to the uncontrolled TIDM patient model (Fig. 2a–c). As a result of this, the *hyperglycemia* condition is prevented by the AP control action. Now, due to BG level drops below RTG value, no further glucose extraction by the kidney takes place and is exposed in Fig. 4c. So, all the model profiles found enhanced by the use of the JAYA-FOPIDC controller-based AP.

4.2 Comparative Investigation

In this section, control performances of JAYA-FOPIDC on comparison with other control methods are discussed. The exercise and meal disturbance effects in the level of BG and insulin infusion rate variations in diabetic patient by the use of this controller are demonstrated in Fig. 4a–c, and Table 2 shows some relevant data.

From patient's BG levels with the proposed controller and an ingested disturbance in meal of 60.00 gm, the settling time, undershoot and overshoot of the adopted controller are of comparatively better stability and controllability to other implemented optimal controllers. As per an exercise disturbance test, the JAYA-FOPIDC controlled BG drops to 80.00 mg/dl and is within 70–120 mg/dl, the *normoglycemic* range. From the results, JAYA-FOPIDC performance is found much better and robustly in eliminating noise and solving the problems of hyperglycemia. The BG-level regulation and reduction in the rate of insulin infusion by this controller

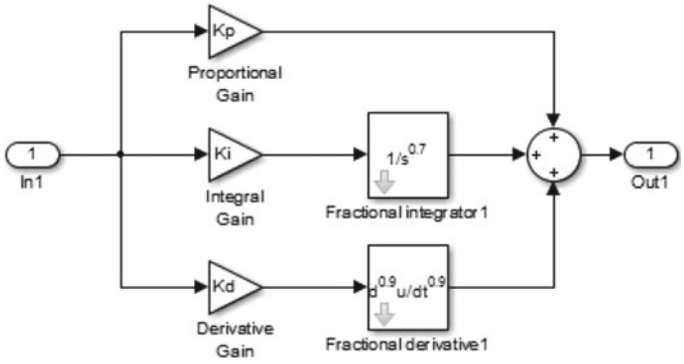

(a)

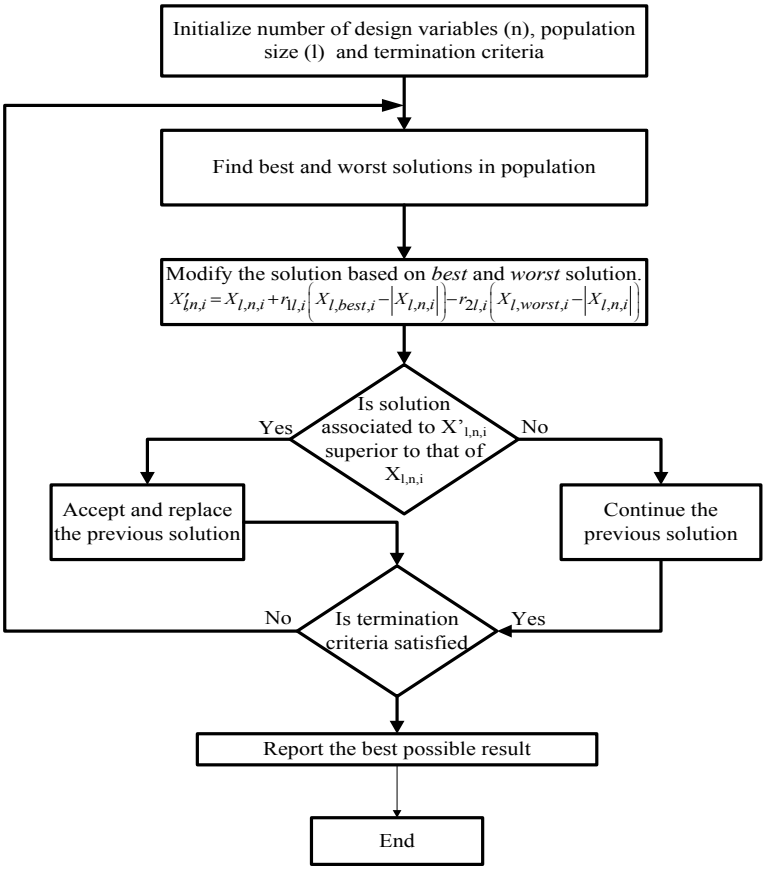

(b)

Fig. 3 **a** Graphical representation of JAYA-FOPIDC; **b** flowchart of the JAYA algorithm

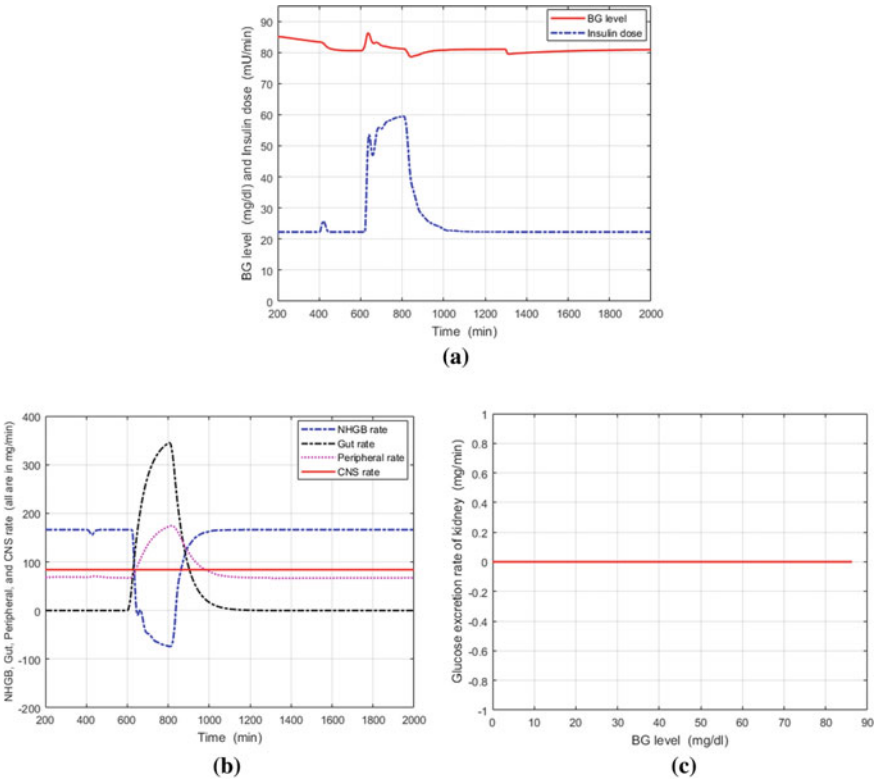

Fig. 4 Characteristics of patient structure along with JAYA-FOPIDC: **a** relationship between the BG level and insulin dose; **b** production and utilization of glucose by the organs; **c** relationship between the glucose excretion rate of kidney and BG level

Table 2 Comparative analysis with other techniques

Control techniques	PID [4]	Fuzzy [5]	H_∞ [11]	SM [13]	JAYA-FOPIDC (Recommended)
Meal intake (mg)	60.0	60.0	60.0	60.0	60.0
Insulin dose in mU/min	59.91	59.90	59.89	59.7	59.2
t_s in min	299	288	267	266	261
O_{peak} in mg/dl	6.1	5.9	6.1	6.2	4.4
U_{Peak} in mg/dl	3.6	3.2	2.1	2.1	1.1
Noise (%)	5.0	5.0	5.0	5.0	1.0
e_{ss} (%)	0.0	0.0	0.0	0.0	0.0

are better compared to other used controllers. The results, with several physiological situations and the mentioned disturbances, revealed higher reliability, stability, accuracy and robust performance using JAYA-FOPIDC-based controller.

5 Conclusions

In the proposed work, there is an enhancement of BG profiles in patient model due to the use of JAYA-tuned FOPIDC, thus resulting in improvements in its accuracy, stability and robustness. For the evaluation of the JAYA-FOPIDC variables, a nonlinear patient structure along with MID is considered. In this approach, JAYA is adopted to accomplish the improved control actions. The comparative investigation indicates that JAYA-FOPIDC is superior then other control techniques. The excellent execution of the JAYA-FOPIDC justifies its real-time application.

References

1. Patra AK (2021) An automatic insulin infusion system based on Kalman filtering model predictive control technique. J Dyn Sys Meas Control 143(2):021004-1-11
2. Patra AK (2021) Model predictive controller design based on the Laguerre functions for blood glucose regulation in TIDM patient. J Inst Eng India Ser B 3(1):1–12
3. Patra AK (2020) Design of artificial pancreas based on the SMGC and self-tuning PI control in type-I diabetic patient. Int J Biomed Eng Technol 32(1):1–35
4. Sutradhar A, Chaudhuri S (2002) Analysis and design of an optimal PID controller for insulin dispenser system. J Inst Eng (India) 82(2):304–313
5. Patra AK (2020) Design of artificial pancreas based on fuzzy logic control in Type-I diabetes patient. In: Innovation in electrical power engineering, communication, and computing technology. Springer, Singapore, pp 557–569
6. Patra AK (2015) Kalman filtering linear quadratic regulator for artificial pancreas in type-I diabetes patient. Int J Model Ident Control 34(1):59–74
7. Patra AK (2015) An automatic insulin infusion system based on LQG control technique. Int J Biomed Eng Technol 17(3):252–275
8. Patra AK (2020) Design of backstepping LQG controller for blood glucose regulation in type I diabetes patient. Int J Autom Control 14(4):445–468
9. Chee F, Andrey V (2005) Optimal H_∞ insulin injection control for blood glucose regulation in diabetic patients. IEEE Trans Biomed Eng 52(10):1625–1631
10. Yasini S, Karimpour A (2012) Knowledge-based closed-loop control of blood glucose concentration in diabetic patients and comparison with H_∞ control technique. IETE J Res 58(1):328–336
11. Patra AK (2014) Optimal H-infinity insulin injection control for blood glucose regulation in IDDM patient using physiological model. Int J Autom Control 8(40):309–322
12. Gallardo H, Ana G (2013) High-order sliding-mode control for blood glucose: practical relative degree approach. Control Eng Pract 21(5):747–758
13. Rmileh A, Gabin W (2012) Wiener sliding-mode control for artificial pancreas: a new nonlinear approach to glucose regulation. Comput Methods Programs Biomed 107(1):327–340
14. Rao RV (2017) A self-adaptive multi-population based Jaya algorithm for engineering optimization. Swarm Evol Comput 37(1):1–26

15. Barger M, Rodbard D (1989) Computer simulation of plasma insulin and glucose dynamics after subcutaneous insulin injection. Diabetes Care 12(1):725–736
16. Parker RS, Doyle III FJ (1999) A model-based algorithm for BG control in type 1 diabetic patients. IEEE Trans Biomed Eng 46(2):148–157
17. Parker RS, Doyle III FJ (1997) Variable-rate implantable insulin infusion pumps—closed loop maintenance of normoglycaemia under patient variability for type 1 diabetes. In: Proceedings of the 11th world congress. International Society for Artificial Organs
18. Lehmann ED, Deutsch T (1992) Physiological model of glucose–insulin interaction in type-1 diabetes mellitus. J Biomed Eng 14(3):235–242
19. Lehmann ED, Deutsch T (1998) Compartmental models for glycaemic prediction and decision support in clinical diabetes care: promise and reality. Comput Methods Programs Biomed 56(1):193–204
20. Sperr G (1997) Biosensor research targets medical diagnostics. Med Device Diagn Ind Mag
21. Cochin L, Cadwallender W (1997) Analysis and design of dynamic systems, 3rd edn. Addison-Wesley, New York
22. Bingul Z, Karahan O (2018) Comparison of PID and FOPID controllers tuned by PSO and ABC algorithms for unstable and integrating systems with time delay. Optimal Control Appl Methods 39(4):1431–1450

Efficiency Enhancement of Solar Photovoltaic Module Based on Different Cooling Arrangement

Roshan Kumar Soni, Sarthak Nayak, Sarita Samal, Prasanta Kumar Barik, Satyabrata Sahoo, and Lipika Nanda

Abstract In this paper, the efficiency of solar photovoltaic (SPV) module has been examined through combined effect of air- and water-cooling arrangements in warm and humid climatic condition. SPV framework requires neither fuel nor creates any toxin coming about into its expanded significance in the present energy area. The electrical yield from a SPV is an element of its effectiveness and some other controlling boundaries which influence the equivalent. One of the significant boundaries controlling the effectiveness of the board is the temperature as it continues expanding while at the same time utilizing the board in the sun. Around 31% of the SPV-based radiation on the board is changed over into the valuable energy, and the rest part is put away in its rear causing the ascent of temperature and antagonistically influencing its yield. The put away warm energy is of no utilization and diminishes the solidness of the in-assembled segments of the board because of the effect of extreme warm weights on them coming about into decrease in its life expectancy and transformation capacity. The least difficult approach to improve the proficiency of the board is to join the different cooling game plans, for example, air cooling, water cooling and consolidated air and water cooling and surveying their viability with no cooling

Present Address:
R. K. Soni · S. Nayak · S. Samal (✉) · S. Sahoo · L. Nanda
School of Electrical Engineering, KIIT Deemed To Be University, Bhubaneswar, India
e-mail: ssamalfel@kiit.ac.in

R. K. Soni
e-mail: 1803044@kiit.ac.in

S. Nayak
e-mail: 1803050@kiit.ac.in

S. Sahoo
e-mail: satyabrata.sahoofel@kiit.ac.in

L. Nanda
e-mail: lnandafel@kiit.ac.in

Present Address:
P. K. Barik
Department of Mechanical and Electrical Engineering, CAET, OUAT, Bhubaneswar, India

M. Mishra et al. (eds.), *Innovation in Electrical Power Engineering, Communication, and Computing Technology*, Lecture Notes in Electrical Engineering 814,
https://doi.org/10.1007/978-981-16-7076-3_4

course of action. From the examinations, it was seen that the efficiencies of SPV module have been improved in the scope of 8–11, 12–15 and 16–20% in air, water, and combined air and water cooling, respectively, compared to without cooling in a clear day.

Keywords Cooling of SPV · Efficiency of SPV · SPV · Tilt angle of SPV

1 Introduction

The importance of the applications of solar photovoltaic systems is increasing day by day due to the profuse availability of solar radiation in the tropical country like India. Solar photovoltaic (SPV) system plays an important role that can make environment-friendly, cost-effective, more flexible, and commercially widespread [1, 2]. That is why it is mainly used in satellite power system, water pumping system and rooftop electricity generation, etc. [3]. A SPV module changes over 6–20% of the episode sun-based radiation to electrical energy relies upon the sort of sun-oriented cells and climatic conditions. The rest of the incident solar radiation is converted into heat which ultimately increases the temperature of SPV module and reduces the conversion efficiency of module as well as shortens the lifespan of solar cell resulting in the structural damage to the SPV material [4–8]. The heat inside SPV cell is created in two ways. First, due to warm energy which is the contrast between the retained sun-based photons and the electrical energy of the created electron opening sets. Second, there are I_2R_s as result of the current flowing through the resistance Rs of the solar cell. The main disadvantage of solar cell is the decrease in its performance with respect to power output and electrical efficiency by the increase in the temperature of module [9–12]. There are various factors affecting the performance of solar cells such as solar radiation, temperature, humidity, air velocity, dust, orientation, and tilt angle. Among these, temperature is the major factor affecting power output and the conversion efficiency of module. As cell temperature of module increases, efficiency of module decreases due to the reduction in the voltage. As operating temperature of module increases, the open-circuit voltage decreases significantly while short-circuit current increases slightly and also the fill factor decreases. This leads to reduction of electrical power output and efficiency of solar cells [13–15]. Therefore, it is required to lower the temperature of solar cell as far as practicable in order to improve the conversion efficiency of PV cells. There are several cooling methods for regulating temperature of PV module such as air cooling, water cooling, cooling with phase change materials, heat pipe cooling, and thermoelectric cooling [16, 17]. Cooling by the flow of air and water may be considered as the most effective method to provide an acceptable level of cooling for the SPV cells. Therefore, the present research work was undertaken with the objective of studying the performance of SPV module with the effects of operating parameters such as change of tilt angle and incorporating air- and water-cooling methods.

2 Methods Implemented

The experiments were conducted, and the data were recorded in an interval of one hour from 9 am to 4 pm from January 2019 to April 2020 by installing the setup at the rooftop of institute situated at Bhubaneswar, Odisha (latitude 20.2650 °N and longitude 85.8117 °E). The place is coming under warm and humid climatic conditions where the annual average rainfall is 1450 mm, and average daily solar insolation is 4.8 kWh/m^2. During the course of investigation, important parameters recorded were solar radiation, ambient temperature, wind velocity, relative humidity and voltage, current and power output from the module. These parameters were recorded at an interval of 1 h. Solar radiation was measured using solar irradiance meter. The details of the experimental setup are shown in Fig. 1. Two solar photovoltaic modules were taken with similar specifications as mentioned in Table 1. The solar modules were installed at a height of 1 m from ground level, and it was oriented in South direction. There was an arrangement provided to vary inclination of solar module with respect to the horizontal plane. Each solar module has 255 W_p. As there were two modules, the total wattage was 510 W_p, which was sufficient to run a 0.5 hp DC water pump. In order to measure the different electrical parameters in connection with evaluation of solar pump used for the study, a solar testing kit was used. It measures the parameters

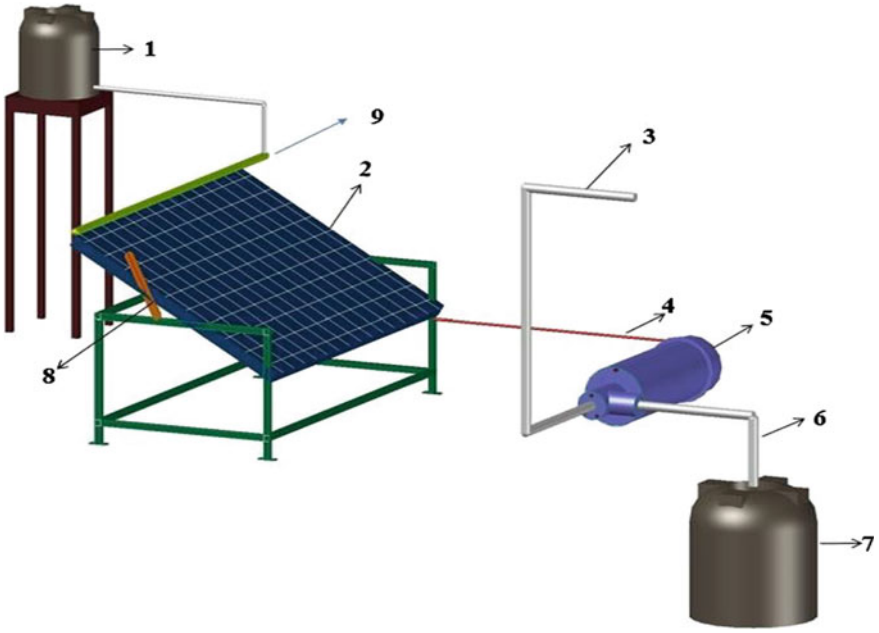

Fig. 1 Experimental setup of the proposed study. 1. Storage tank for flowing of thin film of water on solar module surface, 2. Solar module, 3. Water discharge pipe, 4. Electrical connection from solar module to solar pump, 5. DC solar pump, 6. Suction pipe, 7. Water tank for lifting purposes, 8. Tilt angle adjustment arrangement and 9. Perforated flexible pipe

Table 1 SPV parameters and its specification

Parameter	Specification
Type of solar module	Polycrystalline
Panel connection	Series
Panel dimensions	100 × 166 × 4 cm
Maximum power	255 Wp
Total power of module	2 × 255 Wp = 510 Wp
V_{oc}	37.69 V
I_{sc}	8.89A
V_{mpp}	30.33 V
I_{mpp}	8.41A

such as ambient air temperature, solar radiation, current, voltage, fill factor of solar module.

The instruments used for the measurement of experimental data were solar irradiance meter, SEWARD PV 200 analyzer for measuring electrical parameters to calculate efficiency of module. For air cooling purpose, four number of fans are attached on the backside of the PV module shown in Fig. 2 and specifications are given in Table 2. For effective cooling, fans were operated from 9 am to 4 pm continuously for removing the heat stored in the backside of the module resulting in the lowering of its temperature. The operation of fan is controlled by a charge controller. The fans were powered from the modules used for the study.

For water cooling, a perforated flexible pipe is used and small holes of 2–3 mm are made on the flexible pipe. Water is allowed to flow from the storage tank by the gravitational force. A very thin film of water flows over the surface of the module for effective cooling through evaporation of water. The storage tank was placed on one side and at a height of 2 m from the upper surface of the module. The setup for water cooling is shown in Fig. 3.

3 Results and Discussion

The results in this section consist of two parts. In the first part, the tilt angle of the solar module was decided to fix for the study on the basis of the maximum availability of incident solar radiation on it in the experimental site from January to April. In the second part, all the electrical parameters such as short-circuit current, maximum current, open-circuit voltage, maximum voltage, fill factor of the used solar module were measured on hourly basis from 9 am to 4 pm along with the incident solar radiation on the surface of the module with the help of solar PV analyzer. The data were recorded by following various cooling methods such as air, water, and combined air and water cooling separately and compared these without any cooling method.

Fig. 2 Air cooling arrangement

Table 2 Specification of DC fan

Parameter	Specification
Voltage	12 V
Current	0.83 A
No of fan used	4
Manufacturer	San Ace 120

The efficiency of the solar module is calculated from the measured data and compared with those in case of without using any cooling method.

3.1 Fixing the Tilt Angle of Solar Modules Used Understudy from January to April

The incident solar radiation on the horizontal as well as inclined surface varies from morning to the afternoon due to the change of altitude angle of sun in a day during

Fig. 3 Water-cooling arrangement

its movement in the sky. In order to harvest more solar radiation from any solar device, the tilt angle of the surface needs to be changed on hourly basis in a day or with the change of the season in a year. Without any tracking arrangement, the tilt angle needs to the fixed in a month in a particular location and site in order to get the availability of more solar radiation on the module. The data for the availability of incident solar radiation were measured from 9 am to 4 pm on clear day during January to April 2020. The fixation of tilt angle of module during January–April 2020 has been presented in Fig. 4. From the data collected, it was observed that the availability of incident solar radiation was recorded to be maximum at the tilt angle of 35°, 30°, 20° and 8°, respectively, in the month of January, February, March, and April 2020 for the experimental setup located in Bhubaneswar, Odisha. Accordingly, the tilt angle was fixed in each month and data were recorded for the present study.

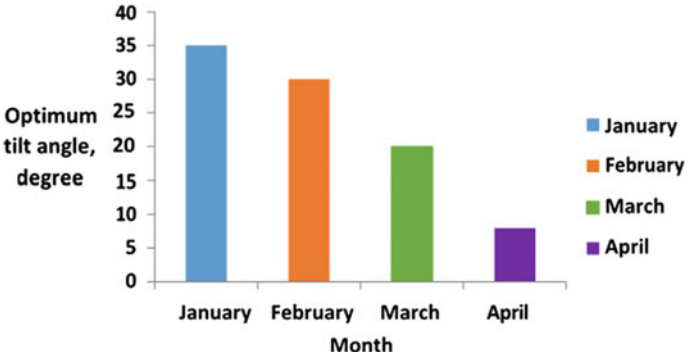

Fig. 4 Fixation of tilt angle of module during January–April 2020

3.2 Measurement of Electrical Parameters of Solar Module Used for the Study

Hourly variations of solar irradiation, ambient temperature, module backside temperature, I_{sc}, V_{oc}, I_{mpp}, V_{mpp}, fill factor, and efficiency of SPV on clear days during January–April 2020 with respect to various cooling arrangements were studied. Data were collected in four consecutive days by following without cooling, cooling with air, water and combined air and water separately, and efficiency of the module was compared with respect to without cooling.

It was revealed from Fig. 5 that the temperatures of SPV system were reduced nearly 4–5 °C in case of air cooling, 6–8 °C in case of water cooling, and 9–12 °C in case of both air- and water-cooling arrangements as compared to without cooling system in a day. Moreover, it is also viewed from Fig. 5 that the efficiency of the SPV module has been increased in the range of 8–11% in case of air cooling, 12–15% in case of water cooling, and 16–20% in case of both air- and water-cooling

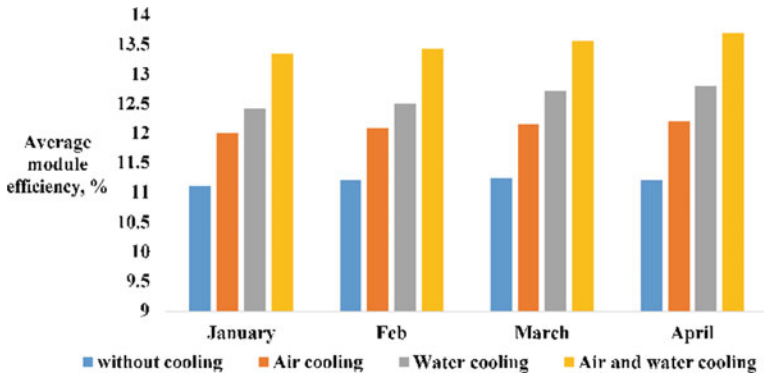

Fig. 5 Variation of SPV efficiency with different cooling arrangement during January–April 2019

arrangements. For air cooling purpose, 4 numbers of fans were fitted to reduce module temperature. From the figure above, it was found that with air cooling, module efficiency increased as open-circuit voltage, fill factor, power output increased. Due to cooling by exhaust fan, temperatures of module were maintained. So, output voltage was increased. Efficiency was calculated to be maximum at noon then decreased as per the changes in the availability of solar radiation. The module temperatures were maintained, and their efficiency was increased as compared to without cooling. The decrease in temperature of the back surface of the module may be attributed due to the dissipation of stored thermal energy from the back surface by convection to the outside through the continuous flow of air with the help of DC fan, powered by the module itself. In case of water cooling, thin film of water was allowed to flow on the upper surface of the module, resulting in a cool environment due to the evaporation of water. The thermal energy at the back surface was decreased due to the spread of cool air at a lower temperature surrounding the module. In combined air and water cooling, the decrease of temperature was found to highest due to the simultaneous effects of flowing of air flow and spread of cool evaporated air both on the lower and upper surfaces of the module. In case of without cooling technique, with increase of solar radiation and ambient air temperature, the temperatures of the back surface of the module increased in the range from 50 to 60 °C resulting in the decrease in the power output and thus efficiency of the module.

4 Conclusion

One of the practical and viable solutions for enhancing the efficiency of the SPV module for a user is to incorporate various cooling arrangements for dissipating stored thermal energy in its backside. This is under the control of the user. This proposition also depends on the climatic conditions where the panels are used. A lot of research activities have been undertaken by the various researchers to increase the output of the solar panel. The present study has been carried out in warm and humid climatic condition by incorporating air, water, and combined air- and water-cooling arrangements for a solar panel, and the following conclusions were drawn out of it. The average solar radiation in a clear day was found to be highest at tilt angle of 35°, 30°, 20°, 8° in month of January, February, March, April, respectively. The temperatures of SPV module were decreased in the range of 4–5 °C in case of air cooling 6–8 °C in case of water-cooling arrangement, and 9–12˚C in case of both air- and water-cooling methods. Correspondingly, the SPV module efficiency was increased in the range of 8–11% in case of air, 12–15% in case of water, and 16–20% in case of both air and water arrangements. The above findings would not only be helpful for the researchers but also for the manufacturers and users for the climatic condition under study. The manufacturers may keep the provision of air- or water-cooling conduits in the backside of the panel for its easy use and cooling, resulting in the enhancement of efficiency by 10–15%.

References

1. Swain MK, Mishra M, Bansal RC, Hasan S (2021) A self-powered solar panel automated cleaning system: design and testing analysis. Electr Power Compon Syst 1–13
2. Mishra M, Dash PB, Nayak J, Naik B, Swain SK (2020) Deep learning and wavelet transform integrated approach for short-term solar PV power prediction. Measurement 166:108250
3. Sainthiya H, Beniwal NS (2020) Thermal modeling and performance analysis of a hybrid photovoltaic/thermal system under combined surface water cooling in winter season: an experimental approach. J Energy Resour Technol 142(1)
4. Muslim NH, Ghadhban SA, Hilal KH (2020) Enhancement of solar photovoltaic module performance by using a water-cooling chamber for climatic conditions of Iraq. Int J Renew Energy Res (IJRER) 10(3):1103–1110
5. Sainthiya H, Beniwal NS (2020) Comparative analysis of electrical performance parameters under combined water-cooling technique of photovoltaic module: An experimental investigation. Energy Sources Part A: Recovery Utilization Environ Effects 42(15):1902–1913
6. Eteruddin H, Atmam A, Setiawan D, Arief YZ (2020) Effects of the temperature on the output voltage of mono-crystalline and poly-crystalline solar panels. Sinergi 24(1):73–80
7. Khalili NNW, Othman M, Abu Bakar MN, Abdullah L (2020) Modelling of a single passage air PV/T solar collector: experimental and simulation design. Processes 8(7):763
8. Ustaoglu A, Ozbey U, Torlaklı H (2020) Numerical investigation of concentrating photovoltaic/thermal (CPV/T) system using compound hyperbolic–trumpet, V-trough and compound parabolic concentrators. Renew Energy 152:1192–1208
9. Barik PK, Shankar G, Sahoo PK (2020) Power quality assessment of microgrid using fuzzy controller aided modified SRF based designed SAPF. Int Trans Electr Energy Syst 30(4):e12289
10. Bevilacqua P, Bruno R, Arcuri N (2020) Comparing the performances of different cooling strategies to increase photovoltaic electric performance in different meteorological conditions. Energy 195:116950
11. Luboń W, Pełka G, Janowski M, Pająk L, Stefaniuk M, Kotyza J, Reczek P (2020) Assessing the impact of water cooling on PV modules efficiency. Energies 13(10):2414
12. Ahmad EZ, Sopian K, Jarimi H, Fazlizan A, Elbreki A, Hamid ASA, Ibrahim A (2021) Recent advances in passive cooling methods for photovoltaic performance enhancement. Int J Electr Comput Eng 11(1). 2088-8708
13. Rout T, Chowdhury A, Maharana MK, Samal S (2018) Analysis of energy management system for photovoltaic system with battery and supercapacitor using fuzzy logic controller. In: 2018 Technologies for smart-city energy security and power (ICSESP). IEEE, pp 1–4
14. Chandan RS, Kiran TS, Swapna G, Muni TV (2020) Intelligent control strategy for energy management system with FC/Battery/SC. JCR 7(2):344–348
15. Zubeer SA, Ali OM (2020) Performance analysis and electrical production of photovoltaic modules using active cooling system and reflectors. Ain Shams Eng J
16. Guichet V, Khordehgah N, Jouhara H (2020) Experimental investigation and analytical prediction of a multi-channel flat heat pipe thermal performance. Int J Thermofluids 5:100038
17. Shittu S, Li G, Zhao X, Zhou J, Ma X, Akhlaghi YG (2020) Experimental study and energy analysis of photovoltaic-thermoelectric with flat plate micro-channel heat pipe. Energy Convers Manage 207:112515

Optimal Compensation of Hydro Governor for Power Oscillation Damping

Samarjeet Satapathy, Narayan Nahak, Ramachandra Agrawal, and Akshaya Kumar Patra

Abstract In this study, phase compensated hydro-turbine governor for stabilizing power system oscillations. As per deregulation in electricity market, much pressures are imparted on optimal use of resources like mechanical turbine governor action. Since mechanical torque control and excitation control of generator are decoupled, regulating generator voltage is not affected by turbine governor control. Also, mechanical torque control is less influenced by system operating condition. So here optimal phase compensation has been included with turbine governor for enhancing damping efficiency of governor which has been found to provide much improvement in dynamic stability: without hampering voltage control and power frequency regulation. The gains of compensation block and governor have been tuned by DE, PSO and squirrel search algorithm (SSA). The results with only governor action and proposed SSA optimized compensated governor have been compared with different case studies like change in mechanical input and reference voltage with system eigenvalues analysis for justifying effectiveness of proposed governor control.

Keywords Governor · Power oscillation damping · Phase compensation · Squirrel search algorithm

S. Satapathy · N. Nahak (✉) · R. Agrawal
Department of Electrical Engineering, Siksha 'O' Anusandhan Deemed to be University, Bhubaneswar, Odisha 751030, India
e-mail: narayannahak@soa.ac.in

A. K. Patra
Department of Electrical and Electronics Engineering, Siksha 'O' Anusandhan Deemed to be University, Bhubaneswar, Odisha 751030, India
e-mail: akshayapatra@soa.ac.in

M. Mishra et al. (eds.), *Innovation in Electrical Power Engineering, Communication, and Computing Technology*, Lecture Notes in Electrical Engineering 814,
https://doi.org/10.1007/978-981-16-7076-3_5

1 Introduction

One of the major challenges for a modern power system is stabilizing power system oscillation which may be brought by varying operating condition, variation in line reactance, change in input turbine power, weak grid connection, etc. These uncontrolled oscillations may lead to out of synchronization and lead to violation in transmission grid security level [1, 2]. As per Ref. [3], hydel turbine governor is not turned efficiently to damp oscillations. Therefore, different set of parameters are to be maintained by the power system operators, for hydro-governor settings. These are isolated made of operation and grid-connected made of operations.

Different model of governors is presented in Refs. [4, 5], for stability studies and enhancement. In Ref. [6], validation of different hydro-turbine governor modelling has been performed, and similarly thermal governors' model in Ref. [7]. Characteristics of steam turbines values are being analysed in Ref. [8]. A review on hydroelectric power station and modelling is given in Ref. [9], and for monitor and analysis by digitized modelling is being performed in Ref. [10]. These characteristics of power system oscillation are analysed in Ref. [11] and turbine controlling strategies are being explained in Ref. [12], for system oscillations. So, damping of system oscillations has been a challenging issue and this has been addressed in many literatures [13, 14], where flexible AC transmission system technologies have been implemented; but most often hydel governors are ignored for oscillation damping which is cheap, simple and easily implementable. Therefore, phase compensation is inserted with turbine governor for better enhancement of capability of governor action in this work. But the next challenge is setting of turbine governor and phase compensation gains. For this suitable control law can be implemented. Different swarm and evolutionary algorithms have been found to be very much popular in this context [15–19], which are DE, PSO and GWO along with their hybridization. Squirrel search algorithm (SSA) has been recently reported in Ref. [20] and has been justified and validated for its effective optimizing efficiency. So SSA is employed here to tune the gains of turbine governor and phase compensation block. Different case studies have been conducted here pertained to change in turbine power and reference voltage. The response has been analysed in time and frequency domain to justify prepared control action for damping system oscillations.

2 Hydro-Turbine Modelling

The hydro-turbine is taken here along with surge tank. The output from turbine is

$$p_t = A_t h_t (q - q_{\text{hl}}) - \text{DG}\Delta\omega \tag{1}$$

where $A_t = \frac{\text{Rated active power output of turbine (MW)}}{(\text{Alternator MVA rating})\, h_{\text{rated}} (q - q_{\text{hl}})}$.

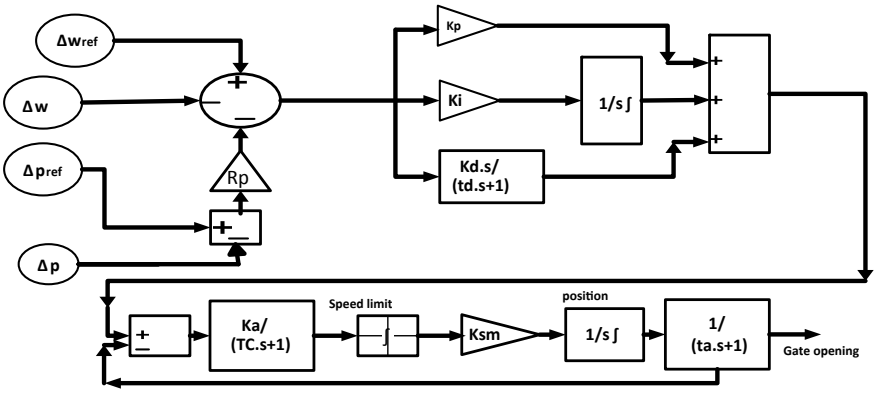

Fig. 1 Governor modelling

Ignoring frictional loss, a small perturbation will lead to change in prime mover output as:

$$\Delta p_t = \frac{A_t(1 - T_1 s)}{(1 + T_2 s)} - DG_0 \Delta\omega \tag{2}$$

3 Governor Modelling

A Woodward governor is taken here which is of PID type, servo motor subsystem, integrator and gain as shown in Fig. 1. The permanent droop is being dependent on open of gate or electrical active power.

4 Generator Model

The small perturbation generator model presented in Fig. 2 has k-constants calculated at initial operating condition $P_o = 0.8$ pu and $Q_o = 0.17$ pu.

$$\Delta\omega = \frac{1}{2Hs + K_D}(\Delta T_M - \Delta T_e) \tag{3}$$

$$\Delta\delta = \frac{2\Pi f_0}{s}\Delta\omega \tag{4}$$

$$T_e \approx P_e = i_d u_d + i_q u_q \tag{5}$$

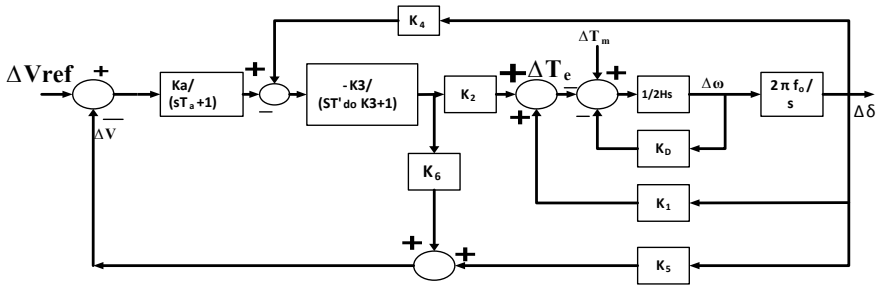

Fig. 2 Generator modelling

$$\Delta T_e = K_1 \Delta\delta + K_2 \Delta e_q^{'} \tag{6}$$

$$\Delta V_t = k_5 \Delta\delta + k_6 \Delta e_q^{'} \tag{7}$$

The K constants of third-order generator model are given by:

$K_1 = \frac{\Delta T_e}{\Delta\delta}\Big|_{e_q'}$ Ratio of deviation in torque and deviation in rotor angle at constant d-axis flux linkages.

$K_2 = \frac{\Delta T_e}{\Delta e_q'}\Big|_{\delta}$ Ratio of deviation in torque and deviation in d-axis flux linkages at constant rotor angle.

$K_3 = \frac{X_d' + X_e}{X_d + X_e}$ Where x_e is a pure impedance.

$K_4 = \frac{1}{K_3}\frac{\Delta e_q'}{\Delta\delta}$ Deviation in rotor angle due to demagnetizing effect.

$K_5 = \frac{\Delta V_t}{\Delta\delta}\Big|_{e_q'}$ Ratio of deviation in terminal voltage and deviation in rotor angle at constant d-axis flux linkages.

$K_6 = \frac{\Delta V_t}{\Delta e_q'}\Big|_{\delta}$ Ratio of deviation in terminal voltage and deviation in d-axis flux linkages at constant rotor angle.

5 Phase Compensation

The phase compensation is a lead–lag type with gain and washout block as shown in Fig. 3. K_g is the gain parameter, and T_{1g}, T_{2g} are time constants of compensation block. The phase lag provided by governor is compensated by the compensation

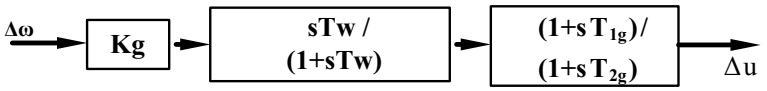

Fig. 3 Phase compensation

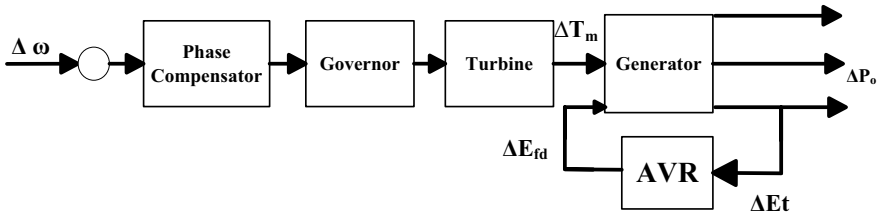

Fig. 4 Overall block diagram of generator with turbine governor and phase compensator

parameter. In steady state, when $s \rightarrow 0$ the value of washout and lead–lag block is 1. So optimal settings of K_g can provide necessary droop. Figure 4 presents the overall block diagram of generator with turbine governor and phase compensator whose gains are to be tuned by optimization technique.

6 Objective Function

In this paper, deviation in angular frequency of alternator has been taken as input signal, which is considered in ITAE-based objective function for minimization as given in Eq. (8).

$$J = \int_0^{tsim} t|\Delta\omega|dt \tag{8}$$

The PID governors gain K_p, $K_{i,}$ K_d and compensation block gain K_g, $T_{1g,}$ T_{2g} are to be tuned by suitable algorithm. The ranges of K_p, Kg are 1–100 and K_i and K_d are 1–10 and time constants T_{1g} and T_{2g} are 0.01 to 1.

SSA is proposed to tune the gains which have been compared with DE and PSO algorithms.

7 SSA Algorithm

A nature-inspired optimization technique is proposed and recently is known as squirrel search algorithm. SSA optimization technique is followed by small mammal's (like flying squirrels) gliding and their searching methods for food in Ref. [20]. These mammals can move an extensive distance quickly and very professionally. The squirrels showed their foraging behaviour for use of food sources. The below steps are followed by SSA.

1. Let there are n numbers of flying squirrels in a forest.
2. For searching food, every flying squirrel is used the present food resources with the help of foraging.
3. There are three types of trees in a forest acorn, hickory and normal tree.

Pseudocode of SSA is given below.

- Initialize input constraints
- Random position of n number of flying squirrels has been generated by Eq. (9).

$$FS_i = FS_L + U(0, 1) \times (FS_U - FS_L) \tag{9}$$

- Fitness value of each flying squirrel's position is calculated and arranged in an ascending order.
- Flying squirrel is being declared on hickory nut trees, acorn nuts trees and normal trees.
- Choose some squirrels randomly on a normal tree which are moving to hickory nut tree and others are moving towards acorn nuts tress.

While (stopping condition is unsatisfied**)**

For t = 1 to n1 (n1 = on acorn tree flying squirrel which are moving to hickory tree)
if $R_1 \geq P_{dp}$

$$\left(FS_{j,k}^{t+1}\right)_{at} = \left\{\left(FS_{j,k}^{t}\right)_{at} + d_g(G_c)\left(\left(FS_{j,k}^{t}\right)_{ht} - \left(FS_{j,k}^{t}\right)_{at}\right)\right\}$$

else

$\left(FS_{j,k}^{t+1}\right)_{at}$ = a random search space position

end
end
For t=2 to n2 (n2 = on normal tree flying squirrel which are moving to acorn tree)
if $R_2 \geq P_{dp}$

$$\left(FS_{j,k}^{t+1}\right)_{nt} = \left\{\left(FS_{j,k}^{t}\right)_{nt} + d_g(G_c)\left(\left(FS_{j,k}^{t}\right)_{at} - \left(FS_{j,k}^{t}\right)_{nt}\right)\right\}$$

else

$\left(FS_{j,k}^{t+1}\right)_{nt}$ = a random search space position

end
end

For t=2 to n3 (n3 = on normal tree flying squirrel which are moving to hickory tree)

if $R_3 \geq P_{dp}$

$$\left(FS_{j,k}^{t+1}\right)_{nt} = \left\{\left(FS_{j,k}^{t}\right)_{nt} + d_g(G_c)\left(\left(FS_{j,k}^{t}\right)_{ht} - \left(FS_{j,k}^{t}\right)_{nt}\right)\right\}$$

else

$\left(FS_{j,k}^{t+1}\right)_{nt}$ = a random search space position

end

end

evaluating seasonal constant (S_c)

if (S_c monitoring condition is satisfying)

flying squirrel is relocated randomly

end

seasonal constant minimum (S_{min}) value is updated

end

The squirrel which is located on hickory tree is the final optimal solution

end

where *j*th represents squirrel and *k*th represents dimension and *t* represents no. of iteration. d_g represents gliding distance that is taken randomly, and G_C represents gliding constant that is taken by exploitation and exploration of search space controlled. R_1, R_2 and R_3 are the uniformly distributed number randomly between the limits (0, 1).

8 Result and Discussion

This work focussed on stabilizing variation in angular frequency of generator subject to different disturbances. The phase compensation has been inserted with governor and gains of phase compensation along with governor PID parameters and tuned by SSA control law. The generator is being initially at steady state at $P_o = 0.8$ pu and $Q_o = 0.17$ pu. Subject to this condition, the mechanical power is varied in case-I. Two different conditions are being taken in case-I. In condition-I, the mechanical input is suddenly raised by 5%, and in condition-II, the mechanical input is suddenly raised by 10%. With only governor action, the bode diagram and root locus plot are presented in Fig. 5 and Fig. 6, respectively. Analysis of speed and real power variations has been performed with proposed control action and only governor control optimized by DE, PSO and SSA control laws. For condition-I, the angular frequency variation is shown in Fig. 7 and real power variation in Fig. 9. System eigen is presented in Table 1, and optimal gains are in Table 2. The result predicts response with only governor tuning and with governor assisted by phase compensation tuning. When phase compensation and governor gains are tuned, the resulting damping capability of governor is much enhanced. System eigenvalues

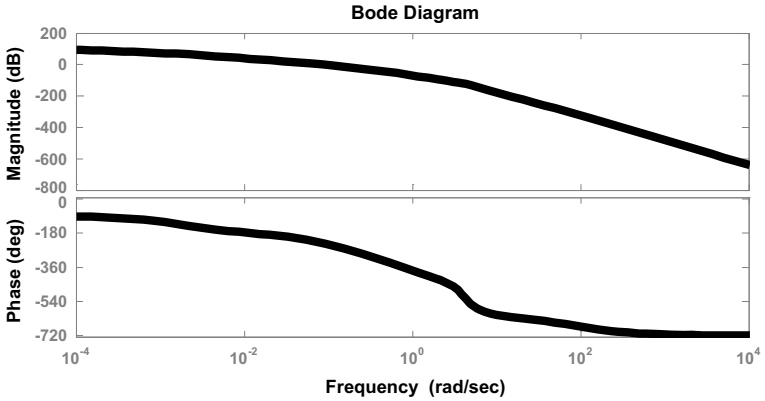

Fig.5 Bode diagram with only governor control

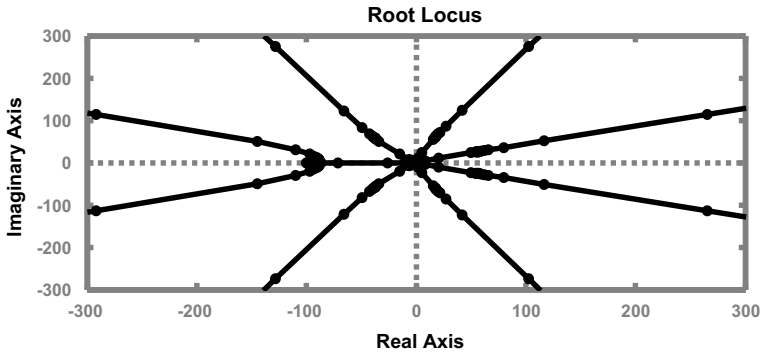

Fig. 6 Root locus with only governor control

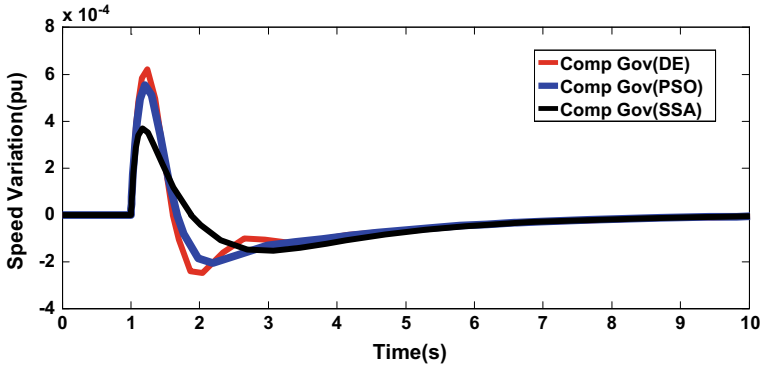

Fig. 7 Speed variation for 10% input mechanical power change

shift to left half of complex plane with reduced imaginary part predict improved damping of oscillation with proposed action. In condition-II, the mechanical power has large variation of 10% sudden raise, which gives rise to move oscillatory response. Figures 8 and 9 present angular frequency and active variation, respectively. System eigen is being provided in Table 1. Result predicts that oscillation is being raised heavily with sudden increase in mechanical power by large amount. Response has been presented without phase compensation block and only optimally set of governor gains and with optimally setting of both phase compensation and governor gains. For both conditions-I and II, the responses have been compared with PSO, DE and SSA algorithms. The SSA algorithm provides much better result for optimal setting of controller gains in contrast to PSO and DE algorithms. In case-II, the disturbance taken in change in reference voltage suddenly raised by 5% subject to reference voltage variation and the system oscillatory response was forward to much enhanced. The response is presented in Fig. 10 for angular frequency variation and system eigen presented in Table 1. Optimal setting of controller gains is given in Table 2. It is observed that governor action assisted by phase compensation improved the damping capability of governor by a large extent, and further, optimal setting of phase compensation and governor parameters also enhances the effectiveness of proposed control action. SSA algorithm is employed to tune the gains and is compared with PSO and DE algorithms.

9 Conclusion

Optimally turned phase compensation block has been inserted with turbine governor in this work for stabilizing power system. SSA is employed to tune gains of governor and compensation block. It has been observed that insertion of additional optimal compensation with governor and also optimally setting of governor gains can enhance damping of system oscillation. The proposed action has been validated with disturbances like change in turbine power and reference voltage, with time and frequency response analysis. A single generator is being considered in this work and connected to infinite bus, and this work can be extended in future for multi-machine system; by the proposed action, it has been observed the efficiency of the turbine control action can be much improved with additional optimal compensation.

Table 1 System eigenvalues

Cases	DE	PSO	SSA
10% input mechanical power	−50.0002, −99.8885, −27.1477, −2.9261 + 4.6284i, −2.9261 − 4.6284i, −4.2285, −2.8156, −1.6500, −0.1000, −0.2488, −0.0000, 0.0000, 0, −0.5556, −0.6667	−50.0009, −99.8885, −27.1459, −2.9262 + 3.6278i, −2.9262 − 3.6278i, −5.4682, −2.8160, −1.6499, −0.1000, −0.2488, −0.0000, −0.0000, 0, −0.5556, −0.6667	−50.0001, −99.8885, −27.1479, −3.9263 + 1.6288i, −3.9263 − 1.6288i, −2.8155, −1.6932, −1.6539, −0.1000, −0.2488, −0.0000, 0.0000, 0, −0.5556, −0.6667
5% input mechanical power	−50.0004, −99.8885, −27.1474, −1.9263 + 4.6284i, −1.9263 − 4.6284i, −2.8156, −1.6500, −1.4081, −0.1000, −0.2488, 0.0000, −0.0000, 0, −0.5556, −0.6667	−50.0005, −99.8885, −27.1470, −2.9264 + 3.6283i, −2.9264 − 3.6283i, −2.8156, −1.6501, −1.6240, −0.1000, −0.2488, 0.0000, 0.0000, 0, −0.5556, −0.6667	−50.0023, −99.8885, −27.1426, −3.9262 + 1.6272i, −3.9262 − 1.6272i, −7.3263, −2.8161, −1.6499, −0.1000, −0.2488, −0.0000, 0.0000, 0, −0.5556, −0.6667
Change in V_{ref}	−50.0126, −99.8885, −27.1069, −15.5301, −2.9248 + 4.6262i, −2.9248 − 4.6262i, −2.8162, −1.6499, −0.1000, −0.2488, 0.0000, 0.0000, 0, −0.5556, −0.6667	−50.0010, −99.8885, −27.1458, −2.9263 + 4.0076i, −2.9263 − 4.0076i, −2.8170, −2.1520, −1.6498, −0.1000, −0.2488, −0.0000, 0.0000, 0, −0.5556, −0.6667	−50.0010, −99.8885, −27.1458, −2.9263 + 4.0076i, −2.9263 - 4.0076i, −2.8170, −2.1520, −1.6498, −0.1000, −0.2488, −0.0000, 0.0000, 0, −0.5556, −0.6667

Table 2 Optimal parameters

Cases	Parameters	DE	PSO	SSA
10% input mechanical power	K_p	18.2715	27.5087	33.7830
	K_i	2.6559	2.3617	4.6008
	K_d	2.9183	5.5277	7.6843
	K_g	17.6466	33.8623	12.1229
	T_{1g}	0.4354	0.4116	0.9644
	T_{2g}	0.4045	0.1336	0.1365
5% input mechanical power	K_p	16.5748	49.0402	55.3444
	K_i	1.9647	1.9380	1.3881
	K_d	4.6975	3.9040	1.6462
	K_g	29.5087	12.0464	25.0093
	T_{1g}	0.2227	0.2937	0.3262
	T_{2g}	0.1115	0.7493	0.5891

(continued)

Table 2 (continued)

Cases	Parameters	DE	PSO	SSA
Change in V_{ref}	K_p	38.4093	3.0736	38.6424
	K_i	4.8692	1.6626	1.7704
	K_d	9.0752	9.1409	3.1483
	K_g	27.1032	15.9448	33.1035
	T_{1g}	0.8807	0.6815	0.5063
	T_{2g}	0.0645	0.4646	0.6343

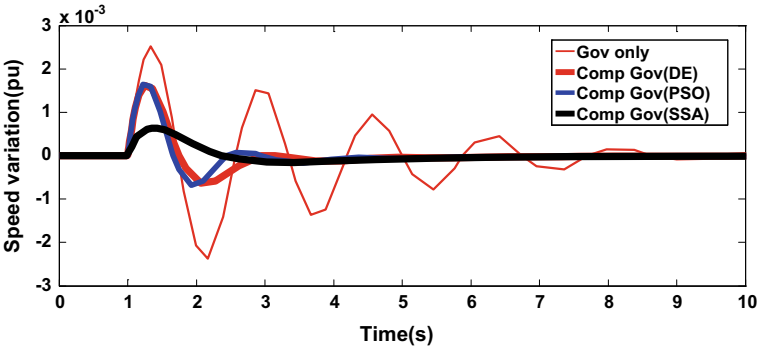

Fig. 8 Speed variation for 5% input mechanical power change

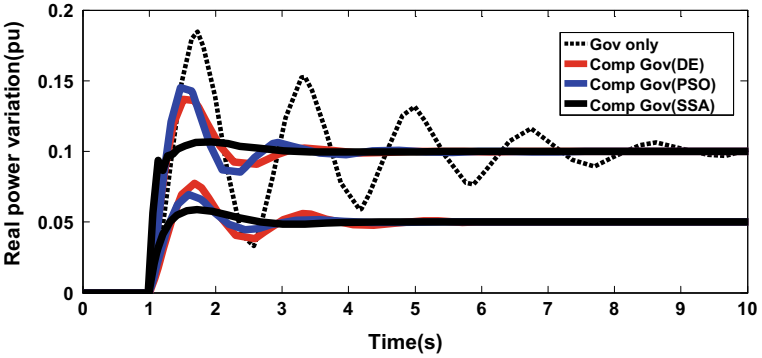

Fig. 9 Real power variations for input mechanical power change

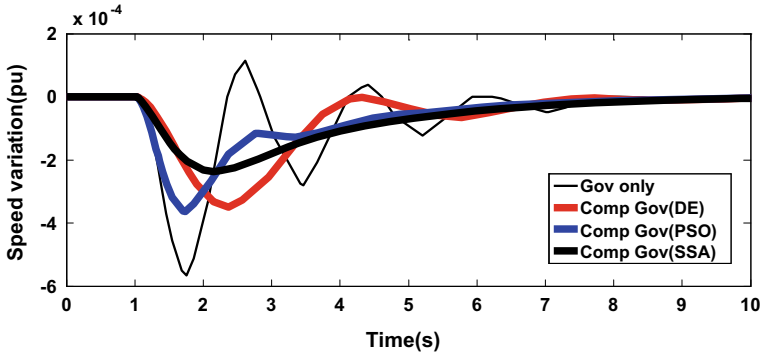

Fig. 10 Speed variation for Change in Vref

References

1. Kundur P (1994) Power system stability and control. McGraw-Hill, Inc.
2. Nahak N, Dei G, Agrawal R, Choudhury AR (2020) Tuning of governor and damping controller parameters of hydro power station for small signal stability enhancement. In: 2020 International conference on computational intelligence for smart power system and sustainable energy (CISPSSE). Keonjhar, India, pp 1–6
3. Nahak N, Satapathy O (2021) Investigation and damping of electromechanical oscillations for grid integrated micro grid by a novel coordinated governor-fractional power system stabilizer. Energy Sources, Part A: Recovery, Utilization Environ Effects. https://doi.org/10.1080/15567036.2021.1942596
4. Working Group on Prime Mover and Energy Supply (1992) Hydraulic turbineand turbine control models for system dynamic studies. IEEE Trans Power Systems 7(1):167–179
5. Working Group on Prime Mover and Energy Supply Models for System Dynamic Performance Studies (1992) Hydraulic turbine and turbine control models for system dynamic studies. IEEE Trans Power Syst 7(1):167–179
6. Deng L, Zhou XJ, Zhang WH (2009) Hydro turbine prime mover model of governor system for power system stability computation. Autom Electr Power Syst 33(5):103–107
7. Kosterev D (2004) Hydro turbine-governor model validation in pacific northwest. IEEE Trans Power Syst 19(2):1144–1149
8. Pereira L, Kosterev D, Davies D et al (2004) New thermal governor model selection and validation in the WECC. IEEE Trans Power Syst 19(1):517–523
9. Sheng K, Liu FP, Liu WL et al (2012) Influence of steam turbine valve discharge characteristics on power systems and its control strategy. Autom Electr Power Syst 36(7):104–109
10. Kishor N, Saini RP, Singh SP (2007) A review on hydropower plant models and control. Renew Sustain Energy Rev 11(5):776–796
11. Chen YT, Li ZH (2005) State monitoring and status analysis of a hydroturbine governor based on the digitized model. Autom Electr Power Syst 29(9):72–76
12. Wang C, Li JH, Li YY (2013) Low frequency oscillation characteristics of East China power grid after commissioning of Huainan-Shanghai UHV project. Autom Electr Power Syst 37(18):120–125
13. Wen XK, Zhong JL, Qian J (2009) Research on the control strategy for turbine on low-frequency oscillation. Proc CSEE 29(26):107–111
14. Nahak N, Mallick RK (2018) Enhancement of small signal stability of power system using UPFC based damping controller with novel optimized fuzzy PID controller. J Intell Fuzzy Syst 35(1):501–512

15. Nahak N, Nabi MM, Panigrahi D, Pandey RK, Samal A, Mallick RK (2019) Enhancement of dynamic stability of wind energy integrated power system by UPFC based cascaded PI with dual controller. In: 2019 IEEE International conference on sustainable energy technologies and systems. Bhubaneswar, India, pp 150–155
16. Nahak N, Mallick RK (2017) Damping of power system oscillations by a novel DE-GWO optimized dual UPFC controller. Eng Sci Tech Int J 20(4):1275–1284
17. Bhukya J, Mahajan V (2020) Optimization of controllers parameters for damping local area oscillation to enhance the stability of an interconnected system with wind farm. Int J Electr Power Energy Syst 119:105877
18. Mallick RK, Nahak N (2016) Design of GWO optimized dual UPFC controller for damping of power system oscillations. In: 2016 IEEE Uttar Pradesh section international conference on electrical, computer and electronics engineering (UPCON). Varanasi, pp 350–355
19. Nahak N, Praharaj K, Mishra A (2021) Dynamic stability enhancement of a variable solar penetrated power system by fractional UPFC-based controller. In: Favorskaya M, Mekhilef S, Pandey R, Singh N (eds) Innovations in electrical and electronic engineering. Lecture notes in electrical engineering, vol 661. Springer
20. Jain M, Singh V, Rani A (2019) A novel nature-inspired algorithm for optimization: Squirrel search algorithm. Swarm Evol Comput 44:148–175

Optimal LFC of Multi-area Interconnected System Applying PI-PID Cascaded Controller

Moayad Ali Deeb and Manoj Kumar Debnath

Abstract The particle swarm optimization (PSO) tuned PI-PID controllers for load frequency control for the hybrid integrated system of thermal, hydro, and gas power plants, as well as an HDVC connection, are presented in this paper. The purpose of this study is to reduce frequency fluctuations of areas and the power of transmission lines due to failure or sudden load change. With and without the HVDC connection, the system output is evaluated. PI-PID controller gains are also determined using the (PSO) formula with the integral time absolute error (ITAE) as the objective function. Through the PSO, the parameters were obtained in proportion to the performance of the system to achieve the best results for each peak overshoot, settling time, and minimum undershoot. Furthermore, the dynamic output of the proposed system has examined its response to load changes that are considered to be 1% phase load disruption (SLP) implemented in area 1. Finally, it has been found that the efficiency of the controller proposed is higher than that of the controller configured for (DE).

Keywords Automatic generation control · Particle swarm optimization algorithm · Hybrid system · Load frequency control

1 Introduction

Connecting power plants together is implemented for economic purposes and to enhance the stability of the system, creating multiple expanded systems. In this system, the different sources are connected by the transmission lines; and the proper operation of this interconnected power system needs constant monitoring to avoid failures and power losses [1, 2].

A large quantity of literature is available on the LFC of the interconnected power system. The transfer function model of the multi-area thermal power system was proposed by Fosha and Elgerd [3]. Researchers around the world are trying to propose a variety of methods for LFC power systems to preserve the system tie-line flow

M. A. Deeb · M. K. Debnath (✉)
Siksha 'O' Anusandhan Deemed to be University, Bhubaneswar, Odisha, India

M. Mishra et al. (eds.), *Innovation in Electrical Power Engineering, Communication, and Computing Technology*, Lecture Notes in Electrical Engineering 814,
https://doi.org/10.1007/978-981-16-7076-3_6

and frequency at their scheduled values during regular service and even through minor disturbances which include modern control theory [4]. Almost all loops in process industries are managed using the PID control algorithm, which also serves as the basis for many sophisticated control algorithms and strategies. Proportional integral (PI) and proportional integral derivative (PID) controllers are commonly used in industrial modules due to their simplicity, rational cost/benefit ratio, and sufficient performance for a class of process models. The PI and PID controller tuning relationships suggested in the literature are defined in detail [5].

Eberhart and colleagues were the first to implement PSO, which is a population-based optimization process [6, 7]. Also, this algorithm, in its different form, has assumed a great deal of significance in the latest years for the optimization of complex control problems and is commonly used in LFC structure. Analysis of the LFC single and multi-area grids using PSO have been published [8, 9].

HVDC transmission has arisen because of its numerous techno-economic advantages. One of the most frequent HVDC transmission implementations disruptions in the system is the operation of a DC connection parallel to an AC link linking two control areas to boost system dynamic efficiency with higher steadiness edges under minor disturbances [10, 11]. For the LFC analysis of a more functional power grid, the LFC theory of an integrated control system with an AC tie line in parallel with a DC tie line is generalized [12]. The PSO algorithm is designed to optimize PID gains, and a new objective function is designed to measure the optimum controller gain more specifically in the shortest time possible [13]. The transient performance indicates the substantial superiority of the proposed architecture approach.

2 System Investigated

The examined structure consists of a two-area power grid that is interconnected by a transmission line and has processing units and loads in each area. The load disruption in an area influences the frequency of both regions and the load distribution of the communication transmission line, as the two regions are related [14]. Each zone's control scheme needs information about all zones' transient state data in order to restore the local frequency to its constant state value. Changes in that region's output frequency or the transmission line's power fluctuation include data from another area. The transmission line power is therefore measured and, since this power must be controlled, the measured signal is sent as feedback to the two-zone local controller [15]. The controller area (ACE) for the controllers, it serves as the actuating signal used in the model. The ACE is expressed in each of the areas presented as:

$$\mathrm{ACE}_1 = \Delta P_{\mathrm{tie}1-2} + B_1 * \Delta f_1 \tag{1}$$

$$\mathrm{ACE}_2 = \Delta P_{\mathrm{tie}2-1} + B_2 * \Delta f_2 \tag{2}$$

where ΔP_{tie} is interline power oscillation in both areas, the frequency bias coefficients of the corresponding regions are, respectively, $B1$ and $B2$. Δf_1 along with Δf_2 distinctive-area frequency oscillations. The rated values are taken from the published article of all the parameters considered in the examined model [16]. Figure 1 demonstrates a multi-source multi-area transition function model with an HVDC relationship and an integral controller.

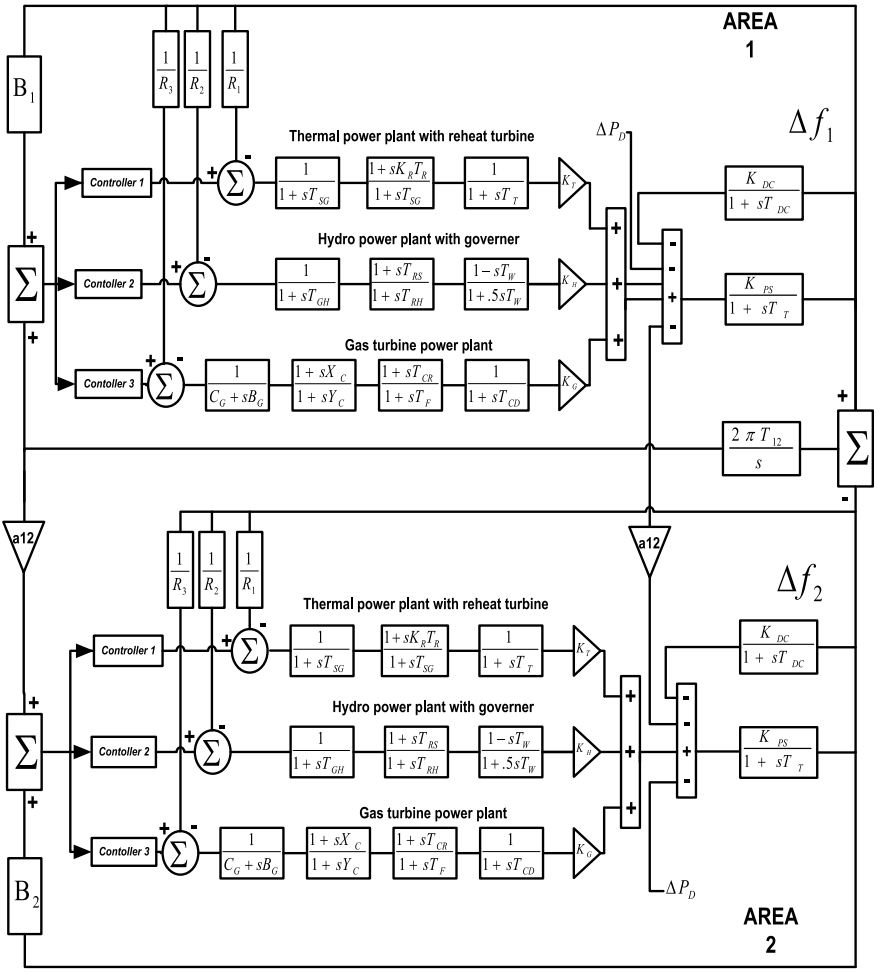

Fig. 1 Transfer function model of a multi-source multi-area with HVDC link

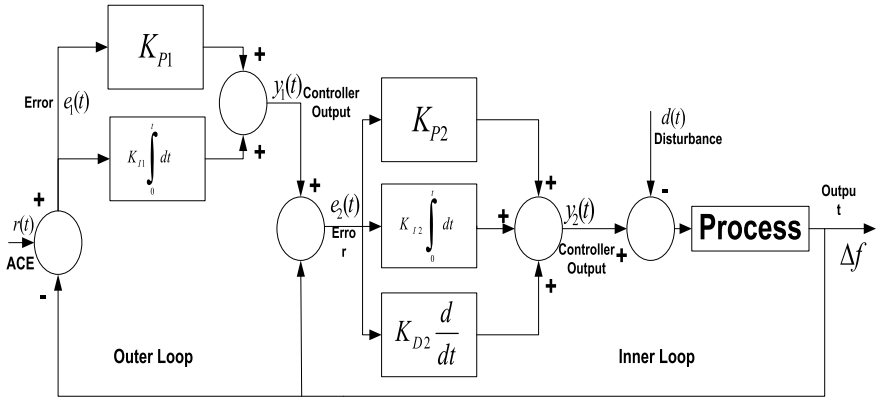

Fig. 2 Configuration of PI-PID controller

3 Controller Structure (PI-PID Cascaded Controller)

The lack of derivative action makes PI controllers less noise-sensitive and more desirable than PID controllers. The PI + PID dual loop controller essentially integrates two sequential inner and outer loops into one loop [17]. The internal process dampens any disturbance in the internal process, while the external process controls the performance of the finished product. The primary objective of using a double loop controller is to reject initial disturbances until they propagate across the farm. The modest PD + PID controller with inner and outer loops is seen in Fig. 2.

The master loop is the name given to the main outer loop. The inner process's output becomes the outer process's input. The process' output is controlled to obey the fixed point's signal. Load disruption is added to the whole system.

The slave loop is a type of secondary inner loop. The inner comparator is used to control the inner step of the inner loop, and the inner loop's output is y_2 (t). Here, y_1 (t) is the inner process's input. Before causing damage to the outside phase, the inner loop corrects the disruptions in the system. As a consequence, the inner loop should react much faster than the outer loop to fulfill the above argument.

4 Result and Discussion

PSO [18] algorithm is used to tune the controller parameters of hybrid source system in the presence of HVAC and HVDC links.

Table 1 Controller parameters for the system

PID									
DE [16]	K_{P1}	K_{I1}	K_{D1}	K_{P2}	K_{I2}	K_{D2}	K_{P3}	K_{I3}	K_{D3}
	0.779	0.2762	0.6894	0.5805	0.2291	0.7079	0.5023	0.9529	0.6569
PI-PID									
PSO	K_{P1}	K_{I1}	K_{D1}	K_{P2}	K_{I2}	K_{D2}	K_{P3}	K_{I3}	K_{D3}
	3.1978	3.9862	3.3859	0.5922	1.0110	0.6701	4.4955	4.6887	4.5700
	K_{P11}	K_{I11}		K_{P22}	K_{I22}		K_{P33}	K_{I33}	
	4.7141	0.9107		0.8117	4.1235		0.8484	2.0680	

4.1 Multi-area Without HVDC Link

Due to its fast-settling functionality, with the support of the following evaluative fitness feature, the PI-PID cascade controller configured by PSO is equipped for load frequency control and tie-power regulation (integral time absolute error). In this analysis, the optimal KP, KI, and KD parameter values for PI-PID controllers are determined conveniently and correctly using a PSO under the evaluated limits [K min $= 0.1$, K max $= 5$] Table 1. The limits of the settling time in the simulation are bigger than 0.05% for both Δf_1 and Δf_2 and 0.01% for ΔP_{tie}.The objectives of good oscillation damping are to monitor frequency and inter-area tie-power, as well as to achieve good efficiency. An unexpected disturbance of the load at 0.01 p.u. in control area 1 is applied. ITAE is represented by the equation:

$$\text{ITAE} = \int (|\Delta f_1| + |\Delta f_2| + |\Delta P_{\text{tie}}|)t.\text{d}t \tag{3}$$

The results obtained in Table 2 for settling time, peak overshoot, and undershoot get through tuning PI-PID by PSO algorithm better performance for a system that makes it superior on peer DE-PID. These satisfactory results were obtained in 50 iterations that lasted 558.199 s. The oscillations of system frequency in area 1, area 2, and the variations of tie-line strength between area 1 and area 2 are seen in Figs. 3, 4, and 5, respectively.

4.2 Multi-area with HVDC Link

By considering the HVDC Link, Tables 3 and 4 show the parameters and results of the analysis of system behavior are studied. To ensure that the system is stable, the load in area 1 is increased by 1%. Figures 6, 7 and 8 display the tie-line amplitude variations in areas 1 and 2 and the system frequency oscillations in areas 1 and 2. Thus, the superiority of the PSO (PI-PID) model over DE-PID is obtained in this situation.

Table 2 System performances for DE-PID controller and PSO (PI-PID) for 1% load at area 1 with AC tie line only

Abnormalities	Time-domain factors	DE-PID	PSO-PID
Δf_1	T_s (s)	13.9200	4.1500
	Overshoot ($O_{sh} \times 10^{-3}$)	0.0020	0.00011
	Undershoots	−0.0266	−0.0042
Δf_2	T_s (s)	8.4800	1.6400
	Overshoot ($O_{sh} \times 10^{-3}$)	0.0008	0.0004
	Undershoots	−0.0221	−0.0006
ΔP_{tie}	T_s (s)	31.9600	6.3500
	Overshoot ($O_{sh} \times 10^{-3}$)	0.0002	0.0003
	Undershoots	−0.0048	−0.0004

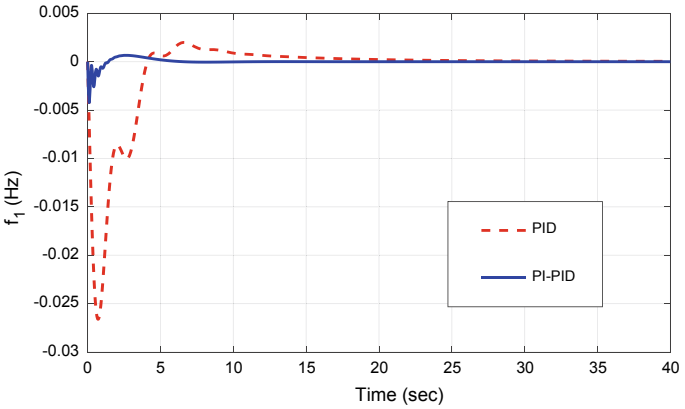

Fig. 3 Rate of frequency oscillation in region 1 with changes in loading

5 Conclusion

This paper presents a model of a power system that contains two areas connected by the tie-line power and each zone contains various plants which are hydro, thermal, and gas; also, there is an HDVC link with the system, where the following algorithm was used PSO (PI-PID) with cascade controller to obtain good results for system performance through to changes in the sudden load that leads to frequency deviations and compared it with DE (PID). Thus, the results that were obtained by PSO (PI-PID) provided good performance and reliability for the proposed system and better than the result that was getting by DE (PID), with two different operating modes one with consider the HVDC link and two without the HVDC link.

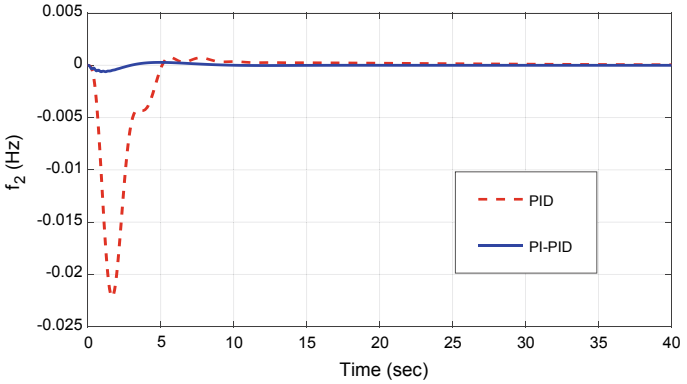

Fig. 4 Rate of frequency oscillation in region 2 with changes loading

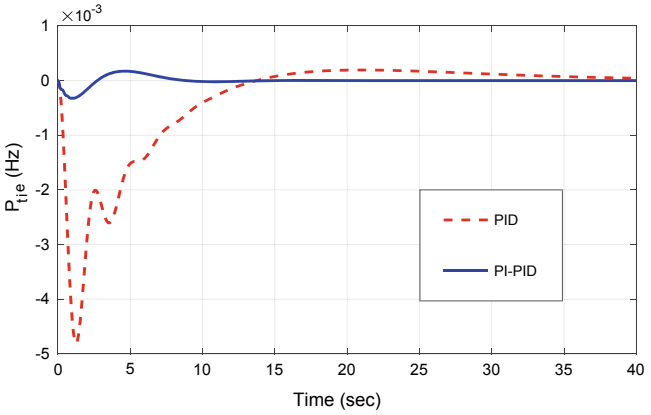

Fig. 5 Rate of frequency oscillation in interline power with changes loading

Table 3 Controller parameters for the system

PID									
DE [16]	K_{P1}	K_{I1}	K_{D1}	K_{P2}	K_{I2}	K_{D2}	K_{P3}	K_{I3}	K_{D3}
	1.6929	1.9923	0.8269	1.7773	0.7091	0.4355	0.9094	1.9425	0.2513
PI-PID									
PSO	K_{P1}	K_{I1}	K_{D1}	K_{P2}	K_{I2}	K_{D2}	K_{P3}	K_{I3}	K_{D3}
	4.4585	0.3046	4.8653	4.1466	0.1877	0.3817	3.3973	4.4250	1.0238
	K_{P11}	K_{I11}		K_{P22}	K_{I22}		K_{P33}	K_{I33}	
	3.1260	4.1145		3.0488	2.1312		0.5300	3.2325	

Table 4 System performances for DE-PID controller and PSO(PI-PID) for 1% load at area 1

Abnormalities	Time-domain factors	DE(PID)	PSO(PI-PID)
Δf_1	T_s (s)	3.2300	3.6300
	Overshoot ($O_{sh} \times 10^{-3}$)	0.3807	0.5430
	Undershoots	−0.0118	−0.0040
Δf_2	T_s (s)	13.4000	1.2000
	Overshoot ($O_{sh} \times 10^{-3}$)	0.5507	0.2930
	Undershoots	−0.0025	−0.0005
ΔP_{tie}	T_s (s)	14.2300	6.9600
	Overshoot ($O_{sh} \times 10^{-3}$)	0.5488	0.1911
	Undershoots	−0.0018	−0.0003

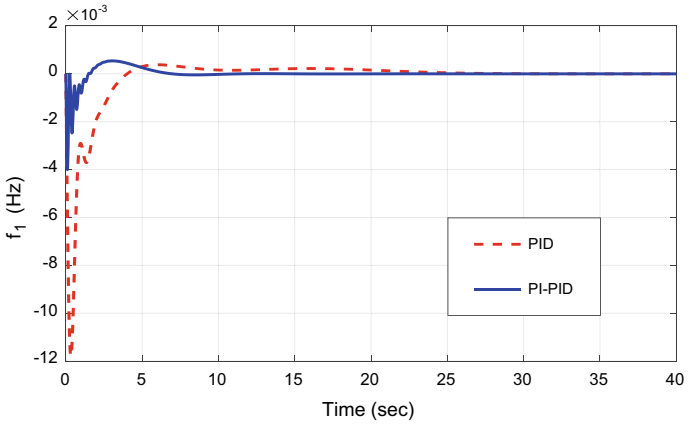

Fig. 6 Rate of frequency oscillation in region 1 with changes loading

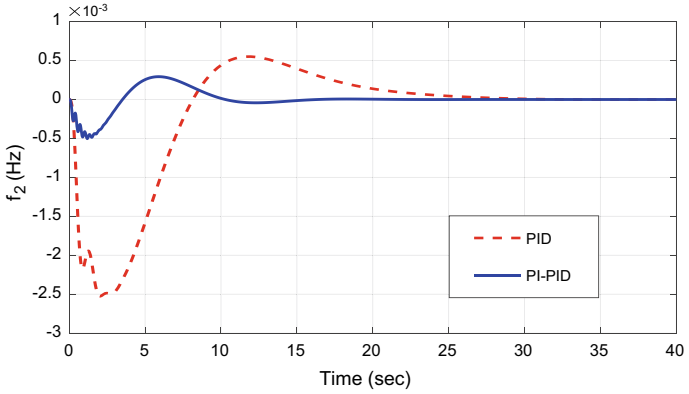

Fig. 7 Rate of frequency oscillation in region 2 with changes loading

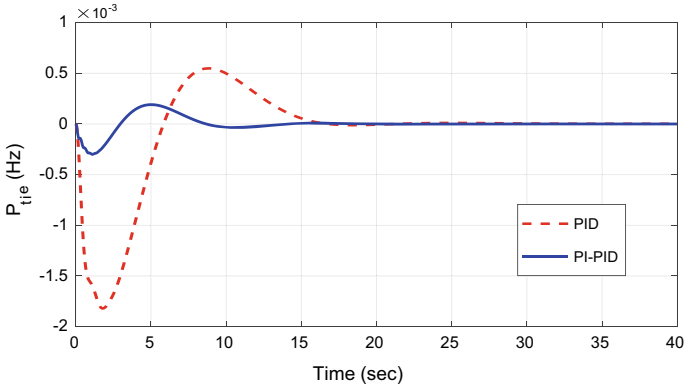

Fig. 8 Rate of frequency oscillation in Interline power with changes loading

Appendix

$B_1 = B_2 = 0.4312$ P.U. MW/Hz; $P_{RT} = 2000$ MW; $P_L = 1840$ MW; $R_1 = R_2 = R_3 = 2.4$ Hz/p.u.; $T_{SG} = 0.08$ s; $T_T = 0.3$ s; $K_R = 0.3$; $T_R = 10$ s; $K_{PS1} = K_{PS2} = 68.9566$ Hz/p.u. MW; $T_{PS1} = T_{PS2} = 11.49$ s; $T_{12} = 0.0433$; $A12 = 1$; $T_W = 1$ s; $T_{RS} = 5$ s; $T_{RH} = 28.75$ s; $T_{GH} = 0.2$ s; $X_C = 0.6$ s; $Y_C = 1$ s; $C_G = 1$; $B_G = 0.05$ s; $T_F = 0.23$ s; $T_{CR} = 0.01$ s; $T_{CD} = 0.2$ s; $K_T = 0.54347$; $K_H = 0.32608$; $K_G = 0.13043$; $K_{DC} = 1$; $T_{DC} = 0.2$ s.

References

1. Kothari DP, Nagrath IJ (2011) Modern power system analysis, 4th edn. McGraw Hill, New Delhi
2. Kundur P (2008) Power system stability and control. Fifth reprint. Tata McGraw Hill, New Delhi
3. Fosha E, Elgerd O (1970) The Megawatt-frequency control problem: a new approach via optimal control theory. IEEE Trans Power Appar Syst 89(4):563–577
4. Parmar KPS, Majhi S, Kothari DP (2012) Load frequency control of a realistic power system with multi-source power generation. Int J Elect Power Energy Syst 42:426–433
5. O'Dwyer A (2006) Handbook of PI and PID controller tuning rules. Imperial College Press, UK
6. Kennedy J, Eberhart RC (1995) Particles swarm optimization. In: Proceedings of IEEE International conference on neural networks, Perth Australia. IEEE Service Center, Piscataway, NJ, IV, pp 1942–1948
7. Eberhart RC, Kennedy J (1995) A new optimizer using particles swarm theory. In: Proceedings of sixth international symposium on micro machine and human science, Nagoya-Japan. IEEE Service Center, Piscataway, NJ, pp 39–43
8. Gautam SK, Goyal N (2010) Improved particle swarm optimization based load frequency control in a single area power system. In: 2010 Annual IEEE India conference (INDICON), pp 1–4
9. Jadhav AM, Vadirajacharya K (2012) Performance verification of PID controller in an interconnected power system using particle swarm optimization. Energy Procedia 14:2075–2080
10. Ganapathy S, Velusami S (2009) Design of MOEA based decentralized load-frequency controllers for interconnected power systems with ACDC parallel tielines. Int J Recent Trends Eng 2(5):357–361
11. Kumar P, Ibraheem (1998) Dynamic performance evaluation of 2-area interconnected power systems: a comparative study. J Inst Eng (India) Electr Eng Div 78:199–209
12. Ramesh S, Krishnan A (2010) Fuzzy rule based load frequency control in a parallel AC DC interconnected power systems through HVDC link. Int J Comput Appl 1(4)
13. Bouallègue S, Haggège J, Ayadi M, Benrejeb M (2012) PID-type fuzzy logic controller tuning based on particle swarm optimization. Eng Appl Artif Intell 25(3):484–493
14. Bhatt P, Ghoshal S, Roy R (2010) Load frequency stabilization by coordinated control of thyristor controlled phase shifters and superconducting magnetic energy storage for three types of interconnected two-area power systems. Int J Electr Power Energy Syst 32:1111–1124
15. Fosha CE, Elgerd OI (1970) The megawatt–frequency control theory. IEEE Trans Power Appl Syst 89:563–571
16. Mohanty B, Panda S, Hota PK (2014) Controller parameters tuning of differential evolution algorithm and its application to load frequency control of multi-source power system. Int J Electr Power Energy Syst 54:77–85
17. Irshad M, Ali A (2018) Optimal tuning rules for PI/PID controllers for inverse response processes. IFAC-PapersOnLine 51(1):413–418
18. Kennedy J, Eberhart R (1995) Particle swarm optimization. In: Proceedings of ICNN'95-international conference on neural networks, vol 4. IEEE

A Novel Fuzzy-Based Model Predictive Adaptive Controller for a PMSG Wind Turbine

Gayatri Mohapatra and Manoj Kumar Debnath

Abstract Wind system has become a reliable and important system to generate power in the recent years. In case of variable wind speed, the conventional method to control the turbine output is quite difficult, which leads to the generation of adaptive control. The proposed model predictive-based adaptive controller improves the performance of systems in terms of the active power stability. This paper imposed a controller based on the concept of prediction of reference values generated by fuzzy using MATLAB/SIMULINK environment on a wind turbine generator. The said technique helps in boosting the PMSG-based wind power industry.

Keywords PMSG wind turbine · MPAC · Fuzzy · Multilevel inverter

Nomenclature

Symbol	Meaning
V_{ds}^{k}	Stator voltage d-axis component for kth instant
R_s	Stator resistance
V_{abcs}	Stator voltage in abc component
i_{abcs}	Stator current in abc component
i_{abcs}	Stator current in abc component
i_{ds}^{k}	Stator current d-axis component for kth instant
i_{ds}^{k}	Stator current d-axis component for kth instant
w_r	Rotor speed in rad/s
J^*	Reference moment of inertia
J	Actual moment of Inertia
λ_{mabcs}	Magnetic flux linkage in abc frame
$\overset{*}{\underset{k}{\omega}}$	Reference rotor speed in rad/s
F	Viscous damping

G. Mohapatra · M. K. Debnath (✉)
Siksha 'O' Anusandhan Deemed To Be University, Bhubaneswar, Odisha, India

M. Mishra et al. (eds.), *Innovation in Electrical Power Engineering, Communication, and Computing Technology*, Lecture Notes in Electrical Engineering 814,
https://doi.org/10.1007/978-981-16-7076-3_7

L_s	Stator Inductance
n_p	No of pole
δ	Torque angle
θ_r	Rotor field angle
λ_m	Magnetic flux linkage
$\overset{*}{T}$	Reference Torque
T_g	Actual Torque
$\overset{*}{e}(t)^k$	Reference error
ξ_{ds}^k	Damping coefficient
x	State vector
$\hat{T}$	Actual Torque

1 Introduction

The renewable energy, in the form of wind generating system, had the "lowest relative greenhouse gas emissions, with the least water consumption demands and the most favorable social impacts" compared to other form of renewable energy. A wind turbine, which acts as a wind energy converter, converting the kinetic energy embedded in wind to electrical form and is classified in vertical and horizontal axis types. The wind turbines find their applications from battery charging to generating domestic power supply, in the same time selling the surplus to grid [1–4]. Due to the unpredictable nature of wind, the predictability of the output power will be difficult without a controller, which needs to make the system very much robust and efficient. The PMSG-based wind system becomes popular due to their variable speed and low maintenance [5–8]. In spite of this, different types of controllers are experimented in the same but the proposed one finds the advantages with predictive controller replacing the PI controller [9–11].

As in [6], detection of the sub-synchronous interactions of the PI parameters in a DFIG is done with non-dominated sorting genetic algorithm (NSGA-III) and the t-distributed stochastic neighbor embedding (t-SNE). Also, the study of the behavior is done for different disturbance. A clear adaptable fuzzy logic controller for the offshore voltage source converter generating station interconnected to a high-voltage DC (HVDC) system, with real-time data obtained for the wind turbine as in paper [7] to obtain realistic response. In paper [9], a customized wide band prediction limit is derived for CHB inverter. The proposed controller in [10] allows both stand-alone and grid-tied operations for voltage–frequency control. In paper [11], a distinct fuzzy logic-based novel firing method for PSWM-based cascaded multi-level inverter for symmetric and asymmetric operations is proposed. A tradeoff between APO and THD of grid components is presented in [12] with a novel adaptable reference input generation to reduce the active power oscillation. This paper [13] delivers a type-2 fuzzy-based direct torque control of the IM drive, with a two-level inverter with

hybrid delay angle modification. In the papers [14, 15], MPC for the T-type inverter with LC filter is proposed to reduce the control variables making the design cost-effective. The paper [16] employs power generation and filtration of a DFIG-based generator with an improved harmonic time-variant isolator.

Model predictive adaptive controller (MPAC) is the basic method which can provide a straightforward controller implementation with very less data computation. In the traditional controllers, the proportional and integral (PI) tuning is adopted but the MPAC predictive method estimates the next possible state to tune the regulator. The limitation of inaccurate and tedious tuning of PI regulator leads to the development of a new MRACS for PMSG wind turbines with the objectives as discussed below:

- An upgraded model predictive control for PMSGs.
- This also patterned a new thriving framework to tune the controller by combining a back-EMF with an I-F controller.
- This also optimizes the output by using fuzzy controller combined with the MPAC.

2 System Investigated

As in Fig. 1, the reference values of dq are given to the predictive controller and then adaptive control is generating the required gate pulse as per Eqs. 1, 2, 3, 4, and 5 described below.

$$\begin{aligned} V_{\mathrm{ds}}^{k} &= (R_s + \delta R_s) i_{\mathrm{ds}}^{k} + (L_s + \delta L_s) \frac{i_{\mathrm{ds}}^{k+1} - i_{\mathrm{ds}}^{k}}{T_s} - (L_s + \delta L_s) w_r i_{\mathrm{qs}}^{k} + \xi_{\mathrm{ds}}^{k} \\ V_{\mathrm{qs}}^{k} &= (R_s + \delta R_s) i_{\mathrm{qs}}^{k} + (L_s + \delta L_s) \frac{i_{\mathrm{qs}}^{k+1} - i_{\mathrm{qs}}^{k}}{T_s} - (L_s + \delta L_s) w_r i_{\mathrm{ds}}^{k} + \xi_{\mathrm{qs}}^{k} \end{aligned} \tag{1}$$

$$V_{\mathrm{abcs}} = \frac{d}{dt} \lambda_{mabcs}(\theta_r) - r_s i_{\mathrm{abcs}} - \frac{d}{dt} (L_s(\theta_r) i_{\mathrm{abcs}}) \tag{2}$$

$$T_g = \frac{3}{2} n_p [\lambda_m + (L_d - L_q) i_d] i_q \tag{3}$$

$$g = (\hat{T} - \overset{*}{T})^2 + \lambda (\hat{\varphi} - \overset{*}{\varphi})^2 \tag{4}$$

$$g = |F(\widehat{i_L} - \overset{*}{i_L})| \tag{5}$$

3 Controller Structures and Their Optimal Design

Predictive control describes as shown in Fig. 2 that finds its advantages in all the areas of the power engineering. It also finds its suitability of being helpful in estimating

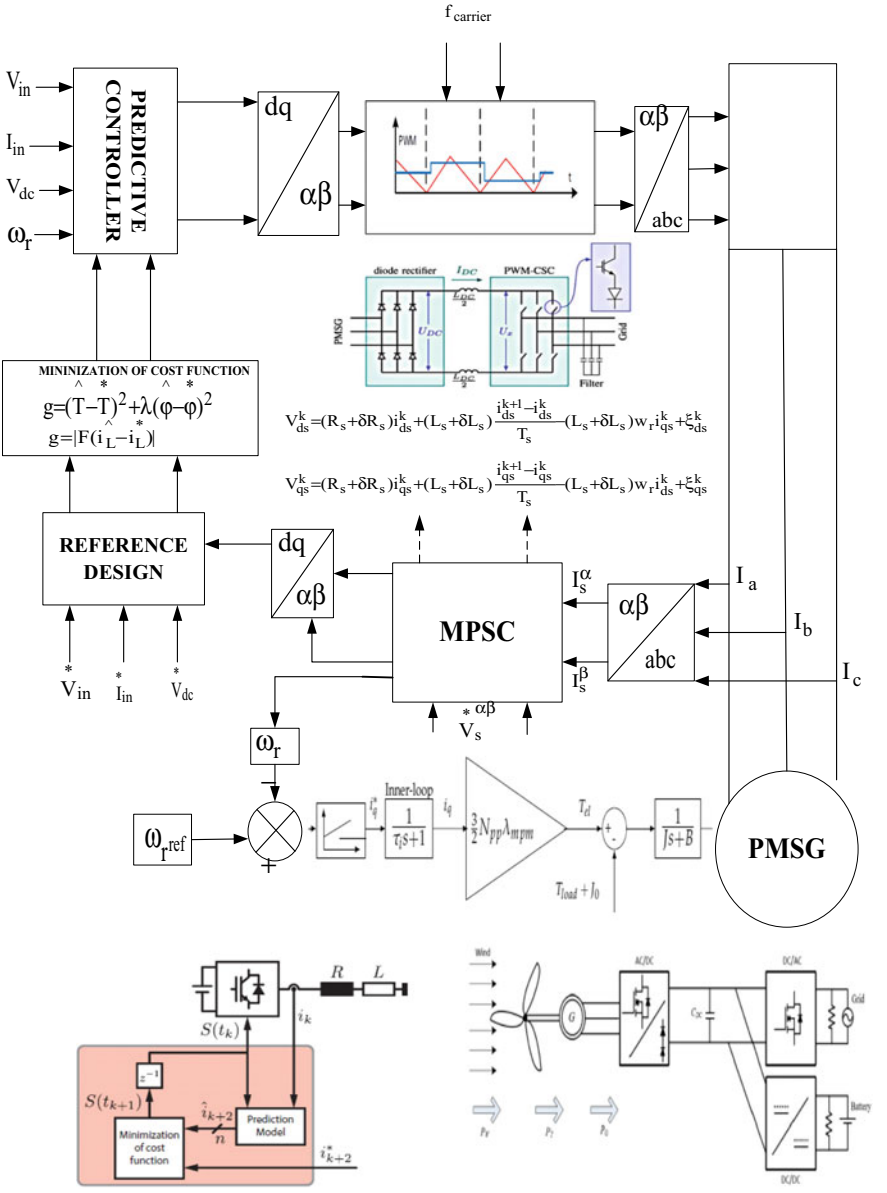

Fig. 1 Describes the complete block diagram of the system

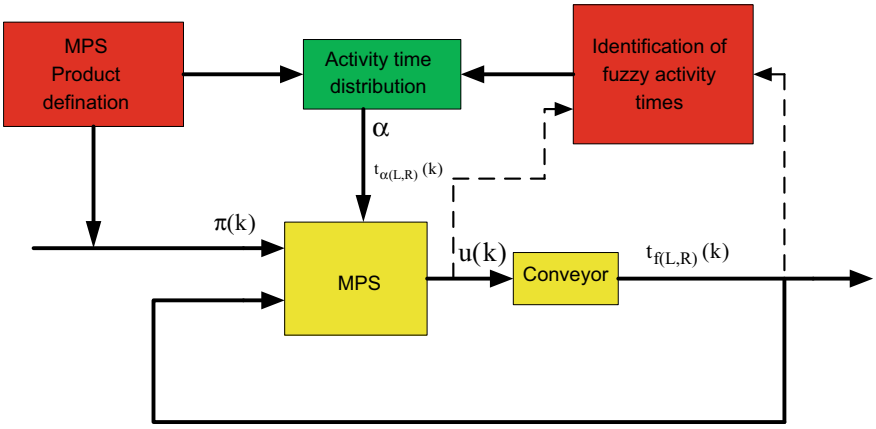

Fig. 2 Describes the complete block diagram of the MPC controller

the upcoming state of the control variable. The selection of the horizon that needs to be used can be done with the help of any optimization tool of fuzzy approach. Longer predictive horizon improves the closed-loop response that can be obtained by considering the minimized cost function as the objective of the optimization as given in Eqs.6, 7, and 8.

$$U_x(k) = [u_x^T(k)u_x^T(k+1)\ldots\ldots u_x^T(k+N_p-1), U_x = U_{x\in}^{N_p} \tag{6}$$

$$J(x(k), U_x(k)) = \sum_{l=k}^{k+N_p-1} J^*(x(l+1), u_x(l)) \tag{7}$$

$$J = \text{Minimize}(\sum_{k=1}^{N} \overset{*}{J}_{t+k|_t} + \sum_{k=1}^{N} \overset{*}{J}_t + w_{g\in_{t+k|_t}}) \tag{8}$$

4 Fuzzy Logic Controller

In this controller, five MFs are described as n-big (n2), n-small (n1), zero (z), p-small (p1), and p-big (p2) as given in Fig. 3 as well as the rule set. This controller needs (MFs) ^2 sets of rules to reproduce the fuzzy output. The rule set for the controller is depicted as per the output requirement in a Mamdani inference system. The fuzzy logic selected on the error and the current error is given in Eqs. 9 and 10.

$$e(t)^k = \overset{*}{\omega}_k - \omega_k, \overset{*}{e(t)} = e(t)^k - e(t)^{k-1} \tag{9}$$

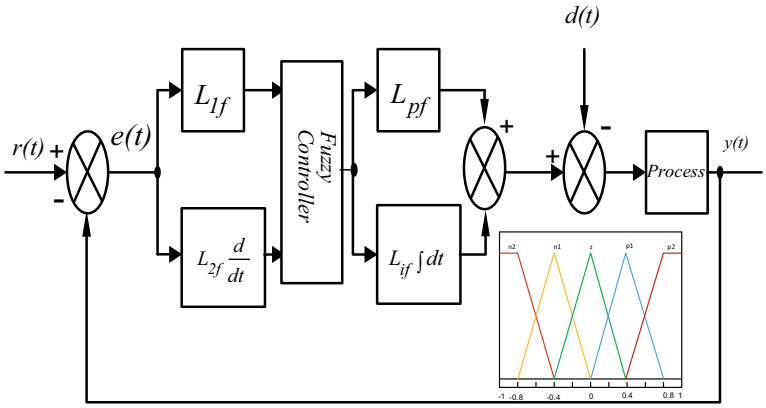

Fig. 3 Describes the complete block diagram of the fuzzy system

$$i_{\mathrm{dqrk}}(t) = \underset{dqr(k-1)}{\overset{*}{i}} + \partial \underset{\mathrm{dqrk}}{\overset{*}{i}} \tag{10}$$

5 Result and Discussion

In the proposed adaptive control strategy, the I-F method of control is applied, where the alignment of dq parameter allows the flux and torque is to be controlled independently. The electrical parameters can attain their steady-state parameters after a period of 0.18 s. Figures 4, 5, and 6 represent the response of the wind turbine, THD, and current error of the proposed and conventional system and the speed error and speed of the proposed and conventional system, respectively.

6 Conclusion

The MRAS controller as applied in the paper generates a combination of the deadbeat predictive MRAS controller for estimating the position and speed of the PMSG rotor. The wind turbine finds the better response in the proposed controller as compared to the conventional one. This controller has great aptitude to improve the dynamics and efficiency of wind turbine generators, thus encouraging the uptake of wind power industry.

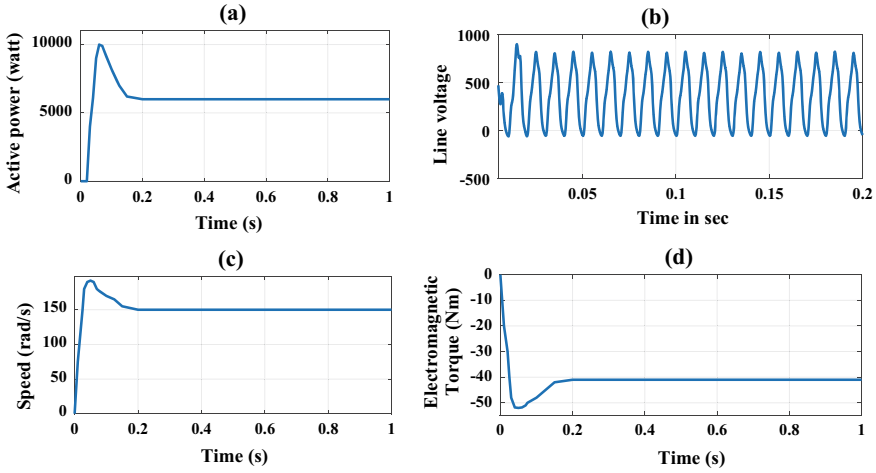

Fig. 4 Describes the response of the wind turbine system

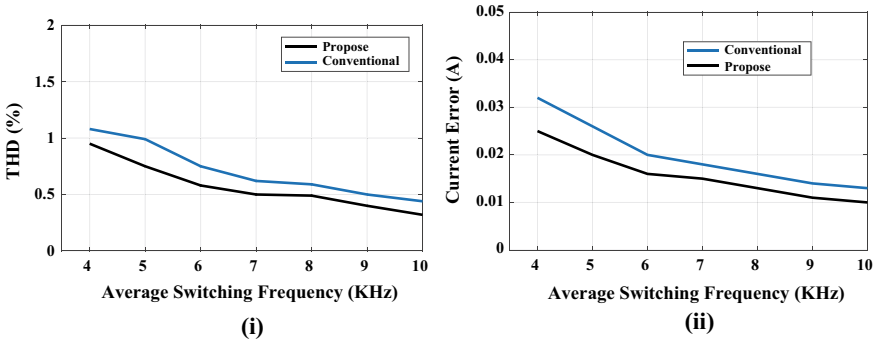

Fig. 5 Describes THD and current error of the proposed and conventional system

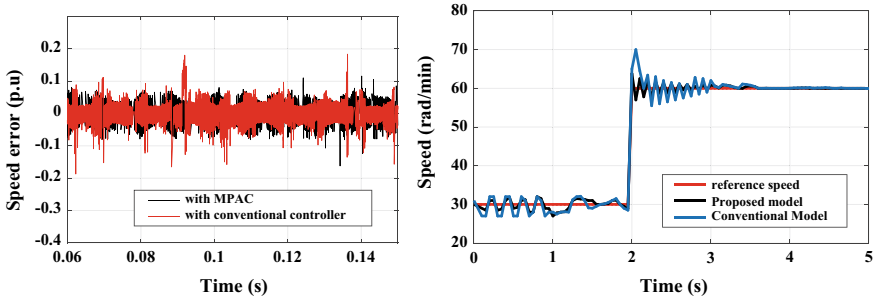

Fig. 6 Describes the speed error and speed of the proposed and conventional system

Appendix

Parameter	Value	Parameter	Value
Power	6000 W	Base Power	9444.44 VA
Speed	153 rad/s	wind speed	12 m/s
Resistance of stator	0.425Ω	No of Pole	4
Flux of rotor coil	0.433wb	Inertia	0.01197 kg m2
Armature inductance	0.000395 H	Density of air	1.225 kg m3
Viscous damping	0.001189 Nms	Stator Inductance	0.000835 H
Swept area	1.06 m^2		

References

1. Kundur P, Balu NJ, Lauby MG (1994) Power system stability and control, vol 7. McGraw-Hill, New York
2. Rodriguez J, Cortes P (2012) Predictive control of power converters and electrical drives, vol 40. Wiley
3. Mohapatra G, Debnath MK (2021) Implementation of fuzzy hysteresis controller for a three-phase photovoltaic multilevel inverter. In Green technology for smart city and society. Springer, Singapore, pp. 129–141
4. Mohapatra G (Mar 2018) Current control of a PV integrated CHB-multilevel inverter using PR controller. In 2018 Technologies for Smart-City Energy Security and Power (ICSESP), IEEE, pp. 1–6
5. Mohapatra G, Debnath MK, Mohapatra KK (2020) Application of 2DOF and 3DOF controller for LFC analysis in multi-generation system. In Innovation in electrical power engineering, communication, and computing technology. Springer, Singapore, pp. 521–529
6. Chen A, Xie D, Zhang D, Gu C, Wang K (2018) PI parameter tuning of converters for sub-synchronous interactions existing in grid-connected DFIG wind turbines. IEEE Trans Power Electron 34(7):6345–6355
7. Muyeen SM, Takahashi R, Tamura J (2010) Operation and control of HVDC-connected offshore wind farm. IEEE Trans Sustain Energy 1(1):30–37
8. Mishra M, Rout PK (2016) Time-frequency analysis based approach to islanding detection in micro-grid system. Int. Rev. Electr. Eng. (IREE) 11(1):116–129
9. Baidya R, Aguilera RP, Acuna P, Vazquez S, du Toit Mouton H (2017) Multistep model predictive control for cascaded h-bridge inverters: formulation and analysis. IEEE Trans Power Electron 33(1):876–886
10. Neves RV, Machado RQ, Oliveira VA, Wang X, Blaabjerg F (2018) Multitask fuzzy secondary controller for AC microgrid operating in stand-alone and grid-tied mode. IEEE Trans Smart Grid 10(5):5640–5649
11. Azeem H, Yellasiri S, Jammala V, Naik BS, Panda AK (2019) A fuzzy logic based switching methodology for a cascaded H-bridge multi-level inverter. IEEE Trans Power Electron 34(10):9360–9364
12. Mohapatra SR, Agarwal V (2019) Model predictive control for flexible reduction of active power oscillation in grid-tied multilevel inverters under unbalanced and distorted microgrid conditions. IEEE Trans Ind Appl 56(2):1107–1115

13. Singh SP, Panda AK (2020) An interval type-2 fuzzy-based DTC of IMD using hybrid duty ratio control. IEEE Trans Power Electron 35(8):8443–8451
14. Ngo VQB, Nguyen MK, Tran TT, Lim YC, Choi JH (2019) A simplified model predictive control for T-type inverter with output LC filter. Energies 12(1):31
15. Chan R, Kwak S (2017) Model-based predictive current control method with constant switching frequency for single-phase voltage source inverters. Energies 10(11):1927
16. Kesraoui M, Chaib A, Meziane A, Boulezaz A (2014) Using a DFIG based wind turbine for grid current harmonics filtering. Energy Convers Manage 78:968–975

Feasibility Study of a Floating Solar Photovoltaic System in Odisha, India

Sonali Goel, Saumya Ranjan Lenka, and Renu Sharma

Abstract India has huge potential to harness solar energy by means of floating solar photovoltaic plant for sustainable energy production. India is encouraging for installation of floating solar power plant in order to increase the share of renewable energy. In this paper, analysis of a 12 kW proposed floating solar photovoltaic system for the Jhumka Dam reservoir near Bhubaneswar ($20^0 18' 54.8'' N\ 85^0 41' 17.82'' E$) is performed by using PVsyst 7.1 software. The findings suggest the floating solar photovoltaic system for electricity generation economical with a levelized cost of energy of INR 9.35/kWh with payback period of 11.9 years and 78.2% return on investment.

Keywords Floating solar panel · Feasibility study · Levelized cost · Payback period

1 Introduction

The floating solar power plant is an emerging method to use solar photovoltaic module to float over the water bodies for energy generation instead of using the land or rooftop for installation. Installation of floating solar photovoltaic (FSPV) over water bodies like pond, lake, and reservoir will not only reduce the dependency of land use for solar power plant but also increase the module efficiency due to lower module temperature. In addition to this, evaporation loss is reduced from the water bodies, thereby conserving water. It is important to affix solar panel to a buoyant structure which holds them above the surface [1]. Installing floating solar PV plants on water reservoir, irrigation canal, large pond, fish farm, and lakes will save the equivalent land space for alternative use. It has become a new concept after its first patent

S. Goel (✉) · S. R. Lenka · R. Sharma
Department of Electrical Engineering, ITER, Siksha 'O' Anusandhan Deemed To Be University, Bhubaneswar, Odisha 751030, India

R. Sharma
e-mail: renusharma@soa.ac.in

M. Mishra et al. (eds.), *Innovation in Electrical Power Engineering, Communication, and Computing Technology*, Lecture Notes in Electrical Engineering 814,
https://doi.org/10.1007/978-981-16-7076-3_8

Fig. 1 Few FSPV installation across India

was registered for this form of technology in 2008. Since then in the countries like Japan, China, UK, the floating solar has been installed predominately. Compared to ground-mounted solar panel, floating solar photovoltaic panels have various benefits like higher energy generation efficiency up to 11%, least or no shading effect, reduce water evaporation, environmental benefit, and no requirement of land space. Few FSPV installation across India is shown in Fig. 1.

1.1 Present Status of Floating Solar Panel in India

The FSPV technology is gaining its popularity in India. The first 10 kW floating solar power system was set up in Rajarhat, Kolkata, in the year 2015 for research activities with a financial assistance from the Ministry of New and Renewable Energy (MNRE), India. Damodar Valley Corporation has started installing 1776 MW of floating solar projects at four of its dams in the state of West Bengal and Jharkhand, while in 2016, 100 kW floating solar power plant was installed by NTPC in Kerala's Kayamkulam District. During the same year, Kerala State Electricity Board installed 500 kW FSPV plant at Banasura Sagar reservoir [2]. Recently the 2 MW FSPV plant, the largest in India till date has been installed at Visakhapatnam, Andhra Pradesh, and with this installation, the total installed capacity of FSPV in the country has reached to 2.7 MW.

By 2022–23, the world's largest floating 600 MW solar power plant is to be set up on a reservoir on Omkareshwar Dam on the Narmada River in Khandwa District of Madhya Pradesh. The 2000 hector project would cost an estimated INR 30 billion [3, 5].

The Energy and Resources Institute (TERI) has conducted a survey to estimate the country's FSPV capacity. Around 18,000 km^2 of water surface area across different states and UTs has been identified for the construction of FSPV plants. The total potential of FSPV to the tune of about 280 GW is possible. In Odisha, there is a FSPV power potential of 21,859 MW from 142 reservoirs (Fig. 2).

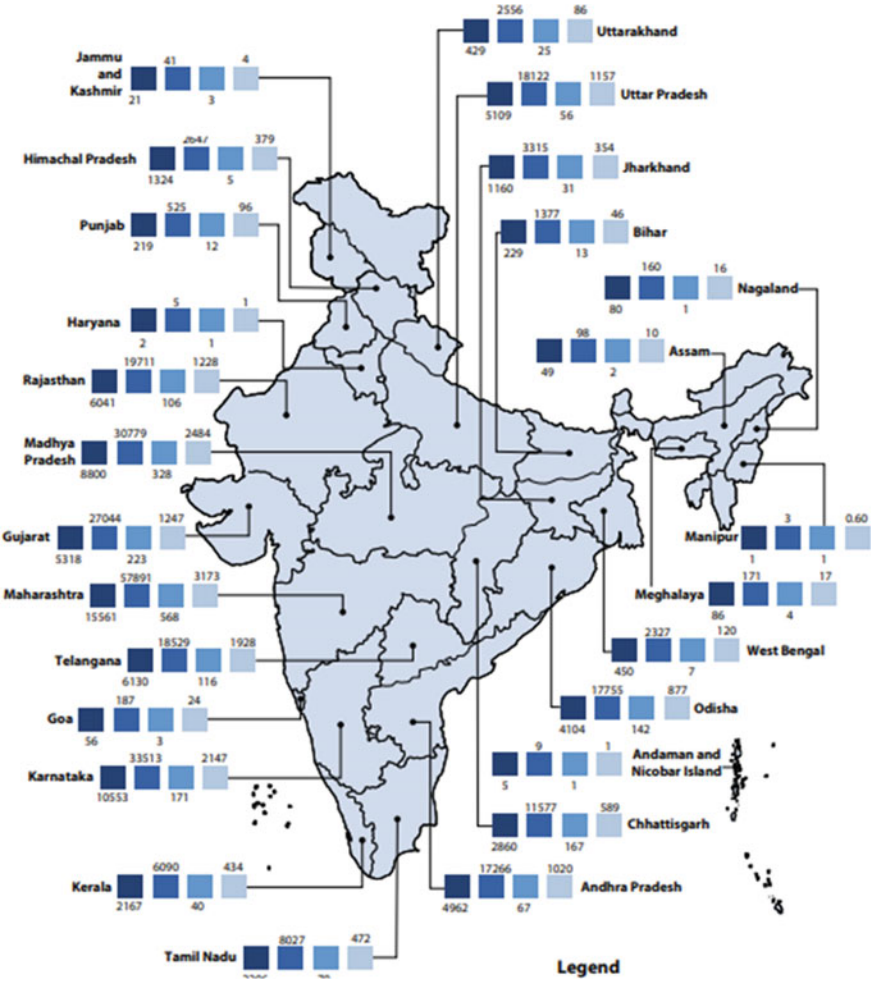

Fig. 2 FSPV installation potential across India [6]

1.2 Major Components of Floating Solar Photovoltaics

The technology used in floating solar power system is similar to that of ground-mounted or rooftop solar plant but in FSPV, floating platform made up of polyvinyl chloride (PVC), steel, etc., is used for mounting solar modules [7]. Multiple floating platforms are connected with specially designated walkways to allow the access of operators or technicians for operation and maintenance. These connected floating platforms are anchored to the shore, to the bottom of the water body, or to floating

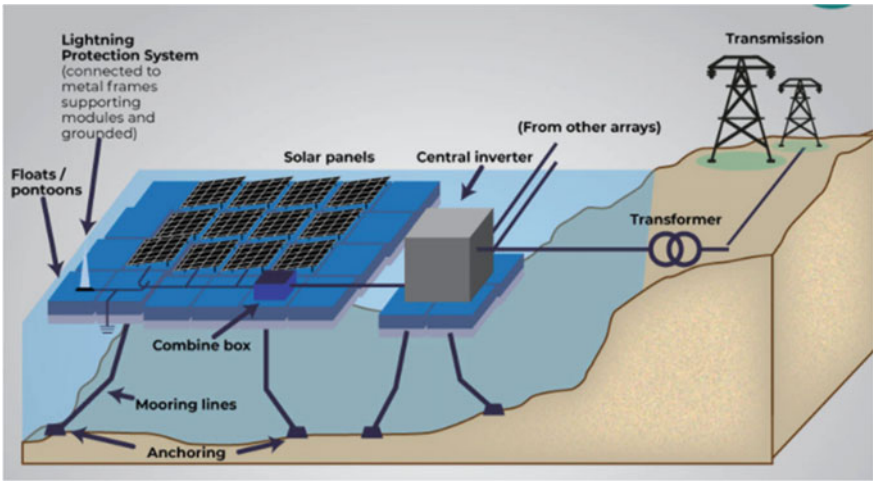

Fig. 3 Schematic of floating solar panel (*Source* World Bank Group, Solar Energy Research Institute of Singapore) [4]

anchors. The main electrical equipment is housed onshore, and electricity is transmitted from the FSPV system to this equipment and the grid or load through underwater cables [7].

The FSPV power plant consists of solar module, central inverter, mounting structure/ floats, combiner box, lightning protection system, cable and connector, and mooring arrangement. The schematic diagram is shown in Fig. 3.

2 Proposed Design of a 12 kW Floating Solar Power Plant

2.1 Study Area—Jhumka Dam and Reservoir

The FPV power plant is proposed for installation on Jhumka Dam reservoir which is 27.4 km away from Bhubaneswar, Odisha. The minimum surface area of the dam is 1,562.45 ha, while water surface area is 101.2 ha [8]. The details of the reservoir are shown in Table 1, and the geographical location of the site and the Jhumka reservoir are shown in Fig. 4 a and b, respectively.

2.2 Solar Energy Resources in Jhumka Reservoir

The monthly solar irradiance, ambient temperature, and wind velocity data of Jhumka region are shown in Table 2. The mean annual global horizontal irradiance of the

Table 1 Geographical location of the site

Sl. No	Particulars	Values
1	Name of the reservoir	Jhumka
2	Geographical location	$20^0 18' 54.8'' N$ $85^0 41' 17.82'' E$
3	Catchment area, km^2	20.80
4	Water surface area, ha	101.2
5	Length of dam, km	410

Fig. 4 a Geographical location of the site b Jhumka reservoir

project site as obtained from NREL site in the year 2014 is 5.16 kWh/m2/d. The highest irradiance of 6.55 kWh/m^2/day and the lowest of 4.32 kWh/m^2/day are observed during the month of May and December, respectively.

3 Simulation Results and Analysis of FSPV

A 12 kW floating solar plant is proposed for installation over the reservoir of Jhumka Dam and is simulated by using PVsyst 7.1 software tool. In the proposed system, 40 nos. of PV modules are arranged in two strings. The total area of the module

Table 2 Meteorological data of Jhumka reservoir, Odisha

Month	Global horizontal irradiation (kWh/m^2/d)	Horizontal diffuse irradiation (kWh/m^2/d)	Temperature ^{0}C	Wind velocity m/s
Jan	4.59	1.82	21.9	0.09
Feb	5.34	2.17	25.2	0.12
Mar	6.01	2.27	30.0	0.13
Apr	6.53	2.64	30.7	0.18
May	6.55	2.81	31.6	0.21
Jun	5.24	2.68	29.6	0.19
Jul	4.52	2.58	28.4	0.16
Aug	4.73	2.58	28	0.16
Sep	4.66	2.36	27.8	0.16
Oct	4.87	2.07	26.5	0.11
Nov	4.61	1.81	24	0.09
Dec	4.32	1.96	21.9	0.08
Year	5.16	2.31	27.1	0.1

is 66.6 m2, and the cell area is 59 m^2. The FSPV power plant is composed of 40 AXI protect AC-300MG/60S, 300 Wp modules in two strings of 20 panel connected in series in each string. The system is connected to a SUN2000-12KTL-M0, 12 kWp inverter. Considering the project life span as 25 years with 4% discount rate and 30% government subsidy on investment, financial analysis was computed. The specifications of PV module and inverter are shown in Table 3, and the detail of system production is shown in Table 4.

Table 3 Solar panel and inverter specification

PV module specification		Inverter specification	
Manufacturer	Generic	Manufacturer	Generic
Model	AXIprotect AC-300MG/60S	Model	SUN2000-12KTL-M0
Unit Nom Power	300 Wp	Unit Nom Power	12 kWac
No of PV modules	40 Units	No of Inverters	1 unit
Nominal (STC)	12 kW	Total Power	12 kWac
Modules	2 string × 20 in series	Operating Voltage	380–850 V
At operating Conditions		Pnom ratio(DC-AC)	1.00
P_{mpp}	10.84 kWp	Total PV Power	
V_{mpp}	588 V	Nominal STC	12 kWp
I_{mpp}	18 A	Total	40 modules
		Module Area	66.6 m^2
		Cell area	59 m^2

Table 4 Detail of system production

	Glob Hor kWh/m^2	Diff Hor kWh/m^2	T_Amb ^{0}C	Glob Inc kWh/ m^2	Glob Eff kWh/ m^2	EArray kWh	E_ Grid kWh	PR ratio
January	142.1	56.27	21.86	186.0	182.9	1883	1850	0.829
February	149.4	60.81	25.16	178.4	175.4	1755	1725	0.806
March	186.4	70.45	30.04	200.3	196.5	1905	1870	0.778
April	195.8	79.28	30.74	188.6	184.2	1807	1774	0.784
May	203.2	87.03	31.58	180.2	175.2	1748	1716	0.793
June	157.2	80.55	29.57	136.0	131.9	1361	1333	0.816
July	140.2	80.11	28.39	121.8	117.3	1231	1205	0.825
August	146.6	79.91	28.03	136.7	132.9	1382	1355	0.826
September	139.8	70.80	27.78	143.1	139.7	1438	1411	0.821
October	150.9	64.13	26.51	173.7	170.4	1737	1706	0.819
November	138.3	54.40	23.99	175.9	173.0	1772	1740	0.824
December	134.0	60.62	21.88	175.1	172.3	1787	1756	0.835
Year	**1883.8**	**844.34**	**27.14**	**1995.8**	**1951.8**	**19,807**	**19,440**	**0.812**

It is found that the maximum energy (1905 kWh) generated during the month of March and the minimum during the month of July (1231 kWh). It is observed that the highest performance ratio of 83.5% (PR) during the month of December and the lowest (77.8%) during March and the annual average PR of the system are 81.2%. The annual energy fed to the grid from the system is estimated as 19,440 kWh. The total installation cost of the system was found to be INR 877,000 with the annual operating cost of INR 144,000. The levelized cost of energy was found to be INR 9.35/kWh. The payback period of the installation is estimated as 11.9 years with 78.2% return on investment (ROI) which indicates the project is viable. The detail cost analysis is shown in Table 6. The simulation results and the detail financial analysis of FSPV plant are shown in Figs. 5 and 6, respectively.

The detailed normalized performance coefficients are shown in Table 5.

From this installation, 15.224 tCO_2 per year is reduced as compared to thermal power plant and total emission of 380.6 tCO2 is eliminated over the lifetime of the project.

4 Conclusion

India has large number of water bodies with a huge potential for energy generation from floating solar PV plants. A 12 kW floating solar PV plant is proposed for installation over the reservoir of Jhumka Dam, and its feasibility was studied by

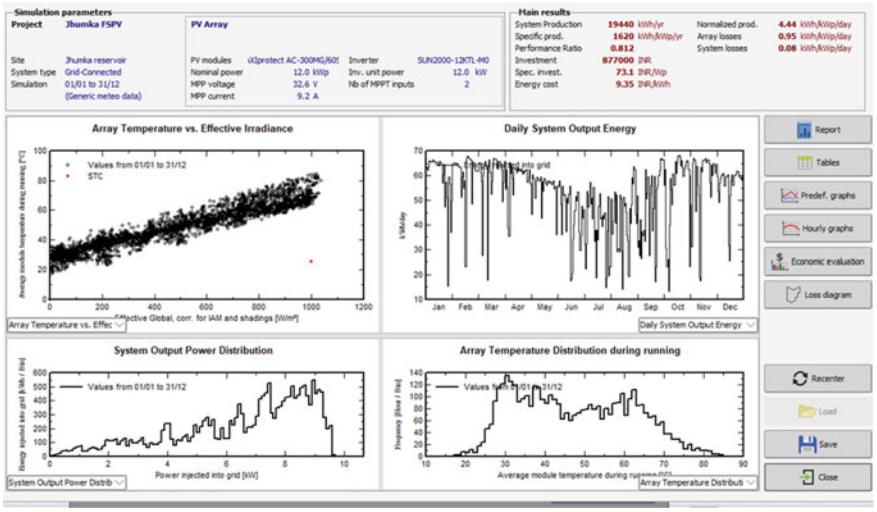

Fig. 5 Simulation results

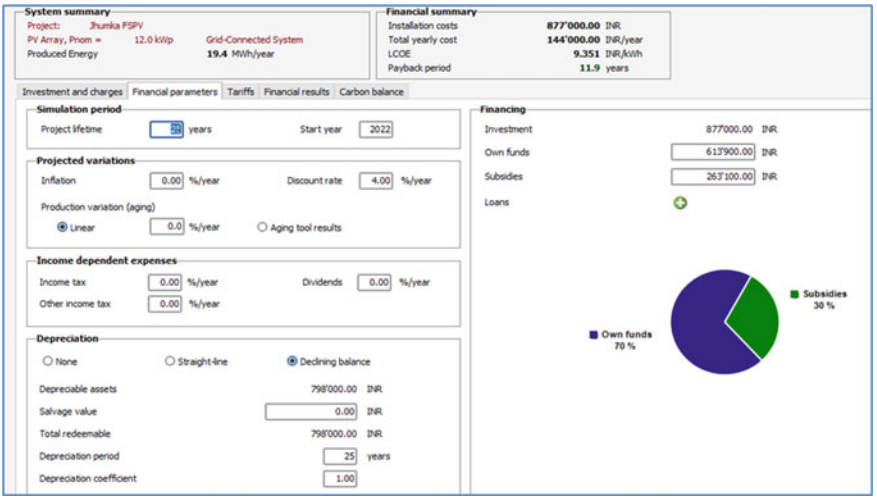

Fig. 6 Detail financial analysis of FSPV Plant

analyzing the system variables by PVsyst. The following conclusions were drawn from the study.

- The installation cost of 12 kWp FSPV is INR 877,000.
- The LCOE was found to be INR 9.35/kWh.
- The payback period of the system is 11.9 years.

Table 5 Normalized performance coefficients of FSPV plant

	Yr kWh/m^2/day	Le ratio	Ya kWh/kW/day	Ls ratio	Yf kWh/kWp/day	Lcr ratio	Lsr ratio	PR ratio
Jan	6.00	0.938	5.06	0.087	4.97	0.156	0.015	0.829
Feb	6.37	1.147	5.22	0.091	5.13	0.18 0	0.014	0.806
Mar	6.46	1.340	5.12	0.094	5.03	0.207	0.015	0.778
Apr	6.29	1.266	5.02	0.090	4.93	0.201	0.014	0.784
May	5.81	1.114	4.70	0.087	4.61	0.192	0.015	0.793
Jun	4.53	0.755	3.78	0.078	3.70	0.167	0.017	0.816
Jul	3.93	0.619	3.31	0.070	3.24	0.158	0.018	0.825
Aug	4.41	0.695	3.72	0.074	3.64	0.158	0.017	0.826
Sept	4.77	0.776	3.99	0.07 6	3.92	0.163	0.016	0.821
Oct	5.60	0.932	4.67	0.085	4.59	0.166	0.015	0.819
Nov	5.86	0.940	4.92	0.090	4.83	0.160	0.015	0.824
Dec	5.65	0.845	4.80	0.085	4.72	0.150	0.015	0.835
Year	**5.47**	**0.946**	**4.52**	**0.08**	**4.44**	**0.173**	**0.015**	**0.812**

Table 6 Detail cost analysis

Financing	
Own funds	613,900 INR
Subsidies	263,100 INR
Electricity sale	
Feed-in-tariff	11.20 INR/kWh
Duration of tariff warranty	20 years
Annual connection tax	0.00 INR/kWh
Annual tariff variation	0.0%/year
Feed-in-tariff decrease after warranty	50.00%
Return on investment	
Payback period	11.9 years
Net Present Value(NPV)	686,052.65 INR
Return on investment(ROI)	78.2%

- Annual reduction of 15.224 tCO_2 and a total lifetime reduction of 380.6 tCO_2 are estimated with this installation.
- The return on investment (ROR) was estimated as 78.2% which indicates the FSPV is viable and profitable.

References

1. https://news.energysage.com/floating-solar-what-you-need-to-know/
2. https://www.jakson.com/blog/floating-solar-power-plants-a-promising-technology-that requires-time-to-evolve/
3. https://www.pv-tech.org/news/plans-progress-for-600mw-floating-solar-project-in-india
4. World Bank Group, Solar Energy Research Institute of Singapore
5. https://www.drishtiias.com/daily-updates/daily-news-analysis/india-s-biggest-floatingsolar-power-plant
6. Acharya M, Devraj S (2019) Floating solar photovoltaic (FSPV): a third pillar to solar PV sector. TERI Discussion Paper: Output of the ETC India Project. New Delhi, The Energy and Resources Institue
7. Sahu A, Yadav N, Sudhakar K (2016) "Floating photovoltaic power plant: a review," Elsevier Renewable and Sustainable Energy Reviews 66
8. Anonymous (2019) Emergency action plan for Jhumka Dam, Odisha Water Resource Department, Bhubaneswar

ASOS-Based Load Frequency Control of Multi-Area Power System Using Degrees of Freedom PID Controller

Sunita Pahadasingh, Chitralekha Jena, and Chinmoy Ku. Panigrahi

Abstract This paper provides adaptive symbiotic organism search (ASOS)-based load frequency control (LFC) for an interconnected three-area thermal-hydro system. Different secondary controllers such as proportional integral derivative (PID), two degrees of freedom (2DOF-PID) and three degrees of freedom (3DOF-PID) are used not only to keep the disparity between generation demand but also achieve zero steady-state error to enhance the frequency and tie power regulations. The controlled parameters are optimized by ASOS algorithm for keen results of difficulties in LFC. Adaptive symbiotic dealings established by an organism to persist in the ecosystem through ASOS imitators. Further, the dynamic behaviors of controller optimized by ASOS and SOS are compared by extensive simulation in MATLAB/Simulink. Finally, system dynamics are compared among PID, 2DOF-PID and 3DOF-PID controllers through numerous simulations.

Keywords Load frequency control · Secondary controllers · Adaptive symbiotic organism search · Cost function · Step load perturbation

1 Introduction

Load frequency control (LFC) is scrutinized in power system as it sustains the frequency at its preferred level by eradicating the disparity between generation and load and also excluding the unintended altercation of power with further areas via tie-line. In past, a large number of researches have been done for single area and interconnected LFC systems. Gupta D. K., et al. have presented the two-area interconnected thermal, hydro and gas power plants [1]. Navuri et al. [2] have analyzed

S. Pahadasingh (✉) · C. Jena · C. Ku. Panigrahi
School of Electrical Engineering, KIIT University, Bhubaneswar, Odisha, India

C. Jena
e-mail: chitralekha.jenafel@kiit.ac.in

M. Mishra et al. (eds.), *Innovation in Electrical Power Engineering, Communication, and Computing Technology*, Lecture Notes in Electrical Engineering 814,
https://doi.org/10.1007/978-981-16-7076-3_9

three-area multi-source power system, and Pahadasingh et al. [3] explored the four-area unequal thermal plants. Limited studies are linked with LFC for an interconnected power system in view of nonlinearity [4]. Many researchers have already deliberated the application of classical controllers [5] such as proportional, proportional integral (PI), proportional integral derivative (PID) controller as a secondary controller for LFC system. Mostly, PID controller is used in LFC for simplification, and less parameter is to be optimized. However, during transient period, it suffers from high settling time and large overshoot. Through multiple control loops, control action is achieved which are basically degrees of freedom [6]. In [7], concept of 2DOF PID controller has discussed which has improved performance characteristics as likened to conventional controller. Three degree-of-freedom PID (3DOF-PID) controller can also be investigated for effective use in the proposed system [8]. Gain parameters of secondary controllers are generally adjusted by optimization techniques. In this area, many researches implemented different optimization techniques such as grey wolf optimization (GWO) [9], hybrid DE-PSO [10], sine cosine algorithm [11], teaching learning-based optimization [12], symbiotic organism search (SOS) [13] and adaptive symbiotic organism search (ASOS) [8–14]. For optimization of controller parameters, objective function is necessary which are basically in time domain. Mostly, integral of time multiplied absolute error (ITAE) is reflected as cost function because its transient behavior is superior as compared to others.

The core involvement of this paper is: (i) design of three-area thermal hydro system using secondary controllers PID, 2DOF-PID and 3DOF-PID. (ii) Superiority of 3DOF-PID controller has proven in comparison with other controllers. (iii) The controller parameters are optimized using ASOS and SOS algorithm, and the results are compared simultaneously.

2 Proposed Model

2.1 Three-Area System

LFC of three-area power system consisting of thermal and hydro units is reflected as multi-sources in area 1, area 2 and area 3. Here in each control area, system nonlinearities are considered. Proposed power system Simulink model is shown in Fig. 1. Input to each controller is taken as area control error, and the general expression of this is expressed in Eq. (1) [15]

$$\mathrm{ACE}_i = B_i \Delta F_i + \Delta P_{ij} \tag{1}$$

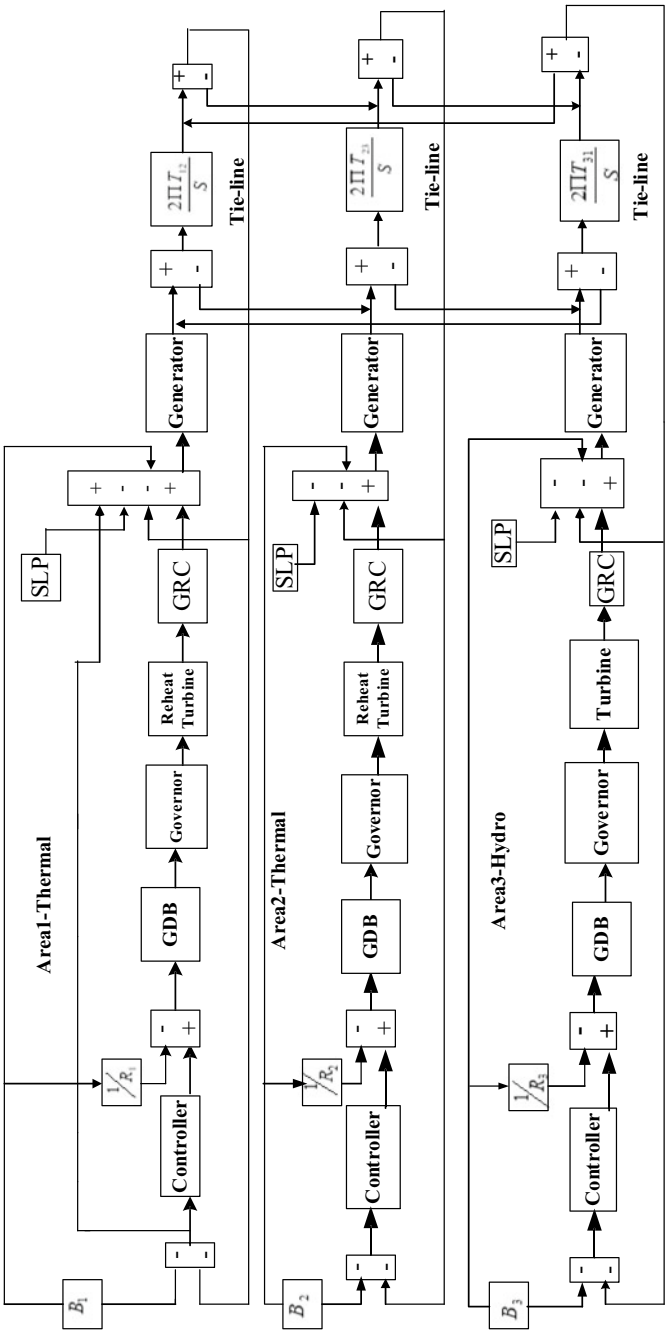

Fig. 1 Representation of Simulink model of three-area power system

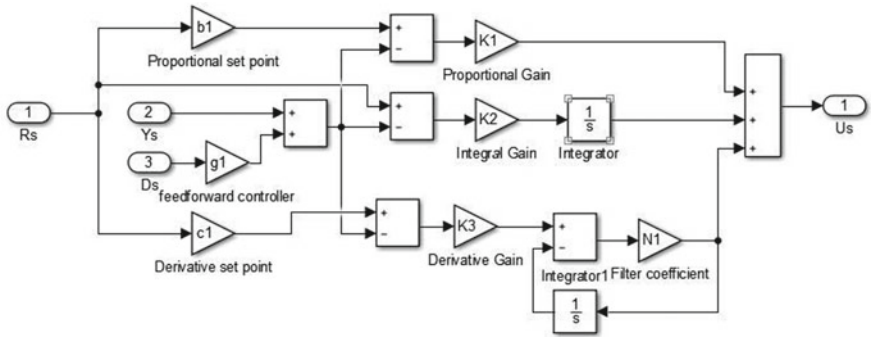

Fig. 2 Arrangement of 3DOF-PID controller

2.2 Controller Design

At first, a PID controller is castoff to reach at zero steady-state error. For this controller, three parameters are optimized (K_P, K_I, K_D). Conversely, it has stark fluctuations with eventual overrun and large settling time causes damage in the system performance.

Control action can be achieved by multiple control loops which are basically called as degrees of freedom. 2DOF-PID controller contains two control loops which are optimized for this system. The response performance essentially hinge on degrees of freedom. Finally, 3DOF-PID controller shown in Fig. 2 has considered for LFC which contains three control loops such as closed-loop stability, modeling of responses and eradication of instabilities.

K_{pi}, K_{Ii} and K_{Di} are the gain of single-order degree of freedom from $C(s)$. N_i is the filter constant for derivative gain. Control signal consists of proportional set point weightings bi and derivative set point weightings, respectively. The feed-forward controller has gain parameter gi.

2.3 Adaptive Symbiotic Organism Search

An efficient technique ASOS has concentrated on particles with best fitness value and the fitness value of the intended particle through modified benefit factors.

(i) Mutualism phase: This phase reveals the mutual benefit symbiotic relationship between two different species. In this phase, X_i and X_j are the two arbitrary organisms. The balance between exploration and exploitation can be achieved by modified benefit factors (BFs) as adaptive benefit factors (ABF) [14]

$$\mathrm{ABF}_1 = \frac{f(X_i)}{f(X_{\mathrm{best}})} \mathrm{if} f(X_{\mathrm{best}}) \neq 0 \tag{2}$$

$$\mathrm{ABF}_2 = \frac{f\left(X_j\right)}{f\left(X_{\mathrm{best}}\right)} \mathrm{if} f\left(X_{\mathrm{best}}\right) \neq 0 \tag{3}$$

$$X_{i,\mathrm{new}} = X_i + \mathrm{rand}(0, 1) * \left(X_{\mathrm{best}} - \mathrm{Mutual\_vector} * \mathrm{ABF}_1\right) \tag{4}$$

$$X_{j,\mathrm{new}} = X_j + \mathrm{rand}(0, 1) * \left(X_{\mathrm{best}} - \mathrm{Mutual}_{\mathrm{vector}} * \mathrm{ABF}_2\right) \tag{5}$$

where

$$\mathrm{Mutual\_vector} = \frac{X_i + X_j}{2} \tag{6}$$

rand (0,1) is the random number and BF_1, BF_2 are the benefit factor within the range from 1 to 2.

Both *i*th and *j*th organisms are restored by receiving aids from this interface with a possibility factors called benefit BF_1 and BF_2.

(ii) Commensalism phase: Two random organisms X_i and X_j from the ecosystem are permitted to interrelate in this phase. In this communication organism, X_i assistances from the interaction, but organism X_j neither assistance nor writhes from the connection. The new updated value of X_i is calculated [13]

$$X_{i,\mathrm{new}} = X_i + \mathrm{rand}(-1, 1) * \left(X_{\mathrm{best}} - X_j\right) \tag{7}$$

(iii) Parasitism phase: In this phase, one species get benefits from ecosystem and other is actively harmed. X_j is selected as a host for parasite vector from the ecosystem. This vector tries to replace X_j for survival in ecosystem, and the fitness values of both are calculated. If parasite vector has better fitness value, then it will kill X_j from the ecosystem and consume this place. If X_j is better, then it gets immunity from parasite vector. Now this PV will no longer alive in the ecosystem.

3 Simulation Results Analysis

Three-area multi-source LFC model is premeditated in MATLAB/Simulink environment. The system performance is evaluated with 1% step load in area 1. At first, SOS-based 3DOF-PID controller is simulated for LFC stud. Then, controller parameters are optimized using ASOS algorithm. The performances of both algorithm-based 3DOF-PID controller are compared through extensive simulations.

Controller parameters of 3DOF-PID optimized by ASOS and SOS algorithm have performed though numerous simulations. The simulation graph Fig. 3 shows the better frequency stability for ASOS-based controller, and Fig. 4 shows the improved performance of tie-line power deviations for ASOS-based controller. From these

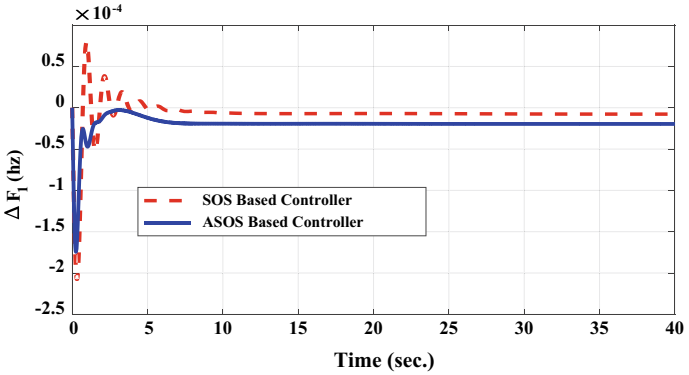

Fig. 3 Frequency variation for area1

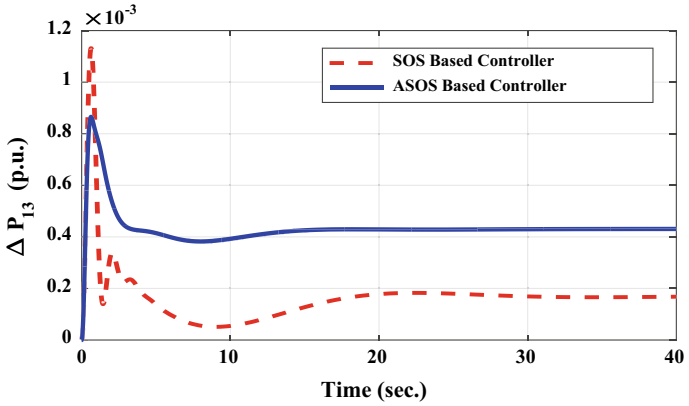

Fig. 4 Power interchange between area 1 and area 2

Table 1 Comparative analysis of 3DOF-PID controller optimized by ASOS and SOS algorithms

Performance	Algorithm	Δf_1(hz)	Δf_2(hz)	Δf_3(hz)	ΔP_{12}(pu)	ΔP_{23}(pu)	ΔP_{31}(pu)
Undershoot (U_{sh}) in pu	ASOS	−0.1742	−0.0592	−0.0481	−1.6213	−0.0000	−0.0000
	SOS	−0.1801	−0.0656	−0.0579	−1.7520	−0.0781	−0.0000
Overshoot (O_{sh}) in pu	ASOS	0.0000	0.0000	0.0000	0.0000	0.7749	0.8653
	SOS	0.0130	0.0048	0.0040	0.0000	0.8364	0.9356

figures, ASOS-based proposed controller has reduced oscillation and peak magnitude as compared to SOS-based controller.

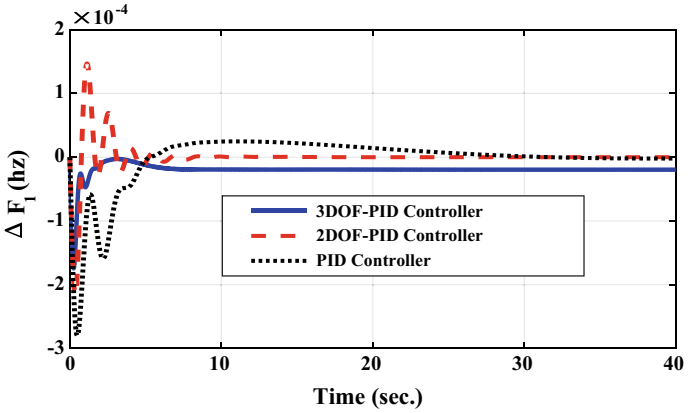

Fig. 5 Frequency deviation for area 1

The dynamic performance values of 3DOF-PID control structure optimized by ASOS and SOS algorithm have depicted in Table 1. Here the superiority of ASOS-based controller over SOS-based controller has notified in terms of diminished undershoots and overshoots values.

At first, PID controller is considered in which three parameters are to be optimized for single control area. Then, 2DOF-PID controller is used here with two extra loops $R(s)$ and $Y(s)$. Hence for this controller, five parameters are to be optimized for singe area.

Finally, 3DOF-PID controller is used in which three control loops are taken in addition of disturbance $D(s)$ to 2DOF-PID, where seven parameters are optimized.

The dynamic assessments of all these controllers are compared through simulations. As analyzed from Fig. 5, 6, 7, 8, 9 and Fig. 10, the 3DOF-PID controller has reduced overshoot and undershoots as compared to others. The 3DOF-PID controller optimized by ASOS algorithm settles quickly as compared to others.

The performance of these controllers tuned by ASOS technique has mentioned in Table 2. The effectiveness of 3DOF-PID controller has performed over 2DOF-PID and PID controller.

4 Conclusion

A 3DOF-PID controller is applied to three area thermal-hydro LFC systems to regulate the frequency and power interchange among control areas. The controller parameters of 3DOF-PID are optimized by a recent heuristic optimization technique adaptive symbiotic organism search (ASOS), which performance is compared with the SOS algorithm. The ASOS based controller has minimum oscillation and peak overshoot as compared to SOS-based controller. The supremacy of 3DOF-PID controller

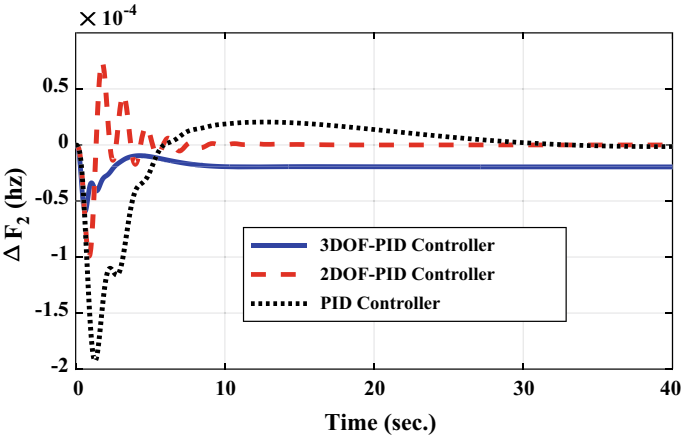

Fig. 6 Frequency deviation for area 2

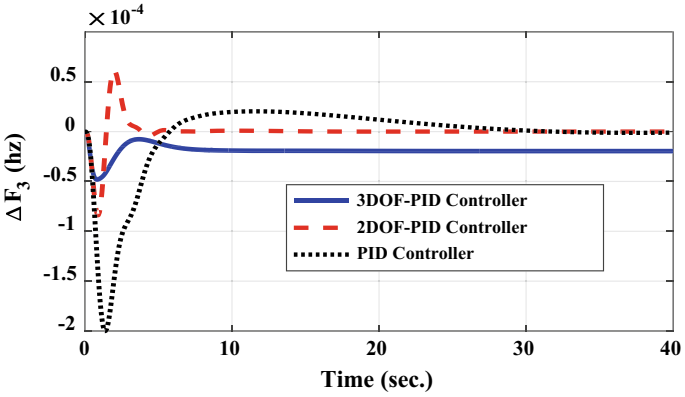

Fig. 7 Frequency deviation for area 3

has achieved in comparison with 2DOF-PID and PID in stand of less overshoot and undershoots with less settling time.

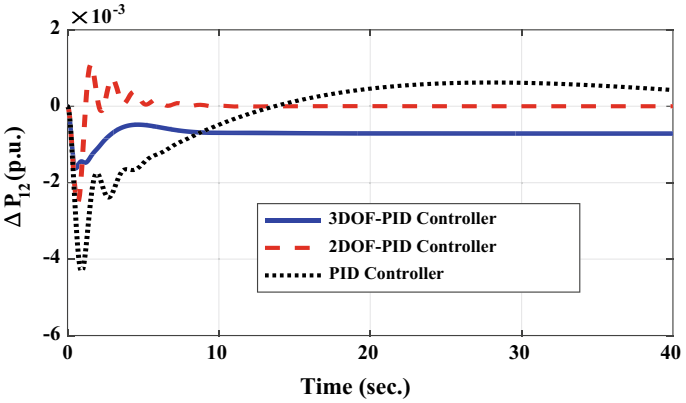

Fig. 8 Power interchange between area 1 and area 2

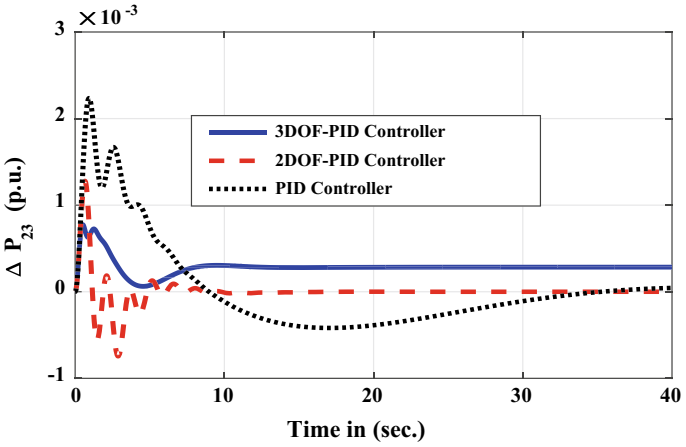

Fig. 9 Power interchange between area 2 and area 3

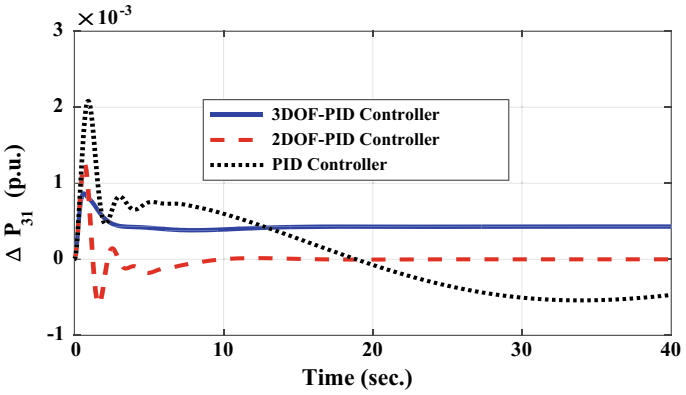

Fig. 10 Power interchange between area 1 and area 3

Table 2 ASOS optimized response values of different controllers

Performance	Controller	Δf_1(hz)	Δf_2(hz)	Δf_3(hz)	ΔP_{12}(pu)	ΔP_{23}(pu)	ΔP_{31}(pu)
Settling time (T_s) in s	3DOF-PID	4.95	5.20	6.31	7.12	8.14	9.70
	2DOF-PID	5.32	6.07	7.78	7.94	10.28	10.02
	PID	5.92	7.21	8.03	8.57	11.67	12.49
Undershoot (U_{sh}) in pu	3DOF-PID	−0.1783	−0.0524	−0.0454	−1.6031	−0.0000	−0.0000
	2DOF-PID	−0.2411	−0.0939	−0.0893	−2.5643	−0.7784	−0.5096
	PID	−0.2876	−0.1879	−0.2001	−4.1458	−0.8278	−0.5440
Overshoot (O_{sh}) in pu	3DOF-PID	0.0000	0.0000	0.0000	0.0011	0.7658	0.8735
	2DOF-PID	0.1496	0.0772	0.0623	1.0668	1.2698	1.2776
	PID	0.2029	0.0811	0.0721	1.3020	2.2523	2.0612

References

1. Gupta DK et al (2021) Load frequency control using hybrid intelligent optimization technique for multi-source power systems. Energies 14:1581
2. Navuri PK, Boddepalli MK (2020) Performance analysis of pidd controllers for automatic load frequency control of multi-area power system. Int J Control Autom 13(4):366–377
3. Pahadasingh S, Jena C, Panigrahi CK (2020) Load frequency control incorporating electric vehicles using FOPID controller with HVDC link. Springer Book Series IEPCCT 630:181–203
4. Tan W, Chang S, Zhou R (2017) "Load frequency control of power systems with nonlinearities." IET Gener Transmission Distribution 11(17)
5. Tungadio DH, Sun Y (2019) Load frequency controllers considering renewable energy integration in power system. Energy Rep 5:436–453
6. Patel NC, Debnath MK, Bagarty DP, Das P (2018) GWO tuned multi degree of freedom pid controller for lfc. Int J Eng Technol 7:548–552
7. Mishra S, Prusty RC, Panda S (2020) Design and analysis of 2dof-pid controller for frequency regulation of multi-microgrid using hybrid dragonfly and pattern search algorithm. J Control Autom Elec Syst 31:813–827

8. Guha D, Roy PK, Banerjee S "Adaptive symbiotic organism search algorithm optimized 3DOF-PID controller for load frequency control of hybrid power system." CALCON 2020, 19670148
9. Patel NC, Debnath MK, Bagarty DP, Das P (2018) GWO tuned multi degree of freedom PID controller for LFC. Int J Eng Technol 7:548–552
10. Pahadasingh S, Jena C, Panigrahi CK (2019) Fuzzy PID AGC of multi area power system optimized by hybrid DEPSO algorithm with FACTS. Int J Recent Technol Eng 8:9563–9569
11. Pahadasingh S, Jena C, Panigrahi CK "SCA based load frequency control incorporating electric vehicle using cascaded controller." ICPEE 2021, 9358648
12. Pahadasingh S, Jena C, Panigrahi CK "TLBO based CC-PID-TID controller for load frequency control of multi area power system." ODICON 2021, 9429022
13. Guha D, Roy PK, Banerjee S (2018) "SOS based load frequency control with tcsc." Proc fourth international conference recent advances in information technology, IIT (ISM) Dhanbad, pp 1–6
14. Nayak JR, Shaw B, Sahu BK (2018) Application of adaptive-SOS (ASOS) algorithm based interval type-2 fuzzy-PID controller with derivative filter for automatic generation control of an interconnected power system'. Eng Sci Technol Int J 21:465–485
15. Kundur P (22 Jan 1994) "Power System Stability & Control", McGraw-Hill Education; 1st edn

Design of Aperture Coupled Microstrip Phased Array Antenna

Pranoti S. Bansode and D. C. Gharpure

Abstract This paper presents the design of aperture coupled microstrip phased array antenna on Rogers TMM4 dielectric substrate for C band (5.8 GHz) frequency range. The proposed antenna consists of two dielectric substrate having thickness of 0.8 mm each stacked on each other. The upper substrate consists of patch antenna elements, and the lower substrate consists of feed network. The ground plane is sandwiched between the two substrates. Corporate feed network technique is used for antenna patch excitations. The direction of the antenna radiation beam has been tilted using the various delay line lengths. The optimized antenna radiation half power bema width is approximately 50° in both phi =0° and phi =90° planes, respectively, at resonant frequency 5.8 GHz. The simulated reflection coefficient of the proposed aperture coupled microstrip phased antenna design is >−20 dB for all antenna delay lines. The all-antenna simulation was carried out in high-frequency structural simulator (HFSS) environment.

Keywords Aperture coupled feeding technique · Delay line phase shifter · Beam steering

1 Introduction

Phased array antenna plays a very important role in modern radar system. The antenna has function to transmit electromagnetic energy through the medium and collect the reflected energy of distant target. For this process, the antenna should have efficient parameters like appropriate impedance matching, high gain, low profile, low side lobe level and precise angular resolution. To achieve these parameters, phased array antennas are best solution to design. Phased array antennas are useful in radar imaging which is widely used in applications such as geographical mapping, security surveillance and collision avoidance [1]. Microstrip patch antennas are used to fabricate a planer phased array, due to their distinct advantages like low profile, light

P. S. Bansode (✉) · D. C. Gharpure
Department of Electronic Science, Savitribai Phule Pune University, Pune, India

M. Mishra et al. (eds.), *Innovation in Electrical Power Engineering, Communication, and Computing Technology*, Lecture Notes in Electrical Engineering 814,
https://doi.org/10.1007/978-981-16-7076-3_10

weight and easy for fabrication. The main disadvantage of microstrip patch antenna is their relatively low bandwidth which can be increased by using aperture coupled feeding techniques [2].

For low frequency, the size of the antenna becomes large. In modern technology to reduce the size of the antenna, the material dielectric constant should be high. Aperture coupled microstrip patch antennas are preferred particularly for phased array antenna because of their advantages of integration of other active devices and circuits [3].

In the electronically steerable phased array antenna (PAA), the antenna elements are arranged to cover an interested range of angle. In a beam steerable antenna, each element in the PAA covers a particular area and it is turned ON when there is need to be radiate in specific direction. They also introduce redundancies to the system, for point-to-point connection [4]. The phase shifter plays an important role in a PAA and can be implemented in different ways. In [5], the phase shifter utilizes interdigital capacitor varactor with inkset-printed BST composite thick films which are based on tunable dielectric concept. Tunable substrate integrity waveguide phase shifter has a drawback that the radiation beam can only be switched to a set of discrete scanning angle [6]. It is better to provide the analog and digital phase shifter with properly designed feed network. In the recent years, the switched line phase shifters are constructed by using RF MEMs switches [7, 8] for low-power-consumption purpose. In [9], phased array antenna with tunable phase shifter based on ferroelectric ceramic material has been designed. This paper describes the phased array antenna with phase shifter operating in wide frequency range of 8 to 10 GHz and maximum insertion loss of 8 dB. In [10], electronically beam scanning reflect array using aperture coupled elements has been designed where three different substrates are used. In [11], the switched line phase shifter is made by using composite right/left-handed transmission line (CRLH-TL) to achieve a relatively constant phase shift over a large bandwidth.

For the substrate, the dielectric constant (ε_r) and the loss tangent (tan δ) were taken into consideration. From the reference studied, a high dielectric constant result reduces the impedance bandwidth, and a high loss tangent increases the feed losses and reduces the antenna efficiency [12]. The advantage of high dielectric constant substrate material is that it reduces the radiation losses because most of the EM field is concentrated between the conductive strip feedline and ground plane. High dielectric constant will also reduce the antenna size by square root of the effective dielectric constant [13]. The review indicates that different techniques to design phase shifters and phased array antenna are being explored. While refereeing the above papers, it is observed that by using tunable substrate integrity and reflect array method, it is difficult to achieve low insertion loss of the phase shifter and high bandwidth of the antenna.

In this paper, an aperture coupled microstrip phased array antenna for 5.8 GHz frequency is proposed. Series feed network is used to excite the patch antenna elements. The main beam of the radiation pattern tilts with the help of delay line phase shifters included in the feed network. The delay lines are designed for four different angles 22.5°, 33.5 °, 45 ° and 56 °. The maximum tilt in the radiation pattern obtained is −18 ° for 56 ° delay line phase shifter.

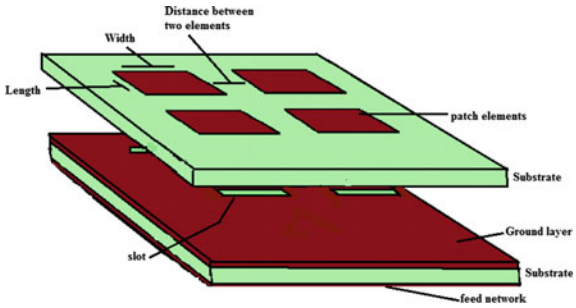

Fig. 1 Structure of 2×2 microstrip aperture coupled patch array antenna

2 Antenna Design

A 2×2 aperture coupled microstrip phased array antenna (ACMPAA) with series feed network was designed using standard formulas [14]. It consists of two layers of TMM4 laminates having dielectric constant of 4.5 and loss tangent of 0.0020. These laminates are etched for appropriate copper patches as per the simulated design and lamented using very thin adhesive material. The antenna consists of patch element on front side of first substrate. The other side of the patch panel substrate is etched completely. On the second substrate, slot is etched for coupling RF energy to the patch element. On the opposite side of the same substrate, transmission line is present to give the excitation to patch elements through the slot. Details of the structure of the complete 2 × 2 aperture coupled patch antenna are shown in Fig. 1.

The calculated length and width of the patch antenna elements are 9.8 mm and 17.8 mm. The interelement spacing (horizontal or vertical) in between the two patch elements should be around λ/2 and greater than λ/4 [6], and it determines the grating lobe level of the main radiation pattern. The horizontal distance between the patch antenna elements is 26 mm, and vertical distance is 28 mm. The substrate dimensions of the 2 × 2 ACMPAA are 60 mm × 58 mm. The ground is present in between the two substrates consisting of etched slots. The slots present exactly at the back side of each patch antenna element having length of 7.6804 mm and width is 0.8528 mm.

Series feed network was placed on the back side of the second substrate. It helps to reduce the antenna size and back lobe levels. The width of the feedline for 50Ω characteristic impedance is 3 mm. A series feed network was designed and includes the quarter wave transformer to match the impedance of 50 Ω. The feed network also includes 100 Ω and 70 Ω impedance transformers. The width of these transformers for 100 Ω was 0.688 mm and for 70 Ω transformers was 1.427 mm.

3 Design Optimization

Various parameters of the patch array antenna were optimized by using Ansoft HFSS software. The effect of return loss, i.e., S11 parameter, was observed for various

lengths and widths of the patch antenna element, length of the transmission line, width and length of the slot present in the ground and width of the transmission line.

3.1 Length and Width of the Patch Array Antenna

Based on dimensions of single patch, the dimensions of width and length of the patch antenna were optimized for ± 25% of calculated length 12 mm and width 15.6 mm. Figure 2 shows the simulated S11 parameter for different lengths of the patch antenna element varied from 5 to 15 mm. The width of the antenna element was kept constant at 15.6 mm. The resonant frequency 5.8 GHz was observed at length of 9.8 mm (i.e., 0.1885λ).

From Table 1, it was observed that the length of the patch antenna varies the resonant frequency of the patch antenna. At a length of 9.8 mm, the patch antenna has a minimum return loss of −26 dB at resonant frequency of 5.8 GHz. The width of the patch antenna greatly affects the radiation efficiency and bandwidth of the antenna, but it has less effect on the resonant frequency. In Fig. 3, the width of the

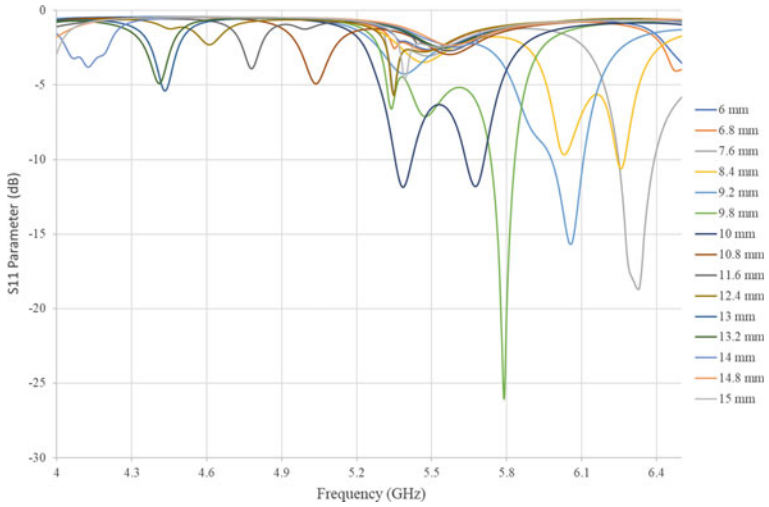

Fig. 2 Effect of different lengths of patch antennas on S11 parameter

Table 1 Patch length variation

Length (mm)	6.8	8.4	9.8	10.8	12.4	13.2	14.8
Frequency (GHz)	6.7	6.26	5.79	7.1	7	6.95	7.6
S11 parameter (dB)	−17.32	−10.62	−26.06	−3.78	−4.40	−3.25	−3.30

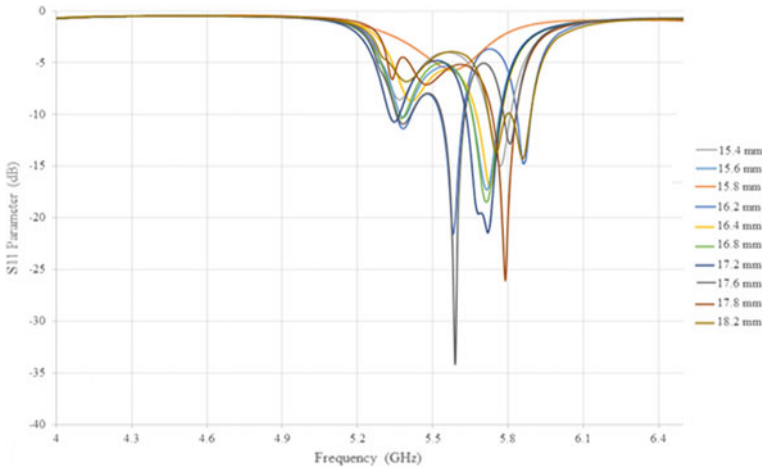

Fig. 3 Effect of different width of patch antenna on S11 parameter

Table 2 Patch width variation

Width (mm)	15.4	15.6	15.8	16.2	16.4	16.8	17.2	17.6	17.8	18.2
Frequency (GHz)	5.59	5.58	5.7	5.71	5.71	5.73	5.75	5.76	5.8	5.86
S11 parameter (dB)	−34.1	−21.55	−22	−18.4	−17	−16.8	−13.7	−14.3	−26	−18.84

patch antenna element was optimized from 15.4 mm to 18.2 mm keeping the length of patch element constant at 9.8 mm.

Table 2 shows that the resonant frequency and S11 parameter change as the width of the patch antenna elements increases. The resonant frequency 5.8 GHz with good impedance match was achieved at 17.8 mm which was 0.3423λ.

3.2 Length and Width of the Slots Present in the Ground

The slot length decides the frequency of the antenna, the coupling and back radiation. The optimization of length and width of the ground slot was carried out. The value of width and length of the slot was calculated as 7.6804 mm and 0.8528 mm. Following Fig. 4 shows the S11 parameter for the various lengths of the slot from 6.5 mm to 8 mm. While varying the slot length, the width of the slot was kept constant at a calculated value of 0.8528 mm.

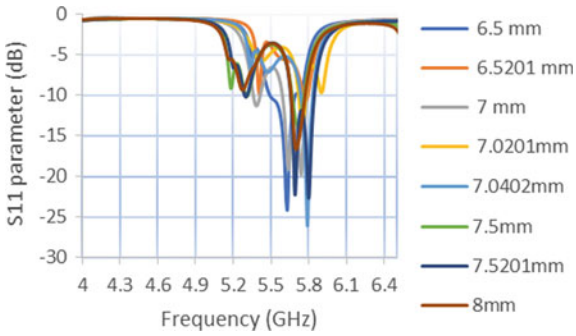

Fig. 4 Effect of different Lengths of the ground slots on S11 parameter

From Table 3, slot lengths were varied from 6.5 mm to 8 mm, and not much variation in resonant frequency of antenna was observed. For 7.04 mm length, i.e., 0.1354λ of slot, the impedance matched perfectly for 5.8 GHz. The width of the slot was also optimized from 0.105 mm to 1 mm. Figure 5 shows the S11 parameter for different widths of ground slots with constant length of 7.04 mm. The slot width affects the frequency and impedance of the patch antenna. The frequency of the antenna changes from 5.43 GHz to 5.84 GHz as the width varies. The impedance of

Table 3 Slot length variations

Slot lengths (mm)	6.5	6.52	7	7.02	7.04	7.5	7.52	8
Frequency (mm)	5.63	5.78	5.74	5.75	5.8	5.72	5.69	5.7
S11 parameter	−24.06	−10.63	−19.73	−13.61	−26	−13.8	−22.21	−16.58

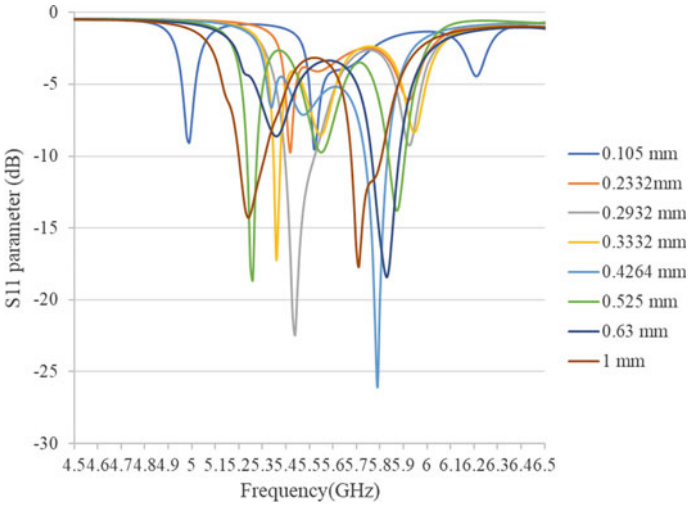

Fig. 5 Effect of different widths of the ground slots on S11 parameter

Table 4 Slot width variations

Slot width (mm)	0.105	0.23	0.29	0.33	0.42	0.52	0.63	1
Frequency (GHz)	5.53	5.42	5.44	5.36	5.8	5.26	5.83	5.71
S11 parameter	−9.26	−9.71	−22.44	−17.21	−26.06	−18.44	−18.44	−17.71

the antenna was matched perfectly at 0.42 mm, i.e., 0.0082 λ for 5.8 GHz resonant frequency. Table 4 shows the variations in slot width. From the table, it concludes that for slot width 0.42 mm, the resonant frequency 5.8 GHz was achieved.

3.3 Optimum Interelement Spacing of the Array Antenna Elements

The interelement spacing of the array antenna was optimized horizontally as well as vertically. According to the literature, the distance between the elements should lie between λ/2 of 26 mm and λ of 52 mm for resonant frequency of 5.8 GHz. The horizontal spacing between the two antennas was optimized from 25 to 29 mm, and the S11 parameter variation is shown in Fig. 6. Table 5 shows the distance variation

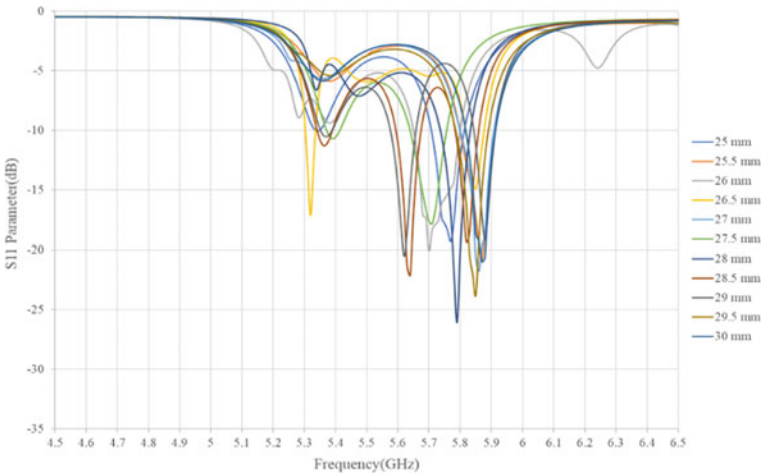

Fig. 6 Effect of varying the horizontal distance between two patch antennas on S11

Table 5 Distance between the two patch variations

Distance (mm)	25	25.5	26	26.5	27	27.5	28	28.5	29
Frequency (GHz)	5.76	5.87	5.7	5.32	5.86	5.71	5.8	5.64	5.62
S11 parameter (dB)	−19.3	−20.8	−20.0	−17.1	−21.7	−17.8	−26.6	−22.7	−20.5

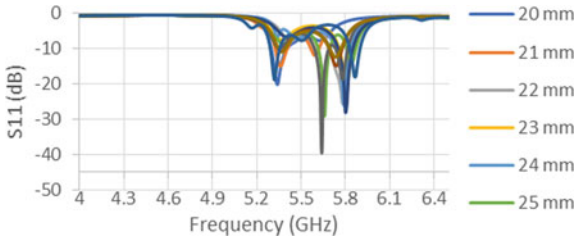

Fig. 7 Effect of vertical distance between the two patch antennas on S11

Table 6 Effect of vertical distance variation on S11 parameter

Distance (mm)	20	21	22	23	24	25
Frequency (GHz)	5.34	5.78	5.78	5.81	5.8	5.66
S11 parameter (dB)	20.13	−19.5	−25	−21.6	−2626	−28.99

between two patches. As we change the horizontal distance between the two patches, the resonant frequency of the patch antenna changes. At distance 28 mm, the resonant frequency 5.8 GHz is achieved with S11 parameter of −26.6 dB.

From the simulation results of interelement spacing, it was observed that if the spacing is small, i.e., at 28 mm, the mutual coupling between two antenna elements becomes very strong. The mutual coupling improves the S11 parameter of the antenna. If the distance is 28 mm, the bandwidth of the antenna is 110 MHz.

The interelement spacing between the antenna elements was simulated for vertical distance 20 mm to 25 mm as shown in Fig. 7. The minimum return loss of −26 dB was observed at vertical distance of 24 mm, i.e., 0.415λ, between the two antennas, and the bandwidth was 100 MHz (5.83–5.73 GHz).

From the Table 6, it is observed that as the vertical spacing varies, the resonant frequency changed. For better performance in the radiation pattern and S11 parameter, the horizontal and vertical distance between the two patches should be greater than lambda by 2. From Table 6, it is observed that at 24 mm, the resonant frequency 5.8 GHz is achieved. At 28 mm horizontal and 24 mm vertical distance, the beam was at very close to the center and gain is maximum at 7 dB.

3.4 Width of the Transmission Line

The width of the feedline calculated was 3 mm. Figure 8 shows the S11 parameter results where the width of transmission line varied from 1.5 mm to 4.5 mm. Figure it was observed that at 3 mm, i.e., 0.05759 λ, width of the transmission line shows return loss of −26 dB at 5.8 GHz frequency.

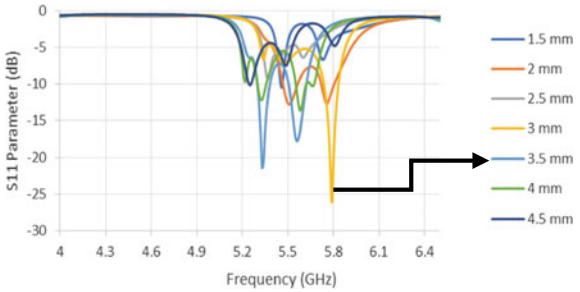

Fig. 8 Effect of different widths of feedline on S11 parameter

4 Final Simulation Results

The 2×2 ACMPAA dimensions were finalized after optimizing all the above parameters. The total substrate dimension is 60 mm × 58 mm. The length and width of the patch element are 9.8 mm and 17.8 mm. The slot present in the ground plane having length and width is 7.6804 mm and 0.8528 mm. The patch elements were excited from the feedlines and through these slots. The horizontal interelement spacing between the antenna elements was 28 mm, and vertical spacing between the elements was 24 mm. This optimum dimension of the 2 × 2 ACMPAA was simulated and discussed.

The variation of return loss versus frequency of aperture coupled microstrip patch array antenna (ACMPAA) is as shown in Fig. 9. From the simulated results, it is observed that the antenna resonates at 5.8 GHz with minimum return loss of -26 dB. The maximum impedance bandwidth obtained for ACMPAA was 0.857%, i.e., 50 MHz (5875−−5825 MHz) with a peak gain of 7 dB.

Figure 10 shows the simulated VSWR of the ACMPAA having a value of 1.1047 at resonant frequency of 5.8 GHz. Figure 11a, b shows the typical 2D and 3D radiation pattern in E and H plane of ACMPAA at 5.8 GHz.

From the radiation patterns, it was seen that the patterns were broadsided and linearly polarized in both E and H planes. The gain of the antenna is 7 dB, and the half power beam width (HPBW) was 40 °. The back-lobe level was −2.92 dB.

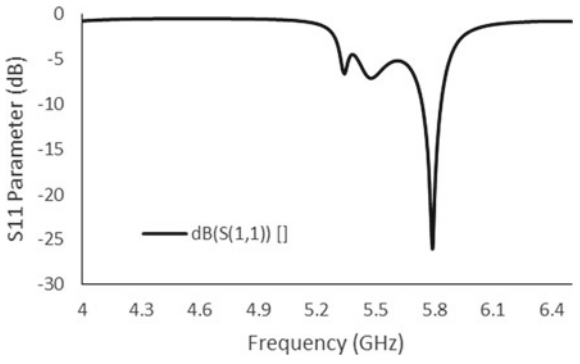

Fig. 9 S11 parameter of the ACMPAA

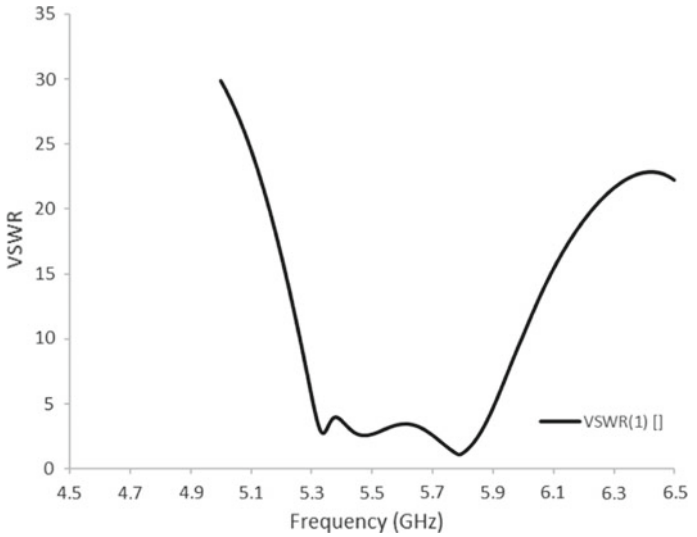

Fig. 10 VSWR of the ACMPAA

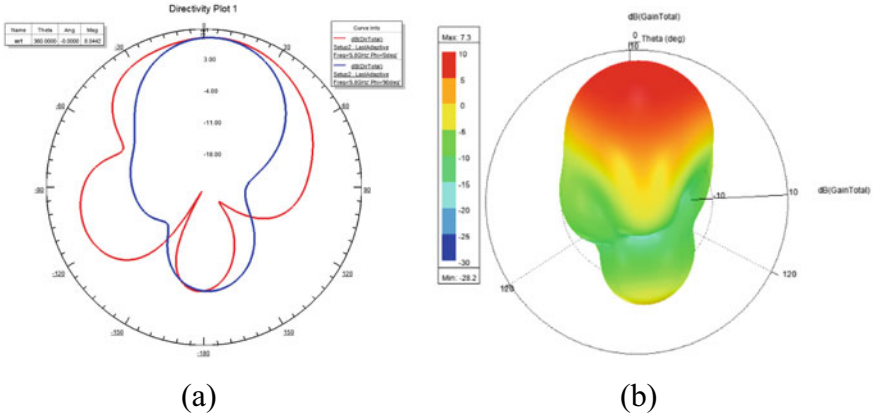

Fig. 11 **a** 2D and **b** 3D radiation pattern of the ACMPAA

The large beam width leads to limitations in the steering angle as shown through simulations.

5 Simulation Studies of 2×2 Phased Array Antenna

To study the effect of input phase variations on the radiation pattern of the antenna, the delay line path of a particular angle has been inserted in the feed network. The delay line length has been calculated for different input phases. The respective delay line length was added in the feed network, and the effect of radiation pattern was observed. As the input phase of the delay line phase shifter changes, the main beam of the antenna steers in different directions. The delay line length for particular input phase was calculated as per the formulae mentioned below.

The following formula is used to calculate the delay line phase [7].

$$\Delta\varphi = \left(\frac{2\pi d}{\lambda}\right)\sin(\theta) \tag{1}$$

where

$\Delta\varphi$: Delay line angle/input phase; d: Distance between two antennas.

λ: Wavelength (in mm); θ: Beam steering angle.

The delay line length is calculated by using formula

$$\Delta L = \left(\frac{\Delta\varphi C}{2\pi f_0}\right) \tag{2}$$

where ΔL: Path difference f_0: Center frequency.

The delay line lengths for 22.5°, 33.5°, 45° and 56° were calculated using above formulae, and the antenna structure was simulated by inserting the delay line as shown in Fig. 12.

The delay line phase shifter was added in the feed network as shown in figure, and the tilt in the main beam of the antenna was measured, with the help of radiation pattern. Figure 13 shows the simulated radiation pattern of the array antenna for 22°, 33°, 45° and 56°delay line phase shifters. At 56° phase shift, maximum tilt was observed beyond this value of phase shift, e.g., 90° side lobe levels start increasing up to a main lobe level and the deep notch comes at the center (heart shape radiation pattern form), i.e., the power of the main beam divides into two beams.

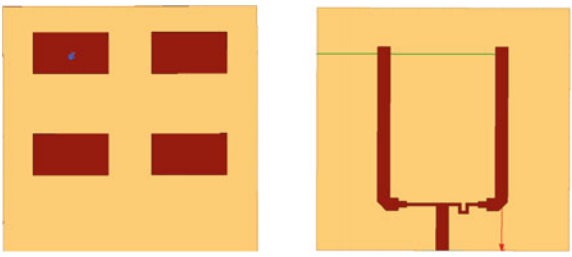

Fig. 12 Phase delay lines in feed network

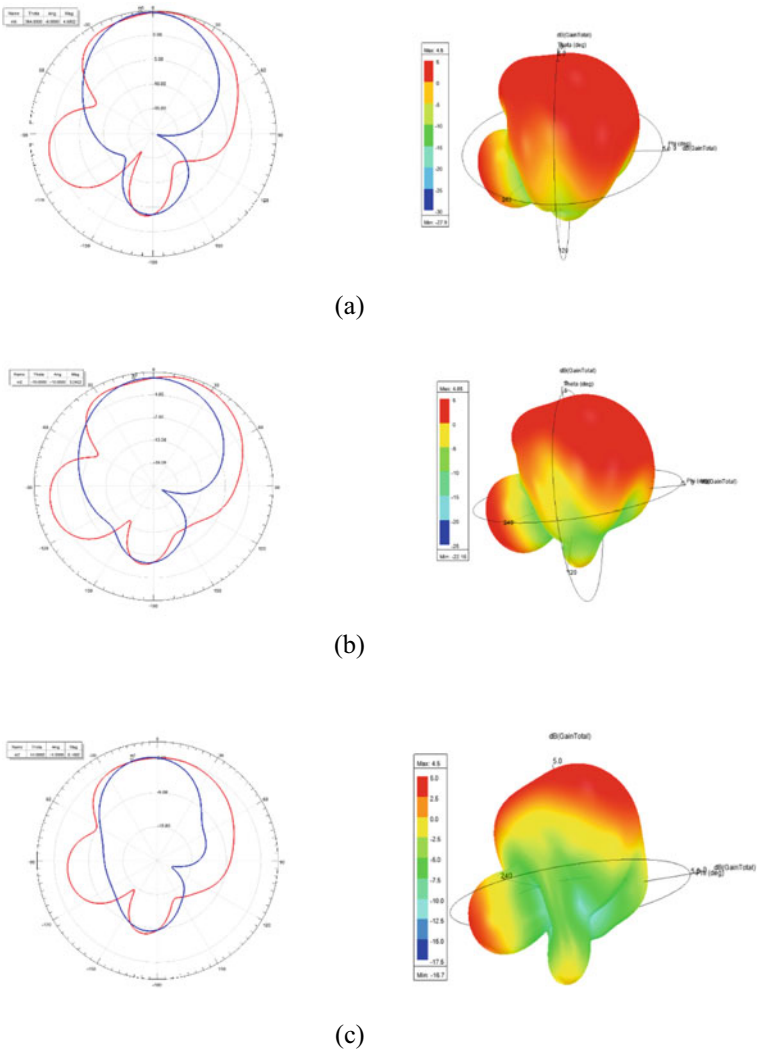

Fig. 13 Radiation pattern at various phase delay lines

Figure 13a shows the main beam of the antenna tilted at −5 °. for the input phase of 22.5 °. From Fig. 13b, the input phase of 33.5 ° the main beam was steered at − 10 °. from the center. Figure 13(c) shows the −15 ° main beam was steered for the input phase of 45 °. Figure 13d shows the beam steering was at −18 ° for input phase of 56 °. It can be concluded that the maximum tilt of the patch array antenna on the left is −18 ° for input phase of 56 °.

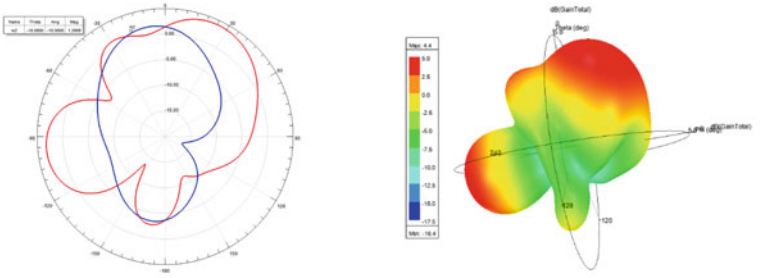

(d)

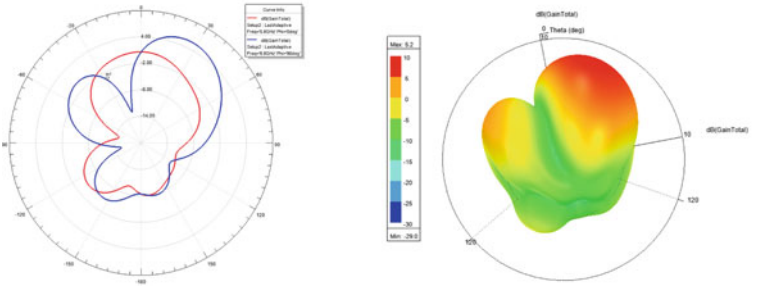

(e)

Fig. 13 (continued)

6 Conclusion

The aperture coupled phased array antenna with delay line phase shifter is simulated, fabricated and tested on spectrum analyzer. In aperture coupled phased array antenna, the slots present in the ground provide the excitation to the patch elements. The slot dimension decides the frequency of the antenna. The corporate feed network is used to provide the power to the antenna. The delay line phase shifter is added in the feed network which provides change in phase which tilts the radiation pattern at particular angle. In [6] to improve switch insertion loss and switch on return loss T line section is added to either side of the switch. The process is quite complicated to add CPW's 90° bend and make RF MEMS switched line phase shifter. In [7], transmission lines are matched to 50 Ω impedance using single-open stub. But, these stubs of unequal length are adding error in the results. In [13], the tunable phase shifters fabricated on the screen-printed barium strontium titanate thick film ceramic material provide the very large insertion loss of 8 dB. This loss is added to the composed performance of the antenna. In [14], the aperture coupled tunable patch elements printed on 25-μm-thick polyimide membrane, microstrip line and ground plane with slot printed on RT duroid 5880 substrate and patch separated from ground

plane with 3-mm-thick Rohacell 71 foam. All the three substrates are bound together by using two 25-μm-thick adhesive film. These substrates increase the thickness of the antenna, and therefore, the losses are increased. Instead of this, aperture coupled feeding technique is useful to improve the bandwidth with smaller thickness. In this antenna, as the power increases will increase the rectification and harmonics of the fundamental frequency. The S11 parameter is optimized by varying length and width of the patch antenna elements, interelement spacing between the patch antenna elements, length and width of the slot and width of the transmission line. From the simulation results, the reflection coefficient is −18.7 dB, and gain is 7 dB at resonant frequency 5.8 GHz. The half power beam width obtained is 50°.

The delay line phase shifter is used to tilt the main beam of the radiation pattern. The simulation was carried out for different delay lines of 22°, 33°, 45° and 56° in the feed network, and tilt in the radiation pattern was observed. At 56° phase shift, maximum tilt in the main beam radiation pattern was observed at −18 °. Microstrip patch antenna is in the fabrication process.

References

1. Xu Z, Hao CX "A compact ku-band active electronically steerable antenna with low-cost 3d t/r module", Hindawi Wireless Commun Mobile Comput 2019, Article ID 5287679, p 8. https://doi.org/10.1155/2019/5287679
2. Professor David M. Pozar, "A Review of Aperture Coupled Microstrip Antennas: History, Operation, Development, and Applications", May 1996.
3. Moreira A, Prats Iraola P, Younis M, Krieger G, Hajnsek I, Papathanassiou KP (2013) A tutorial on synthetic aperture radar. IEEE Geosci Remote Sens Mag 1(1):6–43
4. Iyemeh Uchendu, "Survey of beam steering technique available for millimeter wave applications", 'Progress in Electromagnetics research B, Vol.68,35–54,2016].
5. Mohammad Nikfalazar, "Two-dimensional beam steering phased array antenna with compact tuneable phase shifter based on BST Thick films, IEEE antennas and wireless propagation letters", vol.16,2017.
6. Yuan ji, Lei ge, "Reconfigurable phased array antenna using continuously tuneable substrate integrated waveguide phase shifter", IEEE, DOI https://doi.org/10.1109/TAP.2019.2927813.
7. Li-Ya-Ma, Norhayati soin, " A K-band switched line phase shifter using Novel Low voltage Low pass RF MEMS switch" IEEE regional symposium on Micro and Nano electronics (RSM).
8. Rudra L.Timsina, "A compact design of switched line phase shifter for a microstrip phased array antenna", 'Progress in electromagnetics research symposium-PIER,Singapore,19–22 Nov 2017.
9. Mohsen Sazegar, Yuliang Zheng, "Low-Cost Phased-Array Antenna Using Compact Tunable Phase Shifters Based on Ferroelectric Ceramics", IEEE Transactions on Microwave Theory and Techniques, Vol. 59, No. 5, May 2011, Page No.1265–1273.
10. Mathieu Riel, Jean-Jacques Laurin, "Design of an Electronically Beam Scanning Reflectarray Using Aperture-Coupled Elements", IEEE Transactions on Antennas and Propagation, Vol. 55, No. 5, May 2007, Page No. 1260–1266.
11. Jun Zhang, S. W. Cheung, "Designed of switch line phase shifter with constant phase shifting using CRLH-TL", Proceeding volume 9252, millimetre wave and TeraHz sensors and technology VIII; 92520E (2014).
12. Fredrik Gulbrandsen, "Design and Analysis of an X-band Phased Array Patch Antenna", June 2013 Norwegian University of Science and Technology.

13. Heesu Wang, Kam Eucharist Kedze, and Ikmo Park, “Microstrip Patch Array Antenna Using a Parallel and Series Combination Feed Network”, 2018 International Symposium on Antennas and Propagation (ISAP 2018) October 23~26, 2018 / Paradise Hotel Busan, Busan, Korea
14. Pranoti bansode, Krishna Makhija, R Aiyer, S.A. Gangal, “Non-destructive measurement of dielectric constant using a 2.4 GHz microstrip patch antenna” 2nd International Symposium on Physics and Technology of Sensors (ISPTS) in IEEE Xplore, 2015.

Stability Improvement of Fractional-Order Filters Using Gain Bandwidth and Step Response Approach

Kumar Biswal, Sanjeeb Kumar Kar, and Madhab Chandra Tripathy

Abstract This article focuses on the stability of fractional-order filter circuits, which are characterized by transfer function and their common characteristic equations. Two methods such as gain bandwidth and step response approach are adopted to analyze the transition bandwidth by varying the exponent (order) of fractional capacitor used in filter circuit. The exact analytical solutions are derived for low-pass, high-pass and band-pass filters with different orders of capacitor. The characteristic equation and transfer function of these filters are presented along with simulation results. Here, the stability analysis is presented by considering the bandwidth and step response of the fractional-order filters. Since the bandwidth of the filter is expressed in terms of cutoff frequency which further changes with variation in exponent (order) of capacitor, it is considered for filter circuit in simulation results. Secondly, the steadiness of low-pass filter's response to a step response input is analyzed keeping its DC gain constant for this filter with variable order of capacitor. The response of the filter becomes stable when the exponents of the capacitor are fractional numbers, then compared with that of integer-order filter.

Keywords Fractional calculus · Fractional-order filter · Gain-bandwidth · Step response · Transfer function

K. Biswal (✉)
School of Electronics Engineering, KIIT Deemed To Be University, Bhubaneswar 751024, Odisha, India
e-mail: kumar.biswalfet@kiit.ac.in

S. K. Kar
Department of Electrical Engineering, SOA Deemed To Be University, Bhubaneswar, Odisha, India
e-mail: sanjeebkar@soa.ac.in

M. C. Tripathy
Department of Instrumentation and Electronics, College of Engineering and Technology, Bhubaneswar, Odisha, India
e-mail: mctripathy@cet.edu.in

M. Mishra et al. (eds.), *Innovation in Electrical Power Engineering, Communication, and Computing Technology*, Lecture Notes in Electrical Engineering 814,
https://doi.org/10.1007/978-981-16-7076-3_11

1 Introduction

Fractional calculus is a stream of mathematics which performs complete and integrated work in non-integer orders [1]. The use of arithmetic as a part of ancient and modern physics has a profound effect on our analysis and understanding of complex physical–chemical and bio-physical systems because it provides excellent tools for the interpretation of memory and the properties of various objects and processes incorporated by the development of fractional calculus. The fractional calculus has expanded the area of fractional domain in mathematics which leads the way for research on fractional-order circuits and systems. There are many applications of fractional calculus like control system, process control and analog circuits [2]. The system behavior can be better explained by fractional-order equation than classical integer-order equation Standard capacitors and inductors are identified by their integer-order equation having its first/second derivative present in all electrical system modeling [3].

Nowadays, mostly the integer-order circuits have been generalized to fractional domain that has been evolved as an emerging research area in the field of circuits and systems. It has been observed that in the literature, the fractional-order filters have definitely many advantages as compared to their integer-order counterparts. The gain stability of fractional-order filters is better as compared to its integer-order counterpart. All the filter characteristics (e.g., cutoff frequency, rise time, bandwidth, etc.) are functions of the fractional exponent α, which provides a greater freedom in designing the circuits [4]. The high-frequency applications are mainly found in fractional-order filters keeping the filter coefficients unchanged (i.e., decreasing the fractional capacitor's order, α). Again the speed of response of the filter changes with change in fractional order. So, it has been important to realize and study the performance of fractional-order filters by using fractional capacitors and compare their performance with its integer-order counterpart [5].

The fabrication of fractional capacitor (also called fractance) which obeys fractional calculus is possible due to several circuit applications in its fractional domain representation. A fractional capacitor can be approximated by using a RC ladder network for some experimental work [6, 7]. The purpose of the existing work is to visualize the different uses of circuit application using fractional capacitors [8]. Typical cases of fractional-order filters and their performance have been considered in this work.

Continuous conventional analog-type filters are standard ones because their transfer functions expressions contain the full power of "s." However, if a single or multiple standard capacitors in circuit are replaced by a fractional capacitor with actual power of s, then the fractional capacitor is expressed with its impedance $Z(s)$ as

$$Z(s) = \frac{1}{C_F s^{\alpha}} \quad 0 < \alpha < 1 \tag{1}$$

where C_F is non-integer capacitance and α shows its fractional order. In addition to this an inductor can also be realized by using a generalized impedance converter (GIC) in its fractional domain, due to which the order of the inductor and capacitor can be increased to fractional value in the range of $0 < \alpha < 2$ [9, 10]. Therefore, it is expected that the performance of the filter's transfer function with real power of "s" will improve the design adaptability and improve its performance. The present work investigates a few such programs and attempts to evaluate the effects of simulation on filter's performance [11, 12]. It also proposes a fractional capacitor and its model on the overall performance of fractional-order filter circuits. The main objectives of this article are outlined as investigating the characteristics of a fractional-order filter and compare its performance with an integer-order filter. Again realizations of a fractional-order filter with fractional capacitors and study its performance by observing its simulation results [13]. Finally, the stability analysis of the fractional-order filter is carried out to study the performance of the fractional-order filter by varying the capacitor's exponent used in circuits [14].

2 Fractional Calculus

Fractional calculus is an old research topic that combines different fields of engineering with mathematics. Over the years, the fractional calculus applications began in many areas of technology including control systems, process control and circuits and systems, etc. [1–3]. The integration and derivatives are generalized for fractional-order systems result flexible transfer function with real power of variables. The models having many fractional poles were proposed by Charef et al. (1992); Schlegel and Cech (2005); Schlegel et al. (2014) are appropriate to design industrial processes with dispersed parameters [6, 14]. Such a model provides higher frequency response flexibility than the conventional integer-order models. However, its real-time implementation for the systems is a big challenge for the researchers working in this domain [15]. Typically, an FO system is considered a higher order filter, which always leads to a non-terminating-order filter [16]. The representation is provided by the definition of Grunewald–Letnikov as

$$ {}_aD_t^{k-\alpha} f(t) = \lim_{h \to 0} h^{-\alpha} \sum_{j=0}^{m} W_j^{\alpha} f((m-j)h) \tag{2} $$

The Mittag–Leffler function which contain two complex parameters α and β is defined as

$$ E_{\alpha,\beta}(z) = \sum^{\infty} \frac{z^k}{\Gamma(\alpha k + \beta)} \tag{3} $$

The Oustaloup recursive approximation (ORA) method for partial-order components at two complex parameters is defined as

$$s^{\alpha} = \prod_{n=1}^{N} \frac{1 + \frac{s}{w_z \cdot n}}{1 + \frac{s}{w_p \cdot n}} \tag{4}$$

The above approximation is valid within a frequency range of $\omega_z - \omega_p$, where ω_z and ω_p are the upper and lower frequency limits, respectively, with n is the number of poles and zeroes and N is the order in approximation.

The capacitor is an important part of the electrical circuit and is mostly used in integrated circuits. The current flow mechanism of a capacitor is expressed as $i(t) = C\frac{d}{dt}v(t)$ and for a good capacitor its impedance is leading to form as $\frac{1}{jwc}$ in fractional domain. The current through this capacitor is given by

$$i(t) = C_f \frac{d}{dt^{\gamma}}^{\gamma} v(t) \tag{5}$$

Several documents have shown that a good capacitor is difficult to be practically realized with its desired specifications. For a "very good" capacitor, γ can be in the range of 0.999–0.9999. Taking these values, it has been decided to investigate the effectiveness of upcoming techniques in identifying this exponent value in non-integer region [14].

3 Fractional-Order Systems

Fractional calculus has emerged as a powerful mathematical tool, used in various fields of science and engineering [1–3]. The order of the whole number can be treated as a special case of fractional calculus where the mathematical model representations are assumed to be the non-integer value. Fractional-order systems modeling has become less popular due to lack of suitable tools and strategies for fractional-order system's equation [17]. However, recent advances in numerical techniques and simulation tools have been combined together with the discovery of processors that have been much faster than the system identification method [18]. In general, the robustness of fractional-order systems can be performed by studying the equation with differential order that signifies the filter's operating region, and alternatively, the other way is to study the transfer function of the system [19]. The stability of fractional-order systems has been studied by many researchers from their characteristic equations in Laplace transform representation as well as from the bounded input and bounded output stability criterion for linear time invariant systems [20, 21].

3.1 Mathematical Background

First, the definitions of fractional calculus and its fractions are presented in literature. The findings of the Caputo component of the function $f(x)$ of non-integer order γ in relation to variable t and the starting point at t =0 are described by [9]. Normal capacitors in circuits are replaced by fractional capacitors with its actual power of s. This is because the impedance of a fractional capacitor is expressed as

$$Z(s) = \frac{1}{C_F s^{\alpha}} = \frac{1}{C_F \omega^{\alpha}} \angle\left(-\frac{\pi}{2}\alpha\right) \quad 0 < \alpha < 1 \tag{6}$$

Here, C_F is constant and α shows partial order. The fractional capacitance unit is expressed as $F/s^{(1-\alpha)}$ where's' means second and F means farad [10]. Similarly, the ideal FC magnitude is a straight line with slope of 20α dB/decade with constant phase angle throughout its frequency. The next section explains the various methods used in the literature to obtain fractional capacitors (FC).

3.2 Realization of Fractional Capacitor Using Passive Elements

This section provides different techniques of realizing a fractional capacitor which are derived by various capacitor and resistor combinations. There are lot of works that can be noticed where the study of fractional capacitor is characterized by using ladder networks, e.g., crossed RC ladder, domino ladder, integrated ladder [6, 12]. A non-terminating network of RC ladder is shown in Fig. 1, which provides impedance. The real circuit is the terminating approximate of the actual order, i.e., half order of the infinite length, and the phase difference between the input and output signal is approximately 45°. The alternate α values, i.e., 1 / 2^n when n =2, 3… taking a cross RC ladder structure, but its circuit representation becomes too large and hence difficult to realize. The various structural models of the domino ladder circuits are shown in Fig. 1a, b are found in the literature [15], which are more preferable for

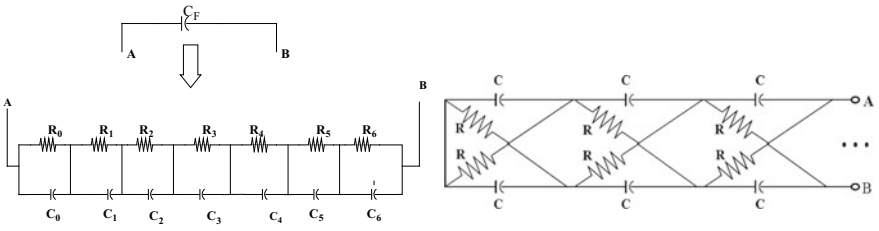

Fig. 1 a Domino ladder network representation of FC b cross RC ladder network of a fractional capacitor

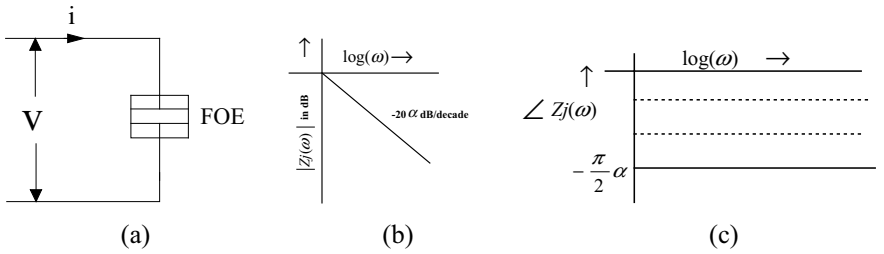

Fig. 2 Plots showing **a** FOE circuit element, **b** magnitude plot, **c** phase plot of a fractional capacitor

realizing the various values of FC. The domino ladder structure presented in Fig.1 a is already popular for fixed-order filtering, whereas Carlson et.al (2008) reported the approximation of fractional-order capacitor by Domino ladder network or by cross RC ladder network is represented in Fig. 1a, b, respectively. Similarly, a cross RC ladder representation which approximates a fractional capacitor (FC) is shown below.

Figure 2a shown below represents the circuit element for FOE which is considered as a fractional capacitor with its magnitude and phase plot represented in Fig. 2b and c, respectively. The magnitude of fractional capacitor changes with respect to the order α by variation of frequency ω in x-axis, whereas the phase remains constant throughout frequency ω for a particular value of α.

$$Z(s) = \frac{V(s)}{I(s)} = \frac{1}{C_F s^{\alpha}}, \Rightarrow Z(j\omega) = \frac{1}{C_F (j\omega)^{\alpha}} = \frac{1}{C_F \omega^{\alpha}} \angle\left(-\frac{\pi}{2}\alpha\right)$$

The MATLAB simulation is done for three possible filters (low-pass, high-pass, and band-pass) whose transfer functions are defined as

$$T_{\text{Lowpass}}(s) = \frac{b}{s^{\alpha+\beta} + as^{\beta} + b} \tag{7}$$

$$T_{Highpass}(s) = \frac{as^{\alpha+\beta}}{s^{\alpha+\beta} + as^{\beta} + b} \tag{8}$$

$$T_{Bandpass}(s) = \frac{as^{\beta}}{s^{\alpha+\beta} + as^{\beta} + b} \tag{9}$$

Now, this method is used here for analyzing the stability of the proposed fractional-order low-pass filter. The characteristics equation of the above filters' transfer function with Eqs. (7) to (9) will be in the form of

$$s^{\alpha+\beta} + as^{\beta} + b = 0 \tag{10}$$

Putting $\alpha = \frac{k_1}{m}$, $\beta = \frac{k_2}{m}$ and $W = s^{\frac{1}{m}}$, then the above equation transfers to $W^{k_1+k_2} + aW^{k_2} + b = 0$.

3.3 Gain-Bandwidth Stability Range of Fractional-Order Filter

The cutoff frequency of 0.4 kHz for a second-order low-pass filter can be increased to 21 kHz by changing the exponent factor α without reducing the time constant RC as in MATLAB simulation shown in Fig. 3, (for all cases time constant, i.e., $RC = 0.515 \times 10^{-3}$). Similarly, the bandwidth of 0.3 kHz for a second-order

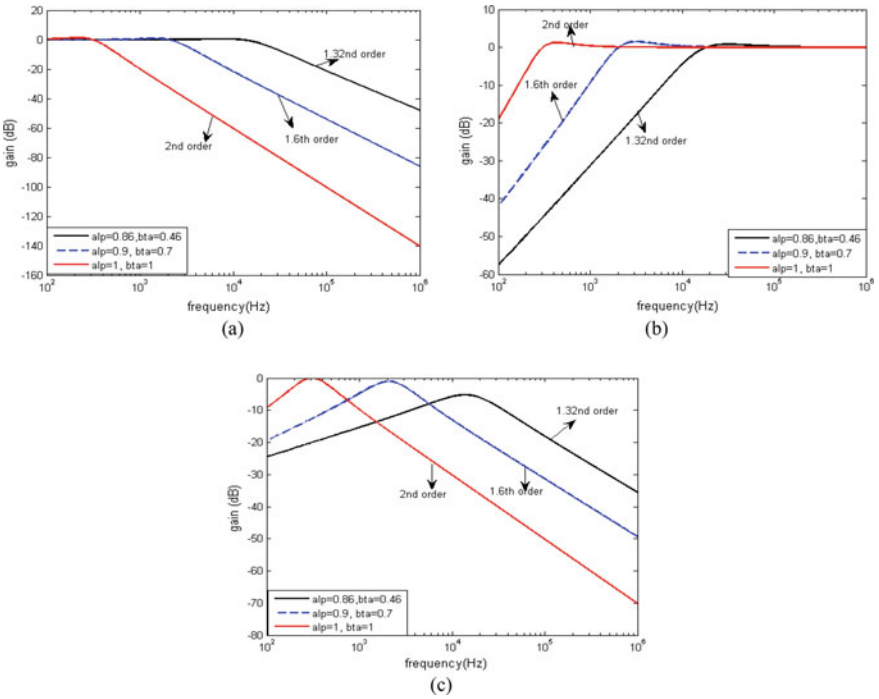

Fig. 3 MATLAB simulation of **a** low-pass **b** high-pass **c** band-pass fractional-order filters of different orders

band-pass filter can be increased to 24 kHz in its fractional domain. However, the slope (dB/decade) is decreased by reducing the order of the filter, which causes the widening the transition band of the filter as shown in Fig. 3c. Here for simulation purposes, we have taken, $b = a^2$ (i.e.,$a = 1.94 \times 10^3$ and $b = 3.76 \times 10^6$). The values of "a" and "b" taken for simulation are same as the experimental value for realizing fractional-order filters. From simulation results, it is observed that the gain-bandwidth stability range of a fractional-order filter is wider than a conventional integer-order filter.

3.4 Stability Analysis of Fractional-Order Filter Using Step Response

In this section, a low-pass filter is considered to study its step response in which the response of the filter settles to steady state over the variation in time. The steadiness of the output can be observed by looking at the filter's step response, where the amplitude slowly diminishes with lesser overshoot and undershoot. The transfer function given in Eq. (7) is used in the following three cases, for which the response plots are represented below.

Case-I (K < 3, α = 1, β = 1): At this scenario, the filter is a complete second (2nd)-order low-pass filter, having DC gain less than three (K<3). From Fig. 4 (b), it is clear that the response to the filter action changes to a fixed amount of time in a fixed period and is therefore stable.

Case-II (K > 3, α = 1, β = 1): At this scenario, the filter is a complete second (2ND)-der low-pass filter where the fixed gain has a value of more than three (> 3) (e.g., K = 4) and reaches unstable state as the steady-state value is not observed in Fig. 4c.

Case-III (K > 3, $\alpha = 0.8$, β = 0.4): At this scenario, the filter is a partial-order (1.2nd order) low-pass filter, and the fixed gain is more than three (>3) (e.g., K = 4). Here, the filter's step response moves toward a steady-state value as it happens in case-1. Hence, the system becomes stable as shown in Fig. 4 d.

To get the step response of a fractional-order low-pass filter, the fractional-order transfer function is approximated to integer order using Oustaloup algorithm in the frequency range of 0.1 Hz–1 MHz, and then, MATLAB code as discussed in [10] is adopted to plot the unit step response of the given fractional-order filter. Here, for simulation, both integer- and fractional-order filters are considered with time constant $RC_F = 0.001$.

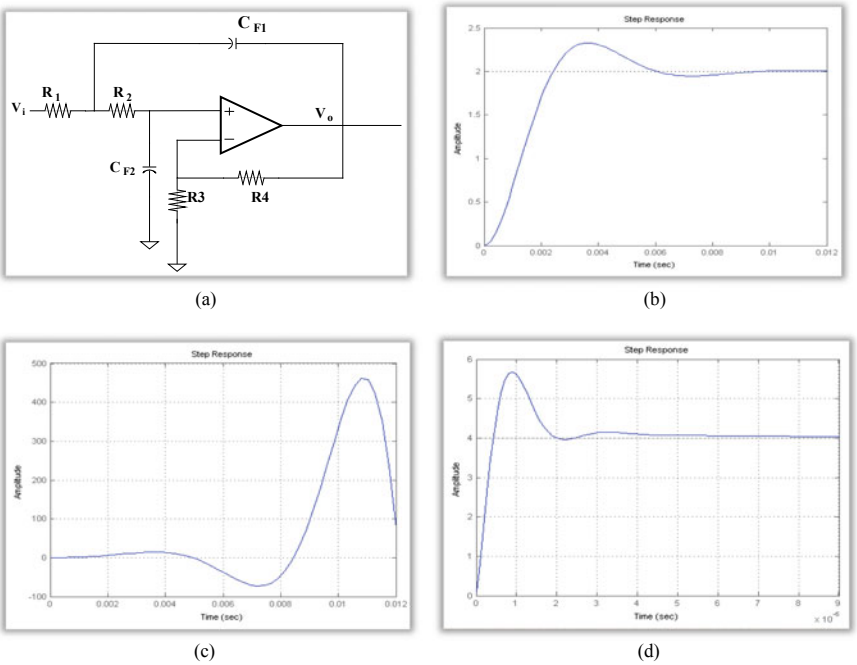

Fig. 4 **a** Circuit diagram of fractional-order low-pass filter **b u**nit step response of second-order low-pass filter (Stable) with dc gain $K = 2$, RC $= 0.001$ **c**) unit step response in second-order low-pass filter, (Unstable) with K $= 4$, $\alpha = 1$, $\beta = 1$, $RC_F = 0.001$ **d** unit step response of second-order low-pass filter response ((Stable) with K $= 4$, $\alpha = 0.8$, $\beta = 0.4$, $RC_F = 0.001$

4 Results and Discussion

The MATLAB simulation carried out for the low-pass, high-pass, and band-pass filters in its integer and fractional domain has been discussed by observing the lower and upper cutoff frequencies. From Fig. 3, it has been confirmed that the filters in fractional domain has comparatively more bandwidth due to their higher value of upper and lower cutoff frequency in case of low-pass, high-pass filters, respectively. For band-pass filter, this results with higher transition bandwidth as the frequency on both sides of the curve shifts forward. So, these changes are noticeably for a fractional-order filter as compared to their integer-order counterpart.

Again, Fig. 4 depicts the performance comparison of a fractional-order filter with its integer-order counterpart. Here in unit step approach, a fractional-order low-pass filter has been investigated with variable gain and order. It is observed that the given filter is stable when the two capacitors are of integer order provided the gain is less than three (i.e., K<3). Furthermore, the same low-pass filter becomes unstable if we increase the gain keeping the orders of the two capacitors unchanged. Finally, the exponents value of the two capacitors used in the low-pass filter is changed to

fractional ones holding the higher value of gain (i.e., $K = 4$), which gives a stable response though the gain is high. This happens due to the fractional values which stands for the order of two capacitors used in given filter circuit.

5 Conclusions

In this paper, the response of the fractional low-pass, high-pass, and band-pass filters is being observed through MATLAB simulation in gain verses bandwidth (frequency) approach, whereas the unit step approach is carried out for low-pass filter only and found to be more stable when two integer-order capacitors are replaced by fractional capacitors. In gain verses bandwidth approach, the order of the capacitor which is a fractional number has certain effect on bandwidth and cutoff frequency. As observed, the stability derived from bandwidth changes with change in order of fractional capacitor used in low-pass, high-pass, and band-pass filters. In step response approach, it is observed that the filter's response quickly reaches steady-state when the orders of the capacitors are fractional values for a fixed gain of the filter circuit.

References

1. Debnath L (2003) Recent applications of fractional calculus to science and engineering. Int J Math Math Sci 54:3413–3442
2. Ortigueira MD (2008) An introduction to the fractional continuous-time linear systems, the 21st century systems. IEEE Circuits Syst Mag 8(3):19–26
3. Elwakil AS (2010) Fractional-order circuits and systems: an emerging interdisciplinary research area. IEEE Circuits Syst Mag 10(4):40–50
4. Caponetto R, Dongola G, Fortuna L, Petras I (2010) Fractional-order systems: modelling and control applications. World Scientific, Singapore
5. Moreles MA, Lainez R (2017) Mathematical modelling of fractional order circuit elements and bio-impedance applications. Commun. Nonlinear Sci. Numer. Simulat. 46:81–88
6. Caponetto R, Dongola G, Fortuna L, Petras I (2019) Fractional-order systems: modeling and control applications. Non-Linear Sci Ser A 72:19–37
7. Zahra WK, Hikal MM, Bahnasy TA (2017) Solutions of fractional order electrical circuits via Laplace transform and nonstandard finite difference method. J Egyptian Math Soc 25:252–261
8. Maundy B, Elwakil AS, Freeborn TJ (2011) On the practical realization of higher order filters with a fractional stepping. Circuit Syst Signal Process. 91:484–491
9. Walczak J, Jakubowska A (2015) "Analysis of resonance phenomena in series RLC circuit with super-capacitor". In Analysis and simulation of electrical and computer systems, lecture notes in electrical engineering, Springer, vol 324, pp 27–34
10. Rousan AA, Ayoub NY, Alzoubi FY, Khateeb H, Al-Qadi M, Hasan (Qaseer) MK, Albiss BA (2006) "A fractional LC-RC circuit", fractional calculus and applied analysis. An Int J Circuit Theory Appl 9(1):33–41
11. Biswal K, Tripathy MC, Kar SK (Feb 2020) "Performance analysis of fractional order low-pass filter". Lecture notes in networks and systems (ICAC), Springer, vol 109, pp 224–231
12. Biswal K, Tripathy MC, Kar SK (Mar 2020) "Performance analysis of fractional order high-pass filter". Lecture notes in electrical engineering (IEPCCT) Springer, vol 630, pp 511–519

13. Swain S, Biswal K, Tripathy MC, Kar SK (Jul 2020) "Performance analysis of fractional order sallen-key high-pass filter using fractional capacitors". International conference on computational intelligence for smart power system and sustainable energy (CISPSSE), Keonjhar, Odisha, India, vol 1, pp 1–5
14. Ahmadi P, Maundy B, Elwakil AS, Belostotski L (2012) High-quality factor asymmetric-slope band-pass filters: a fractional-order capacitor approach. IET Circuits Devices Syst 6:187–197
15. Mondal D, Biswas K (Jul. 2011) Comparative performance study using single component fractional order element, cross RC ladder and domino ladder network. IET Circuits Devices Syst 5(4):334–342
16. Radwan AG, Elwakil AS, Soliman AM (2008) on the first order filter generalized to the fractional domain. J Circuits Syst Comput 17:55–56
17. Biswas K, Sen S, Dutta PK (Sept. 2006) Realization of a constant phase element and its performance study in a differentiator circuits. IEEE Trans Circuits Syst—II 53(9):802–806
18. Tripathy MC, Mondal D, Biswas K, Sen S (Nov. 2015) Experimental studies on realization of fractional inductors and fractional-order bandpass filters. Int J Circuit Theory Appl 43(9):1183–1196
19. Biswal K, Swain S, Tripathy MC, Kar SK (Apr 2021) "Modeling and performance improvement of fractional-order bandpass filter using fractional elements". IETE J Res. https://doi.org/10.1080/03772063.2021.1906334. Published Online (Article in press)
20. Bandyopahyay B, Kamal S (2014) Stabilization and control of fractional-order systems: a sliding mode approach. Berlin, Springer, pp 59–78
21. Radwan AG, Soliman AM, Elwakil AS, Sedeek A (2009) On the stability of linear systems with fractional-order elements. Chaos Solitons Fractals 40(5):2317–2328

Tidal Energy Connected with Grid for Coastal Area

Pushpak Jain and Kanhu Charan Bhuyan

Abstract Tidal renewable energy is one of the underdeveloped power sources that might help meet demand while lowering carbon dioxide emissions. There is enormous potential for generating power from tidal currents. It is a resource used to generate power sustainably. The construction has been developed in MATLAB Simulink of a tidal current turbine and is discussed in this paper. The twin-turbine model has been developed, and the resultant power is 37 kW. Whenever the turbine rotor is in rotational motion, it produces mechanical power, which is then transmitted to the electrical generator. The current control strategy has been used to design a three-phase modified sine wave inverter system for a tidal energy grid-linked structure. The stationary and synchronous reference frames (SRF) are two control techniques applied to an inverter. Park transformation is using to translate AC quantity to DC in the synchronous frame. In $\alpha\beta$-control, proportional-resonant (PR) regulators are commonly used where PI controller converts to PR, which is required for SRF control. The controller implements a phase-locked loop to monitor the power grid's phase angle which responds rapidly enough to fluctuations in demand or grid link conditions. As a consequence, it tends to be successful in providing steady voltage to the load avoiding phase jumps.

Keywords Tidal energy · Clarke and park transformation · Phase locked loop

1 Introduction

The inclination toward the clean energy source for sustainable development leads to the exploration of different forms of renewable energy sources. Energy plight, climate shift due to greenhouse gases increasing the atmospheric temperature, soaring

P. Jain (✉) · K. C. Bhuyan
Department of Instrumentation and Electronics, College of Engineering and Technology, Bhubaneswar 751029, India
URL: https://www.cet.edu.in

K. C. Bhuyan
URL: https://www.cet.edu.in

M. Mishra et al. (eds.), *Innovation in Electrical Power Engineering, Communication, and Computing Technology*, Lecture Notes in Electrical Engineering 814,
https://doi.org/10.1007/978-981-16-7076-3_12

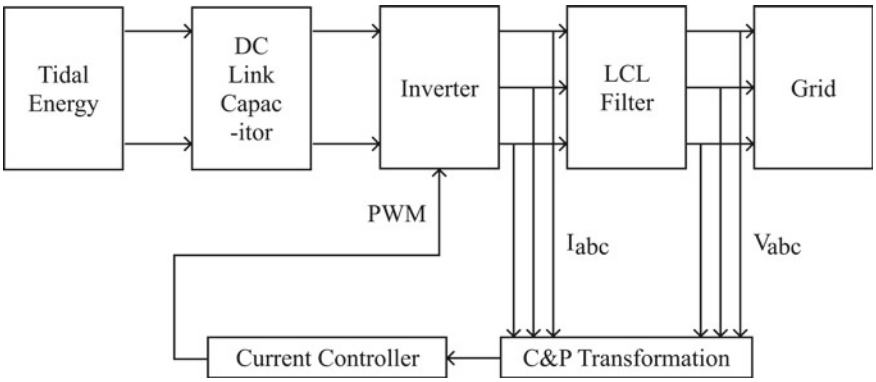

Fig. 1 Block diagram of tidal energy

oil prices, limitation and exhaustion of fossil fuels supply increase the demand in scrutiny of clean energy. Tidal energy is one such green energy where energy is derived from the ocean currents. Tidal energy is a source of motion energy that is stored in oceanic streams because of the gravitational pulls as well as the earth's rotation around its axis [1]. Carbon dioxide emissions are projected to reduce as global environmental perception improves, reducing dependence on fossil fuels and advancing renewable energy production [2]. The cyclic value of the marine current energy supply is being recognized as a significant advantage over other volatile renewable energy technologies [3].

The major focus in this paper is on tidal energy because tides are easily predictable. There are not many sites where high tide can be found, that is why we focused on generating electricity in low-tidal zones. This can be accomplished by employing a low-pressure turbine, which will aid in the construction of compact power plants capable of supplying electricity to small-scale locations.

Figure 1 shows the complete block diagram of tidal energy which is connected to grid. The tidal energy output voltage is fed to the DC-link capacitor, and again, this Dc-link capacitor voltage is transmitted to the DC–AC inverter. The inverter produces a three-phase AC voltage and uses an LCL filter to reduce the harmonic portion of the voltage. The Clarke and Park transition using phase-locked loop (PLL) with current-controlled was used to produce the pulse width modulation (PWM) signal for the inverter. The current control mode (CCM) controls the majority of grid-tied converters. The most enticing aspect of CCM is its tolerance to grid voltage fluctuations. Grid-following and grid-supporting converters will also benefit from CCM-based control. When the voltage needs to be specified in the islanding operation mode in an MG (microgrid), then the voltage control mode (VCM)-based control must be used. Grid-connected processes, such as grid-following and grid-supporting converters, also benefit from VCM [4].

This paper is divided into five sections where Sect. 1, provides a brief introduction to tidal energy. Section 2 describes the modeling and analysis of tidal energy, followed

by Sect. 3 which consists of Clarke and Park transformation for the control of inverter. Section 4, shows the simulation results of grid-connected tidal energy followed by the brief conclusion in Sect. 5.

2 Modeling of Marine Energy

2.1 Tidal Analysis Method

Tidal current systems aim to derive power from water's kinetic activity; these tidal waves are frequently expanded when water is forced to pass via small channels or along beaches. In the world's main shorelines, there are three simple tidal patterns; they are semidiurnal, diurnal, and mixed semidiurnal [5]. The tidal analysis approach used in this paper is the harmonic methods. In a harmonic method, the tides are viewed as long-period waves made up of various harmonic constituents with known frequencies. The sum of harmonic components represents tidal elevation with each component representing a fluctuation at an astronomically determined frequency. The tide is the sum of specific tides, with each specific tide having a distinct amplitude and phase at each position. The waveform that is closer to the measured tide at a specific location by adding up a huge number of selective tides. The established frequencies are used to create equations of the form:

$$h(t) = h_0 + \sum_{j=1}^{m} f_i H_i \cos(\omega_i t + u_i - k_i) \tag{1}$$

where $h(t)$ = depth of expected water level, f_i = factor of the lunar network, H_i = amplitude average, H_o = the average level of water, m = the amount of components, w_j, u_i, k_i = represent the ith tidal components frequency, nodal phase, and phase angle.

The tidal components that have been used in this paper are (S2, K1, N2, O1, and M2). Table 1 shows the resulting quantities of tidal amplitude, phase, and tidal frequency of each tidal component, and the following data is taken from [6].

Table 1 Assets of tidal components [6]

Tidal component	Frequency	Phase	Amplitude
S2	0.0833	52.5	0.11
K1	0.0418	20.5	0.12
N2	0.0790	26.4	0.19
O1	0.0387	218	0.06
M2	0.0805	31	0.86

2.2 Tidal Current and Turbine Profile

The tidal currents are presumed to move inside and outside of the tidal phase in the form of sinusoids. The following equation can be used to model tidal currents as a flow of harmonics:

$$V(t) = \sum A_j \cdot \sin(2\pi f_i t + \theta_i) \tag{2}$$

where $V(t)$ = speed of tidal current as a function of time, A_j = amplitude of jth harmonic, f_j = frequency of jth harmonic, θ_j = phase angel of jth harmonic.

The five main tidal components (S2, K1, N2, O1, and M2) have been designed in Simulink using function blocks. To achieve the resulting tidal current profile, these components were applied. The profile is shown in Figure 2. Establishing a tidal dam across a bay during high tide or drawn out, the energy from free water flow is two ways to generate electricity from water flow. The amount of energy that can be extracted from water flowing by a tidal current turbine is determined by the turbine design [6] and [7]. The diameter of the rotor and the speed of the tidal current determine the power generated by the tidal turbine. The quantity of energy accessible in a free-flowing stream of water is determined by:

$$P_{\text{avl}} = \frac{\delta \cdot A_r \cdot \upsilon^3}{2} \tag{3}$$

where δ = constant depth of seawater (1025), A_r = area of the rotor blades, v = the pace of the tide. The real output from the turbine can be validated as follows:

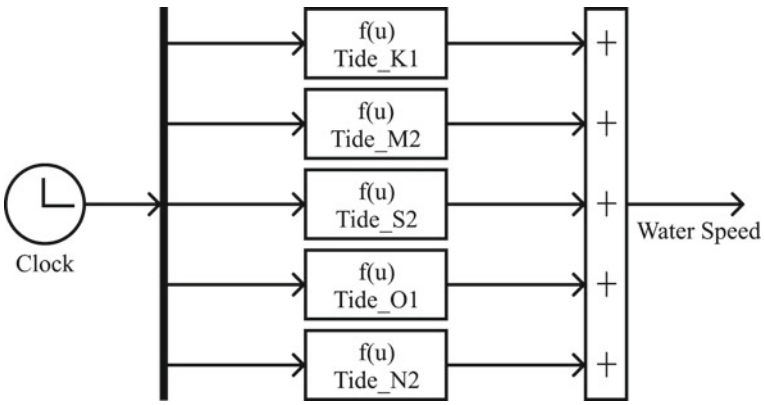

Fig. 2 Block diagram of tidal energy [6]

$$P_{\text{act}} = C_p(\lambda, \theta) * \frac{\delta \cdot A_r \cdot \upsilon^3}{2} \tag{4}$$

where C_p = coefficient of control, λ = ratio of tip pace, θ = pitch angle of turbine blades. The coefficient of control is not constant; it is affected by the ratio of tip pace and the pitch angle of the turbine blades. This information is provided by:

$$C_p(\lambda, \theta) = z_1\left(\frac{z_2}{\beta} - z_3\beta\theta - z_4\theta^x - z_5\right)e^{-\frac{z_6}{\beta}} \tag{5}$$

The term β is often used to describe:

$$\frac{1}{\beta} = \frac{1}{\lambda + 0.08\theta} - \frac{0.035}{\theta^3 + 1} \tag{6}$$

C_p is unable to exceed 0.593. This ensures that the amount of energy derived from water is never more than 59.3 % (Betz's limit). Shifting β indicates that C_p will have its maximal value at one significant value of λ for particular blade pitch for $z_1 = 0.51$, $z_2 = 116$, $z_3 = 0.4$, $z_4 = 0.0$, $z_5 = 5$, $z_6 = 21$ in Eq. (5) [8].

3 Inverter Control

A DC current source or voltage source can be converted into a single-phase or three-phase AC current or voltage with the help of an inverter. Inverters are categorized based on the form of input source which is either the current source inverter or voltage source inverter [9, 10], and [11]. A current-controlled PWM inverter with LCL output filters has been designed as the control structure for the three-phase DC–AC grid connection.

The LCL filter was preferred over the L and LC filters because it produce less grid current deformation and reactive power, have a smaller switching frequency, and have improved attenuation. The voltage sourer inverter (VSI) using an LCL filter is modeled as shown in Figure 3. From a stable DC supply, a voltage source inverter (VSI) produces synchronized three-phase voltages [12] and [13]. The LCL filter mathematical equations in the stationary and synchronous reference frame [14]:

$$\frac{\mathrm{di}_1(t)}{\mathrm{dt}} = \frac{1}{L_1}[-R_1 i_1(t) + V(t) - V_o(t)] \tag{7}$$

$$\frac{\mathrm{dV}_o(t)}{\mathrm{dt}} = \frac{1}{C_g}[i_1(t) - i_2(t)] \tag{8}$$

$$\frac{\mathrm{di}_2(t)}{\mathrm{dt}} = \frac{1}{L_2}[-R_2 i_2(t) + V_o(t) - G_{av}(t)] \tag{9}$$

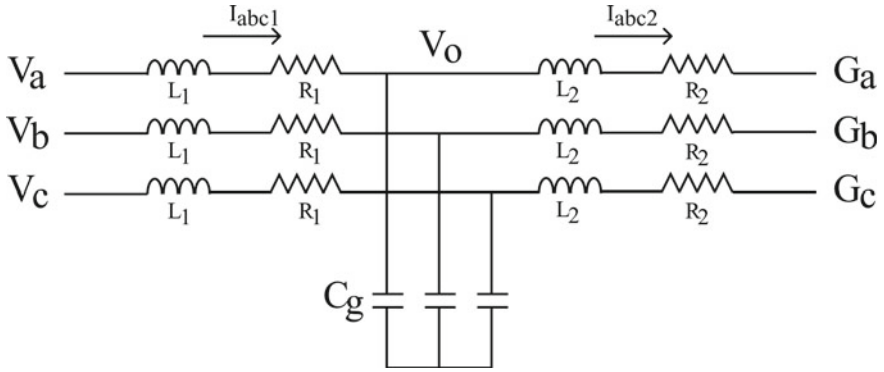

Fig. 3 Block diagram of LCL filter [14]

$$\frac{\mathrm{di}_{1d}(t)}{\mathrm{dt}} - \omega i_q(t) = \frac{1}{L1}[-R_1 i_{1d}(t) + V_d(t) - V_{\mathrm{od}}(t)] \tag{10}$$

$$\frac{\mathrm{di}_{1q}(t)}{\mathrm{dt}} - \omega i_{1d}(t) = \frac{1}{L1}\left[-R_1 i_{1q}(t) + V_q(t) - G_q(t)\right] \tag{11}$$

$$\frac{\mathrm{dV}_{\mathrm{od}}(t)}{\mathrm{dt}} - \omega V_{\mathrm{oq}}(t) = \frac{1}{C_g}[i_{\mathrm{id}}(t) - i_{2d}(t)] \tag{12}$$

$$\frac{\mathrm{dV}_{\mathrm{oq}}(t)}{\mathrm{dt}} - \omega V_{\mathrm{od}}(t) = \frac{1}{C_g}\left[i_{iq}(t) - i_{2q}(t)\right] \tag{13}$$

$$\frac{\mathrm{di}_{2d}(t)}{\mathrm{dt}} - \omega i_{2q}(t) = \frac{1}{L2}[-R_2 i_{2d}(t) + V_{\mathrm{od}}(t) - V_d(t)] \tag{14}$$

$$\frac{\mathrm{di}_{2q}(t)}{\mathrm{dt}} - \omega i_{2d}(t) = \frac{1}{L2}\left[-R_2 i_{2q}(t) + V_{\mathrm{oq}}(t) - V_q(t)\right] \tag{15}$$

Equations (10) to (15) show how the cross-coupling concepts $\omega i_q(t)$ and $\omega i_d(t)$ affect both the capacitor and the current voltages.

3.1 Phase Locked Loop (PLL)

In a microgrid, grid synchronization is critical for power electronic converters. Grid supporting and following converters use the underlying magnitude, frequency, and phase angle of the grid voltage to produce the reference for the converter output current. The frequency-domain strategies and the time-domain strategies are the two most common grid basic component detection methods. The open- and closed-loop types of time-domain technologies can be distinguished. Weighted

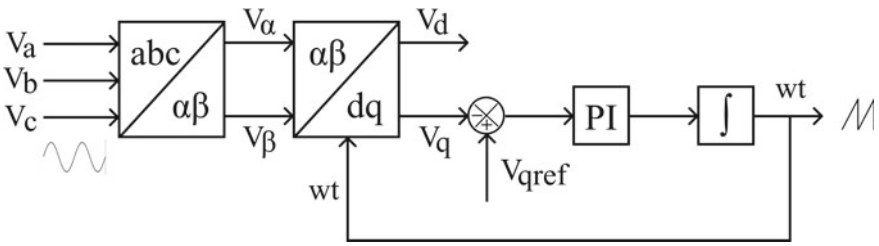

Fig. 4 Block diagram of PLL [15]

least square estimation, zero-crossings detection, adaptive notch filtering, and phase-locked loop techniques are examples of closed-loop techniques. Because of their ease of processing and high accuracy, PLL-based synchronization strategies undoubtedly are the most commonly used for converter control [15, 16], and [17]. For phase tracking, there are three major categories of PLL systems: zero crossings, stationary reference frame, and synchronous rotating frame (Refer Fig. 4).

3.2 Clarke and Park (CP) Transformation

Clarke transformation is being used to transform three-phase grid quantities in an abc frame into two stationary frames. In most cases, proportional-resonant (PR) controllers are used to reduce tracking inaccuracy in fundamental frequency. PR controls, which are gradually increasing in today's control of networked devices, are an alternative to the proportional-integral (PI) controller for output [18]. The response currents or voltages are converted into a $\alpha\beta$ frame that is the $V_\alpha - V_\beta$ and $I_\alpha - I_\beta$. The monitoring errors are then calculated by comparing them to the frame control references. The PR controllers will monitor the resulting tracking errors to zero. The Clarke transformation matrix is [19]:

$$\begin{bmatrix} \alpha \\ \beta \\ \gamma \end{bmatrix} = \begin{bmatrix} 2/3 & -1/3 & -1/3 \\ 0 & 1/\sqrt{3} & -1/\sqrt{3} \\ 1/3 & 1/3 & 1/3 \end{bmatrix} = \begin{bmatrix} A \\ B \\ C \end{bmatrix} \tag{16}$$

The dq0 to ABC transformation, which seems to be an interleaved combination of Park's and Clarke's inverse transformations, is performed by this part. The signals on a synchronously moving reference frame are converted directly to three-phase quantities using this transformation.

4 Simulation Results

The schematic diagram of tidal energy with grid-connected inverter is shown in Figure 1 above. The entire system is made up of a tidal current and turbine profile, filter for power factor correction, DC to AC converter, LCL filter for harmonic reduction, three-phase power grid with current-controlled technique using PLL and CP transformation. The voltage generated by tidal energy is inherently variable. The generated voltage from tidal energy estimated to be 500 to 600V is shown in Figure 5

This tidal energy voltage is then fed into the PFC filter, which produces a more stable DC voltage for the inverter. In a modified sine wave signal, the three-phase AC inverter generates 600V output voltage and 100A output current in a sine wave signal with 6.68% harmonic distortion as shown in Figs. 6, 7, and 8.

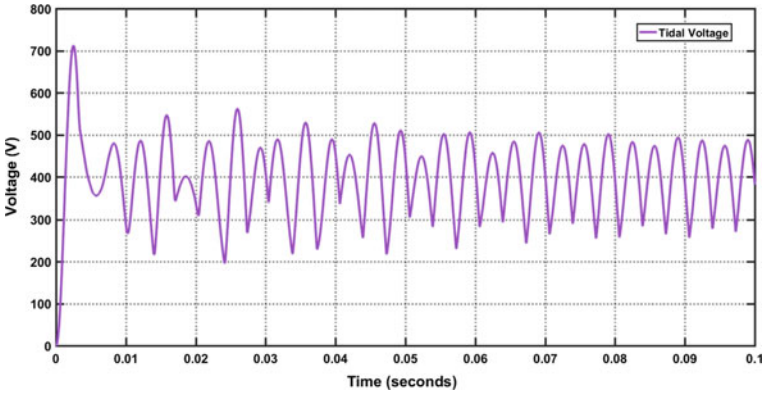

Fig. 5 Voltage of tidal turbine system

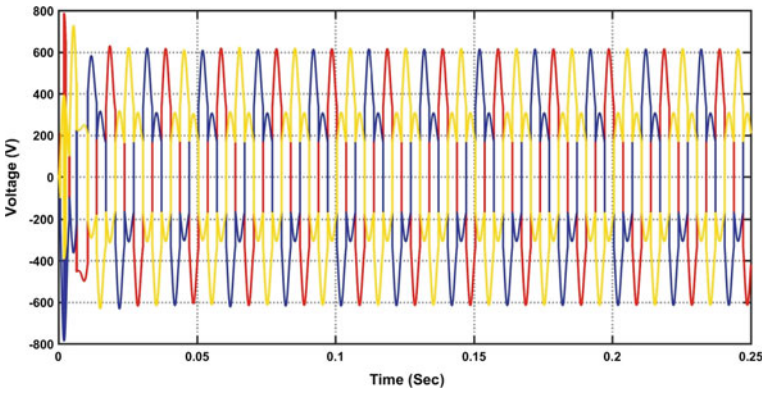

Fig. 6 Output voltage of inverter

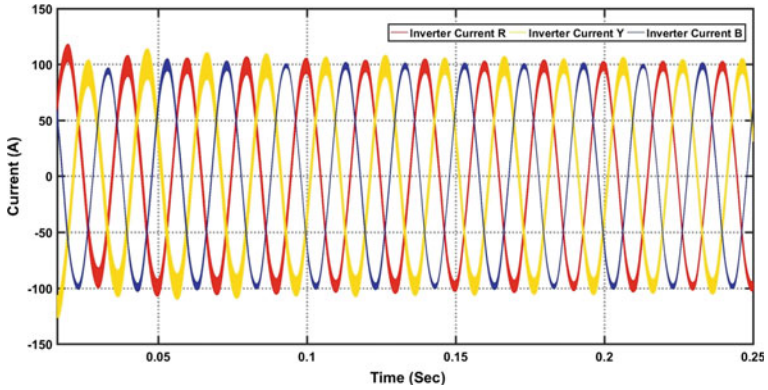

Fig. 7 Output current of inverter

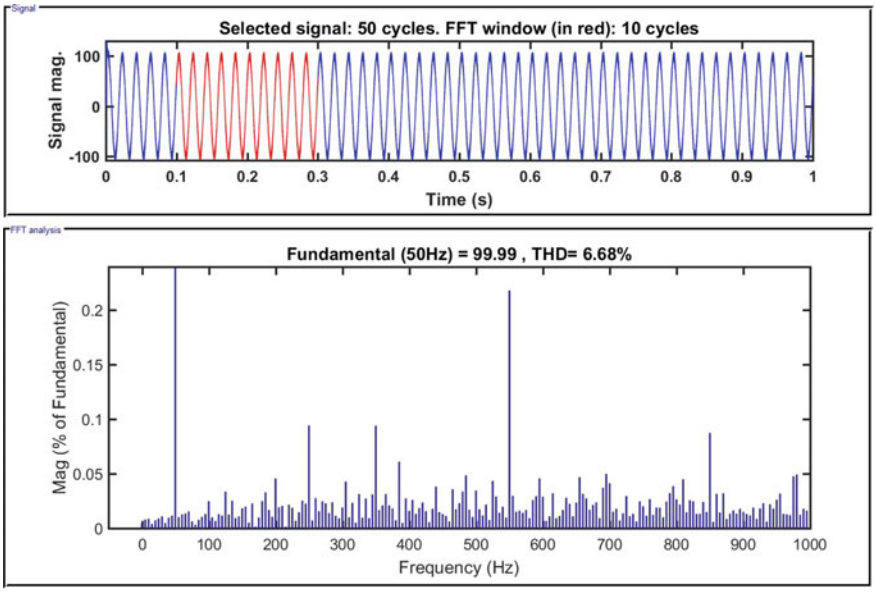

Fig. 8 THD of Inverter Current

Figure 9 shows the phase angle mandated by the dq to abc transition block is tracked using a PLL. The signal is converted to the abc reference frame once again and supplied to the PWM, which generates pulses for a grid-connected inverter. The grid regulation PI controller coefficients KP = 10 and KI = 5000 are used in the control scheme. The grid produces a 400V phase-to-phase output voltage with a 100A output current and frequency of 50Hz. Figure 10 shows the THD of three-phase current waveforms, which are 1.12%, respectively, and are within the IEEE standard of less than 5%. These results demonstrate the effectiveness of the proposed voltage-

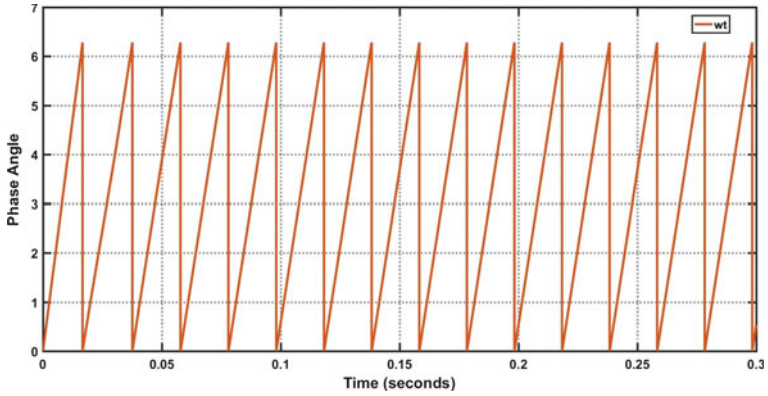

Fig. 9 Phase angle produce by PLL

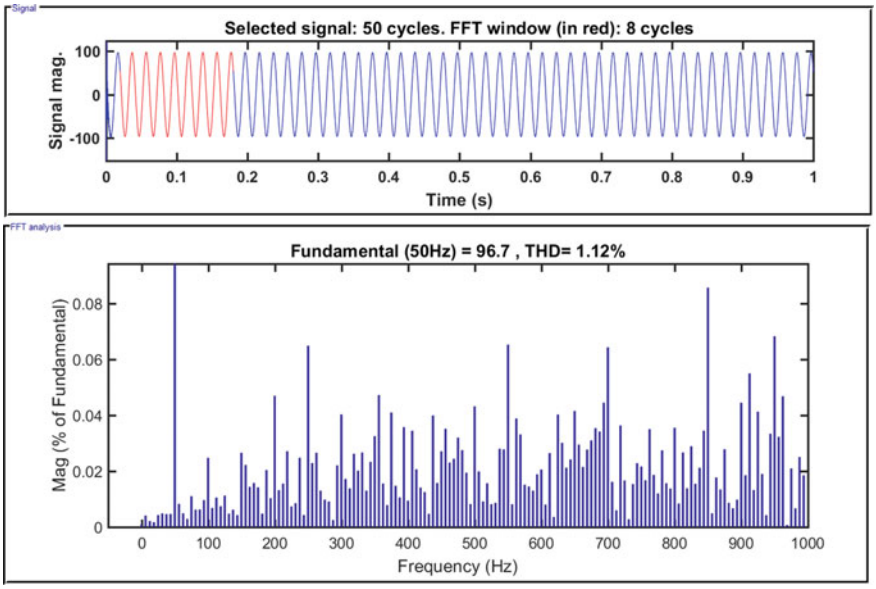

Fig. 10 THD of Grid Current

and current-controlled methodologies, as well as the SPWM mechanism and LCL filter. As seen from Figs. 11 and 12, the grid output current and voltage are in phase with each other with a minimum amount of harmonic component. The LCL filter reduces the harmonic component to 83% as from 6.68% to 1.12%. In a grid-tied environment, the consistency of current pumped into the grid is a big problem that is continually tracked, since power quality can be impaired and contaminated by harmonics produced by the inverter.

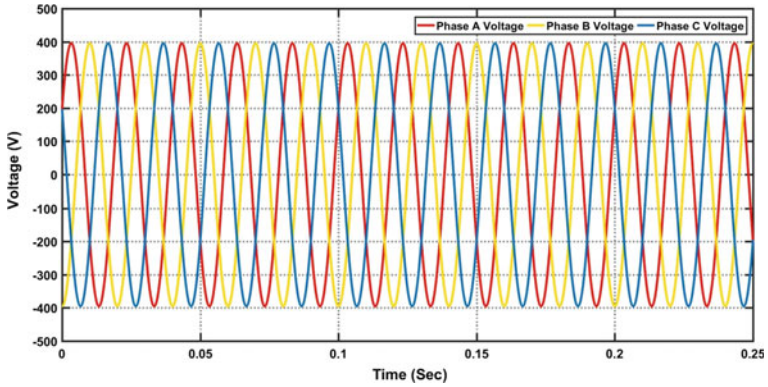

Fig. 11 Grid voltage

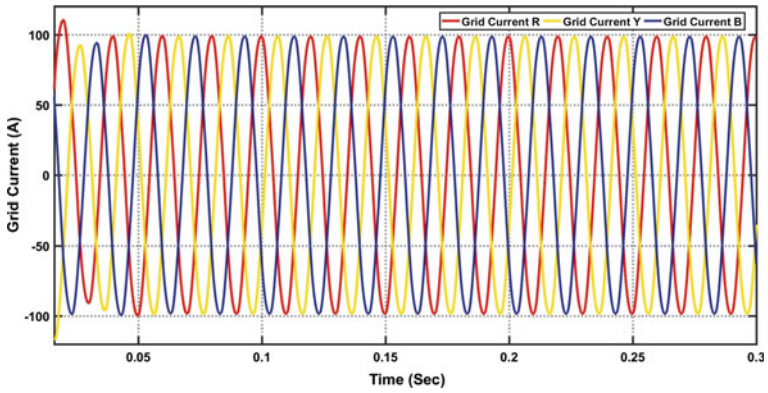

Fig. 12 Grid current

In grid-connected power generation systems, power performance is a key element to consider when the power produced is inserted into the grid.

5 Conclusion

The work provides a simulated model for the tidal acceleration profile, turbine profile, PFC filter, inverter, THD reducer, power grid, and synchronization technique. With a mechanical torque of 228 N.m and a tidal speed of 1 m/s, a specific turbine's resultant energy is 37 kW. The system's architecture generates 36 kW of electricity from the grid with amplitude of 400V, a current of 100 A, and a frequency of 50 Hz. In a synchronously revolving reference frame, the entire control scheme is created. The dq, abc power, and other implementation mechanisms for three-phase inverters have

been mentioned. Since a three-level inverter with a filter circuit is being used, the output noise is minimized. When there are harmonics in the incoming signal, the device functions as a low-pass filter, reducing the effect of the harmonic components in the output. Grid current and inverter current have THDs of 1.12% and 6.48%, respectively, where the filter eliminates grid harmonics in the output by up to 83%.

References

1. Rodrigues N, Pintassilgo P, Calhau F, Gonz´alez-Gorben˜a E, Pacheco A (2021) “Cost-benefit analysis of tidal energy production in a coastal lagoon: the case of Ria Formosa–Portugal.” Energy 229:120812
2. Soundarya G, Sitharthan R, Sundarabalan CK, Balasundar C, Karthikaikan-nan D, Sharma J (2021) “Design and modeling of hybrid DC/AC microgrid with manifold renewable energy sources.” IEEE Canadian J Electric Comput Eng 44(2):130–135
3. Abd Ali L, Haider A, Anssari O (2019) Modeling and simulation of tidal energy. J Eng Appl Sci 14:3698–3706. https://doi.org/10.3923/jeasci.2019.3698.3706
4. Dragi˘cevi´c T, Li Y (2018) “AC and DC microgrid control.” In Control of power electronic converters and systems, Academic Press, pp. 167–200
5. Coles D, Angeloudis A, Goss Z, Miles J (2021) ”Tidal stream versus wind energy: the value of cyclic power when combined with short-term storage in hybrid systems.” Energies 14(4):1106
6. Okoli C, Uhunmwangho R, Nwogu H (2017) ”A simulation model for tidal energy extraction in Nigeria using tidal current turbine.” In 2017 IEEE PES PowerAfrica, IEEE, pp. 500–505
7. Khare V (2019) “Status of tidal energy system in India.” J Marine Eng Technol, pp 1–10
8. Xue J, Ahmadian R, Falconer RA (2019) Optimising the operation of tidal range schemes. Energies 12(15):2870
9. Aihsan MZ, Ahmad NI, Mustafa WA, Rahman NA, Soo JA (2019) Development of square wave inverter using DC/DC boost converter. Int J Pow Elec and Dri Syst ISSN 2088(8694):8694
10. Bhuyan KC, Patjoshi RK, Padhee S, Mahapatra K (2014) “Solid oxide fuel cell with DC-DC converter system: control and grid interfacing.” WSEAS Trans Syst Control 9
11. Rath PK, Bhuyan KC (2018) Vector control of fuel cell based grid connected inverter. J Green Eng 8(3):201–218
12. Cardona JV,Gil JA, Sales FG, Segui-Chilet S, Orts Grau S, Mun˜oz Galeano N (2009) ”Improved control of current controlled grid connected inverters in adjustable speed power energies.” In Internatıonal conference on renewable energies and power qualıty (ICREPQ’09)
13. Bhuyan KC, Sao SK, Mahapatra K (2012) ”Fuel cell connected to grid through inverter.” In 2012 students conference on engineering and systems, IEEE, pp 1–4
14. Sahoo AK, Shahani A, Basu K, Mohan N (2014) “LCL filter design for grid-connected inverters by analytical estimation of PWM ripple voltage.” In 2014 IEEE applied power electronics conference and exposition-APEC 2014, IEEE, pp 1281–1286
15. Wang X, Yaz EE (2016) Smart power grid synchronization with fault tol- erant nonlinear estimation. IEEE Trans Power Syst 31(6):4806–4816
16. Peyghami S, Mokhtari H, Blaabjerg F, Yang Y (2017) ”Grid Synchronization for distributed generations.” In Encyclopedia of sustainable technologies: reference module in earth systems and environmental sciences, Elsevier, pp. 179–194
17. O¨ gren J (2010) ”PLL design for inverter grid connection: Simulations for ideal and non-ideal grid conditions.”

18. Yadav U, Gupta A, Rai HK, Bhalla DK (2021) “Mitigation of harmonic current in grid-connected solar power system.” In Recent advances in mechanical engineering. Springer, Singapore, pp 605–610
19. Jia J, Yang G,Nielsen AH, Rønne-Hansen P (2018) “Study of control strategies of power electronics during faults in microgrids.” In Hybrid—renewable energy systems in microgrids, Woodhead Publishing, pp 109–146

Design of Switched Capacitor-Based Charge Amplifier in 180 nm Technology

Dillip Kumar Sahoo, Kanhu Charan Bhuyan, and Ananya Dastidar

Abstract Charge amplifier is an important member of various amplification unit consisting of processing of the current signals. In this manuscript, a charge amplifier is designed for the conversion of the low magnitude signals to an appropriate level for further processing. The major advantages of this circuit over the conventional Charge Amplifier is the absence of the resistor in the configuration. The design consists of Charge Amplifier that employs Switched-Capacitor-based Techniques. The performance characteristics, such as power consumption, harmonic distortion, figure of merit, and input referred noise are compared. The Switched Capacitor-based configuration has 180 μW of power consumption with third Harmonic Distortion as 15.33 dB with figure of merit as 3.6×10^9 and the input referred noise of the circuit is 110 $\mu V/Hz^{1/2}$

Keywords Charge amplifier · Switched capacitor circuit · CMOS · Figure of merit · Harmonic distortion

1 Introduction

Real-world signals like sound, images, gestures convey information about the physical environments and to interpret them, and they need to be acquired employing signal acquisition systems for analysis and storage. Mathematically, signals are a the function of time, space, or function of some other variables that are used to transport information. But these real-world signals are very weak, and have very low frequencies thus cannot be fed directly to the recording or storage devices due to which proper signal processing needs to be performed on them. The signals from the sensors like piezoelectric are very inadequate to directly being fed into the voltage amplifiers. For signal processing of such signals, it needs charge amplifiers that can properly condition the signals.

D. K. Sahoo (✉) · K. C. Bhuyan · A. Dastidar
Department of Instrumentation and Electronics, College of Engineering and Technology, Bhubaneswar, India
e-mail: dillip55@live.com

M. Mishra et al. (eds.), *Innovation in Electrical Power Engineering, Communication, and Computing Technology*, Lecture Notes in Electrical Engineering 814,
https://doi.org/10.1007/978-981-16-7076-3_13

In this paper, a switched capacitor charge amplifier is implemented that al- lows the real-world signals to be amplified to the proper requisite signal levels. Further, the switched capacitor-based charge amplifiers' characteristics are compared against the conventional charge amplifier, Bias current compensated amplifier, and linear analog feedback network-based charge amplifier. Finally, the switched capacitor-based charge amplifier was designed in 180 nm CMOS technology and the characteristics are compared for all the configurations.

This paper is divided into 6 sections where Sect. 1 gives a brief introduction to the proposed work. Sections 2 and 3 describe the Charge Amplifier. In this section all the previous literature on the Charge Amplifiers are discussed along with the detailed analysis of the switched capacitor-based technique used in the design of the circuit. Section 4, puts a light on the CMOS design of the proposed circuit in the paper, followed by contains the comparison of the characteristics of all the configurations discussed in Sect. 5. Section 6 contains brief conclusion of the work in the manuscript.

2 Charge Amplifier (CA)

A charge amplifier is an integrator with a very high-input impedance that produces a voltage output proportional to the accumulation of current over time. Figure 1 represents the circuit diagram of a CA. The major difference between a CA and voltage amplifier are that, while the former produces an output as a function of time, the latter acts as a trans-impedance amplifier with a capacitor in the feedback path [1]. In conventional CA schematic, V_{IN}, C_S, R_F, R_W, C_F and V_{OUT} are the input signal from the sensors, input capacitance, feedback resistor, wire resistance, feedback capacitor, output voltage, respectively.

The reactance of the of the circuit is given as,

$$X_C = \frac{1}{\omega_C(R_F + R_W)C_F} = \frac{1}{2\pi f_C(R_F + R_W)C_F} \tag{1}$$

where, X_C is the Reactance of the capacitor C_F, ω_C is the Cut-off angular frequency of the CA and f_C is the Cut-off frequency.

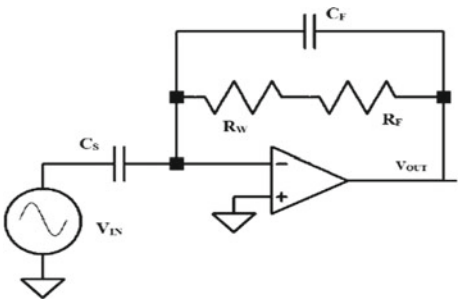

Fig. 1 Circuit diagram of conventional charge amplifier

In CA, the integration functionality secures the circuit from the small amount charge generated by the piezoelectric sensor, and it is not lost due to leakage [2]. The CA offsets the input current with the help of the reference capacitor placed in the feedback loop which is also proportional to the value of the total input charge flowing during the defined time period, so the circuit functions as a charge-to-voltage converter [3]. The gain of the CA circuit depends on the values of the feedback capacitor and the feed-in resistor [4–7]. In the conventional CA configuration, the R_F is served as the DC feedback path for input current of the Operational Amplifier(Op-Amp) inverting-input. The value of the R_F is very high in the range of $G\Omega$ for realizing the low frequencies for the biomedical applications [5, 6, 9]. The worst-case DC offset values of the conventional CA are given as (2),

$$V_{OFF} = R_F|I_b| + |V_{OS1}| \tag{2}$$

where I_b and V_{OS1} are the input current of the inverting-input and input offset voltage of the Op-Amp. In order to decrease the effect of the output offset voltages the JFET-Op-Amps are used [4]. Due to the larger values of the R_F it cannot be used in biomedical applications. Figure 2 represents the bias-current compensated charge amplifier to reduce the large feedback resistor values by decreasing the output offset voltage of the circuit [8]. Here, the values of R_1 and R_2 are quite smaller as compared to the R_F by using the bias-current compensation circuit in the feedback. The worst-case DC offset values of the circuit are given by (3) ,

$$V_{OFF} = R_2|I_{b1}| + R_2|I_{b1}| + |V_{OS1}| + |V_{OS2}| \tag{3}$$

In Fig. 2 the feedback resistor is replaced by the linear analog feedback network thereby reducing the use of the large feedback resistor [4]. In this configuration, the feedback resistor is decreased to MΩ values. Moreover in this configuration, the output DC offset values also decreases. The feedback network used in the schematic Fig. 2 nullifies the total DC offset voltages of the circuit. The worst-case output offset voltage of the circuit is given by (4)

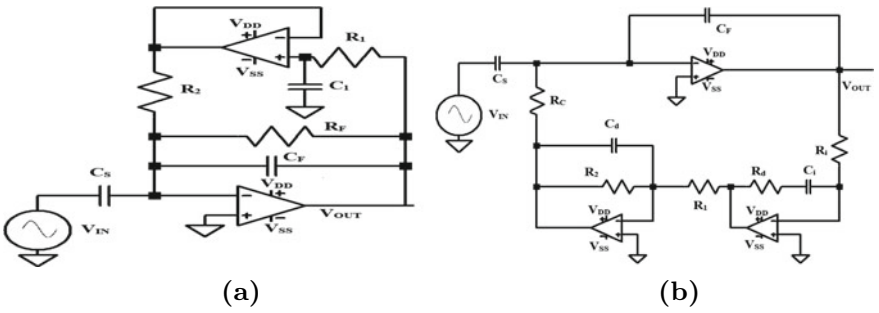

Fig. 2 **a** Circuit diagram of bias-current compensated charge amplifier [8] and **b** circuit diagram of charge amplifier design having linear-feedback network [9]

$$V_{\mathrm{OFF}} \simeq R_i |I_{\mathrm{b2}}| + |V_{\mathrm{OS2}}| \tag{4}$$

The values of the of R_{i} are very small than that of the R_1 and R_2, which makes the output offset smaller than Fig. 2 [9]. But even though the values of the resistances are decreasing it will take much area while making a $M\Omega$ resistances in manufacturing the chips. So in this paper, the switched capacitor-based charge amplifier is proposed which not only has small DC offset values but also the schematic that can be used in designing a CMOS-based circuit.

3 Operating Principle

The new proposed configuration is shown in Fig. 3. In comparison with Fig. 2, the new proposed circuit doesn't contain the feedback resistance. The feedback resistor is replaced by the equivalent switched capacitor. The use of the switched capacitor technique reduces the chip area and the power consumption of the circuit. Moreover, as the resistor is absent the DC output offset voltage is negligible and thus reducing the noise of the circuit. Again the switched capacitor uses the Miller compensation method to further reduce the effect of the feedback resistor. The proposed circuit achieves good linearity in a wide range of frequency for amplification as compared with conventional type circuit.

3.1 Switched Capacitor Technique

The Switched Capacitor circuits are the circuits where analog sampled methods are used to substitute the resistor in a circuit. The Switched Capacitor circuits are very well received for carrying out the task of analog signal processing due to their compatibility with the CMOS technologies, high accurate time constants, good voltage linearity, and temperature features. These circuits are continuous in amplitude and

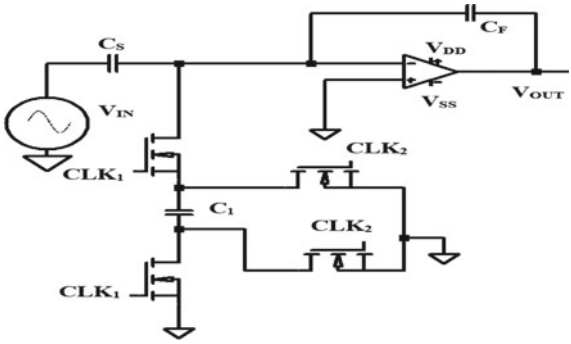

Fig. 3 Schematic of proposed switched capacitor-based charge amplifier

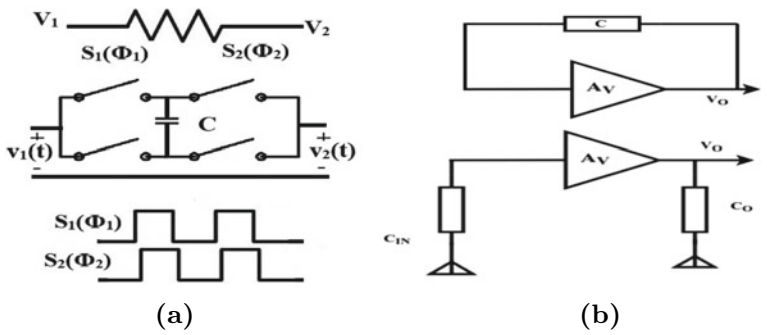

Fig. 4 **a** Switched capacitor-based representation of the resistor [12] and **b** Miller compensation for the feedback capacitances [12]

discrete in time [10–12]. Though the Switched Capacitor circuits have disadvantages like requirement of the non-overlapping clock and proper calculation of bandwidth for its application and the rapport with the CMOS technology makes it a viable means for the usage in microcircuitry [11]. In the later part of the section, the switched capacitor-based circuits are described, followed by the use of the Non-Overlapping Clock signal generator in designing the switched capacitor-based pre-amplifier circuits. In this paper, NOR based Non-Overlapping circuit and inverter-inverter chain are used for the delay of the circuit to produce two non-overlapping clock signals [14]. In Fig. 4 the current flowing through the resistor 'R' is given by, $i\,(\text{avg}) = \frac{V_1 - V_2}{R}$ where V_1 and V_2 are the voltages across the resistors. In switch capacitor-based circuit, the resistor is replaced by the two switches (S_1 and S_2) controlled by non-overlapping clock pulses (ϕ_1 and ϕ_2) and a capacitor 'C' in a billinear two terminal network. When the switch S_1 is ON capacitor C will be charged through the V_1 while discharge via S_2 and vice versa when S_2 is ON. The capacitor charges and discharges periodically between the two nodes V_1 and V_2. Whenever $V_1 > V_2$ the energy is absorbed from $V1$ and delivered to V_2 and vice versa when $V_2 > V_1$ [11]. Mathematically, $i\,(\text{avg}) = \int_0^T i\,(t)\mathrm{d}t$ where 'T' is the time period of the non-overlapping clock pulses and $0 \leq t \leq T$. Also, $i\,(t) = \frac{\mathrm{d}q}{\mathrm{d}t}$, where '$q$' is the charge stored in the Capacitor C, but the charge stored is, $q\,(t) = C(V_1(t) - V_2(t))$. Therefore in the billinear switched capacitor circuit, $I\,(\text{avg}) = \frac{C(V_1(T/2) - V_2(0))}{T} + \frac{C(V_2(T) - V_2(T/2))}{T}$ So, the resistance 'R' is equivalent in terms of the capacitance and the time period of the clock pulse is given by (5),

$$R = \frac{T}{4C} \tag{5}$$

Using (5) and the value of the feedback resistor is 1.1GΩ input capacitance and feedback capacitance as 20 nF and 23 pF respectively, so taking the clock frequency as 10 KHz it gives the switched capacitor as 0.1 pF [9]. As the capacitances used is quite small so Miller compensation method is used to get the stable output. Using the

Miller capacitances the values of the input and output capacitances are used to design the new proposed CA by increasing the capacitance which is practically feasible. The Miller compensation block is shown in Fig. 4

$$C_{\mathrm{IN}} = C(1 - A_{\mathrm{v}}) \tag{6}$$

$$C_{\mathrm{O}} = C(1 - \frac{1}{A_{\mathrm{v}}}) \tag{7}$$

From (6) and (7) the input capacitance is 100 pF and output capacitance is 0.1 pF which neglected due to presence of the load capacitances. Using the above results Fig. 3 is simulated in the LTSPICE circuit simulator tool. In the proposed switched capacitor-based CA, the feedback resistor is replaced by the switched capacitors which help in nullifying the leakage current due to the feedback resistor. As in the proposed circuit, there is no presence of the resistor the output offset voltage is nearly equal to zero. The worst-case output offset voltage is given by (6),

$$V_{\mathrm{OFF}} \simeq |V_{\mathrm{OS1}}| \tag{8}$$

4 CMOS Operational Amplifier

The trend toward the low voltage, low power, and smaller size integrated circuit makes the CMOS Op-amp (Complementary MOSFET Operational Amplifier) the most useful device in analog circuitry. Op-amps are assembled with different functions ranging from a simple dc bias generation to high-speed amplification or filtering. Different Op-amp configurations are used for amplification purposes. The CMOS Op-amp is an Operational Transconductance Amplifier (OTA) that produces current as an output with voltage input. Ideally, Op-amps have single-ended output, differential input, infinite open-loop gain, infinite input resistance, and zero output resistance. For low power and low-voltage specifications in analog circuitry, CMOS technology proves to be an ideal friend. The characteristic of differential amplifier is shown in (9),

$$V_{\mathrm{out}}(s) = A_{\mathrm{v}}(s)[V_1(s) - V_2(s)] \pm A_{\mathrm{c}}(s)\left(\frac{V_1(s) - V_2(s)}{2}\right) \tag{9}$$

where,

$V_{\mathrm{out}}(s)$ = Output Voltage
$V_1(s)$, $V_2(s)$ = Differential input Voltages
$A_{\mathrm{c}}(s)$ = Common mode voltage gain of the differential amplifier

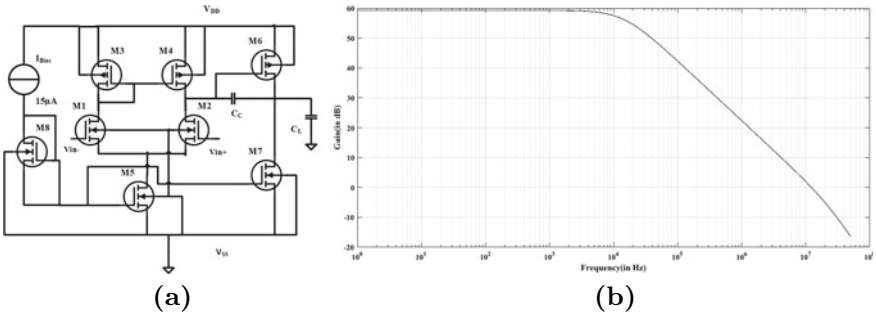

(a) (b)

Fig. 5 **a** Schematic of the two stage CMOS Op-amp with load capacitance (C_L) of 5 pF and V_{DD}=1.8 V and **b** open loop gain of the two-stage op-amp

4.1 Two-Stage CMOS Operational Configuration

The two-stage operational amplifier configuration has two stages for the amplification purpose, i.e., stage-1 is a high gain stage and stage-2 is a high swing stage [10]. In stage-1, high gain is provided for the amplification purpose by using a differential amplifier and cascode stages for the desired output signal. In stage-2, high swing is provided and which uses a common source stage to allow maximum output swing [12]. The circuit diagram depicting the two-stage configuration is shown in Fig. 5 [10, 12]. In this two-stage configuration, single-ended output is provided, while the other end of the output is used for biasing purposes. For the proper stability of the circuit, the Miller compensation method is used to reduce the output resistance. The circuit schematic of the two-stage Op-amp configuration is illustrated in Fig. 5 with following specifications, V_{DD} =1.8V, load capacitance = 5 pF, Slew rate = 10 V/μs and Gain Bandwidth product (GB) = 10 MHz. V_{DS5} is drain to source voltage of MOSFET (M_5) (in Volts), I_D is the drain current, V_{GS} is gate to source voltage. For 180 nm technology, the threshold voltage for CMOS are V_{tnn} =0.48 V, $|V_{thp}|$ =0.43 V with the transconductance values in saturation as $K_n = 289\ \mu A/V^2$, $K_p = 77\ \mu A/V^2$. M_5 transistor provides the tail current to the differential amplifier (M_1 and M_2) with the current mirror load (M_3 and M_4). In the second stage the voltage is converted to current using the Common-Source configuration with M_6 acting as active load to the M_7 NMOS transistor.

Following are the CMOS Op-amp equations for the different W/L ratios of the MOSFETS. The general design consideration of two-stage CMOS Op-amp is as follows [12–16]

- Compensation Capacitance (C_C): $C_C > 0.22 \times C_{Load}$
- Bias Current (I_5)/Slew Rate (SR) requirement: I_5= SlewRate × C_C
- For positive input common mode range requirement gives $(W/L)_3$ aspect ratio and here M_3 and M_4 should be of equal size and area.

$$I_{D1} = I_{D2} = I_{D3} = I_{D4} = \frac{1}{2} I_{D5}$$

$$\left(\frac{W}{L}\right)_3 = \left(\frac{W}{L}\right)_4 = \frac{2I_3}{k_n[V_{DD} - V_{th(mx)} - b]^2} \geq 1 \tag{10}$$

where,

$$b = V_{t_0 3(mx)} + V_{T1(mn)}$$

- Transconductance requirement using the compensation capacitance and gain bandwidth product $(W/L)_{1,2}$ can be determined. The transistor M_1 and M_2 must have equivalent geometry.

$$g_{m1} = g_{m2} = \text{GB} \times C_C$$

giving aspect ratio as,

$$\left(\frac{W}{L}\right)_1 = \left(\frac{W}{L}\right)_2 = \frac{g^2{}_{m2}}{k_n I_5} \tag{11}$$

- To satisfy the output voltage swing requirement, it gives $(W/L)_{5,8}$ aspect ratios using the saturation voltage of M_5. Moreover, it is seen that the aspect ratios of M_5 and M_8 must be exact.

$$V_{DS5} = V_{in}(\min) - V_{SS} - \sqrt{\frac{I_5}{K_n (W/L)_1}} - V_{T1} \tag{12}$$

$$\left(\frac{W}{L}\right)_5 = \left(\frac{W}{L}\right)_8 = \frac{2I_5}{k_n[V_{DS5}(\text{Sat})]^2} \tag{13}$$

- For proper mirroring of the first stage current mirror load aspect ratio $(W/L)_6$ is given as,

$$\left(\frac{W}{L}\right)_4 = \left(\frac{W}{L}\right)_4 \times \frac{g_{m6}}{g_{m4}} \tag{14}$$

- For proper power dissipation of the circuit the aspect ratio of M_7 transistor is kept at,

$$\left(\frac{W}{L}\right)_7 = \frac{I_6}{I_5} \times \left(\frac{W}{L}\right)_5 \tag{15}$$

The open loop voltage gain as shown in Fig. 5 of the OTA for two-stage Op-amp configuration is found to be 59.4 dB with power dissipation 81 μW considering the $L\min = 0.18\,\mu\text{m}$.

4.2 CMOS Based Charge Amplifier

In this section, the proposed configuration along with the conventional CA, bias current CA, and linear feedback CA are simulated in LTSPICE circuit simulator in order to compare the characteristics of the circuits. By assuming the input capacitance C_S = 20 nF for all the circuits from Figs. 1, 2, 3 and 4 were simulated taking sinusoidal input signal with 5 Hz and 2 mV_{P-P}. The feedback resistor and feedback capacitances for Figs. 1 and 2 is taken as,

$$R_F = 1.1\,G\Omega, \quad C_F = 23\,pF$$

From [8] the remaining values of the resistances and capacitances for simulating the CA are as follows:

$$R_1 = R_2 = 5.76\,M\Omega, \quad C_1 = 4.4\,\mu F$$

Similarly from [9] the values of the passive elements to simulate the CA are as follows:

$$C_F = 23\,pF, \quad R_i = 132K\Omega, \quad C_i = 3.3\mu F, \quad R_d = 13K\Omega$$

$$R_1 = 2.2\,K\,\Omega, \quad R_2 = 470\Omega, \quad C_d = 3.3\,nF, \quad R_C = 20\,M\Omega$$

The new CA which is introduced in this paper based on the switch capacitor technique has the following values that are calculated taking in consideration of the input signal values and clock frequency used in the Non-Overlapping Clock Signal Generator are as follows:

$$C_F = 23\,pF, \quad C_S = 20\,nF, \quad C_{IN} = 100\,pF$$

From Sect. 2, the values of the respective capacitance are taken, and it is simulated using the Op-amp specifications as discussed in this section. The following are the values taken to design the proposed CA,

$$C_F = 23\,pF, \quad C_S = 20\,nF, \quad C_{IN} = 100\,pF$$

In place of the Op-Amp, the CMOS Op-amp is taken and the values are simulated and the frequency response for all the different configurations are simulated as discussed in Sect. 2. The response is shown in Fig. 6 along with the gain, bandwidth,power and consumption is tabulated in Table 1.

The performance of any circuit is limited by noise. So, the noise analysis of the Pre-amplifier circuits is shown in Fig. 7 to observe the input-referred noise [17]. As noise is a random phenomenon, it is characterized in terms of spectral density. The input-referred noise specifies how much the input signal is corrupted by the circuit's noise present due to the transistors, i.e., how less the circuit can detect the appropriate signal to noise ratio [10].

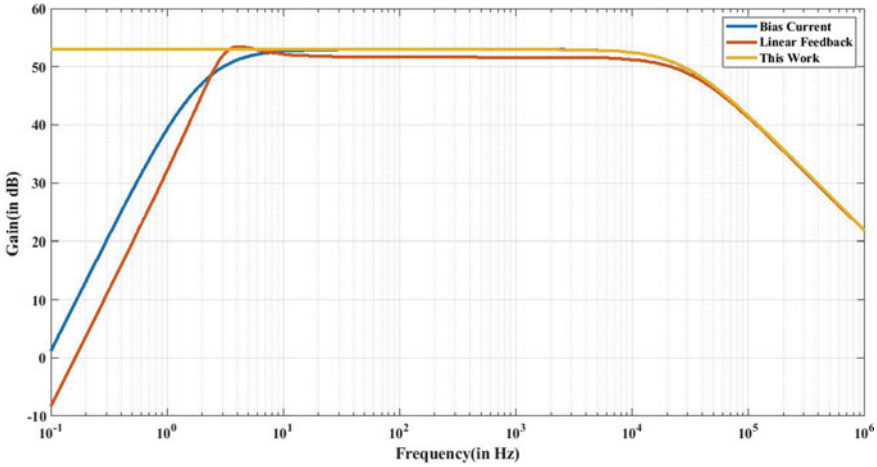

Fig. 6 AC analysis of the charge amplifier configurations using the CMOS-based amplifier

Table 1 Different performance parameters of the charge amplifiers

S. No.	Type of pre-amplifier	Gain (dB)	Bandwidth (KHz)	Power consumption (μW)
1	Bias-current [8]	55	13	300
2	Linear feedback [9]	56	11	220
3	Switch capacitor	54	12	180

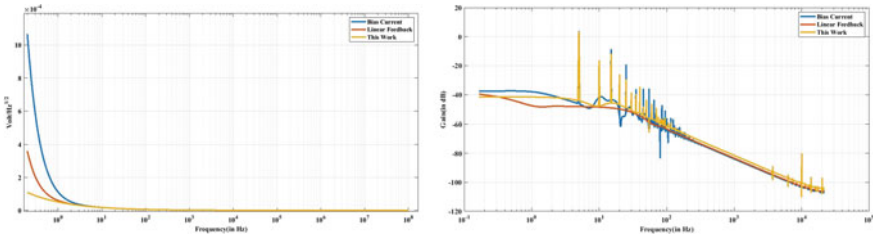

(a) (b)

Fig. 7 **a** Noise analysis and **b** fast Fourier analysis of charge amplifier configurations using the CMOS-based amplifier

The Fast Fourier Transform (FFT) is performed on the circuits to plot the dynamic characteristics of the system. FFT simulation for all the pre-amplifier configurations is shown in Fig. 7. Moreover, for the pre-amplifier design, the third harmonics (HD_3) is used to measure the levels of harmonics and also serves to quantify the system linearities. LTSPICE XVII incorporates the FFT-based algorithms to calculate the HD_3 in dB.

Table 2 Noise parameters of charge amplifier configurations

S. No.	Type of pre-amplifier	Figure of merit	Input referred noise	HD_3 (in dB)
1	Bias-current [8]	2.23×10^9	$1.1\,mV/Hz^{1/2}$	12.1
2	Linear feedback [9]	2.8×10^9	$320\mu V/^{1/2}$	NA
3	Switch capacitor	3.6×10^9	$110.9\mu V/^{1/2}$	15.33

5 Results and Discussion

To study the behavior of the different Charge Amplifier for an input signal of $2\,mV_{PP}$ with 5 Hz the different CA configurations are employed using in LTSPICEXVII. In the behavioral analysis, the harmonic distortion and noise analysis for each of the configurations are also done. The lower the values of the harmonic distortion the better is the design in reducing the effect of the noise in the circuit. Moreover, the noise analysis of the designs is done and the input-referred noise is calculated at the varied frequencies. The noise analysis is done for the effect of the flicker noise at the lower frequencies to determine a good design using the CMOS Op-amp.

The power consumption and Figure of merit (FOM) determine the overall performance of the system, i.e., the higher the FOM better is the performance of the system. Mathematically, FOM can be defined as the ratio of the gain-bandwidth product and power consumption [17].The parameters are tabulated in Table 2.

However, the configuration is experimented on the schematic level and in future research the layout level design will be carried and the chip would be synthesized. In the bias-current literature, the design can be further implemented using switched capacitor technique to further get better offsets and input-referred noise in the future implementations in neurological circuits.

6 Conclusion

The switched capacitor-based charge amplifier for piezoelectric sensors has been introduced in this literature to reduce the usage of high feedback resistance in the feedback. The proposed configuration does not use the feedback resistance, instead, it uses the switched capacitor technique. Thus by this configuration, the large resistors (in MΩ, GΩ ranges) like that of the conventional Charge amplifiers are nullified by the use of capacitors. The simulation results show the low-pass filter response at the output for the Switched capacitor-based circuits. Hence, lower order filter circuits may be used before the analog to digital conversion. Further, the use of the switched capacitors reduces the chip area and power consumption. As a consequence, the cost of implementation of CMOS-based Charge amplifier will drastically reduce.

References

1. Kuntzman ML, Hewa-Kasakarage NN, Rocha A, Kim D, Hall NA (2015) Micromachined in-plane pressure-gradient piezoelectric microphones. IEEE Sens J 15(3):1347–1357. https://doi.org/10.1109/JSEN.2014.2361118
2. Webster JG (1999) The measurement, instrumentation, and sensors: handbook. CRC Press
3. Giannelli P, Calabrese G, Frattini G, Granato M, Capineri L (2019) A buffered single-supply charge amplifier for high-impedance piezoelectric sensors. IEEE Trans Instrum Meas 68(2):368–376. https://doi.org/10.1109/TIM.2018.2849521
4. Durdaut P, Penner V, Kirchhof C, Quandt E, Knochel R, Hoft M (2017) Noise of a JFET charge amplifier for piezoelectric sensors. IEEE Sens J 17(22):7364–7371. https://doi.org/10.1109/JSEN.2017.2759000
5. Smith WJ, LaCourse JR (2004) Non-contact biopotential measurement from the human body using a low-impedance charge amplifier. Bioengineering proceedings of northeast conference 30:31–32. https://doi.org/10.1109/nebc.2004.1299978
6. Peng G, Ignjatovic Z, Bocko MF (2013) Preamplifiers for non-contact capacitive biopotential measurements. In: Proceedings of annual international conference IEEE engineering medical biology social EMBS, vol c, pp 1482–1485. https://doi.org/10.1109/EMBC.2013.6609792
7. Mahbub I, Wang H, Islam SK, Pullano SA, Fiorillo AS (2016) A low power wireless breathing monitoring system using piezoelectric transducer. In: 2016 IEEE international symposium medical measure application MeMeA 2016—Proceedings. https://doi.org/10.1109/MeMeA.2016.7533756
8. Blumen AR, Kenneth R (2008) Knowles. Apparatus for reducing offset voltage drifts in a charge amplifier circuit. U.S. Patent 7,414,466
9. Alnasser E (2020) A novel low output offset voltage charge amplifier for piezoelectric sensors. IEEE Sens J 20(10):5360–5367. https://doi.org/10.1109/JSEN.2020.2970839
10. Razavi B (2002) Design of analog CMOS integrated circuits. Tata McGraw-Hill Education
11. Sedra AS, Smith KC (2010) Microelectronic circuits. Oxford University Press
12. Allen PE, Holberg DR (2011) CMOS analog circuit design. Elsevier
13. Agrawal DV, Patel ML (2014) Non overlapping clocks for switched capacitor circuits. Int J Adv Eng Res Dev 1(05) 1–5. https://doi.org/10.21090/ijaerd.010539
14. Sharma K, Kumar R (2016) Design of a two stage CMOS operational amplifier using 180 nm and 90 nm technology, pp 3624–3634. https://doi.org/10.15662/IJAREEIE.2016.0505026
15. Bandyopadhyay S, Mukherjee D, Chatterjee R (2014) Design of two stage CMOS operational amplifier in 180 nm technology with low power and high CMRR. Int J Recent Trends Eng Technol 11:239–247
16. Maji KB, Kar R, Mandal D, Ghoshal SP (2016) An evolutionary approach based design automation of low power CMOS two-stage comparator and folded cascode OTA. AEU—Int J Electron Commun 70(4):398–408. https://doi.org/10.1016/j.aeue.2015.12.019
17. Razavi B (2013) Fundamentals of microelectronics. Wiley

Optimal Power Trading for a Micro-grid with Demand Response in Competitive Electric Market

Abhilipsa Sahoo and Prakash Kumar Hota

Abstract Nowadays, micro-grids (MG) are happened to be better performer and economically improved electricity provider in deregulated electricity market, and undoubtedly it possesses with enhanced reliability considering amalgamation of renewable sources and demand response. Also, improvised power trading mechanism, prepared by MG operators, is helpful for optimal dispatch of MG utilities in competitive energy market. In this study, optimal power trading has been done by implementing improved whale optimization algorithm (IWOA) for a grid-tied MG to minimize its operating cost. This optimal trading is attained incorporating incentive-based demand response (IBDR) and considering uncertainty of renewable sources, load and market clearing price. These uncertainties are modeled using different probability distribution functions (PDF) by the method of scenario generation and reduction. The applicability and efficacy suggested method are analyzed by simulating a MG test system. The consequences of this approach enhance the performances of MG in terms of economic operation and optimal solution. The impact of demand response significantly curtails grid energy and IBDR provides its optimality for end users by giving high incentives in comparison to curtailment price.

Keywords Micro-grid · Power trading · Demand response · RES · IWOA

1 Introduction

In today's world, MG plays a key role for eliminating energy crisis through the incorporation of distributed energy resources (DERs) and demand response (DR). It provides reliable electrifications which help consumers by reducing their cost of utilization of electricity in a more efficient manner [1, 2]. Generally, a MG adopts method of operation of grid-connected mode. Also it can be operated in island mode [3–6]. In these two modes of operations, MG acts differently regarding to the power flow from source to load. If it approaches the grid-connected mode, then it can

A. Sahoo (✉) · P. K. Hota
Veer Surendra Sai University of Technology (VSSUT), Burla, Odisha, India

M. Mishra et al. (eds.), *Innovation in Electrical Power Engineering, Communication, and Computing Technology*, Lecture Notes in Electrical Engineering 814,
https://doi.org/10.1007/978-981-16-7076-3_14

import or export energy from main grid, whereas for island mode of operation, MG independently accomplishes its demand.

In present situation, DERs based on renewable sources installed in MG are more advantageous than the MG having conventional sources. As these renewable sources are sporadic in nature, so uncertainty modeling of these sources is essential for power trading of MG. In addition, the other parameters like energy market price and load which are varying in nature have impact on power trading. So its modeling is done considering its intermittent characteristics. Due to this sporadic nature of renewable sources, power system faces many constraints during its operation. So for continuation of power supply, energy storage systems (ESS) are integrated in MG [7]. But it requires high maintenance cost for long life span. Considering economical, technical and environmental challenges, MG operator follows proper strategy for optimal power trading by employing demand-side management (DSM) scheme. The demand of end users can be regulated using the concept of DSM approach [8] by providing incentives and financial supports to the users, and its main entity is demand response (DR). Through the process of DR [9], end users can reduce their demand by getting certain incentives. DR can be applied in two forms such as price-based demand response (PBDR) and incentive-based demand response (IBDR). For this proposed work, IBDR is implemented by MG operator.

In recent few years, many researchers have studied [10] on energy management of renewable-integrated MG aiming optimal power dispatch by minimizing the cost. Here MGs were operated in island mode, whereas in [11], the authors have analyzed the MG in grid-connected mode for maximizing their profit by satisfying system constraints. In all of the abovementioned literatures, DR program is not implemented for the operation of MG. The influence of DR on optimum dispatch of MG has been studied by the authors [12–14]. Here, different types of DR like PBDR, IBDR are implemented for the operation of MG considering a day and a week duration. In a competitive market environment by adjusting DR, management of energy for power trading of MG utilities was studied in [15–17] by the authors to meet the load demand by considering constraints associated with the system. Here, different optimization techniques were utilized to minimize the operating cost of MG by implementing DR programs.

In this paper, an attempt has been made by IWOA to determine optimal power trading for grid-tied MG implementing IBDR program. In addition, the uncertainty associated with wind and solar renewable sources, load and MCP required for purchasing of grid power are modeled using Weibull, beta and normal PDF. The proposed IWOA provides more optimal consequences for power trading of MG, grid flexibility in competitive environment and consideration of DR program by MG operator and provides high incentives to end users in comparison to cost of curtailment.

2 Uncertainty Modeling of Load, MCP and Renewable Sources

For power trading of a MG integrated with renewable sources like wind and solar, it is required to model its uncertainty. In addition, uncertainty model is required to make for load and MCP.

MCP & Load Modeling

Normal PDF is utilized to model the stochastic characteristics of hourly load and hourly MCP [18, 19]. Considering its standard deviation (σ_N) and mean value (μ_N), the normal PDF is expressed as:

$$f(N) = \frac{1}{\sigma_N \sqrt{2\pi}} \exp^{\left[-\frac{(N-\mu_N)^2}{2\sigma_N^2}\right]} \tag{1}$$

Wind RES Modeling

Weibull PDF is used for uncertainty modeling [20], which is given as

$$F(W_V) = \frac{h}{c}\left(\frac{v}{c}\right)^{(h-1)} * \left[\exp\left(-\frac{v}{c}\right)^h\right] \tag{2}$$

where v is speed of wind in (m/s), h is shape factor and c is scale factor which are calculated using mean (μ) and standard deviation (σ) of wind speed.

The output of wind power (P_{WT}) obtained from wind speed is expressed as

$$P_{\mathrm{WT}} = \begin{cases} 0 & v < v_{\mathrm{in}} \\ w_r\left(\frac{v-v_{\mathrm{in}}}{v_r-v_{\mathrm{in}}}\right) & v_{\mathrm{in}} < v < v_r \\ w_r & v_r < v < v_o \\ 0 & v > v_o \end{cases} \tag{3}$$

Solar RES Modeling

Beta PDF is used for uncertainty modeling [21], which is expressed as

$$F_{\mathrm{s}}(S) = \frac{\Gamma(a+b)}{\Gamma(a)\Gamma(b)} S^{(a-1)}(1-S)^{(b-1)} \tag{4}$$

For $0 \leq S \leq 1 \& a, b > 0$. where S is a random variable and a, b are shape parameters of beta distribution and estimated through standard deviation (σ_{s}) and mean value (μ_{s}) of solar data.

The output of solar power (P_{PV}) obtained from solar irradiation is given as

$$P_{\mathrm{PV}} = \eta_{\mathrm{pv}} A_{\mathrm{pv}} S \tag{5}$$

3 Mathematical Formulation of MG for Optimal Power Trading

In this work, a grid-tied MG is considered which comprises wind turbine (WT), solar generator (PV), diesel generator (DE) and responsive load. The main aim of MG operator is to trade power economically and securely that satisfy the load of MG. So for optimal power trading, MG operator optimizes the operating cost of MG, i.e., $F_{\mathrm{MG}}(P)$ by minimizing it, and its mathematical formulation is given as follows:

$$F_{\mathrm{MG}}(P) = \min. \sum_{t=1}^{T} \mathrm{OC}(t) \tag{6}$$

where $\mathrm{OC}(t)$ gives operating cost at time 't' hour of MG and is determined as

$$\mathrm{OC}(t) = w_1 * [F_{\mathrm{DE}}(t) + F_{\mathrm{TR}}(t)] + w_2 * [F_{\mathrm{DR}}(t)] \tag{7}$$

where $w_1 \& w_2$ are the weights of objective function, and its values are chosen in such a way that sum of weights must be 1.

$F_{\mathrm{DE}}(t)$ is fuel cost of diesel generator which is considered as a quadratic function, and at 't' hour, it is given as

$$F_{\mathrm{DE}}(t) = a_i P_{i,t}^2 + b_i P_{i,t} + c_i \tag{8}$$

where, a_i, $b_i \& c_i$ are the cost coefficient used for diesel generator. $P_{i,t}$ is its power at 't' hour.

$F_{\mathrm{TR}}(t)$ is cost of trading power happens between MG and main grid. For tth hour, it is given as

$$F_{\mathrm{TR}}(t) = \begin{cases} \alpha_{P,t}.P_{\mathrm{TR},t} & \text{if} \quad P_{\mathrm{TR},t} > 0 \\ -\alpha_{P,t}.P_{\mathrm{TR},t} & \text{if} \quad P_{\mathrm{TR},t} < 0 \\ 0 & \text{if} \quad P_{\mathrm{TR},t} = 0 \end{cases} \tag{9}$$

Here, $\alpha_{P,t}$ is the coefficient of trading power, and its value is considered as MCP [22] of energy market. P_{TR} is the amount of trading power occurs between main grid and MG.

$F_{\mathrm{DR}}(t)$ is cost of incentive given to the end users for curtailment of their load and is expressed as

$$F_{\mathrm{DR}}(t) = \sum_{j=1}^{J} \sum_{t=1}^{T} I_{\mathrm{DR}j,t} - \lambda_{\mathrm{DR}j,t} P_{\mathrm{DR}j,t} \tag{10}$$

Here, $I_{\mathrm{DR}j,t}$ is the incentive paid to the jth customer at 't' hour. $\lambda_{\mathrm{DR}j,t}$ gives the bid price of jth customer at 't' hour taking part in DR program for load curtailment of P_{DR}.

This optimization problem has to be satisfied constraints of the system so as to minimize the operating cost in competitive environment. These constraints are given as follows:

$$\sum_{t=1}^{T} \left(P_{i,t} + P_{\mathrm{WT},t} + P_{\mathrm{PV},t} + P_{\mathrm{TR},t}\right) = D(t) - \sum_{j=1}^{J} P_{\mathrm{DR}j}(t) \tag{11}$$

$$P_i^{\min} \leq P_i \leq P_i^{\max} \tag{12}$$

$$-\mathrm{DR}_i \leq \left(P_{i,t+1} - P_{i,t}\right) \leq \mathrm{UR}_i \tag{13}$$

$$0 \leq P_{\mathrm{WT}} \leq P_{\mathrm{WT}}^{r} \tag{14}$$

$$0 \leq P_{\mathrm{PV}} \leq P_{\mathrm{PV}}^{\max} \tag{15}$$

$$-P_{\mathrm{TR}}^{\max} \leq P_{\mathrm{TR}} \leq P_{\mathrm{TR}}^{\max} \tag{16}$$

where Eq. (11) shows equality constraint and Eqs. (12) to (16) represent the inequality constraints.

While $D(t)$ is the demand of the MG.

$P_i^{\min} \& P_i^{\max}$ are the generation limits of diesel generator. $\mathrm{DR}_i \& \mathrm{UR}_i$ are its ramp limits.

P_{WT}^{r} is the rated wind power, and $P_{\mathrm{PV}}^{\max}$ is the maximum power of solar PV panel.

$-P_{\mathrm{TR}}^{\max} \& P_{\mathrm{TR}}^{\max}$ are the transacted power imported and exported from the main grid.

For IBDR program, the constraints associated with this are given as:

$$\sum_{t=1}^{T} (\lambda_{\mathrm{DR}j,t} P_{\mathrm{DR}j,t} - C(\theta, P) \geq 0 \tag{17}$$

where $C(\theta, P) = k_{1,j} P_j^2 + k_{2,j} P_j - k_{2,j} \theta_j P_j$ is the curtailment cost given to the customer for their load curtailment. $k_{1,j} \& k_{2,j}$ are cost coefficient used for jth customer, and $\& \theta_j$ shows type of customer.

$$\sum_{t=1}^{T}\sum_{j=1}^{J}\left(\lambda_{\mathrm{DR}j,t}P_{\mathrm{DR}j,t}\right) \leq \mathrm{TUB} \tag{18}$$

$$\sum_{t=1}^{T}\sum_{j=1}^{J}P_{\mathrm{DR}j,t} \leq \mathrm{CM}_j \tag{19}$$

TUB&CM$_j$ are the budget of utility and interruptible limits used for jth customer.

4 WOA Technique

Whale optimization algorithm (WOA) proposed by Mirjalili [23] used for enhancing numerous mathematical problems that is stimulated from hunting behavioral characteristic of humpback whales. The bubble-net strategy happens in exploitation stage has two processes as spiral updating and shrinking encircling which are mathematically framed using the following Eqs. (20)–(21).

$$\vec{P} = \left|\vec{G}.\vec{A}^{*}(t) - \vec{A}(t)\right| \tag{20}$$

$$\vec{A}(t+1) = \begin{cases} \vec{A}^{*}(t) - \vec{M}.\vec{P} & j < 0.5 \\ \vec{O}^{'}\mathrm{e}^{bn}\cos(2\pi t) + \vec{A}^{*}(t) & j > 0.5 \end{cases} \tag{21}$$

where $\overrightarrow{P}$ is the distance among whale and prey & t is current iteration.

$\vec{A}^{*}$&$\overrightarrow{A}$ are the position vectors of best solution and each search agents, respectively.

$\overrightarrow{M}$&$\vec{G}$ are coefficients of vectors computed as:

$$\vec{M} = 2\vec{a}.\vec{n} - \vec{a} \tag{22}$$

$$\vec{G} = 2.\vec{n} \tag{23}$$

where j&$\vec{n}$ are haphazard numbers that lies between [0, 1].

$\overrightarrow{a}$ is control parameter that decreases linearly from 2 to 0 over the process of iteration.

4.1 IWOA Technique

In IWOA technique, a control parameter and two improvement factors [24] are employed in original WOA technique to achieve optimal solution as well as to make

a balance between exploration stage and exploitation stage. As in WOA, at preliminary phase target prey is preferred as best search agent and the acquired position of best search agent is unknown, so it is difficult for getting the solution at optimum point. So a control parameter is employed using cosine function which is expressed as below:

$$\vec{a} = (a_{\max} - a_{\min}) * \cos\left(\mu \frac{t}{\text{Iter}_{\max}} \pi\right) \tag{24}$$

where $a_{\max} \& a_{\min}$ are maximum and minimum values of $\vec{a}$.

$t \& \mu$ are the current iteration and adjust factor, respectively.

After inclusion of improvement factors $F_1 \& F_2$ in the exploration and exploitation stages, the modified equations are:

$$\vec{P} = \frac{\left|\vec{C}.\vec{B}^*(t) - \vec{B}(t)\right|}{F_1} \tag{25}$$

$$\vec{B}(t+1) = \frac{\vec{B}^*(t) - \vec{M}.\vec{P}}{F_1} \tag{26}$$

And the update position in the spiral shape path becomes

$$\vec{B}(t+1) = \frac{\vec{D}' e^{bt} \cos(2\pi t) + \vec{B}^*(t)}{F_2} \tag{27}$$

4.2 Performance Evaluation of IWOA

The performance assessment of IWOA technique is analyzed considering optimization problem on standard benchmark functions, i.e., unimodal $\left(f^1 to f^7\right)$ and multimodal $\left(f^8 to f^{13}\right)$. The expression used for evaluation, its ranges and dimensions were taken from [23]. The outcome obtained by IWOA is compared with original WOA [23] and depicted in Table 1. It portrays the mean value and deviation of benchmark functions with relative to the unimodal and multimodal functions. The analysis is done for 300 iterations and 30 search agents, and the results are found for 30 independent runs. The above relative analysis yields that the outcomes attained by IWOA approach in contrast to WOA, PSO and GSA methods for unimodal functions $(f^1 to f^4$ & $f^7)$ are superior. Likewise for multimodal functions $(f^9 to f^{13})$, it yields better outcomes in comparison to other methods.

Table 1 Analysis of performance for benchmark functions using IWOA and WOA

Functions	IWOA	IWOA	WOA	WOA
	Std.-dev.	Std.-dev.	Std.-dev.	Std.-dev.
f^1	0	0	4.9×10^{-30}	1.4×10^{-30}
f^2	0	3.56×10^{-228}	2.3×10^{-21}	1.06×10^{-21}
f^3	0	0	2.93×10^{-06}	5.3×10^{-07}
f^4	0	8.9×10^{-202}	0.39747	7.25×10^{-2}
f^5	0.35002	28.258	0.76362	27.8655
f^6	0.2372	0.74161	0.53242	3.11626
f^7	9.6×10^{-5}	8.77×10^{-5}	1.14×10^{-3}	1.42×10^{-3}
f^8	2859.9	−5948.2	695.7968	−5080.76
f^9	0	0	0	0
f^{10}	9.01×10^{-16}	1.12×10^{-15}	9.897572	7.4043
f^{11}	0	0	1.58×10^{-3}	2.89×10^{-4}
f^{12}	0.02503	0.0481	0.21486	0.33967
f^{13}	0.19104	0.56953	0.26608	1.88901

5 Implementation of IWOA for Optimal Power Trading of MG

For power trading of MG, IWOA technique exhibits to be the most effective approach in competitive power market and maximizing the profit of grid-tied MG. Figure 1 shows implementing flowchart of proposed IWOA for optimal power trading of MG.

6 CASE Studies

The performance of proposed technique is tested on a grid-connected MG which comprises three DE, one WT, one PV and three end users. The data used for this MG [25] is given in Table 2. The rating of wind and solar generator is 11 and 15 KW, respectively. The MG considered for analysis is a grid-connected MG, and it is connected through transformer to main grid where it exports 4 MW and imports − 4 MW. The optimal power trading has been done for 24 h with the implementing DR program. The proposed simulation has been carried out on MATLAB environment, i.e., R-2018a, i5 processor having 4 GB RAM. The suggested IWOA approach is verified for 300 iterations and 30 search agents. The test is done for 30 independent runs. The renewable sources, i.e., wind and solar and load data used for analysis of bidding model of MG, are taken for a day of Harare, Zimbabwe [25]. For this work, 1000 scenarios are generated using Monte Carlo simulation, and backward-reduction

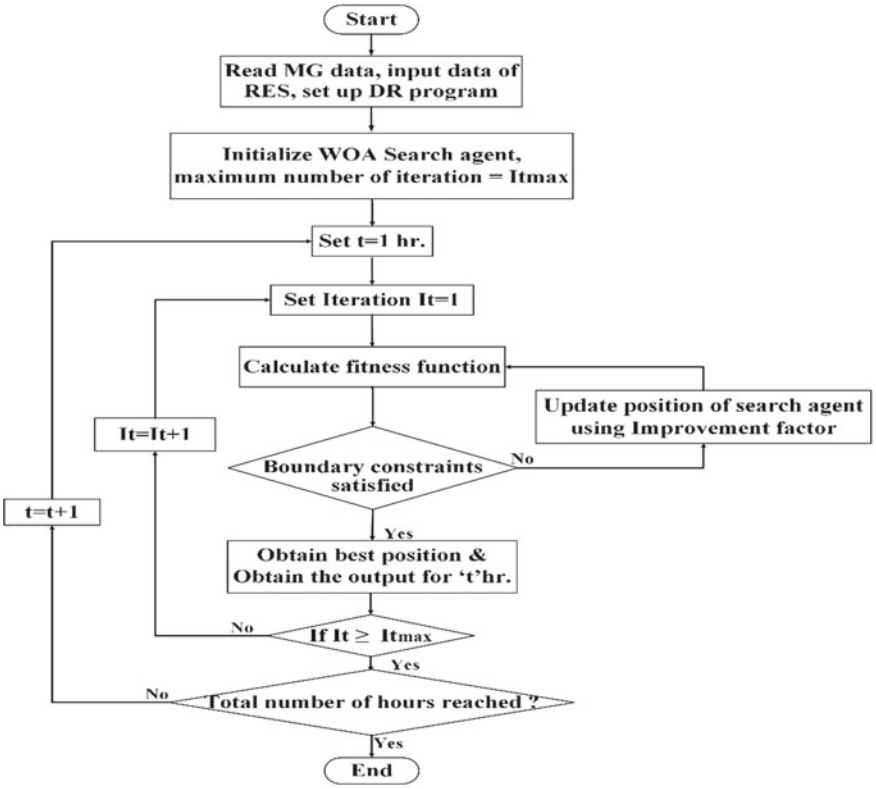

Fig. 1 Implementation of IWOA for optimal power trading of MG

Table 2 Data of cost coefficients of three DE

i	a_i	b_i	$P_i^{\min}$	$P_i^{\max}$	DR_i/UR_i
1	0.06	0.5	0	4	3
2	0.03	0.25	0	6	5
3	0.04	0.3	0	9	8

algorithm is utilized for reducing scenarios. The determined forecasted hourly load, and MCP required for trading is depicted in Fig. 2.

In this study, DR program is implemented for power trading of grid-tied MG. IBDR is analyzed for this study. The customer data is given in Table 3. Here it is assumed that initially all three end users of MG have same limits of power interruptibility and its value is given in Table 4. MG operator has the information of daily limit of power interruption of all end users when IBDR is implemented for the operation of MG. By using this information, the operator arranges the users in order of their

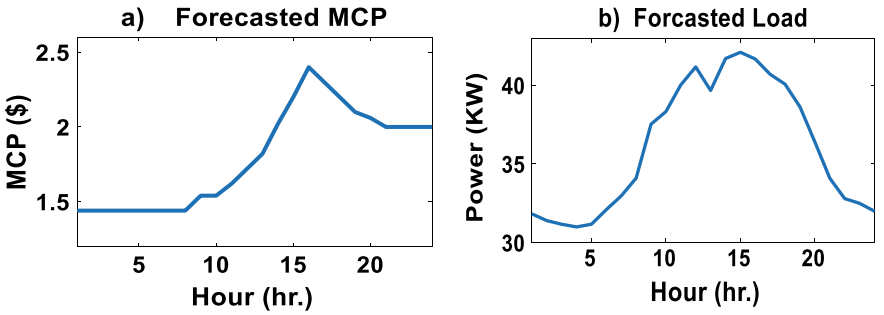

Fig. 2 Forecasted hourly MCP and load

Table 3 Cost coefficients of customer

j	k_1	k_2	θ	CM_j
1	1.079	1.32	0	30
2	1.378	1.63	0.45	35
3	1.847	1.64	0.9	40

Table 4 Power interruptibility price

Hour	1	2	3	4	5	6	7	8	9	10	11	12
λ	1.57	1.4	2.2	3.76	4.5	4.7	5.04	5.35	6.7	6.16	6.38	6.82
Hour	13	14	15	16	17	18	19	20	21	22	23	24
λ	7.3	7.8	8.5	7.1	6.8	6.3	5.8	4.2	3.8	3.01	2.53	1.42

willingness to curtail the power. Also the cost coefficient of participating end user is known to MG operator. The total utility budget of MG is assumed to be 500$.

Due to the implementation of IBDR, the load decreases from the initially forecasted load, and the variation of load is shown in Fig. 3. Accordingly, the optimal dispatch of MG utilities is given in Fig. 4a, b. From this figure, it is shown that as the end users curtail their load during peak load hour so to meet the demand, MG operator bought less power from main grid and sold more power to it. For this curtailment, end users get an incentive which is more than the cost of curtailment attained by proposed method. The curtailment of power for the customers and the incentive received for this power curtailment are given in Fig. 5a, b, respectively. The economic analysis for this case is given in Table 5. From this table, it is obtained that total cost of conventional power generation attained by IWOA increases to 249.17$ from 247.6$ attained by WOA. However, the incentives paid to the customer decreases to 372.16$ for IWOA from 378.11$ attained by WOA. It is also shown that the cost of power trading and total operating cost of MG reduces for proposed IWOA.

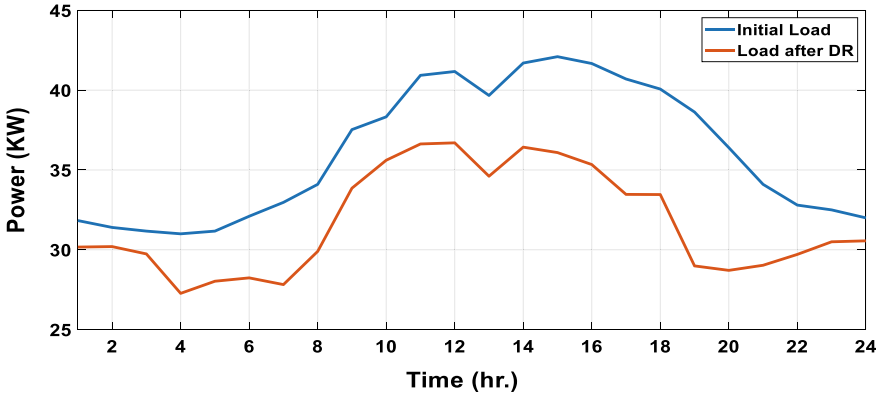

Fig. 3 Load curve after applying DR program

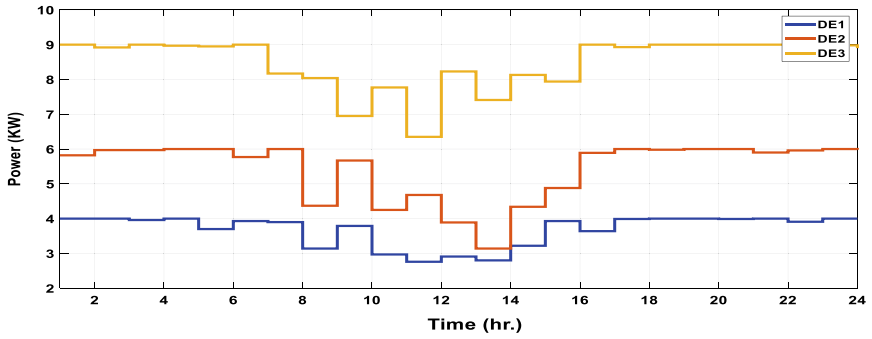

a) Optimal Dispatch of DE1, DE2 and DE3

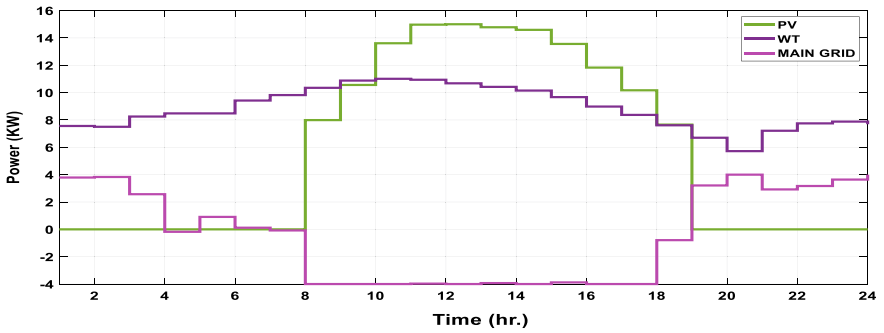

b) Optimal dispatch of PV, WT and MAIN GRID

Fig. 4 Optimal power dispatch implementing DR of **a** DEs and **b** PV, WT and main grid

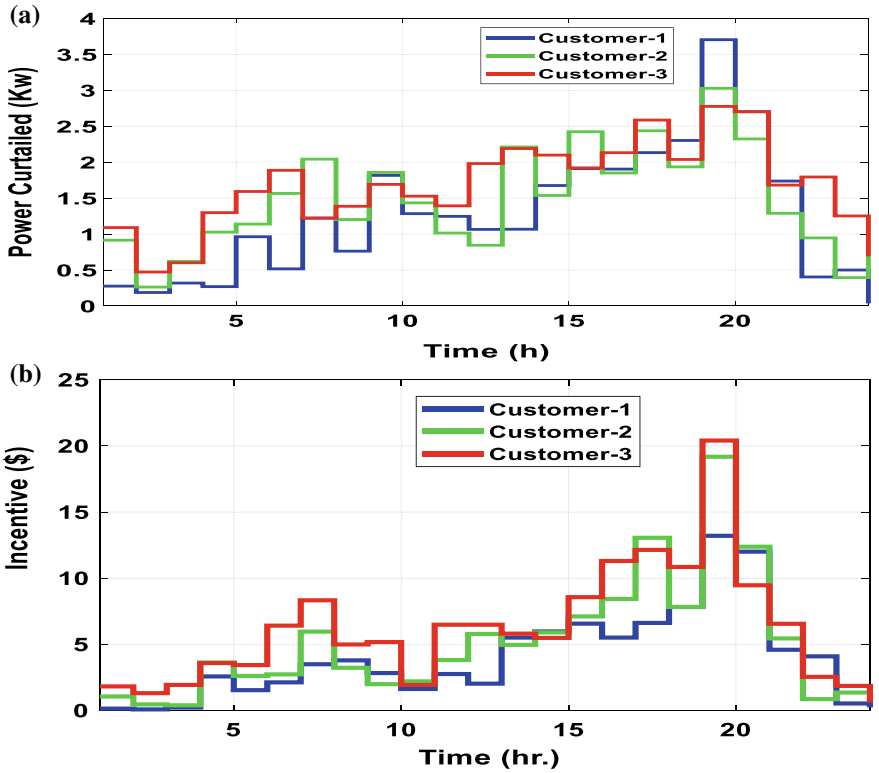

Fig. 5 **a** Power curtailment of customers and **b** incentives received by customers

Table 5 Economic analysis of the study

Economic parameters	WOA	IWOA
Total cost of conventional power generation ($)	247.6	249.17
Total cost of power trading ($)	379.94	372.56
Total operating cost ($)	627.54	621.73
Customer incentives ($)	378.11	372.16
Energy curtailed (KWh)	104.41	104.6
Conventional power generation (KWh)	416.61	422.55
Energy trading (KWh)	76.75	72.91

7 Conclusion

This work shows the implementation of IWOA method in solving the optimal trading problem of grid-tied MG considering uncertainty of renewable generation and load. This proposed technique shows its superiority in terms of cost minimization for

IBDR-implemented MG. In addition, the unpredictability of wind generation, solar generation, load and MCP is characterized by Weibull, beta and normal PDF using scenario generation and reduction. The optimal power trading problem is solved for a grid-tied MG with DR. The implementation of IBDR is more effective in controlling both supply and DR for MG. The impact of DR on optimal trading problem reduces the load of MG by benefiting to the end users as well as reduces the operating cost of MG.

References

1. Hirsch A, Parag Y, Guerrero J (2018) Microgrids: a review of technologies, key drivers, and outstanding issues. Renew Sustain Energy Rev 90:402–411
2. Wu Y, Barati M, Lim GJ (2019) A pool strategy of microgrid in power distribution electricity market. IEEE Trans Power Syst 35(1):3–12
3. Hemmati M, Mohammadi-Ivatloo B, Abapour M, Anvari-Moghaddam A (2020) Day-ahead profit-based reconfigurable microgrid scheduling considering uncertain renewable generation and load demand in the presence of energy storage. J Energy Storage 28:101161
4. Chandak S, Mishra M, Nayak S, Rout PK (2018) Optimal feature selection for islanding detection in distributed generation. IET Smart Grid 1(3):85–95
5. Mishra M, Rout PK (2016) Time-frequency analysis based approach to islanding detection in micro-grid system. Int Rev Electr Eng (IREE) 11(1):116–129
6. Patnaik B, Mishra M, Bansal RC, Jena RK (2021) MODWT-XGBoost based smart energy solution for fault detection and classification in a smart microgrid. Appl Energy 285:116457
7. Rui LI, Wei WANG, Zhe CHEN, Xuezhi WU (2018) Optimal planning of energy storage system in active distribution system based on fuzzy multi-objective bi-level optimization. J Mod Power Syst Clean Energy 6(2):342–355
8. Alasseri R, Tripathi A, Rao TJ, Sreekanth KJ (2017) A review on implementation strategies for demand side management (DSM) in Kuwait through incentive-based demand response programs. Renew Sustain Energy Rev 77:617–635
9. Jordehi AR (2019) Optimisation of demand response in electric power systems, a review. Renew Sustain Energy Rev 103:308–319
10. Wang R, Wang P, Xiao G, Gong S (2014) Power demand and supply management in microgrids with uncertainties of renewable energies. Int J Electr Power Energy Syst 63:260–269
11. Velik R, Nicolay P (2014) A cognitive decision agent architecture for optimal energy management of microgrids. Energy Convers Manage 86:831–847
12. Imani MH, Ghadi MJ, Ghavidel S, Li L (2018) Demand response modeling in microgrid operation: a review and application for incentive-based and time-based programs. Renew Sustain Energy Rev 94:486–499
13. Robert FC, Sisodia GS, Gopalan S (2018) A critical review on the utilization of storage and demand response for the implementation of renewable energy microgrids. Sustain Cities Soc 40:735–745
14. Wang Y, Yang Y, Tang L, Sun W, Zhao H (2019) A stochastic-CVaR optimization model for CCHP micro-grid operation with consideration of electricity market, wind power accommodation and multiple demand response programs. Energies 12(20):3983
15. Fan S, Ai Q, Piao L (2018) Hierarchical energy management of microgrids including storage and demand response. Energies 11(5):1111
16. Hassan MAS, Chen M, Lin H, Ahmed MH, Khan MZ, Chughtai GR (2019) Optimization modeling for dynamic price based demand response in microgrids. J Clean Prod 222:231–241
17. Shayeghi H, Shahryari E (2017) Optimal operation management of grid-connected microgrid using multi-objective group search optimization algorithm. J Oper Autom Power Eng 5(2):227–239

18. Liu C, Wang X, Guo J, Huang M, Wu X (2018) Chance-constrained scheduling model of grid-connected microgrid based on probabilistic and robust optimisation. IET Gener Transm Distrib 12(11):2499–2509
19. Jadidbonab M, Dolatabadi A, Mohammadi-Ivatloo B, Abapour M, Asadi S (2019) Risk-constrained energy management of PV integrated smart energy hub in the presence of demand response program and compressed air energy storage. IET Renew Power Gener 13(6):998–1008
20. Suresh V, Sreejith S, Sudabattula SK, Kamboj VK (2019) Demand response-integrated economic dispatch incorporating renewable energy sources using ameliorated dragonfly algorithm. Electr Eng 101(2):421–442
21. Khaloie H, Abdollahi A, Shafie-Khah M, Siano P, Nojavan S, Anvari-Moghaddam A, Catalão JP (2020) Co-optimized bidding strategy of an integrated wind-thermal-photovoltaic system in deregulated electricity market under uncertainties. J Cleaner Prod 242:118434
22. Kim MK, Park JK, Nam YW (2011) Market-clearing for pricing system security based on voltage stability criteria. Energy 36(2):1255–1264
23. Mirjalili S, Lewis A (2016) The whale optimization algorithm. Adv Eng Softw 95:51–67
24. Sahoo A, Hota PK (2021) Impact of renewable energy sources on modelling of bidding strategy in a competitive electricity market using improved whale optimization algorithm. IET Renew Power Gener 15(4):839–853
25. Nwulu NI, Xia X (2017) Optimal dispatch for a microgrid incorporating renewables and demand response. Renew Energy 101:16–28

A Comparative Study of Deep Learning Algorithms for Identification of COVID-19 Disease Using Chest X-Ray Images

Nour Haj Hammadah, Nilima R. Das, Mamata Nayak, and Tripti Swarnkar

Abstract The COVID-19 deadly disease has appeared as a major health catastrophe in the present days. Since its emergence in Asia in 2019, the virus has spread to almost all continents. It caused more a million of deaths. It is very essential to identify the contaminated patients of COVID-19 as early as possible and keep them in isolation. The technique that uses radiology images to detect the patients is very fast and promising. Generally the patients infected with COVID-19 disease have some abnormalities in their chest images. Thus, there is a possible use of deep learning models in the identification of the disease from the radiology images. This article also uses some learning algorithms to detect the diseased patients from their chest X-ray images. A dataset of 900 chest X-rays was prepared from the databases that widely exist. Three popular convolutional neural networks like ResNet, GoogleNet, and AlexNet were individually used to extract useful features from the chest X-ray images (CXR) to train the classifiers for identifying the COVID-19 disease with greater accuracy. The performance of the classifiers with each network has also been compared for their accuracy level.

Keywords COVID-19 · Deep learning · ResNet · GoogleNet · AlexNet

N. H. Hammadah
Department of Mathematics, SOA(Deemed To Be University), Bhubaneswar, India

N. R. Das (✉) · M. Nayak · T. Swarnkar
Faculty of Engineering and Technology, SOA(Deemed To Be University), Bhubaneswar, India
e-mail: nilimadas@soa.ac.in

M. Nayak
e-mail: mamatanayak@soa.ac.in

T. Swarnkar
e-mail: triptiswarnakar@soa.ac.in

M. Mishra et al. (eds.), *Innovation in Electrical Power Engineering, Communication, and Computing Technology*, Lecture Notes in Electrical Engineering 814,
https://doi.org/10.1007/978-981-16-7076-3_15

1 Introduction

The COVID-19 pandemic, otherwise known as the coronavirus pandemic, is a recent pandemic of coronavirus disease 2019 (COVID-19) caused by severe acute respiratory syndrome coronavirus 2 (SARS-CoV-2) [1]. Symptoms of COVID-19 are greatly changeable. For some there is no symptom, and for others it can be a life-threatening disease. Previously most of the countries were not testing the persons with mild symptoms which resulted in rapid spread of the disease. Studies have anticipated that the statistics provided by the countries related to the disease are expected to be significantly larger than the informed cases. To detect the presence of coronavirus, a lot of research works are being done.

There was no explicit medicine exist to treat the disease and avoid further spreading of the disease. The inadequate test kits and field experts need the application of an automated screening method that can be treated as an aid to reach at a conclusion about the identification of the disease by the specialists as fast as possible, because the infectious persons need isolation and advance clinical verification. The studies say that contaminated patients show distinctive radiographic visual characteristics with fever and cough, etc. CXR is a significant therapeutic method that has a decisive function in the identification of such visual images of the infections. On the other hand, the unavailability of sufficient number of specialist to understand the X-ray images and unclear form of radiographic figures are the main problems in manual identification. To reduce human loss resulted from nCOVID-19 pandemic, the modern machine learning algorithms [2] are employed to build automated systems that can identify the presence of the virus in the patient body in a very early stage. A lot of deep learning techniques like deep convolutional networks and recursive networks, etc., are used to automatically examine the radiological characteristics of the COVID-19 disease [3]. The authors in [4] applied ChexNet-DL to evaluate CXR images and assign a diagnostic label.

In this study, the performance of some well-known classifiers like K-nearest neighbors (KNN) [5], fully connected neural network [6], decision tree [7], and support vector machine (SVM) [8] are compared for identification of nCOVID-19 patients from a dataset of 900 CXR images.

2 Materials and Method

2.1 Dataset Used

The dataset has been collected from six public repositories (publicly accessible dataset, online sources, published papers for CXR images of COVID patients and CXR images (pneumonia) database) [9–15]. The images are found in the Portable Network Graphics abbreviated as PNG format. Resolutions of the images are of 1024*1024 pixels and 256*256 pixels that are transformed into 224*224 and 227*227

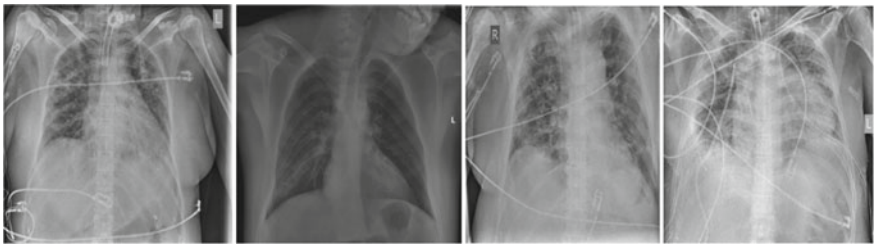

Fig. 1 Sample CXR images of nCOVID-19 patients

pixels, respectively, as needed by profound neural network models. Some CXR images derived from the dataset are presented in Fig. 1.

2.2 Feature Extraction and Classification

Different radiographic texture patterns are found at nCOVID-19-infected patients. In spite of that, all the patterns are not pertinent for precise portrayal of visual pointers related with nCOVID-19. Along these lines, to choose the most instructive features, three popular deep learning networks: AlexNet, GoogleNet, and ResNet are being used to compute the discriminative features present in the image. From the existing literature study, it is found that these networks are extremely quick and are generally utilized for identifying pulmonary sicknesses utilizing CXR images.

After feature extraction, the classifier was ready to receive the features vector to train the classifier model. The size of the extracted features vector was: 4096 for AlexNet, 1024 for GoogleNet, and 512 for ResNet18. For the classification purpose, four different algorithms are used in this work, such as: fully connected neural network (FCNN), KNN, SVM, and decision tree. The output of each network was used with all the classifiers individually. The performance of all the classifiers with each of the network is compared in Table 1. The classification algorithms used in this work can be efficiently trained with smaller dataset without reducing the efficiency. 70% of the dataset was used in training and rest 30% was used for testing.

The training process of the classifiers accomplishes in two stages: stage 1 and stage 2 as shown in Fig. 2. The classifiers were trained with both regular and irregular

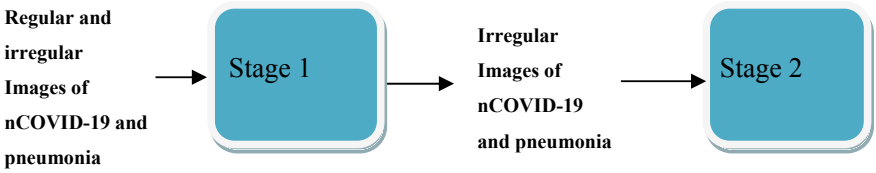

Fig. 2 Stages in training process

images of COVID-19 as well pneumonia cases in stage 1. In stage 2, the models were trained with the irregular images selected in stage 1.

3 Experimental Results

This section of the article presents a comprehensive discussion of the calculated results obtained from the four classification algorithms based on the output of the three networks AlexNet, GoogleNet, and ResNet. The model accuracy and model loss curves for training set are plotted in Fig. 3 for FCNN. The accuracy curves are increasing and linear or constant after 4 epochs. The loss curve smoothly decreases up to 4th epoch and then becomes constant. It is observed that the model is not over fitted. Figure 3a shows the performance of the classifier using the output of AlexNet during the training process with respect to different epochs. The first graph in the figure shows the rate of accuracy, and the second graph shows the rate of loss. Similarly, Fig. 3b, c shows the results of the classifier using the output of other two networks.

3.1 Performance Evaluation

The performances of the above-discussed algorithms are compared using different performance measures existing in the referred literature [8] such as true positive (TP) and true negative (TN), the false positive (FP) and false negative (FN). The confusion matrices generated for the FCNN are presented in the Fig. (4a–c) that describe the sensitivity, accuracy, and precision percentages of the results obtained from this classifier.

The sensitivity percentage for the detection of COVID-19 is 100% for all the networks with FCNN (Fig. 4a–c). The precision percentage of the AlexNet, GoogleNet, and ResNet with FCNN is 77.8, 91.1, and 98.9, respectively, and the accuracy percentage of the networks is 89.3, 91.1, and 93, respectively (Fig. 4a–c).

Table 1 shows the accuracy percentage of the obtained results calculated by the classification algorithms. The accuracy of SVM classifier with the combined networks is the highest among all. Analyzing the obtained output, it can be concluded

Table 1 Analysis of accuracy percentage

Features selected by	Accuracy of the classifiers			
	FCNN	KNN	SVM	Decision tree
AlexNet	89.3	91.11	92.96	89.26
GoogleNet	91.11	93.70	94.81	93.71
ResNet	93	94.82	95.92	90.74

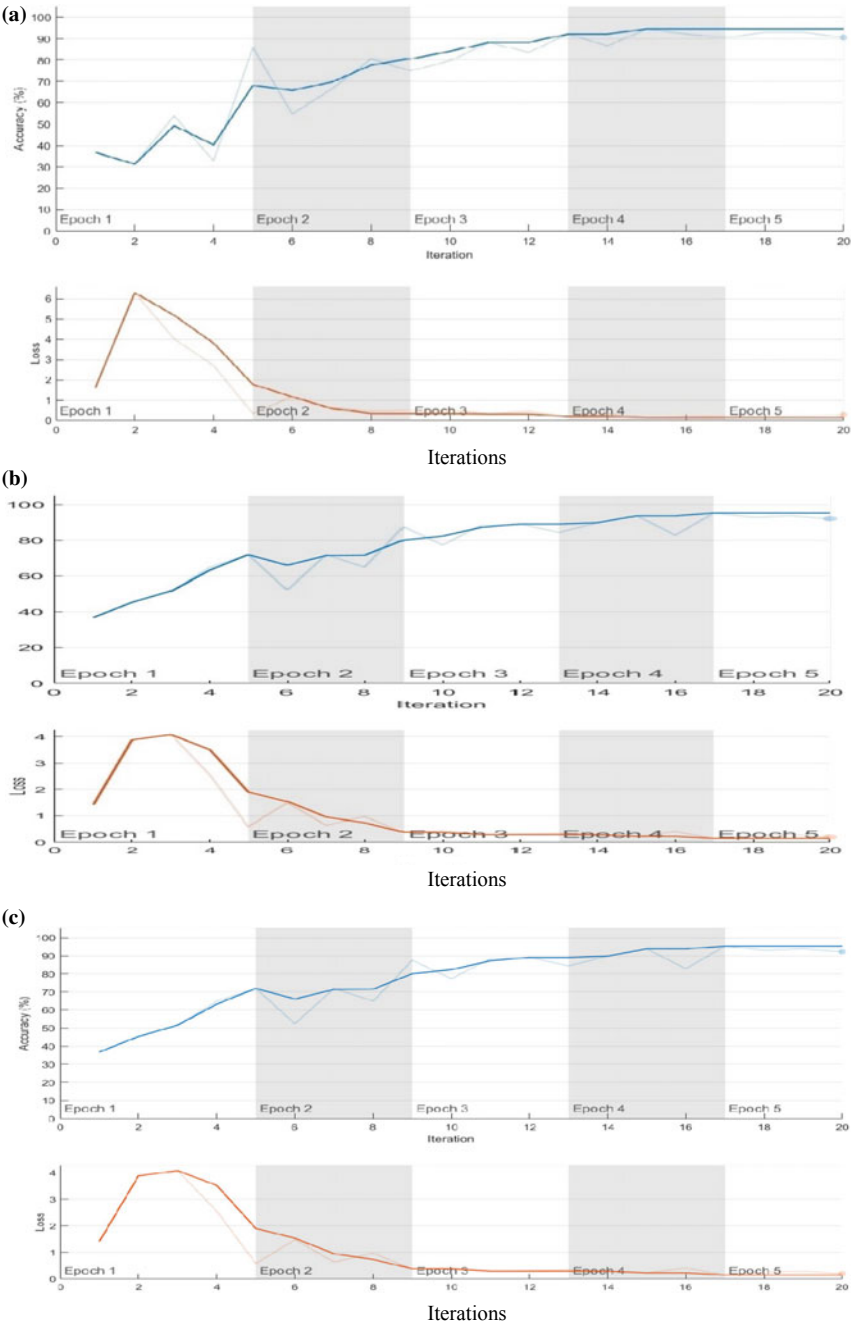

Fig. 3 **a** Accuracy and loss graph with the output of AlexNet. **b** Accuracy and loss graph with the output of GoogleNet. **c** Accuracy and loss graph with the output of ResNet

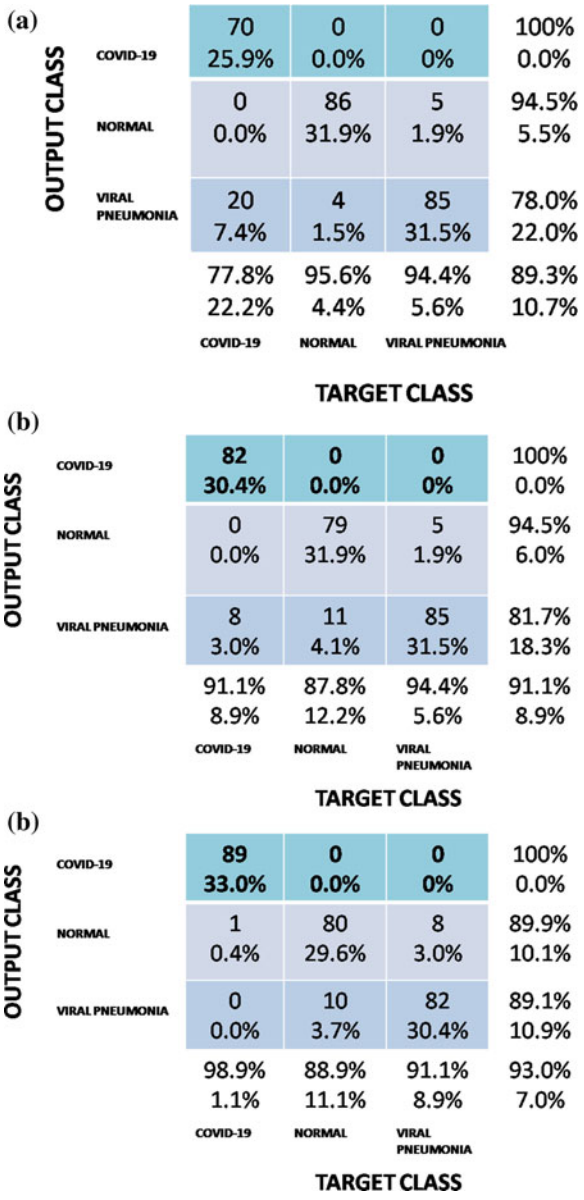

Fig. 4. **a** Confusion matrix for AlexNet. **b** Confusion matrix for GoogleNet. **c** Confusion matrix for ResNet

that SVM is having much more improved performance than the other classifiers that are being studied here.

4 Conclusion

This study addresses a preliminary diagnosis of nCOVID-19-infected patients from CXR images of normal persons and two different types of patients such as COVID-19 and viral pneumonia. The preliminary study can help to identify nCOVID-19 disease at a very early stage, which in turn stop further growth of the infection. With the discussed algorithms, the time taken to classify a large set of images can be significantly reduced having higher accuracy level. The disease nCOVID-19 is very infectious, and a single false negative case may cause a rapid spread of the disease. To decrease the likely possibility of misclassification, the above-discussed convolutional neural networks were used for feature extraction before applying the classifiers. From the performance metrics presented in the results section, it can be concluded that the performance of SVM is comparatively better than other algorithms. In future study, the performance of studied classifiers will be explored with larger dataset, and the result will be compared with some other classifier algorithms which are not taken into consideration in this study. Also, some hybrid approach may be investigated.

References

1. Nayak J, Mishra M, Naik B, Swapnarekha H, Cengiz K, Shanmuganathan V (2021) An impact study of COVID-19 on six different industries: automobile, energy and power, agriculture, education, travel and tourism and consumer electronics. Expert systems, pp 1–32 (2021). doi: https://doi.org/10.1111/exsy.12677
2. Benuwa BB, Zhan YZ, Ghansah B, Wornyo DK, Banaseka Kataka F (2016) A review of deep machine learning. Int J Eng Res Afr 24:124–136
3. Chouhan V, Singh SK, Khamparia A, Gupta D, Tiwari P, Moreira C, Damaševičius R, De Albuquerque VHC (2020) A novel transfer learning based approach for pneumonia detection in chest X-ray images. Appl Sci 10(2):559
4. Purkayastha S, Buddi SB, Nuthakki S, Yadav B, Gichoya JW (2020) Evaluating the implementation of deep learning in Libre health radiology on chest X-Rays. Adv Intell Syst Comput 943:648–657. https://doi.org/10.1007/978-3-030-17795-9_47
5. Guo G, Wang H, Bell D, Bi Y, Greer K (2003) KNN model-based approach in classification. In: OTM confederated international conferences on the move to meaningful internet systems. Springer Berlin, Heidelberg, pp 986–996
6. Schwing AG, Urtasun R (2015) Fully connected deep structured networks, arXiv preprint arXiv:1503.02351
7. Patel H, Prajapati P (2018) Study and analysis of decision tree based classification algorithms. Int J Comput Sci Eng 6(10):74–78
8. Evgeniou T, Pontil M (2001) Support vector machines: theory and applications, machine learning and its applications, advanced lectures
9. Jiao Y, Du P (2016) Performance measures in evaluating machine learning based bioinformatics predictors for classifications. Quant Biol 4(4)
10. https://github.com/armiro/COVID-CXNet
11. https://github.com/ml-workgroup/covid-19-image-repository/tree/master/png

12. https://sirm.org/category/senza-categoria/covid-19/
13. https://eurorad.org
14. https://github.com/ieee8023/covid-chestxray-dataset
15. https://www.kaggle.com/paultimothymooney/chest-xray-pneumonia

Electrical and Dielectric Characteristics of Ethylene Vinyl Acetate/Aluminum Nitride Polymer Composite for Usage in Flexible Electronics

Dillip Kumar Subudhi, P. Ganga Raju Achary, Priyabrata Pattanaik, and Dilip Kumar Mishra

Abstract The polymers have very good flexible properties such as bending, rolling, folding, and stretching capabilities with poor electric and dielectric response. On the other hand, electronic ceramics have suitable electric and dielectric response, but are lacking in flexible properties. New applications in flexible electronics material requires the property of flexibility as well as the electrical and dielectric properties. In this work, we have synthesized a composite material by taking ethylene vinyl acetate (EVA) as a polymer matrix and aluminum nitride (AlN) as an electronic ceramic material by the solution casting method and report the electrical and dielectric characteristics of the composite material. The XRD of ethylene vinyl acetate/aluminum nitride (EVA/AlN) composite material is studied for the presence of the AlN and EVA phase. The electrical and dielectric properties such as the capacitance (C), dielectric constant (ε), AC conductivity (σ_{ac}), and the dielectric loss (tan δ) are obtained by the impedance spectroscopy in the frequency range of 1–1000 kHz. Its electric and dielectric responses are an indication of its suitability in the flexible electronics industry.

D. K. Subudhi (✉)
Department of CSIT, Faculty of Engineering and Technology (ITER), Siksha 'O' Anusandhan Deemed To Be University, Bhubaneswar, Odisha 751030, India
e-mail: dillipsubudhi@soa.ac.in

P. Ganga Raju Achary
Department of Chemistry, Faculty of Engineering and Technology (ITER), Siksha 'O' Anusandhan Deemed To Be University, Bhubaneswar, Odisha 751030, India
e-mail: pgrachary@soa.ac.in

P. Pattanaik
Department of ECE, Faculty of Engineering and Technology (ITER), Siksha 'O' Anusandhan Deemed To Be University, Bhubaneswar, Odisha 751030, India
e-mail: priyabratapattanaik@soa.ac.in

D. K. Mishra
Department of Physics, Faculty of Engineering and Technology (ITER), Siksha 'O' Anusandhan Deemed To Be University, Bhubaneswar, Odisha 751030, India
e-mail: dilipmishra@soa.ac.in

M. Mishra et al. (eds.), *Innovation in Electrical Power Engineering, Communication, and Computing Technology*, Lecture Notes in Electrical Engineering 814,
https://doi.org/10.1007/978-981-16-7076-3_16

Keywords Flexible electronics · Aluminum nitride · Ethyl vinyl acetate · Dielectric · Dielectric loss (tan δ) · AC conductivity

1 Introduction

Flexible electronics is becoming the next big revolution in the electronics industry. These devices are expected to be used in biomedical implantable devices, wearable devices, ultra-thin lifestyle consumer electronics, etc. [1]. Polymers as a dielectric material can be easily processed with low cost but have poor thermal conductivity. When materials with high thermal conductivity, like aluminum oxide, aluminum nitride, boron nitride, silicon nitride, and beryllium oxide, etc., are added as fillers to polymers, the synthesized composite materials shows good thermal conductivity and acceptable electrical parameters.

In this paper, we have taken aluminum nitride as a filler as it has high intrinsic thermal conductivity and low thermal expansion coefficient with high electrical resistivity [2, 3]. We have taken ethylene vinyl acetate (EVA) which is an elastomeric polymer, prepared by ethylene and vinyl acetate monomer with appropriate resin and elastomeric properties with 7.5 wt% of AlN, to form EVA/AlN polymer composite. We measure the dielectric and electrical properties of neat EVA to EVA/AlN composite materials. The major objective is to accurately find the dielectric and electrical properties of EVA/AlN composite using high-precision LCR meter. The second major objective is to find out the frequency ranges where the dielectric value remains constant, and varies linearly or nonlinearly with the excitation frequency. This gives the background analysis on the applications that is dependent on the frequency. The third objective is to find the temperature range where the flexible material can be used, so that the working temperature range of the device can be defined properly.

This experiment data gives an evidence of the behavior of dielectric and electrical characteristics of neat EVA and nanocomposite EVA/AlN. The characteristics of the samples can be effectively used while creating sensors in general and capacitive sensors in particular. The data accurately measures the value of capacitance for a given configuration, which can be utilized to make a high-precision capacitive sensor with small in size and low power consumption device.

2 Literature Review

Flexible electronics is an exciting area having a lots of applications in flexible displays, sensor arrays, electronic textiles, biomedicine, artificial skin, and wearable electronics, etc., by following low temperature processing techniques. The use of flexible electronics has been originated from thin single crystalline solar cell in

satellite communications in the year 1960. In 1994, Landin et al. have created techniques to implement logic devices on polyamide substrates [4]. This triggers a lot of focus on flexible electronics using polymers. Nathan et al. demonstrated the thin-film material technology for flexible electronics whose performance is comparable to traditional solid-state electronics. He predicted that eventually the flexible electronics will take over the solid-state electronics just like the IC-based design took over circuit board-based electronics. He explained different plastic substrate materials to find the desired properties like thermal expansion, chemical resistance, and low moisture absorption [5]. X. Chen et al. reported new innovations in materials, design process, and device design that will boost flexible electronics [6]. Fabrication of flexible electronics can be done by using printing circuit (roll to roll for high volume and sheet to sheet for high precision low volume) techniques. R. Pelrine et al. reported that polymers can function as dielectric for a flexible capacitors [7]. Henderson, A. M reported the general overview of EVA copolymers with its physical, chemical, and electrical properties [8]. M. Rahaman et al. reported the practical applications of EVA in capacitors, electrode, pH sensors, electromagnetic interference shielding materials, etc. [9]. The EVA polymer is slowly replacing traditional polymer composites because of its acceptable properties such as softness, good mechanical properties, good physical properties, good flexibility, and resistance to chemicals [10]. EVA copolymer is widely used in industrial application starting from hot melt adhesive to wine bottle closures, insulating, sheathing product for high voltage cables, foot wear and toys, etc. [11]. However, the major disadvantage of EVA in electronic industry is its poor electrical and dielectric properties coupled with its thermal instability [12]. To improve the usability of this EVA copolymer in thermally elevated application, different approaches are adopted by the material scientists such as incorporation of permitted fraction of filler materials like aluminum nitride, aluminum oxide, silicon carbide, zinc oxide, etc. [10]

3 Experimental Section

Highly purified chemicals like AlN from M/s HIMEDA (India), EVA from PIL (India), and toluene from MERCK (India) are used to prepare the desired sample. The polymer (EVA) is dissolved properly in the solvent (toluene) with continuous stirring for 30 min in a magnetic stirrer at slightly above room temperature. Once the EVA is completely dissolved in toluene, then 7.5 wt % of AlN is slowly added to it. The solution is again stirred for another 30 min followed by 1 h and 30 min sonication to obtain a clear uniform composite solution. The uniform mixture is transferred to a teflon tray followed by drying in hot air oven for 6–8 h. The EVA/AlN composite is carefully removed and labeled for characterization and studied using XRD. After confirmation by XRD analysis, a set of samples of 1 cm by 1 cm with 1 mm thickness is prepared and labeled for measurements.

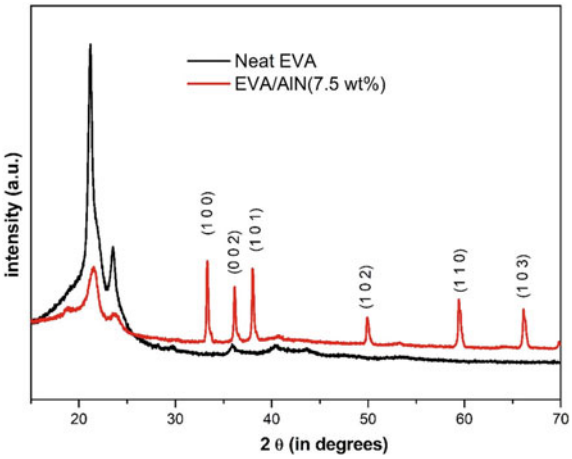

Fig. 1 XRD patterns of EVA and EVA/AlN composite

4 Result and Finding

4.1 XRD Study of EVA/AlN Composite

Figure 1 shows the XRD patterns of (neat EVA and composite of EVA/AlN). The XRD pattern clearly shows that the neat EVA does not have any sharp peaks between 2θ in the range of (25–70°). The response of intensity of neat EVA at 2θ at 25°, which demonstrates its amorphous nature. However, the sharp peaks from the reflection planes (1 0 0), (0 0 2), (1 0 1), (1 0 2), (1 1 0), and (1 0 3) of AlN are clearly visible in the EVA/AlN polymer composite. The presence of sharp peaks certainly increases the crystallinity of the composite material.

4.2 Electrical and Dielectric Study of EVA/AlN Composite at Room Temperature

The electrical and dielectric study is carried out in a high-precision LCR meter. The data for capacitance, dielectric loss (tan δ), dielectric permittivity (ε), and ac-conductivity (σ_{ac}) are obtained from the high-precision LCR meter with varying frequencies and temperatures. From LCR measurement, the capacitance and dielectric loss factor are directly measured whereas the real part of the dielectric permittivity and the AC conductivity are derived using the mathematical expression [13]. In the AC analysis, dielectric constant is a complex quantity. It is represented by

$$\varepsilon = \varepsilon\prime - j\varepsilon\prime\prime.$$

where ε = the complex dielectric.

ε' = the real part of complex dielectric, an indication of the degree of polarization.

ε'' = the loss factor of the dielectric, indication of loss of electrical energy in the form of heat energy.

The dielectric constant signifies the efficiency of dielectric material to store the electrical energy, and the dielectric loss indicates the loss of electrical energy in the form of heat energy. The dielectric constant is a function of frequency. As frequency increases, the value decreases due to polarization mechanisms no longer being able to follow the rapidly changing field.

Imaginary part of the dielectric is always positive quantity and represents loss factor. Dielectric loss factor represented as $\tan \delta = \varepsilon''/\varepsilon'$. Figure 2 represents the variation of capacitance, dielectric loss factor, dielectric constant, and AC conductivity as a function of frequency of pure EVA as well as EVA/AlN polymer composite at room temperature.

Capacitance: For neat EVA, it varies from 3.5 pF at 1 kHz to 4.15 pF at 1000 kHz. At lower end of frequency, the capacitance tends to decrease slightly and then rises up from 100 to 1000 kHz. For EVA/AlN composite, it varies from 2.1 pF at 1 kHz to 3.1 pF at 1000 kHz. At lower end of frequency, the capacitance tends to remain

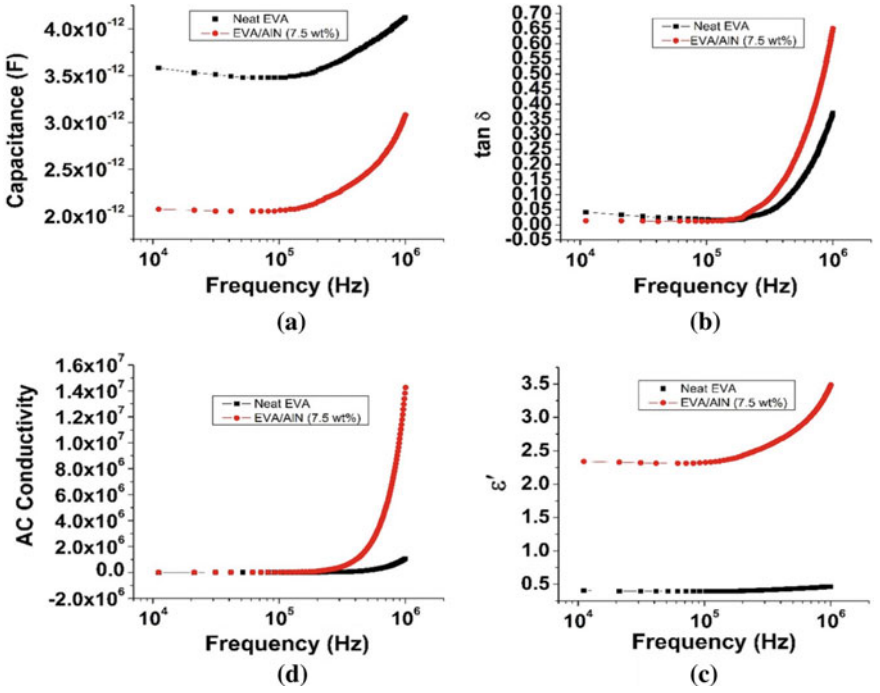

Fig. 2 Capacitance (**a**), tan δ (**b**), ε' (**c**), and σ_{ac} (**d**) versus frequency of neat EVA and EVA/AlN composite measured at room temperature

constant at 2.1 Pico Farad from 1 to 200 kHz. Then it increases with frequency till 1000 kHz.

Real part of dielectric ε': The real part of dielectric (ε') remains unaffected with the increase in logarithmic frequencies in case of neat EVA (Fig. 2c) [14]. However, with the incorporation of AlN filler in the EVA matrix, the permittivity (ε') increases considerably [15, 16]. The ε' value of neat EVA slowly decreases from 0.405 to 0.39 within the frequency range of 1–100 kHz. Beyond 100 kHz, the ε' rises up to a value of 0.465 at 1000 kHz. The ε' value of EVA/AlN slowly decreases from 2.3 to 2.4 within the frequency range of 1–100 kHz. Beyond 100 kHz, the ε' rises up to a value of 3.5 at 1000 kHz. The ε' value of EVA/AlN composite has a sevenfold rise to that of neat EVA at 1000 kHz.

Dielectric loss (tan δ): Dielectric loss (tan δ) is an important parameter in designing a good capacitor. A good capacitor should have low dielectric loss [17]. The dielectric loss of composite films is influenced by several factors like direct current conduction, Maxwell–Wagner–Sillars (MWS) relaxation [18], and Debye loss factor [19]. The dielectric loss is slightly more in the EVA/AlN composite as compared to pure EVA, which is clearly visible above 5 × 105 Hz frequency. The loss factor of neat EVA remains static with the value 0.05 within the frequency range of 1–200 kHz. Beyond that it rises up to a value of 0.37 at 1000 kHz. For EVA/AlN composite, the loss factor remains close to 0 within the frequency range of 1–200 kHz. Beyond that it rises up to a value of 0.65 at 1000 kHz. The loss factor of EVA/AlN composite has a twofold rise to that of neat EVA at 1000 kHz.

AC conductivity (σ_{ac}): The AC conductivity represents how good the device conducts with respect to the AC excitation. The AC conductivity is mathematically calculated as $\sigma_{ac} = 2\pi f\varepsilon''$.

At lower frequency, the AC conductivity value is almost zero which shows the polymer is an insulator. The AC response of the sample is measured in the frequency range of 1 kHz to 1 MHz. The AC conductivity for EVA/AlN composite increases with frequency above 500 kHz. The frequency dependence of conductivity for EVA/AlN composite is due to hopping mechanism of AlN particles and percolating network. For neat EVA, σ_{ac} remains close to zero from 1 to 500 kHz. Beyond that it rises up to a value of 11×10^6 S/m at 1000 kHz. For EVA/AlN composite, σ_{ac} value is close to zero from 1 to 500 kHz. Beyond 500 kHz that it rises up to 15×10^7 S/m at 1000 kHz which indicates a 13-fold rise from the neat EVA value.

4.3 Electrical and Dielectric Study of EVA/AlN Composite at Higher Temperature

The data for capacitance, tan δ, ε', and σ versus frequency at various temperatures of EVA/AlN composites are plotted in Fig. 3. From the figure, it is inferred that the electrical parameters like capacitance, tan δ, ε', and σ versus frequency remains same up to temperature of 80° C. Beyond 80° C, the EVA/AlN composite tends to deform

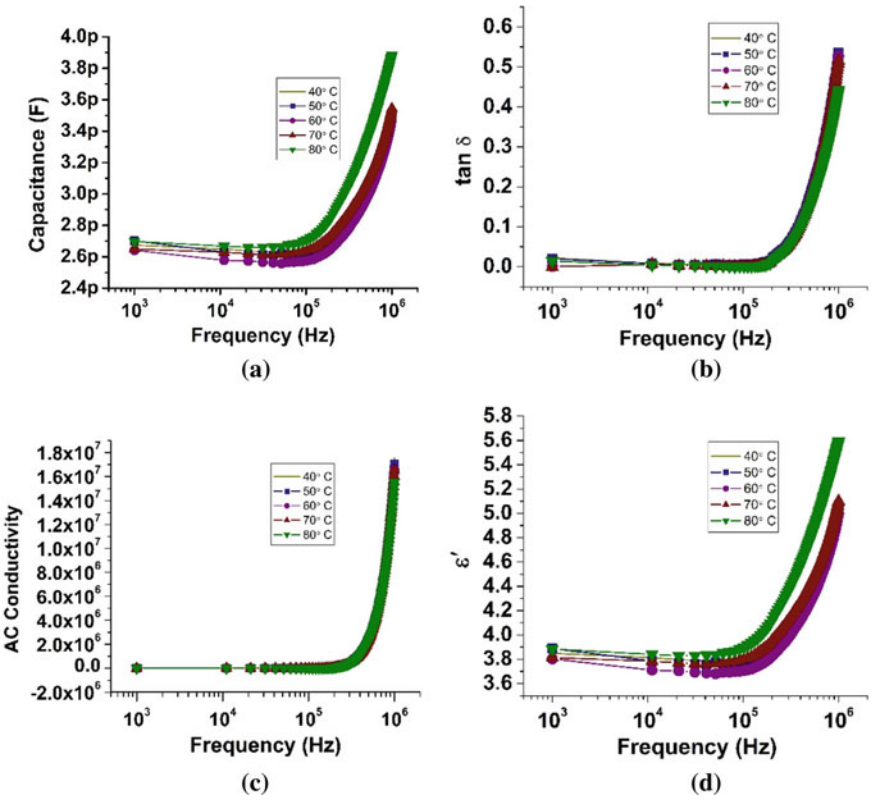

Fig. 3 Capacitance (**a**), tan δ (**b**), ε' (**c**), and σ_{ac} (**d**) versus frequency of EVA/AlN composite measured at different temperature intervals

its shape and size. The consistence characteristics are found within the temperature of 80° C and used as the upper limit for flexible electronic devices.

5 Conclusion

The electric and dielectric characteristics of the composite EVA/AlN material show a promising trend in flexible electronics like flexible sensors, wearable devices, implantable biomedical devices, etc. The composite material has higher dielectric values to that of neat EVA. We are reporting the electrical parameters within a limit of temperature up to 80 °C. Further study can be done in the mechanical property and thermal property of the material to verify its wide usefulness in the flexible electronics industry.

Conflict of Interest The authors declare that they have no conflict of interest.

References

1. Rogers JA, Huang Y (2009) A curvy, stretchy future for electronics. Proc Natl Acad Sci 106(27):10875–10876
2. Xu Y, Chung DDL, Mroz C (2001) Thermally conducting aluminum nitride polymer-matrix composites. Compos Part A Appl Sci Manuf 32(12):1749–1757
3. Vijayalakshmi K, Pillay VV (2014) Influence of deposition time on the microstructure and dielectric properties of AlN/Si thin films for enhanced hydrogen sensing application. Microelectron Eng 113:29–34
4. Landin A, Schmidt D, Thielen C, Olympie F, Schumacher T (1995) Alan Constant, Stanley G. Burns, Howard Shanks, Carl Gruber. In: Proceedings of the second symposium on thin film transistor technologies, vol 94(35), p 392
5. Nathan A et al (2012) Flexible electronics: the next ubiquitous platform. In: Proceedings of IEEE, vol 100, no. Special Centennial Issue, pp 1486–1517
6. Chen X, Rogers JA, Lacour SP, Hu W, Kim D-H (2019) Materials chemistry in flexible electronics. Chem Soc Rev 48(6):1431–1433
7. Pelrine R et al (2001) Applications of dielectric elastomer actuators. In: Smart structures and materials 2001: electroactive polymer actuators and devices, vol4329, pp 335–349
8. Henderson AM (1993) Ethylene-vinyl acetate (EVA) copolymers: a general review. IEEE Electr Insul Mag 9(1):30–38
9. Rahaman M, Chaki TK, Khastgir D (2012) Consideration of interface polarization in the modeling of dielectric property for ethylene vinyl acetate (EVA)/polyaniline conductive composites prepared through in-situ polymerization of aniline in EVA matrix. Eur Polym J 48(7):1241–1248
10. Khobragade PS, Hansora DP, Naik JB, Njuguna J, Mishra S (2018) Ethylene vinyl acetate properties improved with layered hybrid nanofillers. Polym Compos 39(10):3519–3727. https://doi.org/10.1002/pc.24371
11. Valentová H, Il M, Czaniková K (2014) Dynamic mechanical and dielectric properties of ethylene vinyl acetate/carbon nanotube composites. J Macromol Sci Part B: Phys 37–41. doi: https://doi.org/10.1080/00222348.2013.846814
12. Di H, Deng C, Li R, Dong L, Wang Y (2015) RSC Advances A novel EVA composite with simultaneous fl ame retardation and cerami fi able capacity. RSC Adv 5:51248–51257. https://doi.org/10.1039/C5RA05781G
13. Raymond WJK, Chakrabarty CK, Hock GC, Ghani AB (2013) Complex permittivity measurement using capacitance method from 300 kHz to 50 MHz. Measurement 46(10):3796–3801
14. Dash BK, Achary PGR, Nayak NC, Choudhary RNP (2017) Dielectric relaxation behavior of exfoliated graphite nanoplatelet-filled EPDM vulcanizates. J Electron Mater 46:563–572. https://doi.org/10.1007/s11664-016-4935-1
15. Dang Z, Yuan J, Zha J, Zhou T (2012) Progress in materials science fundamentals, processes and applications of high-permittivity polymer—matrix composites. Prog Mater Sci 57(4):660–723. https://doi.org/10.1016/j.pmatsci.2011.08.001
16. Yu S, Hing P, Hu X (2000) Dielectric properties of polystyrene-aluminum-nitride composites. J Appl Phys 88(1):398–404. https://doi.org/10.1063/1.373672
17. Anithakumari P, Mandal BP, Abdelhamid E, Naik R, Tyagi AK (2016) RSC advances composites: a step towards miniaturizated electronic devices. RSC Adv 6:16073–16080. https://doi.org/10.1039/C5RA27023E
18. Samet M, Levchenko V, Boiteux G, Seytre G, Kallel A, Serghei A (2015) Electrode polarization vs. Maxwell-Wagner-Sillars interfacial polarization in dielectric spectra of materials: characteristic frequencies and scaling laws. J Chem Phys 142(19):194703

19. Hui S, Chaki TK, Chattopadhyay S (2010) Dielectric properties of EVA/LDPE TPE system: effect of nanosilica and controlled irradiation. Polym Eng Sci 50(4):730–738. https://doi.org/10.1002/pen.21577

Advanced Adaptive Filter-Based Control Strategy for Active Switch Inverter Operation

Buddhadeva Sahoo, Sangram Keshari Routray, Pravat Kumar Rout, and Mohammed M. Alhaider

Abstract This study proposes an advanced filter-based control strategy for nonlinear load-based grid-integrated system applications. In addition to that, a reduced switch multilevel inverter is proposed for improving the voltage levels and obtains a linear voltage as compared to other traditional inverter-based system applications. As the inverter is capable to generate a five-level inverter voltage, the name of the proposed inverter is termed as a five-level active switch inverter (5LASI). The proposed controller is able to track and regulate both active and reactive current separately and provides the actual information regarding the harmonic/nonlinearity presence in the undertaken system. To evaluate the performance of the proposed inverter and control, the undertaken system is tested at different load conditions. Further, to guarantee stability, different stability curves are presented.

Keywords Power quality (PQ) · Five-level active switch inverter (5LASI) · Nonlinear load · Advanced adaptive filter (AAF)

1 Introduction

Nowadays, the power quality (PQ) problems are raised due to the excess application of higher pulse nonlinear load application [1]. This is a most common challenge in day-to-day life as the need for energy demand is increased gradually. To resolve the PQ problems, shunt active filter-based advanced power electronic device is raised

B. Sahoo (✉)
Department of Electrical Engineering, Siksha 'O' Anusandhan University, Bhubaneswar, Odisha, India

S. K. Routray · P. K. Rout
Department of Electrical and Electronics Engineering, Siksha 'O' Anusandhan University, Bhubaneswar, India

M. M. Alhaider
College of Engineering at Wadi Addawaser, Prince Sattam Bin Abdulaziz University, Al-Kharj 11991, Saudi Arabia

M. Mishra et al. (eds.), *Innovation in Electrical Power Engineering, Communication, and Computing Technology*, Lecture Notes in Electrical Engineering 814,
https://doi.org/10.1007/978-981-16-7076-3_17

their interest. With the elimination of harmonic current, lesser DC-link voltage selection reduced harmonics and decreased flickers, the three-phase shunt active filters are widely applied [2, 3]. However, the traditional inverters are not enough suitable for complex system applications due to their lesser voltage levels and high DC-link voltage requirement. As a solution, multilevel inverters such as diode clamped, flying capacitor, and cascaded H-bridge-based inverters are widely accepted. However, diode clamped and flying capacitor-based inverters are decreased its performance due to the excess requirement of power electronic components [4–6]. To solve the above problems, cascaded H-bridge inverters are widely implemented for real-time applications. The excess switching requirement also produces additional switching losses and computational burden to the system. This motivates us to develop an improved multilevel inverter with reduced switching requirements.

After the development of the multilevel inverter, the most important part of the controller is to properly develop the detection and control circuit by which the system eliminates the nonlinearity effectively [7]. The amount of nonlinearity elimination and reactive power support is completely related to filter design and power electronic components and energy storage device capacity [8, 9]. To solve the above-raised problem, many novel control algorithms are proposed in the literature. In [10], Fourier transform (FT)-based control technique is suggested for similar applications due to easier design and implementation. However, the performance of the FT-based control technique decreases the suitability at variable nonlinear load application and necessitate additional component such as phase-locked loop (PLL). As a solution, an enhanced instantaneous control method is proposed to sense the direct $\alpha\beta$ components for fulfilling the appropriate active and reactive power need [11, 12]. However, due to the use of an excess transformation device, the performance of the controller is affected. In [13], the synchronous frame-based control method is implemented to detect the active and reactive voltage and current components. However, the above method is less sensitive to harmonic grid voltage application. In addition to that, the need of extra transformation and synchronizer affects the controller performance and increases the controller complexity. In [14, 15], a peak calculation-based control technique is proposed for a similar application, in which the filter is used to track the appropriate reference signal. This technique offers excellent harmonic regulation capability by avoiding extra transformation need. However, the above technique decreases the suitability due to the synchronizing tool need and creating a lower DC-link voltage fluctuation problem.

To resolve the sensing problem, an adaptive sensing technique is proposed in [16–18]. In [16, 17], for availing better active filter performance, an adaptive control method based on the noise cancelation method is suggested for the same nonlinear load application. The above technique is applicable only when the sensitive load contains both nonlinear and fundamental components. However, the proposed method decreases the performance during the presence of interharmonics. To solve the above problem, in [18–20], the adaptive method is enhanced by using a multistage control operation. However, the modified adaptive method-based controller is decreased due to the complex design and integration. Looking at the above problem,

an advanced adaptive control method is necessary to develop for real-time complex system applications.

The main findings of the proposed system are illustrated below.

- To improve the voltage level, a novel five-level active switch inverter is proposed with a reduced switch component.
- The proposed ATF control technique is based upon the self-adaptation technique and able to vary the respective weights at different input conditions.
- During the variable input condition, the stability of the proposed controller is checked accordingly.
- The proposed control and inverter method are applicable to eliminate the nonlinearity, interharmonics, and noise in the nonlinear load current application.

2 System Under Study and Five-Level Active Switch Inverter

The overall undertaken system model is illustrated in Fig. 1. In this study, a novel 5LASI is proposed for a three-phase system application. By using 18 IGBTs, six diodes, two equal rating capacitors (C_1 and C_2), and three flying capacitors (C_{FC}), the proposed inverter is designed and connected to the grid-integrated nonlinear system application. Due to the proposed approach, the proposed system is capable to generate the five-level inverter output voltage. In this study, two nonlinear loads are connected to the grid in series through delta-delta and delta-star transformers. The used nonlinear load is designed by using two diodes based on inductive systems. One

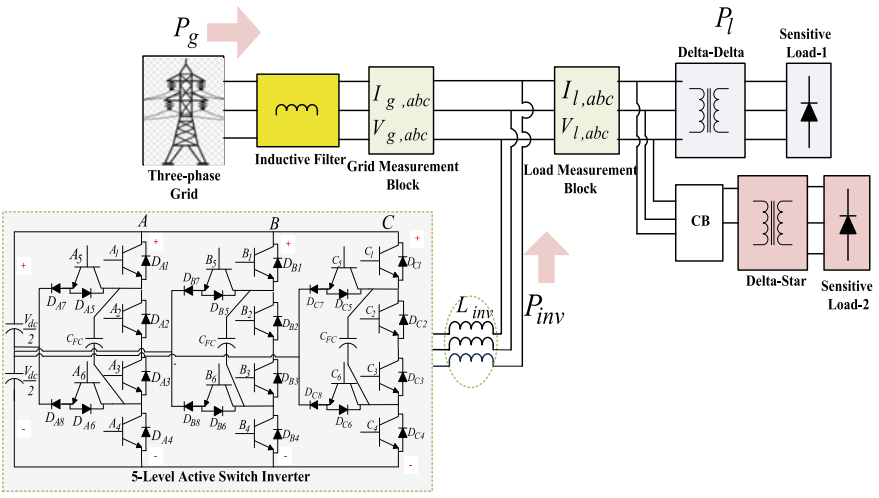

Fig. 1 SAHF-based test system model

Table 1 Operating switching sequence of phase A

Operating switching state							Flying capacitor state	
No.	A_1	A_2	A_3	A_4	A_5	A_6	$I_O > 0$	$I_O < 0$
1	✓	✓	×	×	×	✓	–	–
2	✓	×	✓	×	×	✓	Charge	Discharge
3	×	✓	×	×	×	✓	Discharge	Charge
4	×	×	✓	×	×	✓	–	–
5	×	✓	×	×	✓	×	–	–
6	×	×	✓	×	✓	×	Charge	Discharge
7	×	✓	×	✓	✓	×	Discharge	Charge
8	×	×	✓	✓	✓	×	–	–

load is connected in phase with the grid, and the other is connected with a 30-degree phase shift. Initially, sensitive load-1 is activated through a delta-delta transformer and after 10 cycles the delta-wye transformer is connected to increase the load rating from 6 to 12 pulses.

2.1 5LASI Working Model

The detailed structure of the proposed 5LASI is illustrated in Fig. 1. The proposed inverter is designed by using two DC-link capacitors such as (C_1 and C_2) having an equal voltage level and half of the total DC-link voltage ($V_{dc}/2$). In addition to that, a flying capacitor (C_{FC}) is used to provide one-fourth of the total DC-link voltage ($V_{dc}/4$). By using the above design and circuit configuration, the proposed 5LASI is capable to generate five additional output voltage levels as $+0.5V_{dc}$, $+0.25V_{dc}$, 0, $-0.25V_{dc}$, and $-0.5V_{dc}$, respectively. The one-leg switching states of the proposed inverter are presented in Table 1. Similarly, the other two phases are 120° and 240° phase-shifted from A-phase. During the grid integration, the active power is flown through the forward conduction of IGBT, and reactive power is flown through the antiparallel diode of the IGBT.

3 Adaptive Filter-Based Control Design

The proposed adaptive harmonic elimination strategy based on the Wiener concept has been globally selected for different signal processing problems. This strategy proves its significance by updating the system parameters and the self-adjusting capability according to the system conditions. Figure 2 illustrates the detailed adaptive harmonic elimination method and complete control strategy for the proposed 5LASI

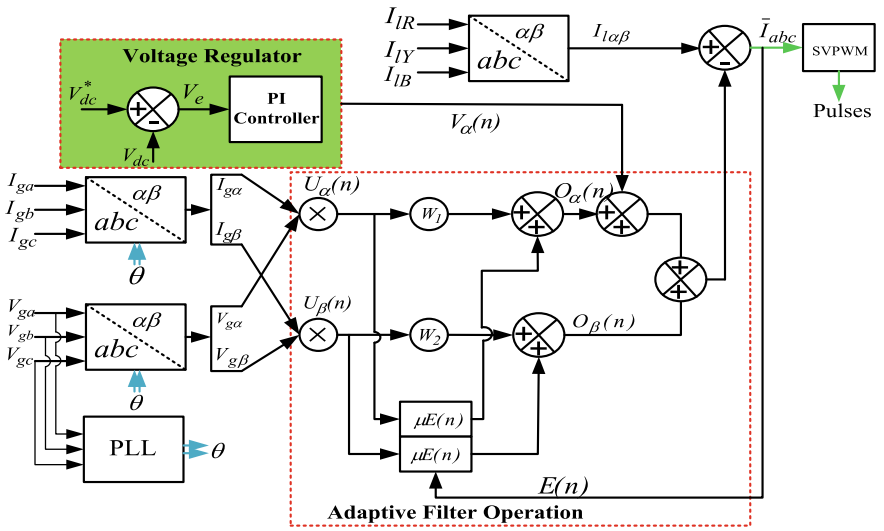

Fig. 2 Adaptive filter-based control approach

operation. From Fig. 2, it is observed that by considering the nonlinear load ($I_{l,abc}$) and grid current ($I_{g,abc}$), the overall control structure of the system is developed. The sinusoidal $I_{g,abc}$ always in-phase with the grid voltage ($V_{g,abc}$) obtained by the phase-locked loop (PLL). The sinusoidal grid current is passed through the adaptive filter to compute the output signal ($Y(n)$) and used to track the fundamental signal present in $I_{l,abc}$. The main objective of the adaptive filter is to compute the fundamental current component present in the load current. Therefore, the proposed approach easily estimates the harmonic contained by comparing the $Y(n)$ and $I_{l,abc}$ signals. The coefficients of the proposed filter are decided through adaptation techniques.

In this study, an adaptive notch filter is used to estimate the fundamental load current component. The complete structure of the filter is illustrated in Fig. 2. The proposed structure uses two orthogonal signals obtained from the grid current and voltage component, one is in-phase and the other is 90° phase-shifted to actual grid current, respectively. In this study, only two constraints are required for adaptation. The adaptation technique operation is similar to the normal adaptive filter operation and the fundamental $Y(n)$ is varied according to the variable load current conditions. For the adaptation process, two methods such as least mean square (LMS) and recursive least square (RLS) are used for adaptive filter operation [17, 18]. The recursive formula related to the LMS technique is estimated as follows.

$$E(n) = I_{l,abc} - Y(n) = I_{l,abc} - X^T(n)W(n) \tag{1}$$

$$W(n+1) = W(n) + \mu E(n)X(n) \tag{2}$$

where $X(n)$ is the input current vector (grid current and voltage component), μ is the step size, and $W(n)$ is the weight vector. μ regulates the convergence rate of the proposed technique to find the optimum solution. In this study, μ is selected as 0.0015 [10]. The recursive method applied to optimize the weights is presented as.

$$W_1(n+1) = W_1(n) + \mu E(n) X(n) \tag{3}$$

$$W_1(n+1) = W_1(n) + \mu E(n) X_{90^\circ}(n) \tag{4}$$

where $X_{90^\circ}(n)$ is the phase-shifted component of $X(n)$. The RLS strategy is divided into five steps and each step is discussed below.

Step-1 (Starting)

$P_{\tau_1}(0) = 0.1, P_{\tau_2}(0) = 0.1, W_1(0) = 0, W_2(0) = 0, \tau = 0.9995$(Practical value).

Step-2 (Parameter gain computation)

$$l_1(n) = \frac{P_{\tau_1}(n-1)X(n)}{\tau + X(n)^2 P_{\tau_1}(n-1)} \tag{5}$$

$$l_2(n) = \frac{P_{\tau_2}(n-1)X_{90^\circ}(n)}{\tau + X_{90^\circ}(n)^2 P_{\tau_2}(n-1)} \tag{6}$$

Step-3 (Output and system error computation)

$$Y(n) = W_1(n-1)X(n) + W_2(n-1)X_{90^\circ}(n) \tag{7}$$

$$E(n) = I_{l,abc}(n) - Y(n) \tag{8}$$

Step-4 (Updating coefficients)

$$W_1(n) = W_1(n-1) + E(n) l_1(n) \tag{9}$$

$$W_2(n) = W_2(n-1) + E(n) l_2(n) \tag{10}$$

Step-5 (Inverted autocorrelation)

$$P\tau_1(n) = \tau^{-1}(P_{\tau_1}(n-1) - l_1(n)X(n)P_{\tau_1}(n-1)) \tag{11}$$

$$P\tau_2(n) = \tau^{-1}(P_{\tau_2}(n-1) - l_2(n)X_{90^\circ}(n)P_{\tau_2}(n-1)) \tag{12}$$

By considering the above equations, it can be visualized that the constant gain ($l(n)$) is converted to the constant gains $l_1(n)$ and $l_2(n)$, and the related equations are presented in Step-2. Similar to the gain, the inverted autocorrelation matrix ($P(n)$) is converted to two scalar terms as $P\tau_1(n)$ and $P\tau_2(n)$, and the related formula is

presented in Step-5. By using this method, the controller complexity is decreased, and the proposed method becomes simpler and easier to implement. The forgetting term τ is a positive constant, which is smaller than 1. Due to the selection of $\tau < 1$, the proposed scheme gives more stress on the new sample and forgets the old sample. To generate the orthogonal component, a PLL is integrated in the controller design.

In this study, a novel technique is used to extract the orthogonal current input component. These components are obtained by using Clarke transformation of the load current. The formula is illustrated below.

$$\begin{bmatrix} I_{l0} \\ I_{l\alpha} \\ I_{l_\beta} \end{bmatrix} = \sqrt{\frac{2}{3}} \begin{bmatrix} 1/\sqrt{2} & 1/\sqrt{2} & 1/\sqrt{2} \\ 1 & -1/2 & -1/2 \\ 0 & \sqrt{3}/2 & -\sqrt{3}/2 \end{bmatrix} \begin{bmatrix} I_{la} \\ I_{lb} \\ I_{lc} \end{bmatrix} \tag{13}$$

After obtaining two orthogonal components, it is filtered through a low-pass filter with a 100 Hz cutoff frequency. The proposed approach guaranteed that the orthogonal input signals follow the load current.

4 Result Analysis

To validate the superiority of the proposed inverter and controller, the developed MATLAB model is tested under variable nonlinear load conditions. Initially, the stability of the proposed control approach is tested through different Bode and Nyquist plot analysis. After testing the stability, the robustness of the proposed approach is tested under constant and variable load conditions. In addition to that, the proposed system results are compared with the traditional system results for showing the actual requirement of the proposed controller.

Case-1: Stability proofing

Initially, the open-loop condition is derived from the DC-link voltage regulator. The open-loop transfer function of the control loop is illustrated below.

$$G_o(s) = \left(K_{\text{po}} + \frac{K_{\text{io}}}{s}\right)\left(\frac{1}{C_{\text{dc}}s}\right) \tag{14}$$

where $G_o(s)$ is the open-loop transfer function, K_{po} and K_{io} are the PI controller constraints, and C_{dc} is the DC-link capacitor present in the inverter. To make the system closed, a unit feedback signal is attached to the open-loop system. After using the unit feedback signal, the closed-loop response becomes

$$H_c(s) = \left(\frac{1}{C_{\text{dc}}}\right) \times \left(\frac{K_{\text{pc}}s + K_{\text{ic}}}{s^2 + \frac{K_{\text{pc}}}{C_{\text{dc}}}s + \frac{K_{\text{ic}}}{C_{\text{dc}}}}\right) \tag{15}$$

From Eq. 15, it is illustrated that it is a second-order system. From the second-order system, the damping factor (ξ) and bandwidth (ω_c) of the undertaken system are estimated as.

$$2\xi\omega_c = \frac{K_p}{C_{\mathrm{dc}}} \Rightarrow K_p = 2\xi C_{\mathrm{dc}}\omega_c \tag{16}$$

$$\omega_c^2 = \frac{K_i}{C_{\mathrm{dc}}} \Rightarrow K_i = C_{\mathrm{dc}}\omega_c^2 \tag{17}$$

To offer enhanced stability, the Bode response of the open-loop system at different band width is illustrated in Fig. 3a. From Fig. 3a, it is found that at $\omega_c = 345$ the open-loop system offers a better stability response as compared to other bandwidth values. As per the internationally acceptable standard, ξ value must lie between 0.5

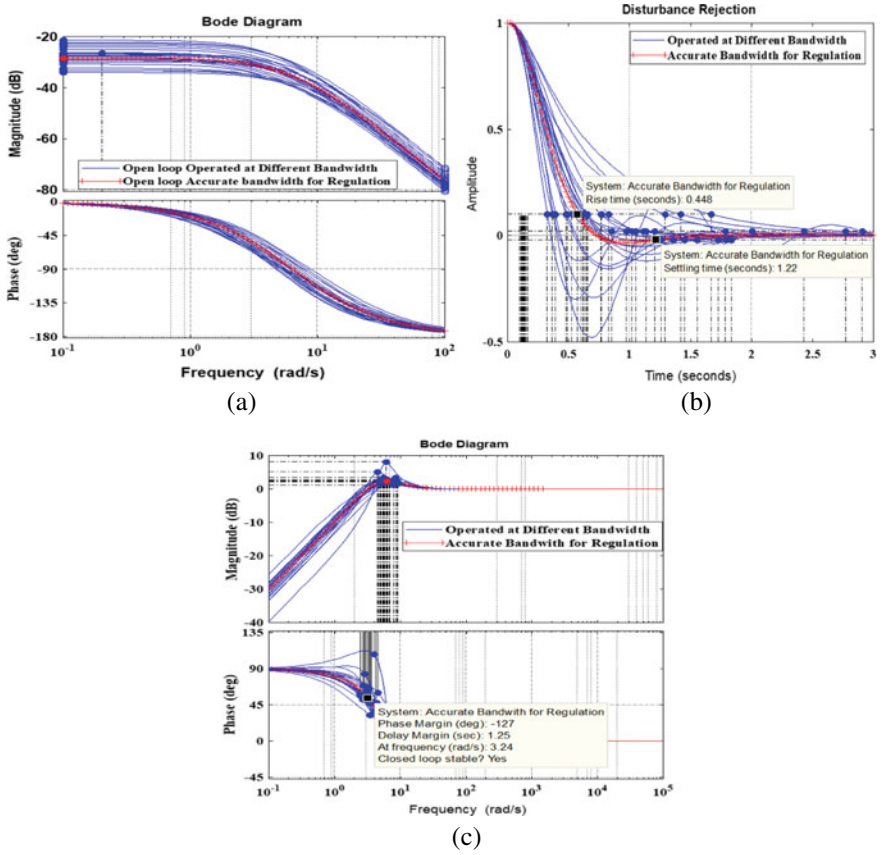

Fig. 3 At different bandwidth: **a** open-loop system Bode response, **b** disturbance rejection, and **c** closed-loop system Bode response

and 0.8. The obtained bandwidth and DC-link capacitor voltage are used to compute the K_p and K_i constraints of the regulator through Eqs. 16 and 17. In this test case, 20 samples of bandwidth are taken to compute the PI controller parameters. In Fig. 3b, by using different bandwidths, the rejection of the disturbance curve is illustrated. It is visualized that by using the selected bandwidth values, the system offers a faster response as compared to others. Similarly, by using the K_p and K_i values, the closed-loop response of the system offers better stability as compared to others as illustrated in Fig. 3c. This shows the robust stability conditions of the undertaken controller and suggested for higher power application.

Case-2: Adaptive filter-based 5LASI operation at variable load condition

To test the proposed control and inverter model performance, the modeled system undergoes through variable load situation. As illustrated in Fig. 1, initially, the delta-delta-connected transformer is connected to the proposed system. Due to the connection of Load-1, during 0–0.07 s, the load current is set at 1000 A, and during 0.11–0.15 s, the load current is increased to 3000 A. At 0.15 s, Load-2 is connected to the model system and the current is increased to 6000 A. This type of system model and load demand is set to validate the control model and inverter performance.

In Fig. 4a–o, the obtained results are presented during variable load conditions. Figure 6a illustrates that the grid voltage is estimated as 6000 A. As per the set condition, the load voltage and current results are illustrated in Fig. 4b, c. To generate the appropriate load voltage and current, the required DC-link load-1 and load-2 voltage results are illustrated in Fig. 4d, e, respectively. By using the proposed DC-link voltage regulator, the system can maintain the voltage and current at their rated value as illustrated in Fig. 4f, g, respectively. The absolute voltage error curve is illustrated in Fig. 4h, which shows that during any type of load change the voltage error is slightly changed to zero. By using the proposed controller, the proposed 5LASI generates appropriate voltage and current to compensate the load harmonics as illustrated in Fig. 4i, j, respectively. The proposed inverter is also capable to generate the five-level phase voltage output as illustrated in Fig. 4k. Due to the increased voltage level, the system can reduce the voltage error and improved its quality significantly. By using the traditional inverter and control approach, the system is able to flow the required grid current results as per the load demand. However, it is visualized that Fig. 4l contains more harmonic, which significantly decreases the power quality of the system. By using the proposed inverter and control approach, the proposed system not only fulfills the desired load demand but also maintains the linear load current. Due to the improved grid current as illustrated in Fig. 4m, the system improved the power quality significantly. The proposed control approach provides a better linear relationship result between the grid and the load current as illustrated in Fig. 4n. Figure 4o illustrates that the control approach tracks the reference grid current results efficiently. The above findings indicate that by using the proposed 5LASI and control approach, the system improves its performance and suitable for real-time application.

Study-3: Comparative study

To obtain a clear analysis, the obtained load, traditional, and proposed grid current results are passed through fast Fourier transform (FFT) analysis. From the FFT analysis, the load current harmonic percentages are computed and presented in Fig. 5a–c.

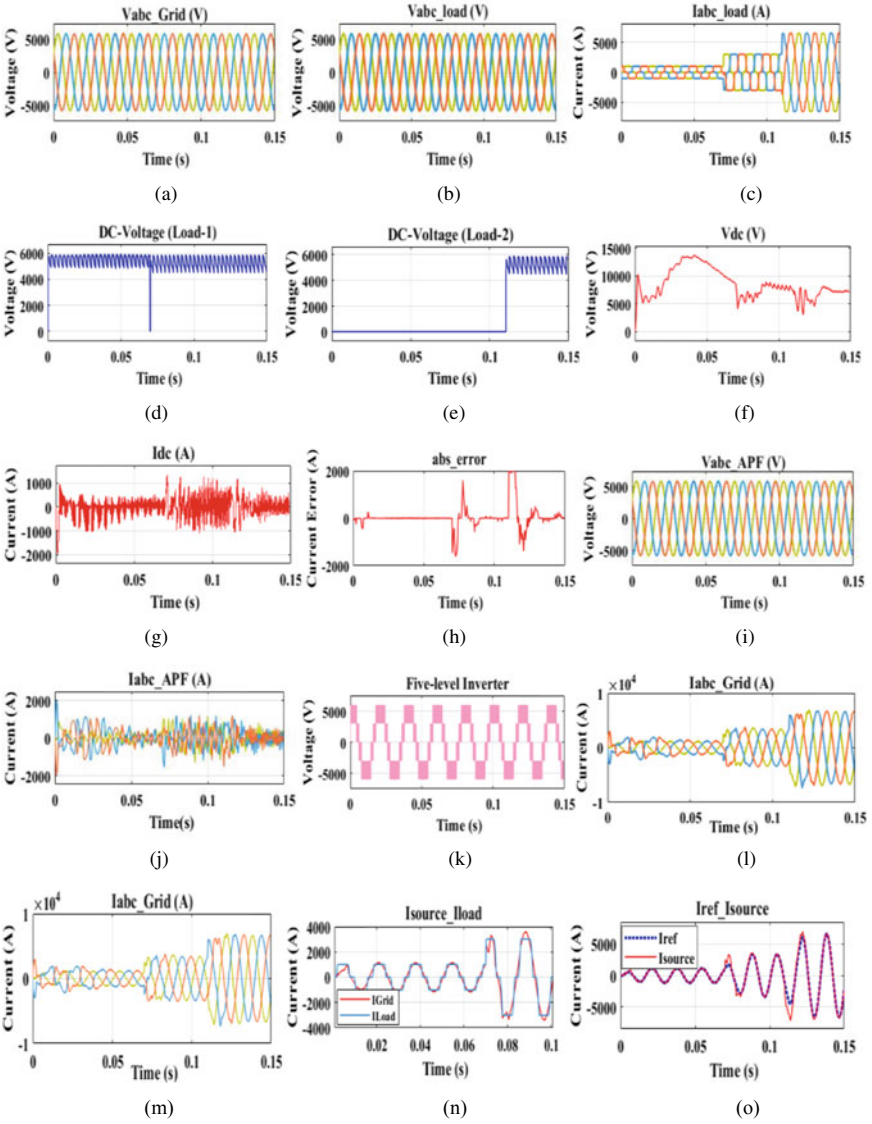

Fig. 4 **a** Grid voltage, **b** sensitive load voltage, **c** sensitive load current, **d** DC-link load voltage-1, **e** DC-link load voltage-2, **f** DC-link capacitor voltage, **g** DC-link capacitor current, **h** absolute voltage error, **i** APF voltage, **j** APF current, **k** 5LASI phase voltage, **l** traditional grid current, **m** proposed grid current, **n** relation between source and load current, **o** relation between reference and grid current

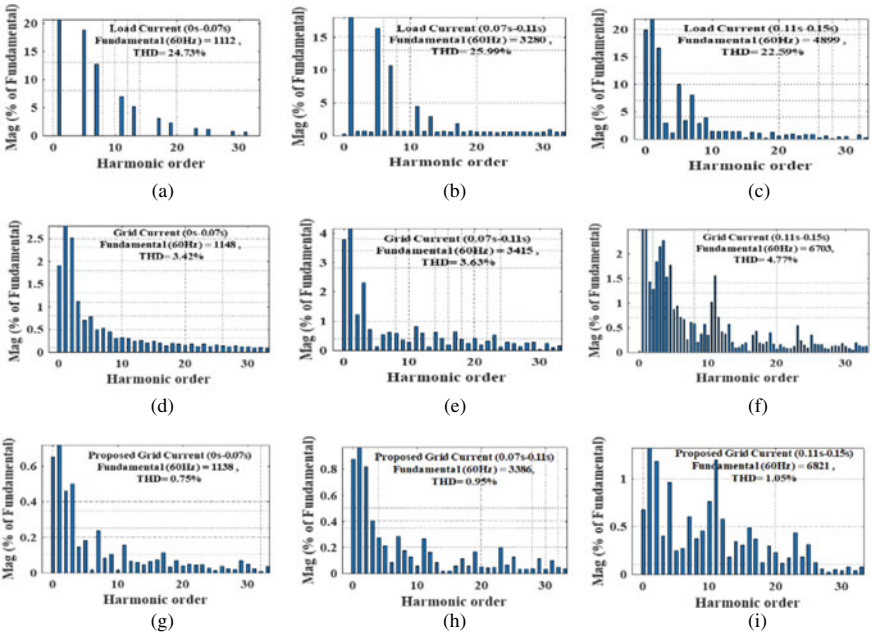

Fig. 5 **a** Load current (0–0.07 s), **b** load current (0.07–0.11 s), **c** load current (0.11–0.15 s), traditional: **d** grid current (0–0.07 s), **e** grid current (0.07–0.11 s), **f** grid current (0.11–0.15 s), proposed: **g** grid current (0–0.07 s), **h** grid current (0.07–0.11 s), **i** grid current (0.11–0.15 s)

In Fig. 5a–c, it is found that the load current harmonics are 24.73%, 25.99%, and 22.59 at $t = 0$, 0.07, and 0.11 s, respectively. These percentages are quite high as per the IEEE-1541 standards. By using the traditional filter and inverter strategy, the grid current nonlinearity percentage is reduced to 3.42%, 3.63%, and 4.77% for the same period and illustrated in Fig. 5d–f, respectively. However, as per the IEEE standard, this percentage of harmonics is also not acceptable. By using the proposed inverter and control strategy, the harmonic contained in the grid current is significantly reduced to 0.75, 0.95, and 1.05% for the same period, and the results are illustrated in Fig. 5g–i, respectively. For a clear representation, a comparative Table 2 is presented and calculated the improvement percentage from the traditional approach. Therefore, looking at the necessity, it is suggested to integrate the proposed model for real-time application.

5 Conclusion

In this study, by using the advanced adaptive filter-based controller and 5LASI, the proposed system performance is significantly improved. The combined controller stability curves guarantee the stability of the proposed system at variable load

Table 2 Comparative study

Conditions	THD%		
	0–0.07 s (%)	0.07–0.11 s (%)	0.11–0.15 s (%)
Load current	24.73	25.99	22.59
Conventional inverter and controller	3.42	3.63	4.77
Improvement	86.17	86.03	78.88
5LASI + controller	0.75	0.95	1.05
Improvement	96.96	96.34	95.35

conditions. The proposed control algorithm is capable to calculate the appropriate harmonic current and eliminate it from the nonlinear load system. Due to this, the system reduces the harmonic percentage significantly. In addition to that, by using the proposed control and modulation strategy, the inverter generates an increased five-level output voltage. The improved voltage level also increases the power quality as well as the voltage of the undertaken system at variable load conditions. The above findings indicate that the proposed inverter and controller provide an improved result regarding voltage and current results. The compared traditional results with the proposed results indicate that the overall improvement percentage is 96.21%, and this is a very good response. The obtained and analyzed results serve as a basis for designing an appropriate system and controller for real-time applications.

Acknowledgements Assistance provided by the Council of Scientific & Industrial Research, Gov. of India, under the acknowledgment number 143460/2K19/1 (File no: 09/969(11117)/2021-EMR-I).

Appendix

Linear voltage (V_S): 4160*(2/3)$^{1/2}$ V, 60 Hz, Source inductance = 1e^{-5}, Resistance, inductance (Line): 8Ω, 7mH, SHAF integrating inductor: 2mH, Load resistance and inductance: 26.66 Ω, 10mH, SHAF dc voltage and capacitor: 6000 V, 2500 μF.

References

1. Sahoo B, Routray SK, Rout PK (2021) AC, DC, and hybrid control strategies for smart microgrid application: a review. Int Trans Electr Energy Syst 31(1):e12683
2. Biricik S, Redif S, Özerdem ÖC, Khadem SK, Basu M (2014) Real-time control of shunt active power filter under distorted grid voltage and unbalanced load condition using self-tuning filter. IET Power Electron 7(7):1895–1905
3. Sahoo B, Routray SK, Rout PK (2020) Robust control approach for stability and power quality improvement in electric car. Int Trans Electr Energy Syst 30(12):e12628

4. Akagi H (1996) New trends in active filters for power conditioning. Indus Appl 32(6):1312–1322
5. Sahoo B, Routray SK, Rout PK (2020) A novel centralized energy management approach for power quality improvement. Int Trans Electr Energy Syst:e12582
6. Akagi H (1996) New trends in active filters for improving power quality. In: Proceedings of international conference on power electronics, drives and energy systems for industrial growth, vol 1. IEEE, , pp 417–425
7. Sahoo B, Routray SK, Rout PK (2021) Execution of robust dynamic sliding mode control for smart photovoltaic application. Sustain Energy Technol Assessm 45:101150
8. Yan J et al (2017) A novel phase performance evaluation method for particle swarm optimization algorithms using velocity-based state estimation. Appl Soft Comput 57:517–525
9. Sahoo B, Routray SK, Rout PK (2021) Advanced Speed-and-current control approach for dynamic electric car modelling. IET Electr Syst Transp
10. Balasubramaniam PM et al (2021) An efficient control strategy of shunt active power filter for asymmetrical load condition using time domain approach. J Discr Math Sci Cryptogr 24(1):19–34
11. Routray SK, Sahoo B, Dash SS (2020) A novel control approach for multi-level inverter-based microgrid. Advances in electrical control and signal systems. Springer, Singapore, 983–996
12. Nguyen BH (2018) "Evolutionary computation for feature selection in classification
13. Sahoo B, Routray SK, Rout PK (2020) Hybrid generalised power theory for power quality enhancement. IET Energy Syst Integr 2(4):404–414
14. Badal FR, Das P, Sarker SK, Das SK (2019) A survey on control issues in renewable energy integration and microgrid. Prot Control Mod Power Syst 4(1):8
15. Sahoo B, Routray SK, Rout PK (2021) Robust control and inverter approach for power quality improvement. Green technology for smart city and society. Springer, Singapore, 143–156
16. Hekss Z et al (2021) Nonlinear adaptive control design with average performance analysis for photovoltaic system based on half bridge shunt active power filter. Int J Electr Power Energy Syst 125:106478
17. Sahoo B, Routray SK, Rout PK (2020) Integration of wind power generation through an enhanced instantaneous power theory. IET Energy Syst Integr 2(3):196–206
18. Fallah M et al (2021) A modified indirect extraction method for a single-phase shunt active power filter with smaller DC-link capacitor size. Sustain Energy Technol Assessm 45: 101039
19. Sahoo B, Routray SK, Rout PK (2020) Robust control approach for the integration of DC-grid based wind energy conversion system. IET Energy Syst Integr 2(3):215–225
20. Sahoo B, Routray SK, Rout PK (2021) Advanced control technique based neutral clamped inverter operation. In: 2021 1st Odisha international conference on electrical power engineering, communication and computing technology (ODICON). IEEE

Bypass Diodes Configurations for Mismatch Losses Mitigation in Solar PV Modules

Priya Ranjan Satpathy, Pritam Bhowmik, Thanikanti Sudhakar Babu, Renu Sharma, and Chiranjit Sain

Abstract Partial shading among the photovoltaic modules is the most commonly observed scenario that can permanently damage the modules by creating mismatch among cells, hotspot, and unexpected losses in the system. Basically, modules are provided with bypass diodes for prevention from destructive effect of the hotspot. Bypass diodes configuration plays a crucial role in the operation and performance of the modules during shading. In this paper, the sensitivity of PV modules with no bypass diode, grouped bypass diodes, overlapped bypass diodes, and single bypass diodes during partial shading is investigated. The investigation is carried out in the MATLAB/Simulink environment for a module under various cell-level shadings. The comparison is done using power generation, losses, efficiency, and number of peaks analysis. It is found that the performance and characteristics of the modules are highly susceptible to the bypass diodes configurations and nature of shading.

Keywords Photovoltaic (PV) · Bypass diodes · Hotspot · Mismatch loss · Partial shading · Power generation

P. R. Satpathy (✉) · R. Sharma
Department of Electrical Engineering, ITER, SOA Deemed To Be University, Bhubaneswar, India

R. Sharma
e-mail: renusharma@soa.ac.in

P. Bhowmik
Department of Electrical Engineering, Budge Budge Institute of Technology, Kolkata, India

T. S. Babu
Department of Electrical and Electronics Engineering, Chaitanya Bharathi Institute of Technology, Hyderabad, India

C. Sain
Department of Electrical Engineering, Siliguri Institute of Technology, Siliguri, India
e-mail: chiranjitsain@nitm.ac.in

M. Mishra et al. (eds.), *Innovation in Electrical Power Engineering, Communication, and Computing Technology*, Lecture Notes in Electrical Engineering 814,
https://doi.org/10.1007/978-981-16-7076-3_18

1 Introduction

Photovoltaic (PV) power generation is widely accepted among all renewables due to source abundance, noiseless generation, no emission, eco-friendly, and low maintenance characteristics [1–3]. In PV system, modules are the most expensive components that play a crucial role in overall power generation [4]. Basically, PV modules are the series combination of a number of PV cells encapsulated together to increase the overall voltage and power. Generally, PV modules are installed in an open space to receive maximum irradiance for generating higher power. However, the performance of the PV arrays and connected modules gets harmed due to various factors such as low and fluctuating irradiance, temperature, and shading [5–9].

Partial shading is the resultant of various unexpected environmental scenarios such as deposition of tree leaves, snow, dust, soiling, bird waste, and debris in module, shadow of the nearby buildings, poles, and tress, cloud coverage, broken or cracked module glass [10–12]. During these scenarios, the module receives multiple irradiance levels resulting mismatch among the connected cells. The cells under shading receive reduced irradiance and starts behaving as a load by consuming the current of the healthy unshaded cells instead of generating current. The parallel-connected cells have no effect of partial shading and mismatch as the total current of the array is the sum of the current generated by the individual cell [13]. However, the series cells get most affected by shading as same current flows through the entire string and forcing the shaded cells to carry higher current. Hence, the extra current generated by the unshaded cells gets stuck in the shaded one resulting proportional lower current output. The effect of partial shading in strings and parallel strings-based PV arrays is examined and concluded that short strings arrays generated maximum power during shading [14]. Also, partial shading in the cells can result in generation of local heat among the shaded cells causing hotspot phenomenon [15]. The hotspot phenomenon aims to damage the PV module physically, and hence, detection is considered to be a major part of the system [16]. The fast, simple, reliable, and inexpensive way of hotspot detection in the cells is done by using infrared thermography (IRT) diagnostic tool [17]. However, long-term existence of the shading and hotspot in the modules can lead to permanent damage and early degradation of modules by causing glass cracking or breaking, soldier joints meltdown, and cell detachment.

Bypass diodes (BDs) are connected in antiparallel manner with a group of cells in order to bypass the higher current generated by the unshaded PV cells [18]. During shading, the bypass diode of the shaded cells/module gets forward biased forming a low resistive path for current generated by the unshaded cells or modules to pass through them avoiding hotspot formation in the shaded ones. In practice, one bypass diode per cell increases the cost and module side so, for feasibility, one bypass diode is connected to a group of cells. For example, for a 36 cells PV module, two bypass diodes are connected, each for a group of 18 series connected cells. However, in the group string of cells, single cell shading can lead to turning on of the bypass diode that reduces the respective string voltage giving rise to voltage proportional to the forward-biased voltage of the diode [19]. A smart bypass diode concept has

been proposed that uses SM74611 IC for each cell in order to increase the shade resilience and reliability of the PV module, but using these types of ICs increases the overall module cost and complexity [20]. Generally, bypass diodes are mounted in the modules using two configurations, i.e., overlapped and non-overlapped structures that have been mathematically explained in the literature [21, 22]. However, the performance comparison bypass diodes configurations in the modules under shading have not been done.

This paper examines the performance of the bypass diodes and its configurations in PV modules under various shading scenarios. The operation and working of the modules with no BD (NBD), grouped BD (GBD), overlapped BD (OBD), and single BD (SBD) are studied. The entire comparisons have been done using the power–voltage (P–V) curves and various electrical performance parameters. The investigation is conducted in MATLAB/Simulink environment using various real-time-based partial shading scenarios.

2 System Configuration and Test Benches

The modeling of cells and modules has been explained in this section. Also, various partial shading scenarios along with the formulations involved and bypass diodes operation in PV modules have been explained.

2.1 Mathematical Modeling of Cells and Module

The cell is a semiconductor device that generates electricity from solar irradiance (G) by mean of the photoelectric effect which is represented by a current source with a parallel diode (D) and some resistances. The equivalent electrical circuit of a PV cell is depicted in Fig. 1 where I_{Ph} is the photogenerated current, I_{PV} is the output current, V_{PV} is the output voltage, R_{S} is the series resistance, and R_{Sh} is the shunt

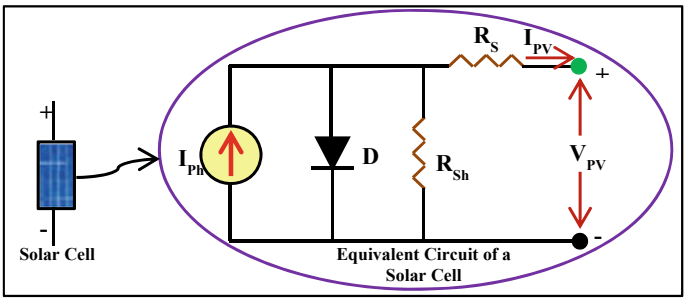

Fig. 1 Equivalent circuit representation of a PV cell

Table 1 Specification of the module at STC (1000 W/m^2, 25 °C, and 1.5 AM)

Parameters	Rating at STC	Rating at OC
Power at MPP (P_M) (W)	50	34.55
Voltage at MPP (V_M) (V)	17.47	15.09
Current at MPP (I_M) (A)	2.866	2.28
Open-circuit voltage (V_{OC}) (V)	21.566	19.35
Short-circuit current (I_{SC}) (A)	3.104	2.509
Maximum efficiency (η) (%)	16.89	14.54
Fill factor (FF) (%)	74.69	71.17

resistance of the cell.

$$I_{PV} = I_{Ph} - I_o\left[\exp\left(V_{PV} + R_s I_{pv}/V_t\right) - 1\right] - \left[\left(V_{pv} + I_{pv} R_s\right)/R_{Sh}\right] \quad (1)$$

The mathematical expression to model the cells has been given in Eq. (1) where I_O symbolizes diode current, $I_{ph} = G/G_{STC} * \left(I_{PV\_STC} + K_I \Delta T\right)$ indicates photonic current, $V_t = nkT/q$ represents the thermal voltage, n, k, T, q, K_I, G, and G_{STC} symbolize diode factors, Boltzmann's constant, module temperature, electron charge, short-circuit current temperature coefficient, irradiance received by the module, and irradiance at the standard testing condition (STC), respectively.

A module comprises of numerous series connected cells (mainly 36 or 72 cells) encapsulated together in a glass frame resulting in higher system voltage.

The PV modules have been operated at 800 W/m^2 and 50 °C during the normal or unshaded condition and considered as operating condition (OC) of the modules. The specification of the module used in the study at STC and OC has been represented in Table 1 [23].

2.2 Formulations

The maximum power (P_M) from module/arrays is calculated in Eq. (2) where V_M and I_M are the maximum voltage and current outputs.

$$P_M = V_M \times I_M \quad (2)$$

The generating efficiency (η) is expressed in Eq. (3) where G and A denote the received irradiance and area of the module, respectively.

$$\eta(\%) = (P_M/G \times A) \times 100 \quad (3)$$

The mismatch loss (ML) encountered by the module/array during partial shading can be calculated using Eq. (4) where P_{MU} and P_{MS} denote the maximum power generated by the module/array under unshaded and shaded conditions, respectively.

$$\mathrm{ML} = P_{\mathrm{MU}} - P_{\mathrm{MS}} \tag{4}$$

The percentage of power loss (PL) in the module/array during shading is calculated in Eq. (5) where P_{MSTC} indicates the maximum power of module/array at STC.

$$\mathrm{PL}(\mathrm{in}\%) = ((P_{\mathrm{MSTC}} - P_{\mathrm{MS}})/P_{\mathrm{MSTC}}) \times 100 \tag{5}$$

3 Bypass Diode Configurations

Bypass diode (BD) is a Schottky barrier diode (or hot carrier diode) that has a low forward voltage drop with a very fast switching action. So, these types of diodes are connected in parallel with the PV cells to reduce the effect of the hotspot and maximize the power generation with a reduced voltage rate. In general, commercial small-scale PV module consists of cells in series configuration with one or two antiparallel installed bypass diodes. Also, various modules having no bypass diodes are available in the market that is specially intended to charge the batteries with 12 or 48 V voltage. There also exist six bypass diodes (each for twelve cells)-based PV modules in the market with 72 cells in series. The configurations of bypass diodes have a huge contribution in the mitigation of hotspot and losses in the modules due to partial shading. In this study, the effect of partial shading on the power generation of modules and arrays has been investigated considering different BD configurations. The widely used bypass diode configurations include grouped cell bypass diodes, overlapped bypass diodes, and single bypass diodes shown in Fig. 2b–d, respectively. Figure 2a illustrates the structure of a 36 series cells-based PV module without any parallel-connected bypass diodes. The module has been divided into two groups: Group 1: From positive terminal cell numbered as 1 to 18th cell and Group 2: From negative terminal, cell numbered 36 to the 19th cell.

4 Results and Discussions

The partial shading scenarios used in the study are based on various patterns, intensity, area, uniformity, and level of irradiance received as shown in Fig. 3. The shading scenario A occurs due to deposition of tree leaf in the module that covers four cells of different cells group receiving two irradiance levels, i.e., unshaded cells receive 800 W/m^2 and shaded cells receive 50 W/m^2. Scenario B is the temporary shadings occur due to cloud passage where the module receives three different irradiance levels 800, 250, and 100 W/m^2. Scenario *C* occurs due to snow coverage where the cells receive very low or zero irradiance as compared to the unshaded cells. Shading scenario *D* occurs due to dust deposition in the module whereas scenario *E* reflects shading due to the presence of certain buildings or poles near the installation area.

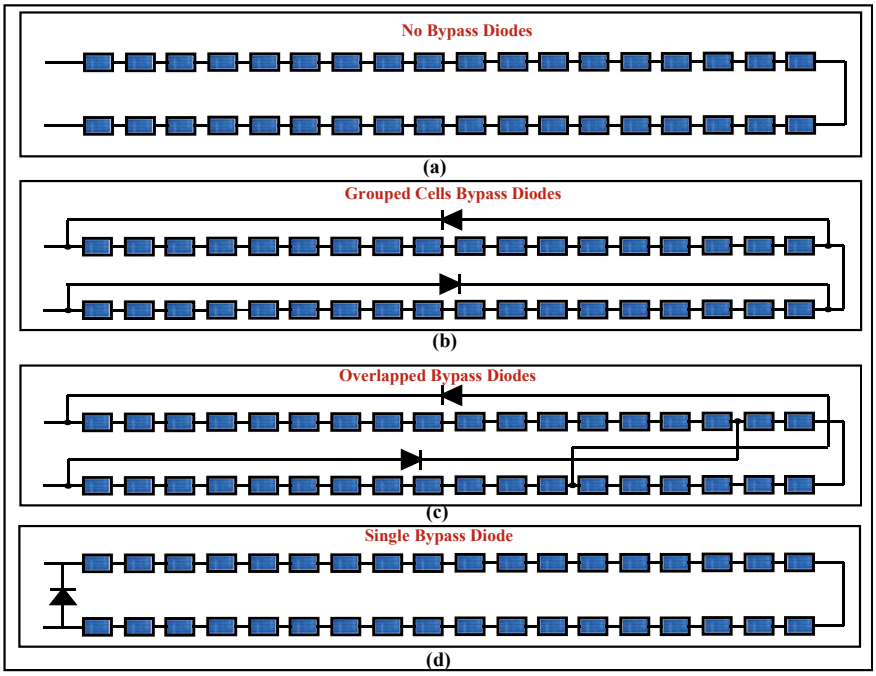

Fig. 2 Bypass diodes configurations in PV module. **a** No bypass diodes, **b** grouped bypass didoes, **c** overlapped bypass diodes, and **d** single bypass diodes

The variation of maximum power output (P_M) and efficiency (η) of the module with respect to different irradiance levels and operating temperature conditions have been represented as a 3D graph shown in Fig. 4a, b, respectively. In Fig. 4a, it can be seen that the power output (P_M) of the module gradually decreases from 50 W at 1000 W/m^2 (white color) to 0 W at 0 W/m^2 (black color). Also, it has been noticed that the power output of the module decreases from 50 W at 25 °C (white color) to 32 W at 100 °C (orange color). Similarly, the efficiency (η) of the PV module (Fig. 4b) has been found to be decreasing from 16.83% at 1000 W/m^2 (dark red color) to 13.8% at 100 W/m^2 (red color). Similarly, the efficiency of the module hardly reduces to 13.8% at 100 °C temperature. The efficiency of the module reduces to 0% as the module has been subjected to receive 0 W/m^2. This makes a sense that the power generation and efficiency of the PV module are largely dependent on the irradiance received by it and has a puny dependence on the operating temperature.

During unshaded scenario or operating condition (at 800 W/m^2 and 50 °C), the module generated maximum power equal to 34.55 W whereas at STC (1000 W/m^2 and 25 °C) generated the maximum power equal to 50 W with zero mismatch loss. However, during shading, the performance of the module degrades as the cells under shading receive low irradiance levels resulting in reduced power output. The maximum power (P_M), maximum voltage (V_M), maximum current (I_M), efficiency

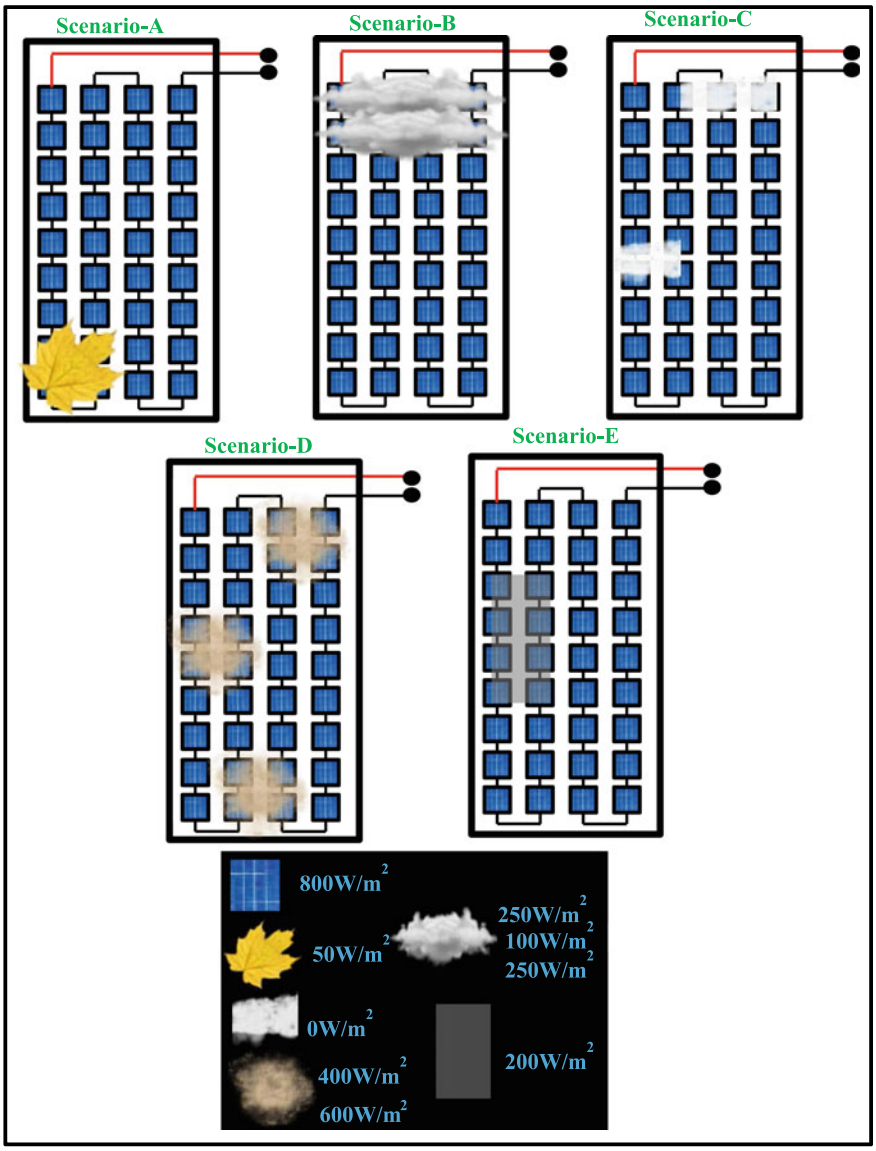

Fig. 3 Various partial shading scenarios considered for PV module

(η), mismatch loss (ML), power loss (PL), number of peaks generated by different bypass diode configurations of PV module during all shading scenarios (Fig. 3) have been tabulated in Table 2.

The power–voltage (P–V) curve of the module with BD configurations during shading scenario A has been shown in Fig. 5. The graph clearly indicates that the

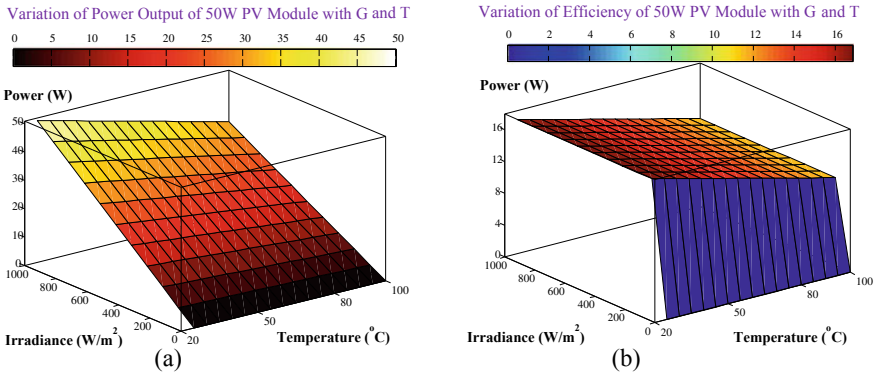

Fig. 4. 3D graph showing the variation of power output and efficiency of the PV module with irradiance and temperature conditions. **a** Maximum power (PM) and **b** efficiency (η)

Table 2 Performance of modules with bypass diodes configurations during shading scenarios

	Shading A				Shading B			
Parameters	NBD	GBD	OBD	SBD	NBD	GBD	OBD	SBD
P_M (W)	5.46	14.8	10.6	5.46	5.15	5.15	5.76	5.15
V_M (V)	17.8	6.73	4.73	17.8	16.9	16.9	18.8	16.9
I_M (A)	0.3	2.2	2.23	0.3	0.3	0.3	0.34	0.3
η (%)	2.29	6.22	4.46	2.29	6.37	6.37	6.63	6.37
ML (W)	29	19.7	23.9	29	29.4	29.4	28.7	29.4
PL (%)	89	70.4	78.8	89	89.7	89.7	88.4	89.7
Peaks	1	2	2	1	1	1	1	1

	Shading C				Shading D				Shading E			
Parameters	NBD	GBD	OBD	SBD	NBD	GBD	OBD	SBD	NBD	GBD	OBD	SBD
P_M (W)	0	1.18	1.66	0	19.6	19.6	20.1	19.6	10.3	15	11.3	10.3
V_M (V)	0	7.77	5.4	0	16.3	16.3	16.6	16.3	16.9	6.78	18.5	16.9
I_M (A)	0	0.15	0.3	0	1.2	1.2	1.21	1.2	0.6	2.21	0.61	0.6
η (%)	0	0.49	0.69	0	8.24	8.24	8.45	8.24	4.33	6.31	4.75	4.33
ML (W)	34.5	33.37	32.8	34.5	14.9	14.9	14.4	14.9	24.2 79.4	19.5	23.2	24.2
PL (%)	100	97.6	96.6	100	60.8	60.8	59.8	60.8	1	70	77.4	79.4
Peaks	0	1	2	0	1	1	1	1		2	2	1

module with grouped cell BDs (GBD) has generated higher power of 14.8 W followed by the module with overlapped BDs (OBD), i.e., 10.6 W. It has been found that the module with no BD (NBD) and single BD (SBD) generated the equal and lowest power (5.46 W) as the unshaded cells current get no path to flow and forcefully flow through the shaded cells resulting in low power output and hotspot. The module with

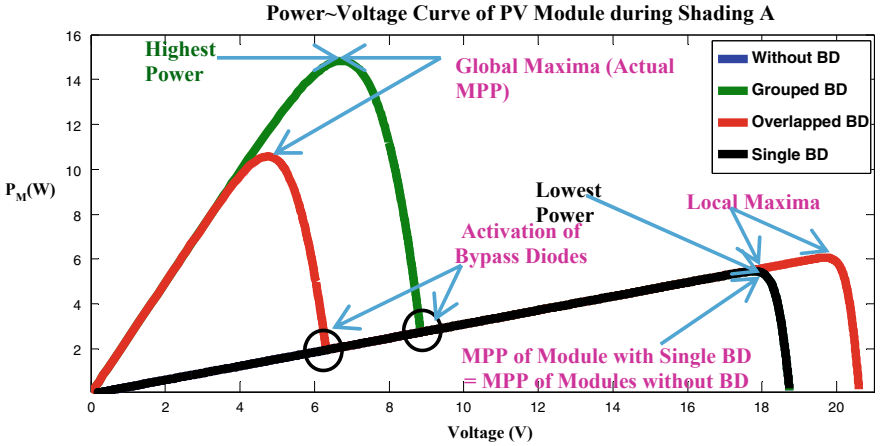

Fig. 5 *P–V* characteristics curves of the module with different bypass diodes configuration during shading scenario A

NBD and SBD encountered the highest mismatch loss (29 W) as compared to the module with OBD (23.9 W) and GBD (19.7 W). The efficiency of the module with GBD has been found to be at maximum (6.22%) followed by OBD (4.46%) and NBD/SBD (2.29%).

During shading scenario B, the module with OBD generates slightly higher power (5.76 W) than the NBD, GBD, and SBD modules (5.15 W). Similarly, the modules with NBD, GBD, and SBD have encountered higher mismatch and power losses of 29.4 W and 89.7%, respectively, as compared to the module with OBD (28.7 W and 88.4%). The *P–V* curves shown in Fig. 6a clearly represents that all the BD configurations have generated convex curves with one maximum power point (MPP) each.

During shading *C*, some cells of the modules have been covered by the snow receiving 0 W/m^2 irradiance resulting in zero power output from the modules with NBD and SBD encountering 100% power loss. However, the module with OBD generated slightly higher power (1.66 W) with 96.6% power loss as compared to the module with GBD (1.18 W, 97.6%). The *P–V* characteristics curves of the PV modules during shading *F* have been shown in Fig. 6b.

The *P–V* characteristics curves of all the BD configurations during shading scenario *D* have been depicted in Fig. 6c indicating that all the configurations have generated convex peaks. The modules with NBD, GBD, and SBD have generated equal power, i.e., 19.6 W encountering mismatch and power losses equal to 14.9 W and 60.8%, respectively. The PV module with OBD generated slightly higher power (59.8 W) with reduced mismatch (14.4 W) and power (59.8%) loss.

In this case of shading E, the GBD module generated the higher power, i.e., 15 W with puny mismatch (19.5 W) and power (70%) losses. The PV module with OBD has generated lower power than the GBD, i.e., 11.3 W with mismatch and power

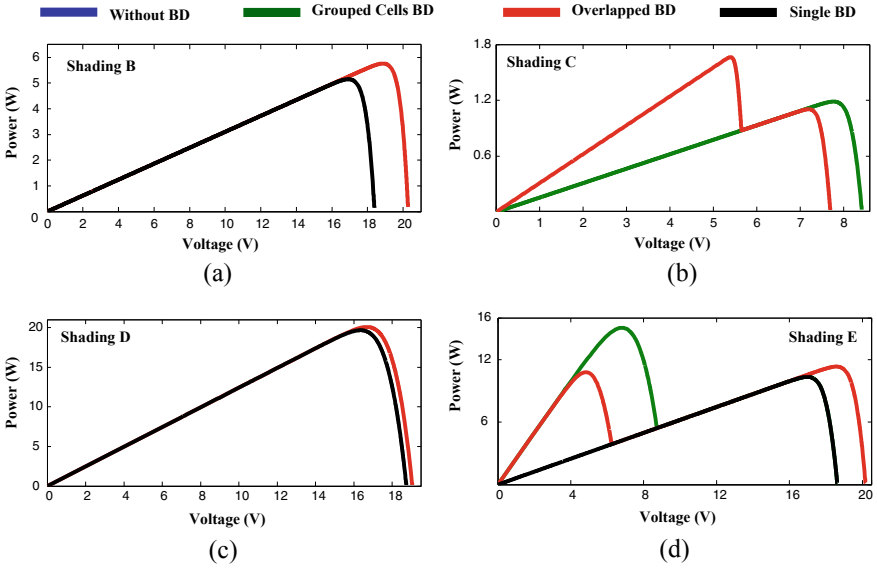

Fig. 6 *P–V* curves of the various BD configured modules during various shading scenarios. **a** Shading scenario B, **b** shading scenario C, **c** shading scenario D, **d** shading scenario E

losses equal to 23.2 W and 77.4%, respectively. The PV modules with NBD and SBD have the lowest power output (10.3 W) and higher mismatch (24.2 W) and power (79.4%) losses.

Hence, from the results, it has been found that the OBD has generated higher power with GMPP lying at the first position of the *P–V* curve and reduced the possibility of the hotspot. The module with GBD has generated the second higher power with GMPP lying at the first position of the *P–V* curve in most of the cases and hence reduces the hotspot. The module with NBD and SBD has generated the lowest power with the highest possibility of hotspot during shading.

5 Conclusion

In this paper, the performance of different bypass diode configurations under partial shading is studied. The study is conducted for modules using various partial shading scenarios. The results show that the PV module with overlapped bypass diodes has generated higher power during most of the shading scenarios followed by module with grouped bypass diodes. It is established that the presence of bypass diodes in the modules can increase the power generation of the module and reduces the possibility of hotspot. However, bypass diodes activation can form non-convex characteristics curves that can complicate the operation of the maximum power point tracker algorithms. The modules with no bypass diodes have the lowest power generation and

can form hotspot resulting damage and fire hazards sometimes. Hence, bypass diodes play a major role in power generation of the modules whose performance largely depend on the adopted configuration and nature of the partial shading.

Acknowledgements This work has been supported by the Council of Scientific and Industrial Research (CSIR), Govt. of India under the File No- 09/0969(11258)/2021-EMR-I.

References

1. Nazeri MNR, Tajuddin MFN, Babu TS, Azmi A, Malvoni M, Kumar NM (2021) Firefly algorithm-based photovoltaic array reconfiguration for maximum power extraction during mismatch conditions. Sustainability 13(6):3206
2. Mishra M, Dash PB, Nayak J, Naik B, Swain SK (2020) Deep learning and wavelet transform integrated approach for short-term solar PV power prediction. Measurement 166:108250
3. Swain MK, Mishra M, Bansal RC, Hasan S (2021) A self-powered solar panel automated cleaning system: design and testing analysis. Electric power components and systems, pp 1–13
4. Shen L, Li Z, Ma T (2020) Analysis of the power loss and quantification of the energy distribution in PV module. Appl Energy 260:114333
5. Yousri D, Babu TS, Mirjalili S, Rajasekar N, Abd Elaziz M (2020) A novel objective function with artificial ecosystem-based optimization for relieving the mismatching power loss of large-scale photovoltaic array. Energy Convers Manag 225:113385
6. Satpathy PR, Sharma R, Jena S (2017) A shade dispersion interconnection scheme for partially shaded modules in a solar PV array network. Energy 139:350–365
7. Satpathy PR, Jena S, Sharma R (2018) Power enhancement from partially shaded modules of solar PV arrays through various interconnections among modules. Energy 144:839–850
8. Winston DP, Kumaravel S, Kumar BP, Devakirubakaran S (2020) Performance improvement of solar PV array topologies during various partial shading conditions. Sol Energy 196:228–242
9. Mansoor M, Mirza AF, Ling Q, Javed MY (2020) Novel grass hopper optimization based MPPT of PV systems for complex partial shading conditions. Sol Energy 198:499–518
10. Satpathy PR, Sharma R (2020) Parametric indicators for partial shading and fault prediction in photovoltaic arrays with various interconnection topologies. Energy Convers Manag 219:113018
11. Yousri D, Allam D, Eteiba MB (2020) Optimal photovoltaic array reconfiguration for alleviating the partial shading influence based on a modified Harris Hawks optimizer. Energy Convers Manag 206:112470
12. Eltamaly AM, Al-Saud MS, Abokhalil AG (2020) A novel bat algorithm strategy for maximum power point tracker of photovoltaic energy systems under dynamic partial shading. IEEE Access 8:10048–10060
13. Satpathy PR, Sharma R, Panigrahi SK, Panda S (2020) Bypass diodes configurations for mismatch and hotspot reduction in PV modules. In 2020 international conference on computational intelligence for smart power system and sustainable energy (CISPSSE). IEEE, pp 1–6
14. Satpathy PR, Sharma R (2020). Reliability and losses investigation of photovoltaic power generators during partial shading. Energy Convers Manag 223:113480
15. Niazi KAK, Akhtar W, Khan HA, Yang Y, Athar S (2019) Hotspot diagnosis for solar photovoltaic modules using a Naive Bayes classifier. Sol Energy 190:34–43
16. Gallon J, Horner GS, Hudson JE, Vasilyev LA, Lu K (2015) PV module hotspot detection. Tau Science Corporation
17. Salazar AM, Macabebe EQB (2016) Hotspots detection in photovoltaic modules using infrared thermography. In: MATEC web of conferences, vol. 70. EDP Sciences, p 10015

18. Silvestre S, Boronat A, Chouder A (2009) Study of bypass diodes configuration on PV modules. Appl Energy 86(9):1632–1640
19. Dhere NG, Shiradkar N, Schneller E, Gade V (2013) The reliability of bypass diodes in PV modules. In: Reliability of photovoltaic cells, modules, components, and systems VI (Vol 8825). International Society for Optics and Photonics, p 88250I
20. Pannebakker BB, de Waal AC, van Sark WG (2017) Photovoltaics in the shade: one bypass diode per solar cell revisited. Prog Photovolt Res Appl 25(10):836–849
21. Teo JC, Tan RH, Mok VH, Ramachandaramurthy VK, Tan C (2020) Impact of bypass diode forward voltage on maximum power of a photovoltaic system under partial shading conditions. Energy 191:116491
22. Diaz-Dorado E, Suárez-García A, Carrillo C, Cidras J (2010) Influence of the shadows in photovoltaic systems with different configurations of bypass diodes. In: SPEEDAM 2010. IEEE, pp 134–139
23. Satpathy PR, Sharma R (2018) Power loss reduction in partially shaded PV arrays by a static SDP technique. Energy 156:569–585

Sentiment Analysis of Bengali Facebook Data Using Classical and Deep Learning Approaches

Partha Chakraborty, Farah Nawar, and Humayra Afrin Chowdhury

Abstract The process of assessing the emotional tone behind a document in order to comprehend the expressed opinions, views and emotions is known as sentiment analysis. A sentiment detecting approach is presented in this paper that uses seven machine learning algorithms to detect the polarity of textual Facebook posts and comments in Bengali, including five classical approaches and two deep learning approaches. We preprocessed our initial raw data through several steps and applied the TF-IDF technique for feature extraction. In classical approaches, we have used Naive Bayes (NB), Support vector machine (SVM), Decision tree (DT), AdaBoost, Random forest classifier (RF) and in deep learning approaches we have used Long Short Term Memory Network (LSTM), and Convolutional Neural Network. We have shown a comparative analysis of the classifiers used in sentiment detection. In our study, deep learning approaches have shown better performance than classical approaches with an accuracy of 96.95% by LSTM. Among the classical approaches, Support vector machine and Random forest classifier have achieved maximum accuracy of 78.23% and 78.37%, respectively.

Keywords Sentiment analysis · Opinion · Facebook · TF-IDF · Deep learning

1 Introduction

In recent days, social media like Facebook has become one of the main platforms for expressing opinions [13]. The feelings expressed on Facebook through comments, suggestions, and criticism are a great source of analyzing the sentiment of an individual and can be used for a variety of reasons, such as marketing, sales, product evaluation, decision making, etc.

P. Chakraborty (✉) · F. Nawar · H. A. Chowdhury
Department of Computer Science & Engineering, Comilla University, Cumilla 3506, Bangladesh
e-mail: partha.chak@cou.ac.bd

M. Mishra et al. (eds.), *Innovation in Electrical Power Engineering, Communication, and Computing Technology*, Lecture Notes in Electrical Engineering 814,
https://doi.org/10.1007/978-981-16-7076-3_19

In the Bengali language, very few works have been done on analyzing Bengali text, and there are no appropriate NLP techniques for conducting sentiment analysis studies. The purpose of the research is to build an efficient sentiment analysis system for Bangla text data.

In this paper, we analyzed Bengali text extracted from the social media platform Facebook to perform sentiment analysis. Our data set comprises 10,819 data points gathered from Facebook. We removed noises and redundancies from the initial raw data through several preprocessing steps. We applied stemming and TF-IDF vectorizer for feature extraction. After that we have trained the processed data with both classical and deep leaning classifiers. Deep learning algorithms can be considered as a sophisticated complex approach for learning which imitates biological networks of neural connections. The majority of classical algorithms use statistics and probabilistic reasoning for analysis.In classical approaches, we have used NB, AdaBoost, SVM, DT, RF classifiers and in deep learning approaches we have used LSTM and CNN.

The remaining section of the manuscript is arranged in this manner—the second section consists of works that are relevant, the third and fourth sections describe the architecture and methodology of the system, respectively. Result analysis and comparison are presented in Sect. 5. Finally, the conclusion of the study is stated in Sect. 6.

2 Related Work

Even though Bangla is a widely spoken language around the world, very few NLP tools have been developed for it. To minimize this gap, many researchers are working with the Bangla language.

Chakraborty et al. [11] used attention mechanism-based models, BERT and ELECTRA, to classify Bangla text documents. For their experiment, they used three different Bangla text datasets, with two of the models providing excellent results for two of the three datasets.

Pang et al. [9] used NB classification, Maximum Entropy classification and SVM to classify emotions as positive or negative based on categorization features. These approaches are incorporated into n-grams. Their research shows that SVMs are effective.

Abinash Tripathy [15] presented a comparison of the findings obtained from the Naive Bayes (NB) and SVM classification algorithms to determine whether a sentimental review is positive or negative.

A polarity detection method was presented in by Faruque et al. [4] based on public opinion about Bangladesh Cricket on Facebook. They have used Naive Bayes, Logistic Regression (LR) and Support vector machine (SVM) algorithms for training the classifiers. In their study, LR achieved slightly better accuracy than the other algorithms.

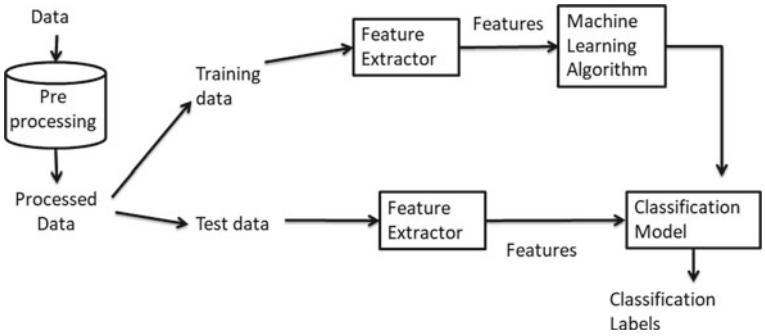

Fig. 1 System architecture of the proposed representation

Boia et al. [3] experimented with using emoticons to label tweets. This shows the precise distinction between positivity and negativity in emoticon-based marking, but not between neutral messages.

Haque et al. [5] introduced a review analysis system in Bengali and Phonetic Bengali, using restaurant reviews to identify reviews using several machine learning techniques. A comparison of vectorizers based on different classifiers is shown, with SVM providing the highest accuracy of 75.58% .

Tuhin et al. [16] detected emotion from Bengali text using Naive Bayes Algorithm and Topical Approach. A comparison of the effectiveness of these two approaches was conducted, with the topical method producing the best outcomes at both magnitude levels.

3 System Architecture

Our data went through several phases of preprocessing. The preprocessing process removes any irrelevant tokens and characteristics to minimize computational difficulty and redundancy. We have used TF-IDF for text vectorization. In total, seven classifiers were used in the study, including five classical approaches and two deep learning approaches. The training data set was used to train these classifiers. In the end, the classifiers were evaluated using the test data set. The schematic diagram in Fig. 1 depicts the underlying learning and classification model.

4 Methodology

4.1 Data Collection

Our data set includes 10,819 data points gathered from Facebook. We used the Facebook Graph API to extract data from Facebook. At first, we selected a topic that

মাদ্রিদ হারার পর পুরা মনটাই ভাইঙ্গা গেছে :(কিছুই ভালো লাগেনা ... ২ তারিখ কোপেনহেগেন এর সাথে হোম ম্যাচ http://fb.me/2MIEwzs4Z

Fig. 2 A snippet of Bengali Facebook data set

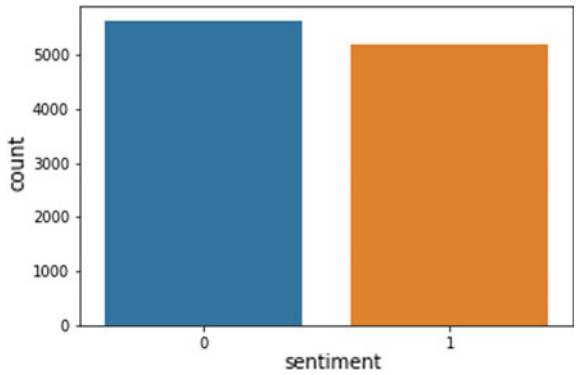

Fig. 3 Frequency of data in each class where class 0 indicates negative polarity and class 1 contains positive polarity

has recently become popular. Then, comments from the first 30,000 s were gathered for each post. A snippet of extracted data is shown in Fig. 2.

The data was automatically labeled using the python programming language. In our approach, we assumed that any comment or post that included positive emoticons, such as :), was positive, and negative emoticons, such as :(, was negative. The frequency of the data in each class is shown in Fig. 3.

4.2 Data Preprocessing

The initial raw data gathered from Facebook included redundant, unnecessary, and noisy information (e.g., punctuation, emoticons, URLs) which doesn't contribute anything to the sentiment of an individual. We removed this noise and redundancy through the following preprocessing steps:

1. *The removal of URLs*: URLs do not provide any emotion from the individuals. They must be removed in order for the system to run faster and more efficiently.
2. *The removal of emoticon*: Small emoticons are used in social media texts so that the user can express his feelings about a subject. We omitted the emoticons because we are only working with textual information.
3. *The removal of punctuation marks*: In documents, the Bengali language employs a significant number of punctuation characters, which play a minor role in determining the sentiment. As a result, the data was stripped of all punctuation marks.
4. *The removal of stopwords*: Stopword refers to a word that appears regularly in a data set but does not provide any negative or positive emotions. Removing stopwords will reduce our computation complexity. So we have used BLTK tools for removing Bengali stopwords.

Sentence	পরিচিত	পথচলা	তেমনি	মেসি	বাংলাদেশকে	যাও	ছিলে	গর্বিত	একজন	উপযুক্ত	বাংলাদেশি	আলহামদুলিল্ল
0	0.000000	0.000000	0.000000	0.000000	0.000000	0.000000	0.0	0.0	0.055556	0.0	0.000000	0.0555
1	0.000000	0.000000	0.000000	0.000000	0.000000	0.000000	0.1	0.1	0.000000	0.1	0.000000	0.0000
2	0.000000	0.055556	0.000000	0.000000	0.000000	0.000000	0.0	0.0	0.000000	0.0	0.000000	0.0555
3	0.000000	0.000000	0.071429	0.071429	0.000000	0.000000	0.0	0.0	0.000000	0.0	0.071429	0.0000
4	0.045455	0.000000	0.000000	0.000000	0.045455	0.045455	0.0	0.0	0.090909	0.0	0.000000	0.0000

Fig. 4 A sample of TF-IDF representation of the first five comments of the dataset

4.3 Feature Extraction

Feature extraction is the process of making the initial set of raw data more manageable while the processed data represents the original data without losing any important information [10]. We made use of a vectorizer, TF-IDF, to convert our textual information into number representations as it is a great way to evaluate the relevancy of a word in a corpus. TF and IDF are measured by the following equations:

$$\mathrm{Tf}_{\mathrm{w,d}} = \frac{\text{Frequency of the word w in the document } d}{\text{sum of all words in the document}} \tag{1}$$

$$\mathrm{IDF}_{\mathrm{w}} = \log \frac{\text{The number of documents}}{\text{The number of documents with word } w} \tag{2}$$

The $\mathrm{TFIDF}_{\mathrm{w,d}}$ score of a word is measured by the following equation,

$$\mathrm{TFIDF}_{\mathrm{w,d}} = \mathrm{TF}_{\mathrm{w,d}} \times \mathrm{IDF}_{\mathrm{w}} \tag{3}$$

TF-IDF Vectorization generates a matrix of features, which is subsequently sent into the ML algorithm for training. A sample of the feature matrix generated from our dataset is given in Fig. 4.

The TF-IDF score is useful for balancing the weight of more common or general terms against less common or specific words. After the TF-IDF vectorization step, the feature matrix is used to train the machine learning.

4.4 Classical Approaches

In this study, we used five classical algorithms for predicting purposes. They are the NB classifier, Ada Boost, DT, SVM, and RF classifier.

Naïve Bayes Classifier The classification of Naive Bayes is a probabilistic statistical classification founded on the Bayes theorem. It presupposes that the effect of one feature in a category is unaffected by the effects of other features.

Naïve Bayes is the simplest supervised technique, and it produces excellent results in real-world scenarios [17]. As this algorithm is fast, accurate, and reliable, it works efficiently on large corpus of text data. The main limitation of Nave Bayes is that it

assumes that all the features are mutually independent, where there is always some degree of relationship between the features.

Decision Tree A decision tree is a supervised classification technique that employs a hierarchical structure that looks like a tree for classification in which a leaf node represents each class and the features are presented as the internal nodes of the tree [14]. In our decision tree, we used Gini impurity and entropy for the purpose of gathering information and determining the split's quality. As the cost of a decision tree is logarithmic, it can work well on large text corpus. But it often generates overfitting issues.

Random Forest Classifier Random forest is a technique for group categorization, which creates a classification group instead of a single classification and then classifies additional points based on classification predictions [8]. The Random forest algorithm can work with large amounts of data with high dimensionality and resolves the overfitting issue that arises in models of decisions.

Support Vector Machine SVM is an algorithm for classification and regression [6] that provides a decision limit which splits data while maximizing the limit. An SVM model shows data as space points and is mapped to distinguish features from the various categories as broadly as possible. In our text dataset, the SVM algorithm produces a model for assigning fresh data to one (positive or negative) category given the set of training input that was designated as one or the other category.

Ada Boost Ada Boost is the algorithm for adaptive stimulation which combines the results of weak learner algorithms. This algorithm is less susceptible to overfitting than noise. Moreover, it just works on statistical functions and reduces the dimension of the data [7].

4.5 Deep Learning Approaches

LSTM LSTM is a specific type of recurrent, long-term dependence-learning neural network. The Recurring Network is an ANN type in which the outcome of a typical artificial neural network that feeds back information is fed back to the neurons as new input based on new input values [12].

A diagram of our LSTM model is depicted in Fig. 5. Our LSTM model takes a sentence as input, including all the words from first to last, and makes a vector representation of the sentence. It then processes the representation vectors to investigate the connection between terms from beginning to end.

CNN CNN is a multi-layered artificial neural network model that feeds back information [1]. The features of the object are extracted from CNN by capturing its spatial features. A fully connected layer, pooling, and convolution are the three layers that make up CNN.

A diagram of our CNN model is depicted in Fig. 6. Our CNN model takes the preprocessed sentences as an input in a vectorized form. With the assistance of different

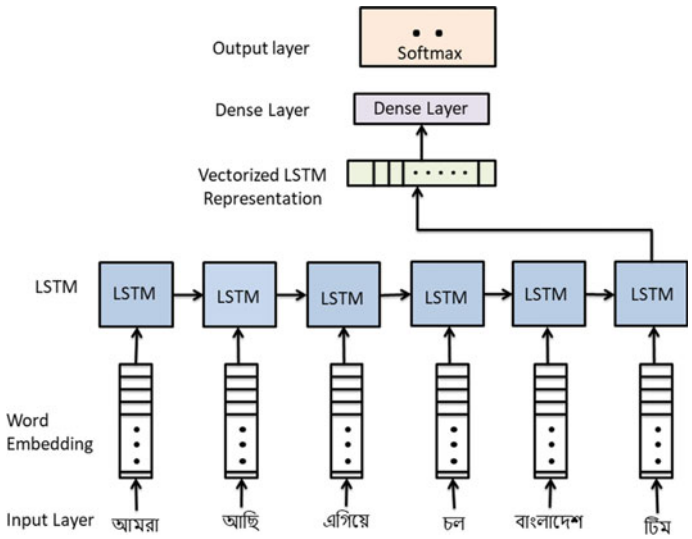

Fig. 5 LSTM model for sentiment analysis

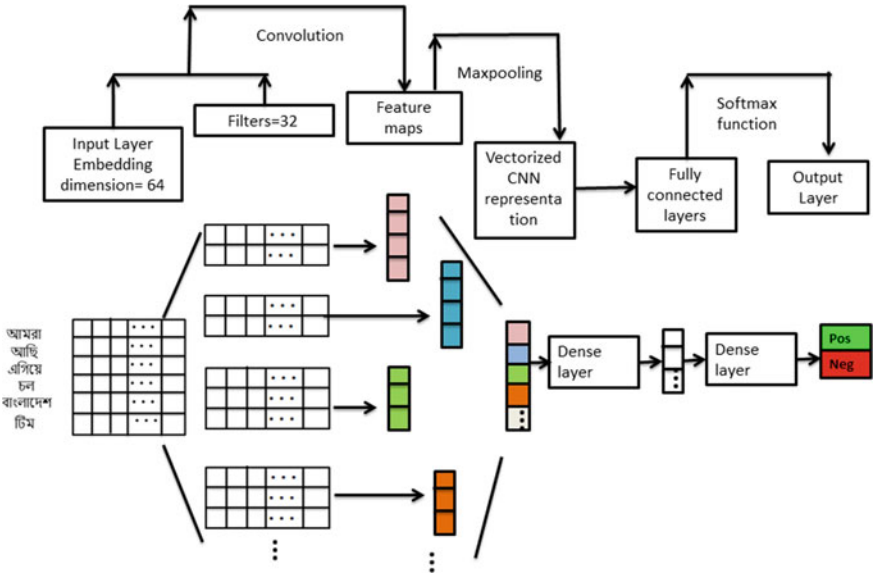

Fig. 6 CNN model for sentiment analysis

filters, the convolution layer extracts features of the input sentences and information about their spatial position. The pooling layer reduces the feature dimension. The convolution neural network's final layer is a traditional fully connected artificial neural network. The new text is fed into CNN as an input.After the training, CNN calculates the predictive class chance.

5 Result Analysis and Comparison

The accuracy of a classifier is not the only criterion used to assess its effectiveness. There are three more useful metrics to consider (precision, recall, and F-measure) [10]. They will give us a lot more details on how well a binary classifier does. Precision is a metric for how accurate a classifier is. Recall is used to calculate the completeness of a classification. Precision may be harmed by improving recall [2]. The F1 score reflects the combination of precision and recall.

As a common evaluation metric, we were aiming for accuracy, recall, F-measure, and overall accuracy. The positive class in our scheme was 1, while the negative class was 0. The equations for the performance metrics are given below, where true negative and true positive are represented respectively as TN and TP and false negative and false positive are represented, respectively, as FN and FP and m stands for entire size of the sample (TP + TN + FP + FN):

$$\text{Precision} = \frac{\text{TP}}{(\text{TP} + \text{FP})}$$

$$\text{Accuracy} = \frac{\text{TP} + \text{TN}}{m}$$

$$\text{Recall} = \frac{TP}{(\text{TP} + \text{FN})}$$

$$F\text{-measure} = \frac{(2 \times \text{Precision} \times \text{Recall})}{(\text{Precision} + \text{Recall})}$$

Table 1 shows that the Adaboost Classifier has the lowest accuracy of 66.29%, while the Deep Learning algorithm LSTM has the highest accuracy of 96.95%. Convolutional neural networks come in second place with an accuracy of 88.22%. We can observe from the table that deep learning algorithms have a better accuracy rate with an average of 92.58% than classical approaches, which have an average accuracy of 73.92%.

Figure 7 shows a comparison of all the classifiers used based on $F1$-score, Recall, Precision. From Fig. 7, we can see that deep learning approaches have showed better performance than the classical approaches. Among the traditional methods, Support Vector Machine and Random forest classifier have achieved maximum accuracy of 78%.

Table 1 Performance ratings of the proposed model

Feature	Recall	Precision	*F*-measure	Accuracy
Naïve Bayes	0.73	0.73	0.73	72.80%
SVM	0.78	0.78	0.78	78.23%
Random forest	0.78	0.78	0.78	78.37%
Decision tree	0.74	0.74	0.74	73.97%
Ada boost	0.66	0.67	0.66	66.29%
LSTM	0.97	0.97	0.97	96.95%
CNN	0.88	0.88	0.88	88.22%

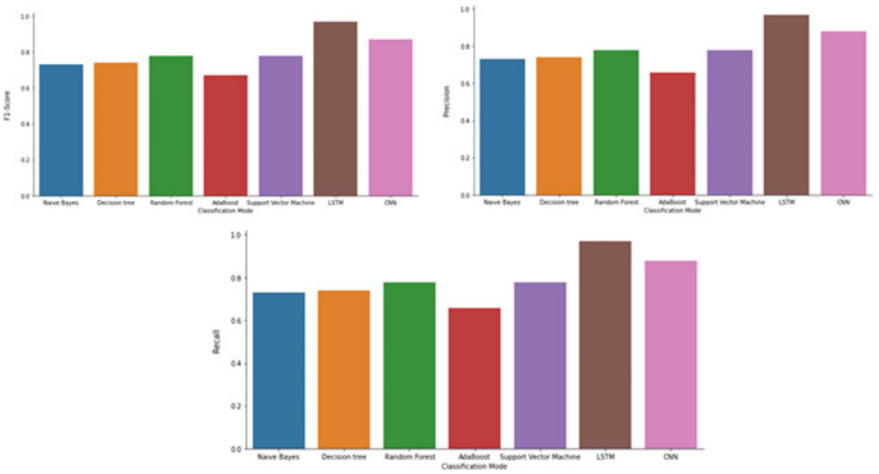

Fig. 7 Visualization of performance metrics

6 Conclusion

We have presented a sentiment categorization method in this paper for textual Bengali data acquired from Facebook. The data is preprocessed after the automatic annotation to remove noise and shrink the function space. To prepare the data for classification, it is stemmed, tokenized, and vectorized.

The system that was developed uses a total of seven classifiers, including five classical classifiers: Naive Bayes, Decision tree, Random forest classifier, AdaBoost, SVM and two Deep Learning classifiers, LSTM and CNN. From the study, we can see that deep learning approaches have a higher accuracy rate than classical approaches. From all the classifiers used in this study, the AdaBoost Classifier has the lowest accuracy of 66.29%. The deep learning classifier LSTM, on the contrary, with a precision of 96.95%, is the most accurate. The study not only predicted the sentiment of Bengali text data as positive or negative, but it also presented a clear comparative analysis between the dataset and several machine learning models.

References

1. Ahammad K, Shawon JAB, Chakraborty P, Islam MJ, Islam S (2021) Recognizing Bengali sign language gestures for digits in real time using convolutional neural network. Int J Comput Sc Inf Secur (IJCSIS) 19(1)
2. Banik N, Rahman MHH (2018) Evaluation of naïve bayes and support vector machines on Bangla textual movie reviews. In: 2018 International conference on Bangla speech and language processing (ICBSLP). IEEE, pp 1–6
3. Boia M, Faltings B, Musat C-C, Pu P (2013) A:) is worth a thousand words: how people attach sentiment to emoticons and words in tweets. In: 2013 International conference on social computing. IEEE, pp 345–350
4. Faruque MA, Rahman S, Chakraborty P, Choudhury T, Um J-S, Singh TP (2021) Ascertaining polarity of public opinions on Bangladesh cricket using machine learning techniques. Spatial Inf Res 1–8
5. Haque F, Manik MMH, Hashem MMA (2019) Opinion mining from Bangla and phonetic Bangla reviews using vectorization methods. In: 2019 4th International conference on electrical information and communication technology (EICT). IEEE, pp 1–6
6. Hossain MF, Islam S, Chakraborty P, Majumder AK (2020) Predicting daily closing prices of selected shares of Dhaka stock exchange (DSE) using support vector machines. Internet Things Cloud Comput 8(4):46
7. Khan M, Malik K (2018) Sentiment classification of customer's reviews about automobiles in roman Urdu. In: Future of information and communication conference. Springer, pp 630–640
8. Makassar BBPSDMPK (2019) Sentiment analysis using random forest algorithm-online social media based
9. Pang B, Lee L, Vaithyanathan S (2002) Thumbs up? sentiment classification using machine learning techniques. In: Proceedings of the 2002 conference on empirical methods in natural language processing (EMNLP 2002). Association for Computational Linguistics, pp 79–86
10. Partha C, Ahmed S, Yousuf MA, Azad A, Alyami SA, Moni MA (2021) A human-robot interaction system calculating visual focus of human's attention level. IEEE Access 9:93409–93421
11. Rahman M, Pramanik M, Sadik R, Roy M, Chakraborty P (2021) Bangla documents classification using transformer based deep learning models. In: Proceedings of the IEEE, pp 1–6
12. Rahman S, Chakraborty P (2021) Bangla document classification using deep recurrent neural network with BiLSTM. In: Proceedings of international conference on machine intelligence and data science applications. Springer, Singapore, pp 507–519
13. Sarker A, Chakraborty P, Sha SMS, Khatun M, Hasan MR, Banerjee K (2020) Improvised technique for analyzing data and detecting terrorist attack using machine learning approach based on twitter data. J Comput Commun 8(7):50–62
14. Timoney J, Raj A, Davis B (2018) Nostalgic sentiment analysis of youtube comments for chart hits of the 20th century
15. Tripathy A, Agrawal A, Rath SK (2015) Classification of sentimental reviews using machine learning techniques. Procedia Comput Sci 57:821–829
16. Tuhin RA, Paul BK, Nawrine F, Akter M, Das AK (2019) An automated system of sentiment analysis from Bangla text using supervised learning techniques. In: 2019 IEEE 4th international conference on computer and communication systems (ICCCS). IEEE, pp 360–364
17. Zhang H, Li D. Naïve bayes text classifier. In: 2007 IEEE international conference on granular computing (GRC 2007). IEEE, pp 708–708

Analysis and Recognition of Emotions from Voice Samples Using Ant Colony Optimization Algorithm

Surjyo Narayana Panigrahi and Hemanta Kumar Palo

Abstract In this work, the authors attempt to an improved speech emotion recognition (SER) using ant colony optimization (ACO) algorithm. Observation shows mostly discussed spectral features consider the entire frequency range hence containing irrelevant information. The desired modeling requires a larger memory, reduces the system response, and decreases the accuracy. Thus, the authors focus only on the spectral roll-off (SR), spectral centroid (SC), and spectral flux (SF), log energy, and formants at a few chosen sub-bands for the intended analysis. The emotional voice samples have been collected from the surrey audio-visual expressive emotion (SAVEE) dataset which is easily accessible and is in the English language. The ACO algorithm is further explored to develop a more discriminative and relevant feature set of the baseline techniques. Finally, the individual optimized feature sets are concatenated to develop suitable identification system models. The K-nearest neighbor (KNN) classifier has been chosen for the proposed investigation due to its simplicity and suitability in the reduced feature domain. Results show the hybridized optimized feature set using the ACO technique has indeed improved the SER accuracy as compared to the baseline feature sets.

Keywords Speech emotion · Recognition · Feature extraction · Ant colony optimization · Classification

1 Introduction

SER deals with the automatic recognition of emotional states in a speech signal and is an active research field during the last few decades. It remains the quickest and natural means to interact among humans and computers. The SER sensors can provide

S. N. Panigrahi
YBN University, Namkum, Ranchi, Jharkhand 834001, India

H. K. Palo (✉)
ITER, Siksha 'O' Anusandhan (Deemed to be University), Bhubaneswar, Odisha 751030, India
e-mail: hemantapalo@soa.ac.in

M. Mishra et al. (eds.), *Innovation in Electrical Power Engineering, Communication, and Computing Technology*, Lecture Notes in Electrical Engineering 814,
https://doi.org/10.1007/978-981-16-7076-3_20

important inputs to the signal processing tools for the identification of the emotional states of a speaker through voice samples qualitatively. The domain has gained more popularity and attention with the advancement of next-gen artificial intelligence, machine learning, and intelligent assistant systems such as Amazon's Alexa, Microsoft's Cortana, and Apple's Siri [1]. Such analysis benefits many vivid application domains such as criminal investigation, psychological findings, bio-medical engineering, online tutoring, robotics, security, banking, and finance. The recognition system uses simulation models to characterize and classify emotional cues from speech samples using computers based on emotionally relevant features.

Among the baseline prosodic features, the energy and pitch predominate since these parameters vary among emotions. For example, a higher pitch and energy have been reported for high arousal emotional states such as anger, surprise, and happiness as compared to boredom and sad states. Similarly, several frame-level features have been successfully employed in this field, but the feature set remains high dimensional. It has resulted in slower system response besides requiring a large storage space hence cannot be easily and economically adaptable. On the contrary, the hybridization of features containing complementary information has improved the SER accuracy, thus remain a common technique in recent years. Nevertheless, the curse of dimensionality persists due to the presence of irrelevant features contributing very little emotional information. It warrants the application of feature selection and optimization algorithms for better accuracy and lower computational complexity [2–10]. In the feature selection algorithm, a subset of the raw feature set is considered. However, reducing the size of the feature vector leads to an uncertain loss of information causing instability in the system performance. The feature optimization aims to transform the original feature space into another domain and concentrate on the discriminant information containing in a specific region of interest, hence remains a better alternative. Several feature optimization algorithms such as principal component analysis, linear discriminant analysis, singular value decomposition, locally linear embedding, and nonnegative matrix factorization, based on feature selection have been successfully applied in the field of SER [7]. Similarly, the application of the genetic algorithm (GA), particle swarm optimization (PSO), ant-colony optimization (ACO), etc., and their variants has provided better SER accuracy than the non-optimized feature sets [6, 11–14]. Among these, the ACO has been chosen for our purpose for the reason explained below. The regulation of direction and speed in PSO remains lower; hence, it suffers from the partial optimization problem. Further, it provides ambiguous results in dealing with both optimization and scattering, hence difficult to handle non-coordinated systems. Similarly, the GA cannot guarantee a universal optimum discovery unconditionally, hence suitable for some specific optimization problems. On the contrary, the ACO is a versatile heuristic-based approach that remains robust in dealing with wide varieties of combinatorial optimization issues. The positive feedback in this algorithm provides a good solution with rapid discovery. It is suitable for dynamic applications and is inherently parallel. Since the speech frequencies occur in parallel, ACO remains a potential candidate for our purpose. However, hardly any researches have been carried out using this algorithm in the field of SER that creates the desired motivation for this work.

The classification algorithm to detect the desired emotions based on the extracted feature sets remains an important organ of the SER system. Literature survey shows the simulation of several efficient classification algorithms such as the decision tree (DT), support vector machine (SVM), random forest (RF), discriminant analyzer, K-nearest neighbor (KNN), naïve Bayes' (NB), Gaussian mixture model, hidden Markov model, probabilistic neural network, etc., in the field of SER [15, 16]. The choice of the classifier is broadly made based on the size of the feature set and complexity. For example, the RF is a complex classifier as it utilizes several DTs, thus remains slow similar to SVM. The classifier can deal with overfitting issues accurately; hence, it can handle large feature sets similar to GMM. The SVM needs the selection of a suitable kernel for efficient operation and is task-dependent. Although the DT is inherently simple, the classifier it is subjected to poor convergence due to fragmentation issues in finding an optimal solution. On the contrary, the KNN is a simple algorithm that requires the adjustment of minimum variables and is faster. It can accurately predict different patterns if the data dimension is small. As this work aims to extract an optimized set of discriminative low-dimensional feature sets based on ACO, KNN suits our purpose, hence chosen for this work.

Results show the ACO technique has indeed improved the SER accuracy by 3.02, 2.83, 2.46, and 1.07% when applied to formants, SC, SF, and SR, respectively, as compared to the baseline feature sets. An improvement in SER accuracy amounting to 4.52% has been experienced using the hybridized optimized feature set as the outcome.

The organization of the paper is as follows. Section 2 provides the background of this work. The proposed methodology has been described in Sect. 3. The simulated results have been discussed in Sect. 4, while Sect. 5 concludes the work.

2 Background

Cepstral analysis extracts feature over the entire frequency spectra. It makes the technique noise-sensitive with a distorted power spectrum. For low noise and distortion, its extraction domain must concentrate at high frequencies or formant reasons where the signal-to-noise ratio is more. Further, the extraction of spectral features at sub-band frequencies makes them less susceptible to the merging of spectrum peaks. In this way, it is possible to prevent the peaks of the spurious spectrum. Hence, the authors attempt to concentrate on features residing only at the sub-bands. The chosen features are the spectral roll-off, spectral centroid, spectral flux, and the formants. In addition to that, the log energy at these sub-bands is extracted and concatenated with the spectral features. However, these features are extracted at utterance-level traditionally; hence, it do not consider the dynamics associated with a signal. To resolve this issue, the extraction of these features is formalized at the frame level before the application of the optimization algorithm. This work has resolved the issue by following the frame-level extraction of the features. A frame size of 30 ms with

10 ms overlapping between frames has been considered using a Hamming window for such purpose.

2.1 Spectral Flux (SF)

The SF indicates the variation in a signal spectrum. It provides information on rapid change in signal power spectrum among frames. The equation for SF is given by

$$S_p = \sum_{f=1}^{N/2} \left(\left| X_p[f] \right| - \left| X_{p-1}[f] \right| \right)^2 \tag{1}$$

where $X_p[f]$ is the magnitude of the normalized spectrum and $p = 1, 2, \ldots, M, M$ denotes the number of frames of an emotional speech signal.

2.2 Spectral Centroid (SC)

The SC is computed based on the filter shape, the number of sub-bands, and the center of the cutoff frequency. It is estimated using the relation

$$C_p = \frac{\sum_{f=1}^{N/2} \left| X_p[n] \right| * f'(f)}{\sum_{f=1}^{N/2} \left| X_p[f] \right|} \tag{2}$$

where $f'(f)$ is the frequency at bin f. The SC signifies the spectral tilt or slope. Within a frame, it denotes the balancing point of the spectral magnitude, hence shows brighter texture or sound sharpness at higher frequencies.

2.3 Spectral Roll-Off (SR)

The SR provides the desired information on the frequency below which a certain percentage of the whole signal energy exists. It gives information on the shape of the signal spectrum. It can compute the number of high-frequency contents in a speech signal. In the calculation of the SR, the chosen percentage is kept in the range of 85–95%. It is estimated using the relation as given below.

$$\sum_{f=1}^{F_t} \left| X_p[f] \right| = 85\% * \sum_{f=1}^{\frac{N}{2}} \left| X_p[f] \right| \tag{3}$$

where F_t denotes the frequency below which 85% of the spectrum $X_p[n]$ of a frame p occurs.

2.4 Formants

The formants differ with age, gender, among speakers, and their affective states. In general, high arousal affecting states have higher formants than the low arousal affecting states. Thus, the formants can provide important inputs of a speaker's emotional state. The voiced emotional speech sequences with the excitation term $u(n)$ and vocal tract impulse response $h(n)$ can be expressed in the time domain as $x(n) = u(n) * h(n)$ and the frequency domain as

$$X(\omega) = U(\omega).H(\omega) \tag{4}$$

The logarithm of the spectrum or the cepstrum is represented as

$$F^{-1}\{\log[X(\omega)]\} = F^{-1}\{\log[U(\omega)]\} + F^{-1}\{\log[H(\omega)]\} \tag{5}$$

The low-frequency components of the cepstrum provide the formants.

2.5 Log Energy

The energy of an emotional signal varies with the arousal level of the affected state [12]. It is higher for high-frequency signals such as anger or happy states. The log energy provides important information on the affected states, as the human ear happens to be logarithmic. It is computed as

$$G_x = \log \sum_{n=-\infty}^{\infty} |x(n)|^2 \tag{6}$$

3 Problem Definition

The speech signal is non-stationary and can be represented adequately within a short duration by extracting the features at the frame level. Within a short frame, the signal can be assumed periodic and involves feature dynamism compared to utterance-level feature extraction. Hence, the authors have extracted the chosen feature sets at the frame level for the intended task. However, the feature dimension becomes large

containing redundant data which has increased the computational complexity and the classification time. To alleviate these issues, the authors have proposed optimizing the feature vectors using ACO. This way, the resultant feature vector contains only relevant emotional information and becomes low dimensional. It has indeed improved the classification time as shown in the result section.

The ACO optimization technique is applied to each feature sets separately to obtain the corresponding optimized feature set. The classifier is simulated with each optimized feature vector individually. Further, all these optimized feature sets are concatenated and fed to the classifier at once to investigate the classification accuracy.

4 The Proposed Methodology

The input emotional speech signal is initially preprocessed to remove any background noise and spectrally flatten the signal. This step includes the pre-emphasis filter, normalization, framing, and windowing sections. The chosen feature extraction techniques such as the SC, SR, SF, log energy, and the formants have been applied to each pre-processed signal individually as shown in Fig. 1.

The ACO suggested by Marco Dorigo is a population-based metaheuristic optimization approach adapted from swarm intelligence [17]. It deals with the social behaviors of swarms comprised of a group of ants without any central control. Although, the ants are considered unintelligent, however, they acquire the desired intelligent behavior by coordination and synchronization. During foraging, these species release a pheromone substance that helps the trailing ants during their journey to form a large group. However, their behavior remains stochastic that drives a few species to divert their path yet to be explored. In case the explored path founds to be shorter, more ants choose that path wherein more pheromone is likely to be deposited in that path after some time. Nevertheless, there is an obvious reduction in the amount

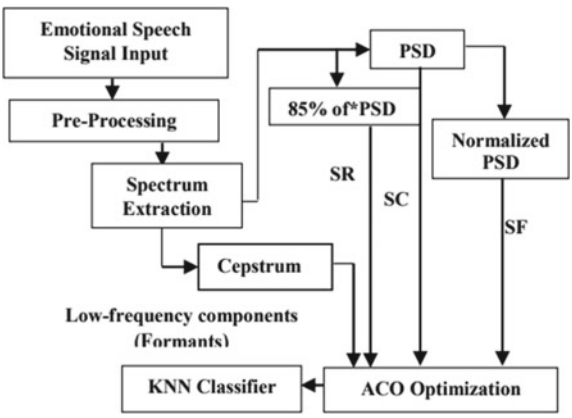

Fig. 1 Proposed methodology

of pheromone on every trail due to evaporation as time elapses. Consequently, the shortest path will have the highest pheromone concentration at a certain stage.

There are four input feature vectors to which the ACO is applied individually. It should be noted that each input vector is extracted at the frame level for adequate analysis of the aperiodic speech signal. This way, it is possible to assume the signal is stationary. It also includes the dynamism associated with the feature extraction technique which is not possible if we consider the utterance-level statistics or extraction. Consider the SR frame-level feature extraction technique. Thus, each input feature vector to the ACO has a size $P \times Q$, where $i = 1, 2, \ldots, P$ is the number of SR features extracted from each frame of the signal and $j = 1, 2, \ldots, Q$ denotes the number of frames of a signal. However, using the optimized ACO algorithm, we intend to reduce the feature dimension to retain only the emotionally relevant information. Thus, the output of the ACO has the SR feature dimension of $1 \times Q$ which is very less as compared to $P \times Q$ before the application of the ACO. The KNN is individually trained using each optimized feature vector corresponding to a chosen spectral feature extraction technique. The authors have aimed to minimize the objective function with an increase in pheromone quantity associated with the P number of ants corresponding to the P number of spectral features per frame of a signal for the optimization of the feature vector. The ACO algorithm has been briefed below.

Let the time elapsed since the beginning of the experiment as t. Considering that A_1 and A_2 number of ants have utilized the first and second bridge, respectively. Then, the $(A_1 + 1)$th ant will select the first bridge with a probability p_1

$$p_{1(A+1)} = \frac{(A_1 + h)^m}{(A_1 + h)^m + (A_2 + h)^m} \tag{7}$$

Here, the h and m denote the variable for developing the model based on the extracted feature sets. Similarly, the probability $p_{2(A+1)}$ indicates the same $(A + 1)$th ant selects the second bridge, where $p_{2(A+1)} = 1 - p_{1(A+1)}$. A value of $h \approx 20$ and $m \approx 2$ has provided a good fit model using Monte Carlo simulations as in [18], hence chosen for this work. The steps of the ACO algorithm are briefed below.

- Let $P, i = 1, 2, , \ldots, P$ is the number of SF features denoted by s^p vector of a frame of a signal associated with P ants.
- When the first cycle begins, the ants randomly search for the best possible feature from the chosen feature vector by creating an old ant colony in the initialization phase.
- The pheromone quantity is updated for the creation of a new ant colony in the solution phase, by considering the best solution from the old ant colony as per the equation given below.

$$s_t^{p(new)} = s_t^{p(old)} \pm \gamma, t = 1, 2, \ldots, I \tag{8}$$

where $s_t^{p(\text{new})}$ and $s_t^{p(\text{old})}$ are the solution vectors corresponding to the ith ant at ith cycle and the previous cycle, respectively. The search direction is expressed as

$$\bar{s}_t^{\text{best}} = s_t^{\text{best}} \pm \left(s_t^{\text{best}} * 0.01\right) \tag{9}$$

where $f\left(\bar{s}_t^{\text{best}}\right) \leq f\left(s_t^{\text{best}}\right)$, the $\pm$ sign indicates the direction of search to achieve the global optimum, and γ provides the length of the jump.

- In the update process, the pheromone quantity (τ_t) is minimized as per the following equations

$$\tau_t = 0.1 * \tau_{t-1} \tag{10}$$

$$\tau_t = \tau_{t-1} + 0.1 * f\left(s_t^{\text{best}}\right) \tag{11}$$

The objective function is minimized with an increase in pheromone quantity to reach an optimized solution. The process continues till the chosen number of cycles I is completed.

The optimized feature sets from the baseline features extracted from the SAVEE dataset are used to simulate the k-NN classifier to determine the SER accuracy. The algorithm recognizes the emotional patterns using a distance function or similarity measure. During the class assignment, the KNN uses the majority vote corresponding to its neighbors based on the distance criteria. The Euclidean distance norm has been used in this work as given by

$$d(x,t) = \sqrt{\sum_{j=1}^{J}\left(x_j - t_j\right)^2} \tag{12}$$

For $K = 1$, the problem is simply confined to the nearest neighbor class. By varying the values of K, the modelling structure varies. A value of $K = 1, 2, 3$, and 4 has been trailed to obtain the desired model. However, with the change of value greater than $K = 3$, not significant variations in the SER accuracy and simulation time have been experienced. Thus, $K = 3$ has been retained in this work.

5 Simulation Results and Discussion

The work chooses the SAVEE dataset to collect the emotional voice samples for classification. The dataset is funded by the University of Peshawar (Pakistan) and CVSSP at the University, Surrey (UK) [19]. Among other accessible datasets, the SAVEE is in the English language, hence is easy to understand. Further, it comprises most of the basic emotions such as anger, disgust, sadness, fearful, happiness, surprise, and

neutral, which help in the investigation. There are sixty emotional voice samples in each of the available states in the dataset, except the neutral state which comprises 120 utterances. The sampling frequency has been 44.1 kHz. However, for our convenience, it has been downsampled to 16 kHz. Among the available emotional states, this work considers six classes for analysis of the SER. These states are happy, sad, anger, fear, disgust, and neutral. The individual feature extraction technique is applied at the frame level to each sample of a chosen class. The extracted feature set of an emotional state comprising of sixty utterances is then concatenated to form a feature vector corresponding to the chosen feature extraction technique. The feature vector is then used to simulate the KNN to determine the SER accuracy.

Tables 1 and 2 compare the average magnitude and variance of the extracted feature sets among the chosen emotional states. The features have the highest average magnitude for anger state among all the chosen states. It indicates, the state has the highest level of arousal and contains more high-frequency components. On the contrary, the sad state has shown the lowest average magnitude irrespective of the feature set chosen as compared to other chosen states. Thus, the sad state is considered to have the lowest arousal level just above the neutral state. For a similar reason, the sad state has shown to have the lowest variance irrespective of the feature sets chosen, while the anger state has shown the highest variance among all the states as shown in Table 2.

The SER accuracy of each chosen emotional class using the extracted baseline feature sets with KNN is shown in Fig. 2.

Table 1 Comparison of average magnitude of the extracted feature sets among the chosen emotions

Emotions	SC	SR	SF	Log-energy
Happy	1.6318	0.0326	1.276	74.570
Sad	0.6569	0.0296	1.2067	67.070
Anger	1.8405	0.0360	1.364	75.525
Fear	1.251	0.0353	1.258	72.674
Disgust	0.8162	0.03328	1.478	68.640
Neutral	0.6707	0.0297	1.014	65.401

Table 2 Comparison of variance of the extracted feature sets among the chosen emotions

Emotions	SC	SR	SF	Log-energy
Happy	0.2825	0.0068	0.3005	109.62
Sad	0.1653	0.0045	0.4271	110.92
Anger	0.4188	0.0013	0.2315	117.80
Fear	0.3718	0.0106	0.2835	124.09
Disgust	0.1931	0.0104	1.0645	88.799
Neutral	0.1803	0.0064	0.4352	72.061

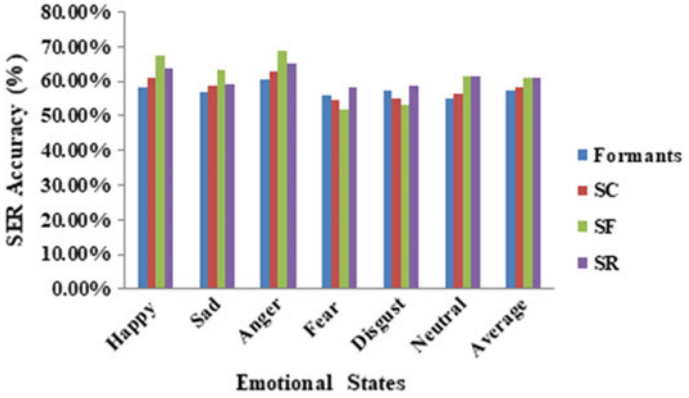

Fig. 2 KNN average accuracy using the baseline feature sets

The accuracy of the anger state has been the highest followed by the happy state, whereas the fear state is least classified as observed from this table. The SER accuracy of the anger state has been 60.35, 62.88, 68.81, and 65.35% with formants, SC, SF, and SR feature sets, respectively. On the contrary, the corresponding accuracy for the fear state has been 55.82%, 54.42%, 51.68%, and 58.27%. Among the baseline feature extraction techniques, the SR has provided the highest average accuracy of 61.17% followed by the SF with 61.03%. The formants have witnessed a lowest average accuracy of 57.25% as observed from the results.

The SER accuracy of each chosen emotional class using the extracted ACO-based feature sets with KNN is shown in Fig. 3. Similar results have been manifested with the optimized feature sets in classifying the emotional states. However, the optimized feature sets have provided better SER accuracy as compared to the baseline feature sets validates our novelty. The average SER accuracy has been 60.27, 60.97, 63.49,

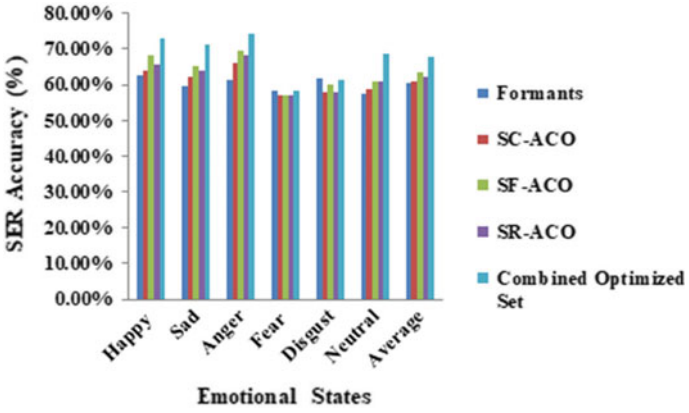

Fig. 3 KNN average accuracy using the optimized feature sets

and 62.24% using the formants-ACO, SC-ACO, SF-ACO, and SR-ACO, respectively, which is better as compared to the baseline feature sets in Fig. 1. Further, the concatenation of the optimized feature sets to form a combined feature matrix has indeed improved the SER accuracy as compared to any of the individual optimized feature sets. The SER accuracy using the combined optimized feature set has been 73.05, 71.43, 74.28, 58.31, 61.18, and 68.68% with the happy, sad, anger, fear, disgust, and neutral states, respectively. Again, in this case, the anger state is better classified followed by the happy state as compared to all other chosen states. The availability of more complementary emotional attributes in the combined optimized feature set is the possible reason for the enhanced accuracy. The average SER accuracy of 67.82% has been manifested using the combined ACO feature set which is better than any of the ACO-based individual optimized feature sets. Another reason for improved SER with the optimized feature set is the feature dimension. The baseline features are of large dimension with redundant information as compared to the optimized feature sets. The use of the ACO algorithm has discarded the irrelevant data, thus providing more discriminating features representing the emotional information. The choice of the KNN classifier which suits well for low-dimensional feature sets has helped in provided an enhanced accuracy with the optimized features as revealed from the simulation work.

Table 3 compares the SER accuracy between the baseline and ACO-based feature sets. The average accuracy has been improved by 3.02, 2.83, 2.46, and 1.07% with formants, SC, SF, and SR, respectively, using the ACO technique as compared to the baseline feature sets. The table shows, the combined optimized feature set has experienced a 4.52% increase in SER accuracy as compared to the baseline feature sets.

The baseline feature vectors are high dimensional, containing redundant data. The use of the ACO optimized algorithm of the proposed model provides emotionally relevant information and the feature vector is low dimensional. It has reduced the computational complexity of the classifier and hence the classification time as shown in Table 4. The optimized technique has resulted in a more reliable and discriminating feature set with an improvement in the speech emotion recognition accuracy observed in Table 3.

Table 3 Comparison of SER between the baseline and the ACO features using KNN

Features	Baseline (%)	Optimized (%)	% Improvement in accuracy
SR	63.23	68.07	1.07
SC	63.15	65.83	2.83
SF	66.21	72.96	2.46
Formants	59.44	61.99	3.02
SR + SC + SF + Formants	65.72	70.24	4.52

Table 4 KNN classification time comparison between the baseline and the proposed optimized feature extraction techniques

Feature extraction technique	Classification time corresponding to the feature vectors				
	SR (s)	SC (s)	SF (s)	Formants	SR + SC + SF + Formants (s)
Baseline	1.63	1.45	1.23	1.86	4.32
Optimized	0.71	0.67	0.55	0.79	2.07

6 Conclusions

This work attempts to develop a novel and effective feature set to analyze a few chosen emotional states from voice samples using the ACO technique. It considers and extracts the baseline features at formant frequency regions, where these features remain less prone to noise and contain more emotionally relevant information. The application of the ACO algorithm helps to map the high-dimensional frame-level feature space into a low-dimensional effective feature space. The optimized and the baseline feature vectors have been compared individually for their efficacy by simulating the KNN classifier. Further, the individually optimized feature vectors are concatenated to develop the desired hybrid feature matrix for better SER accuracy. Other efficient feature selection and optimization may further be explored for such analysis and are kept as our feature perspective.

References

1. Haridas VA, Marimuthu R, Sivakumar VG (2018) A critical review and analysis of techniques of speech recognition: the road ahead. Int J Knowl-Based Intell Eng Syst 22(1):39–57
2. Gomathy M (2021) Optimal feature selection for speech emotion recognition using enhanced cat swarm optimization algorithm. Int J Speech Technol 24(1):155–163
3. Özseven T (2019) A novel feature selection method for speech emotion recognition. Appl Acoust 146:320–326
4. Agarwal G, Om H (2020) Performance of deer hunting optimization based deep learning algorithm for speech emotion recognition. Multimedia Tools Appl 1–32
5. Palo HK, Kumar P, Mohanty MN (2017) Emotional speech recognition using optimized features. IJRECE 5(4):4–9
6. Bandela SR, Kumar TK (2019) Speech emotion recognition using semi-NMF feature optimization. Turk J Electr Eng Comput Sci 27(5):3741–3757
7. Langari S, Marvi H, Zahedi M (2020) Improving of feature selection in speech emotion recognition based-on hybrid evolutionary algorithms. Int J Nonlinear Anal Appl 11(1):81–92
8. Singh A (2020) Speech emotion recognition using enhanced cat swarm optimization algorithm. Int J Inf Technol (IJIT), 6(5) (2020).
9. Shahzadi A, Ahmadyfard A, Harimi A, Yaghmaie K (2015) Speech emotion recognition using nonlinear dynamics features. Turkish J Electr Eng Comp Sci 23
10. Palo HK, Sahoo S, Subudhi AK (2021) Dimensionality reduction techniques: principles, benefits, and limitations. data analytics in bioinformatics: a machine learning perspective. Wiley, pp 77–107

11. Daneshfar F, Kabudian SJ (2020) Speech emotion recognition using discriminative dimension reduction by employing a modified quantum-behaved particle swarm optimization algorithm. Multimedia Tools Appl 79(1):1261–1289
12. Palo HK (2020) The effect of age, gender, and arousal level on categorizing human affective states. In: Emotion and information processing, Springer, Cham, pp 97–124
13. Hong-zhang Y (2013) Feature selection of speech emotional recognition based on ant colony optimization algorithm. Comput Simul 4 (2013)
14. Nayak J, Vakula K, Dinesh P, Naik B, Mishra M (2020) Ant colony optimization in data mining: critical perspective from 2015 to 2020. In: Innovation in electrical power engineering, communication, and computing technology, pp 361–374
15. Paliwal KK (1998) Spectral sub-band centroid features for speech recognition. In: Acoustics, speech and signal processing (ICASSP), vol 2, pp 617–620
16. Palo HK, Behera D, Rout BC () Comparison of classifiers for speech emotion recognition (SER) with discriminative spectral features. In Advances in intelligent computing and communication, Springer, Singapore pp 78–85
17. Dorigo M, Socha K (2006) An introduction to ant colony optimization. In: Handbook of metaheuristic, vol 26, issue 1. IRIDIA, Brussels. ISSN 1781-3794
18. Pasteels JM, Deneubourg J-L, Goss S (1987) Self-organization mechanisms in ant societies (i): Trail recruitment to newly discovered food sources. Experientia Suppl 54:155
19. Palo HK, Mohanty MN (2020) Analysis of speech emotions using dynamics of prosodic parameters. In: Cognitive informatics and soft computing. Springer, Singapore, pp 333–340

Moth Flame Optimized Automatic Generation Control with PIDF Controller for the Integration of Plug-In Electrical Vehicles with Interconnected Power System

B. V. S. Acharyulu, Kumaraswamy Simhadri, B. Seshasai, and B. Mohanty

Abstract The purported values of tie-line power and frequency ought to be perpetuated for steady functioning of power system. The process of maintaining purported values of frequency is the process of automatic generation control (AGC). This paper bestows AGC using the proportional integral derivative (PIDF) controller with filter accomplished by plug-in electric vehicles (PEV). Two areas, area-1 and area-2, comprehended with power generations of hydro, gas and thermal sources each for a two-area six-unit power system. The major contribution of this paper concentrates on comparison of response of AGC with and without inclusion of PEVs. It is observed that the inclusion of PEV reduces the settling time as well as peak over shoot. The inclusion of plug-in electric vehicle to the conventional system improves the time of response of the system, whereas the time taken by the system response is more without PEV. Into the bargain, the system parameters are changed from their purported values to analyze robustness of the system. A new natural inspired optimization called moth-flame optimization (MFO) is used in AGC.

Keywords Moth-flame optimization (MFO) · Automatic generation Control (AGC) · Proportional integral derivative (PIDF) controller · Plug-in electric vehicles (PEV)

1 Introduction

Mainly, tie-line power frequencies are the crucial properties of AGC to maintain the power system in prop state [1]. Thus, to correlate the accumulated real power

B. V. S. Acharyulu (✉) · B. Seshasai
Department of EEE, LIET, Vizianagaram, Andhra Pradesh, India

K. Simhadri
Department of EEE, Aditya Institute of Technology And Management, Tekkali, Andhra Pradesh, India

B. Mohanty
Department of EE, VSSUT, Burla, Odisha, India

M. Mishra et al. (eds.), *Innovation in Electrical Power Engineering, Communication, and Computing Technology*, Lecture Notes in Electrical Engineering 814,
https://doi.org/10.1007/978-981-16-7076-3_21

generation in each and every unit, AGC becomes main portion of each unit while considering load losses. AGC takes expository supervising action with respect to generation under vast interconnected power system. The AGC guarantees that the system stays stable by restoring the mismatch between both the output and load [2].

Furthermore, evolutionary strategies are used to obtain optimal values and to solve AGC problems for various deregulated systems. The evolutionary algorithms such as genetic algorithm (GA) [3], differential evolution algorithm (DE) [4], particle swarm optimization (PSO) [5], bacterial foraging algorithm (BFOA) [6], firefly algorithm (FA) [7], fruit fly optimization algorithm (FOA) [8], moth-flame optimization (MFO) [9] etc., are implied. To resolve AGC issues in multi-source multi-area hydro-thermal power systems, Sahu et al. proposed hFA-PS methodology [10]. The study of an integrated power grid in the deregulated power environment of multi-source electricity generation is taken from [11]. The diversity of electricity generation sources have been stated in standard or traditional power system generation methods [9, 12]. To bring forth frequency response assistance, the load of PEVs might be governed [13].

A PIDF regulator with PEV is brought forward by the stimulation and influence of the above survey of literature for AGC of two-area multi source with PEV, and to improve power system efficiency, MFO is used to adjust the regulator for settling time, overshoot and under shoot.

The substantial relevance of present work is therefore diminished as follows.

- To develop and establish a PIDF regulator.
- To optimize parameters and control via MFO
- To assert the PEV with PIDF controller's superiority over PIDF without PEV Controller
- To research controller robustness in a wide range of variables.

2 System Modeling

Figure 1 indicates the examination of the integrated two or double-area grid. Each field is composed of hydraulic, thermal and gas sources. A single heat turbine is installed in the thermal environment. The system parameters are extracted from [9].

The three separate PIDF controllers are monitored for each region and a total of twenty-four control parameters are optimized simultaneously. An ITAE function is used as a benchmark function to detect a frequency error [14].

$$J = \text{ITAE} = \int_0^t (|\Delta f_1| + \Delta f_2 + |\Delta P_{\text{tie}}|).t\,\mathrm{d}t \tag{1}$$

Here, Δf_1 and Δf_2 are the deviations in frequency from the areas area-1 and area-2, respectively, ΔP_{tie} is the tie-line power and t is the simulation time. Hence, the model problem might be articulated as optimization problem by lowering the above benchmark function which is subjected to.

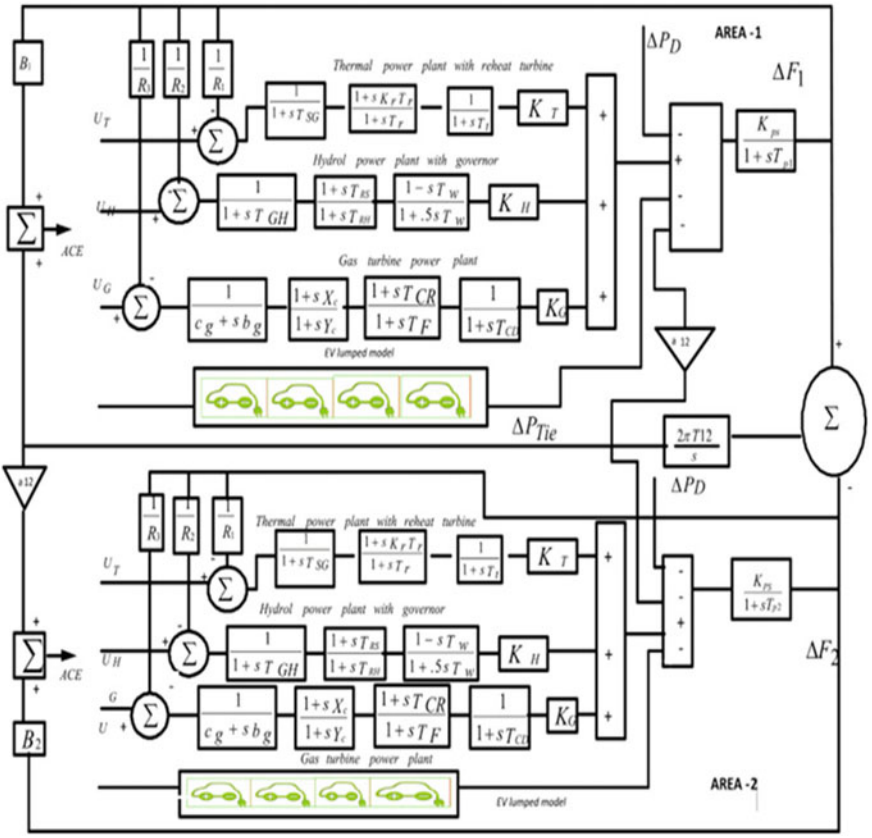

Fig. 1 PEV enabled multi-source two area power system

$K_{p\max} \geq K_p \geq K_{p\min} K_{i\max} \geq K_i \geq K_{i\min}, K_{d\max} \geq K_d \geq K_{d\min}, Z_{\max} \geq Z \geq Z_{\min}$ and where J is the objective function, and optimal and efficient PIDF parameters are measured between -1 and 1 for K_p, K_i, K_d, and the range of filter constant (F) can be taken from 0 to 200.

MFO is used in this paper to refine the PIDF controller parameters, and the MFO algorithm flow chart is shown in [15].

3 Moth-Flame Optimization (MFO)

A person named Seyedali Mirjalili developed this nature-inspired algorithm called moth-flame optimization. The flexure alignment behavior of moths in nature-influenced this algorithm. A moth's mechanism for traveling in a straight path over a long distance is very effective. It can be seen moving in a straight line as well as

spiraling around the lights. Inevitably, the moths fall on the flames. In this paper, the data point is taken as the moth, and the variable quantities are the moth's location in space. The moth is defined by an $m * d$ matrix with m number of moths and a dimension of d represented by N.

$$N = \begin{bmatrix} n_{11} & n_{12} & \cdots & n_{1d} \\ n_{21} & n_{22} & \cdots & n_{2d} \\ \vdots & \vdots & \vdots & \vdots \\ n_{m1} & n_{m2} & \cdots & n_{md} \end{bmatrix} \tag{2}$$

The fitness function is determined by

$$\text{FIT} = \begin{bmatrix} \text{FIT}_1 \\ \text{FIT}_2 \\ \vdots \\ \text{FIT}_m \end{bmatrix} \tag{3}$$

Moths always have their best position due to the release of flag during searching the flame. Moths update their location in relation toward flame according to the following equation,

$$\text{MOFL}_{i_j} = \text{SP}\big(\text{MO}_i, \text{FL}_j\big) \tag{4}$$

Here, MOFL_{i_j} is the updated position of moth, SP is the function called spiral function, MO_i is the ith moth and FL_j is the jth flame. Further, the spiral function is defined as

$$\text{SP}\big(\text{MO}_i, \text{FL}_j\big) = D_{i_j} * e^{at} \cos(2\pi t) + \text{FL}_j \tag{5}$$

where a is called shape constant of spiral movement, t is random variable within $[-1, 1]$, D_{i_j} is the distance from ith moth to jth flame

$$D_{i_j} = \big|\text{MO}_i - \text{FL}_j\big| \tag{6}$$

The updation of flame is done by using the following equation

$$\text{FL} = \text{round - up}\left(\text{FL}_{\max} - I * \frac{\text{FL}_{\max} - 1}{I_{\max}}\right) \tag{7}$$

where $\text{FL}_{\max}$ is the max value of flame, I is present iteration value, $I_{\max}$ is max iteration value.

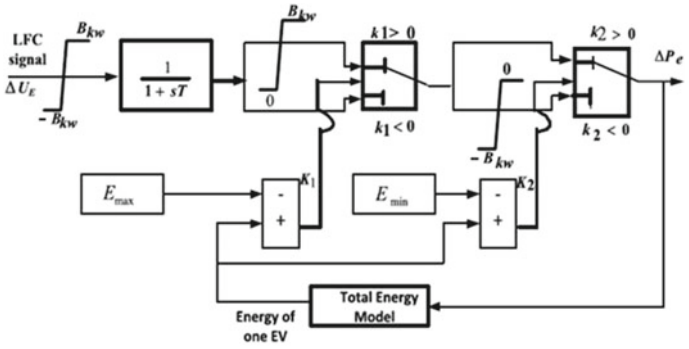

Fig. 2 Model of lumped PEV

4 Modeling of PEV

Because vast quantities of PEVs will be roaming on roads in the coming days, the modeled PEV is addressed in the current analysis. In the existing research, the lumped model of PEV is discussed in Fig. 2 [16]. Here, the input to PEV is ΔU_{E} which is specified as the AGC signal and the output is the discharging/charging power of one PEV. In each local control center, the net amount of energy stored in batteries is evaluated by the stored energy model shown in Fig. 2. Assorted numbers of EVs are controlled by the local control center which serves as imparting medium for EVs and grid.

5 Result and Discussions

MATLAB/SIMULINK software is used to design a two-area system with PEVs as shown in Fig. 1, and the algorithm for moth-flame optimization is written in mfile or script file. A maximum of 100 iterations and 30 number of moths' are taken into consideration for this evaluation. The worthwhile accomplishment of the proposed system is inspected using an MFO tuned PIDF controller or restrainer accompanied by PEV and unaccompanied by PEV. The best points of parameter gains of PIDF with no PEV are $K_{\mathrm{P1}} = -0.0626$, $K_{\mathrm{I1}} = -0.433$, $K_{\mathrm{D1}} = -0.469$, $F_1 = 102.04$, $K_{\mathrm{p2}} = -0.5$, $K_{\mathrm{I2}} = -0.311$, $K_{\mathrm{D2}} = -0.5$, $F_2 = 8.23$, $K_{\mathrm{P3}} = -0.5$, $K_{\mathrm{I3}} = -0.5$, $K_{\mathrm{D3}} = -0.231$, $F_3 = 87.6$, $K_{\mathrm{p4}} = 0.349$, $K_{\mathrm{i4}} = -0.5$, $K_{\mathrm{d4}} = -0.296$, $F_4 = 112.45$, $K_{\mathrm{P5}} = 0.5$, $K_{\mathrm{I5}} = -0.5$, $K_{\mathrm{D5}} = -0.372$, $F_5 = 98.32$, $K_{\mathrm{P6}} = -0.5$, $K_{\mathrm{I6}} = -0.5$, $K_{\mathrm{D6}} = -0.489$, $F_6 = 198.3$, and the optimal parameter gain values of PIDF controller accompanied by PEV are $K_{\mathrm{P1}} = -0.5$, $K_{\mathrm{I1}} = -0.5$, $K_{\mathrm{D1}} = -0.4225$, $F_1 = 98.14$, $K_{\mathrm{p2}} = -0.5$, $K_{\mathrm{I2}} = -0.003$, $K_{\mathrm{D2}} = 0.5$, $F_2 = 58.43$, $K_{\mathrm{P3}} = -0.5$, $K_{\mathrm{I3}} = -0.5$, $K_{\mathrm{D3}} = -0.116$, $F_3 = 17.4$, $K_{\mathrm{p4}} = -0.443$, $K_{\mathrm{i4}} = -0.484$, $K_{\mathrm{d4}} = -0.498$, $F_4 = 152.55$, $K_{\mathrm{P5}} = 0.5$,

$K_{I5} = -0.385$, $K_{D5} = -0.498$, $F_5 = 48.32$, $K_{P6} = -0.2772$, $K_{I6} = -0.06$, $K_{D6} = -0.498$, $F_6 = 98.2$.

The correlated system accomplishment is briefed in Fig. 3a–c. Table 1 shows the fluctuations of frequency at area-1 and 2, and the inter-area power variance of an MFO-optimized PIDF controller accompanied and unaccompanied by PEV. Table 1 showcases that MFO-tuned PIDF controllers with PEV achieve the lowest value of ITAE compared to MFO-tuned PIDF controllers without PEV. Table 1 also reveals

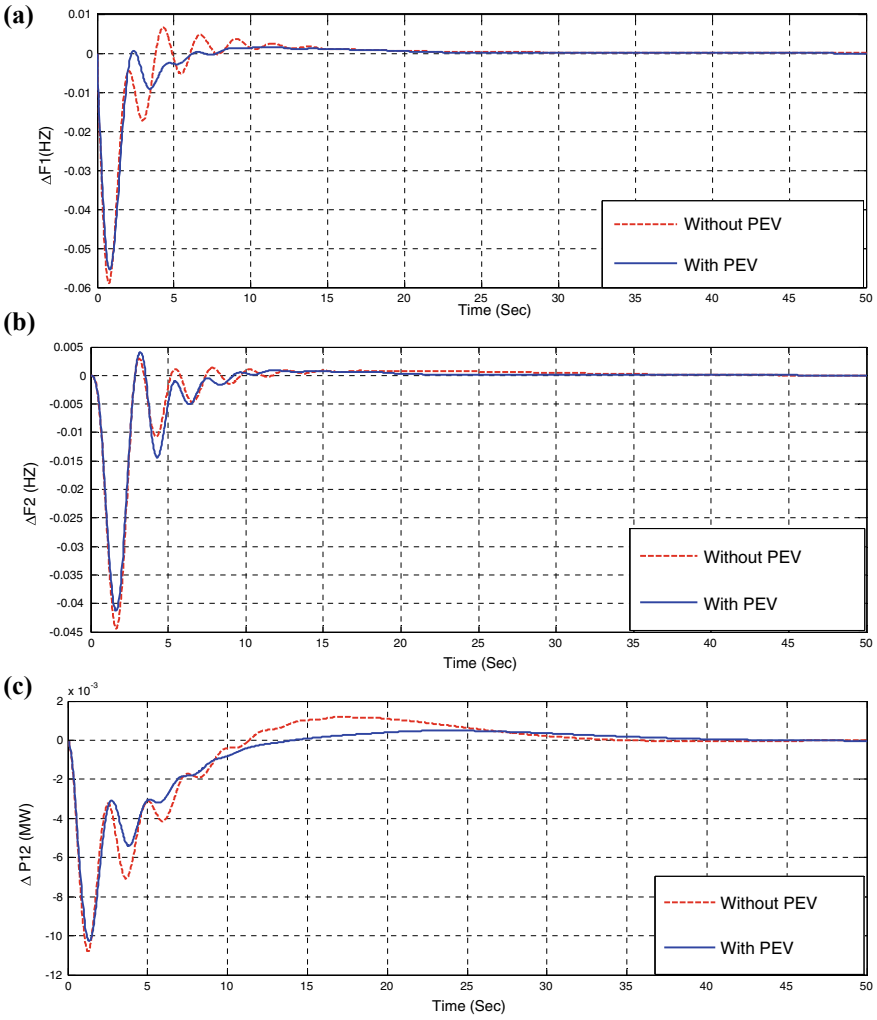

Fig. 3 **a** Area-1 Frequency deviation for two-area power system under 2% SLP. **b** Area-2 Frequency deviation for two-area power system under 2% SLP. **c** Deviation of tie-line power for two-area system under 2% SLP

Table 1 Performance comparison

Performance index	Parameter	Without PEV	With PEV
	ITAE	1.77	1.29
ΔF_1	ST	24.31	23.11
	OS	0.0066	0.0017
	US	0.059	0.055
ΔF_2	ST	31.11	22.31
	OS	0.0037	0.0029
	US	0.0449	0.0442
ΔP_{tie12}	ST	27.81	27.12
	OS	0.0012	0.0004
	US	0.0118	0.0101

that when the PEV is taken into account, the settling time (ST) for ΔF_1, ΔF_2 and ΔP_{tie} is enhanced.

Figure 4a–c depicts the proposed controller's stability review. For the proposed scheme, the variables Tt, TGH, and TCD are varied from +25 to −25%, and the resulting STs and overshoots are furnished in Table 2. The proposed controller's capacity is shown by the frequency variance simulation findings at first area.

6 Conclusion

To reduce frequency fluctuations and increase inter-area power transaction, the proposed PIDF regulator with PEV is checked for two-area multi-source for AGC scheme. To obtain the controller's optimum gains, the suggested modern MFO algorithm has been used. The findings reveal that the PIDF controller accompanied by PEV outperforms the PIDF controller unaccompanied by PEV. The controller's reliability is shown by the structural rigidity. As a result, it is proposed that the PIDF controller was used for a wide range of engineering problems using the PEV.

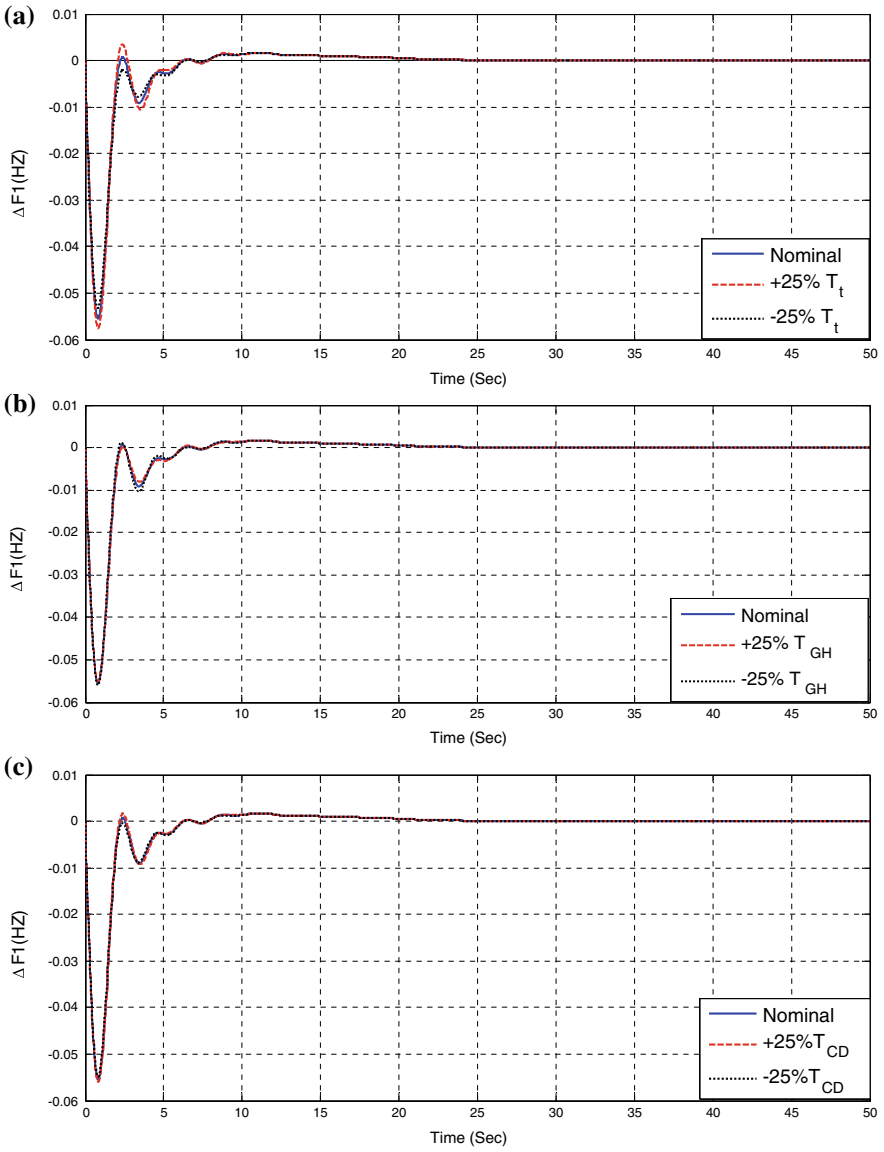

Fig. 4 **a** Deviation of frequency of area-I for SLP of 2% with variation in T_t. **b** Deviation of frequency of area-I for SLP of 2% with variation in T_{GH}. **c** Deviation of frequency of area-I for SLP of 2% in with variation in T_{CD}

Table 2 Sensitive analysis

Parameter variation	% change	ITAE	Settling time		
			ΔF_1	ΔF_2	ΔP_{tie12}
Nominal	0	1.29	23.11	22.31	27.12
T_{t}	−25	1.289	23.31	22.54	27.22
	+25	1.29	23.91	22.32	27.32
T_{GH}	+25	1.29	23.45	22.23	27.23
	−25	1.288	23.71	22.58	27.24
T_{CD}	−25	1.29	23.16	22.11	27.54
	+25	1.291	23.18	22.54	27.34

References

1. Cohn N (1956) Some aspects of tie-line bias control on interconnected power systems. IEEE Trans Power Appar Syst 75:1415–1436
2. Elgerd OI, Fosha CE (1970) Optimum megawatt-frequency control of multi-area electric energy systems. IEEE Trans Power App Syst 89:556–563
3. Demiron A, Zeynelgil HL (2007) GA application to optimization of AGC in three-area power system afterderegulation. Int J Electr Power Energy Syst 29(3):230–240
4. Hota PK, Mohanty B (2016) Automatic generation control of multi-source power generation under deregulated environment. Int J Electr Power Energy Syst 75:205–214
5. Bhatt P, Roy R, Ghoshal SP (2010) Optimized multi area AGC simulation in restructured power systems. Int J Electr Power Energy Syst 32(4):311–322
6. Debbarma S, Saikia LC (2012) Bacterial foraging based FOPID controller in AGC of an interconnected two-areareheat thermal system under deregulated environment. In: Proceedings of international conference on advances engineering, science and management, Nagapattinam, Tamil Nadu, India, pp 303–308
7. Shekhar GTC, Sahu RK, Baliarsingh AK, Panda S (2016) Load frequency control of power system underderegulated environment using optimal firefly algorithm. Int J Electr Power Energy Syst 74:195–211
8. Mohanty B, Hota PK (2015) Comparative performance analysis of fruit fly optimization algorithm for multi-areamulti-source automatic generation control under deregulated environment. IET Gener Transm Distrib 9(14):1845–1855
9. Mohanty B, Acharyulu BVS, Hota PK (2017) Moth-flame optimization algorithm optimized dual-mode controller for multiarea hybrid sources AGC system. Optim Control Appl Meth 1–15
10. Sahu RK, Panda S, Pradhan S (2015) A hybrid firefly algorithm and pattern search technique for automatic generation control of multi area power systems. Int J Electr Power Energy Syst 64:9–23
11. Parmar KPS, Majhi S, Kothari DP (2014) LFC of an interconnected power system with multi-source power generation in deregulated power environment. Electric Power Energy Syst 57:277–286
12. Mohanty B, Panda S, Hota PK (2014) Controller parameters tuning of differential evolution algorithm and its application to load frequency control of multi-source power system. Electric Power Energy Syst 54:77–85
13. Qazi HW, Flynn D, Rather ZH (2016) Impact of electric vehicle load response variation on frequency stability. In: Proceedings of IEEE PES innovative smart grid technologies conference Europe, Ljubljana, Slovenia, 9–12 Oct 2016, 6 pp

14. Acharyulu BVS, Mohanty B, Hota PK (2020) Analysis of moth flame optimization optimized cascade proportional-integral-proportional-derivative controller with filter for automatic generation control system incorporating solar thermal power plant. Optim Control Appl Meth 1–16
15. Acharyulu BVS, Mohanty B, Hota PK (2019) Performance analysis of a cascade controller for conventional and deregulated power systems. Int J Model Simul. https://doi.org/10.1080/02286203.2019.1610690
16. Padhy S et al (2017) A modified GWO technique based cascade PI-PD controller for AGC of power systems in presence of plug in electric vehicles. Eng Sci Tech Int J

Cost and Feasibility Analysis for Designing a PV–Wind Hybrid Renewable Energy System (A Case Study for Campus-3, KIIT University, Bhubaneswar)

Satyabrata Sahoo, Sarat Chandra Swain, Kantipudi V. V. S. R. Chowdary, and Arjyadhara Pradhan

Abstract This paper presents the cost analysis for the design of a hybrid renewable energy system for Kathajodi campus, KIIT University (20° 20′ 56.26″ N 85° 49′ 11.80″ E), Bhubaneswar, India. The proposed system is an approach for designing a reliable, clean, and environment-friendly renewable energy system to deliver the load requirement of the study area. The various energy resources data such as solar irradiance, wind speed, and temperature of the study area are investigated before designing the system. The cost analysis of the system is performed by using HOMER Pro software for various possible configurations by using the available data for energy resources. Moreover, the sensitivity analysis is done for various possible changes in the input parameters for the optimal design of the proposed system. The objective of this analysis is to design a hybrid renewable energy system with minimum net present cost and minimum cost of energy (COE) by considering the various constraints for the design of the system.

Keywords PV · Wind · HOMER · Optimization · Net Present Cost (NPC) · Cost of Energy (COE)

1 Introduction

Nowadays, in order to meet the increase in power demands and to reduce greenhouse gas emissions, renewable energy-based systems are used. Among all other renewable

S. Sahoo (✉) · S. C. Swain · K. V. V. S. R. Chowdary · A. Pradhan
Kalinga Institute of Industrial Technology, Bhubaneswar 751024, India

S. C. Swain
e-mail: scswainfel@kiit.ac.in

K. V. V. S. R. Chowdary
e-mail: rchowdaryfel@kiit.ac.in

A. Pradhan
e-mail: arjyadhara.pradhanfel@kiit.ac.in

M. Mishra et al. (eds.), *Innovation in Electrical Power Engineering, Communication, and Computing Technology*, Lecture Notes in Electrical Engineering 814,
https://doi.org/10.1007/978-981-16-7076-3_22

energy systems, solar and wind energy systems are mostly used nowadays [1–3]. A hybrid power plant consisting of solar energy, wind energy, battery, diesel generator, and converter can be designed with or without a grid to meet the electrical load demand of a particular area [4]. But due to the discontinuous nature of solar radiation and wind speed, the renewable energy system must be connected to the energy storage devices such as batteries, fuel cells, or hydrogen energy storage devices. On the other hand, the renewable energy system can also be connected to a diesel generator or to the grid to ensure continuity in the power supply. These additional components to ensure the continuity in power supply increase the cost of the system. Hence, the cost of various configurations of the power plants must be analyzed before the actual design [5].

But the challenges lie in the cost-effective design of a hybrid innovative renewable energy system. Also, the technical, economic, and environmental effect analysis must be done before the actual design [6]. Homer software facilitates the optimal design of the various configurations of a power plant in terms of net present cost (NPC), cost of energy (COE), initial cost, operating and maintenance cost, fuel cost, etc. considering the various constraints. Sensitivity analysis can be done of various configurations [7]. According to the optimization results of HOMER software, we can select a power plant model for delivering a particular load. HOMER checks the feasibility of a particular configuration and its life cycle cost.

2 System Description

The proposed hybrid renewable energy system is designed for the Kathajodi campus of KIIT University, Odisha. The various energy resource data such as solar irradiance, wind speed, and temperature of the study area are taken from NREL (National Renewable Energy Laboratory) and NASA (National Aeronautics and Space Administration) as input for designing the system. The proposed standalone renewable energy system is designed by using PV, wind turbine, storage, converter, diesel generator, and load components available in the HOMER Pro software. The PV panel, wind turbine, and battery act as the primary components to provide power to the study area. Diesel generator acts as standby for very bad weather conditions. The converter is connected between the DC and AC bus for AC–DC/DC–AC power conversion. The system architecture is shown in Fig. 1.

2.1 Energy Resources of the Location

The solar energy and wind energy production at a particular location depends on the average solar irradiance, wind speed, and temperature of the particular location.

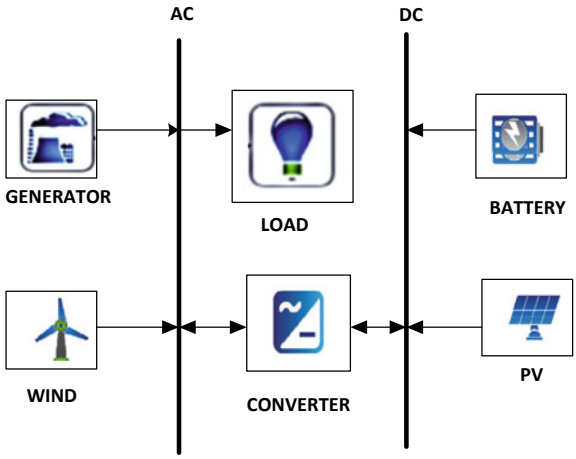

Fig. 1 Architecture of the proposed model

Hence, the various energy resources data of the site must be analyzed before designing the system [8, 9].

(A) Solar Irradiance

The monthly average solar irradiance of the study area for one year has been shown in Fig. 2. The figure below shows that the solar irradiance is maximum (6.066 kWh/m^2/day) on the month of April and minimum (4.09 kWh/m^2/day) on the month of December and has an average value of 4.81 kWh/m^2/day throughout the year.

(B) Wind Speed

The monthly average wind speed of the study area is shown in Fig. 3. The wind speed is maximum (6.370 m/s) on the month of June and minimum (3.160 m/s) on the month of December and has an average value of 4.79 m/s throughout the year.

(C) Temperature

The monthly average temperature of the location for one year is shown in Fig. 4. The temperature of the study area is maximum (38 °C) in the month of June and minimum (20 °C) in the month of December and has an average value of 29 °C.

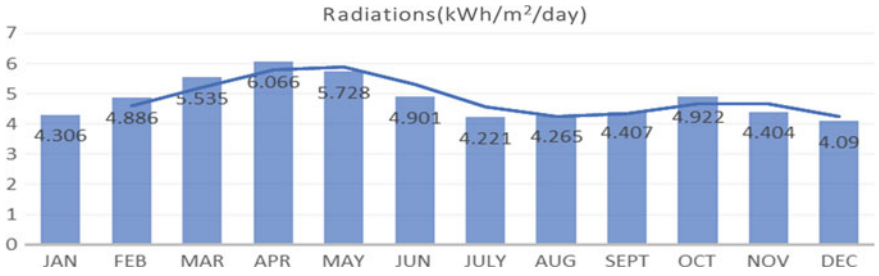

Fig. 2 Average solar irradiance of each month

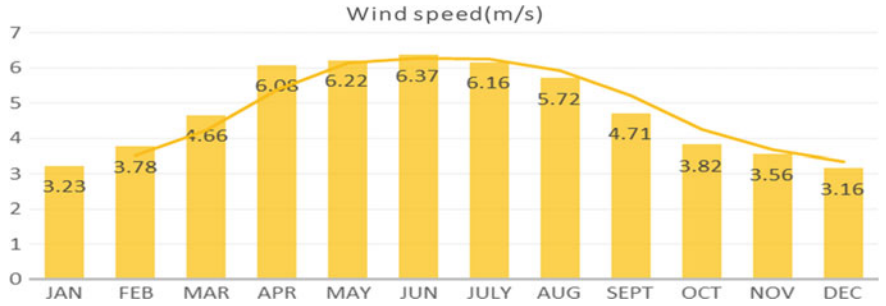

Fig. 3 Average wind speed of each month

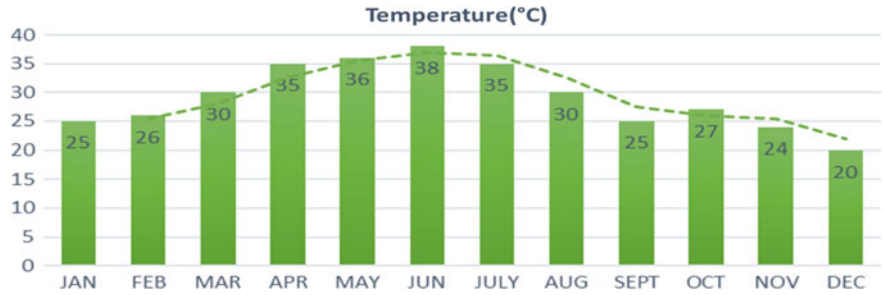

Fig. 4 Average temperature of each month

2.2 Load Profile

The various departments that are present in campus-3 of KIIT University are the School of Electrical Engineering, School of Civil engineering, School of Humanities, Chemistry block, and a Sports and Gymnasium center. The major loads that are connected are tube lights, ceiling fans, exhaust fans, air conditioner, LED floodlights, Lab machinery, and experimental setup of different schools. The load demand is very high from 9.00 am to 6.00 pm as compared to morning and night hours as all the schools are closed by 6.00 pm. The power consumption of various labs and classrooms are enlisted in Table 1, and the daily and monthly load profile of the whole campus has been shown in Figs. 5 and 6, respectively [9]. In Fig. 6, if we observe, the load profile, the peak load is less than 200 kW, and the average load is 150–160 kW from the month of August to December. The peak load is less than 300 kW from the month of January to July and the average load is less than 200 kW. So, this load variation is due to the air-conditioned classrooms, labs, offices, and faculty chambers.

Table 1 Load demand

S. No	Different labs and class rooms	Maximum load demand (KW)	S. No	Different labs and class rooms	Maximum load demand (KW)
1	Electrical drives lab	17.1	12	Simulation lab	2.5
2	Electrical science lab	11.9	13	Project lab	2
3	Electrical machine lab	116	14	Geotechnical engineering lab	10
4	Power system lab	4.5	15	Computational lab	2.5
5	Power electronics lab	2	16	Hydraulic water resource lab	25
6	Electrical measurement lab	1	17	Structural engineering lab	26.2
7	Control system lab	1.4	18	Concrete and material testing lab	10
8	Energy system lab	4	19	Light, Fan and AC	150
9	Microprocessor lab	1	20	Chemistry lab	1
10	Plc lab	2.25	21	Sports and gymnasium centre	1
11	Faculty chamber	2 kW	22	Others	10
			Total demand		**403.35**

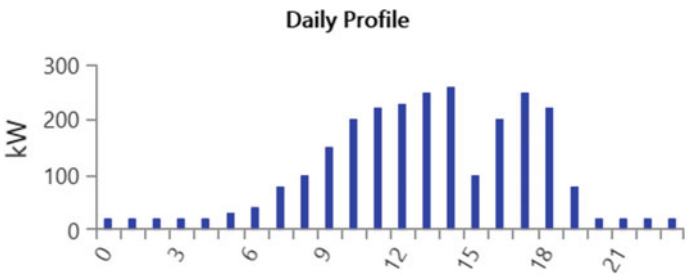

Fig. 5 Daily load profile

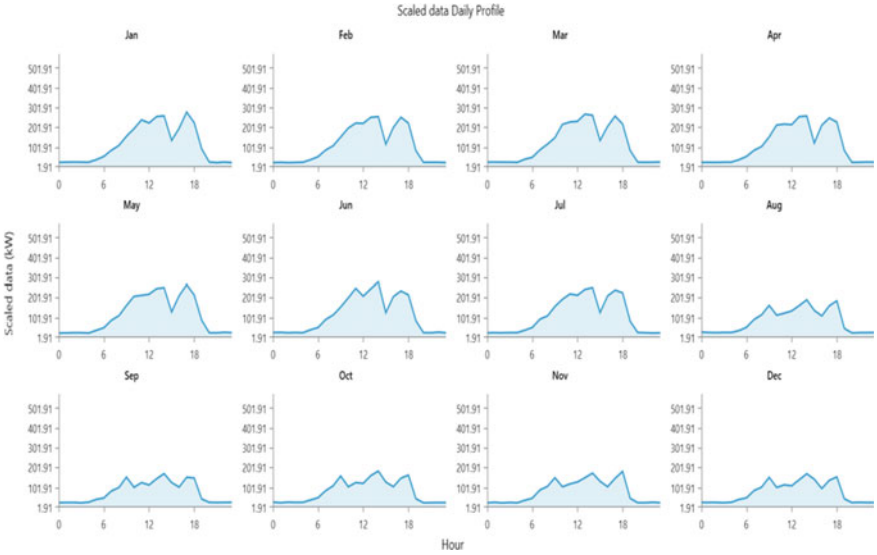

Fig. 6 Monthly load profile

2.3 Components of Hybrid Renewable Energy System

The various components that are available in HOMER for designing a microgrid or power plant are PV, wind turbine, generator, energy storage, converter, boiler, hydro generator, hydrogen tank, grid, electrolyzer, thermal load controller, etc. The different types and sizes of the components can be selected according to the requirement of the design [10–12].

(A) PV Panel

A generic flat plate solar PV panel of 1 kW is considered for the proposed system. HOMER optimizer optimizes the best size and the number of PV panels required for the proposed system based on the load demand. The capital investment of the solar PV panel is ₹30,000 for 1 kW, the cost of replacement is ₹27,000, and operation and maintenance charges are ₹100 per year. The solar PV module has a lifetime of 25 years and has a derating factor of 85%.

(B) Wind Turbine

A 10-kW wind turbine (Bergey Excel 10-R) is selected for this application manufactured by Bergey Wind Power. The capital investment for a 10-kW wind turbine is approximately ₹250,000, the cost of replacement is ₹230,000, and operation and maintenance charges are ₹100 per year. The wind turbine has a lifetime of 20 years, and the optimum height of operation is considered as 30 m. HOMER optimizer optimizes the most suitable size and cost of the wind turbine.

(C) Diesel Generator
A 320-kW diesel generator (CAT-400 kVA-50 Hz-pp) is selected for this application. The capital investment of the DG set is approximately to be ₹150,000, the cost of replacement is ₹145,000, operation and maintenance charges are ₹3000 per hour, and the fuel price is ₹70 per liter.

(D) Battery Energy Storage
A 10-kWh battery manufactured by Power Safe SBS XC is selected for this application. The initial cost of the battery is approximately ₹20,000, the cost of replacement is ₹16,000, and operation and maintenance charges are ₹100 per year. HOMER optimizer selects the required size and number of batteries required for different configurations.

(E) Converter
A 250-kW converter (Dyno Power MPS 250) has been selected for this application. The initial capital investment for 1 kW is ₹6,000, the cost of replacement is ₹5000, and operation and maintenance charges are ₹10 per year. The converter has a lifetime of 15 years and an efficiency of 96%. The converter size is selected based on the peak load demand.

3 Homer Pro Software

HOMER Pro developed by National Renewable Energy Laboratory (NREL) can be used for the optimal design of both standalone and grid-connected microgrids. The different configurations of microgrids and power plants can be designed by using the different components available in HOMER [13]. HOMER simulates all the possible combinations of components considering the sensitivity variables. The minimum net present cost with the best feasible configuration is the optimization problem in HOMER software. HOMER uses Graham's algorithm to solve the optimization problems [14]. The equations for the calculation of net present cost are given below.

$$C_{\text{NPC}} = \frac{C_{\text{annual, total}}}{\text{CRF}(K, \text{project})} \tag{1}$$

where $C_{\text{annual, total}}$ is the total annual cost, R_{project} is the project lifetime, K is the annual interest rate. The capital recovery factor can be calculated by the following equation,

$$\text{CRF}(K, N) = \frac{k(1+k)^N}{k(1+k)^N - 1} \tag{2}$$

where N is the number of years.

Levelized cost of energy (COE) is calculated by using the below given equation.

$$\text{Levelized OE} = \frac{C_{\text{annual, total}}}{E_{\text{load}}} \tag{3}$$

where E_{load} is the total load connected to the system.

4 Results and Discussion

The hybrid renewable energy system is simulated in HOMER Pro software to meet the required load demand. The various sensitivity parameters that have been considered for simulation are lifetime of battery (7 years, 6 years), PV panel derating factor (80, 90%), wind turbine height (30, 20 m), minimum load ratio of diesel generator (25, 30%). The sensitivity analysis result has been shown in Table 2. If we observe, first and second row results in Table 2, the hub height of the wind turbine is varied from 25 to 30 m; hence, the NPC is reduced from ₹40.7 M to ₹40.20 and the COE is reduced from ₹3.76 to ₹3.71.

The optimal configuration of the system considering all the sensitivity parameters has a net present cost (NPC) of ₹40.7 million, operating cost of ₹588,418 per year and cost of energy (COE) ₹3.76/kWh. The configuration consists of generic flat plate PV panels of 515 kW, Bergery Excel-10 wind turbine of 384 kW, Energy Power Safe SBS XC 780 battery-194 string, Dynapower MPS-250 converter of 355 kW. The detailed cost analysis of the optimal configuration has been shown in Fig. 7. In Fig. 7, we can observe that PV panel cost is higher than the wind turbine, battery, and converter cost. Maximum power generation is from solar energy than wind energy. The best four optimization results having different configurations with an ascending order of NPC have been shown in Table 3. In Table 3, we can observe that the NPC and COE are minimum with the combination of both solar and wind energy resources. Now, if we add a diesel generator to this existing system for increasing the reliability, then NPC and COE are increased significantly. PV power generation, wind turbine power generation, battery charging and discharging characteristics, w.r.t total electrical load

Table 2 Sensitivity analysis result

BAT	DG	PV	Wind	PV (kW)	Wind (kW)	Bat (kW)	Converter (kW)	NPC (M)	COE/kWh
6	25	80	25	514.96	34	194	354.85	₹40.7	₹3.76
6	25	80	30	521.63	33	173	421.160	₹40.20	₹3.71
7	25	80	25	514.96	34	194	354.85	₹39.7	₹3.67
7	25	80	30	521.63	33	173	421.16	₹39.3	₹3.64
6	25	90	25	534.53	30	159	366.82	₹38.7	₹3.58
6	25	90	30	479.40	32	169	388.91	₹37.9	₹3.50
7	25	90	25	534.54	30	159	366.82	₹37.9	₹3.50
7	30	90	30	505.64	30	156	456.51	₹37.4	₹3.46

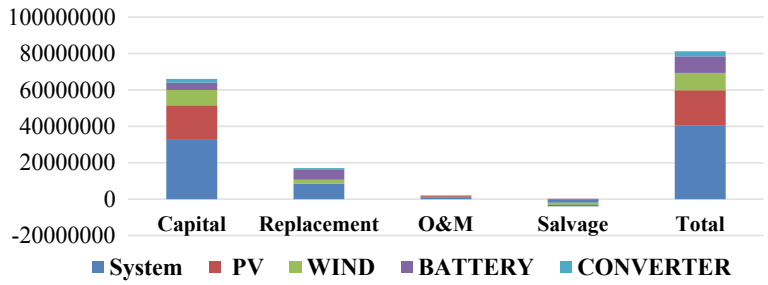

Fig. 7 Detailed cost analysis of the optimal configuration

Table 3 The best four optimization results having different configurations

PV (kW)	Wind (kW)	DG (kW)	Bat (kW)	Converter (kW)	NPC (₹) (M)	COE/kWh (₹)	Operating cost (₹)	Initial cost (₹) (M)
514.96	34	×	194	354.85	40.7	3.76	588,419	33.1
860.124	×	×	273	453.68	48.6	4.54	727,261	39.2
×	250	×	329	390.078	60.5	5.69	1.09 M	46.4
600.47	35	320	355	541.82	61.1	5.34	1.46 M	42.2

served on each day for one week in the month of July has been shown in Fig. 8. In Fig. 8, we can clearly observe that the battery goes to charging mode when PV and wind power generation is high and goes to discharging mode when PV and wind power generation is low. Total electrical energy production of each month for one year has been shown in Fig. 9. In Fig. 9, we can clearly observe that the total renewable power generation is high from the month of March to August. In the other months,

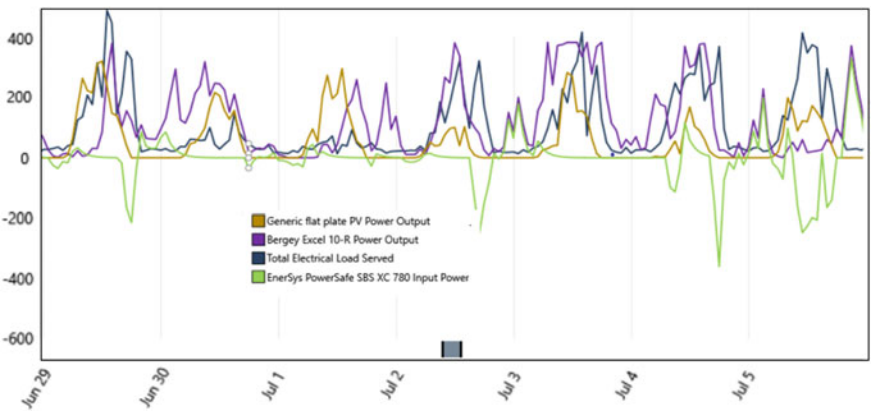

Fig. 8 Total power generation by PV, wind and battery w.r.t load

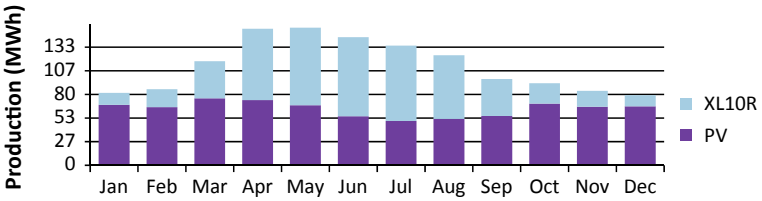

Fig. 9 Total Renewable energy generation

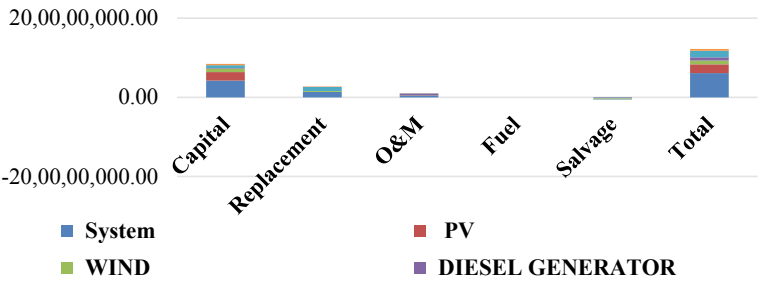

Fig. 10 Cost analysis of the configuration with diesel generator

solar power generation is more as compared to wind power generation. The most reliable configuration consisting of PV, wind, battery, converter, and diesel generator has a net present cost of ₹61.1 million. The optimal cost analysis of the configuration with diesel generator has been shown in Fig. 10.

5 Conclusion

A hybrid standalone renewable energy system consists of PV, wind, battery, converter, and diesel generator has been proposed in this paper. With the help of HOMER Pro version 3.14.2, simulation is done for all the possible combinations of components and the simulation results are arranged in the ascending order of net present cost. Solar irradiance and wind speed data have been taken for the study area, KIIT University, Bhubaneswar. The optimal configuration of the system has a net present cost of ₹40.7 million, operating cost of ₹588,418 and cost of energy ₹3.76/kWh. The optimal configuration consists of PV, wind, battery, and converter without a diesel generator. But if we want to design a more reliable system which consists of PV, wind, battery, converter, and a diesel generator, then the net present cost, operating cost, and the cost of energy will be ₹61.1 million, ₹1.46 million and ₹5.34/kWh, respectively. Hence, the cost and feasibility analysis of the proposed model has been analyzed successfully by using HOMER Pro software, and the same analysis can be done for any location around the world.

References

1. Elmaadawy K, Kotb KM, Elkadeem MR, Sharshir SW, Dán A, Moawad A, Liu B (2020) Optimal sizing and techno-enviro-economic feasibility assessment of large-scale reverse osmosis desalination powered with hybrid renewable energy sources, Energy Convers Manage 224:113377. ISSN 0196-8904
2. Mishra M, Dash PB, Nayak J, Naik B, Swain SK (2020) Deep learning and wavelet transform integrated approach for short-term solar PV power prediction. Measurement 166:108250
3. Swain MK, Mishra M, Bansal RC, Hasan S (2021) A self-powered solar panel automated cleaning system: design and testing analysis. In: Electric power components and systems, pp 1–13
4. Kellogg WD, Nehrir MH, Venkataramanan G, Gerez V (1998) Generation unit sizing and cost analysis for stand-alone wind, photovoltaic, and hybrid wind/PV systems. IEEE Trans Energy Convers 13(1):70–75
5. Srivastava R, Giri VK (2016) Optimization of hybrid renewable resources using HOMER. Int J Renew Energy Res (IJRER) 6(1):157–163
6. Sharma A, Singh A, Khemariya M (2013) Homer optimization based solar PV; wind energy and diesel generator based hybrid system. Int J Soft Comput Eng (IJSCE) 3(1). ISSN 2231-2307
7. Asrari A, Ghasemi A, Javidi MH (2012) Economic evaluation of hybrid renewable energy systems for rural electrification in Iran—A case study. Renew Sustain Energy Rev 16(5): 3123–3130. ISSN 1364-0321
8. Vendoti S, Muralidhar M, Kiranmayi R (2018) HOMER based optimization of solar-wind-diesel hybrid system for electrification in a rural village. In: 2018 International conference on computer communication and informatics (ICCCI), Coimbatore, India, pp 1–6
9. Balachander K, Suresh Kumaar G, Mathankumar M, Manjunathan A, Chinnapparaj S (2020) Optimization in design of hybrid electric power network using HOMER. Mater Today: Proc. ISSN 2214-7853
10. Khalil L, Liaquat Bhatti K, Arslan Iqbal Awan M, Riaz M, Khalil K, Alwaz N (2020) Optimization and designing of hybrid power system using HOMER pro. Mater Today: Proc. ISSN 2214-7853
11. Mishra S, Panigrahi C, Kothari DP (2014) Design and simulation of a solar–wind–biogas hybrid system architecture using HOMER in India. Int J Ambient Energy 37:1–8. https://doi.org/10.1080/01430750.2014.915886
12. Singh A, Baredar P, Gupta B (2015) Computational simulation & optimization of a solar, fuel cell and biomass hybrid energy system using HOMER Pro software. Procedia Eng 127:743–750
13. Dash RL, Behera L, Mohanty B Hota K (2018) Cost and sensitivity analysis of a microgrid using HOMER-Pro software in both grid connected and standalone mode. In: 2018 International conference on recent innovations in electrical, electronics & communication engineering (ICRIEECE), Bhubaneswar, India, pp 3444–3449
14. Sandeep G, Vakula VS (2016) Optimal combination and sizing of a standalone hybrid power system using HOMER. In: 2016 international conference on electrical, electronics, and optimization techniques (ICEEOT), Chennai, India, pp 4141–4144

Design of Optimal Multi-band PSS for Variable Solar-Penetrated Power System

Samarjeet Satapathy, Arjit Gourav Patel, Bighnesh Samal, Narayan Nahak, and Pravati Nayak

Abstract Power system stabilizer (PSS) has been traditionally used to damp low-frequency oscillation (LFO). But multi-band PSS (MBPSS) provides damping of local, inter-plant, and inter-area oscillations. Again, pertaining to random SPV penetration, LFO damping is going to be a challenging task. In this work, optimal MBPSS is proposed to damp LFO, subject to random variation in SPV penetration, where the parameters of MBPSS are tuned by modified DE (MDE) technique. Time and frequency analysis has been performed with step and random change in SPV output, and oscillations are investigated with only PSS and MBPSS optimized by DE and MDE algorithm. Time domain simulation for 200 s has been performed with detail Eigen analysis. It has been found that damping capability of PSS is much enhanced with MBPSS and effective tuning of MBPSS parameters by MDE, enhances damping efficacy of PSS. To verify effectiveness of proposed control action, multi-machine system with varying SPV penetrations has been considered in this work.

Keywords PSS · MBPSS · Low frequency oscillations · SPV · Modified DE

1 Introduction

The LFO is becoming more challenge for system operators, particularly with increased renewable penetration and interconnection of different power systems [1]. LFO is classified as local, inter-plant, inter-area oscillation [2, 3]. Local oscillations exist between generators with remaining power system. These are generally 0.8 Hz to 4 Hz. Inter-plant oscillations occur between two generators which are electrically closed, and this is generally between 1 and 2 Hz. Inter-area oscillations occur between two different groups of generators which are in different areas and lies between 0.2 Hz

S. Satapathy · A. G. Patel · B. Samal · N. Nahak (✉) · P. Nayak
Department of Electrical Engineering, Siksha 'O' Anusandhan Deemed to be University, Bhubaneswar, Odisha 751030, India
e-mail: narayannahak@soa.ac.in

P. Nayak
e-mail: Pravatinayak@soa.ac.in

M. Mishra et al. (eds.), *Innovation in Electrical Power Engineering, Communication, and Computing Technology*, Lecture Notes in Electrical Engineering 814,
https://doi.org/10.1007/978-981-16-7076-3_23

and 0.8 Hz. These oscillations if not damped adequately in early stage, then may lead finally to lose of synchronism [4, 5]. PSS has been used traditionally to damp LFO and recent research in [6] proposed a new coordinated PSS and governor action. PSS provides a stabilizing signal in excitation system of generator for compensating phase lag that result from voltage regulator, exciter, and synchronous generator. So due to this, overall damping of oscillation has been improved. Many researches have been performed for oscillation damping using FACTS devices and co-ordination of PSS with FACTS devices [7–11]. Tuning of FACTS with PSS is costly and has complicated control structure. SPV being an important renewable source and its integration with conventional power generation is in the path progress [12]. When SPV output varies randomly, LFO is being instigated much with increased solar penetration [13]. Conventional PSS (CPSS) is modified as MBPSS in [14] where three pairs of different lead-lag compensators are employed in the place of one lead-lag compensator to handle the three oscillations through three frequency bands. So, in this work, random variation in SPV has been performed with application of proposed MBPSS controller. Another important issue is optimally setting of PSS parameter for this modern optimization can be implemented. DE is the most powerful optimization technique applied by many researchers, for different optimizing problems. Mostly, conventional DE depends on mutation strategies and control parameters like F, CR, G, and NP. To select the particular parameters and strategies for the objective function is a very big task. So, to eliminate this demerit of DE, MDE has been reported in [15]. In MDE, to select appropriate F and CR value in the time of program run has been improved.

2 Generator Modelling

The small perturbation generator model presented in Fig. 1.has k-constants calculated at initial operating condition $P_0 = 0.8$ pu and $Q_0 = 0.17$ pu.

$$\Delta\omega = \frac{1}{2Hs + K_{\mathrm{D}}}(\Delta T_{\mathrm{M}} - \Delta T_e) \tag{1}$$

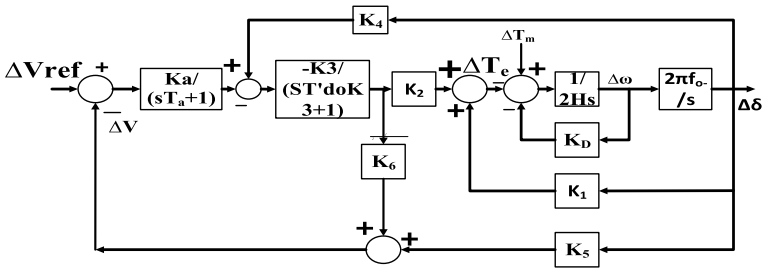

Fig. 1 Generator model

$$\Delta\delta = \frac{2\Pi f_0}{s}\Delta\omega \tag{2}$$

$$T_e \approx P_e = i_d u_d + i_q u_q \tag{3}$$

$$\Delta T_e = K_1\Delta\delta + K_2\Delta e'_q \tag{4}$$

$$\Delta V_t = k_5\Delta\delta + k_6\Delta e'_q \tag{5}$$

The K constants of third-order generator model are given by:

$K_1 = \frac{\Delta T_e}{\Delta\delta}\Big|_{e'_q}$ Ratio of deviation in torque and deviation in rotor angle at constant d axis flux linkages.

$K_2 = \frac{\Delta T_e}{\Delta e'_q}\Big|_{\delta}$ Ratio of deviation in torque and deviation in d-axis flux linkages at constant rotor angle.

$K_3 = \frac{X'_d + X_e}{X_d + X_e}$ where x_e is a pure impedance.

$K_4 = \frac{1}{K_3}\frac{\Delta e'_q}{\Delta\delta}$ deviation in rotor angle due to demagnetizing effect.

$K_5 = \frac{\Delta V_t}{\Delta\delta}\Big|_{e'_q}$ Ratio of deviation in terminal voltage and deviation in rotor angle at constant d-axis flux linkages.

$K_6 = \frac{\Delta V_t}{\Delta e'_q}\Big|_{\delta}$ Ratio of deviation in terminal voltage and deviation in d-axis flux linkages at constant rotor angle.

3 Multi-machine System Modelling

To justify the control action of MBPSS, single machine system and multi-machine system have been considered in this work. The configuration of single machine system is shown in Fig. 2a and for multi-machine, three generators system is connected to three generators as in Fig. 2b and an SPV is connected to bus 1, 2, and 3 with G_1, G_2, and G_3, respectively.

4 Multi-band PSS

Conventional PSS (CPSS) is modified as MBPSS in which three pairs of different lead–lag compensators are employed in the place of one lead–lag compensator as shown in Fig. 3. MBPSS handles inter-area oscillation through a low-frequency band (LFB) whose range is from 0.01 to 0.1 Hz, inter-plant oscillation through an intermediate-frequency band (IFB) whose range is from 0.1 to 1 Hz, and local area oscillation through a high-frequency band (HFB) whose range is from 1 to 4 Hz. $\Delta\omega$

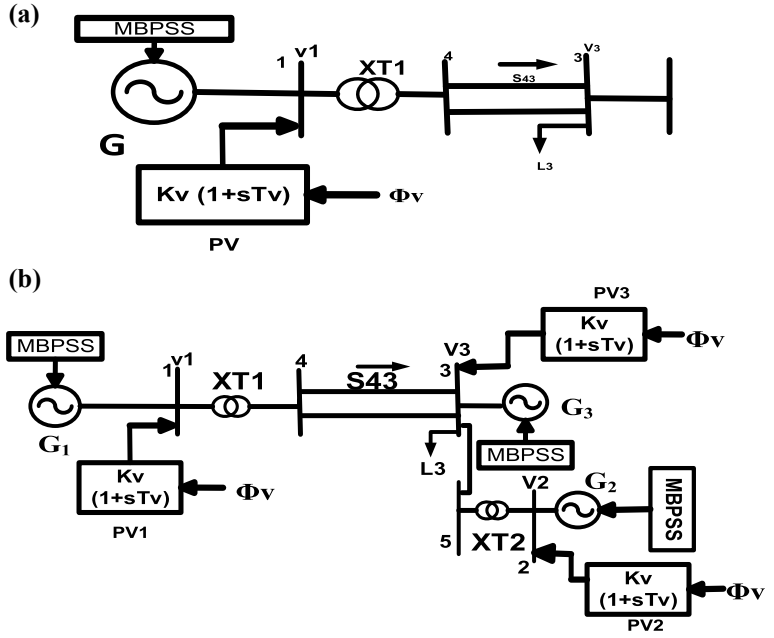

Fig. 2 **a** Single machine model with MBPSS. **b** Multi-machine model with MBPSS

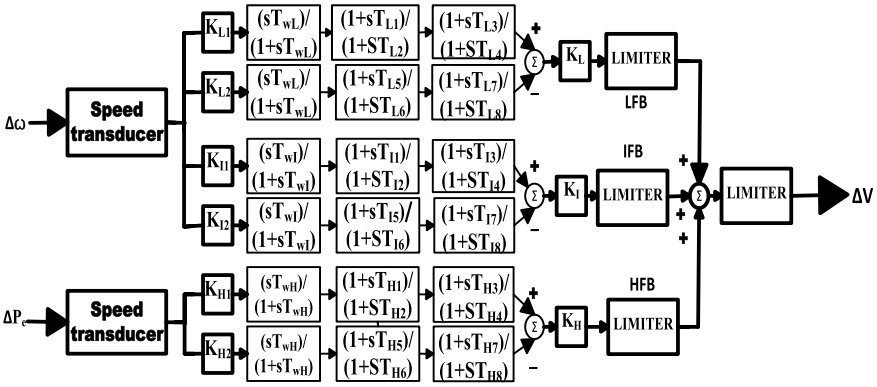

Fig. 3 MBPSS model

input is given to LFB and IFB. ΔP_e input is given to HFB. Both the bands output has a gain ($K_{L,}$ K_I, and K_H) and a limiter. Finally, the output of both the bands are summed and give to a limiter whose range from is $VST_{min}$to VST_{max}.

$$G_{\mathrm{LMBPSS}} = \left(K_{\mathrm{L1}} \frac{sT_{\mathrm{WL}}}{1+sT_{\mathrm{WLI}}} \frac{1+sT_{\mathrm{L1}}}{1+sT_{\mathrm{L2}}} \frac{1+sT_{\mathrm{L3}}}{1+sT_{\mathrm{L4}}} - K_{\mathrm{L2}} \frac{sT_{\mathrm{WI}}}{1+sT_{\mathrm{WI}}} \frac{1+sT_{\mathrm{L5}}}{1+sT_{\mathrm{L6}}} \frac{1+sT_{\mathrm{L7}}}{1+sT_{\mathrm{L8}}} \right) K_{\mathrm{L}} \quad (6)$$

$$G_{\mathrm{IMBPSS}} = \left(K_{\mathrm{I1}} \frac{sT_{\mathrm{WI}}}{1+sT_{\mathrm{WI}}} \frac{1+sT_{\mathrm{I1}}}{1+sT_{\mathrm{I2}}} \frac{1+sT_{\mathrm{I3}}}{1+sT_{\mathrm{I4}}} - K_{\mathrm{I2}} \frac{sT_{\mathrm{WI}}}{1+sT_{\mathrm{WI}}} \frac{1+sT_{\mathrm{I5}}}{1+sT_{\mathrm{I6}}} \frac{1+sT_{\mathrm{I7}}}{1+sT_{\mathrm{I8}}} \right) K_{\mathrm{I}} \quad (7)$$

$$G_{\mathrm{HMBPSS}} = \left(K_{\mathrm{H1}} \frac{sT_{\mathrm{WH}}}{1+sT_{\mathrm{WH}}} \frac{1+sT_{\mathrm{H1}}}{1+sT_{\mathrm{H2}}} \frac{1+sT_{\mathrm{H3}}}{1+sT_{\mathrm{H4}}} - K_{\mathrm{H2}} \frac{sT_{\mathrm{WH}}}{1+sT_{\mathrm{WH}}} \frac{1+sT_{\mathrm{H5}}}{1+sT_{\mathrm{H6}}} \frac{1+sT_{\mathrm{H7}}}{1+sT_{\mathrm{H8}}} \right) K_{\mathrm{H}} \quad (8)$$

Equations (6)–(8) are the transfer function of LFB, IFB, and HFB, respectively.

5 Objective Function

In this paper, deviation in angular frequency of alternator has been taken as input signal. Which is considered in ITAE-based objective function for minimization as given in Eq. (8). For multi machine system, $\Delta\omega$ is the sum of speed deviations of all generators.

$$J = \int_{0}^{\mathrm{tsim}} t|\Delta\omega|\mathrm{d}t \quad (9)$$

LFB parameters K_{L}, K_{L1}, T_{L1}, T_{L3}, K_{L2}, T_{L5}, $T_{\mathrm{L7,}}$ IFB parameters K_{I}, K_{I1}, T_{I1}, T_{I3}, K_{I2}, T_{I5}, T_{I7}, and HFB parameters, K_{H1}, T_{H1}, T_{H3}, K_{H2}, T_{H5}, T_{H7} are tuned by suitable algorithm and the range of K_{L}, $K_{\mathrm{L1,}}$ $K_{\mathrm{L2,}}$ K_{I}, K_{I1}, K_{I2}, K_{H}, K_{H1}, K_{H2} is from 1 to 100 and the range of T_{L1}, $T_{\mathrm{L3,}}$ T_{L5}, $T_{\mathrm{L7,}}$ T_{I1}, T_{I3}, T_{I5}, T_{I7}, T_{H1}, T_{H3}, T_{H5}, T_{H7} is from 0.001 to 1. MDE is proposed to tune the gains which has been compared with DE and PSO algorithm.

6 SPV (Solar Photovolatic) System

The output power of SPV is given in Eq. (10)

$$P_{\mathrm{v}} = \eta_c S_{\mathrm{a}} \varphi_v [1 - 0.005(T_{\mathrm{a}} + 25)] \quad (10)$$

where η_c, $S_{\mathrm{a,}}$ ϕ_{v} and T_{a} are the SPV efficiency, 4084 m^2 SPV array area,1kw/m^2 SPV radiation and ambient temperature in °C, respectively. P_{V} is independent on η_c and S_{a} and changes with the value of ϕ_{v} and $T_{\mathrm{a,}}$ P_{V} value changes. In this work, T_{a} is taken as 25 °C and P_{V} depends on ϕ_{v}. The first-order transfer function model of

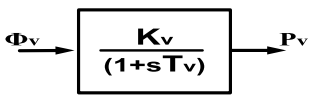

Fig. 4 Transfer function model of SPV system

SPV is shown in Fig. 4 because present work based on low-frequency oscillation and for simplified transfer function model losses are not considered here.

7 Modified DE

DE is the powerful optimization technique which depends on mutation methods and control parameters such as scaling factor F crossover rate CR, population of NP and generation G. But it is a difficult task to select the appropriate methods and parameters for optimization run. To overcome from this type of problem, in this paper, MDE is improved in which fond CR value are selected during the program run. In MDE, range of F and CR are taken 1–0.01 which is decreased exponentially. F and CR values are evaluated as given in Eq. (11) and Eq. (12)

$$F_G = F_{\max} e^{\frac{-a_1 G}{G_{\max}}} \tag{11}$$

$$CR_G = \mathrm{CR}_{\max} e^{\frac{-a_2 G}{G_{\max}}} \tag{12}$$

The maximum value of F_{G} and CR_G comes at $\mathrm{G} = 0$ and the minimum value of F_G and CR_G comes at $G = G_{\mathrm{MAX}}$.

8 Result Analysis

A MBPSS has been employed here to damp local and inter-area oscillations subject to change in mechanical input power and varying solar penetrations. PSS provides additional electrical torque through excitation system, thereby providing damping action to system oscillations. MBPSS can be used to damp both local mode and inter-area oscillations. Both speed and real power deviation are taken as input to MBPSS. PSO, DE, and MDE techniques are employed to tune the gains of MBPSS. ITAE objective function being considered for optimization problem to minimize variation in angular speed. Case studies have been considered with varying mechanical turbine power and solar power generation. A single machine system shown in Fig. 2a is considered for case-1 and case-2. In case-1, input power is step increased by 10% and in case-2, SPV output power is raised to 0.2 pu and then 0.6 pu. Step raise of input power by 10% is considered for objective function. Initially, the system was in steady state at real and reactive power output of 0.8 pu and 0.17 pu, respectively. For case-1, the input power is suddenly raised by 10% and optimal MBPSS being employed for oscillation damping. PSO, DE, and MDE are employed to tune the gains of MBPSS. Figure 5 shows variation in angular speed with proposed MBPSS control action for sudden change in mechanical power. Table 1 presents optimal values of parameter, and Table 2 presents Eigen values of case-1. In case-2, the solar

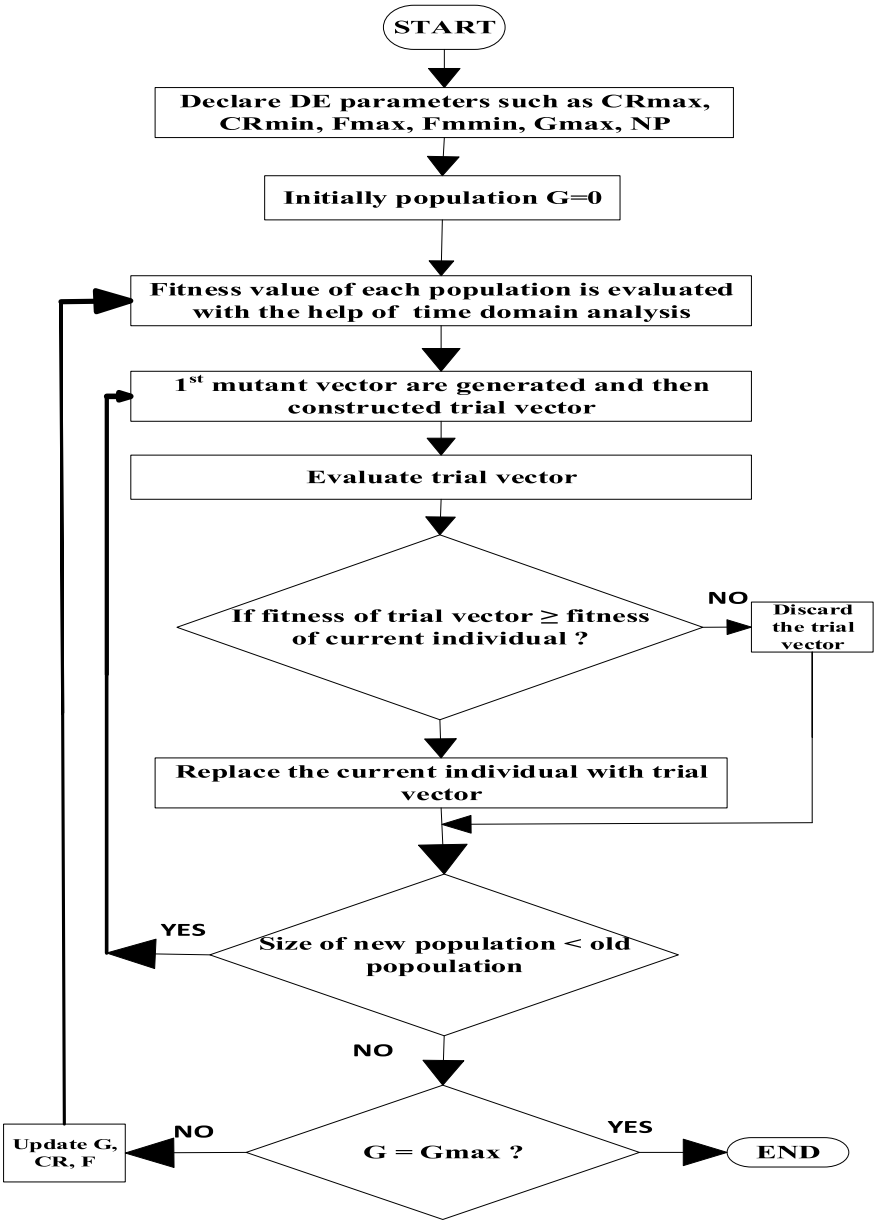

Fig. 5 Flow chart of MDE

Table 1 Optimal parameters

Cases	Optimization technique	Frequency pass section	K	K_1	K_2	T_1	T_3	T_5	T_7
10% raised in input mechanical power	DE	Low	5.7619	5.2135	13.514	0.6665	0.2758	0.6758	0.2970
		Intermediate	23.6241	22.8370	10.1209	0.7483	0.7581	0.1312	0.0818
		High	4.2315	38.5086	4.9409	0.2556	0.5216	0.6371	0.9966
	PSO	Low	16.7035	1.0028	15.1694	0.16679	0.67832	0.99992	0.64066
		Intermediate	1.1633	12.8833	20.5728	0.11875	0.67030	0.49049	0.19724
		High	3.9018	16.2307	17.3833	0.02939	0.43634	0.45383	0.01000
	MDE	Low	8.4305	12.3588	8.4705	0.5551	0.1404	0.9379	0.4297
		Intermediate	19.9126	14.1902	16.0217	0.5030	0.7488	0.1415	0.5124
		High	33.7270	26.8941	43.5678	0.8079	0.5606	0.0795	0.7569
SPV output raised by 0.2pu	DE	Low	12.1845	7.3962	3.2393	0.9670	0.9456	0.5629	0.1638
		Intermediate	20.0075	21.7822	11.0050	0.5120	0.1200	0.2415	0.7140
		High	38.2328	19.0002	25.8153	0.2737	0.8935	0.5453	0.4167
	PSO	Low	6.6886	2.4068	8.3160	0.6515	0.3684	0.9323	0.4441
		Intermediate	8.8411	6.5747	17.6860	0.2775	0.5665	0.8199	0.3567
		High	21.3096	44.4975	23.0984	0.2956	0.4292	0.2159	0.7556
	MDE	Low	12.8821	17.5163	12.1162	0.6907	0.5739	0.1469	0.27705
		Intermediate	8.6901	11.0698	12.5723	0.0978	0.9477	0.7223	0.8079
		High	8.0622	19.4656	3.4381	0.6083	0.9126	0.0468	0.6177
SPV output raised by 0.6pu	DE	Low	10.0052	8.1970	9.2308	0.0356	0.0100	0.5112	0.7380
		Intermediate	2.1631	17.5320	22.4882	0.034	0.0181	0.2269	0.5426
		High	37.1260	18.4368	3.5908	0.7032	0.0474	0.2784	0.0890

(continued)

Table 1 (continued)

Cases	Optimization technique	Frequency pass section	K	K_1	K_2	T_1	T_3	T_5	T_7
	PSO	Low	12.1991	1.71468	9.4591	0.7848	0.8322	0.0101	0.1997
		Intermediate	2.6489	1.0036	8.5560	0.2793	0.5156	0.8192	0.3747
		High	44.4873	17.2094	23.7611	0.3062	0.4190	0.2159	0.0.77545
	MDE	Low	10.6457	4.07734	18.4898	0.9523	0.5201	0.7908	0.5734
		Intermediate	22.4439	4.0366	20.0029	1.0000	0.5833	0.0010	0.7796
		High	32.7091	21.8429	8.8074	0.2336	0.7968	0.5236	0.5200

Table 2 System Eigen values for mechanical mode

Cases		DE	PSO	MDE
10% raised in input mechanical power	G_1	$-0.0005 + 0.8000i$ -0.0005 - $0.8000i$	$-0.6500 + 0.31258i$ - $0.6500 - 0.31258i$	$-0.833 + 0.1200i$ $-0.833 - 0.1200i$
	G_2	$-0.0332 + 0.198i$ $-0.0332 - 0.198i$	$-0.0147 + 0.0051i$ $-0.0147 - 0.0051i$	$-0.9100 + 0.0039i$ $-0.9100 - 0.0039i$
	G_3	$-0.0083 + 0.0012i$ $-0.0083 - 0.0012i$	$-0.0005 + 0.0008i$ $-0.0005 - 0.0008i$	$-0.6993 + 0.0009i$ $-0.6993 - 0.0009i$
SPV output raised by 0.2 pu	G_1	$-0.0107 + 0.0044i$ $-0.0107 - 0.0044i$	$-0.0136 + 0.0054i$ $-0.0136 - 0.0054i$	$-0.7957 + 0.8143i$ $-0.7957 - 0.8143i$
	G_2	$-0.0016 + 0.0036i$ $-0.0016 - 0.0036i$	$-0.0007 - 0.0090i$ $-0.0007 + 0.0090i$	$-0.1000 + 0.0999i$ $-0.1000 - 0.0999i$
	G_3	$-0.0043 + 0.0197i$ $-0.0043 - 0.0197i$	$-0.0056 + 0.0091i$ $-0.0056 - 0.0091i$	$-0.7222 + 0.0028i$ $-0.7222 - 0.0028i$
SPV output raised by 0.6 pu	G_1	$-0.0084 + 1.0449i$ $-0.0084 - 1.0449i$	$-0.0054 + 0.0012i$ $-0.0054 - 0.0012i$	$-0.136 + 0.0044i$ $-0.136 - 0.0044i$
	G_2	$-0.0030 + 0.0168i$ $-0.0030 - 0.0168i$	$-0.2385 + 2.4027i$ $-0.2385 - 2.4027i$	$-0.3700 + 0.0056i$ $-0.3700 - 0.0056i$
	G_3	$-0.0016 + 0.0285i$ $-0.0016 - 0.0285i$	$-0.0048 + 0.0091i$ $-0.0048 - 0.0091i$	$-0.0954 + 0.0035i$ $-0.0954 - 0.0035i$

penetration has been charged and system oscillatory response has been observed with and without proposed MBPSS action. In case-2, two different condition are taken; in condition-1, the solar power output is step raised by 0.2 pu, and in condition-2, the solar power output is step raised to 0.6pu. It was observed that with large change in solar output, the system oscillation is more enhanced. DE, PSO, and MDE are employed to tune the gains of MBPSS. Figure 6 shows variation in angular frequency for condition-1, and Fig. 7 shows variation in angular frequency for condition-2. The optimal parameter and Eigen values are presented in Tables 1 and 2, respectively. In case-3, for three machines system as shown in Fig. 2b, SPV variation is executed in random manner as shown in Fig. 8. Figure 9 presents rotor speed derivations for G_1, G_2, and G_3, respectively. At $t = 0$, SPV suddenly rises to 0.9 pu resulting in heavy oscillation as given in Fig. 9, where the damped response is presented with

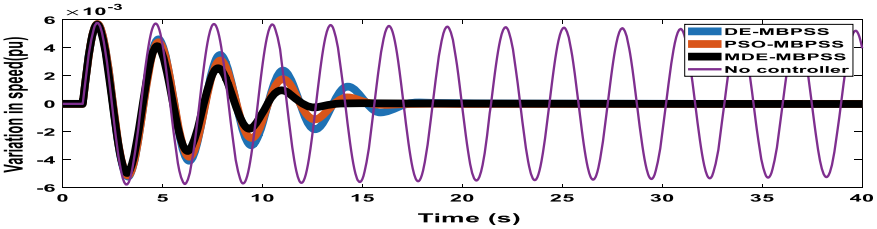

Fig. 6 Speed variation for 10% mechanical input

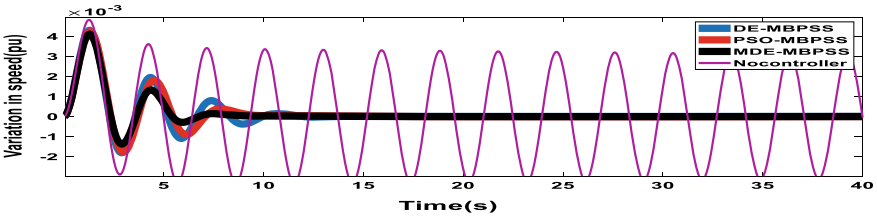

Fig. 7 Speed variation for SPV output raised by 0.2 pu

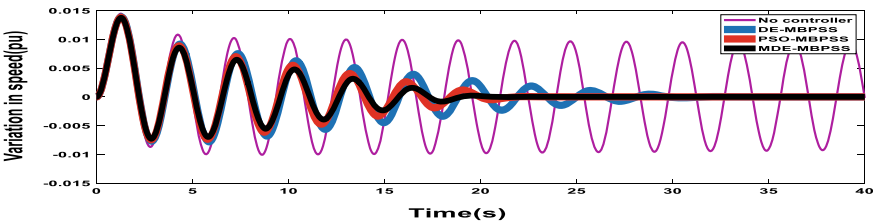

Fig. 8 Speed variation for SPV output raised by 0.6 pu

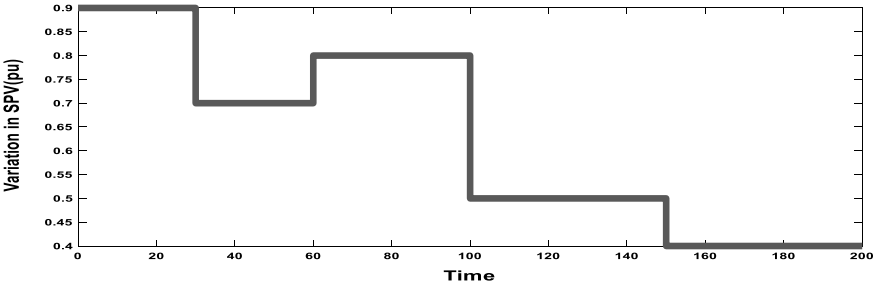

Fig. 9 SPV random variation

proposed optimal MBPSS for G_1, G_2, and G_3 where it is observed that with proposed control actions, the oscillations are much damped with random variations in SPV penetrations (Fig. 10).

9 Conclusion

In this work, MBPSS is employed to provide damping torque for electro-mechanical oscillation resulting from disturbances such as varying input mechanical power and varying SPV penetration. It observed that the varying input turbine power to generator and varying solar penetration excites system oscillation. These oscillations are damped by proposed MBPSS whose parameters are optimally tuned by PSO, DE,

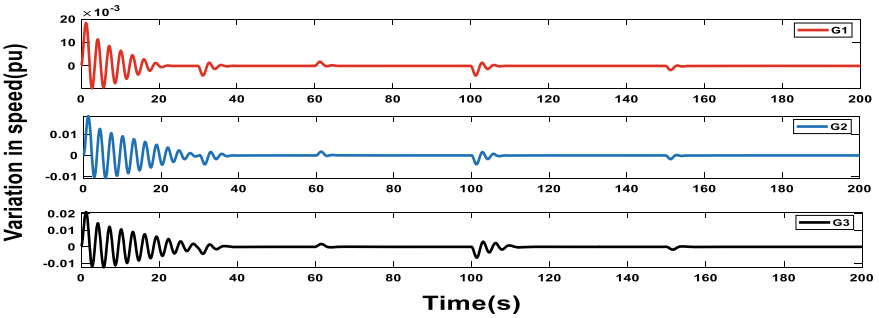

Fig. 10 Speed deviations due to random SPV variations

and proposed MDE control laws. MBPSS can provide damping to local intra-plant and inter-area oscillations, in comparison to single PSS. Also, MDE proposed in this work can provide better performance as compared to PSO and DE algorithms. The proposed MBPSS can be employed in future for large inter-connected power system network with more distribution generation.

References

1. Anderson PM, Fouad AA (1977) Power system control and stability. Iowa State University Press, Ames, IA
2. Padiyar KR (2007) FACTS controllers in power transmission and distribution. New age International (P) Limited
3. Nahak N, Bohidar S, Mallick RK (2018) Investigation of UPFC based Damping controller parameter and a novel multi input dual controller with time delay for multi machine system by Grey-Wolf optimizer. Int Rev Autom Control 11(1)
4. Noroozian M, Anderson G (1994) Damping of power system oscillations by use of controllable components. IEEE Trans PWRD 9:2046–2054
5. Nahak N, Mallick RK (2017) Damping of power system oscillations by a novel DE-GWO optimized dual UPFC controller. Eng Sci Tech Int J (2017) 20(4):1275–1284
6. Nahak N, Satapathy O (2021) Investigation and damping of electromechanical oscillations for grid integrated micro grid by a novel coordinated governor-fractional power system stabilizer. In: Energy sources, Part A: recovery, utilization, and environmental effects. https://doi.org/10.1080/15567036.2021.1942596
7. Gholipour E, Nostratabadi SM (2015) A new coordination strategy of SSSC and PSS controllers in power system using SOA algorithm based on Pareto method. Electr Power Energy Syst 67:462–471
8. Nahak N, Sahoo SR, Mallick RK. Small signal stability enhancement of power system by modified GWO optimized UPFC based PI-lead-lag controller. In: Advances in Intelligent System and computing, vol 817. Springer. https://doi.org/10.1007/978-981-13-1595-4_21
9. Mallick RK, Nahak N (2016) Design of GWO optimized dual UPFC controller for damping of power system oscillations. In: IEEE UPCON conference 09-11 Dec 2016, IIT, BHU Varanasi
10. Wang HF (2000) A unified model for the analysis of FACTS devices in damping power system scillations—Part III: unified power flow controller. IEEE Trans Power Deliver 15(3):978–983

11. Yao W, Jiang L, Wen J, Wu QH, Cheng S (2014) Wide-area damping controller of FACTS devices for inter-area oscillations considering communication time delays. IEEE Trans Power Syst 29(1)
12. Tan YT, Kirschen DS (2007) Impact on the power system of a large penetration of photovoltaic generation. In: Proceedings of IEEE PES general meeting, pp 1–8
13. Nahak N, Mallick RK (2019) Investigation and damping of low frequency oscillations of stochastic solar penetrated power system by optimal dual UPFC. IET Renew Power Gener 13(3):376–388
14. Khodabakhshian A, Hemmati R, Moazzami M (2013) Multi-band power system stabilizer design by using CPCE algorithm for multi-machine power system. Electric Power Syst Res 101:36–48
15. Sahoo DK, Sahu RK, Chandra Sekhar GT, Panda S (2018) A novel modified differential evolution algorithm optimized fuzzy proportional integral derivative controller for load frequency control with thyristor controlled series compensator, J Electr Syst Inf Technol 5(3):944–963

TLBO Designed 2-DOFPIDF Controller for LFC of Multi-area Multi-source Power System

Nimai Charan Patel, Binod Kumar Sahu, and Ramesh Chandra Khamari

Abstract This article explains the load frequency control (LFC) in multi-area multi-unit interlinked power system by employing two degree of freedom proportional integral derivative controller with filter (2-DOFPIDF controller). A PID controller is also separately implemented for performance comparison. Every control area in the system possesses with a non-reheat thermal plant and a hydro generating unit. The parameters of the implemented controllers are fine-tuned by application of teaching learning based optimisation (TLBO) algorithm using integral time absolute error (ITAE) as the fitness function. A comprative performance analysis is accomplished between the two controllers by injecting an instantaneous load of 15% in area-1. It is seen that the proposed 2-DOFPIDFcontroller yields significantly superior transient response when compared to the PID controller. Finally, the robustness of the TLBO optimised 2-DOFPIDF controller is verified by injection of a random step load in area-1.

Keywords Load frequency control · Area control error · 2-DOFPIDF controller · Objective function · Teaching learning based optimisation · Transient response

1 Introduction

Frequency control is an essential task in interlinked power system. It is required to keep the frequency at a constant value to ensure the stability and power quality of a given power system. The system frequency at any given point of time depends on the real power demand on the system at that time [1–3]. Practically, the real power demand is dynamic in nature, and it never remains constant. Hence, it is essential to implement a suitable secondary controller for regulation of the generated power

N. C. Patel · R. C. Khamari
Government College of Engineering, Keonjhar, Odisha, India

B. K. Sahu (✉)
Siksha 'O' Anusandhan University, Bhubaneswar, Odisha, India

M. Mishra et al. (eds.), *Innovation in Electrical Power Engineering, Communication, and Computing Technology*, Lecture Notes in Electrical Engineering 814,
https://doi.org/10.1007/978-981-16-7076-3_24

according to the active power demand to keep the frequency within the prescribed limit and this method of balancing the load and generation is known as LFC.

The foremost work on LFC was first carried out by Cohn in 1956 [4]. Since then, numerous research works have been performed on LFC issues as mentioned in the literature. In 1970, Elgerd and Fosha carried out an important research work on LFC issues and presented an optimum method for LFC in multi-area system [5]. Many control strategies for LFC including the application of various artificial intelligence techniques along with the conventional controllers are mentioned in the literature. Design of PI controller with fuzzy gain sceduling approach is described for LFC of four area interlinked system [6]. Implementation of artificial neural newtork (ANN) controller is described for LFC in multi-area system with various generation sources [7]. Performance comparision of various classical controllers for LFC has been outlined in [8]. Implementation of differential evolutionary (DE) algorithm tuned 2-DOFPID controller has been illustrated for LFC of dual-area interlinked thermal plant taking the effect of governor dead band (GDB) into account [9]. DE and particle swarm optimisation (PSO) algorithm are hybridised for optimal tuning of the fuzzy PID controller in interlinked power system [10]. DEPSO optimised PID controller is implemented for controlling the frequency in interlinked power system with nonlinearities [11]. Application of sine cosine algorithm (SCA) is explained for optimum design of double loop PD + PI controller in dual area system with different generating units [12]. LFC of dual-area solar thermal system by invasive weed optimisation (IWO) algorithm tuned multi-staged PID controller is explained in [13]. LFC analysis of thermal plant with electric vehicle (EV) aggregators having time varying delay has been eplained in [14]. Cascading of moth flame optimisation (MFO) based PDF and 1PI controller is discussed for LFC of dual-area thermal plant [15]. LFC with realistic high-voltage direct current (RHVDC) and realistic dish-stirling solar thermal system (RDSTS) is demonstrated under dergulated environment [16]. LFC of restructured power system incorporating phase locked loop (PLL), and virtual inerial is illustrated [17].

In this study, a dual-area interlinked system with every area consisting of a non-reheat thermal and a hydro plant is considered for LFC analysis with 2-DOFPIDF controller. In the first step, the PID controller is fine-tuned separately by the application of TLBO algorithm and the system response is observed. In the next step, TLBO optimised 2-DOFPIDF controller is employed for further improvement of system performance and stability. In both the cases, an instantaneous disurbance of 15% is imparted in area-1 to analyse the transient system performance. It is witnessed that the 2-DOFPIDF controller gives significantly better result when compared with the other controller. Finally, the robustness of the recmmended TLBO optimised 2-DOFPIDF controller is verified by the injection of a random step load in area-1.

2 System Modelling

The model of the power system is sketched in Fig. 1. It comprises of two control areas which are interlinked via the tie-line. The tie-line facilitates the power interchange between the two control areas. Every area of the considered system possesses with a non-reheat thermal and a hydro plant. Each area of the power system has a capacity of 2000 MW.

Area control error (ACE) of every area is given by the following equations.

$$\mathrm{ACE}_1 = B\Delta f_1 + \Delta P_{\mathrm{tie}} \tag{1}$$

$$\mathrm{ACE}_2 = B\Delta f_2 + \Delta P_{\mathrm{tie}} \tag{2}$$

where, ACE_1 and ACE_2 denote area control errors of area-1 and area-2 respectively. B is the frequency bias factor, Δf_1 and Δf_2 represent the frequency changes in area-1 and area-2, respectively, and ΔP_{tie} is the tie-line power change. Various parameters of the considered model are mentioned in Appendix 1 [18, 19].

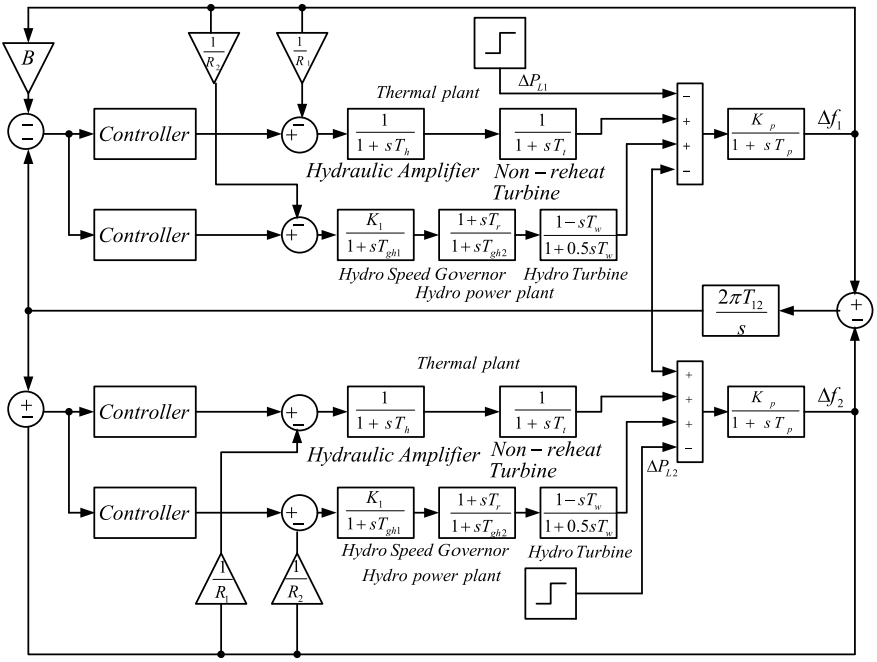

Fig. 1 Power system model under investigation

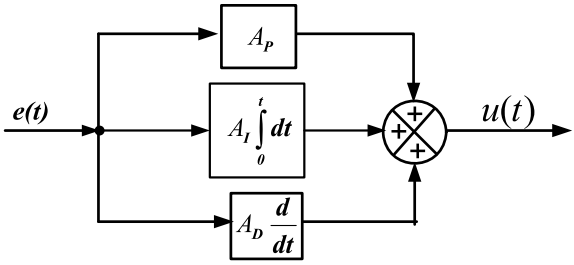

Fig. 2 Configuration of the PID controller

3 Proposed Control Approach

The various controllers used in this work are the PID and 2-DOFPIDF controller. The description of theses controllers are outlined below.

3.1 PID Controller

PID controllers are very popular controller due to its simple design and robustness. Also, it delivers better dynamic response and therefore, PID controller has always been the 1st choice of engineers since many decades. Schematic arrangement of the controller is sketched in Fig. 2. Here, ACE is the input to the PID controller.

3.2 2-DOFPIDF Controller

2-DOFPIDF controller has two control loops as shown in Fig. 3. Due to the presence of two control loops in this controller, it delivers improved performance than the PID controller. The two inputs in this case are the ACE and the frequency error. Different setpoint weights are allocated at the input for proportional as well as derivative actions

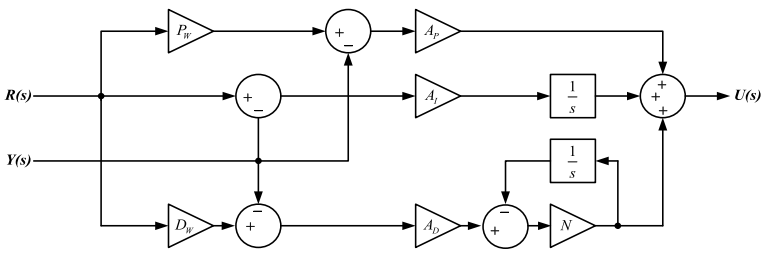

Fig. 3 Configuration of 2-DOFPIDF controller

to obtain a weighted difference signal but no setpoints are allocated at the input for integral action as illustrated in Fig. 3.

3.3 Optimal Design of Controllers

The time response of any given system is greatly dependent on the parameters of the controller, and therefore, the parameters of controller must be properly selected by using suitable optimisation technique. Optimisation technique employs a function known as the objective function or fitness function denoted by J and then the optimisation problem is formulated by minimsation of this objective function under the constraints of lower and upper limits of the parameters to be optimised. Various objective/fitness functions for LFC analysis are mentioned in the literature. In the present work, ITAE is selected as the objective/fitness function. ITAE is expressed by the Eq. (3), and the optimisation problem is structured as minimisation of J under the restrictions described by the Eqs. (4–5).

$$J = \text{ITAE} = \int_0^{t_s} (|\Delta f_1| + |\Delta f_2| + |\Delta P_{\text{tie}}|) t \, \mathrm{d}t \tag{3}$$

$$0.01 \leq A_{\text{P,D,I}}, P_{\text{W}}, D_{\text{W}} \leq 5 \tag{4}$$

$$10 \leq N \leq 500 \tag{5}$$

where, $A_{\text{P,D,I}}$ represent the proportional, derivative and integral coeffeicients of the PID and 2-DOFPIDF controller as per the subscripts used at any particular instance. D_{W} and P_{W} are the setpoint weights corresponding to derivative and proportional actions and N is the derivative filter coefficient of the 2-DOFPIDF controller. Various optimisation techniques have been mentioned in the literature for solution of different optimisation problems in engineering and appropriate selection of the optimisation technique is vital for a given problem otherwise it may lead to unsatisfactory result. After a careful examination of the literature, TLBO has been chosen in this work to solve the optimisation problem so as to get the optimum parameters of the controllers.

3.3.1 Teaching Learning Based Optimisation (TLBO)

TLBO was developed by Rao et al. in the year 2011 [20]. It is a metaheuristic population oriented search algorithm stimulated by the teaching and learning procedure. This algorithm simulates the effect of teacher's impact on the outcome of students in a particular class. The outcome of a student is assessed by the result or grades secured by the student. The teacher is considered to be higly educated person than the

students as he shares his experience and knowledge with the students and the quality of the teacher considerably influences the output of the students. A quality teacher imparts training on the students in such a way that the outcome of the students is improved. The students can further enhance their knowledge and produce good results by interaction amongst themselves. The working method of TLBO is composed of two phases. The first phase is the teacher phase which comprises of learning from the teacher, whereas the second phase is the learner phase which comprises of learning by interactions between the learners or students. Various steps of TLBO alorithm are described below.

1. Initialisation: Initially, a population with size [NP $\times$ D] is generated randomly, where NP represents the number of all learners and D represents dimension of search region denoting the number of various subjects provided.
2. Teacher phase: Each teacher put his best effort to enhance the mean class result in his assigned subject. The teacher is considered to be the highly educated person as he trains the learners, and therefore, he is taken to be the ultimately best learner. Hence, the best solution (X_{best}) is found out and designtated as teacher. The average or mean value of the marks secured in each subject by different students is computed as:

$$M_{\text{d}} = [m_1, m_2, ..., m_D] \tag{6}$$

The difference between mean value of the grades in a given subject and the grade of respective teacher is determined by:

$$M_{\text{diff}} = \text{rand} \times [X_{\text{best}} - T_{\text{F}} M_{\text{d}}] \tag{7}$$

where, T_{F} denotes the teaching factor, rand denotes a random positive real number of value less than 1. The value of T_{F} may be 1 or 2 and randomly decided using the equations given below.

$$T_{\text{F}} = \text{round}(1 + \text{rand}) \tag{8}$$

where, rand denotes a positive real random number of value less than 1.

The existing population gets updated by using the following equation.

$$X_{\text{new}} = M_{\text{diff}} + X \tag{9}$$

Elements of X_{new} are retained if $J(X_{i,\text{new}}) < J(X_i)$, else elements of X_{new} are replaced by corresponding elements of X. Here, J denotes the objective function as defined by Eq. (3).

3. Learner phase: A learner arbitrarily selects another learner and tries to enrich his knowledge by mutual interactions with the other learner. The learner enhances his knowledge through mutual interaction when the other learner is more knowledgeable than him. The procedure of learning in this step is described by the

equations given below.

$$X_{\text{new}} = \text{rand}(X_i - X_j) + X_i, \text{ if } J(X_i < X_j) \tag{10}$$

Otherwise,

$$X_{\text{new}} = \text{rand}(X_j - X_i) + X_i \tag{11}$$

where, X_i and X_j are two arbitrarily selected learners and $i \neq j$.

If X_{new} performs better then it is kept. Step (ii) and (iii) will be repeated till the stopping criterion is arrived and lastly the elements with best solution is retained.

4 Result Analysis

Figure 1 shows the scrutinised power system model. Each parameters of this system are depicted in Appendix 1. The considered system is modelled and simulated in the MATAB and Simulink environment. The controllers employed for LFC analysis of considered power system are PID and 2-DOFPIDF controllers. TLBO algorithm is scripted in the.m file and integrated with the considred model for optimal tuning of the controllers. The numbers of population is taken as 50 (i.e., NP = 50) and numbers of iteration is taken as 500 in each case.

4.1 Transient Performance Analysis

An abrupt disruption of 0.15 p.u. is imparted in area-1, and the transient system response is examined independently by implementation of TLBO tuned PID and 2-DOFPIDF controllers. The optimal parameters of the various controllers obtained by the injection of an abrupt disturbance of 15% in area-1 are given in Table 1. The transient response of the tie-line power oscillations and frequency oscillations in both areas with the two controllers are depicted in Figs. 4, 5 and 6 and the corresponding transient response specifications with ITAE values for a simulation time of 40 s are depicted in Table 2.

By careful examination of transient performance specifications and ITAE values given in Table 2 and transient responses shown in Figs. 4, 5 and 6, it can be inferred that the TLBO optimised 2-DOFPIDF controller performs better than the TLBO optimised PID controller. Comparing the performance of both the controllers, it is obvious that the TLBO optimised 2-DOFPIDF controller exhibits significantly less peak undershoot (U_{sh}), peak overshoot (O_{sh}) and settling time (T_{S}) for frequency oscillation in area-1 and area-2 as well as tie-line power oscillation than the TLBO optimised PID controller. Moreover, the TLBO optimised 2-DOFPIDF controller

Table 1 Optimum Parameters of the TLBO optimised controllers

Controllers	Controller parameters of area-1						Controller parameters of area-2					
	A_{P1}	A_{I1}	A_{D1}	P_{W1}	D_{W1}	N_1	A_{P2}	A_{I2}	A_{D2}	P_{W2}	D_{W2}	N_2
TLBO-PID	5.0000	5.0000	1.1121	–	–	–	0.0100	0.8121	3.0805	–	–	–
TLBO-2-DOFPIDF	2.8002	5.0000	2.0527	3.9942	0.0100	343.6048	0.0100	0.5724	1.6502	1.3771	0.0100	107.7592

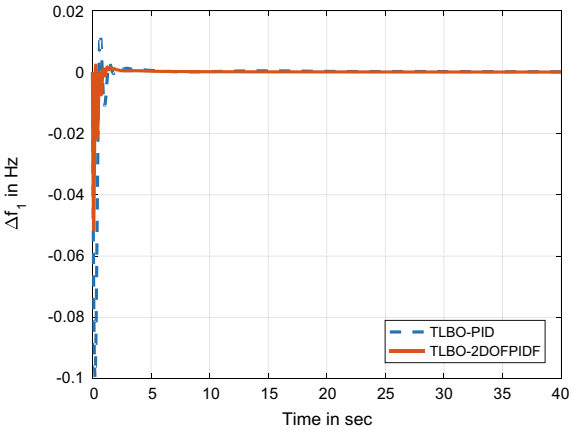

Fig. 4 Variation of the area-1 frequency

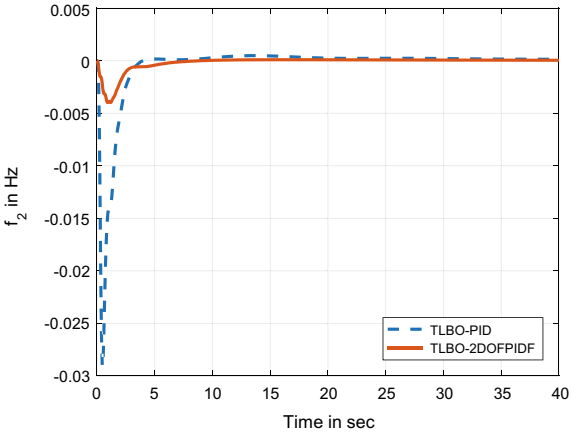

Fig. 5 Variation of the area-2 frequency

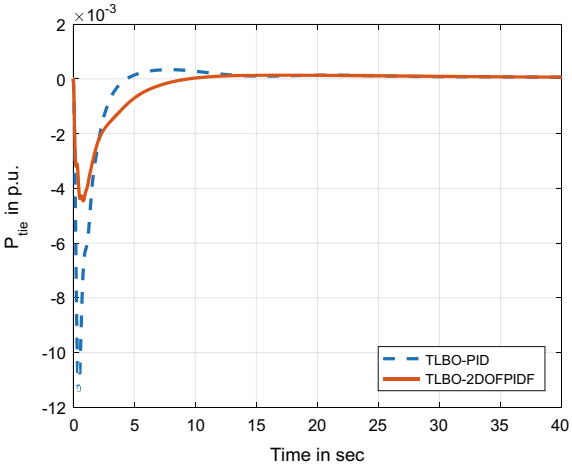

Fig. 6 Tie-line power variation

Table 2 Transient performance specifications due to application of abrupt load in area 1

Controllers	Δf_1			Δf_2			ΔP_{tie}			ITAE
	$U_{sh} \times 10^{-3}$	$O_{sh} \times 10^{-3}$	T_S	$U_{sh} \times 10^{-3}$	$O_{sh} \times 10^{-3}$	T_S	$U_{sh} \times 10^{-3}$	$O_{sh} \times 10^{-3}$	T_S	
TLBO-PID	−99.7359	12.6561	29.6367	−29.1176	0.4814	30.3815	−11.4084	0.3337	11.4588	0.4908
TLBO-2-DOFPIDF	−51.5129	2.2881	7.4258	−3.9813	0.0925	6.2259	−4.4589	0.1319	7.3449	0.2275

gives significantly less ITAE value than the TLBO optimised PID controller. Therefore, it is obvious that the recommended TLBO optimised 2-DOFPIDF controller delivers appreciably superior performance than the TLBO optimised PID controller.

4.2 Robustness Analysis

The robustness of the TLBO designed 2-DOFPIDF controller is verified with the obtained controller parameters as depicted in Table 1 by injection of a random step load in area-1 varying in the range [0.3–0.3] p.u.. The nature of the random load (ΔP_{L1}) and the corresponding frequency deviations in both areas (Δf_1 and Δf_2) along with the tie-line power variation (ΔP_{tie}) are depicted in Figs. 7, 8, 9 and 10.

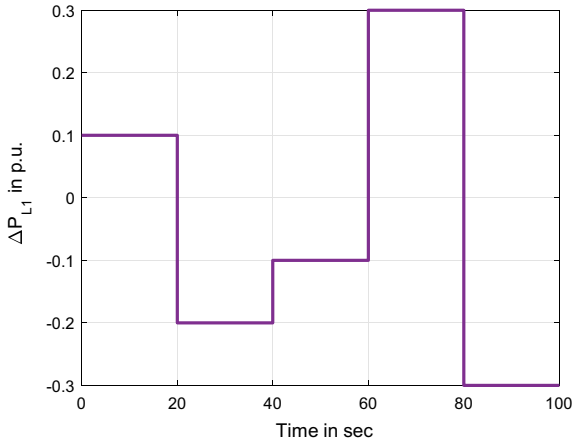

Fig. 7 Random step load injected in area-1

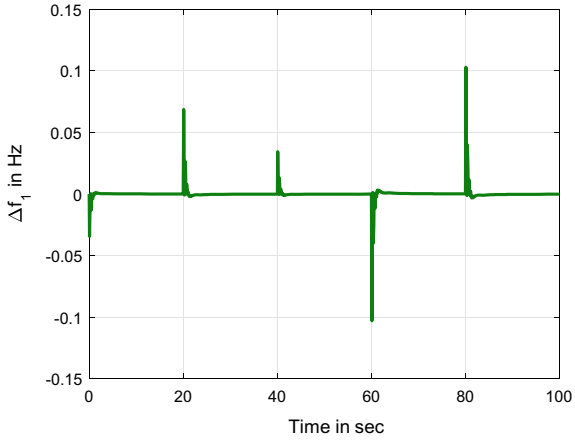

Fig. 8 Frequency variation in area-1 due to injection of random step load in area-1

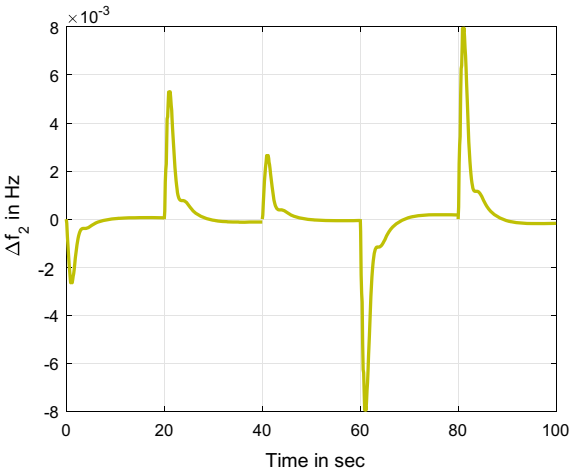

Fig. 9 Frequency variation in area-2 due to injection of random step load in area-1

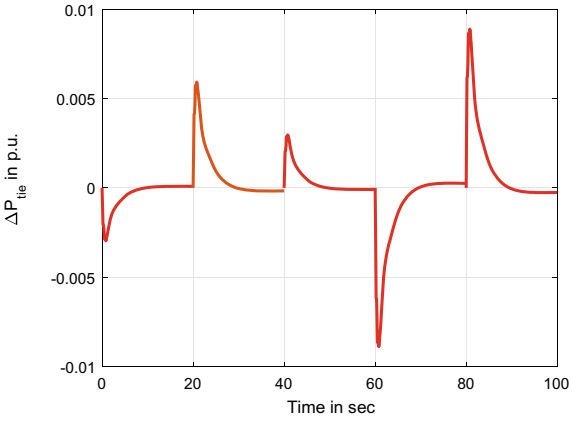

Fig. 10 Tie-line power variation due to injection of random step load in area-1

From Figs. 8 and 9, it is witnessed that the frequency deviation in area-1 and area-2 is effectively damped out. Also, it is seen from Fig. 10 that the tie-line power oscillation is effectively damped out. Hence, the controller is proficient in retaining the system stability even under the application of random load varied over a wide range.

5 Conclusion and Future Scope

In this paper, a dual-area interlinked system consisting of a non-reheat thermal and a hydro generating unit in each area is modelled and PID controller alongwith 2-DOFPIDF controller are implemented for load frequency control. An instantaneous

disruption of 15% is applied in area-1 to examine the transient system response with various controllers. At first, the PID controller is optimised by TLBO algorithm and the obtained response of the considered system is observed. In the next step, the performance of the considered system is examined with the TLBO optimised 2-DOFPIDF controller. It is found that the proposed TLBO optimised 2-DOFPIDF controller gives the least ITAE value and delivers supreme performance when compared to TLBO optimised PID controller. Finally, robustness of the proposed controller is verified by injecting a randomly varying step load in area-1.

The research work presented in this paper leaves ample of scope to carry out further research such as the presented control techniques can be applied for AGC of power system under deregulated environment, new optimisation techniques may be employed for optimal tuning of the controller parameters in the existing work for further improvement of the system dynamics.

Appendix 1

Invesigated system parameters are given below.

$$T_{\mathrm{h}} = 0.08\,\mathrm{s},\ T_{\mathrm{t}} = 0.3\,\mathrm{s},\ T_{\mathrm{gh1}} = 48.7\,\mathrm{s},\ T_{\mathrm{gh2}} = 0.513\,\mathrm{s},$$
$$K_1 = 1.0,\ T_{\mathrm{r}} = 5\,\mathrm{s},\ T_{\mathrm{W}} = 1.0s,\ B = 0.425\,\mathrm{p.u.\,MW/Hz},$$
$$R_1 = 2\,\mathrm{Hz/p.u.},\ R_2 = 2.4\,\mathrm{Hz/p.u.},$$
$$T_{12} = 0.0707\,\mathrm{p.u.},\ K_{\mathrm{P}} = 100\,\mathrm{Hz/p.u.},\ T_{\mathrm{P}} = 20\,\mathrm{s}.$$

References

1. Kundur P, Balu NJ, Lauby MG (1994) Power system stability and control, vol 7. McGraw-Hill, New York
2. Elgard OI (1982) Electric energy systems theory. McGraw-Hill, New York, pp 299–362
3. Saadat H (1999) Power system analysis. McGraw-Hill
4. Cohn N (1956) Some aspects of tie-line bias control on interconnected power systems. Trans Am Inst Electr Eng Part III: Power Apparatus Syst 75(3):1415–1436
5. Elgerd OI, Fosha CE (1970) Optimum megawatt-frequency control of multiarea electric energy systems. IEEE Trans Power Appar Syst 4:556–563
6. Chang CS, Fu W (1997) Area load frequency control using fuzzy gain scheduling of PI controllers. Electr Power Syst Res 42(2):145–152
7. Zeynelgil HL, Demiroren A, Sengor NS (2002) The application of ANN technique to automatic generation control for multi-area power system. Int J Electr Power Energy Syst 24(5):345–354
8. Nanda J, Saikia LC (2008) Comparison of performances of several types of classical controller in automatic generation control for an interconnected multi-area thermal system. In: Australasian universities power engineering conference. IEEE, pp 1–6

9. Panigrahi TK, Behera A, Sahoo AK (2017) Novel approach to automatic generation control with various non-linearities using 2-degree-of-freedom PID controller. Energy Procedia 138:464–469
10. Sahu BK, Pati S, Panda S (2014) Hybrid differential evolution particle swarm optimisation optimised fuzzy proportional–integral derivative controller for automatic generation control of interconnected power system. IET Gener Transm Distrib 8(11):1789–1800
11. Patel NC, Debnath MK, Bagarty DP, Das P (2017) Load frequency control of a non-linear power system with optimal PID controller with derivative filter. In: IEEE ınternational conference on power, control, signals and ınstrumentation engineering (ICPCSI). IEEE, pp 1515–1520
12. Patel, NC, Debnath MK, Sahu BK, Das P (2018) Solution of LFC problem using PD+ PI double loop controller tuned by SCA. In: International conference on recent ınnovations in electrical, electronics & communication engineering (ICRIEECE). IEEE, pp 337–342
13. Patel NC, Debnath MK, Sahu BK, Dash SS, Bayindir R (2019) Application of invasive weed optimization algorithm to optimally design multi-staged PID controller for LFC analysis. Int J Renew Energy Res 9(1):470–479
14. Patel NC, Sahu BK, Debnath MK (2019) Automatic generation control analysis of power system with nonlinearities and electric vehicle aggregators with time-varying delay implementing a novel control strategy. Turk J Electr Eng Comput Sci 27(4):3040–3054
15. Patel NC, Agrawal R, Pradhan P, Satapathy S, Ahmed I, Debnath MK (2020) Two-staged (PDF+ 1PI) controller design for load frequency control. In: International conference on computational ıntelligence for smart power system and sustainable energy (CISPSSE). IEEE, pp 1–6
16. Babu NR, Saikia LC (2021) Load frequency control of a multi-area system incorporating realistic high-voltage direct current and dish-Stirling solar thermal system models under deregulated scenario. IET Renew Power Gener 15(5):1116–1132
17. Bhagat SK., Saikia LC., Babu NR, Saha D (2021) Impact of PLL and virtual ınertia on deregulated AGC system ıntegrated with parallel AC/HVDC. IETE J Res 1–4 (2021)
18. Chandrakala KV, Balamurugan S, Sankaranarayanan K (2013) Variable structure fuzzy gain scheduling based load frequency controller for multi source multi area hydro thermal system. Int J Electr Power Energy Syst 53:375–381
19. Sahu RK, Panda S, Padhan S (2015) A hybrid firefly algorithm and pattern search technique for automatic generation control of multi area power systems. Int J Electr Power Energy Syst 64:9–23
20. Rao RV, Savsani VJ, Vakharia DP (2012) Teaching–learning-based optimization: an optimization method for continuous non-linear large scale problems. Inf Sci 183(1):1–5

Automatic Generation Control of an Interconnected Power System Using 2-degree of Freedom Fractional Order PID Controller

S. Sahoo, N. K. Jena, D. P. Das, and B. K. Sahu

Abstract Here, in this work, two-degree of freedom non-integer order PID controller is applied for the generation control of an equal two-area power system. Diversified generating sources including renewable sources are present in each area. The system is made more realistic by introducing governor dead band (GDB) and generation rate constraint (GRC) in thermal unit and GRC in hydro unit. An innovative optimization technique named as selfish herd optimization (SHO) is preferred to obtain the gain values of the proposed controller. The superiority of the designed control technique is established by comparing its dynamic response with that of most widely accepted PID controller. From the results, it is verified that the proposed controller improves the transient response of frequency and tie line power (T-L power) and minimizes the area control error (ACE) due to which the system can be able to supply good quality of electricity.

Keywords Automatic generation control (AGC) · Fractional order PID controller (FOPID) · Selfish herd optimization (SHO) · Renewable energy sources (RES)

Abbreviations

B	Frequency parameter
R	Speed regulation parameter torque
K_{ps}	Power system gain
T_{ps}	Power system time constant

S. Sahoo · N. K. Jena · D. P. Das · B. K. Sahu (✉)
Department of Electrical Engineering, ITER, Siksha O Anusandhan Deemed to be University, Bhubaneswar, India
e-mail: manojdebnath@soa.ac.in

S. Sahoo
e-mail: subhadrasahoo@soa.ac.in

N. K. Jena
e-mail: narendrajena@soa.ac.in

M. Mishra et al. (eds.), *Innovation in Electrical Power Engineering, Communication, and Computing Technology*, Lecture Notes in Electrical Engineering 814,
https://doi.org/10.1007/978-981-16-7076-3_25

T_g Time constant of governor
T_t Time constant of turbine
K_r Gain of the reheater
T_r Reheat time constant
T_{ij} Synchronization coefficient
T_w Water turbine time constant
T_{GH} Hydro governor time constant
T_{RH} Hydro reheat time constant

1 Introduction

The modern power system becomes larger in size and more complex due to continuous increase in load demand. It consists of number of control areas, and each area may consist of different kind of conventional or non-conventional sources to satisfy the peak load of existing power system. Due to shortage of fossil fuel and to meet the future load demand, nowadays non-conventional energy sources are preferred. It also helps to reduce the pollution level in the environment. To maintain the equilibrium of the power system, the generated power should match with the load demand and loss. Any sudden change in power demand causes deviation in system parameter such as frequency and voltage. For successful and stable operation of an interconnected power system, the voltage and frequency should remain constant after any load disturbance. Hence, automatic generation control (AGC) concept is used to keep the system frequency and T-L power at a constant level during normal and abnormal condition. The summation of change in system frequency and change in T-L power is known as area control error (ACE) which is the controlled output of AGC.

Literature Review reveals that primary controller which includes the speed governor system of the power plant may not able to maintain the frequency and tie-line power due to frequent and large load change. Hence, various types of secondary controllers are developed as a solution for AGC issues in an interconnected power system. At first Elgerd et al. [1] developed the concept of conventional I/PI controller for AGC. To obtain the better response of the conventional PID controller, different optimization techniques are used to tune the parameters of the controller. Guha et al. [2] applied differential search algorithm (DSA) for tuning the parameters of PIDF controller for LFC of a two-area thermal system. The firefly algorithm is used to tune PID controller of two equal area non-reheat thermal system by Pradhan et al. [3]. Hasanein et al. [4] proposed SSA to optimize the gains of PID controller of a multi-area power system. BBO optimized PID controller is demonstrated by Rahman et al. [5] for LFC of an interconnected system. Acharyalu et al. [6] used MFO technique for tuning of PIDF controller for AGC of a multisource three-area power system.

In case of the system having nonlinearities and uncertainties, the classical PID controller may not provide the desired dynamic response. Hence, several artificial intelligence-based controllers such as fuzzy logic controller [7], sliding

mode control [8, 9], self-adaptive fuzzy logic controller [10], adaptive neuro-fuzzy controller(ANFIS) [11], non-integer controller [12], and cascaded controller [13] are designed to make the system more stable. Though fuzzy logic-based controller and neural network-based controllers are mostly used in the market, still they may not always give better response because these are based upon assumed value of membership function and predefined rule base. Hence, non-integer-type PID controller is preferred which may give better transient response of frequency and tie-line power for a wide range of step load perturbation. A non-integer ID controller is proposed by Debbarma et al. [14] to stabilize the frequency of three unequal area thermal system. Ismyil et al. [15] developed GA-based fractional order PID (FOPID) controller for the AGC of a two-area thermal system. Tasnin et al. [16] demonstrated fractional order cascaded controller for AGC of a deregulated multiarea system. The same controller optimized with selfish herd optimization is proposed by Jena et al. [17] for the AGC of a two-area system with renewable energy sources. Sahu et al. [18] took a maiden attempt for the application of two-degree of freedom PID controller for the LFC of an interconnected power system. Jena et al. [19] demonstrated two-degree of freedom cascaded controller for AGC of a two-area multisource power system. Two-degree of freedom fractional order PID controller is proposed by Mohapatra et al. [20] for AGC.

From the above study, it is very clear that the performance of AGC depends upon controller design and its gain parameters. To obtain the accurate gain value, several optimization methods are used such as TLBO [7], WGA [10], GA [15], DE [18], and QOSSA [20]. For the stability of an interconnected power system, an efficient controller structure along with proper gain parameters is on demand. In this paper, a new, efficient, and bio-inspired optimization method called selfish herd optimization [21] is used for the tuning of two-degree of freedom fractional order PID controller with filter for the LFC of an equal two-area multisource system.

Objective of the paper

(i) The two-degree of freedom fractional order PID (2DOFFOPIDF) controller with filter is employed as supplementary controller for the stability of a multisource two-area system.
(iI) The transient behavior of frequency and tie-line power is examined by taking a wind power source in each area.
(iII) A comparative analysis is done in between 2-DOFFOPIDF controller and classical PID controller to show the superiority of the 2-DOFFOPIDF controller.
(iv) To establish the robustness of two-degree of freedom FOPIDF controller, a random load is introduced in first area.

2 System Under Study

A two equal area diversified power system is considered to prove the efficiency of designed controller as shown in Fig. 1. The MATLAB/Simulink platform of version

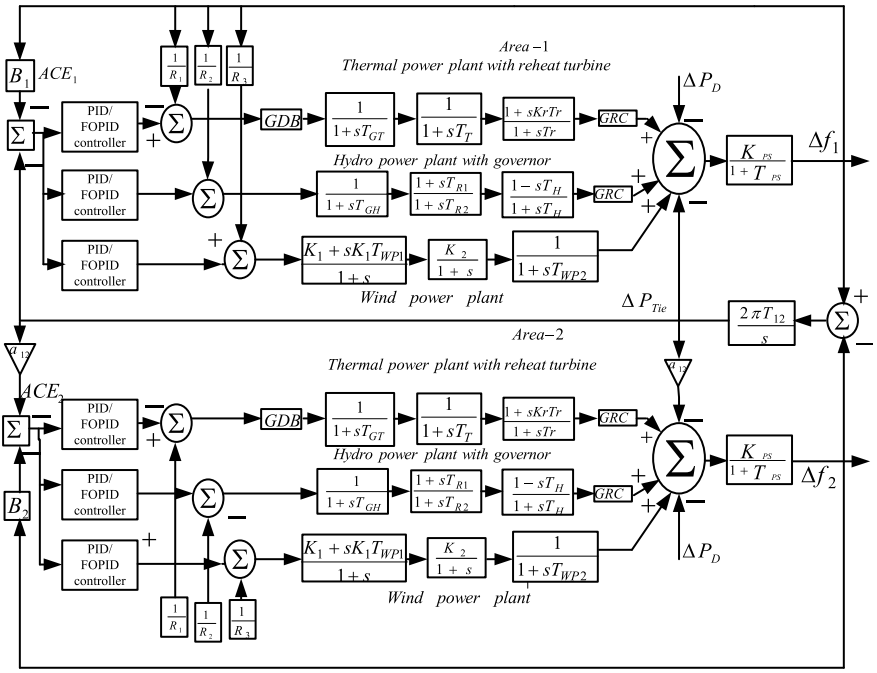

Fig. 1 Two-area interconnected power system

2016b is chosen for the simulation. Three different sources are present in each area. Due to exhaustion of raw material for the traditional sources and to meet the growing demand of load, renewable energy sources are introduced along with the conventional system. In the proposed system, wind power system is added in each area with thermal and hydro units. The system parameters for thermal and hydro units are taken from reference [22] and that of wind system is taken from reference [19]. For the analysis of LFC, step load perturbation (SLP) of 0.01 pu is introduced in area-1 and the area control error (ACE) of each area is the input to the controllers for minimizing.

3 Controller Structure and Objective Function

Different controllers are deployed as a secondary controller to reduce the frequency deviation and T-L power deviation of an interconnected system after any disturbance, thereby reduces the area control error (ACE) up to a remarkable extent. Here, in this work, to reduce the frequency deviation, 2DOFFOPID controller with filter is proposed and its response is juxtapposed with the result of conventional PID controller. The fractional order PID controller is based upon fractional calculus. Since it has more degree of freedom and more no. of tuning parameters, it outperforms the

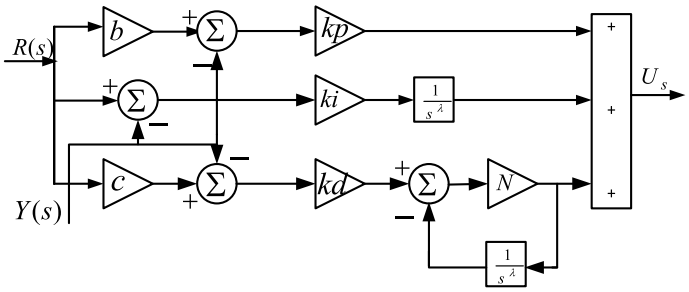

Fig. 2 2DOFFOPIDF controller structure

integer order PID controller in terms of overshoot and settling time. Filter is provided to mitigate the noise quickly. To the proposed controller two inputs are given, one is the reference signal R(s) and other one is measured output Y(s). U(s) is the controlled output of the controller. Three analogous controllers having different gain parameters are used for each unit of each control area of the proposed model. Figure 2 shows the block diagram of the designed controller.

$$(bR(s) - Y(s))k_p + (R(s) - Y(s))\frac{k_i}{s^{\lambda}} + (cR(s) - Y(s))\left(\frac{k_d s^{\mu} N}{s^{\mu} + N}\right) = U(s) \quad (1)$$

Controller structure with proper gain value plays a vital role for the stability of any system. Hence, various optimization algorithms are used to obtain the controller gain parameters. In this study, in order to die out the oscillations in frequency and tie-line power, integral time absolute error (ITAE) is considered as the fitness function.

$$J = \text{ITAE} = \int_0^t [|\Delta f_1| + |\Delta f_2| + |\Delta ptie_{12}|]t \cdot \mathrm{d}t \quad (2)$$

where $\Delta f_1 \rightarrow$ Frequency excursion of area-1.
$\Delta f_2 \rightarrow$ Frequency excursion of area-2.
$\Delta ptie_{ij} \rightarrow$ T-L power excursion between area 'i' and 'j'.

4 Selfish Herd Optimization (SHO) Algorithm

Fausto et al. [21] developed selfish herd optimizer (SHO) as an efficient, bio-inspired algorithm for global optimization, which is based upon the selfish herd theory as described by Hamilton (1971). This theory describes predatory interactions between two groups of animals. The two groups are (a) prey and (b) predator. Each prey moves one position to another to escape themselves from the hungry predators. The prey

with maximum survival value is considered as safe and vice versa. The members of predator move to destroy the prey. A predator will be able to kill a herd only if the herd is within a predefined distance known as area of risk and the herd is less fit than the predator. Figure 3 shows the flowchart for the SHO algorithm.

5 Result Analysis

Case-1: Transient study of given system
To analyze the dynamic stability of frequency and T-L power, a two equal area system with both conventional and non-conventional sources is considered. MATLAB/Simulink (2016b) platform is used to simulate the system, under study as shown in Fig. 1. Here PID controllers and 2-DOFFOPID controllers with filter are proposed to study the transient behavior of various parameters. To obtain the optimized values of controller gain parameters, a novel swarm optimization algorithm named as SHO technique is used. To carry out the transient study of the system, a step load of magnitude 0.01 pu is inserted in first area at $t = 0$ s. The dynamic behavior of frequencies and T-L power are given in Fig. 4. The performance indicators such as undershoot (U_{sh}), overshoot (O_{sh}), and settling time (t_s) are shown in Table 1. Table 1 and Fig. 4 show that the 2-DOFFOPIDF controller provides better transient response than classical PID controller in every aspects of the performance indicators. Also, the ITAE in case of 2-DOFFOPIDF controller (0.0047) is less than that of the PID controller (0.0511).

Case-2: Robustness analysis
The demonstrated controller is validated by injecting a randomly varying the load. The random load in inserted in area-1. Figure 5 shows the random load, the change in frequency in area-1 and change in tie-line power between area-1 and area-2. From the transient response, the dynamic stability of the system is established also maintained by randomly varying the load.

6 Conclusion

This work focuses on the performance of 2-DOF FOPIDF controller for minimizing the frequency deviation and tie-line power deviation of an interconnected power system having different sources. For the tuning of the gain parameters of the different controllers, selfish herd optimization technique is preferred. In the recommended system, wind power systems are inserted in each area to meet the required load demand without pollution. The dynamic response of frequencies and tie-line power concluded that 2DOFFOPIDF controller optimized by SHO technique is more powerful than conventional PID controller in all aspects such as undershoot, overshoot, and settling time.

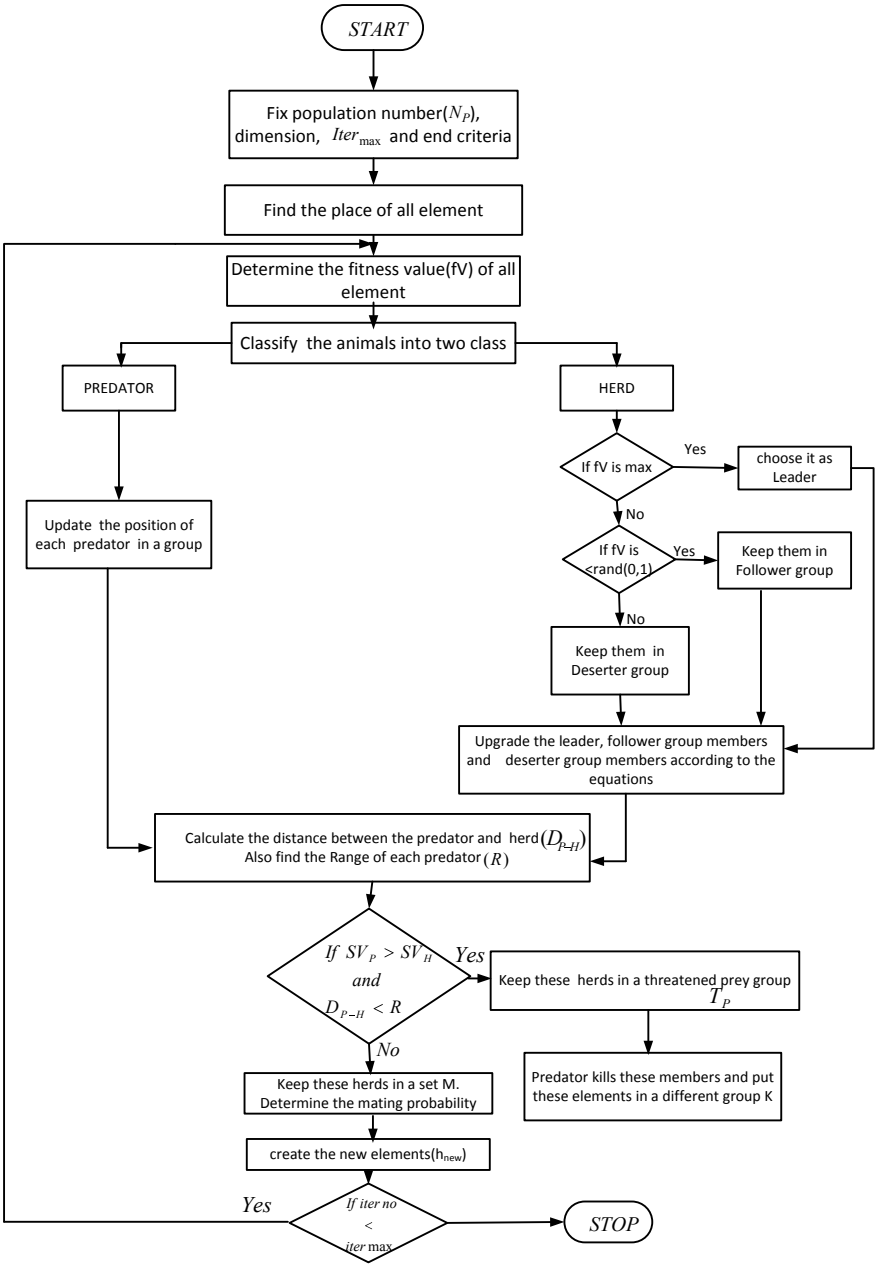

Fig. 3 Flowchart of SHO

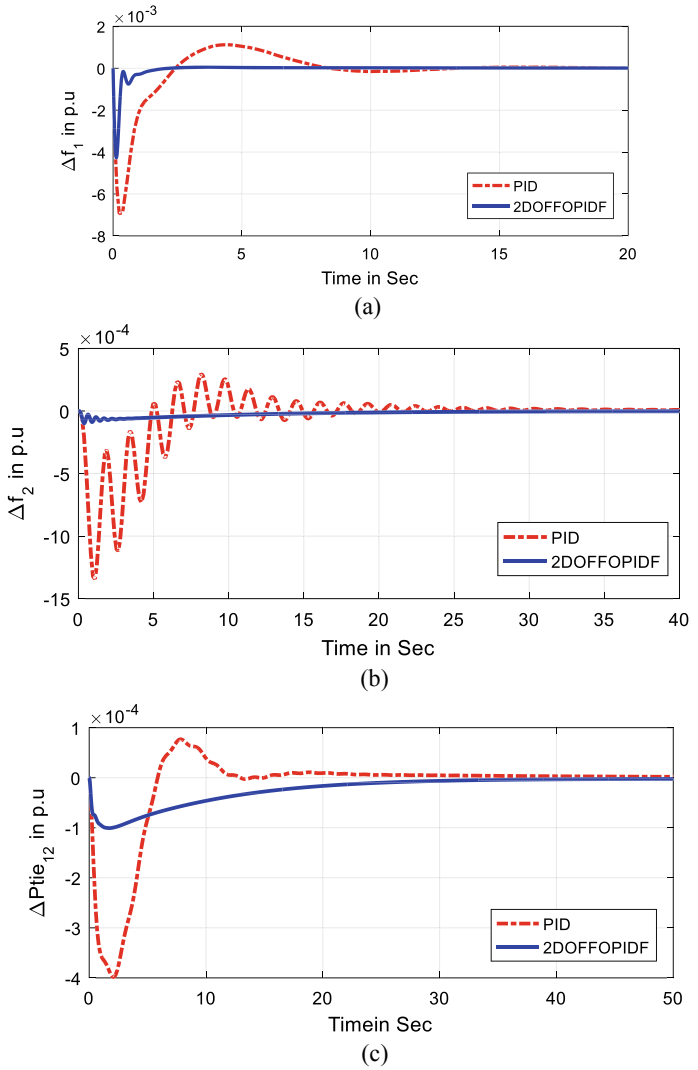

Fig. 4 Transient response curve of area frequencies and tie-line powers **a** frequency deviation in area-1, b frequency deviation in area-2, and **c** tie-line power deviation between areas 1 and 2

Table 1 Transient parameters

	PID			FPIDF		
	U_{sh}	O_{sh}	t_s	U_{sh}	O_{sh}	t_s
Δf_1	−6.9291	1.1209	8.798	−4.2720	0.0470	1.74
Δf_2	−1.3419	0.2953	17.5	−0.0985	0	4.021
$\Delta ptie_{12}$	−0.3984	0.0770	9.589	−0.1006	0	7.893

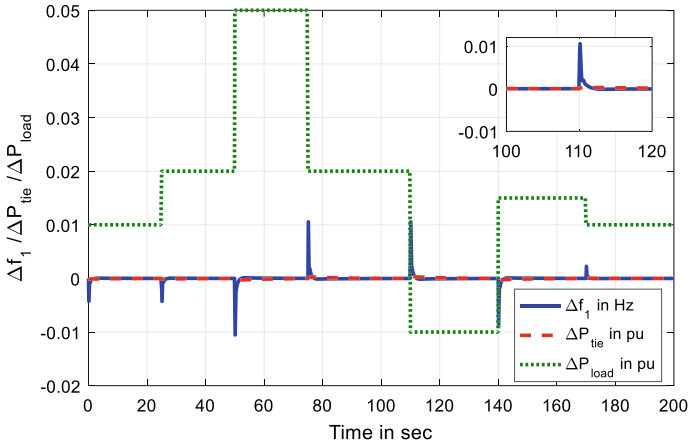

Fig. 5 Random load and its effect on the transient response

7 Future Work

- This work can be extended by adding another area having different energy sources to the existing power system. Again the system may be restructured to prove the efficacy of the controller.
- Further to improve the performance of the proposed 2-DOFFOPIDF controller, another degree of freedom may be added which results in 3-OFFOPIDF controller.

Appendix

$K_{ps1} = K_{ps2} = 120$ Hz/puMW, $T_{ps1} = T_{ps2} = 20$ s, $T_{sg1} = T_{sg2} = 0.08$ s, $T_{T1} = T_{T2} = 0.3$ s, $R_1 = 2.4$ Hz/puMW, $R_2 = 2.4$ Hz/puMW, $R_3 = R_1 B_1 = B_2 = 0.425$ puMW/Hz, $T_{12} = 0.0137$ puMW/rad.

$T_{RH1} = T_{RH2} = 28.75$ s, $T_{RS1} = T_{RS2} = 5$ s, $T_{GH1} = T_{GH2} = 0.2$ s, $T_w = 1$ s, $k_{r1} = k_{r2} = 0.3$, $T_{r1} = T_{r2} = 10$s,

$K_1 = 1.25$, $K_2 = 1.4 T_{P1} = 0.6$ s, $T_{P2} = 0.041$ s.

References

1. Elgerd OI, Fosha CE (1970) Optimum megawatt-frequency control of multi-area electric energy systems. IEEE Trans Power App Syst 89(4)

2. Guha D, Roy PK, Banerjee S (2017) Study of differential search algorithm based automatic generation control of an interconnected thermal-thermal system with governor dead-band. Appl Soft Comput 52:160–175
3. Padhan S, Sahu RK, Panda S (2014) Application of firefly algorithm for load frequency control of multi-area interconnected power system. Electric power components and systems 42(13):1419–1430
4. Hasanien HM, El-Fergany AA (2019) Salp swarm algorithm-based optimal load frequency control of hybrid renewable power systems with communication delay and excitation cross-coupling effect. Electric Power Syst Res 176
5. Rahman A, Saikia LC, Sinha N (2017) Automatic generation control of an interconnected two-area hybrid thermal system considering dish-stirling solar thermal and wind turbine system. Renew Energy 105:41–54
6. Acharyulu BV, Mohanty B, Hota PK (2019) Comparative performance analysis of PID controller with filter for automatic generation control with moth-flame optimization algorithm. In: Applications of artificial intelligence techniques in engineering. Springer, Singapore, pp 509–518
7. Sahu BK, Pati S, Mohanty PK, Panda S (2015) Teaching–learning based optimization algorithm based fuzzy-PID controller for automatic generation control of multi-area power system. Appl Soft Comput 27:240–249
8. Mohanty B (2015) TLBO optimized sliding mode controller for multi-area multi-source nonlinear interconnected AGC system. Int J Electr Power Energy Syst 73:872–881
9. Jena NK, Sahoo S, Sahu BK, Mohanty KB (2021) Frequency stability analysis with fuzzy adaptive selfish herd optimization based optimal sliding mode controller for microgrids. Int J Emerg Electr Power Syst. https://doi.org/10.1515/ijeeps-2021-0105
10. Sahoo S, Jena NK, Dei G, Sahu BK (2019) Self-adaptive fuzzy-PID controller for AGC study in deregulated power system. Indonesian J Electr Eng Informatics (IJEEI) 7(4):650–663
11. Bharath Kumar T, Vani MU (2014) Load frequency control in two area power system using ANFIS. Comput Eng Intell Syst 5:27–35
12. Gorripotu TS, Samalla H, Rao CJM, Azar AT, Pelusi D (2019) TLBO algorithm optimized fractional-order PID controller for AGC of interconnected power system. In: Soft computing in data analytics. Springer, Singapore, pp 847–855
13. Debnath MK, Jena T, Mallick RK (2016) Novel PD-PID cascaded controller for automatic generation control of a multi-area interconnected power system optimized by grey wolf optimization (GWO). In: IEEE 1st International Conference on Power Electronics, Intelligent Control and Energy Systems (ICPEICES). IEEE, pp 1–6
14. Debbarma S, Saikia LC, Sinha N (2014) Solution to automatic generation control problem using firefly algorithm optimized IλDμ controller. ISA Trans 53(2):358–366
15. Ismayil C, Kumar RS, Sindhu, T.K.: Optimal fractional order PID controller for automatic generation control of two area power systems. Int Trans Electr Energy Syst 25(12):3329–3348
16. Tasnin W, Saikia LC (2018) Deregulated AGC of multi-area system incorporating dish-Stirling solar thermal and geothermal power plants using fractional order cascade controller. Int J Electr Power Energy Syst 101:60–74
17. Jena NK, Sahoo S, Sahu BK (2020) Fractional order cascaded controller for AGC study in power system with PV and diesel generating units. J Interdisc Math 23(2):425–434
18. Sahu RK, Panda S, Rout UK (2013) DE optimized parallel 2-DOF PID controller for load frequency control of power system with governor dead-band nonlinearity. Int J Electr Power Energy Syst 49:19–33
19. Jena NK, Patel NC, Sahoo S, Sahu BK, Dash SS, Bayindir R (2020) Application of fractional order cascaded controller for AGC study in power system integrated with renewable sources. Int J Renew Energy Res (IJRER) 10(1):89–100
20. Mohapatra T, Dey AK, Sahu BK (2020) Implementation of Quasi oppositional SSA based two-degree-of freedom fractional order PID controller for AGC with diverse source of generations. IET Gener Transmiss Distrib

21. Fausto F, Cuevas E, Valdivia A, González A (2017) A global optimization algorithm inspired in the behavior of selfish herds. Biosystems 160:39–55
22. Shankar R, Kumar A, Raj U, Chatterjee K (2019) Fruit fly algorithm-based automatic generation control of multiarea interconnected power system with FACTS and AC/DC links in deregulated power environment. Int Trans Electr Energy Syst 29(1)

Performance Assessment of Three-Phase Standalone PV System with Machine Learning-Based Controller

Debswarup Rath, Akshaya Kumar Patra, Bidyadhar Rout, Dillip Kumar Subudhi, and Sanjeeb Kumar Kar

Abstract This work demonstrates simulation and design of standalone PV system. PV system consists of boost converter, multilevel inverter and proposed controller (machine learning-PID controller). In this control approach, the disturbances which caused tuning of PID controller cumbersome are eliminated by using machine learning-based controller. Amongst various techniques, machine learning provides various tools like regression analysis, forecasting, etc. which when used improves efficiency of system. Levenberg–Marquardt algorithm also goes by the name damped least squares method and is designed to work specifically to work with loss function, and it optimizes the parameters of machine learning-PID controller (MLPIDC). The proposed PV system along with MLPIDC has been checked for accuracy, robustness, and stability through MATLAB/Simulink for better justification and real-time implementation.

Keywords Multilevel inverter · PV system · MLPIDC · Levenberg–Marquardt algorithm

1 Introduction

Over the years, solar energy had emerged as one of the viable alternatives to fossil fuel [1, 2]. The basic energy elements of solar energy system are solar cells [3–5].

D. Rath (✉) · S. K. Kar
Department of EE, ITER, S'O'A University, Bhubaneswar 751030, India

S. K. Kar
e-mail: sanjeebkar@soa.ac.in

A. K. Patra
Department of EEE, ITER, S'O'A University, Bhubaneswar 751030, India

B. Rout
Department of EE, VSSUT, Burla 768017, India

D. K. Subudhi
Department of CSIT, ITER, S'O'A University, Bhubaneswar 751030, India

M. Mishra et al. (eds.), *Innovation in Electrical Power Engineering, Communication, and Computing Technology*, Lecture Notes in Electrical Engineering 814,
https://doi.org/10.1007/978-981-16-7076-3_26

Energy generated from solar cell is direct current (DC) in nature. It moreover is very low in magnitude to be inverted to alternating current (AC). There is thus a need to boost the DC voltage which is achieved through boost converters. Some of the approaches that a boost converter can be modelled are classical, canonical approach, discrete time approach, and interleaved models [6, 7]. Almost all of these approaches suffer from performance related issues.

Essentially controllers aid in reduction of error, stabilizing circuit, smooth operation, and making system robust. A few well-known control algorithms include PID controller (PIDC) [8], fractional order controllers (FOC) [9], proportional resonant derivative (PRD) controller [10], LQG controller [11], model predictive controllers (MPC) [12], fuzzy logic controllers (FLC) [13], sliding mode controller [14] amongst others. PIDC are the most common type of controllers. It is a three-input controller. Limitations of PIDC include there exists overshoot and undershoot in outputs, it gives late response to disturbances, it is not stable over entire control process, and it has poor or no recovery rate. However, the problems are not limited by choice of controllers alone but by choice of optimization of controller parameter. It is seen eminently that may not cope up with disturbances present in system. It became eminent that researchers require more robust methods like machine learning techniques to over disturbance issue. ML techniques like Levenberg–Marquardt algorithm (LMA) may also be efficient [15].

Machine learning-based controllers are realized by using artificial neural networks (ANNs). ANNs consist of number of highly interconnected information processing units. MLPIDC is realized with feed forward neural network using LMA machine learning architecture. After choosing and tuning the controller, it is imperative to step up PV-generated voltage.

The stepped-up voltage is fed from inverter to convert into AC. This is done by using reduced switch multilevel inverter (RSMLI). Triggering to these switches is provided by third harmonic injected sinusoidal pulse width modulation (THISPWM) technique which is a proven technique for performance improvement [16]. The measure of total harmonic distortion (THD) and robustness forms the basis of performance assessment. IEEE standards provide a measure for measuring harmonic [17–19].

The remainder of proposed work is organized as follows. Section 2 contains details about mathematical modelling of solar cell, boost converter, THISPWM, and RSMLI. The detailed description of MLPIDC is in Sect. 3. Results and performance analysis are discussed in depth in Sect. 4. Section 5 consists of conclusion following future scope.

2 System Modelling and Problem Formulation

The proposed PV-based system model consists of PV cell, boost converter, controller, RSMLI, and THISPWM triggering circuits. The outline of the PV system is shown

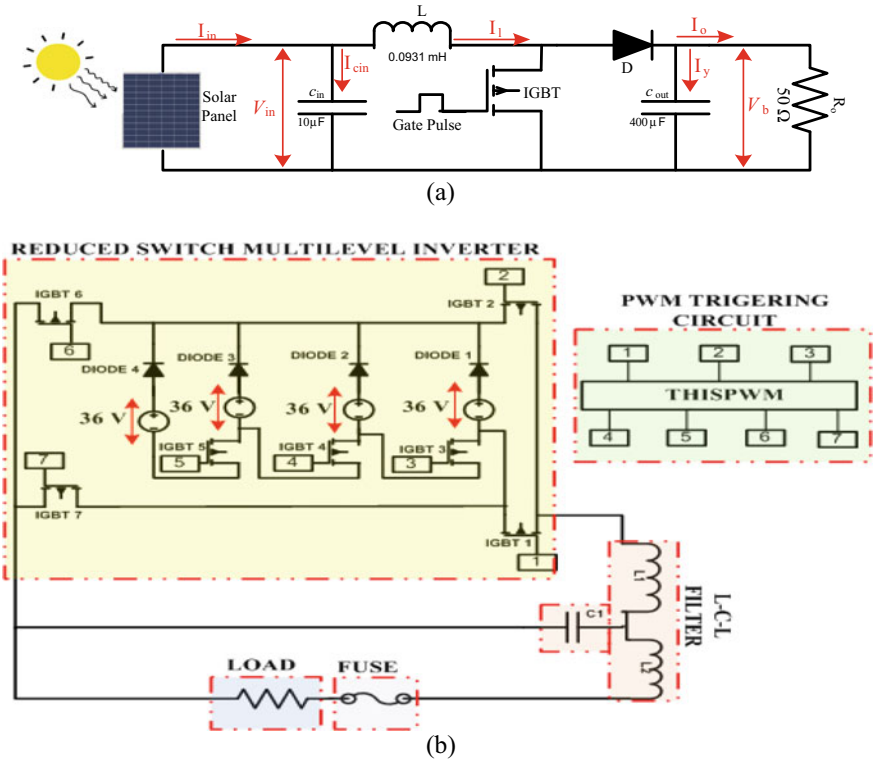

Fig. 1 Block diagram representation of: **a** boost converter system; **b** reduced switch multilevel inverter system

in Fig. 1. In order to generate energy, solar cell uses solar irradiance and temperature as its input. The detailed model of PV system is analysed in subsequent subsections.

2.1 PV Cell

In ideal case, solar cell is a current source in parallel with diode. However, it is not the case. Hence, there are series and shunt compensators associated with the basic solar cell structure [3–5]. Solar cell is modelled by analysing its mathematical equations. Equations (1)–(3) represents output current of solar cell, current through diode, and current through shunt resistance while Eq. (4) voltage across shunt resistance.

$$J = J_l - J_d - J_{\text{sh}} \tag{1}$$

Table 1 Performance indexes

Performance index	Formula	Machine learning equivalent	Formula
ITAE	$\int t * \lvert e(t)\rvert dt$	PSTAE	$\sum t_{peak} * \lvert e_{peak}\rvert$
IAE	$\int e(t)dt$	PSAE	$\sum \lvert e_{\text{peak}}\rvert$
ISE	$\int e(t)^2 dt$	PSSE	$\sum \lvert e_{\text{peak}}\rvert^2$

$$J_d = J_o\left(e^{\frac{V_j}{nV_t}} - 1\right) \tag{2}$$

$$\mathrm{J_{sh}} = \frac{\mathrm{V_j}}{\mathrm{R_{sh}}} \tag{3}$$

$$V_j = V + JR_s \tag{4}$$

Substituting the values of shunt current and diode current in Eq. (1), while R_S, J_0, R_{sh} and n are not measured directly so by using lambert function and using nonlinear regression for compensating, we get Eq. (5). Table 1 lists out the meaning of various symbols used.

$$J = \frac{J_l + J_0\frac{V}{R_{\text{sh}}}}{1 + \frac{R_s}{R_{\text{sh}}}} - \frac{nV_t}{R_s}W\left(\frac{J_0R_s}{nV_t\left(1 + \frac{R_s}{R_{\text{sh}}}\right)}e\left(\frac{V}{nV_t}\left(1 - \frac{R_s}{R_s+R_{sh}}\right) + \frac{(J_l + J_0)R_s}{nV_t\left(1 + \frac{R_s}{R_{sh}}\right)}\right)\right) \tag{5}$$

2.2 *Boost Converter*

Boost converter as the name suggests is used to step up the magnitude of DC voltage. The details of its modelling are described in appending sections.

2.2.1 Working Principle of Boost Converter

Figure 1a represents a boost converter. It has two switches. IGBT is a controlled switch, and diode is an uncontrolled switch. It also has three energy storage elements which are one inductor and two capacitors.

The boost converters are designed to convert fluctuating DC input voltage to a constant magnitude output voltage [6–9]. IGBT and diode make a good switching pair and are switched alternatively which provides better switching. These boost converters have an efficiency (η) of 95%. The magnitude of output voltage depends on duty cycle which is the ratio between changes in voltage to output voltage. It is

expressed in per unit terms. It is represented by Eq. (6).

$$\text{DutyCycle} = D = \left(1 - \frac{V_{\text{in}}}{V_b}\right)^{*} \eta \tag{6}$$

The relationship between output current (I_o) and current (I_y) across output capacitor (C_{out}) is expressed by Eqs. (7, 8), respectively.

$$I_o R_o - \frac{1}{C_{\text{out}}} \int_0^t I_y \mathrm{d}t = 0 \tag{7}$$

$$V_b = I_o R_o = \frac{1}{C_{\text{out}}} \int_0^t I_y \mathrm{d}t \tag{8}$$

$$I_y = I_l - I_o \tag{9}$$

$$\frac{1}{C\text{in}} \int (I_{\text{in}} - I_l)\mathrm{d}t - \frac{1}{C_{\text{out}}} \int I_y \mathrm{d}t = L \frac{\mathrm{d}I_l}{\mathrm{d}t} \tag{10}$$

Equation (9) expresses the relationship between I_y,I_o and current from inductor (I_l). Equation (10) expresses relationship between input current (I_{in}), I_y, and I_l respectively. Input voltage (V_{in}) is expressed mathematically in Eq. (11). Equation (12) represents the current across input capacitor (C_{in}).

$$V_{in} = \frac{1}{C_{\text{in}}} \int_0^t (I_{\text{in}} - I_l)\mathrm{d}t \tag{11}$$

$$I_{ci\text{n}} = I_{\text{in}} - I_l \tag{12}$$

2.3 *Reduced Switch Multilevel Inverter (RSMLI)*

The inverter converts DC electricity from sources like solar cells, batteries, etc. to AC electricity. In this proposed model, the use of reduced number of switches in a multilevel inverter is an efficient way to improve the performance of multilevel inverters. The number of switches and sources required for realizing the structure of RSMLI is given by Eq. (13–14)

$$\text{Totality of controlled switching devices} = \frac{P + 5}{2} \tag{13}$$

$$\text{Totality of source} = \frac{P-1}{2} \tag{14}$$

where P is the level of RSMLI. In proposed RSMLI, P is taken as 9, and it has seven switches and four sources.

In case of the reduced switch multilevel inverter (RSMLI), the pair of S_1, S_5, S_6, and S_7 form the basic bridge circuit. S_1, S_5, S_6, and S_7 are complementary to each other in pairs. First S_6 and S_7 triggered and then S_1 and S_5 turned on. S_2, S_3, and S_4 are triggered to give the peak voltages.

2.3.1 Harmonics in RSMLI

Total harmonic distortion is defined as the ratio of sum of the powers of all harmonic components to the power of the fundamental component. It is expressed mathematically by the expression Eq. (15), v_1 is the fundamental component, and the harmonic components are v_2, $v_3 \ldots v_n$. Low values of harmonic distortions indicate low peak current, high power factor, and high efficiency.

$$\text{THD} = \sqrt{\frac{((v_2)^2 + (v_3)^2 \ldots\ldots (v_n)^2)}{v_1}} \times 100\% \tag{15}$$

2.4 *Third Harmonic Injected Sinusoidal Pulse Width Modulation (THISPWM)*

In third harmonic injected sinusoidal pulse width modulation (THISPWM), a third harmonic wave is added to the reference sinusoidal. The amplitude of the harmonic injected wave is one-sixth of the sinusoidal reference. V_{car}, V_{ref} are maximum magnitude of the carrier and sinusoidal wave, respectively. The load frequency and the modulation index are controlled by frequency. Modulation index controls root mean square (RMS) value of the output voltage. The output voltage (V_{outRMS}) and the modulation index (m_a) are expressed as Eq. (16–17), where T is the total time period, and T_{on} is the width of the n^{th} pulse, then respectively. The modified sinusoidal reference is expressed in Eq. (18)

$$V_{\text{outRMS}} = V_s \sqrt{\left(\sum_{b=1}^{2n} \frac{2T_{\text{on}}}{T}\right)} \tag{16}$$

$$m_a = \frac{V_c}{V_{\text{car}}} \tag{17}$$

$$V_{\text{ref}} = V_1 c_{\max} \text{Sin}(\omega t) + V_3 c_{\max} \text{Sin}(3\omega t) \tag{18}$$

where $V_{1_{\max}}$, $V_{3_{\max}}$ represent the fundamental and injected third harmonic component of modified reference.

2.5 Feed Forward Neural Network (FNN)

The proposed controller is designed using feed forward neural network (FNN) architecture. FNN is a type of ANN where connections between nodes do not form a cycle. It only moves in forward direction. It moves from input to output layer. Neural network consists of input layer, output layer, and hidden layer. It only moves in forward direction. In FNN, information moves in forward direction only. It moves from input to hidden layer to output layer. Hidden layer does the intermediate computations before processing data forward. The proposed MLPIDC is modelled as multilayer neural network with 22 hidden layers and one input layer and one output layer.

3 Weight Updating Algorithm

Broadly, the algorithms of interest for designing machine learning-based PIDC are Levenberg–Marquardt algorithm (LMA).

3.1 Levenberg–Marquardt Algorithm (LMA)

LMA is also known as damped least square method. It is designed to work for cost function or loss function. It works by computing gradient vector and Jacobian matrix. Let us consider a cost function or loss function f. It is defined below in Eq. (19).

$$f = \sum_{i=1}^{m} e_i^2 \tag{19}$$

where m is number of data sets. As per our classical practice, we often choose one between integral time absolute error (ITAE), integral square error (ISE), integral absolute error (IAE), etc. as performance indexes. However, with a slight modification, the same formulas can be used as cost or loss functions. Machine learning equivalent of performance indexes is Peak Sum Time Absolute Error (PSTAE), Peak

Sum Absolute Error (PSAE), and Peak Sum Square Error (PSSE). Table 1 highlights the relation between machine learning equivalents of performance indexes.

We can define cost function or loss function by Eq. (20)

$$f = \sum_{\text{peak}=1}^{m} t_{\text{peak}} * \left| e_{\text{peak}} \right| \tag{20}$$

We can define Jacobian matrix by Eq. (21)

$$J_{i \cdot j} = \frac{\partial e_i}{\partial w_j} \tag{21}$$

where e_i and w_j are error vector and parameter vector respectively. i and j are number of instances of dataset and number of parameters, respectively. Gradient vector (∇f) and hessian approximation (H_f) of cost function are defined by Eq. (22)

$$\begin{aligned} \nabla f &= 2J^T \cdot e \\ H_f &\approx 2J^T \cdot J + \lambda I \end{aligned} \tag{22}$$

where λ and I are damping factor and identity matrix, respectively. The improvements in parameter are expressed by formula in Eq. (23).

$$w^{(i+1)} = w^i = -\left(J^{(i)T} \cdot J^{(i)} + \lambda^{(i)} I\right)^{-1} \cdot \left(2J^{(i)T} \cdot e^{(i)}\right) \tag{23}$$

If an iteration fails, then λ increases by some factor but, however, if it is successful, loss or cost function decreases with decrease in λ. This process is on contrary speeds up iteration. Flowchart is represented in Fig. 2b.

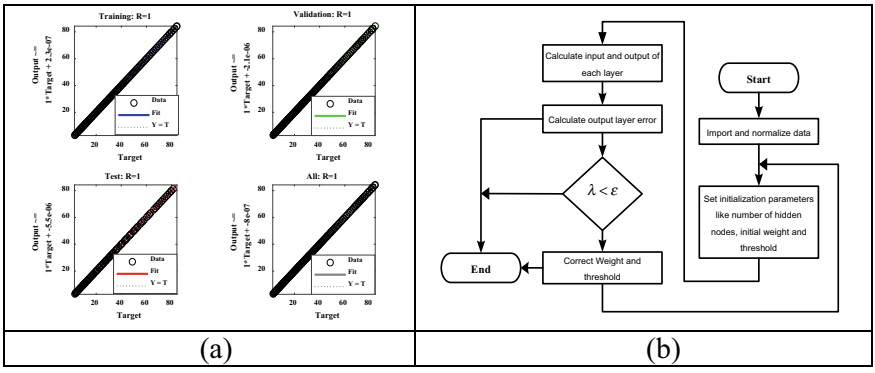

Fig. 2 **a** Regression analysis plot for Levenberg–Marquardt algorithm; **b** flowchart for Levenberg–Marquardt algorithm

4 Results

The comparison between the above-mentioned algorithms is given by Table 2.

The performance of algorithms is evaluated by obtaining different plots such as error plot, regression plot, error histogram, plot fit, and training state, Mean Square Error (MSE) and regression. Regression plots give the information about how the data are scattered. It as maximum value of 1 and minimum value of 0.1 means model is a perfect fit and 0 means model is not a fit; it is represented in Fig. 2a.

Number of bars in error histogram indicates how many times error had occurred. Error histogram is plotted between error and its instance of occurring. If maximum instances have no or less error, then training is good with minimum anomalies, and error histogram is represented Fig. 3.

Training failures are highlighted by training state plot. It is observed that training state plots give less or minimum number of failures; hence, it is best fit. Pool training failures are represented in Fig. 4.

Table 2 Performance of Levenberg–Marquardt algorithm

Category of data	Samples	MSE	*R*	Algorithm
Training	147,023	1.4433e−8	1	Levenberg–Marquardt algorithm
Validation	42,007	1.16927e−8	1	
Testing	21,003	1.10563e−8	1	

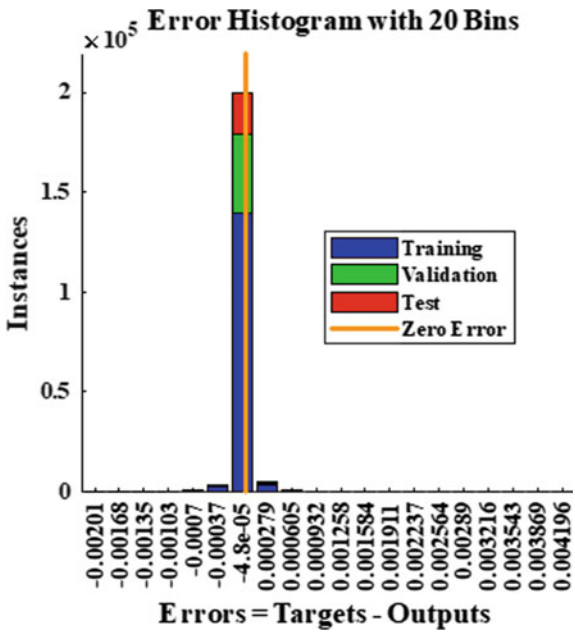

Fig. 3 Error histogram analysis plot for Levenberg–Marquardt algorithm

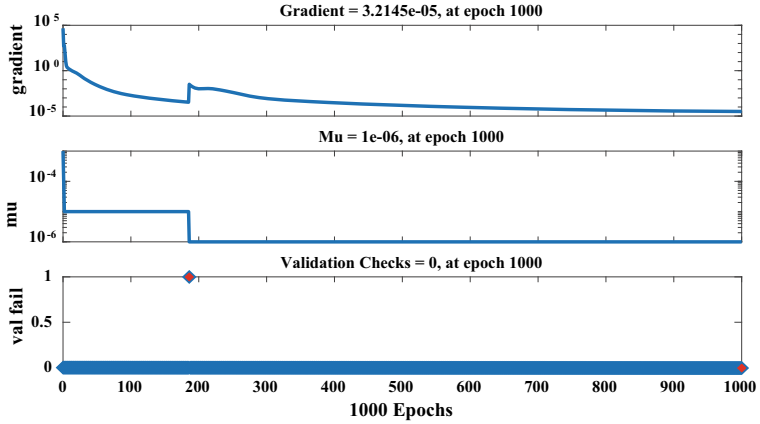

Fig. 4 Training validation analysis plot for Levenberg–Marquardt algorithm

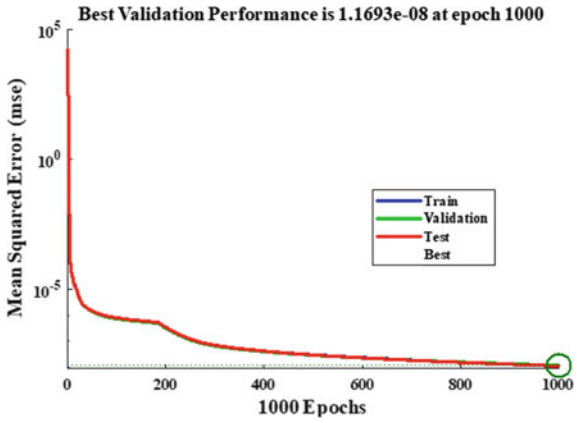

Fig. 5 Performance analysis plots for Levenberg–Marquardt algorithm

Training performance of algorithms is evaluated by training state plot. The performance is satisfactory if the error value is less for every epoch, and the best validation performance value should be minimum. Performance validation is represented in Fig. 5.

The solar array output is very low to be inverted to alternating quantity. Boost converter steps up direct current voltage. It steps up voltage from 17 to 36 V. This is represented in Fig. 6.

After stepping up voltage, it is fed to inverter. The inverter is reduced switch multilevel inverter. In this inverter, the direct quantity is inverted into three-phase alternating quantity. This is represented in Fig. 7a, b. This three-phase supply is then fed to load, while three-phase voltage and current are seen to be 550 V and 5 A.

The harmonic of load current is found out to be 0.19%, and its induced voltage harmonic is 0.38%. This is represented in Fig. 8a, b.

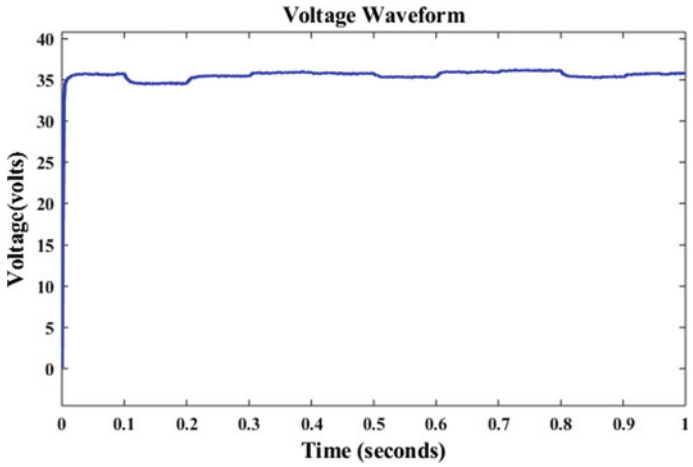

Fig. 6 Output of boost converter

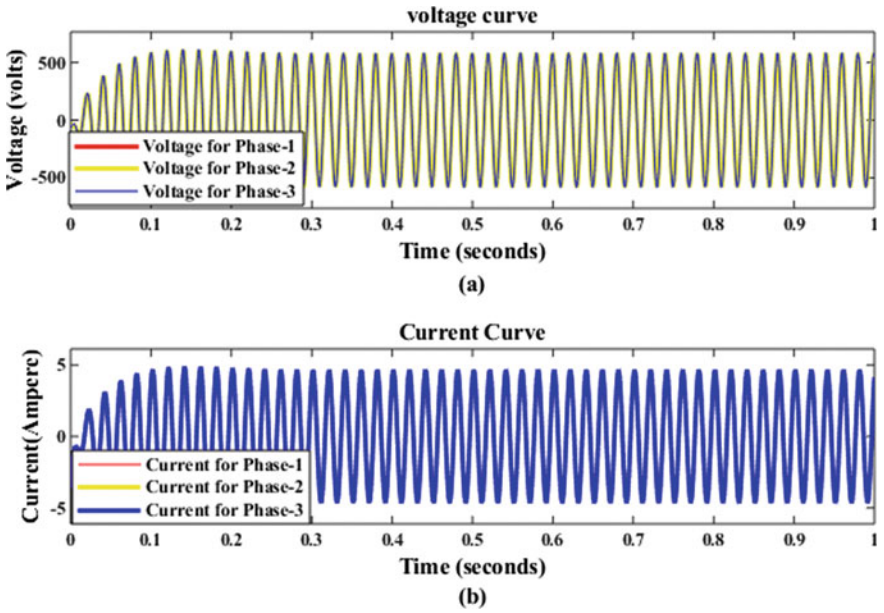

Fig. 7 Output of three-phase multilevel inverter

Stability of any controller or for the matter of entire proposed PV system is essential for any validation of model. The proposed model is analysed for a wide range of frequency spectrum. It is seen from Fig. 9 that the proposed model is stable for higher-order frequency response. It can be seen from Fig. 9 that smoothness for the higher-order frequency explains its stability and validity.

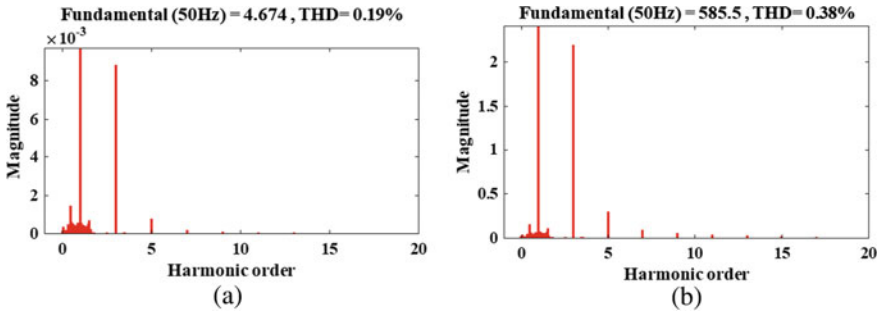

Fig. 8 **a** Current harmonic of three-phase multilevel inverter; **b** voltage harmonic of three-phase multilevel inverter

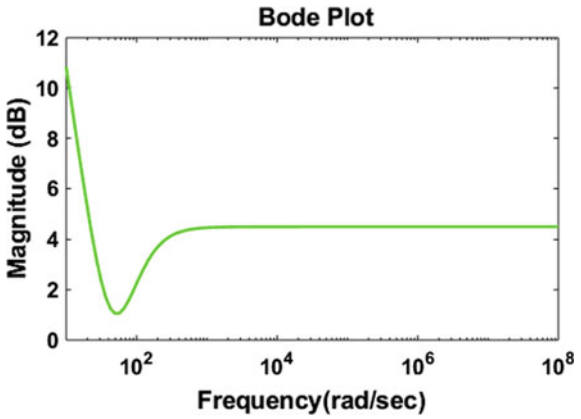

Fig. 9 Stability response (bode plot) of three-phase multilevel inverter

Robustness is the ability of system to maintain constant output irrespective of input fluctuations. The variation of irradiance is ten from 800 to 1300 W/m^2. The voltage of boost converter varies from 35 V to 35.9 V, while three-phase voltage and current are seen to be invariant and remain fixed at 550 V and 5 amperes. Figure 10a–d represents robustness of proposed PV system.

5 Conclusions

The work demonstrated simulation and design of PV system. PV system consisted of boost converter, multilevel inverter, and proposed controller (machine learning-PID controller). This proposed controller is seen to have inherited the characteristics of PIDC, but it overcame the entire basic problem (which is already highlighted in previous sections) associated with traditional PIDC. Machine learning-based approach proved effective which can be explained by simulations of proposed

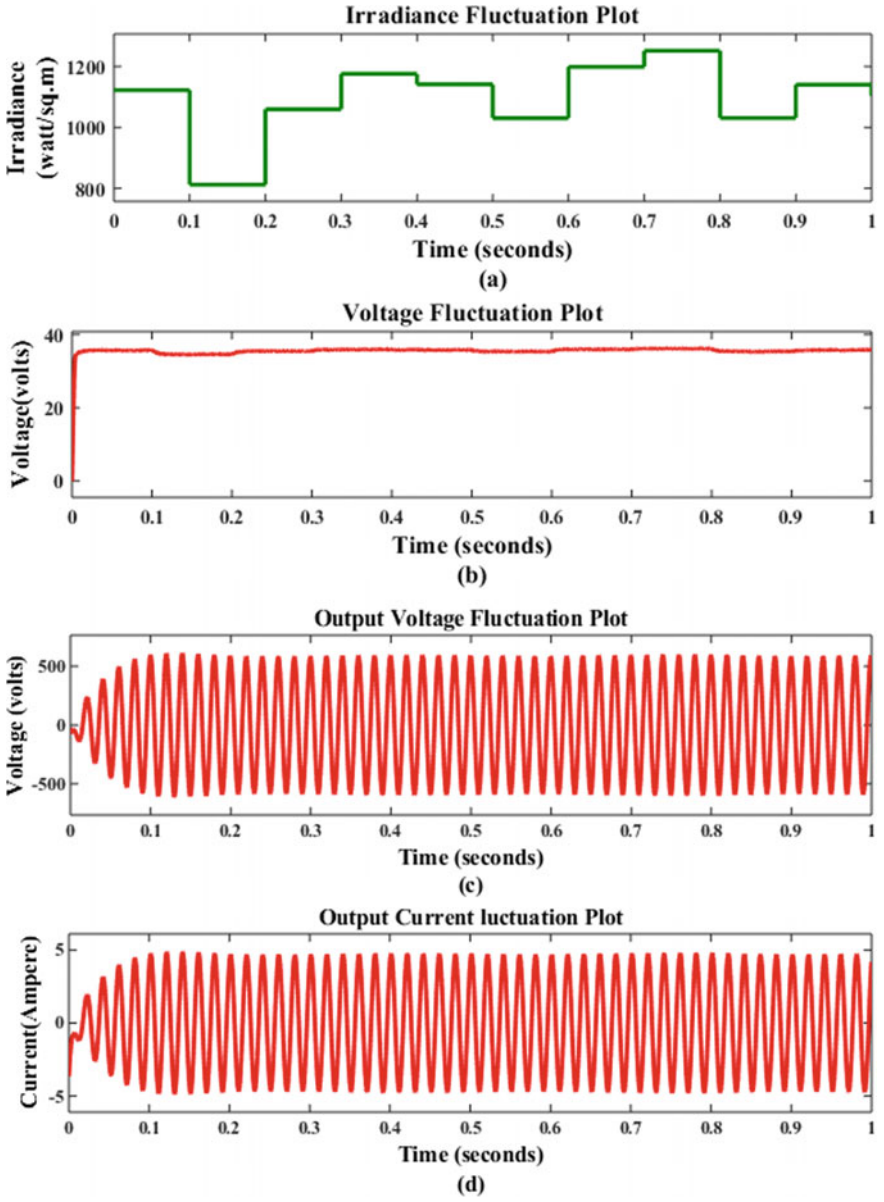

Fig. 10 Robustness analysis of proposed PV system **a** variation of irradiance; **b** fluctuation of output voltage of boost converter; **c** fluctuation of output voltage of three-phase multilevel inverter; **d** fluctuation of output current of three-phase multilevel inverter

model. The model was analysed for performance, stability, and robustness. The simulation results predict better performance, improved stability, and better robustness ability, hence paving way for its real-time implementation.

References

1. Swain MK, Mishra M, Bansal RC, Hasan S (2021) A self-powered solar panel automated cleaning system: design and testing analysis. Electr Power Compon Syst 1–13
2. Mishra M, Dash PB, Nayak J, Naik B, Swain SK (2020) Deep learning and wavelet transform integrated approach for short-term solar PV power prediction. Measurement 166:108250
3. Ghani F, Rosengarten G, Duke M, Carson JK (2014) The numerical calculation of single-diode solar-cell modelling parameters. Renew Energy 72:105–112
4. Louzazni M (2015) An analytical mathematical modeling to extract the parameters of solar cell from implicit equation to explicit form. Appl Solar Energy 51(3):165–171
5. Sira-Ramirez H, Ilic-Spong M (1989) Exact linearization in switched-mode DC-to-DC power converters. Int J Control 50(2):511–524
6. Alkrunz M, Yazici I (2016) Design of discrete time controllers for the DC-DC boost converter. Sakarya Univ J Sci 20(1):75–82
7. Chaiyatham T, Ngamroo I (2014) Improvement of power system transient stability by PV farm with fuzzy gain scheduling of PID controller. IEEE Syst J 11(3):1684–1691
8. Rath D, Kar S, Patra AK (2021) harmonic distortion assessment in the single-phase photovoltaic (PV) system based on SPWM technique. Arab J Sci Eng. https://doi.org/10.1007/s13369-021-05437-6
9. Hemakesavulu O, Chellammal N, Dash SS, Lalitha S (2017, November) A new PR-D (Proportional Resonant and Derivative) controller for resonance damping in a grid connected reverse voltage topology multi-level inverter. In: 2017 IEEE 6th international conference on renewable energy research and applications (ICRERA), pp 653–658. IEEE
10. Huerta F, Perez J, Cóbreces S, Rizo M (2018) Frequency-adaptive multiresonant LQG state-feedback current controller for LCL-filtered VSCs under distorted grid voltages. IEEE Trans Industr Electron 65(11):8433–8444
11. Talbi B, Krim F, Laib A, Sahli A (2020) Model predictive voltage control of a single-phase inverter with output LC filter for stand-alone renewable energy systems. Electr Eng 1–10
12. Zeb K, Islam SU, Din WU, Khan I, Ishfaq M, Busarello TDC, Ahmad I, Kim HJ (2019) Design of fuzzy-PI and fuzzy-sliding mode controllers for single-phase two-stages grid-connected transformerless photovoltaic inverter. Electronics 8(5):520
13. Cortajarena JA, Barambones O, Alkorta P, De Marcos J (2017) Sliding mode control of grid-tied single-phase inverter in a photovoltaic MPPT application. Sol Energy 155:793–804
14. Ata A, Khan MA, Abbas S, Ahmad G, Fatima A (2019) Modelling smart road traffic congestion control system using machine learning techniques. Neural Netw World 29(2):99–110
15. Lin CM, Hsu CF (2003) Neural-network hybrid control for antilock braking systems. IEEE Trans Neural Netw 14(2):351–359
16. Quraan M, Tricoli P, D'Arco S, Piegari L (2016) Efficiency assessment of modular multilevel converters for battery electric vehicles. IEEE Trans Power Electron 32(3):2041–2051
17. IEEE Recommended Practice and Requirements for Harmonic Control in Electric Power Systems (2014), in IEEE Std 519–2014 (Revision of IEEE Std 519–1992), pp 1–29
18. Sadeghkhani I (2018) Analysis of hybrid reference frame limiting strategy performance in the presence of secondary control of inverter based islanded microgrids. J Intell Proced Electr Technol 9(33):3–14
19. Malla N, Tamrakar U, Tonkoski R (2017) Online learning control for harmonics reduction based on current controlled voltage source power inverters. IEEE J Autom Sinica 4(3):447–457

A Hybrid-Based Ensemble Learning Model and DNN for Automated Diagnosis of Brain Tumor from MRI Images

Basra Jehangir and Soumya Ranjan Nayak

Abstract A brain tumor is a life-threatening condition that can disrupt the human body's normal functioning. Manual detection of the type of tumor may be time-consuming and sometimes may have many human errors. Hence, a need for an automated process arises. This paper focuses on detecting brain tumor and tumor classification into 3 types: meningioma, glioma, and pituitary tumor. In this work, a simple convolutional neural network (CNN) for feature extraction and, finally, an ensemble of Machine Learning algorithms for classification is used. The ensemble of machine learning algorithms includes Random Forest Classifier, Support Vector Classifier, K Neighbors classifier, Gaussian Naive Bayes, and boosting classifiers such as XGBoost and gradient boosting classifiers. Finally, voting classification is used, and the type of voting used is hard voting. In which, the support vector classifier acquired the maximum classification accuracy of 92.72%.

Keywords Random forest classifier · K neighbor classifier · Support vector classifier · Gaussian naïve bayes · Boosting classifiers · Ensemble

1 Introduction

A brain tumor is a mass of flesh with irregular cell growth and their multiplication. There are 130 different brain tumors, each originating in different brain regions depending on the cell type. The most common diagnostic tools for the detection and examination of Brain Tumors are Computed Tomography (CT) scan and Magnetic Resonance Imaging (MRI). Since digital Image processing is currently gaining high popularity and is used in image classification, we have classified the images based on whether the brain has a tumor and which type of tumor. In the health care system, CNN has gained massive importance because of the advancements in biomedical

B. Jehangir · S. R. Nayak (✉)
Amity School of Engineering and Technology, Amity University Uttar Pradesh, Noida, India

B. Jehangir
e-mail: basra.jehangir@s.amity.edu

M. Mishra et al. (eds.), *Innovation in Electrical Power Engineering, Communication, and Computing Technology*, Lecture Notes in Electrical Engineering 814,
https://doi.org/10.1007/978-981-16-7076-3_27

image processing, reducing time and human resources [1–3]. It has reduced the pressure on radiologists and doctors to diagnose and classify various diseases such as chest disease, cancer cell, and tumor detection.

A multiclass classification of brain MRIs is performed in this work, and classification of data into glioma, meningioma, pituitary, and no tumor is performed. The methodology followed is a combination of the CNN model and an ensemble of several Machine Learning models. The CNN model used here is a 22 layered model and is used for feature extraction of the data. These extracted features are then inserted into the Machine Learning models. Based on extracted features, to classify brain tumors, machine learning models are prepared. Finally, after all of these machine learning models have been combined to construct a voting ensemble that is more effective than a single model, and the results are finally recorded.

2 Related Work

There are over 130 different types of brain tumors. These are majorly classified into cancerous or malignant and non-cancerous or benign brain tumors. They can develop in every part of our brain or spinal cord. We divided the data into three groups of tumors in this study: meningioma, pituitary, and glioma tumor, and the fourth one of no tumor. The meningioma tumor begins in the membrane that covers the brain and spinal cord, known as the meninges. Glioma tumor starts in the glial cells. The pituitary tumor starts in the pituitary gland. The classification dataset we used is an open-source data collection available on GitHub that includes 3160 images of three different types of tumors and no tumor.

Feature extraction reduces the dimensionality of data by removing redundant data, which increases the training speed of the learned model. Kaplan et al. [4] extracted brain tumor features and then classified their data using K-Nearest Neighbor (Knn) and Artificial Neural Networks (ANN), Random Forest (RF), Averaged One dependency estimator (AODE), and Linear Discriminant Analysis (LDA) classification methods, with a 95.56 percent accuracy. Gumaei et al. [5] extracted the features by a hybrid method and then classified the brain tumors by Regularized extreme machine learning (REML). Sachdeva et al. [6] performed feature extraction, segmentation, and multiclass classification in which classification was done using the combination of PCA and ANN into six classes. Kumar et al. [7] extracted the features by the discrete wavelet transform, Genetic algorithms for diminishing the number of features, and SVM for image classification. Rammurthy and Mahesh [8] used cellular automata and rough set theory to segment the data, then extracted features from the segments, and used deep convolutional neural networks to detect brain tumors. Finally, the proposed Whale Harris hawks optimization (WHHO) method is used to classify the data. Tuba et el. [9], classification and feature selection by brainstorm optimization and support vector machines is done.

Two types of neural networks were used by Paul et al. [10] to identify brain tumor types: fully connected and convolutional neural networks. Mehrotra et al. [11]

performed binary classification of brain tumors into malignant and benign by transfer learning of artificial neural networks. Mohammed et al. [12] also performed binary classification by using CNN and achieved an accuracy of 95%. K. Machhale et al. [13] performed a classification of 50 images by SVM, K-NN, and a hybrid of SVM and KNN. For feature extraction, Cheng et al. [14] used a strength histogram, a gray level matrix, and a bag of words (BOW). Hashemzehi et al. [15] used a hybrid of NADE and CNN to train the images for the classification of a brain tumor.

Ghassemi et al. [16] used a pre-trained deep neural network as a discriminator of GAN on different data sets of MR images, and then the fully connected layers (FCLs) are replaced. The model is trained to produce a classification of 3 types of brain tumor. In the work of Z. N. K. Swati et al. to close the distance between the low-level features captured by MRIs of the brain and the high-level features captured by the human eye, researchers used a content-based image retrieval (CIBR) system. Rai Hari Mohan and Kalyan Chatterjee [17], in their work, tried to perform binary classification of the normal and abnormal brain with the dataset of 233 MRIs and Precision, Recall, Specificity, F-score, and Accuracy were used to test the proposed model's results, which was compared to the performance of the other two forms of model, Le-Net and VGG-16.The accuracy of the proposed model was 98% and was compared with VGG-16 and Le-net [18]. In Shahriar Sazzad et al. [19], threshold-based OTSU segmentation is used in brain tumor classification, and the accuracy of batch1, batch2 and batch 3 are 95 92.5, and 87.5, respectively. Lavanyadevi et al. [20] performed classification and segmentation of brain tumor. The classification was done by PNN algorithm, and the segmentation was done by k means clustering algorithm.

This study's work is based on a binary classification done by Saha et al. [21] in classifying the chest x-rays as COVID-19 affected or healthy. Feature extraction is done by a simple CNN model and the classification by an ensemble of Machine Learning models. Similar kind of work also reported where CNN based architecture and machine learning based algorithm used for feature extraction [22–24]. The accuracy acquired by this model is 98.91%. However, in this study, multiclass classification is performed, and the number of Machine Learning models is increased more to increase the scope of getting higher accuracy.

3 Proposed Work and Methodology

The data that is used for this study was acquired through GitHub. This data set contains a total of 3160 images of different types of brain tumors. These images were initially imported and then resized so that there is uniformity in terms of image size. The data is then normalized for similarity in pixel distribution. After that the data is divided into various parts of training, validation, and testing. Using the former two, the CNN model is trained. The model is run over 60 epochs, at which the model gave an expected result. The extracted features are taken just before the fully connected layer and after which they are inserted into the Machine Learning algorithms. These

ML algorithms are Random Forest, SVC, K Neighbor Classifier, Gaussian Naive Bayes, and boosting algorithms such as XGBoost and gradient boosting Classifier.

3.1 Dataset Used

The brain tumor dataset used is a freely available data collection on GitHub [25] that includes 3160 weighted photographs from patients with three different types of brain tumors: meningioma, glioma, pituitary tumor, and no tumor. The Glioma Tumor has 926 images, the Meningioma tumor has 937 images, the pituitary tumor has 901 images, and the remaining 396 images are of no tumor. The MRIs provided in this dataset is a combination of T1 and T2 types. The data is then divided into Testing and Training as per requirement. Some of the images can be seen in Fig. 1.

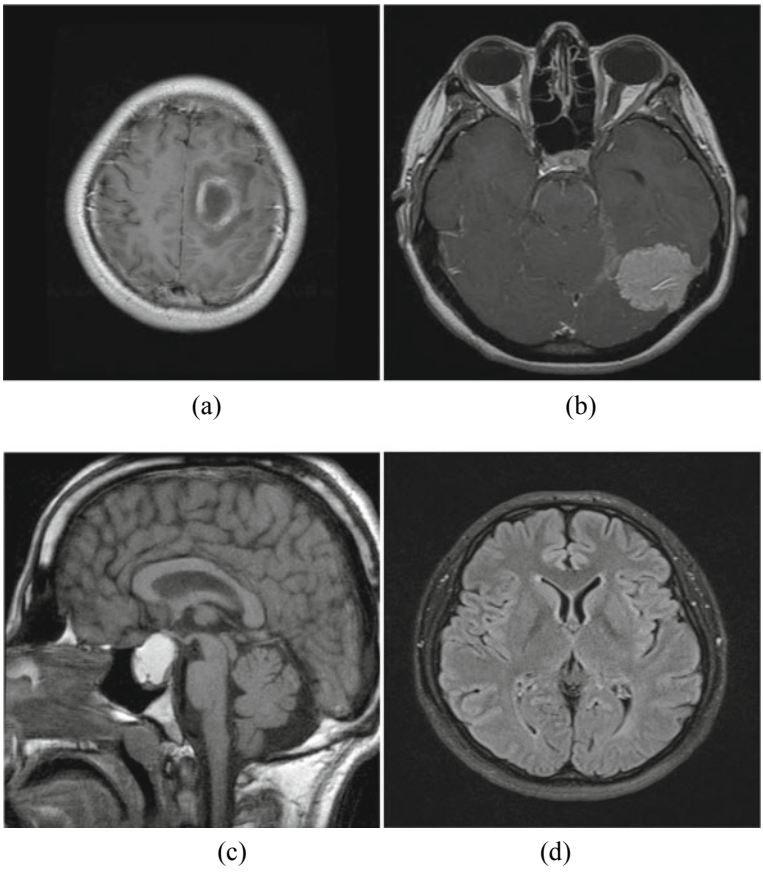

Fig. 1 Sample images from data set, **a** glioma tumor, **b** meningioma, **c** Pituitary tumor, **d** no tumor

That contains sample images each from Glioma tumor in Fig. 1a, meningioma in Fig. 1b, Pituitary tumor in Fig. 1c, and no tumor in Fig. 1d.

3.2 Preprocessing

All images are of different sizes. These images are resized to the scale of (70, 70) in RGB format of equal sizes. Data normalization is also performed so that the images can be inserted into a CNN model. The data is then separated into three categories: training data, validation data, and testing data. Training data is used to train the model, validation data is used to validate the model and perform hyper parameter tuning, and testing data is used to test the model. The entire data set is divided into a ratio of 6:2:2 for training, validation, and testing purposes. Further, this data is normalized before passing through the CNN model.

3.3 Proposed Model

The proposed approach uses a Convolutional Neural Network and several ML models combined to form an ensemble. For feature extraction, the CNN model is used, and Machine Learning algorithms are used for classification. The features extracted by the CNN model connect the two models, and this can be seen diagrammatically in Fig. 2.

3.3.1 The CNN Model

CNN is a deep learning model that is often used to explore visual imagery. The main benefit of using a CNN over other DL models is that it is constrained to deal with image data exclusively. The CNN sequential model that is used in this work is relatively simple than other transfer learning models as it contains only 22 layers. After performing image normalization, the pixels are inserted into the CNN model in an array. The initial layer is a convolutional 2-dimensional input layer that receives an input and outputs the shape (70, 70, 3). The CNN model can be seen structurally in Fig. 3.

The deeper layers perform the feature extraction until the first fully connected layer (FCL). The Convolutional layer, Rectified Linear Unit and Pooling layer extract features from the data set in the model.

The convolutional layer is the first layer that extracts features from the data. It performs mathematical operations between the input image matrix and the filter or kernel. The filter moved step by step and performed element-wise product between the image and the filter. For the first layer, a filter size of 32 was used, which was increased to 64, 128,256,512, and 1024 as the layers keep on increasing. The value

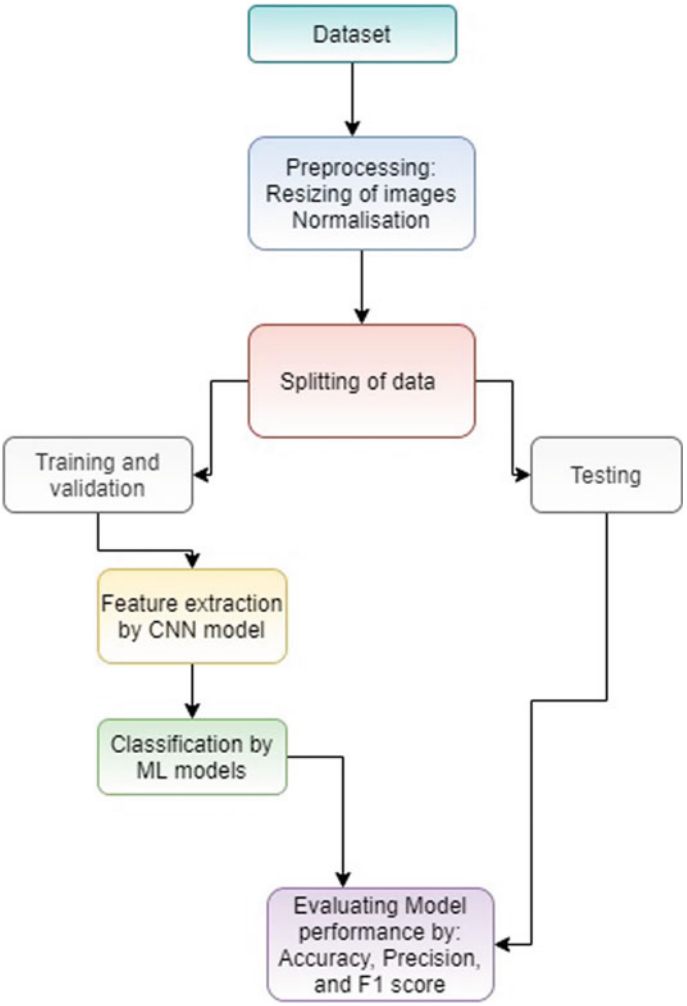

Fig. 2 Proposed Hybrid model for brain tumor analysis

of stride determines how much we move the filter across the image. In this work, the stride value is 1, lower the stride value higher is the output volume. The padding that we used for the model in this work is the same so that the filter fully covers the image.

The ReLu (Rectified Linear Unit) introduces non-linearity to our data by setting all the negative values to zero. The shallow layers of the model are used to detect low-level features such as edges and boundaries. However, as we go deeper into the model, the complexity of features is increased gradually with each layer until the fully connected layer.

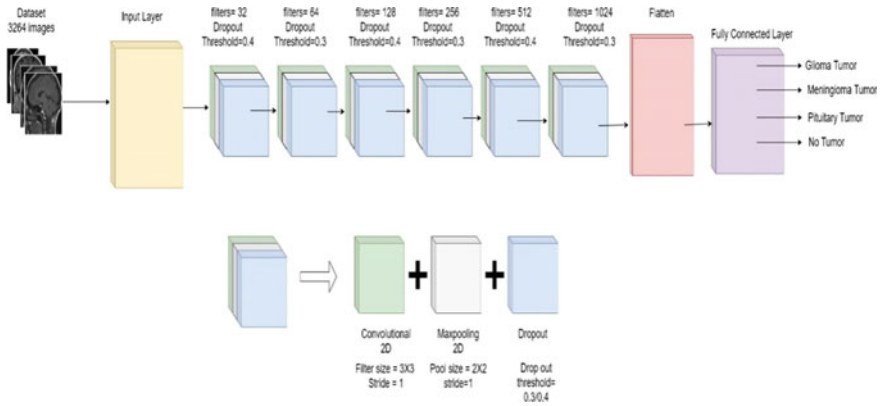

Fig. 3 Structure of CNN model deployed in proposed hybrid model

The pooling layer is similar to the convolutional layer because it reduces the spatial size of the feature maps. The type of pooling used in this model is max pooling with a pool size of (2, 2). This max pooling layer returns the maximum value in the portion covered by the kernel. The main use of this max pooling layer is to prevent over fitting and de-noising the data by providing an abstract form of data.

Convolution is an effective way of extraction of features as it is very efficient in reducing the dimensions of data and producing less redundant data, which is then fed to the flatten layer, which converts the resultant two-dimensional arrays into a single long linear vector. After fattening the matrix, we feed it to the fully connected layer (FCL). The number of neurons in FCL is 32. The activation function used in the fully connected layer is "Softmax." The structure of the CNN model can be seen in Table1.

The model was run over 60 epochs; however, on using higher values, accuracy started to saturate.

3.3.2 Machine Learning Model for Classification

After extracting features by the deeper layer of the CNN, the shape of the CNN output produced is (1860, 1024), this output is then taken as input into the ML algorithms combined to develop an ensemble classifier. The classification is done based on voting classification. The type of voting classification used is hard voting. Each model votes for a class in hard voting, also known as majority voting, and the model with the most votes wins. The different Machine Learning models used are Random Forest Classifier, SVC, K Neighbor classifier, Gaussian Naive Bayes, and boosting classifiers such as XGBoost and gradient boosting classifiers. The entire structure can be seen in Figs. 4 and 5.

Table 1 Structure of CNN

Layer	Patch size/stride	Number of filters	Dropout threshold	Activation
Conv2D	3 × 3/1	32	–	ReLu
Max pooling 2D	2 × 2/1	–	–	–
Dropout	–	–	0.4	–
Conv2D	3 × 3/1	64	–	ReLu
Max pooling 2D	2 × 2/1	–	–	–
Dropout	-	–	0.3	–
Conv2D	3 × 3/1	128	–	ReLu
Max Pooling 2D	2 × 2/1	–	–	–
Dropout	–	–	0.4	–
Conv2D	3 × 3/1	256	–	ReLu
Max pooling 2D	2 × 2/1	–	–	–
Dropout	–	–	0.3	–
Conv2D	3 × 3/1	512	–	ReLu
Max pooling 2D	2 × 2/1	–	–	–
Dropout	–	–	0.4	–
Conv2D	3 × 3/1	1024	–	ReLu
Max pooling 2D	2 × 2/1	–	–	–
Dropout	–	–	0.3	–
Flatten	–	–	–	–
Dense	–	32	–	ReLu
Dense	–	4	–	Softmax

4 Result Analysis

Google collaborator was used to run the model. Google Collaborator is a free cloud-based Jupyter notebook environment that lets us train algorithms using Google's free GPU. The data was initially run over a CNN model, which acquired accuracy and loss of, and 90%, and 38.06 over validation data. The features acquired by the CNN model were passed over an ensemble of Machine Learning models, which consisted of Random forest, K nearest neighbor classifier, Gaussian NB, SVC, and boosting classifiers such as gradient boosting and XGBoost classifier, the accuracies that were recorded by each of them are 92.71%, 89.39%, 89.70%, 92.72%, 91.29%, and 92.24% respectively. Precision, Recall, F1 score of machine learning, and CNN models were also recorded in Table 2.

The value of Precision, Recall, and F1 score for the CNN model and ensemble of machine learning models for each class is shown in Tables 3 and 4.

The confusion matrix for the CNN model and ensemble of machine learning models for each class is shown in Figs. 6 and 7.

The graphical comparison of ML models can be seen in Fig. 8

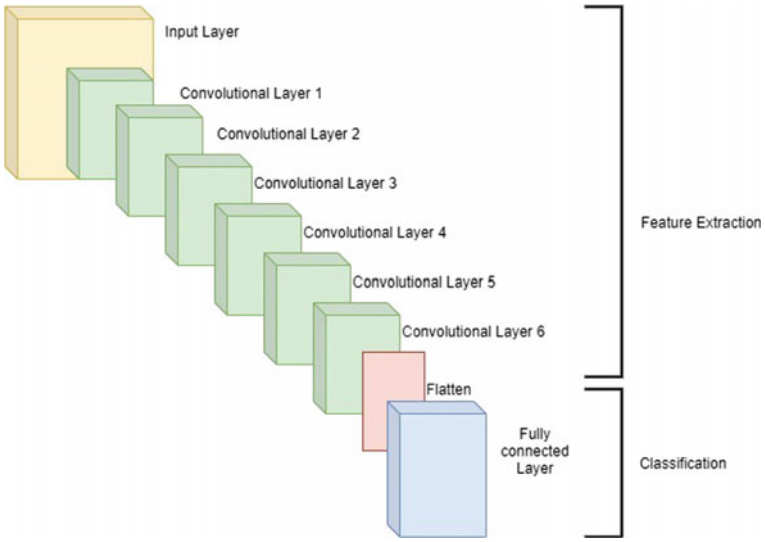

Fig. 4 Overall Structure of CNN model deployed in proposed hybrid model

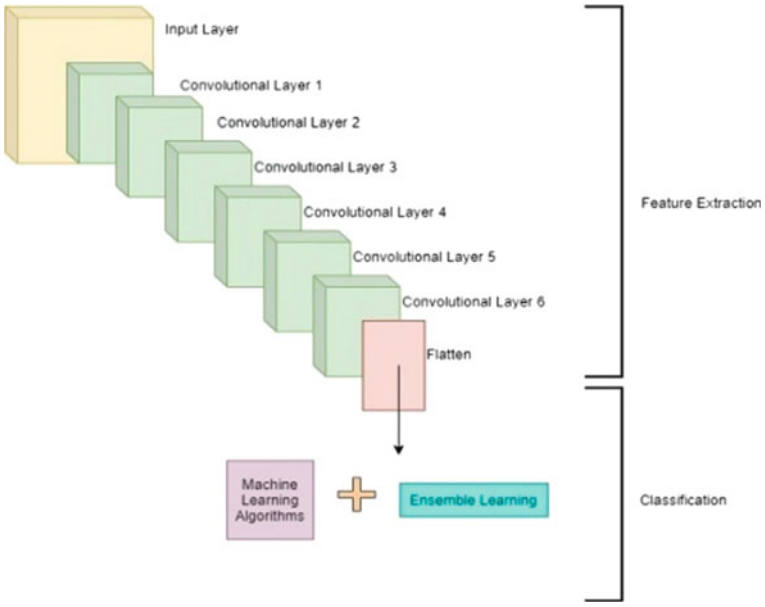

Fig. 5 Classification Model using proposed Ensemble model

Table 2 Accuracy, precision, recall, F1 score of CNN model and Ensemble of ML models

Model	Accuracy (%)	Precision (%)	Recall (%)	F1 Score (%)
CNN model	90.82	90.21	91.44	90.46
Ensemble of machine learning models	92.72	92.88	92.52	92.62

Table 3 Precision, Recall, F1 Score for our CNN model as per the tumor type

Class	Precision (%)	Recall (%)	F1 Score (%)
Glicoma	93.41	86.66	89.91
Meningioma	86.56	94.56	90.38
Pituitary	98.28	96.62	97.45
No Tumor	93.23	92.22	92.73

Table 4 Recall, F1 score for an ensemble of machine learning models as per the tumor type

Class	Precision (%)	Recall (%)	F1 Score (%)
Glicoma	96.02	80.55	87.61
Meningioma	92.69	89.65	91.16
Pituitary	89.44	100	94.42
No tumor	82.69	95.55	88.65

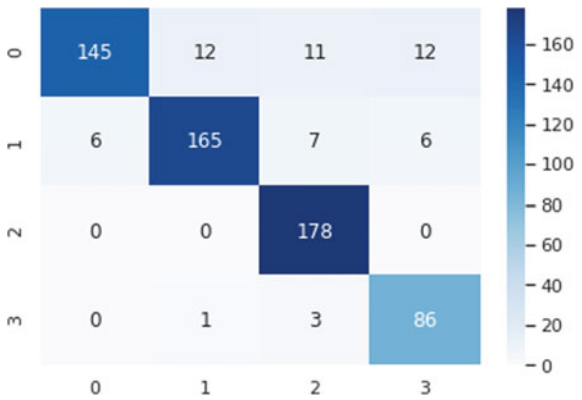

Fig. 6 Confusion Matrix for CNN model

5 Conclusion

Brain tumor is a life-threatening disease and may have severe consequences if not treated at the right time. The treatment may include many procedures like surgery or radiotherapy, depending on the scenario. However, to start the treatment early, we need early detection of the tumor and the type of tumor. We aim to minimize the burden on the health workers by automating detecting brain tumors and determining

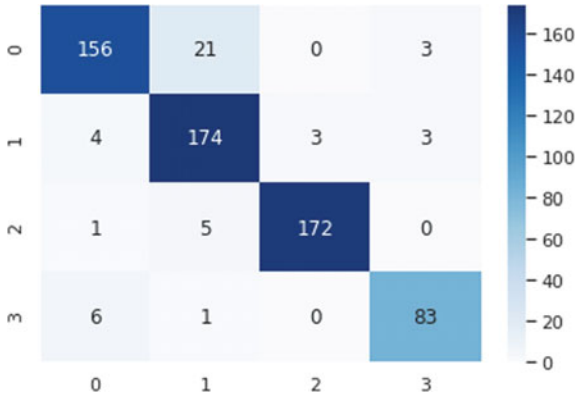

Fig. 7 Confusion Matrix for ensemble of ML models

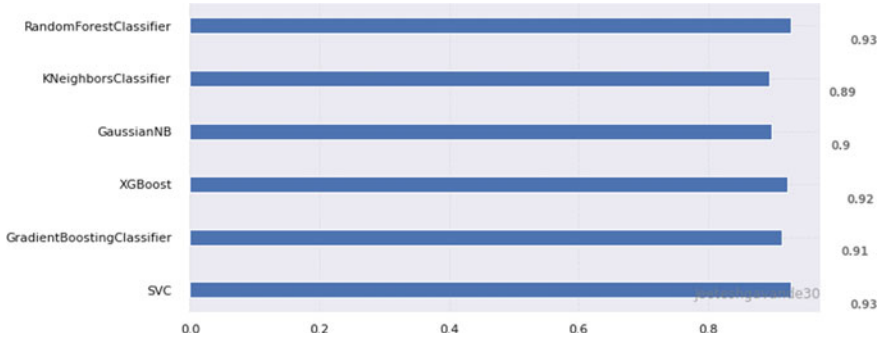

Fig. 8 Bar graph depicting the accuracies of ML models

the type of tumor a patient has for his/her early treatment. For this purpose, we have made a model that uses CNN for feature extraction and an ensemble of machine learning algorithms for classification. After performing experimentation, the model showed an accuracy of 92.72%. Although the model is not entirely accurate, it may have limitations and may sometimes misclassify brain tumors. However, this study aims to decrease the human resources required in detecting the disease and can be used instead of manually examining the MRI of the brain.

References

1. Mohapatra S, Swarnkar T, Mishra M, Al-Dabass D, Mascella R (2021) Deep learning in gastroenterology: a brief review. Handb Comput Intell Biomed Eng Healthc 121–149
2. Mohapatra S, Swarnkar T, Das J (2021), Deep convolutional neural network in medical image processing. In: Handbook of deep learning in biomedical engineering. Academic Press, pp

25–60
3. Mohapatra S, Nayak J, Mishra M, Pati GK, Naik B, Swarnkar T, Wavelet transform and deep convolutional neural network-based smart healthcare system for gastrointestinal disease detection. Interdisc Sci Comput Life Sci 1–17
4. Kaplan K, Kaya Y, Kuncan M, Ertunç HM (2020) Brain tumor classification using modified local binary patterns (LBP) feature extraction methods. Med Hypotheses 139. https://doi.org/10.1016/j.mehy.2020.109696
5. Gumaei A, Hassan MM, Hassan MR, Alelaiwi A, Fortino G (2019) A hybrid feature extraction method with regularized extreme learning machine for brain tumor classification. IEEE Access 7(c):36266–36273. https://doi.org/10.1109/ACCESS.2019.2904145
6. Sachdeva J, Kumar V, Gupta I, Khandelwal N, Ahuja CK (2013) Segmentation, feature extraction, and multiclass brain tumor classification. J Digit Imaging 26(6):1141–1150. https://doi.org/10.1007/s10278-013-9600-0
7. Kumar S, Dabas C, Godara S (2017) classification of brain MRI tumor images: a hybrid approach. Procedia Comput Sci 122:510–517. https://doi.org/10.1016/j.procs.2017.11.400
8. Rammurthy D, Mahesh PK (2020) Whale Harris hawks optimization based deep learning classifier for brain tumor detection using MRI images. J King Saud Univ Comput Inf Sci. https://doi.org/10.1016/j.jksuci.2020.08.006
9. Tuba E, Strumberger I, Bezdan T, Bacanin N, Tuba M (2019) Classification and feature selection method for medical datasets by brain storm optimization algorithm and support vector machine. Procedia Comput Sci 162(Iii):307–315. https://doi.org/10.1016/j.procs.2019.11.289
10. Paul JS, Plassard AJ, Landman BA, Fabbri D (2017) Deep learning for brain tumor classification. In: Medical imaging 2017: biomedical applications in molecular, structural, and functional imaging, vol 10137, issue no 2, pp 1013710. https://doi.org/10.1117/12.2254195
11. Mehrotra R, Ansari MA, Agrawal R, Anand RS (2020) A transfer learning approach for AI-based classification of brain tumors. Mach Learn Appl 2:100003. https://doi.org/10.1016/j.mlwa.2020.100003
12. Mohammed M, Nalluru SS, Tadi S, Samineni R (2019) Brain tumor image classification using convolutional neural networks. Springer Singapore, vol 29, issue no 5
13. Machhale K, Nandpuru HB, Kapur V, Kosta L (2015) MRI brain cancer classification using hybrid classifier (SVM-KNN). In: 2015 international conference on industrial instrumentation and control (ICIC 2015), pp 60–65. https://doi.org/10.1109/IIC.2015.7150592.
14. Cheng J et al (2015) Enhanced performance of brain tumor classification via tumor region augmentation and partition. PLoS ONE 10(10):1–13. https://doi.org/10.1371/journal.pone.0140381
15. Hashemzehi R, Mahdavi SJS, Kheirabadi M, Kamel SR (2020) Detection of brain tumors from MRI images base on deep learning using hybrid model CNN and NADE. Biocybern Biomed Eng 40(3):1225–1232. https://doi.org/10.1016/j.bbe.2020.06.001
16. Ghassemi N, Shoeibi A, Rouhani M (2020) Deep neural network with generative adversarial networks pre-training for brain tumor classification based on MR images. Biomed Signal Process Control 57:101678. https://doi.org/10.1016/j.bspc.2019.101678
17. Swati ZNK et al (2019) Content-based brain tumor retrieval for MR images using transfer learning. IEEE Access 7(c):17809–17822. https://doi.org/10.1109/ACCESS.2019.2892455
18. Rai HM, Chatterjee K (2020) Detection of brain abnormality by a novel Lu-Net deep neural CNN model from MR images. Mach Learn Appl 2:100004. https://doi.org/10.1016/j.mlwa.2020.100004
19. Shahriar Sazzad TM, Tanzibul Ahmmed KM, Hoque MU, Rahman M (2019) Development of automated brain tumor identification using MRI images. In: 2nd International conference on electrical, computer and communication engineering (ECCE 2019), pp 1–4. https://doi.org/10.1109/ECACE.2019.8679240
20. Lavanyadevi R, MacHakowsalya M, Nivethitha J, Niranjil Kumar A (2017, December) Brain tumor classification and segmentation in MRI images using PNN. In: Proceedings of—2017 IEEE International conference on electrical, instrumentation and communication engineering (ICEICE 2017), vo. 2017, pp 1–6. https://doi.org/10.1109/ICEICE.2017.8191888

21. Saha P, Sadi MS, Islam MM (2021) EMCNet: automated COVID-19 diagnosis from X-ray images using convolutional neural network and ensemble of machine learning classifier. Informatics Med Unlocked 22:100505. https://doi.org/10.1016/j.imu.2020.100505
22. Nayak SR, Nayak DR, Arora V, Sinha U, Pachuri RB (2021) Application of deep learning techniques for detection of COVID-19 cases using chest X-ray images: a comprehensive study. Biomed Signal Process Control 64:102365
23. Garg M, Gupta S, Nayak SR (2021) detection of bifurcations and crossovers points from retinal vasculature map using Modified Windows Feature-Point Detection (MWFD) approach. Int J Comput Appl Technol 64(4):361–374
24. Jena KK, Mishra S, Mishra S, Bhoi S, Nayak SR (2019) MRI brain tumor analysis using fuzzy rule based approach. J Res Lepidoptera 50(2):98–112
25. SartajBhuvaji/Brain-Tumor-Classification-DataSet. https://github.com/SartajBhuvaji/Brain-Tumor-Classification-DataSet. Accessed on 1 July 2021

Design and Implementation of Elliptic Curve Digital Signature Using Bit Coin Curves Secp256K1 and Secp384R1 for Base10 and Base16 Using Java

Deepak S. Sakkari and Mohammed Mujeer Ulla

Abstract Public key ciphers like Rivest, Shamir, and Adleman algorithm (RSA) have been implemented extensively in computer network security. Earlier researchers found RSA is not computationally feasible due to exponential growth of key size and is not suitable for resource constrained devices where speed, storage, and bandwidth play a prime importance. Due to which RSA cannot be used with Internet of things [IoT]—end nodes like Raspberry Pi and Arduino. Elliptic curve cryptography is a special type of cryptographic technique which actually is based upon geometrical interpretations and is a classic combination of algebraic properties and geometric techniques. In this paper, elliptic curves used by bit coins like secp256K1 and secp384R1 for base10 and base16 are implemented using Java programming language on Raspberry Pi. This paper focuses on implementation of elliptic curve digital signature (ECDH) on Raspberry Pi using bit coin curves secp256K1 and secp384R1.

Keywords Internet of things (IoT) · Elliptic curve cryptography (ECC) · Elliptic curve digital signature algorithm (ECDSA) · Rivest–Shamir–Adleman (RSA) · Elliptic curve discrete logarithm problem (ECDLP) · National Institute of Standards and Technology (NIST) · Radio-frequency identification(RFID)

1 Introduction

Internet of things is a network in which every object or thing is given with a uniform resource identifier, and data are transmitted without any human intervention [1]. Advancement in IoT technology has made things smarter and opening up for attacks over the data [2]. Basically, IoT comprises of three layers such as sensing layer,

D. S. Sakkari · M. M. Ulla (✉)
Presidency University, Bengaluru 560064, India
e-mail: mohammedmujeerulla@presidencyuniversity.in

D. S. Sakkari
e-mail: deepakssakkari@presidencyuniversity.in

M. Mishra et al. (eds.), *Innovation in Electrical Power Engineering, Communication, and Computing Technology*, Lecture Notes in Electrical Engineering 814,
https://doi.org/10.1007/978-981-16-7076-3_28

data transmission layer, and application layer. Many end devices in sensing layer are prone to denial of service attacks and many other problems exist like authentication and authorization of sensor nodes [3]. Elliptic curve cryptography is used in public key cryptographic protocols such as digital signatures and key exchange protocols [4]. Today many international standards are available for selection of elliptic curves. The curve selection is done based on security requirement and computational speed [5].

During the initial, release of cryptographic standards for practical use of elliptic curves was given with different key sizes. The recommended standards for different security levels are defined over prime field or binary extension fields. Many of the elliptic curves deployed over Internet are mostly defined over prime fields. In this paper, we focus on analyzing elliptic curves over prime field. In world of elliptic curve cryptography, an exponential time algorithm to choose between different forms of elliptic curves based on multiplicative group of finite field is absent, so one could achieve same level of security with an elliptic curve group that is smaller in size. Some of the advantages of using smaller elliptic curves are shorter key sizes, lesser bandwidth, and less computation times which remain the primary requirement for deployment of resource constrained applications. Therefore, to implement elliptic curve cryptography in e-commerce domain, it is quite important to find a suitable curve that could work efficiently with resource constrained devices such as edge nodes like Raspberry Pi, Arduino boards, RFID cards, and wireless devices.

2 Theoretical Principle

2.1 Elliptic Curve

Elliptic curve systems, as applied to cryptography, were first proposed in 1985 independently by Neil Koblitz and Victor Miller. Elliptic curves are based upon discrete logarithm problem. A discrete logarithm problem is defined as given Q ∈ G, find x such that $Q = xP$. The discrete logarithm problem on which elliptic curve is believed to be more difficult than the corresponding problem in (the multiplicative group of non-zero elements) the underlying field. An elliptic curve is a plane defined by equation of form $y^2 = x^3 + ax + b$, over a finite field F_P where p is prime (refer Fig. 1). Elliptic curves are usually defined over prime p also known as GF_P or binary fields also known as $GF(2m)$ in cryptography. An elliptic curve over finite field has finite number of coordinates within that field. Consider an elliptic curve defined over $y^2 = x^3 + ax + b$ where $a = 2$, $b = 3$, and modulo prime field $p = 5$. The values of *a, b, and p (prime)* are random.

$x = 0 \Rightarrow y^2 = 3 \Rightarrow$ No solution (mod 5)
$x = 1 \Rightarrow y^2 = 6 \Rightarrow 1$ $y = 1, 4$ (mod 5)
$x = 2 \Rightarrow y^2 = 15 \Rightarrow 0$ $y = 0$ (mod 5)
$x = 3 \Rightarrow y^2 = 36 \Rightarrow 1$ $y = 1, 4$ (mod 5)

Fig. 1 Elliptic curves

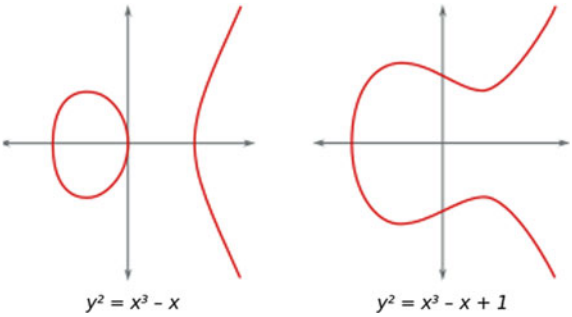

$x = 4 \Rightarrow y^2 = 75 \Rightarrow 0\ y = 0 \pmod 5$)

Then, points on elliptic curve are (1,1), (1,4)(2,0), (3,1), (3,4)(4,0).

The values of *x, y* will always be within the prime field $(n - 1)$. The elliptic curve looks continuous, but is not continuous rather it is a collection of discrete set of points, where the curve is symmetric over x-axis and variable x is cubic, i.e., elliptic curve has three roots. Elliptic curves have nothing to do with ellipses and should not be mistaken with ellipses [6].

2.2 *Elliptic Curve Over Real*

The elliptic curves are defined by the equation of form $y^2 = x^3 + ax + b$, where collection of points (a, b) is derived from R. Elliptic curves are called as singular curve if $4a^3 + 27b^2 = 0$ else they are known as nonsingular elliptic curve, i.e., $4a^3 + 27b^2 \neq 0$. This condition will ensure that we have third point of intersection and there exists three real roots on elliptic curve [7], i.e., let $a, b \in R$ such that $4a^3 + 27b^2 \neq 0$. $\mathrm{E} = (\mathrm{x}, \mathrm{y}) \mid y^2 = x^3 + ax + b$ and $a, b \in R$ such that $4a^3 + 27b^2 \neq 0$ where θ is point at infinity.

Base point selection: Selection of base point or generator point in elliptic curve cryptography is very crucial step for its security. To reduce overall computation, cost optimal selection of base point is needed. One could choose random point on the curve as base point while some choose the smallest point on the curve as generator point. There are some algorithms which give optimum base point selection method. Initially, we select a random point on the curve and then we perform scalar multiplication using a random point. Finally, the resultant of multiplication is being used to judge the base point of the elliptic curve. Let us assume a and p are integers, where $p > 0$ [8].

Algorithm: ECC base point selection algorithm on GF_P.
Input: *a, b, p, n, h.*
Output: Base point *G* on curve having order n.
S1. Select random value x such that ($0 \leq x < p$).
S2. a = $(x^3 + ax + b) mod p$**.**

S3. If a € to quadratic residue of *mod p*, if yes go the step S4, if not, go to S1.

S4. Compute $G = hG$, then judging whether G meets $y^2 = x^3 + ax + b$ and G is not infinite point. If so G is the solved base point, then go S5, if not, go to S1.

S5. Return *G*.

Case 1: Point addition when $x_1 \neq x_2$

Figure 2 demonstrates given two points $P(x_1, y_1)$ and $Q(x_2, y_2)$ on elliptic curve and by drawing a tangent passing through (P, Q) will definitely hit the third intersection point on elliptic curve which we call it as $-R(x_3, -y_3)$, this is due to cubic properties of a variable x in elliptic curve equation, i.e., $y^2 = x^3 + ax + b$ [9]. By drawing a perpendicular line from intersected point $-R(x_3, -y_3)$ will give us the fourth intersection point $R(x_3, y_3)$ on the elliptic curve, which we call it as sum of points $(P + Q)$. Let us have an equation of elliptic curve $y^2 = x^3 + ax + b$ and we choose values for (a, b) such that non singularity condition exists, i.e., $4a^3 + 27b^2 \neq 0$ [10]. The below sequence of derived equations helps us to recursively find the remaining points (x, y) on elliptic curves [11].

The slope of the line is given by

$$\lambda = \frac{y_2 - y_1}{x_2 - x_1} \tag{1}$$

Equation of straight line is given by

$$y - y_1 = \lambda(x - x_1) \tag{2}$$

Figure 2 demonstrates line with points $P(x_1, y_1)$, $Q(x_2, y_2)$ is passing through point $R(x_3, y_3)$, and therefore, Eq. (2) can be rewritten as

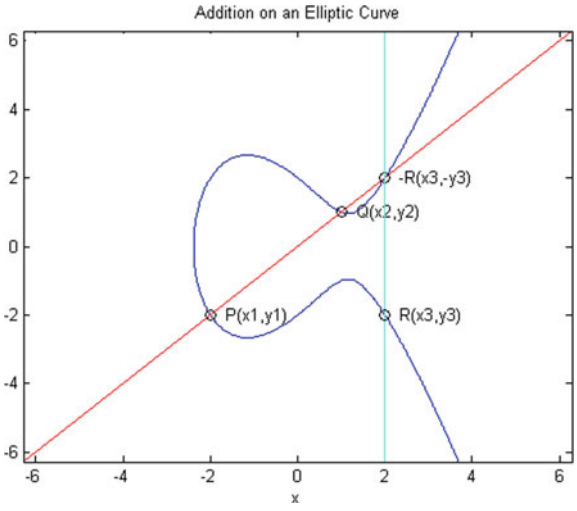

Fig. 2 Point addition

$$-y_3 - y_1 = \lambda(x_3 - x_1) \tag{3}$$

Rearranging the terms in above Eq. (3) to find y_3

$$\therefore y_3 = \lambda(x_1 - x_3) - y_1 \tag{4}$$

Using Eq. (2) and rearranging terms to find value of y

$$y = y_1 + \lambda(x - x_1) \tag{5}$$

The elliptic curve is defined by equation of form

$$y^2 = x^3 + ax + b \tag{6}$$

Substituting Eq. (5) in Eq. (6)

$$(y_1 + \lambda(x - x_1))^2 = x^3 + ax + b \tag{7}$$

$$x^3 - \lambda^2 x^2 + \cdots\cdots\cdots\cdots = 0 \tag{8}$$

The roots of an equation are the values of x for which the function will be zero. A root is nothing but value of x as y is zero. An algebraic equation of third-degree is known as cubic equation. The general form of a cubic function is $f(x) = ax^3 + bx^2 + cx + d$, and the cubic equation is of form $ax^3 + bx^2 + cx + d = 0$, where *a, b,* and *c* are the coefficients, and d is the constant. Suppose, we wish to find roots of a cubic equation $x^3 - 6x^2 + 11x - 6 = 0$, after factorization cubic equation has three real roots, the solutions are $(x = 1)$, $(x = 2)$, and $(x = 3)$. The curve passes the x-axis three times, once where $x = 1$, once where $x = 2$, and once where $x = 3$. This is demonstrated in Fig. 3.

Equation 8 shows the partial expansion of Eq. 7, expansion is done until we find the first negative coefficient in the equation, i.e., $-\lambda^2 x^2$. As discussed earlier and from theory of equations, any cubic equation will have three roots. The expanded Eq. 8 is a cubic equation which means the equation has three roots. By theory of equation, we know that addition of all three roots is equal first negative coefficient value, i.e.,$x_1 + x_2 + x_3 = \lambda^2$.

$$\therefore x_3 = \lambda^2 - x_1 - x_2 \tag{9}$$

Case 2: Point doubling

Figure 4 demonstrates when $P(x_1, y_1) = Q(x_2, y_2)$, we obtain a tangent that touches the points P and R, from equation [9], we have $x_3 = \lambda^2 - x_1 - x_2$. As stated earlier $P = Q$, values of $x_1 = x_2$ and $y_1 = y_2$ and therefore the Eq. 9 can be rewritten as

Fig. 3 Cubic equation

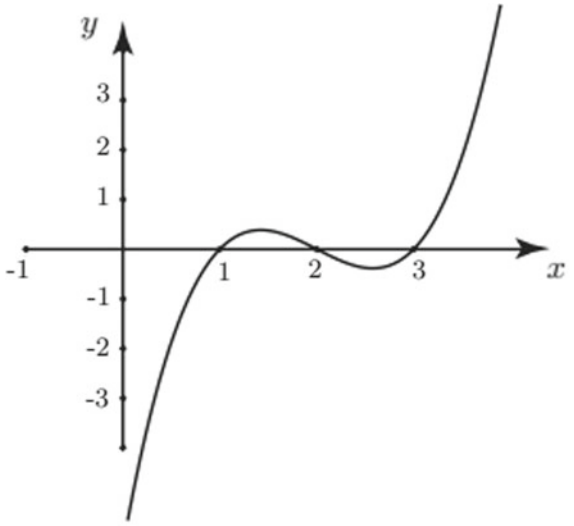

The graph of $y = x^3 - 6x^2 + 11x - 6$.

Fig. 4 Point doubling

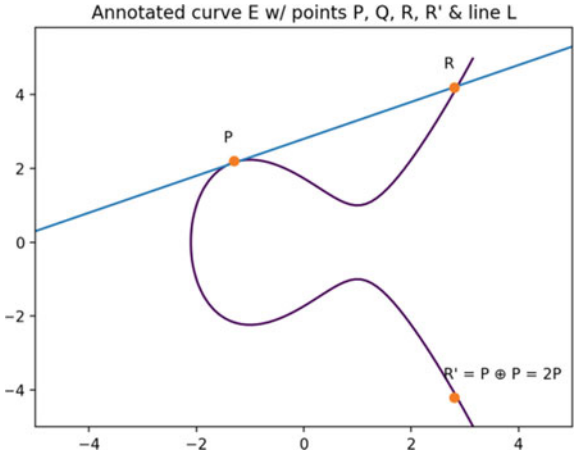

$$x_3 = \lambda^2 - 2x_1 \tag{10}$$

From Eq. (4), we have $y_3 = \lambda(x_1 - x_3) - y_1$

The equation of elliptic curve is given by $y^2 = x^3 + ax + b$

To find the value of λ, for case 2, we differentiate above equation of elliptic curve y in terms of x at point $(x_1,\ y_1)$

Fig. 5 Point at infinity

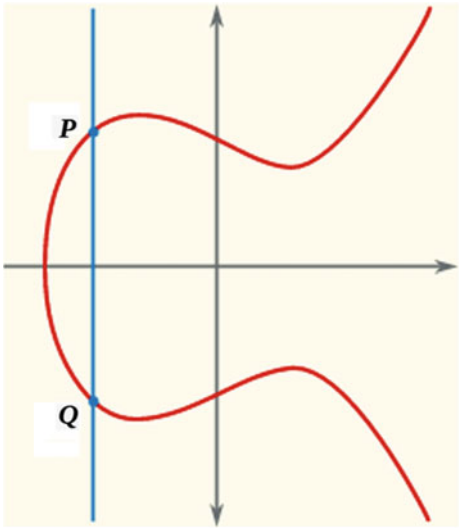

$$2y\frac{dy}{dx} = 3x^2 + a\frac{dy}{dx}(x_1, y_1) = \frac{(3x^2 + a)}{2y}$$

$$\lambda = \frac{3x^2 + a}{2y} \tag{11}$$

Substituting Eq. (11) in Eq. (4), we obtain

$$y_3 = \frac{3x^2 + a}{2y}(x_1 - x_3 - y_1)) \tag{12}$$

Case 3: Point at infinity
In this case, we assume two points $P(x_1, y_1)$ and $Q(x_2, -y_2)$ meet each other at third intersection which is point at infinity $x_1 = x_2$ and $y_1 = -y_2$. (Refer Fig. 5)

$P + Q = \theta$.
$Q = -P$.
$P + (-P) = \theta$, where θ is an identity element.

3 Generic Procedure of ECDSA

Both parties agree on publicly known data items as follows:

1. Elliptic curve equations
2. Values of a and b

3. Prime p
4. The elliptic group computed from the elliptic curve equation
5. The base point B taken from the elliptic group
6. Similar to the generator used in current crypto systems
7. Each user generates their public/private key pair
8. Private key = an integer, x selected from interval $[1, p - 1]$
9. Public key = product Q of private key and base point ($Q = X * B$)

4 Proposed Elliptic Curve Digital Signature Algorithm

In this section, we present implementation of signature-based scheme provided in Fig. 6. As shown in the Figure, two users communicate with each other with set of message exchanges. The above implementation is tested on platforms like Raspberry Pi, Arduino UNO with ESP8266 and Microsoft windows with eclipse integrated development environment (IDE) and Java development kit (JDK). The client server communication is achieved with server listening to requests coming from local host on port 4444. The concept of local host can be extended to work within a wide area network (WAN) by replacing local host name by client IP address provided both the client and server machines are connected to network.

Message exchanges between client and server are achieved by using JavaScript object notation (JSON). Multithreading concept from Java is used to create multiple instances of server to handle multiple requests from multiple clients. The bit coin curves secp256K1 and secp384R1 recommended by National Institute of Standards and Technology (NIST) are used in the implementation of both base10 and base16 modes.

The communication between Alice and Bob begins as follows

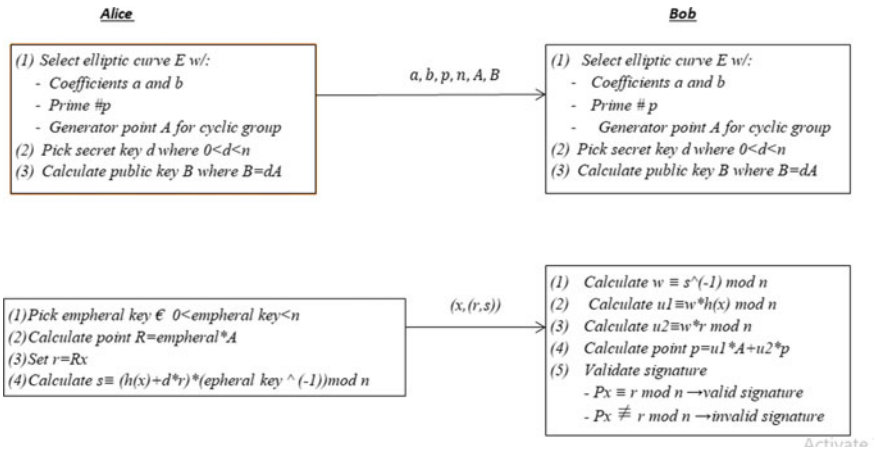

Fig. 6 Design and implementation of ECDSA using secp256K1 and secp384R1 curves

- Alice wants to send a signed message to Bob so she selects domain parameters (*a, b, p, n, A, B*) elliptic curves, coefficients *a* and *b*, prime number #p, and generator point *A* for cyclic group with prime order *n*. Later, she picks secret key d where value of *d* is $0 < d < n$ and calculate the Alice's public key *B* which is *d* hops from generator point A.
- Once the exchange of public key between Alice and Bob is completed. The Alice selects the ephemeral key such that 0 < ephemeral key < n holds good. Then, calculates point *R* which is ephemeral key hops. Generator point A and sets r = Rx finally computes $s \equiv (h(x) + D * r) *$ inverse of ephemeral key mod n, i.e., sends the signed message (x, (r,s)) to Bob.

- Now Bob starts to calculate the following things to validate the message exchanges

1. calculate $w \equiv s^{-1} \bmod n$
2. $u1 \equiv w * h(x) \bmod n$
3. $u2 \equiv w * r \bmod n$
4. calculate point $p = u1 * A + u2 * B$
5. finally, validate signature
6. $-Px \equiv r \bmod n \Rightarrow$ valid signature
7. $-Px \cong r \bmod n \Rightarrow$ invalid signature

5 Experiments

First experiment is ECDSA for base10 where the parameters for a, *b, p, n, h, g* are listed in Table 1 and 2 for Alice and Bob, respectively

5.1 Alice's Key Generation and Encryption Process for BASE10

Alice begins with public key generation using the domain parameters in Table 1 as follows:

1. Alice selects the secret key d from < 2 ……..$n - 1$ >

Table 1 ECC parameters in Base10 for alice

$a = 4$	$n = 37$	$b = 20$
$h = 1$	$p = 29$	$G = (8,10)$

Table 2 ECC PARAMETERS IN BASE10 FOR BOB

$a = 2$	$n = 19$	$b = 2$
$h = 1$	$p = 1$	$G = (5,1)$

2. Alice's public key is computed B = dA and shared with Bob.
3. Secure hash key is generated SHA(x)
4. Alice selects ephemeral key between 0 < ephemeral > n.
5. Alice waits for public key of Bob, once it is received. The data are encrypted and transmitted to Bob.

5.2 BOB'S Key Generation and Decryption Process for BASE10

Bob generates his public key to be shared with Alice using the domain parameters in Table 2 and secret key for self as follows:

1. Bob selects the secret key d from
2. Bob's public key is computed B = dA and shared with Alice.
3. Secure hash key is generated SHA(x)
4. Calculate w $\cong s^{-1}$ mod n
5. Calculate u1 $\cong$ w*SHA(x) mod n
6. Calculate u2 $\cong$ w*r mod n
7. Calculate P = u1*A + u2*B
8. V = Px
9. Validate V $\cong$ r mod n

Finally, message is accepted only if it is signed by Alice's private key.

5.3 Server Communication as Eavesdropper for BASE10

Server does eavesdropping on all communications between Alice and Bob but finds only the values of *a, b, p, n, h, Gx, Gy* and public key but will not find the private key of both the parties. To sign messages, as being Alice, eavesdropper needs to solve elliptic curve discrete logarithm problem (ECDLP) and compute private key d or ephemeral key of Alice.

System name: Alice

a: 2

b: 2

p: 17

n: 19

h: 1

Generator X: 5

Table 3 Alice's Base10-domain parameters obtained by eave

Name: Alice
a:4
b:20
p:29
n:37
h:1
Generator X:8
Generator Y:10
Public key X:6
Public key Y:17
[Eave]: to sign messages, as being ALICE needs to solve ECDLP and compute his/her private key d or ephemeral key

Generator Y: 1

Public key X: 0

Public key Y: 6

Eave has domain parameters (curve and generator point) for Alice.

5.4 Alice's Key Generation Encryption Process for Base16 Hex Input (Secp256K1 Curve)

The next elliptic curve for our experiment is secp256K1 for Alice and secp384R1 for Bob. Alice begins with public key generation using the domain parameters in Table 3 and shares it with Bob as follows:

1. Alice selects the secret key d from $< 2 \ldots\ldots\ldots n - 1 >$
2. Calculates send public key $B = dA$
3. Secure hash key is generated SHA(x)
4. Alice selects ephemeral key between $0 <$ ephemeral $> n$.
5. Once the public key of Bob is received. The data are encrypted and transmitted to Bob.

5.5 BOB'S Key Generation Decryption Process for Base16 Hex Input (Secp384R1 Curve)

Bob generates his public key using domain parameters in Table 4, to be shared with Alice and secret key for self.

Table 4 BOB'S base10-domain parameters obtained by eave

Name: Bob
a:2
b:2
p:17
n:19
h:1
Generator X:5
Generator Y:1
Public key X:6
Public key Y:3

1. Initially, Bob selects the secret key d from < 2 ……..$n - 1$ > .
2. Bob's public key is computed B = dA and shared with Alice.
3. Secure hash key is generated SHA(x).
4. Calculate w ≅ s^{-1}mod n.
5. Calculate u1 ≅ w*SHA(x) mod n.
6. Calculate u2 ≅ w*r mod n.
7. Calculate P = u1*A + u2*B.
8. V = Px.
9. Validate V ≅ r mod n.

Finally, message is accepted only if it is signed by Alice's private key.

5.6 Server Communications as Eavesdropper for Base16

Server does eavesdropping on all communications between Alice and Bob but finds only the values of *a*, *b*, *p*, *n*, *h*, *Gx*, *Gy* and public key but will not find the private key of both the parties. To sign messages, as being Alice or Bob, eavesdropper needs to solve ECDLP and compute his/her private key d or ephemeral key as shown in Tables 5, 6, and 7.

6 Performance Analysis

For analyzing different curves under secp, ESCDSA algorithm is applied for each of the selected curve. Computation time needed for signature generation and signature verification is recorded as shown in Figs. 7 and 8, respectively. Both Figures 7, 8 and Tables 8, 9 indicate that the curve secp384R1 requires less computation time for the signature generation and secp512R1 requires less computation time for verification processes compared to other selected curves when the ECDSA is applied. The curve

Table 5 ECC parameters in base16 for alice (NIST recommended parameters secp256K1)

$a = 0$
$b = 7$
$p =$ FFFFFFFFFFFFFFFFFFFFFFFFFFFFFFFF FFFFFFFFFFFFFFFFFFFFFFFEFFFFFC2F
$n =$ FFFFFFFFFFFFFFFFFFFFFFFFFFFFFFFE BAAEDCE6AF48A03BBFD25E8CD0364141
$h = 1$
$Gx =$ 79BE667EF9DCBBAC55A06295CE870B07 029BFCDB2DCE28D959F2815B16F81798
$Gy =$ 483ADA7726A3C4655DA4FBFC0E1108A8F D17B448A68554199C47D08FFB10D4B8

Table 6 ECC parameters IN base16 for BOB (NIST recommended parameters secp384R1)

$a =$ FFFFFFFFFFFFFFFFFFFFFFFFFFFFFFFF FFFFFFFFFFFFFFFFFFFFFFFFFFFFFFFEFFFFF FFF0000000000000000FFFFFFFC
$b =$ FFFFFFFFFFFFFFFFFFFFFFFFFFFFFFF FFFFFFFFFFFFFFFFFFFFFFFFFFFFFFFFFFFFFEF FFFFFFF0000000000000000FFFFFFFC
$p =$ FFFFFFFFFFFFFFFFFFFFFFFFFFFFFFFFF FFFFFFFFFFFFFFFFFFFFFFFFFFFFFEFFFFFFFF 0000000000000000FFFFFFFC
$n =$ FFFFFFFFFFFFFFFFFFFFFFFFFFFFFFFFFFFFF FFFFFFFFFFFFFFC7634D81F4
$h = 1$
$Gx =$ AA87CA22BE8B05378EB1C71EF320AD746E 1D3B628BA79B9859F741E082542A385502F25D BF55296C3A545E3872760AB7
$Gy =$ 3617DE4A96262C6F5D9E98BF9292DC29F8F4 1DBD289A147CE9DA3113B5F0B8C00A60 B1CE1D7E 819D7A431D7C90EA0E5F

Table 7 Base16 domain parameters obtained by eave

x: *ABC*
$r =$ 3002719260124138234864644293005553694107074621611323149430212532410635475904301642043243286192603916432052661917741
$s =$:212023627282593087235718421965745837495934069460383858508397637227006170026649520856917088465725290817349107331914690

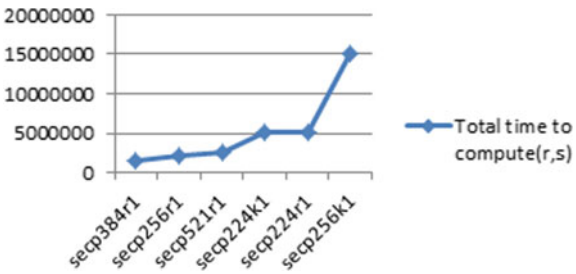

Fig. 7 Total time required for signature generation (μs)

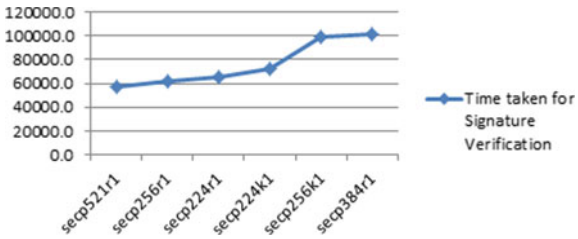

Fig. 8 Total time for signature verification in milliseconds (ms)

Table 8 Signature generation times IN μ seconds of curves when used for ECDSA

Type of curve	Time to compute (r)	Time to compute (s)	Time to compute (r, s)
Secp384R1	4345	31,612,001	1,616,347
Secp256R1	3998	2,204,409	2,208,407
Secp521R1	4915	2,639,882	2,644,798
Secp224K1	3172	5,032,156	5,035,329
Secp224R1	3052	5,044,813	5,047,866
Secp256K1	4562	15,161,901	15,166,463

Table 9 Signature verification times of curves in milliseconds when used for ECDSA

Type of curve	Time taken for signature verification
Secp521R1	57,288
Secp256R1	62,097
Secp224R1	64,719
Secp224K1	72,134
Secp256K1	98,503
Secp384R1	101,509

secp384R1 and secp512R1 are suitable for resource-constrained applications. The advantage of using secp384R1, secp512R1 is that it has a smaller prime field.

7 Conclusions

The proposed elliptic curve cryptography implemented an asymmetric digital signature algorithm using Java programming language to protect the data. The results demonstrated proposed algorithm is robust against eavesdropping and requires him to solve discrete logarithm problem and obtain ephemeral key and secret key in order to portray him as Alice or Bob. From the analysis, it is clear that when the field size of the curves increases so does the required computation time. In future, we have planned to use this concept to compare the time complexity involved with ECDH

and RSA. The proposed implementations will help the common people to validate themselves with each other on Internet of things platform and give an idea to select best secp elliptic curves.

Acknowledgements The authors would like to acknowledge the support provided by Presidency University- Bengaluru, India.

Compliance with Ethical Standards

Funding: Presidency University, Bengaluru, Karnataka, India.

No Conflict of Interest: Author Dr. Deepak S. Sakkari declares that he has no conflict of interest. Author Mohammed Mujeerulla declares that he has no conflict of interest.

Ethical Approval

This article does not contain any studies with human participants or animals performed by any of the authors. Informed consent: Informed consent was obtained from all individual participants included in the study.

References

1. Khan MA, Quasim MT, Alghamdi NS, Khan MY (2020) A secure framework for authentication and encryption using improved ECC for IoT-based medical sensor data. In: 2020 IEEE Access 8:52018–52027. ISSN 2169–3536
2. Patel C, Doshi N () Secure light weight key exchange using ECC for user gateway paradigm. IEEE Trans Computer 1. https://doi.org/10.1109/TC.2020.3026027
3. Zhang X, Wang X (2018) Digital image encryption algorithm based on elliptic curve public cryptosystem. In: 2018 IEEE Access, vol 6, pp 70025–70034. ISSN 2169–3536
4. Hammi B, Fayad A, Khatoun R, Zeadally S, Begriche Y (2020) A lightweight ECC-based authentication scheme for Internet of Things (IoT). In: 2020 IEEE Syst J 14:3440–3450. https://doi.org/10.1109/JSYST.2020.2970167
5. Shaikh JR, Nenova M, Iliev G, Valkova-Jarvis Z (2017) Analysis of standard elliptic curves for the implementation of elliptic curve cryptography in resource-constrained E-commerce applications. In: 2017 IEEE-COMCAS ISBN:978–1–5386–3169–0
6. Guicheng S, Zhen Y (2013) Application of elliptic curve cryptography in node authentication of Internet of Things. In: 2013IEEE-IIHMSP. ISBN 978–0–7695–5120–3. https://doi.org/10.1109/IIH-MSP.2013.118
7. Kishore RK, Naikoti A (2016) ECDH based security model for IoT using ESP 8266. In: 2016 IEEE- ICCICCT. https://doi.org/10.1109/ICCICCT.2016.7988026
8. Bai TDP, Raj KM, Rabara SA (2017) Elliptic curve cryptography based security framework for Internet of Things (IoT) enabled smart card. In: 2017 IEEE-WCCCT. https://doi.org/10.1109/WCCCT.2016.20. ISBN 978-1-5090-5573-9
9. Dhillon PK, Kalra S (2016) Elliptic curve cryptography for real time embedded systems in IoT networks. In: 2016 IEEE-WECON ISBN:978–1–5090–0893–3
10. Bettoumi B, Bettou B (2018) Evaluation of Authentication Based Elliptic Curve Cryptography in Wireless Sensor Networks in IoT Context" 2018 IEEE SoftCOM ISSN: 1847–358X
11. The Department of Computer Science and Engineering at the Indian Institute of Technology Kharagpur, Available: http://cse.iitkgp.ac.in/

Development of Conceptual Framework for Reinforcement Learning Based Optimal Control

Smriti Gupta, Sabita Pal, Kundan Kumar, and Kuntal Ghosh

Abstract The framework of reinforcement learning-based optimal control depends on a mathematical formulation of intelligent decision making. In this article, we demonstrated the comprehensive design framework for offline reinforcement learning algorithms that utilizes sparse and discrete data space for efficient decision-making purposes. Learning is often difficult with the sparse reward function under the absence of optimization. Hence, an optimized map can be used in the reward function to improve efficacy. Some reward functions outperform sparse reward, such as "map completeness" and "information gain". "Map completeness" is proportional to the difference between the current time step and the previous time step, while "information gain" utilizes the entropy information for measuring the uncertainty in the map. On a whole. this article proposes a framework for the development of optimized reward function-based reinforcement learning based control strategy.

Keywords Markov decision process · Reinforcement learning · Temporal difference · Q learning · Sparse reward function

1 Introduction

Reinforcement learning was induced by an experimentation (TE) method, directed by Thorndike in an investigation of feline's practices in 1898. Later, in 1954, Minsky planned the principal neural PC called stochastic neural simple support number crunchers (SNARCs), which reproduced the rodent's cerebrum to tackle the labyrinth puzzle. Practically following twenty years, Klopf incorporated worldly difference(TD) learning in TE to upgrade the computational conduct of the calcula-

S. Gupta (✉) · S. Pal · K. Kumar
Department of Electronics and Communication Engineering, ITER, Siksha 'O' Anusandhan (Deemed to Be University), Bhubaneswar 751030, Odisha, India

K. Ghosh
Department of Aerospace Engineering, Indian Institute of Science (IISc), Banglore 560012, Karnataka, India

M. Mishra et al. (eds.), *Innovation in Electrical Power Engineering, Communication, and Computing Technology*, Lecture Notes in Electrical Engineering 814,
https://doi.org/10.1007/978-981-16-7076-3_29

tion. Finally, in 1989, Watkins and Dayan introduced the concept of ideal control, which includes bellman equality and the Markov decision process (MDP), as well as TD finding out how to frame a significant Q-learning. Since then Q-learning is boundlessly used to take care of genuine issues yet this calculation has a limit in tackling the issue in the high dimensional environment as the quantity of estimations increments radically [1]. As true issues turned out to be logically convoluted, there are circumstances where one RL agent can't manage and comes the requirement of multiple agents. In a multi-agent system (MAS), learning agents ought to battle or get together to get the best-optimized results. Busoniu et al. [2] provides a comprehensive survey of multi-agent reinforcement learning (MARL) techniques for fully cooperative, fully competitive, and mixed tasks which focuses on autonomous multiple agents learning to solve complex tasks online using learning strategies based on dynamic programming and temporal-difference RL. Sadhu et al. [3] proposed an algorithm for MAQL with two appealing features which were unavailable in convention Q learning. To begin with, an agent only needs to adapt one Q-table in joint state-action space during the learning process, as opposed to m joint Q-tables for, m agents in CQL. Second, instead of evaluating the computationally costly CE, a clever method is used, in which the composite Q-values are computed during the learning process, and the best option is chosen during the planning phase using the learned composite Q-values. This has advantages in real-time planning because the suggested technique avoids the time-consuming calculation of a CE. Spiros et al. [4] presented a novel estimated value feature and test it on two particularly challenging coordination problems: the climbing game and the penalty game. The action selection strategy chosen was the Boltzmann strategy. MARL can speed up the task by parallel computation, but it has several challenges like the difficulty of specifying a learning goal, the nonstationarity of the learning problem, and the need for coordination [2].

Wang et al. [5] combines Q-learning with Boltzmann policy in the multi-robot system for path planning optimization. Q-learning is delineated as a grid-based formula that solves the low-dimensional issues and Boltzmann policy as applied mathematics finds a globally optimum solution. This approach cuts down on the number of iterations and hence the number of explorations. This helps in the convergence of the process. Sadhu et al. [3] has efficient convergence as it implements team-goal exploration and joint action selection for the specified state. Chaplot et al. [6] focuses on Active Neural SLAM, a modular navigational model. It uses analytical path planners and policies both local as well as global. It can relocalize the existing map to enhance efficiency. Botteghi et al. [7] uses Deep Reinforcement Learning (DRL) to generate a map-less path planning algorithm. The reward function is derived from the generated map. It helps in obstacle avoidance in a complex environment with high convergence. Arana-Daniel et al. [8] creates a robust navigation system using an artificial intelligence approach. It applies reinforcement learning with SLAM for creating a computational efficient map of an unknown environment. Reinforcement learning has numerous applications, like multi-robot collaboration in the creative manufacturing plants, multiplayer online AI ongoing interaction in PC, mechanical controller control, traffic light frameworks, and self-sufficient military frameworks like Unmanned Aerial vehicles (UAVs), surveillance, and shuttle etc. [1, 9].

In this article, we demonstrated a detailed design framework for offline reinforcement learning algorithms, which utilizes the advantage of sparse and discrete data space for efficient decision-making. Under this framework, we demonstrate the working of the coupled function for policy optimization that is comprised of different parameters such as learning rate, discount factor and exploration rate. This paper aims to provide a basis for the creation of reward function-based reinforcement learning with optimized reward functions.

The rest of this article is segmented as follows. The background and preliminary ideas about reinforcement learning and its mathematical formulation using MDP are described in Sect. 2. Different variations of RL methods are presented in Sect. 3. Section 4 discusses the challenges in RL, and Sect. 5 concludes the paper.

2 Background and Preliminaries

2.1 Reinforcement Learning

Reinforcement Learning is a TE-based learning algorithm where the learner is the agent a decision-maker, and anything outside it is considered as the environment. The agent learns directly by interacting with the environment, self teaches itself, and learns what decision to take to reach a designated goal. Agent, Environment, reward, and action are the four basic components of RL. In RL, an agent's main goal is to optimize the reward for a sequence of actions to reach a designated goal in a dynamic environment [10]. Reinforcement learning offers a mathematical formalism for management-based learning. An agent can mechanically acquire near-optimal behavioral skills, expressed by policies, using reinforcement learning to optimize custom reward functions.

The reciprocity between an agent and its environment, as depicted in Fig. 1, occurs in three stages:

1. The agent begins by interacting with the world by performing an action a_t
2. The agent performs action a_t and transitions from state s_t to state s_{t+1}.
3. Following that, the agent will be rewarded r_{t+1} for the action it took.

Based on reward the agent will decide whether to proceed with the same action or to take some different activities that will maximize the reward. Most feasible moves give a small negative reward, which punishes moves that don't make progress and

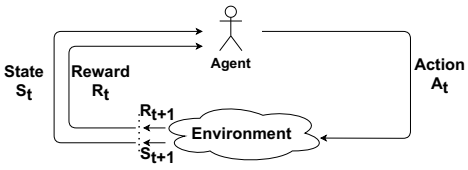

Fig. 1 Agent-environment interaction model diagram

therefore discourage going in circles. Obstacle state and goal state are assigned with high negative and positive reward respectively. The main objective of the agent is to reach the desired target with maximum cumulative reward and minimal number of iteration steps at the same time should avoid collision with obstacles [7]. The agent's choice of action is standardized by defining the concept of policy. A policy π is a function that maps any perceived state s to the action that should be taken as a result of that state [1].

$$\pi = \Psi(s) = \left\{ p\left(a_n \mid s\right) \mid \forall a_n \in \Delta_\pi \wedge \sum_n p\left(a_n \mid s\right) = 1 \right\} \tag{1}$$

where Δ_π represents all probable actions of the policy π.

Reinforcement learning entails iteratively accumulating knowledge by engaging with the environment, usually the most recently learned policy, and then using that experience to enhance the policy [11]. RL satisfies an oblivious condition known as the Markov decision Process (MDP) since the succeeding state s_{t+1} and reward r_{t+1} are exclusively dependent on the present state-action pair inadvertent of the previous history.

2.2 Markov Decision Process (MDP)

Any RL problem is formulated using the Markov Decision Method. A tuple (*S, A, R, P*) defines it, where *S* and *A* are a finite set of states and actions taken by an entity. $\mathrm{P}(s_t, a_t, s_{t+1})$ is the transition function, that provides the likelihood of achieving next state s_{t+1} after performing action a_t in state s_t. Finally, $\mathrm{R}(s_t, a_t, s_{t+1})$ provides an immediate reward for the transformation (s_t, a_t, s_{t+1}) [12]. The reward function is classified into two types: a sparse function in which reward is given when the agent reaches the desired state or failure state, and the other one is a dense function that rewards all state activity by a basis of assessment [8]. The expected discounted cumulative reward that an agent receives when starting from state s and following policy is denoted by the value of a state, $V^\pi(s)$ [13].

$$V^\pi(s) = \mathbb{E}\left[\sum_{k=0}^{\infty} \gamma^k r_{t+k+1} \mid s_t = s \right] \tag{2}$$

where the expectation operator is employed to average over random transitions and probably over a stochastic policy and a stochastic reward function.

For a given policy π, the state-action value function is given by [13]

$$Q^\pi(s, a) = \mathbb{E}\left[\sum_{k=0}^{\infty} \gamma^k r_{t+k+1} \mid s_t = s, a_t = a \right] \tag{3}$$

It is the expected sum of the discounted rewards for an agent starting at state s, taking an action a, and then following policy π.

The goal of MDP is to find an optimal policy that will result in a maximum cumulative reward for all states.

$$\pi^* = argmax \mathrm{V}^{\pi}(s), \forall s \in S \tag{4}$$

We can represent the optimal value function using bellman optimality equation

$$V^*(s) = \max \sum_{s' \in S} P^a_{ss'} \left[R^a_{ss'} + \gamma V^* \left(s' \right) \right] \tag{5}$$

3 RL Methods

Two conventional RL strategies are 1) Monte-Carlo (MC) and 2) TD learning. These strategies don't need the environment's complex knowledge and can handle larger state-space issues.

1. The Monte-Carlo method entails the following steps: It is a model-free method of learning. By Creating and recording episodes regularly, the average return at each state is used to evaluate the value function. Two assumptions must be made: first, the episode must have a large number of episodes, and second, each state must be inspected a sufficient number of times.
2. The Temporal-Difference process, unlike MC, does not attempt to wait until the end of the scene to make a change. It uses the Bellman equation to create a report on each venture within the scene, resulting in faster convergence [1]. TD method uses a TD update rule to find state-action value function, which is defined as:

$$V^i(s_t) \leftarrow V^{i-1}(s_t) + (1 - \alpha) \left(r_{t+1} + \gamma V^{i-1}(s_{t+1}) \right) \tag{6}$$

Both of these methods are again classified as the on-policy and off-policy methods. On-policy uses the same policy for exploration as well as exploitation process, whereas off-policy uses different policies for the same. Due to simplicity, off-policy is more desirable, but for stability, on policy are best suited [1].

3.1 Q-Learning

Q-learning is a model-free reinforcement learning technique for determining the best action-selection strategy for any (finite) MDP. It functions by looking at an action-value function that calculates the expected utility of taking a particular action in a given state and then implementing the best policy. [5]. It is an off-policy TD control learning which is the most widely used reinforcement learning method. Q- learning

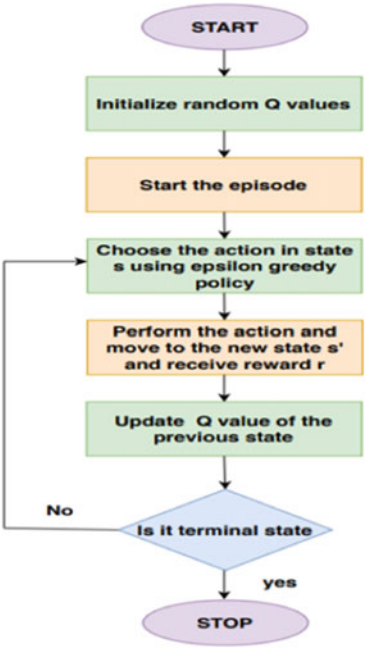

Fig. 2 Flow chart of classical Q-learning algorithm

is an iterative computation and incremental learning process. The flow chart of the algorithm is shown in Fig. 2. The algorithm beings with the initialization of the Q-table, which represents the state-action value. Then agent takes an action by a certain strategy, reaches to next state, and gets an immediate reward. Q(s,a) is update using TD update rule as given below [14]. The process continues until the agent reaches the target state.

$$Q(s,a) = (1-\lambda)Q(s,a) + \lambda\left[r + \gamma \max_{a'} Q\left(s', a'\right)\right] \tag{7}$$

3.1.1 Meta Parameters in Q-Learning

For successful reinforcement learning, three parameters i.e. α, ϵ, and γ need to be chosen carefully.

- The learning rate (α) is key to maximize the rate of learning. If chosen very small, it results in slow learning, at the same time large value will induce oscillations [15]. The learning rate affects how much fresh information will take precedence over old information. A factor of 0 means the agent will learn nothing, whereas a factor of 1 means the agent will only evaluate the most recent input. Larger values of the learning rate increase the influence of both current and future rewards at the

expense of past rewards. For a stochastic environment, the procedure converges under some technical constraints that need the learning rate to decline to zero [16]. Most Optimal policy is achieved by initializing a higher learning rate close to 1, for faster learning but with time it should decay for getting an optimum result. If there is a learning disability, then the optimization process will be affected.

- The exploration parameter (ϵ) is also an important parameter, which controls the exploitation-exploration trade-off. When the robot enters a new state, it must choose and act as the action list. It should be possible to attempt as many different actions as possible to complete the task, but this will raise problems with algorithmic convergence [5]. As a result, an appropriate exploration strategy must be devised. In starting, exploration is required but as time passes the agent gets acquainted with the environment, and exploitation should be done. This is possible by using a decaying function for updating the exploration rate. Depending on the type of strategy chosen, its value varies. Some of the well-known strategies are:
  - Epsilon greedy policy: This is a common policy, in which a parameter of $0 < \epsilon(t) < 1$ is used to select an action based on a set of criteria [3, 17].

$$\mu_t(x) = \begin{cases} \text{random } b \in A(x), & \text{with } p = \epsilon(t) \\ \arg\max_{b \in A(x)} Q(x, b), & \text{with } p = 1 - \epsilon(t) \end{cases} \tag{8}$$

    where p signifies the likelihood of taking a particular action. A lower value of $\epsilon(t)$ indicates that the agent is using more previous experience and exploiting the optimal policy. Typically, the parameter $\epsilon(t)$ is a decaying function with an initial value close to 1 for better exploration.
  - Boltzmann policy: The policy is typically described using the action-value function $Q(s, a)$, which indicates the amount of future rewards the agent would receive if the action was taken at state s and followed the current policy in later stages. The probability of action selection is given by the function

$$P(a \mid x(t)) = \frac{e^{\beta Q(s,a)}}{\sum_{a'=1}^{M} e^{\beta Q(s,a')}} \tag{9}$$

    The exploitation-exploration trade-off is controlled by the inverse temperature β. Ideally, β should start low to allow for a lot of exploration when the agent doesn't have a solid map of which activities will be lucrative, and then steadily grow as the agent starts reaping higher and higher benefits [15].

- Each discount factor (γ) option will result in a different MDP optimal policy. For $\gamma = 0$, the agent acts myopically to maximize immediate reward as it changes reinforcement learning to supervised learning. Using $\gamma = 1$ would, on the other hand, frequently result in minimal task efficiency, a situation is known as the positive circuits problem and the expectation of return from states will consequently be infinity [18]. The complexity of learning a value function increases with the increase of $\frac{1}{1-\gamma}$ [15].The ideal value of γ chosen in most practical real-world problems varies between 0.7 and 0.9.

ALGORITHM 1: PSEUDOCODE OF Q-LEARNING ALGOITHM

Define the environment, actions, rewards and no. of training episode (M)
Initialize discount factor, learning rate, and exploration rate
Initialize Q-function Q (s, a) =0
for t=1,2,3…M ***do***
    Choose a starting location
    while (not a goal state) ***do***
        Check next possible N states
        Choose action according to epsilon greedy policy

$$a(x) = \begin{cases} random\ b \in A, with\ p = \epsilon \\ \underset{b \in A}{argmax}\ Q(x, b), with\ p = 1 - \epsilon \end{cases}$$

        Perform the chosen action
        Transitions to the next state
        Receives the immediate reward
        Update Q-table
    end while
    Update the exploration rate and learning rate using some decay function
end for
The optimal policy is $\pi^* = \underset{a \in A}{argmax}\ Q^*(s, a),\ \ (\forall\ s\ \in S)$

Fig. 3 Pseudo-code of Q-learning algorithm using epsilon greedy policy

The pseudo-code for Q-learning algorithm using epsilon greedy algorithm is given in Fig. 3 [9].

3.1.2 Variations in Q-Learning

As In classical Q-learning an infinite number of iterations are required to update the Q-table, which increases run time complexity and is not suitable for large state space. So to improve CQL, Konar et al. [19] proposed a new deterministic Q-learning which uses a locking property once an optimal action is taken. Thus updating the Q-table requires less number of states and increasing the performance.

4 Practical Challenges in Reinforcement Learning

Applying reinforcement learning to robotics is not yet a simple task, but rather one that necessitates a certain level of expertise. In this segment, we discuss some practical challenges faced in RL. Future research in this area results from the practical challenges that robot reinforcement learning faces.

- Exploiting data sets in a better way: Locally learned information from previous data sets must be reused for training an agent at a global level for complex tasks.
- Comparable Experiments and Consistent Evaluation: The cost, fragility, and variations in hardware make large-scale experiments difficult to perform and reproduce. This is a major limitation in robotic reinforcement learning which must be resolved for self-improving robot research to progress.
- Sparsity in reward function: When the reward is sparse, there is a significant delay between an action and the associated meaningful reward and it can lead to learning disability [20].

5 Conclusion

Reinforcement learning has been validated in several simulated environments, but RL algorithms have limitations in real-world applications. A real-world environment presents more obstacles than a virtual environment, including larger state spaces, increased technical complexity, major safety concerns, and longer performance processing times. RL algorithms fall short when dealing with complex high-dimensional functions like deep neural networks, high-dimensional state or observation spaces, and temporally extended tasks. Also, the learning problem is difficult with sparse reward function. Results show that the RL agents that manipulate the information stored in the map, outperform the "sparse" reward function in training environments. Also, it helps in obstacle avoidance in a complex environment with high convergence.

References

1. Nguyen TT, Nguyen ND, Nahavandi S (2020) Deep reinforcement learning for multiagent systems: a review of challenges, solutions, and applications. IEEE Trans Cybern 50(9):3826–3839
2. Busoniu L, Babuska R, De Schutter B (2008) A comprehensive survey of multiagent reinforcement learning. IEEE Trans Syst Man Cybern Part C (Appl Rev) 38(2):156–172
3. Sadhu AK, Konar A (2017) Improving the speed of convergence of multi-agent q-learning for cooperative task-planning by a robot-team. Robot Auton Syst 92:66–80
4. Spiros K, Daniel K (2002) Reinforcement learning of coordination in cooperative mas. In: The 18th national conference on AI, Alberta, Canada: ACM Press, pp 326–331 (2002)
5. Wang Z, Shi Z, Li Y, Tu J (2013) The optimization of path planning for multi-robot system using Boltzmann policy based q-learning algorithm. In: 2013 IEEE international conference on robotics and biomimetics (ROBIO), pp 1199–1204. IEEE
6. Chaplot DS, Gandhi D, Gupta S, Gupta A, Salakhutdinov R (2020) Learning to explore using active neural slam. arXiv preprint arXiv:2004.05155
7. Botteghi N, Sirmacek B, Mustafa KA, Poel M, Stramigioli S (2020) On reward shaping for mobile robot navigation: a reinforcement learning and slam based approach. arXiv preprint arXiv:2002.04109

8. Arana-Daniel N, Rosales-Ochoa R, López-Franco C (2011) Reinforced-slam for path planing and mapping in dynamic environments. In: 2011 8th international conference on electrical engineering, computing science and automatic control, pp 1–6. IEEE
9. Osmanković D, Konjicija S (2011) Implementation of q-learning algorithm for solving maze problem. In: 2011 proceedings of the 34th international convention MIPRO, pp 1619–1622. IEEE
10. Zhang D, Han X, Deng C (2018) Review on the research and practice of deep learning and reinforcement learning in smart grids. CSEE J Power Energy Syst 4(3):362–370
11. Levine S, Kumar A, Tucker G, Fu J (2020) Offline reinforcement learning: tutorial, review, and perspectives on open problems. arXiv preprint arXiv:2005.01643
12. He YS, Tang YY (2008) Path planning of virtual human by using reinforcement learning. In: 2008 international conference on machine learning and cybernetics, vol 2, pp 987–992. IEEE
13. Chen Y, Schomaker L, Wiering MA (2021) An investigation into the effect of the learning rate on overestimation bias of connectionist q-learning. In: ICAART (2), pp 107–118
14. Wen S, Chen X, Ma C, Lam HK, Hua S (2015) The q-learning obstacle avoidance algorithm based on EKF-SLAM for NAO autonomous walking under unknown environments. Robot Auton Syst 72:29–36
15. Schweighofer N, Doya K (2003) Meta-learning in reinforcement learning. Neural Netw 16(1):5–9
16. Iyer V, Jadhav R, Mavchi U, Abraham J (2016) Intelligent traffic signal synchronization using fuzzy logic and q-learning. In: 2016 international conference on computing, analytics and security trends (CAST), pp 156–161. IEEE
17. Yu X, Wu Y, Sun XM, Zhou W (2021) A memory-greedy policy with guaranteed convergence for accelerating reinforcement learning. J Auton Veh Syst 1(1):011005
18. Knox WB, Stone P (2012) Reinforcement learning from human reward: discounting in episodic tasks. In: 2012 IEEE RO-MAN: the 21st IEEE international symposium on robot and human interactive communication, pp 878–885. IEEE (2012)
19. Konar A, Chakraborty IG, Singh SJ, Jain LC, Nagar AK (2013) A deterministic improved q-learning for path planning of a mobile robot. IEEE Trans Syst Man Cybern Syst 43(5):1141–1153
20. Kober J, Bagnell JA, Peters J (2013) Reinforcement learning in robotics: a survey. Int J Robot Res 32(11):1238–1274

Stock Index Movement Prediction: A Crow Search-ELM Approach

Sidharth Samal and Rajashree Dash

Abstract Predicting the direction of the stock index is a challenging task to tackle because of the inconsistent and noisy stock market data. Extreme learning machine (ELM) being a simpler yet faster machine learning algorithm has the potential to be used for stock market trend analysis due to its better generalization ability. However, the performance of ELM is heavily affected by the input weights allocated to the edges connecting the input layer and hidden layer neurons. On this basis, the crow search (CS) optimization algorithm being a recent and unexplored metaheuristic approach has shown very promising outcomes in various fields of research. This study develops a stock index movement prediction framework combining ELM and CS called CS-ELM. CS-ELM optimizes the weights of ELM for getting an improved accuracy. Furthermore, its performance is compared with default ELM as well as traditional optimization algorithms in particular particle swarm optimization and differential evolution implemented on similarly developed ELM models. The empirical analysis has been carried out utilizing BSE SENSEX and NIFTY 50 benchmark stock index datasets and the outcomes show that CS-ELM achieves better forecasting performance in contrast with other prediction models.

Keywords ANN · ELM · Crow Search · Stock prediction

1 Introduction

Financial time series movement forecasting is considered to be a crucial affair as it can be helpful to investors and traders. However, the high volatility and uncertainty in stock market data escalate the dilemma of developing a prediction model with lower complexity and higher accuracy. An ample amount of machine learning frameworks such as K-nearest neighbor [1], support vector machines [2], and radial basis function network [3], etc., have been experimentally analyzed in the literature with the intention of stock index movement prediction. The main drawbacks of these models are the

S. Samal (✉) · R. Dash
Department of Computer Science and Engineering, Siksha O Anusandhan (Deemed To Be University), Bhubaneswar, India

M. Mishra et al. (eds.), *Innovation in Electrical Power Engineering, Communication, and Computing Technology*, Lecture Notes in Electrical Engineering 814,
https://doi.org/10.1007/978-981-16-7076-3_30

network complexity, several parameter tuning, iterative learning process, and back-propagated error minimization. These drawbacks can be overcome by using another popular machine learning model known as ELM. Huang et al. proposed ELM in 2006 having a single-hidden layer feed-forward neural network (SLFN) architecture [4]. As the name suggests, SLFN architecture consists of only one hidden layer in between its input and output layer [5, 6]. A comprehensive literature review also shows that ELM has held its position as the faster learning model in various areas of research such as medical diagnostics, signal and image processing, financial time series prediction and so on [7, 8].

The main advantage of using ELM is its single-iteration learning scheme with no further back-propagated error minimization which reduces the network training time. One of the key components of ELM which affects the prediction performance is the weights assigned to the edges connecting the input layer neurons and hidden layer neurons. The fundamental theory of ELM suggests to assign these input weights with random values in a certain range [9]. However, it is not guaranteed that we will obtain the most optimum weight by random weight assignment. Therefore, optimizing those random weights using a suitable optimization technique is recommended.

In this paper, the CS optimization algorithm proposed by Askarzadeh [10] has been implemented over ELM weight assignment for stock index movement prediction over BSE SENSEX and NIFTY 50 benchmark stock indices. This experiment aims to generate the most optimal input weights for increasing the accuracy of the framework. CS has been used in various fields of research as well as in solving real-world optimization problems [11, 12] as CS has a simpler implementation, adaptability, flexibility, and lesser control parameters. A comparative study among default ELM, PSO-ELM, DE-ELM, and the proposed CS-ELM is also carried out in this experiment which shows the superiority of CS-ELM over other prediction models. The results obtained after experimentation also shows that CS-ELM has faster convergence and better results than other optimization-based ELMs.

The remainder of this paper is arranged in the following format. Section 2 depicts a detailed flow of the proposed stock index movement prediction using CS-ELM model. Section 3 specifies the empirical result analysis. Subsequently, Sect. 4 provides the concluding remarks.

2 Proposed CS-ELM Based Predictor Framework

The working principle of suggested CS-ELM-based stock index movement prediction framework is explained in this section. Six popular technical indicators such as simple moving average (SMA), moving average convergence and divergence (MACD), stochastic K and D, relative strength index (RSI), and William's R% are adopted from [3] and normalized using min–max normalization scheme. The proposed CS-ELM scheme is represented in Fig. 1. The output data values are calculated using the formula in Eq. (1) given below.

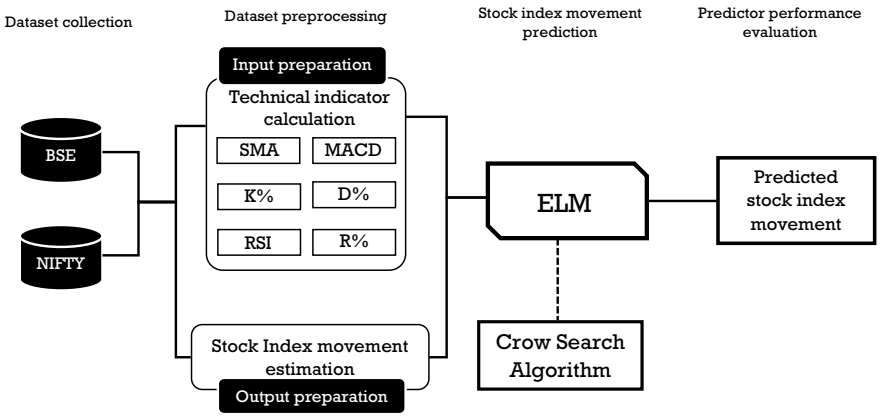

Fig. 1 Architecture of CS-ELM-based stock index movement predictor framework

$$\text{movement}(i) = \begin{cases} 1, & \text{cPrice}(i-1) < \text{cPrice}(i) \\ 0, & \text{cPrice}(i-1) > \text{cPrice}(i) \end{cases} \tag{1}$$

where, movement (i) represents the stock index movement of current trading day, cPrice(i-1) is the closing price of previous trading day, cPrice(i) is the closing price of current trading day.

The preprocessed data consists of 1208 samples which are further split into 70:30 as training and testing set sequentially. The mathematical operating principle of ELM for this experiment has been adopted from [4]. During the training phase, the input weights of the ELM model are updated using the CS algorithm adopted from [10] to get the best accuracy for a given iteration. The workflow of ELM and CS algorithm is given in this section. The optimized weights are used for testing the generalization ability of ELM using testing data. Both training and testing performance of the proposed predictor are evaluated based on 3 performance measures given in Eq. (2)–(4). Finally, the proposed model generates the predicted stock index movement.

$$\text{Accuracy} = \frac{\text{True Positive} + \text{True Negative}}{\text{Total number of samples}} \tag{2}$$

$$F\text{ - measures} = 2 \times \frac{\text{Precision} \times \text{Recall}}{\text{Precision} + \text{Recall}} \tag{3}$$

$$G\text{ - Mean} = \sqrt{\text{Specificity} \times \text{Sensitivity}} \tag{4}$$

2.1 Crow Search-Extreme Learning Machine

ELM is an SLFN model in which only one hidden layer is present in between the input layer and output layer. ELM is also a single-pass training network, i.e., ELM takes only one run to be trained over any dataset and no back-propagated error minimization is needed. ELM has very few parameters to be tuned; hence, it has extreme learning capability unlike other traditional machine learning algorithms such as MLP, SVM, KNN, etc. The input weights of ELM are generated randomly, and the output weights are mathematically calculated using Moore–Penrose pseudo-inverse matrix. In this paper, the ELM network architecture and mathematical modeling are adopted from [4].As the input weights of ELM are generated arbitrarily; we need to perform multiple runs to find the best result yielding weights. However, we may or may not achieve the most suitable weights in those runs. Therefore, using an optimization scheme for acquiring, the input weights of ELM are the most feasible and efficient way. Crow search is a recently developed optimization scheme which has shown tremendous outcome in various fields of research and in solving optimization issues existing in the real-world. CS tries to imitate the behavior of crow birds present in nature. The pseudo-code of CS-ELM is given below.

CS-ELM pseudo code

```
Initialize crows: position, memory, flock size
Initialize ELM parameters: input (X), actual output(O)
Begin training ELM
    for iteration = 1 to max iteration do
        for i = 1 to flock size do
            Obtain input layer weight (w)
            Calculate hidden layer output (H)
            Calculate output weight
                β = H†O
            Compute final(predicted) output of network
            Evaluate fitness value (Accuracy)
        end for
        Apply CS to improve fitness
    end for
end
Store best fitness value and memory of the respective crow
ELM testing using optimized weights
```

Where, X = input to the ELM (6 technical indicators)
O = actual output (0 or 1 class labels).
w = input weights between input layer and hidden layer neurons.
b = bias.
H = hidden layer output

$$\Rightarrow Z = wX + b$$
$$\Rightarrow H = f(Z)$$

f(Z) = activation function
β = output weights
$H^{\dagger}$ = Moore–Penrose pseudo-inverse matrix (adopted from [4]).

3 Experimental Result Discussion

The experiments carried out using CS-ELM for stock index movement prediction are described in this section. This research aims to obtain the optimum input weights needed in ELM architecture for stock index movement prediction by using CS algorithm. As the input weights are randomly generated in ELM, it may hamper the performance of the prediction. Therefore, optimizing the input weights using CS optimization algorithm can provide a better prediction outcome. This hypothesis is simulated using BSE SENSEX and NIFTY 50 benchmark indices data collected over a time frame of May 2014 to May 2019 which consist of 1234 days of the raw stock index day to day data. Data preprocessing step yields a total of 1208 samples for both the datasets consisting of 6 stock market technical indicators which are additionally split into 847:361 training and testing samples, respectively. Their respective class labels are calculated using Eq. (1), i.e., 0 or 1. The number of hidden neurons for the entire experiment is set to 6 through trial and error. In this experiment, the activation function used for hidden layer neurons is Leaky Rectified Linear Unit which can be calculate using Eq. (5).

$$f(x) = \begin{cases} 0.001 \times x & \text{for } x < 0 \\ x & \text{for } x \geq 0 \end{cases} \tag{5}$$

During training stage, the input weights are optimized using CS algorithm, and the output weights are calculated using the Moore–Penrose pseudo-inverse technique. Afterward, the testing is done using the optimized weights and output weights obtained from the training phase to evaluate the generalization ability of ELM. The prediction performance is evaluated using accuracy, f-measure, and g-mean using Eqs. (2)–(4). A comparative analysis has been done among the proposed CS-ELM with default ELM, PSO-ELM, and DE-ELM which are represented in Tables 1 and 2 over BSE SENSEX and NIFTY 50 dataset, respectively, over testing dataset. The parameters utilized for CS algorithm for this experiment are 0.1 for awareness probability, flight length as 2, lower bound as -1, and upper bound as 1.

The testing results obtained from proposed CS-ELM over BSE SENSEX and NIFTY 50 datasets are represented in bold face in Tables 1 and 2 respectively. The data in Tables 1 and 2 show that CS-ELM outperforms other prediction models in terms of all three performance measures in both datasets. The testing prediction

Table 1 Predictor performance comparison for BSE SENSEX dataset

Predictor framework	Accuracy	F-Measure	G-Mean
ELM	0.8088	0.8011	0.8095
PSO-ELM	0.8531	0.8481	0.8542
DE-ELM	0.8670	0.8554	0.8650
CS-ELM	**0.8919**	**0.8800**	**0.8881**

Table 2 Predictor performance comparison for NIFTY 50 dataset

Predictor framework	Accuracy	F-Measure	G-Mean
ELM	0.8060	0.7784	0.7997
PSO-ELM	0.8698	0.8544	0.8670
DE-ELM	0.8559	0.8255	0.8414
CS-ELM	**0.8864**	**0.8706**	**0.8816**

Table 3 Predictor accuracy improvement comparison of CS-ELM with other models

Predictor model	BSE sensex (%)	NIFTY 50 (%)
PSO-ELM	4.55	1.91
DE-ELM	2.87	3.56
ELM	10.27	9.97

accuracy improvement of CS-ELM over other prediction models is represented in Table 3. From Table 3, it can be observed that CS-ELM has an improved accuracy than ELM, PSO-ELM, and DE-ELM with more than 10.27%, 4.55%, and 2.87%, respectively, for the BSE SENSEX dataset and 9.97%, 1.91%, and 3.56% for NIFTY 50 dataset.

The convergence curves of CS-ELM along with PSO-ELM and DE-ELM obtained after 200 iterations over testing dataset represented in Fig. 2 and 3 show that CS-ELM has a faster convergence as well as better accuracy in the case of both datasets.

4 Conclusion

This study proposes a CS-based ELM predictor scheme for predicting the upcoming movement of stock index. The experiment is carried out over BSE SENSEX and NIFTY 50 benchmark indices. The recommended framework takes the advantage of ELM's faster learning ability and CS's faster convergence property to capture the non-linearity in stock market data. Instead of the traditional random weight assignment, here the input weights of a basic SLFN model are optimized using CS algorithm.

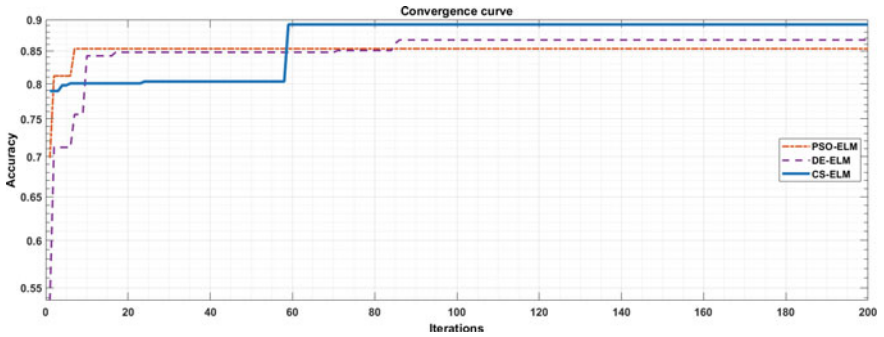

Fig. 2 Performance of optimization techniques for BSE SENSEX dataset

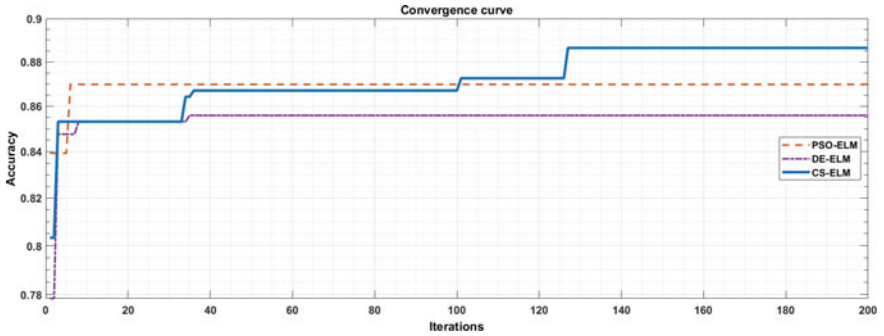

Fig. 3 Performance of optimization techniques for NIFTY 50 dataset

A comparative study among default ELM, PSO-ELM, DE-ELM, and proposed CS-ELM is also provided with the aid of accuracy, f-measure, and g-mean. The results show that CS-ELM shows more than 10%, 2%, and 4% more accuracy in the case of BSE SENSEX dataset and 9%, 3%, and 1% better accuracy in the case of NIFTY 50 dataset over ELM, PSO-ELM, and DE-ELM, respectively. In addition to accuracy, the experimental result shows that CS-ELM performs superior in terms of f-measure and g-mean than other models. This experiment shows that in an ELM based stock index movement predictor, instead of random weight assignment, optimized weights can yield a better outcome.

References

1. Imandoust SB, Bolandraftar M (2013) Application of k-nearest neighbor (knn) approach for predicting economic events: theoretical background. Int J Eng Res Appl 3(5):605–610
2. Huang W, Nakamori Y, Wang SY (2005) Forecasting stock market movement direction with support vector machine. Comput Oper Res 32(10):2513–2522

3. Dash R, Dash PK (2015) A comparative study of radial basis function network with different basis functions for stock trend prediction. In: IEEE power, communication and information technology conference (PCITC), pp 430–435
4. Huang GB, Zhu QY, Siew CK (2006) Extreme learning machine: theory and applications. Neurocomputing 70(1–3):489–501
5. Mishra M, Sahani M, Rout PK (2017) An islanding detection algorithm for distributed generation based on Hilbert-Huang transform and extreme learning machine. Sustain Energy Grids Netw 9:13–26
6. Mishra M, Panigrahi RR, Rout PK (2019) A combined mathematical morphology and extreme learning machine techniques based approach to micro-grid protection. Ain Shams Eng J 10(2):307–318
7. Dash R, Dash PK, Bisoi R (2014) A self adaptive differential harmony search based optimized extreme learning machine for financial time series prediction. Swarm Evol Comput 19:25–42
8. Huang GB, Wang DH, Lan Y (2011) Extreme learning machines: a survey. Int J Mach Learn Cybern 2(2):107–122
9. Mishra M, Rout PK (2019) Fast discrete s-transform and extreme learning machine based approach to islanding detection in grid-connected distributed generation. Energy Syst 10(3):757–789
10. Askarzadeh A (2016) A novel metaheuristic method for solving constrained engineering optimization problems: crow search algorithm. Comput Struct 169:1–12
11. Sheta AF (2017) Solving the economic load dispatch problem using crow search algorithm. In: 8th international multi-conference on complexity, informatics and cybernetics (IMCIC 2017) pp 95–100
12. Dash R, Samal S, Dash R, Rautray R (2019) An integrated TOPSIS crow search based classifier ensemble: In application to stock index price movement prediction. Appl Soft Comput 85:105784

Small Signal Stability Improvement of Wind Penetrated Power System by Lightning Search Algorithm Tuned Fractional STATCOM

Sankalpa Bohidar, Samarjeet Satapathy, Narayan Nahak, and Ranjan Kumar Mallick

Abstract In this work, a fractional STATCOM-based controller action is proposed for small signal stability enhancement of a variable wind integrated power system. The controlled action is provided by a fractional lead-lag compensation based on STATCOM whose parameters are optimized using lightning search algorithm (LSA) in contrast with PSO and DE techniques. The system response and eigenvalues are analyzed prior to and post damping action of the power system with step and random wind penetrations and also varying turbine input power. Eigenvalue analysis of mechanical modes of system with different case studies has been analyzed. Also, time domain analysis has been performed for 200 s with random wind penetrations to prove the efficiency of proposed controller. It is observed that fractional control action based on STATCOM with parameters tuned by LSA can much enhance system oscillation damping subject to step and random mechanical and wind power variations.

Keywords STATCOM · Wind source · Small signal stability · Lightning search algorithm

S. Bohidar · S. Satapathy · N. Nahak (✉)
Department of Electrical Engineering, Siksha 'O' Anusandhan Deemed to be University, Bhubaneswar, Odisha 751030, India
e-mail: narayannahak@soa.ac.in

S. Bohidar
e-mail: sankalpabohidar@soa.ac.in

R. K. Mallick
Department of Electrical and Electronics Engineering, Siksha 'O' Anusandhan Deemed to be University, Bhubaneswar, Odisha 751030, India
e-mail: ranjanmallick@soa.ac.in

M. Mishra et al. (eds.), *Innovation in Electrical Power Engineering, Communication, and Computing Technology*, Lecture Notes in Electrical Engineering 814,
https://doi.org/10.1007/978-981-16-7076-3_31

1 Introduction

In the modern power system, continuously, more efforts are put on renewable penetrations to existing synchronous generations. There are several aspects of such integrations and challenges faced by power system operators subject to such integrations. Wind sources with wind energy conversion systems are prime renewable sources as per researches. Also, wind generations costs are nearly same as the generations by fossil fuels [1–3]. Different experiments have been conducted by many researches pertaining to small signal stability (SSS) of a variable wind penetrated power system [4]. In [5], investigations conducted for grid integrated wind sources by probabilistic methods. Also, case studies are conducted in [6] for observing the effect of wind penetrations on power system. As per [7], SSS is dependent on the system operating conditions. Also, as per [8], the SSS is affected by system oscillations due to varying wind generations. In [9], simulations have been conducted in time domain with different renewable sources for SSS enhancements and FACTS-based controllers are found to be much efficient in comparison with conventional PSS as reported by many researches [10–14]. In [15], STATCOM coordinated control action is proposed and in [16] imperial competitive algorithm [ICA] is proposed for STATCOM controller. Also detailed analysis of STATCOM-based stabilization has been performed in [17]. STATCOM, being as shunt compensating device, can be used for SSS enhancement. Currently, fractional order controllers are gaining more popularity in industrial applications to enhance robustness of PID control. Podlubny [18] proposed fractional PID action involving differentiator and integrator of order μ and λ, respectively. In [19], FOPI UPFC is presented to mitigate SSR. In [20], fractional SSSC is proposed for enhancing the dynamic stability of power system. The next issue is tuning of the damping controller parameter. Different swarm and evolutionary optimization techniques have been reported by different researches for optimal setting of FACTS-based controller in [21, 22]. STATCOM provides simple controlled action to improve oscillatory instability. LSA is proposed in [23], and in [24], lightning search algorithm (LSA) is proposed for voltage and frequency control, and LSA is justified to be a challenging algorithm for controller design. In this work, LSA has been implemented to tune fractional STATCOM controller parameters to enhance SSS subject to variable wind generations.

2 SMIB System Installed with STATCOM

The single machine system installed with STATCOM is depicted in Fig. 1 where wind generation has been integrated. STATCOM modulating index and phase angles being represented by m_{E} and δ_{E}. These parameters can alter operation and control of power system.

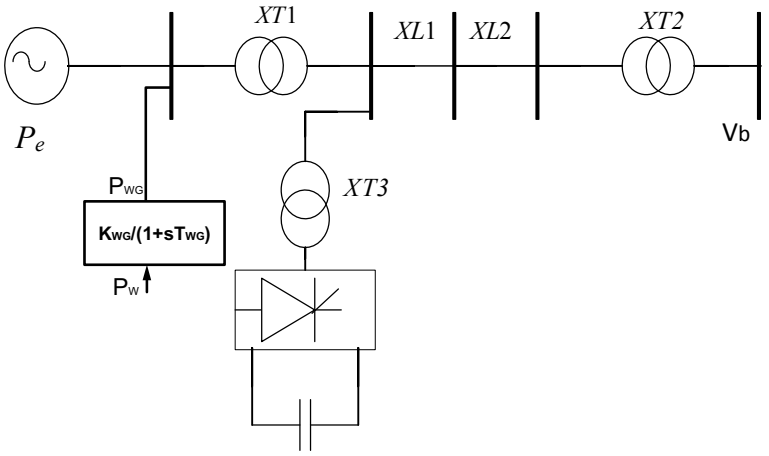

Fig. 1 Single machine wind integrated power system

3 Small Signal Modelling of Power System with STATCOM

The modelling of STATCOM with power system is represented by the following equations. Figure 2 presents low frequency model of STATCOM with power system and the fractional control action based on STATCOM is depicted in Fig. 3.

$$\dot{\delta} = \omega_0.\omega \tag{1}$$

$$\dot{\omega} = (P_m - P_e - D.\omega)/M \tag{2}$$

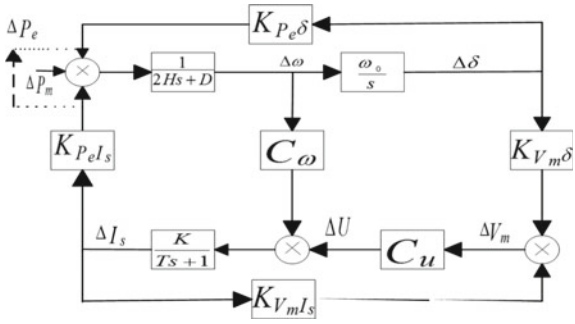

Fig. 2 Small signal modelling of power system with STATCOM

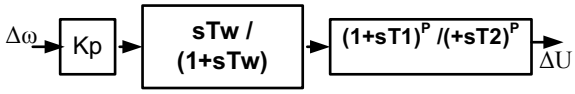

Fig. 3 Fractional lead-lag controller

$$\dot{I_s} = \tfrac{1}{T}[-I_s + k.u] \tag{3}$$

$$P_e = \tfrac{e_q^{'} V_m}{x_d^{'}+x_1} \sin\theta + \tfrac{V_m^2}{2} \cdot \tfrac{x_d^{'}-x_q}{\left(x_d^{'}+x_1\right).\left(x_q+x_1\right)} \sin 2\theta \tag{4}$$

$$V_{md} = \tfrac{\left(x_q+x_1\right) V \sin\delta + I_s X_2 \sin\theta \left(x_q+x_1\right)}{X_1+X_2+x_q} \tag{5}$$

$$V_{mq} = \tfrac{\left(x_d^{'}+x_1\right) V \cos\delta + e_q^{'} X_2 + I_s X_2 \cos\theta \left(x_d^{'}+x_1\right)}{X_1+X_2+x_d^{'}} \tag{6}$$

$$V_m = V_{md} + jV_{mq} \tag{7}$$

$$\theta = \tan^{-1}\left(\tfrac{V_{mq}}{V_{md}}\right) \tag{8}$$

$$\dot{\delta} = \omega_0.\Delta\omega \tag{9}$$

$$\dot{\Delta\omega} = (\Delta P_m - \Delta P_e - D.\Delta\omega)/M \tag{10}$$

$$\dot{\Delta I_s} = \tfrac{1}{T}[-\Delta I_s + k.\Delta u] \tag{11}$$

$$\Delta P_e = K_{P_e\delta}\Delta\delta + K_{P_e I_s}\Delta I_s \tag{12}$$

$$K_{P_e\delta} = \frac{\partial P_e}{\partial\delta} \tag{13}$$

$$K_{P_e I_s} = \tfrac{\partial P_e}{\partial I_s} \tag{14}$$

$$\Delta u = -C_u.\Delta V_m + C_\omega.\Delta\omega \tag{15}$$

$$\Delta V_m = K_{V_m\delta}.\Delta\delta + K_{V_m I_s}.\Delta I_s \tag{16}$$

$$K_{V_m\delta} = \tfrac{\partial V_m}{\partial\delta} \tag{17}$$

$$K_{V_m I_s} = \tfrac{\partial V_m}{\partial I_s} \tag{18}$$

4 Objective Function

In this paper, deviation in angular frequency of alternator has been taken as input signal which is considered in ITAE-based objective function for minimization as given in Eq. (19). For SMIB, $\Delta\omega$ is the sum of speed deviations of all generators.

$$J = \int_0^{t\text{sim}} t|\Delta\omega|\mathrm{d}t \tag{19}$$

where gains range is 1–100 for Kp and T_1, T_2 between 0.01 and 1 and the p range is 0–1. LSA is proposed to tune the gains which have been compared with DE and PSO algorithm.

5 Model of Wind Energy Generation

The speed V_w varies with coefficient C_p in proportion to λ_p, tip speed ratio and β_p angular blade pitch [9].

$$\lambda_\mathrm{p} = \frac{R_\mathrm{b}\omega_\mathrm{b}}{V_\mathrm{W}} \tag{20}$$

where R_b is blade radius (23.5 m.) and ω_b = blade speed (3.14 rad/s). C_p is given as

$$C_\mathrm{P} = (0.44 - 0.0167\beta_\mathrm{p})\sin\left[\frac{\pi(\lambda_\mathrm{p} - 3)}{15 - 0.3\beta_\mathrm{p}}\right] - 0.0184(\lambda_\mathrm{p} - 3)\beta_\mathrm{p} \tag{21}$$

So, the wind power is given by

$$P_\mathrm{w} = (1/2)\rho_\mathrm{a}\mathrm{A_s}C_\mathrm{p}V_\mathrm{W}^3 \tag{22}$$

where ρ_a is air density (=1.25 kg/m^3). A_s is blade swept area (=1735m^2). Wind energy modelling is being presented in Fig. 4 and shown by Eq. 23.

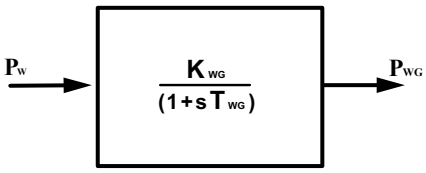

Fig. 4 Modelling of wind generator system

$$G_{\mathrm{WG}} = \frac{K_{\mathrm{WG}}}{1 + sT_{\mathrm{WG}}} = \frac{\Delta P_{\mathrm{WG}}}{\Delta P_{\mathrm{W}}} \tag{23}$$

6 Lightning Search Algorithm (LSA)

LSA is a challenging metaheuristic [23]. Considering cloud change differences, this algorithm is developed imitating natural lightning mechanism. There are transition, space and lead projectiles as represented by the following equations [23].

Transition projectile: Initial input (population) is provided by this transition projectile. By using a uniform distribution probability function, the random values are generated from tip of step leader in thunder as projectiles and hence named. PDF is given by

$$f(x^T) = \begin{cases} \frac{1}{b-a} & \text{for } a \le x^T \le b \\ 0 & \text{otherwise} \end{cases} \tag{24}$$

where x^T = a randomly generation number.

The space projectile function is

$$f(x^s) = \begin{cases} \frac{1}{\mu} e^{\left(\frac{-x^s}{\mu}\right)} & \text{for } x^s \ge b \\ 0 & \text{for } x^s \le b \end{cases} \tag{25}$$

where x^s = randomly generation variable managing direction of projectiles and initial location is given by

$$p^s_{i\_\mathrm{new}} = p^s_i \pm \exp \mathrm{rand}(\mu_i) \tag{26}$$

Lead projectile equations are depicted by

$$f(x^L) = \frac{1}{\sigma\sqrt{2\pi}} e^{\left(\frac{-\left(x^L-\mu\right)}{2\sigma^2}\right)} \tag{27}$$

Here, σ = scale parameter governing exploitations of LSA.

$$P^L_{\mathrm{new}} = P^L + \mathrm{norm\ rand}(\mu_L, \sigma_L) \tag{28}$$

7 Result Analysis

In this work, LSA optimized fractional STATCOM action is proposed to damp oscillations of a variable and random wind penetrated power system. To verify the effectiveness of proposed action, three different cases have been taken under consideration. ITAE-based objective function being implemented for minimizing speed variations, which is the input for control action. In case-1, the prime mover power is step raised by 10% and proposed control action being employed for oscillation damping in contrast to PSO and DE optimizations. Figure 5 presents speed variations with DE, PSO and LSA optimized fractions STATCOM action. It was found that the fraction STATCOM tuned by LSA, and oscillations are damped heavily in comparison with DE, PSO optimal action. Tables 1 and 2 present optimal parameters and system mechanical eigen. In case-2, step variation in wind power output has been considered taking Pw = 0.2 pu and Pw = 0.6 pu with two different conditions. DE, PSO and LSA optimized fractional STATCOM actions are implemented to damp resulting speed variations. Figures 6 and 7 depict speed variations for Pw = 0.2 pu and Pw =

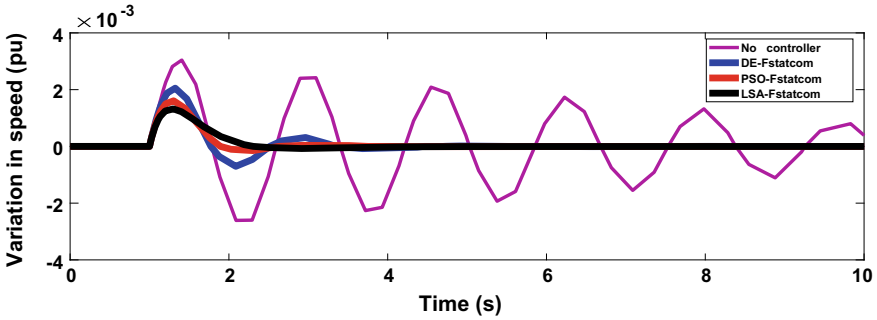

Fig. 5 Speed variation for 10% mechanical input change

Table 1 Optimal parameters

Cases	Optimization technique	K_p	p	T_1	T_2
10% raised in input mechanical power	DE	25.7219	0.4420	0,2613	0.6095
	PSO	37.2529	0.9898	0.4657	0.7630
	LSA	31.53350	0.9423	0,7353	0.6254
Wind power output raised by 0.2pu	DE	47.1446	0.7889	0.3457	0.4797
	PSO	34.9531	0.8202	0,3724	0.2614
	LSA	39.6084	0.6342	0.5046	0.7816
Wind power output raised by 0.6pu	DE	43.0498	0.2620	0.8644	0.5904
	PSO	39.5214	0.4432	0.3026	0.6234
	LSA	59.0808	0.3676	0.3963	0.1230

Table 2 System eigenvalues for mechanical mode

Cases	DE	PSO	LSA
10% raised in input mechanical power	−1.2411 +4.4024i −1.2411 −4.4024i	−2.2874 +3.8385i −2.2874 −3.8385i	−2.1995 +1.0002i −2.1995 −1.0002i
Wind power output raised by 0.2pu	−1.6984 +2.8057i −1.6984 −2.8057i	−1.6580 +1.5820i −1.6580 −1.5820i	−2.8851 +0.1075i −2.8851 −0.1075i
Wind power output raised by 0.6pu	−0.6000 +4.4289i −0.6000 −4.4289i	−0.7868 +3.2929i −0.7868 −3.2929i	−0.9133 +1.8980i −0.9133 −1.8980i

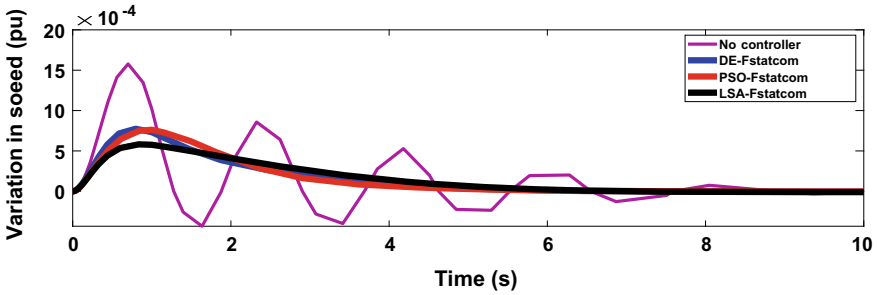

Fig. 6 Speed variation for wind power output raised by 0.2pu

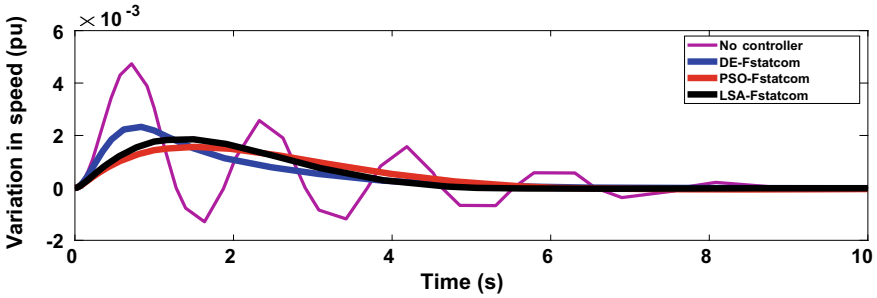

Fig.7 Speed variation for wind power output raised by 0.6pu

0.6 pu, respectively. Tables 1 and 2 present optical parameters and system mechanical modes. It is found that increased heavy wind penetrations excite oscillations in speed, and LSA tuned fractional STATCOM action is observed to be much efficient for oscillation damping in contrast to DE and PSO tuning actions. The system eigen is observed to be shifted to much left side with proposed action justifying efficacy of proposed action. In case-3, a time domain stimulation being performed pertained to random variations in wind power generations. The pattern of variations in wind generation is shown in Fig. 8. The variation in speed subject to random wind penetration is shown in Fig. 9. By implementing proposed control action, the variation in speed is much damped as compared to only PSO and DE algorithms tuned action.

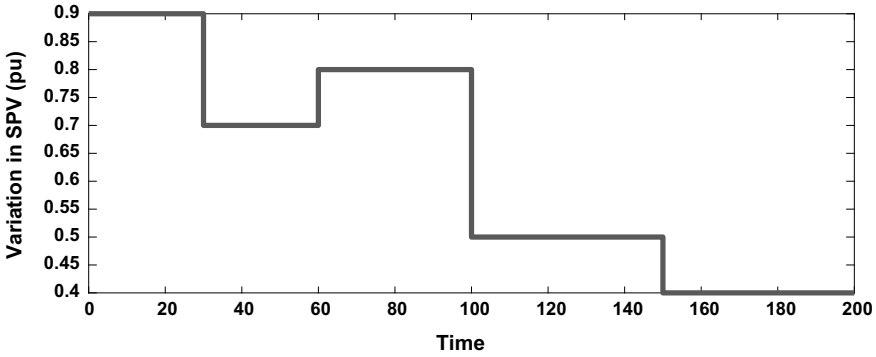

Fig. 8 SPV random variation

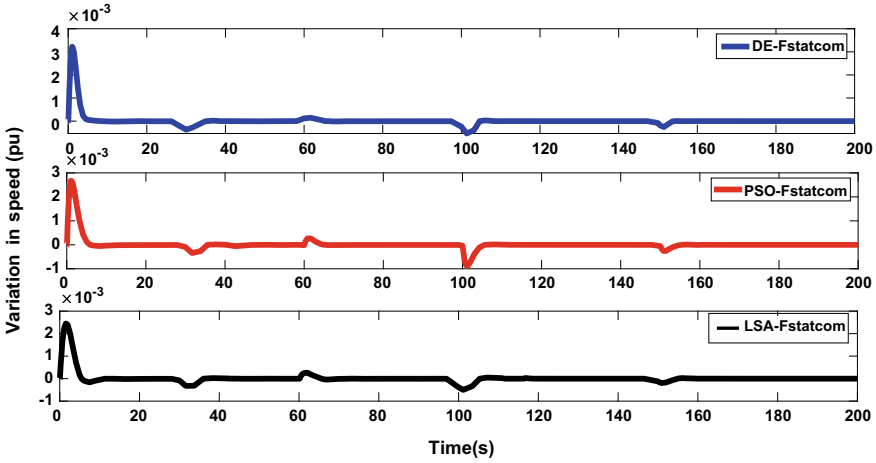

Fig. 9 Speed deviations due to random wind power output variations

8 Conclusion

A random wind penetration power system is considered, here, the SSS enhancer. An optimal fractional STATCOM-based control action is proposed in this work, the gains of control action are optimized by LSA and put in comparison with PSO and DE algorithms. Different case studies are conducted with varying input prime mover power, step and random variations in wind penetration. Time stimulations have been conducted with 200 s for random wind variations with proposed control actions. The eigenvalues are analyzed for different conditions. From speed variations response and eigen analysis, it is observed that fractional STATCOM controller optimized by LSA can much efficiently damp system oscillations resulting from varying mechanical power and wind power output variations. The efficacy of control action has been

verified with PSO and DE tuned control actions. This work can be further modified for large extended power system in the future.

References

1. Anderson PM, Bose A (1983) Stability simulation of wind turbine system. IEEE Trans Power App Syst 102(12):3791–3795
2. Kodama N, Matsuzaka T, Inomata N (2001) The power variation control of a wind generator by using probabilistic optimal control. Trans Inst Elect Eng Jpn 121-B(1):22–30
3. Wang P, Billinton R (2001) Reliability benefit analysis of adding WTG to a distribution system. IEEE Trans Energy Convers 16(2):134–139
4. Shi LB, Wang C, Yao LZ, Wang LM, Ni YX (2011) Analysis of impact of grid-connected wind power on small signal stability. Wind Energy 14:518–537
5. Bu SQ, Du W, Wang HF, Chen Z, Xiao LY, Li HF (2011) Probabilistic analysis of small-signal stability of large-scale power systems as affected by penetration of wind generation. IEEE TransPower Syst. 27:1–9
6. Slootweg JG, Kling WL (2003) The impact of large scale wind power generation on power system oscillations. Electr Power Syst Res 67:9–20
7. Nahak N, Satapathy O (2021) Investigation and damping of electromechanical oscillations for grid integrated micro grid by a novel coordinated governor-fractional power system stabilizer. In: Energy sources, part a: recovery, utilization, and environmental effects. https://doi.org/10.1080/15567036.2021.1942596
8. Liu W, Ge R, Li H, Ge J (2014) Impact of large-scale wind power integration on small signal stability based on stability region boundary. Sustainability 6:7921–7944
9. Lee D-J, Wang L (2008) Small-signal stability analysis of an autonomous hybrid renewable energy power generation/energy storage system part i: time-domain simulations. IEEE Trans Energy Convers 23(1)
10. Nahak N, Sahoo SR, Mallick RK Small signal stability enhancement of power system by modified GWO optimized UPFC based PI-lead-lag controller. Adv Intell Syst Comput, vol 817. https://doi.org/10.1007/978-981-13-1595-4_21
11. Mallick RK, Nahak N, Sinha RR (2015) Fuzzy sliding mode control for UPFC to improve transient stability of power system. In: 2015 annual IEEE India conference (INDICON), 2015, pp 1–6. https://doi.org/10.1109/INDICON.2015.7443182
12. Nahak N, Nabi MM, Panigrahi D, Pandey RK, Samal A, Mallick RK (2019) Enhancement of dynamic stability of wind energy integrated power system by UPFC based cascaded PI with dual controller. In: 2019 IEEE international conference on sustainable energy technologies and systems (ICSETS), 2019, pp 150–155
13. Nahak N, Sahoo SR, Mallick RK (2018) Design of dual optimal UPFC based PI controller to damp low frequency oscillation in power system. In: 2018 technologies for smart-city energy security and power (ICSESP), 2018, pp 1–5. https://doi.org/10.1109/ICSESP.2018.8376732
14. Panda S (2011) Robust coordinated design of multiple and multi-type damping controller using differential evolution algorithm. Int J Electr Power Energy Syst 33:1018–1030
15. Guo C, Jiang W, Zhao C (2019) Small-signal instability and supplementary coordinated damping-control of LCC-HVDC system with STATCOM under weak AC grid conditions. Int J Electric Power Energy Syst 104:246–254
16. Abd-Elazim SM, Ali ES (2016) Imperialist competitive algorithm for optimal STATCOM design in a multimachine power system. Int J Electr Power Energy Syst 76:136–146
17. Abido MA (2005) Analysis and assessment of STATCOM-based damping stabilizers for power system stability enhancement. Electric Power Syst Res 73(2):177–185
18. Podlubny I (1999) Fractional-order systems and PID-controllers. IEEE Trans Autom Control 44:208–214

19. Koteswara Raju D, Umre BS, Junghare AS, Chitti Babu B (2017) Mitigation of subsynchronous resonance with fractional-order PI based UPFC controller. Mech Syst Signal Process 85:698–715
20. Nahak N, Bohidar S, Routray D, Mallick RK, Patra AK, Agrawal R (2020) Dynamic stability improvement of a variable wind integrated power system by fractional parallel SSSC controller. In: 2020 IEEE international conference on power electronics, smart grid and renewable energy (PESGRE2020), 2020, pp 1–6. https://doi.org/10.1109/PESGRE45664.2020.9070279
21. Nahak N, Bohidar S, Mallick RK (2018) Investigation of UPFC based damping controller parameter and a novel multi input dual controller with time delay for multi machine system by Grey-Wolf optimizer. Int Rev Autom control 11(1)
22. Panda S, Padhy NP (2008) Comparison of particle swarm optimization and genetic algorithm for FACTS-based controller design. Appl Soft Comput 8(4):1418–1427
23. Sarker MR, Mohamed A, Mohamed R (2017) Improved proportional-integral voltagecontroller for a piezoelectric energy harvesting system converter utilizing lightning search algorithm. Ferroelectrics 514(1):123–145
24. Rajbongshi R, Saikia LC (2017) Combined control of voltage and frequency of multiarea multisource system incorporating solar thermal power plant using LSA optimised classical controllers. IET Gener Transm Distrib 11(10):2489–2498

Improved Grid Synchronization Technique Under Adverse Grid Condition

Banishree Misra, Poonam Tripathy, and Byamakesh Nayak

Abstract The identification and extraction of positive sequence fundamental component from an unbalanced and polluted grid signal have a vital role in controlling the grid integrated electrical power converters. The mostly used synchronous reference frame phase lock loop (SRF-PLL) fails in executing this task for an unbalanced and harmonically distorted grid voltage. In this paper, the SRF-PLL along with a low pass filter (fourth order Butterworth filter) is utilized to extract the positive sequence fundamental signal from a distorted grid voltage. The detailed study of the proposed low pass filter with second order generalized integrator (SOGI) and SRF-PLL is presented to exhibit its adaptability to adverse grid conditions and power quality issues. The proposed synchronization structure will provide fast and robust performance under voltage sag, harmonics, and sudden phase jump without compromising the dynamic performance and stability of the overall synchronization structure. To validate the performance of the proposed technique, a detailed dynamic analysis and harmonic analysis are carried out in MATLAB/Simulink environment.

Keywords Synchronous reference frame · Second order generalized integrator · Low pass filter · Voltage sag · Harmonics · Phase jump

1 Introduction

Maintaining good power quality is a challenging task for power electronic converter-controlled grid integrated distributed power generation system. During grid synchronization process, maintenance of desired phase, frequency, and grid magnitude at the point of common coupling (PCC) [1, 2] is a major concern. Hence, monitoring, detection and extraction of correct magnitude, phase and frequency of the utility voltage signal have the foremost significance in reference signals generation. Under healthy grid condition, grid voltage is balanced and sinusoidal; but in case of faulty grid or

B. Misra (✉) · P. Tripathy · B. Nayak
School of Electrical Engineering, KIIT Deemed to be University, Bhubaneswar 751024, India
e-mail: bmisrafel@kiit.ac.in

M. Mishra et al. (eds.), *Innovation in Electrical Power Engineering, Communication, and Computing Technology*, Lecture Notes in Electrical Engineering 814,
https://doi.org/10.1007/978-981-16-7076-3_32

nonlinear loads usage, grid voltage is unbalanced and distorted. Under such situation, it is highly essential to maintain the continuity of grid supply for uninterrupted generation and running. Hence, proper synchronization of the grid converters must be ensured.

But increased nonlinear loads usage or transient fault conditions make the grid signal no longer sinusoidal which affects the accuracy in the information given to the PLL creating a weak distributed generation system. Therefore, the performance of the PLL must be robust in both normal and abnormal grid operating conditions and this can be ensured by injecting a perfect sinusoidal fundamental grid signal [3, 4] to the input of the PLL. In the balanced grid condition, the grid voltage comprises of only positive sequence component with identical synchronization angle for both grid voltage and its positive sequence component. During unbalanced grid conditions, the grid voltage is decomposed into its positive and negative sequence integrant where the positive sequence component is provided as the feed in to the phase lock loop. So, the positive sequence, negative sequence, and all harmonic components must be extracted from the grid input current before processing in the PLL or for the generation of current command signal [5]. This paper proposes a method to segregate out the major harmonics, fundamental positive sequence, and negative sequence component of grid current signal using second order generalized integrator (SOGI) with synchronous reference frame phase lock loop (SRF-PLL) and a low pass filter [6, 7].

2 SRF-PLL Synchronization Structure

By using park's transformation $\left[T_{dq}\right]$ SRF-PLL method can be represented as shown in Fig. 1. The grid voltage is transformed from the natural/*abc* reference frame to the synchronously rotating/*DQ* reference frame. In the *DQ* reference frame, the angular position is administered by a feedback response by making the *q* component zero. The *d* component represents the amplitude of the voltage vector, and the output of the feedback loop indicates its phase in steady-state condition.

In ideal utility conditions having balanced system voltage with no harmonics, a SRF-PLL with high bandwidth can precisely detect the magnitude and phase of the main voltage vector while for a utility voltage, unbalanced or polluted with higher-order harmonics, a reduced bandwidth of SRF-PLL can reject and nullify the effect

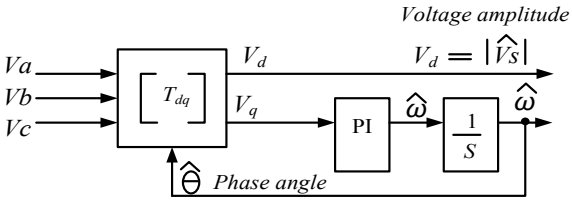

Fig. 1 Basic arrangement of SRF-PLL

of harmonics. But the SRF-PLL with reduced bandwidth in polluted grid will lead to inaccurate estimation of the grid phase angle and amplitude, thereby deteriorating the quality of power delivered to the main grid [8]. So, the proposed technique uses adaptive filters like second order generalized integrator (SOGI) and a low pass filter connected with the SRF-PLL synchronization structure for accurately estimating the phase angle and amplitude of the utility grid signal.

3 SOGI Low Pass Filter SRF-PLL Synchronization Technique

3.1 SOGI-Based Filter

The second order generalized integrator (SOGI)-based adaptive resonant filtering technique is designed on the basis of fundamental frequency of grid. The higher-order harmonics (fifth, seventh, and more) can be filtered out by adjusting the bandwidth of the adaptive filter [9]. Stability of the filter depends on its bandwidth and damping factor. Proper choice of bandwidth [10, 11] can eliminate higher-order harmonics from the output of SOGI, keeping the system stability intact. However, the full magnitude of negative sequence current appears with positive sequence current component at the filter output which is confirmed by the following equation:

The voltage vector represented in the Cartesian $\alpha\beta$ stationary reference frame using Clarke transformation for the nth harmonic voltage is given as

$$v_{\alpha\beta} = \begin{bmatrix} v_\alpha \\ v_\beta \end{bmatrix} = \left[T_{\alpha\beta} \right].v_{abc} = \sum_{n=1}^{\infty} v^n \begin{bmatrix} \cos(n\omega t + \emptyset^n) \\ \sin(n\omega t + \emptyset^n) \end{bmatrix} + \sum_{n=1}^{\infty} v^{-m} \begin{bmatrix} \cos\left(-m\omega t + \emptyset^{-m}\right) \\ \sin\left(-m\omega t + \emptyset^{-m}\right) \end{bmatrix} \quad (1)$$

where

$$\left[\mathrm{T}_{\alpha\beta} \right] = \frac{2}{3} \begin{bmatrix} 1 & -\frac{1}{2} & -\frac{1}{2} \\ 0 & \frac{\sqrt{3}}{2} & -\frac{\sqrt{3}}{2} \end{bmatrix}$$

To filter or extract the negative sequence component current, an algorithm must be developed and placed in between the SOGI and the PLL. This section proposes a new algorithm by combining the SOGI structure with a low pass filter for extraction of positive sequence fundamental signal from unbalanced and polluted grid signals.

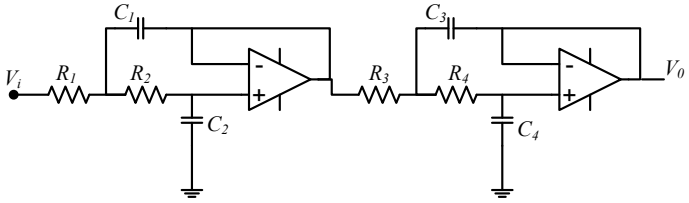

Fig. 2 Fourth order Butterworth filter [12]

3.2 Butterworth Fourth Order Low Pass Filter

The proposed synchronization structure comprises of the SOGI filter with a fourth order Butterworth filter to generate the required positive sequence fundamental component for the SRF-PLL as shown in Fig. 2. The structure of fourth order Butterworth filter in Fig. 2 comprises of two cascaded op-amps integrated with four capacitors and four resistors producing maximally flat frequency/magnitude response in the passband.

The transfer function for the Butterworth filter can be written as

$$\frac{V_0(s)}{V_i(s)} = \frac{w_{c1}^2 . w_{c2}^2}{\left(S^2 + {}^{w_{c1}}/_{Q_1} + w_{c1}^2\right)\left(S^2 + {}^{w_{c2}}/_{Q_2} + w_{c2}^2\right)} \tag{2}$$

The cut-off frequencies (w_{c1}, w_{c2}) and quality factors (Q_1, Q_2) can be derived as

$$w_{c1} = \frac{1}{\sqrt{R_1 R_2 C_1 C_2}} \quad w_{c2} = \frac{1}{\sqrt{R_3 R_4 C_3 C_4}} \tag{3}$$

$$Q_1 = \frac{\sqrt{R_1 R_2 C_1 C_2}}{R_1 C_1 + R_2 C_1} \quad Q_2 = \frac{\sqrt{R_3 R_4 C_3 C_4}}{R_3 C_3 + R_4 C_3} \tag{4}$$

Quality (Q) factor corresponds to the ratio of cut-off frequency to bandwidth. Higher quality (Q) factor means smaller bandwidth that is comparatively lower rate of energy loss in comparison with its stored energy and vice versa.

3.3 Proposed Synchronization Technique Under Adverse Grid Condition

The structure of the proposed synchronization technique is provided in Fig. 3. The effectiveness of the proposed filtering techniques is validated in MATLAB/Simulink

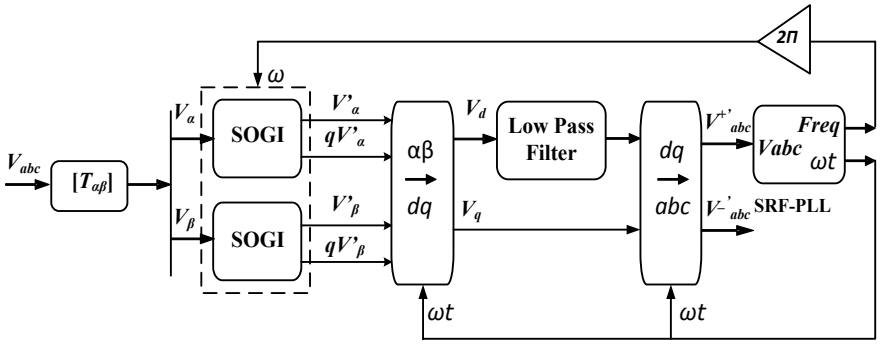

Fig. 3 Structure of SOGI low pass filter with SRF-PLL

environment for different case studies. The main purpose of the new filtering technique is the extraction of fundamental positive sequence voltage $V^{+'}_{abc}$ from an asymmetrical and distorted three-phase grid voltage. Initial grid parameters are at their normal value with grid fundamental frequency at 60 Hz. In the case study, the pre-fault voltage is set to $V_{abc} = 1\angle 0°$ in per unit base. Then, different faults or instabilities like two-phase voltage sag, harmonics, and phase jump were applied at various instants and the system dynamic response was studied. The details of the faults or instabilities applied at different intervals of time are as follows:

(Test case I) *Two-phase voltage sag*:

Initially, a two-phase voltage sag registering a drop of voltages to 0.6 pu in two phases at the point of common coupling is considered.

(Test case II) *Harmonics*:

In the second interval, addition of fifth and seventh order harmonics with magnitude 0.2 pu and 1/7 pu, respectively, to the grid voltage along with a two-phase sag (voltage drop in two phases to 0.6 pu) is considered.

(Test case III) *Phase jump*:

In the last interval, C type asymmetrical fault is considered where there is a change in magnitude as well as phase angles of two phases. Accordingly, the positive and negative sequence fault voltages are given by $V^{+1} = 0.75\angle 30°$ pu and $V^{-1} = 0.25\angle -30°$ pu.

For the proposed synchronization technique, resonating frequency of the SOGI-QSG filter is assumed to ideally synchronize with the grid frequency given by $\omega = 2\pi 60$ rad/s and setting the gain at $k = 1.414$. Next section discusses simulation results of the proposed synchronization method including the response of the separated fundamental signal in both natural and DQ frame of reference. Here, detail simulated results are provided to get the phase angle information, the total harmonic distortion of the extracted waveforms and the settling time analysis of the SRF-PLL response.

4 Simulation Results

4.1 Conventional SRF-PLL System

Figure 4 shows the SRF-PLL performance under both balanced andpolluted grid conditions. Figure 4a shows introduction of different disturbances at different intervals. When the grid signal is perfectly balanced at $t = 0$ s with no oscillations, d-axis component provides absolute amplitude of the extracted fundamental component and zero value of the q-axis component confirms the accurate estimation of phase angle of the extracted signal. Figure 4b, c showing all the disturbance intervals for which both d-axis and q-axis components fluctuate about the mean value. It concludes that the amplitude as well as the phase angle of the extracted fundamental signal cannot be exactly determined by simply using the SRF-PLL structure.

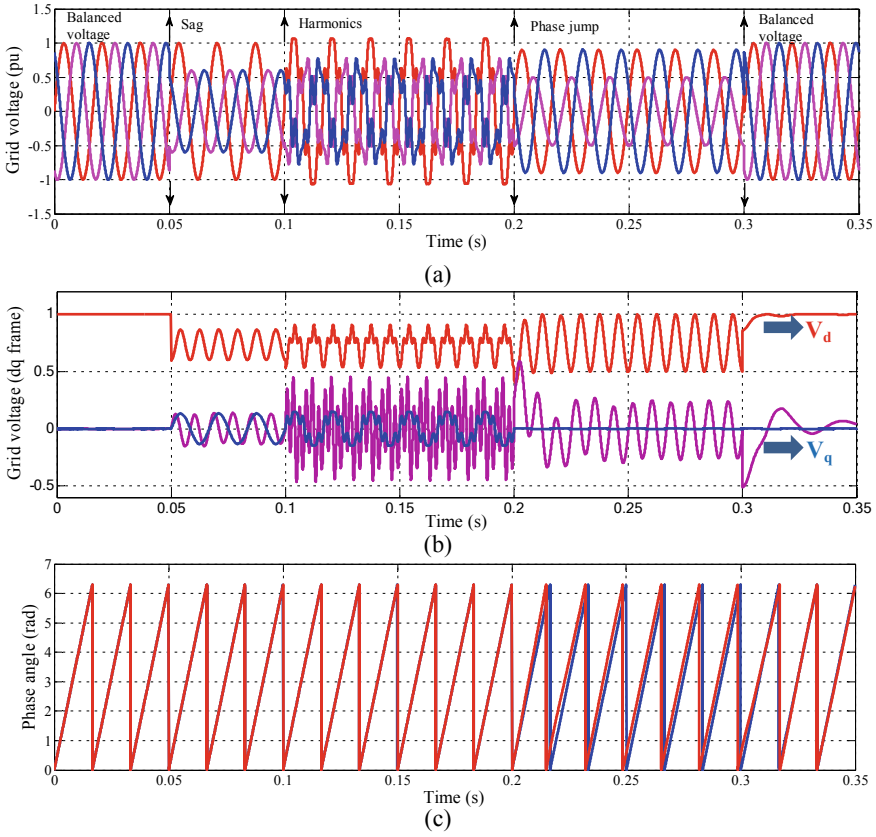

Fig. 4 SRF-PLL response at polluted grid conditions **a** in natural reference frame, **b** in DQ reference frame, and **c** detected phase angle (rad)

A second order low pass Butterworth filter with the SOGI-SRF-PLL can be used to compensate the fluctuating mean value of the d-axis and q-axis component providing a better response for amplitude plus phase angle restoration which is explained in the next section.

4.2 SOGI Low Pass Filter-Based SRF-PLL

Figure 3 shows the synchronization structure using a low pass fourth order Butterworth filter along with a SOGI filter to estimate the mean value of the extracted signal which determines the amplitude of the positive sequence fundamental voltage component. Figure 5 shows the SOGI low pass filter SRF-PLL responses. From Fig. 5b, c the mean value of the extracted *d*-axis component is used to estimate the fundamental grid signal amplitude. Figure 5d confirms accurate estimation of phase angle. A little distortion in the amplitude of extracted three-phase fundamental component is registered during phase jump with a THD of 0.8%. The THD after compensation of voltage sag is 0.17% and harmonics is 0.16%, which are very low. The *q*-axis and *d*-axis components are stable and also accurately estimated as desired by the SRF-PLL. The response time of SOGI low pass filter-based SRF-PLL under various grid fault conditions are analyzed.

The assessment of the proposed synchronization technique is provided in Table 1. A comparison of SRF-PLL and SOGIlow pass filter SRF-PLL with respect to different features under distorted grid conditions is provided in Table 2.

5 Conclusions

The simulation results, dynamic analysis, and response time of the proposed low pass filter-based SOGI PLL synchronization technique confirm its robustness and accuracy. The results are validated based on the quality of the extracted fundamental positive sequence component from the distorted grid signal. The dynamic behavior and stability of the synchronization technique are well studied in both natural and DQ reference frames. The steady-state error in the phase angle of the extracted signal is almost zero except a minimum amplitude error, which can be noticed in case of phase jump. The response time is a little more in case of two-phase voltage sag condition but the harmonic profile confirms the precision of the proposed technique.

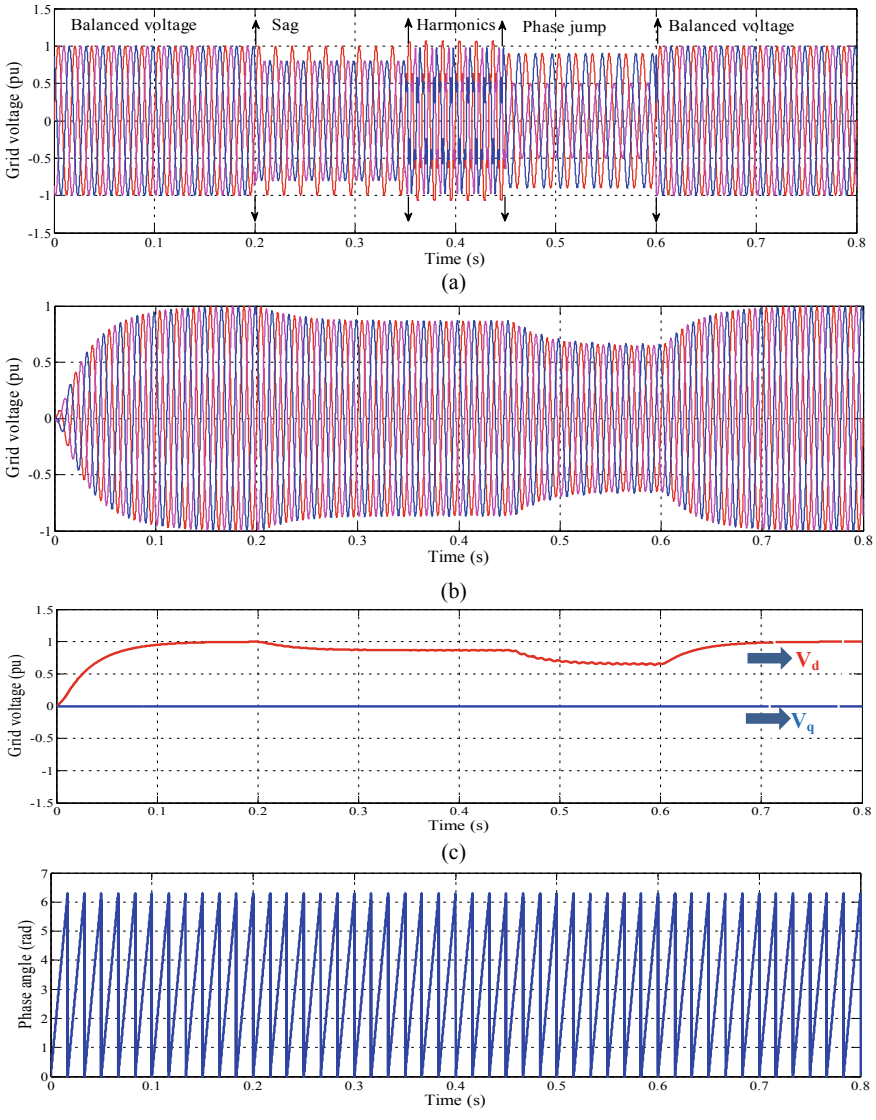

Fig. 5 SOGI low pass filter with SRF-PLL response at **a** polluted grid conditions like voltage sag, harmonics, and phase jump before compensation, **b** in natural reference frame after compensation, **c** in DQ reference frame after compensation, and **d** detected phase angle (rad)

Table 1 Assessment of the proposed synchronization technique

Test case	Two-phase voltage sag (0.2–0.35 s)	Harmonics (0.35–0.45 s)	Phase jump (0.45–0.6 s)
Settling time (ms)	120	0.8	10
THD of the extracted signal (%)	0.17	0.16	0.8
Observation	Little sluggish response with accurate estimation of amplitude	Fast response and accurate restoration of amplitude	Exact estimation of phase angle with a small amplitude error

Table 2 Performance comparison of SRF-PLL and SOGI low pass filter SRF-PLL

Features	SRF-PLL	SOGI low pass filter SRF-PLL
Computational burden	Lowest	Low
Phase error	Exist	Less as compared to SRF-PLL
Dynamic Performance	Poor	Better
Filtering Performance	Poor	Better
Application	Works effectively under ideal grid condition. Fails to perform under distorted and unbalanced grid condition	Performs effectively under distorted and unbalanced grid conditions like two-phase voltage sag, harmonic distortion, and phase jump condition

References

1. Rodríguez P, Luna A, Muñoz-Aguilar R, Etxeberria-Otadui I, Teodorescu R, Blaabjerg F (2012) A stationary reference frame grid synchronization system for three-phase grid-connected power converters under adverse grid conditions. IEEE Trans Power Electron 27(1):99–112
2. Ullah I, Ashraf M (2019) Comparison of synchronization techniques under distorted grid conditions. IEEE Access 7:101345–101354
3. Gonzalez-Espin F, Figueres E, Garcera G (2012) An adaptive synchronous-reference-frame phase-locked loop for power quality improvement in a polluted utility grid. IEEE Trans Industr Electron 59(6):2718–2731
4. Hui N, Luo Z, Feng Y, Han X (2020) A novel grid synchronization method based on hybrid filter under distorted voltage conditions. IEEE Access 8:65636–65648
5. Karimi-Ghartemani M, Iravani M (2004) A method for synchronization of power electronic converters in polluted and variable-frequency environments. IEEE Trans Power Syst 19(3):1263–1270
6. Kaura V, Blasko V (1997) Operation of a phase locked loop system under distorted utility conditions. IEEE Trans Ind Appl 33(1):58–63
7. Timbus A, Liserre M, Teodorescu R, Rodriguez P, Blaabjerg F (2009) Evaluation of current controllers for distributed power generation systems. IEEE Trans Power Electron 24(3):654–664
8. Rodriguez P, Pou J, Bergas J, Candela J, Burgos R, Boroyevich D (2007) Decoupled double synchronous reference frame PLL for power converters control. IEEE Trans Power Electron 22(2):584–592

9. Rodríguez P, Teodorescu R, Candela I, Timbus A, Liserre M, Blaabjerg F (2006) New positive-sequence voltage detector for grid synchronization of power converters under faulty grid conditions. In: 37th IEEE power electronics specialists conference, pp 1–7
10. Misra B, Nayak B (2017) Second order generalized integrator based synchronization technique for polluted grid conditions. In: 2017 2nd International conference for convergence in technology (I2CT), pp 1080–1084
11. Misra B, Majumdar A, Pal S (2020) Performance of second-order generalized integrator based adaptive filter under adverse grid conditions. In: 2020 1st International conference on innovation in electrical power engineering, communication, and computing technology, 630, pp 685–695
12. Schaumann R, Valkenburg MV (2001) Design of analog filters. Oxford University Press, New York

Automated Visual Inspecting System for Fruit Quality Estimation Using Deep Learning

Debaniranjan Mohapatra, Niva Das, Kalyan Kumar Mohanty, and Janhawi Shresth

Abstract Automated visual inspection using deep learning is widely used in recent years. In the field of agriculture, deep learning can be deployed to reduce effective man power, best time utilization, and supreme classification with improved accuracy. In agriculture, DL can be imported in many applications like soil identification, disease classification, fruit grading, and many more. Fruit quality classification is an essential part in farming as it implies to the return directly. Hence, an automated system is much needed to improve the classification of fruits with high accuracy and less time. In this paper, three different CNN models are proposed, namely simple CNN, ResNet50, and VGG19 for the said purpose. A comparison between CNN and two other forms of CNN (ResNet50 and VGG19) is presented in terms of performance. This work has achieved the optimum result with grading accuracy over 94% using VGG19 model.

Keywords Deep learning · CNN · ResNet50 · VGG19

1 Introduction

Agriculture is the main source of national income for a country. The national economy is directly related to agricultural outcome [1]. When we think about a developing country like India, agriculture is the backbone of Indian economy. Farming provides 17% of total GDP and also 60% of employment out of 1.3 billion people in India. The fulfillment of basic requirements like food, shelter, and cloths is not possible for

D. Mohapatra (✉) · N. Das
ITER, S'O'A Deemed to be University, Bhubaneswar 751030, India

N. Das
e-mail: nivadas@soa.ac.in

K. K. Mohanty
Tech Mahindra, Bhubaneswar 751023, India

J. Shresth
Kalinga Institute of Industrial Technology, Bhubaneswar 751024, India

M. Mishra et al. (eds.), *Innovation in Electrical Power Engineering, Communication, and Computing Technology*, Lecture Notes in Electrical Engineering 814,
https://doi.org/10.1007/978-981-16-7076-3_33

government when it is dealing with huge number of populations. Hence, we need to satisfy the basic requirements like food so as to proceed toward technological growth.

Crop or fruit quality detection is very much essential for farmers as the whole income depends on it. A good fruit quality will capture high price as well as demand and the price will decrease according to decreased fruit grade. Fruit quality is an important parameter in estimating shelf life, and it is directly reflected in customers purchasing choice. Presently, fruit market is operated with the brokers or middle men who takes the fruit at very less price from Farmers. Hence, farmers are not getting the exact value of it though they worthy of it. Hence, an automated system is needed to classify the healthy and diseased crops so that a farmer can easily justify his price according to the cultivated fruit [2]. The application of this system is that farmers can get notified about the exact price of their fruits by suppressing the role of middle men or brokers.

In this work, images of apple, banana, and oranges have collected from Kaggle site. A total of 849 data of both healthy and diseased images were collected. We have used 80% of the total data for training phase and rest images (170) for testing the data. Proposed paper is organized as follows. Section 2 presents literature review, Sect. 3 explains the proposed methodology, Sect. 4 consists of results and analysis followed by a conclusion at Sect. 5.

2 Literature Review

In order to conduct research, a proper literature review should be maintained so as to extract the research gap; hence, we have explored some of the related works of this research. Nandi et al. [3] have worked in this sector to contribute their effort for the development of a fine fruit grading system. They have developed a grading system of mango (*Mangifera Indica* L.) fruit according to its maturity. They have followed some attributes like size, shape, surface defect, etc., they have graded mangoes in four categories based on local market distance and market values. They have captured the images from videos taken by charged couple device (CCD). Then, they have applied several image processing techniques to collect those features which are sensitive to fruit maturity and quality. They have employed support vector regression (SVR) for maturity prediction. Fuzzy incremental learning algorithm was adopted by them to support multi-attribute decision making process and they have reached to accuracy about 87%.

Hu et al. [4] have worked on crop disease detection with the combination of both IoT and deep learning. The application of their work is their system identifies the crop disease automatically and sends the corresponding precautions to the farmers directly. They have implemented ResNet architecture which is a multidimensional feature compensation network model. ResNet model considers mainly three dimensions, namely species, coarse grained, and fine grained and generates a compensation layer

for disease identification purpose. They have concluded that ResNet model performs better than any other existing deep learning model.

Ponce et al. [5] have worked on olive fruit classification using image processing and CNN model. They have taken 2800 numbers of data of olive fruit with seven different categories. They have preprocessed the images with image processing techniques and then trained the model with these images. They have got remarkable hit rates after testing the data in Inception-ResNet-V2 architecture. They have reached accuracy near about 95.91% in the entire work.

Hossain et al. [6] have developed an efficient frame work for fruit classification using deep learning. The entire architecture is composed of two learning models, out of which the first one is a six layered CNN and the second is a fine-tuned visual geometry group-16 (VGG16) deep learning model. Moneny et al. [7] have introduced an accurate cherry fruit classification based on deep CNN model. This work aims to detect the appearance of cherries and provide an appropriate grading system. The authors have estimated the image properties through KNN, ANN fuzzy EDT, and compared the results of CNN model with HOG and LBP algorithms as well.

3 Proposed Methodologies

Proposed work comprises with three different forms of CNN that are simple CNN, ResNet50, and VGG19. The structural and functional analysis is listed below.

CNN stands for convolutional neural network, it is a class of deep learning which aims to analyze visual imagery. In CNN, the convolution is done between kernel filters and the input matrix by the means of shifting; hence, it is also known as shift invariant or space invariant artificial neural networks (SIANN) [8, 9]. This convolution process brought feature maps which contain important and key points from the input and pooling operation are done on it to collect the important characteristics. The architecture of CNN model is given in Fig. 1. Nowadays, CNN is used in image and video processing, medical image analysis, recommendation system, natural language processing, etc., [10]. Some architectures of CNNs are LeNet, AlexNet, VGG, GoogleNet, ResNet, and more. CNN is composed of multiple layers (input, hidden, and output) with neurons, in which each neuron of a particular layer is connected to other neuron of different layer and hence supporting multilayer perceptron. The fully connectivity of CNN network provides data overfitting. CNN provides many ways of regularization by means of weight decay, skip connection, dropout, etc. In this work, weight and bias values are used as CNN parameters for training. These features make CNN into a self-learning model by which the model provides an optimum accuracy. The key concept of the model is forward propagation and backward propagation. Forward propagation receives input data, process it, and generates output, whereas backward propagation calculates the error and updates the parameters.

In this work, we have six predictions at the outputs like $y_1, y_2 \ldots y_6$ for classification. The modified neuron is obtained by "$((\text{img.} * w) + b)$," where "w" is the

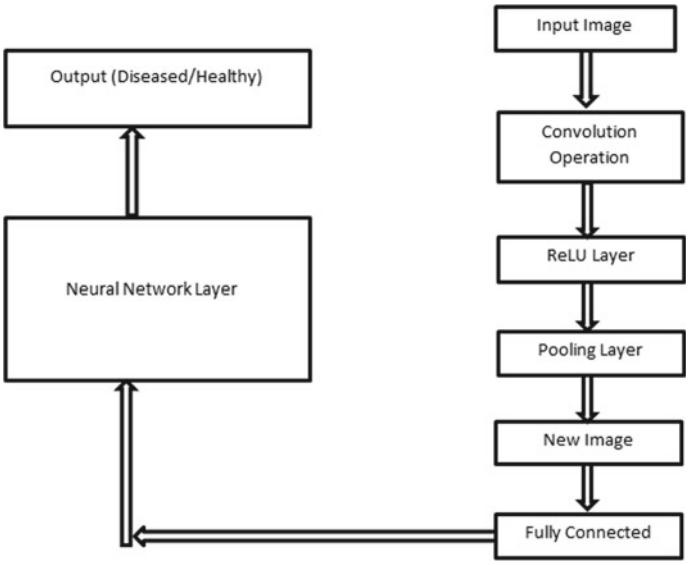

Fig. 1 Architecture of entire work in CNN

weight filter of size $3 * 3$ and "b" is the bias associated with each individual filters. Here, we are using ten filters so the size of bias is $10 * 1$.Then, we are taking the ReLU function in Eq. 1 as

$$\beta = \text{ReLU}((\text{img.} * w) + b) \tag{1}$$

where "β" is the ReLU operation operated on the image. After the completion of ReLU operation, we are using max pooling operation as "max pool(β)." After pooling, we are able to obtain a reduced height and width image with constant channel. Now, this process propagates in a loop manner to the last layer. Now, we are leading toward backward propagation to update the weights of the filters. Suppose we are getting the estimated results as y_n and the original results Y_n then we can find the error or loss as $L = l_1, l_2 \ldots l_n$ by taking the differences. To update the weight and bias, we need to find the derivative of loss function with respect to weights and bias as $\left[\frac{\partial L}{\partial w}, \frac{\partial L}{\partial b}\right]$. Now, we are able to obtain the new weight and bias using gradient descend formula as shown in Eqs. 2 and 3. So mathematically:

$$W_{\text{new}} = W_{\text{old}} - \alpha * \frac{\partial L}{\partial w} \tag{2}$$

$$B_{\text{new}} = B_{\text{old}} - \alpha * \frac{\partial L}{\partial b} \tag{3}$$

where W_{new} and B_{new} corresponds to new weight and bias.

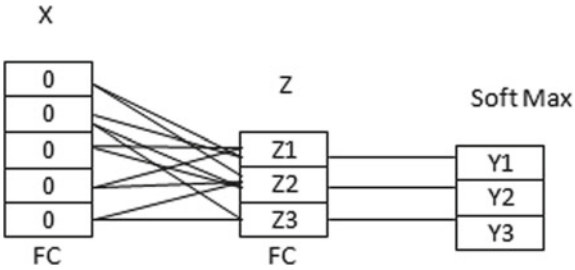

Fig. 2 Intermediate stages in CNN

Here, in Fig. 2, "x" is the input neurons, "z" is called as logits, and finally, softmax layer is places. The transformation of logits is mapped to softmax layer in terms of probability. The relationship is established in Eqs. 4–6 as follows:

$$Y_1 = \frac{e^{Z_1}}{\sum_{k=1}^{3} e^{Z_k}} \tag{4}$$

$$Y_2 = \frac{e^{Z_2}}{\sum_{k=1}^{3} e^{Z_k}} \tag{5}$$

$$Y_3 = \frac{e^{Z_3}}{\sum_{k=1}^{3} e^{Z_k}} \tag{6}$$

The generalized form of softmax output is represented in Eq. 7 as

$$Y_i = \frac{e^{Z_i}}{\sum_{k=1}^{3} e^{Z_k}} \tag{7}$$

where

$$Z_i = \sum_{J=1}^{5} w_{ji} * X_j + b \tag{8}$$

In the final layer which is sometimes called a loss layer too, softmax function is used mostly to solve the overfitting problem. Now, the cross-entropy loss to this multiclass classification is defined in Eq. 9 as

$$\text{Loss} = -\sum_{i=1}^{3} Y_i \log(y_i) \tag{9}$$

This loss explains the model behavior after each iteration of optimization, and it is tried to be minimized to achieve the best result.

ResNet is also a class of deep learning and resembles with simple CNN but utilizes skip connection as shown in Fig. 3. Skip connection or shortcut is introduced

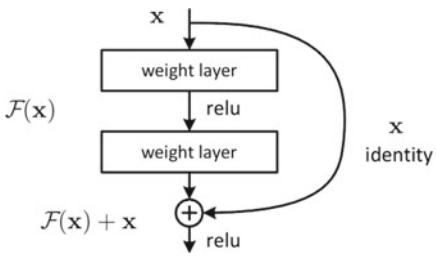

Fig. 3 ResNet50 functional block diagram

in ResNet to avoid vanishing gradient problem and higher training error. In simple terms, let us consider a database is to be trained where input is equals to output using multilayer perceptron model. The easiest solution to this problem is to fix weight value = 1 and bias = 0 in hidden layers but practically the model will generate a complex mapping value after back propagation. This complex mapping will lead to a wide range of weight and bias value. Skipping connection provides a simpler network in the initial training phase. An enhanced speed and lower execution time are also achieved after reducing vanishing grading problem. A neural network without residual parts consists more feature space; hence, it will create more confusion [11].

VGGNet is a convolutional neural network invented at Oxford University by Simonyan and Zisserman in the year 2014 [12]. This was awarded as the runner up in classification task in ImageNet large scale visual recognition competition. VGGNet is very useful in object detection and classification of unseen objects as it is capable of good feature extraction. Idea behind the introduction of VGG is to enhance the classification accuracy by increasing the depth of CNNs [13, 14]. Five max pooling filters having been embedded with CNN model in this work to down sample the input information.

We have implemented a confusion matrix to check the degree of performance of our system. We have estimated the parameters like precision, recall, accuracy percentage (AP), and error associated with the model. The confusion matrix is shown in Table 1 for concept visualization-

The parameters are estimated as follows:

$$\text{Precision} = \frac{\text{TP}}{\text{TP} + \text{FP}}, \text{Recall} = \frac{\text{TP}}{\text{TP} + \text{FN}},$$
$$\text{Accuray} = \frac{\text{TP} + \text{TN}}{\text{TP} + \text{TN} + \text{FP} + \text{FN}}$$

Table 1 Comparison of confusion matrixes of all models

Category	Disease	Healthy
Disease	True positive (TP)	False positive (FP)
Healthy	False negative (FN)	True negative (TN)

4 Results and Analysis

In this work, a total of 849 images of three different fruits (apple, banana, and orange) with healthy and rotten category is taken for each fruit class. Hence, a total of six predictions is obtained. Some sample images of the fresh and rotten fruits are given in Fig. 4 for understanding. The objective of this section is to classify the fruit quality (healthy or rotten) with proposed models and to extract a comparison between the respective models by means of some parameters.

Here (Fig. 5), the graphical representation of CNN accuracy and loss is provided. It is observed that the validation accuracy has reached over 78% in CNN model and the loss is about 0.30%.

Here (Fig. 6), the graphical representation of ResNet50 accuracy and loss is provided. It is observed that the validation accuracy has reached over 83% in ResNet50 model and the loss is about 0.1%.

Here (Fig. 7), the graphical representation of VGG19 accuracy and loss is provided. It is observed that a high degree of validation accuracy has reached over 94% in VGG19 model, and the loss is optimum about 0.02%. It is noted that VGG19 issues best result despite 20 epochs which is 100 in other cases.

In this section (Table 2), a confusion matrixes of all respective models are provides which inform about true positive, true negative, false positive, and false negative predictions done by the models. The number of true positive in the VGG19 model

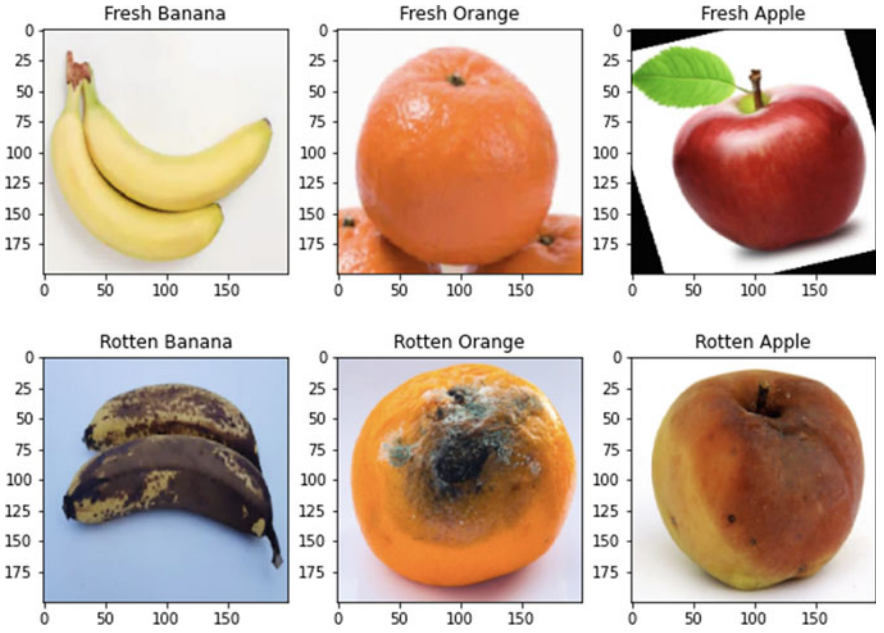

Fig. 4 Some sample images of the fresh and rotten fruits

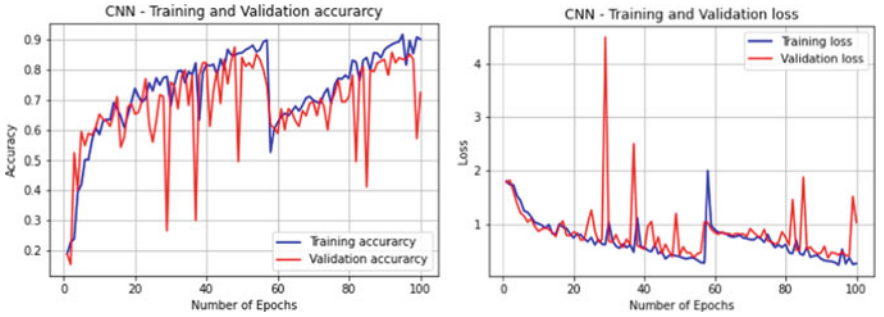

Fig. 5 Graphical representation of accuracy and loss using CNN

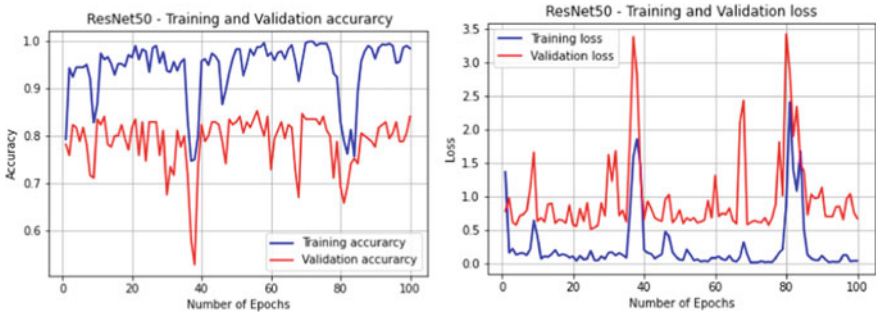

Fig. 6 Graphical representation of accuracy and loss using ResNet50

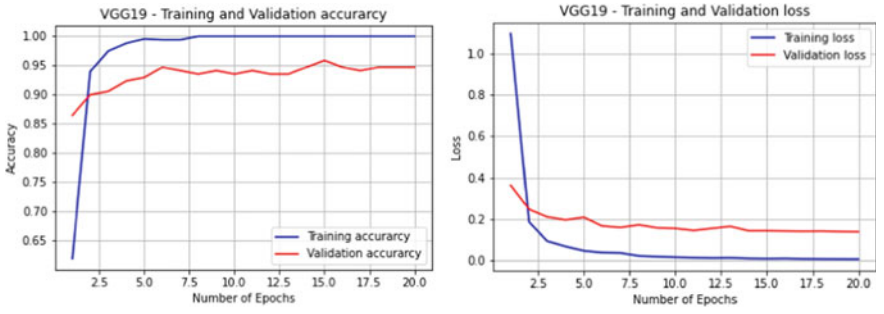

Fig. 7 Graphical representation of accuracy and loss using VGG19

is 163, whereas CNN and ResNet have 132 and 136, respectively. The accuracy that clearly implies VGG19 performance is more accurate compared to another two models.

In this section (Tables 3, 4, and 5), a detailed analysis of deep neural network models is given by means of classification report. Here, the notations from 0 to 5 are the categorical variables corresponding to the six classes present in the confusion

Table 2 Comparison of confusion matrixes of all models

Labels	CNN	ResNet50	VGG19
Fresh Banana Fresh Orange Rotten Apple Fresh Apple Rotten Banana Rotten Oranges	[[13 0 0 0 3 1] [0 17 6 0 0 3] [0 1 24 0 2 2] [0 0 0 38 0 0] [1 0 0 0 19 9] [0 2 7 0 1 21]]	[[13 0 1 0 1 2] [1 15 8 0 1 1] [0 1 27 0 0 1] [0 0 0 38 0 0] [0 0 0 0 28 1] [0 0 16 0 0 15]]	[[14 0 0 0 3 0] [0 25 0 0 0 1] [0 0 27 0 0 2] [0 0 0 38 0 0] [0 0 0 0 29 0] [0 2 2 0 0 27]]
	Fresh banana Fresh Orange Rotten Apple Fresh Apple Rotten Banana Rotten Orange	Fresh banana Fresh Orange Rotten Apple Fresh Apple Rotten Banana Rotten Orange	Fresh banana Fresh Orange Rotten Apple Fresh Apple Rotten Banana Rotten Orange

Table 3 Classification report of CNN

Notation	Precision	Recall	F1 score	Support
0	0.93	0.76	0.84	17
1	0.85	0.65	0.74	26
2	0.65	0.83	0.73	29
3	1.00	1.00	1.00	38
4	0.76	0.66	0.70	29
5	0.58	0.68	0.63	31

Table 4 Classification report of ResNet50

Notation	Precision	Recall	F1 score	Support
0	0.93	0.76	0.84	17
1	0.94	0.58	0.71	26
2	0.52	0.93	0.67	29
3	1.00	1.00	1.00	38
4	0.93	0.97	0.95	29
5	0.75	0.48	0.59	31

Table 5 Classification report of VGG19

Notation	Precision	Recall	F1 score	Support
0	1.00	0.82	0.90	17
1	0.93	0.96	0.94	26
2	0.93	0.93	0.93	29
3	1.00	1.00	1.00	38
4	0.91	1.00	0.95	29
5	0.90	0.87	0.89	31

Table 6 Model comparison

Model type	Accuracy	Execution time (s)	Support
CNN	0.78	1.63	170
ResNet50	0.80	0.92	170
VGG19	0.94	1.10	170

matrix. These reports are generated inside the code sections and placed here for clear and better understanding.

In Table 6, a comparison between the parameters is given on different models. It is clearly viewed that VGG19 model performs best among all models and ResNet50 exhibits less computational time as compared to rest two models.

5 Conclusion

In this paper, a novel fruit quality estimation system is proposed for agricultural applications. Three models (CNN, ResNet50, and VGG19) have been investigated on a dataset, and it is found that VGG19 performs the best in terms of accuracy. ResNet19 also performs well and its performance is best as far as execution time is considered. In RseNet and VGG, testing accuracy is a bit less than training; indicating overfitting due to some noise and fluctuations. This application can be deployed in real-time as it can solve some primary requirement for farmers. Transferred learning models like ResNet and VGG are basically a derived CNN models with some modifications in hidden layers. In future, we will try to improve the accuracies with introducing other transfer learning models like VGG16 and Inception-ResNet.

References

1. Mohapatra D, Tripathy J, Patra TK (2021) Rice disease detection and monitoring using CNN and Naive Bayes classification. In: Borah S, Pradhan R, Dey N, Gupta P (eds) Soft computing techniques and applications. Advances in intelligent systems and computing, vol 1248. Springer, Singapore. Retrieved from https://doi.org/10.1007/978-981-15-7394-1_2
2. Li K, Lin J, Liu J, Zhao Y, Dou S, Zhang Y, Liu X (2019) Disease based on deep learning. Icsai, 1228–1232. Retrieved from https://doi.org/10.1007/s11263-019-01247-4
3. Nandi CS, Tudu B, Koley C (2016) A machine vision technique for grading of harvested mangoes based on maturity and quality. Retrieved from https://doi.org/10.1109/JSEN.2016.2580221
4. Hu W, Fan JIE, Du Y, Li B, Xiong NN, Bekkering E (2020) MDFC—ResNet: an agricultural IoT system to accurately recognize crop diseases, 1–13. https://doi.org/10.1109/ACCESS.2020.3001237
5. Ponce JM, Aquino A, Andújar JM, Member S (2019) Olive-fruit variety classification by means of image processing and convolutional neural networks. 147629–147641. https://doi.org/10.1109/ACCESS.2019.2947160

6. Hossain MS, Member S, Al-hammadi M, Muhammad G (2018) Automatic fruit classification using deep learning for industrial applications. 3203(c). Retrieved from https://doi.org/10.1109/TII.2018.2875149
7. Moneny M, Jahanbakhshi A, Mahmoudi M, Zhang Y-D (2020) Classification of sour lemons based on apparent defects using stochastic pooling mechanism in deep convolutional neural networks. Sci Hortic 263:109133. Retrieved from https://doi.org/10.1016/j.scienta.2019.109133
8. Radovanović D, Đukanovic S (2020) Image-based plant disease detection: a comparison of deep learning and classical machine learning algorithms. In: 2020 24th International conference on information technology (IT), 2020, pp 1–4. https://doi.org/10.1109/IT48810.2020.9070664
9. Park H, JeeSook E, Kim S (2018) Crops disease diagnosing using image-based deep learning mechanism. In: 2018 International conference on computing and network communications (CoCoNet), 2018, pp 23–26. https://doi.org/10.1109/CoCoNet.2018.8476914
10. Shaw AK, Chakraborty A, Mohapatra D, Dutta S (2020) Scalable IoT solution using cloud services—an automobile industry use case. In: 2020 Fourth international conference on I-SMAC (IoT in social, mobile, analytics and cloud) (I-SMAC), Palladam, India, 2020, pp 326–331. https://doi.org/10.1109/I-SMAC49090.2020.9243544
11. Kulkarni O (2018) Crop disease detection using deep learning. In: 2018 Fourth international conference on computing communication control and automation (ICCUBEA), pp 1–4. https://doi.org/10.1109/ICCUBEA.2018.8697390
12. Sun Y, Zhang W, Gu H, Liu C, Hong S, Xu W, Yang J, Gui G (2019) Convolutional neural network based models for improving super resolution imaging, vol 7. IEEE, pp 43042–43051 https://doi.org/10.1109/ACCESS.2019.2908501
13. Kurniawati NN, Abdullah S (2009) Texture analysis for diagnosing paddy disease. In: International conference on electrical engineering and informatics (ICEEI'09), vol 1. IEEE, pp 23–27. https://doi.org/10.1109/ICEEI.2009.5254824
14. Mohapatra D, Shaw AK, Chakraborty A (2021) Exploring novel techniques to detect aberration from metal surfaces in automobile industries. In: Sabut SK et al (eds) International conference on communication, circuits, and systems IC3S 2020, vol 728. Springer, Singapore. https://doi.org/10.1007/978-981-33-4866-0_5

Multi-objective Optimal Allocation of DSTATCOM Using an Improved Student Psychology Based Algorithm

Subrat Kumar Dash, Swapnil Pani, and Sivkumar Mishra

Abstract The placement and sizing problem of DSTATCOM are solved in this paper using a new meta-heuristic approach. For this, a new improved student psychology-based algorithm is proposed. The considered objectives are minimization of the real power loss, voltage deviation minimization and maximization of a voltage stability index. The proposed approach is validated using a standard 33-bus radial test distribution system with a multi-objective framework for four different loading scenarios. The results and their comparision with recent approaches are included in the analysis.

Keywords DSTATCOM · Optimal allocation · Improved student psychology-based algorithm · Real power minimization

1 Introduction

With the rising trend of energy demand, distribution networks (DN) are worst affected in minimizing real power loss (RPL), curbing voltage deviation (VD) within the nominal range and keeping an adequate voltage stability margin (VSM). Further, with rapid industrialization, a lot of non-linear loads operating at low power factors are also regularly getting connected to the DN which adds to the misery. Traditionally, several planning methods such as shunt capacitor bank (SCB) allocation, interconnection of the synchronous condenser (SC), integration of distributed generation (DG) units are being practiced to improve the performance of DN. However, the intermittent nature of DGs poses additional challenges for their integration to DN. Similarly, SCBs can not provide variable reactive power support at the time of need and also can cause ferroresonance effect in the DN. SC rated below 200 H.P. are not economically viable as well as need frequent maintainance. Due to recent developments in power electronics technology, flexible AC transmissions (FACTS) devices are now available

S. K. Dash · S. Pani
Government College of Engineering Kalahandi, Bhawanipatna, Odisha, India

S. Mishra (✉)
Centre for Advanced Post Graduate Studies, BPUT, Rourkela, Odisha, India

M. Mishra et al. (eds.), *Innovation in Electrical Power Engineering, Communication, and Computing Technology*, Lecture Notes in Electrical Engineering 814,
https://doi.org/10.1007/978-981-16-7076-3_34

in downsize, suitable for distribution voltage level especially aimed at improving the power quality of DN. These devices are now called custom power devices (CPD) [1]. One such CPD is distribution static compensator (DSTATCOM) which is now projected as an alternative to improve the performance of the DN by providing variable reactive power at a competitive cost. Better reactive power management is possible if DSTATCOM of optimal capacity is placed at a strategic location. So for distribution utilities (DU) optimal DSTATCOM allocation (both placement and sizing) (ODA) plays a crucial role to draw maximum benefits.

In the past, a lot of research articles are published that addresses ODA. Modeling and incorporation of DSTATCOM to distribution load flow is proposed in [2]. Some of the DSTATCOM allocation approaches utilize various sensitivity based techniques to pre locate the candidate nodes of DSTATCOM such as loss sensitivity factor (LSF) [3], index vector method (IVM) [4], voltage stability index (VSI) [5], new voltage stability index (NVSI) [6], power stability index (PSI) [7]. Kanwar et al. [8] used an intelligent search mechanism to reduce the search space and then obtained optimal capacities of distributed generation (DG) units and DSTATCOM simultaneously. Though, reduce search space may offer less computational burden but are not efficient to deliver optimal results.

Several metaheuristic approaches such as improved cat swarm optimization (ICSO), immune algorithm (IA), harmony search algorithm (HSA), differential evolution algorithm (DEA), gravitational search algorithm (GSA) and, firefly algorithm (FFA) presented in [8–13], respectively, are used to determine the optimal capacities of DSTATCOM units at the pre located nodes. However, these metaheuristic approaches struggle with local and or premature convergence. So, to overcome these deficiencies improvised or hybrid metaheuristic approaches are also applied to solve ODA. A hybrid of whale and grey wolf optimizers is proposed in [14] to decide the optimal allocations of DSTATCOM. A new discrete and continuous version of the Chu–Beasley genetic algorithm is suggested to solve ODA in [15]. Further, a brief review of the ODA methods including analytical and metaheuristic approaches are presented in [16]. The application of metaheuristic approaches for both DG and DSTATCOM allocations is reviewed in [17]. A study on the impact of DSTATCOM allocation on various load models is presented in [18] for minimizing RPL only. However, the effect of load modeling for DSTATCOM allocation on VD and VSM is not investigated.

In the light of the above discussions, this manuscript proposes an improved student psychology-based optimization algorithm (ISPBOA) to determine the optimal location as well as the size of the DSTATCOM unit considering a multi-objective framework encompassing several load models. The remaining of the paper is structured as follows. Section 2 introduces DSTATCOM and its modelling. In Sect. 3, the detailed problem formulation is presented. ISPBOA and its implementation strategy for obtaining ODA are elucidated in Sect. 4. The results and analysis of the proposed work are presented in Sect. 5. Finally, Sect. 6 concludes the findings of the work.

2 Static Compensator (D-STATCOM)

A GTO/IGBT based voltage source converter acts as the heart of DSTATCOM which is supported by a DC capacitor bus and a tuned filter is connected to limit the harmonics. This arrangement is connected across the compensating bus via a coupling transformer to alleviate the power quality issues of the DN by fast exchange of the reactive power.

A DN reduced to two-bus equivalent, and without DSTATCOM is depicted in Fig. 1. The KVL for the equivalent DN without DISTACOM can be written as:

$$U_{t+1}\angle\theta_{t+1} = U_t\angle\theta_t - (R_m + jX_m)I_m\angle\delta_m \tag{1}$$

The modified KVL equation for DN with DSTATCOM connected at $(t+1)$th bus, can be expressed as in Eq. (2). Figures 2 and 3 portrays the DN with DSTATCOM placed at $(t+1)$th bus and the resulting phasor diagram, respectively. Where, $\boldsymbol{R_m}$ and $\boldsymbol{X_m}$ are the branch resistance and reactance, respectively. $\boldsymbol{I_{DSTATCOM}}$ is the current injected by the DSTATCOM and at $\boldsymbol{\psi}$ is its corresponding phase angle.

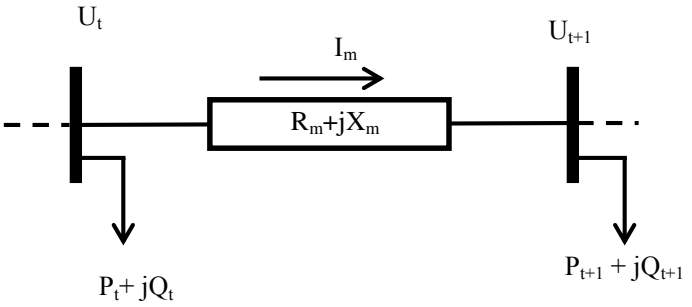

Fig. 1 Two bus equivalent of a DN

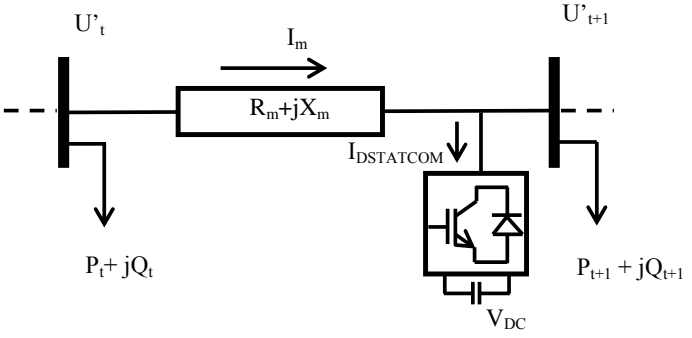

Fig. 2 DN with DSTATCOM placed at $(t+1)$th bus

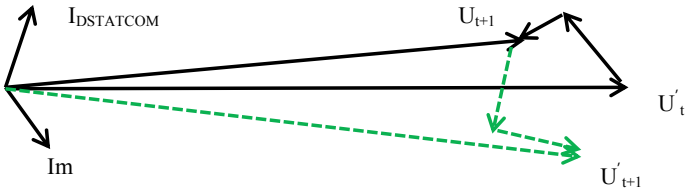

Fig. 3 Phasor diagram of DN with DSTATCOM

$$U'_{t+1}\angle\theta'_{t+1} = U'_t\angle\theta'_t - (R_m + jX_m)(I_m\angle\delta_m + I_{\text{DSTATCOM}}\angle\psi \tag{2}$$

DSTATCOM being a source of reactive power will force, the phase angle between the compensated bus and the current injected by the DSTATCOM to be in quadrature Therefore, one can write:

$$\psi = \frac{\pi}{2} + \theta'_{t+1} \tag{3}$$

Now, the power pushed by the DSTATCOM at compensating bus is expressed as:

$$-jQ_{\text{DSTATCOM}} = U'_{t+1}\angle\theta'_{t+1}I^*_{\text{DSTATCOM}}\angle\left(\frac{\pi}{2} + \theta'_{t+1}\right) \tag{4}$$

3 Problem Formulation

To solve ODA, a weighted sum multi-objective function (MOF) is proposed, whilst satisfying the system operational constraints. MOF is optimized using an improved student psychology-based optimization algorithm to determine both the placement as well as the size of the DSTATCOM unit simultaneously.

3.1 Multi-objective Function (MOF)

A DN owing to its radial mode of operation experiences huge RPL, increased VD and mostly operates at the verge of stability. Increased load demand causing reactive power scarcity further worsens this condition. Hence, it is essential to put a check on RPL, VD and VSM. Therefore, a multi-objective function is formulated by suitably combining the indices of three solo objectives namely index of real power loss (IRPL), index of voltage deviation (IVD) and index of voltage stability margin (IVSM) through appropriate weights as given in Eq. (5).

$$\text{MOF} = \lambda_1 \times \left(\frac{\text{ploss}^{\text{dstat}}}{\text{ploss}^{\text{base}}}\right) + \lambda_2 \times \left(\frac{\text{VD}^{\text{dstat}}}{\text{VD}^{\text{base}}}\right) + \lambda_3 \times \left(\frac{(1/\text{VSI}^{\text{dstat}})}{(1/\text{VSI}^{\text{base}})}\right) \quad (5)$$

where, $\mathbf{ploss^{dstat}}$, $\mathbf{ploss^{base}}$, represents RPL with and without integration of DSTATCOM, respectively. Similarly, $\mathbf{VD^{dstat}}$ and $\mathbf{VD^{base}}$, are the voltage deviation of the DN with and without DSTATCOM, respectively. VSM with and without DSTATCOM is denoted as $\mathbf{VSI^{dstat}}$ and $\mathbf{VSI^{base}}$, respectively. Where, λ_1, λ_2 and λ_3 are the weights that glorify the importance of respective indices on the overall MOF. In the present work the values of λ_1, λ_2 and λ_3 are considered as 0.4, 0.3 and 0.3, respectively [19].

3.2 Constraints

For optimizing Eq. (5) to solve ODA, the following constraints are formulated.

Node Voltage Constraint:

The voltage of each node of the DN is allowed to vary between 0.95 p.u. and 1.05 p.u. of the substation voltage.

$$Ui_{\max_{\min}} \quad (6)$$

Feeder Flow Constraint:

It restricts the branch currents within the thermal limit of the feeder which may be altered due to the integration of D-STATCOM.

$$|I_m| \leq \left|I_m^{\text{specified}}\right| \quad (7)$$

D-STATCOM Position Constraint:

The candidate bus for D-STATCOM allocation is uniquely created for all buses except the substation bus.

$$2 \leq L_{\text{dstat}} \leq \text{NB} \quad (8)$$

D-STATCOM Sizing Constraints:

The size of the D-STATCOM is allowed to be within a minimum and maximum limits of the total reactive power load as defined in (Eq. 9).

$$0.2 \times \sum_{i=1}^{\text{NB}} Q_{\text{load}}(i) \leq Q_{\text{DSTATCOM}} \leq 0.8 \times \sum_{i=1}^{\text{NB}} Q_{\text{load}}(i) \quad (9)$$

3.3 Load Modeling

The active and reactive powers for different load models (LM) such as constant power, industrial, residential and commercial loads can be expressed as in Eqs. (10) and (11). Where, P_n and Q_n are the active and reactive power at nominal bus voltage U_n, respectively. The exponents α and β assume different values for different load models [18].

$$P = P_n\left(\frac{U}{U_n}\right)^{\alpha} \tag{10}$$

$$Q = Q_n\left(\frac{U}{U_n}\right)^{\beta} \tag{11}$$

4 Optimal DSTATCOM Allocation

In this work, the ODA is solved using an improved student psychology-based optimization algorithm (ISPBOA). So, at first, the ISPBO algorithm is described followed by the implementation strategy of the proposed method for ODA is presented.

4.1 Improved Student Psychology Based Optimization Algorithm (ISPBOA)

Student psychology-based optimization (SPBO) is a recently proposed [20] population-based algorithm that emulates student psychology to perform better in class performance. Based on the class performance students are first categorized into four groups namely best student (BS), good student (GS), average student (AS) and below-average student (BAS). The class performance is a random process that can be modeled as a normal distribution curve. So, this paper proposes a normal distribution based approach of classifying students into the above categories. The psychology of students belonging to different groups are different to excel in their class performance. The best student (student having the best marks in the class) tries to perform better than any other student of the class. So, his/her performance can be modeled as:

$$p_{mn}^{k+1} = p_{\text{best},mn}^{k} + (-1)^{a} \times \text{rand} \times \left(p_{\text{best},mn}^{k} - p_{rn}^{k}\right) \tag{12}$$

A good student tries to compete with the best and to be the next best student. So Eq. (13) will describe his /her class performance.

$$p_{mn}^{k+1} = p_{\text{best},mn}^{k} + \text{rand} \times \left(p_{\text{best},mn}^{k} - p_{mn}^{k}\right) \tag{13}$$

However, few GS try to follow the BS as well as try to do better than any AS. So, the performance of, GS can also be expressed as Eq. (14). A random number is generated to select any one of the performance improvement mechanisms between Eqs. (13) or (14).

$$p_{mn}^{k+1} = p_{mn}^{k} + \left|\text{rand} \times \left(p_{\text{best},mn}^{k} - p_{mn}^{k}\right)\right| + \left|\text{rand} \times \left(p_{mn}^{k} - p_{\text{avg}}^{k}\right)\right| \tag{14}$$

An average student often puts average effort to improve his/her performance which can be expressed as in Eq. (15).

$$p_{mn}^{k+1} = p_{mn}^{k} + \left|\text{rand} \times \left(p_{\text{avg}}^{k} - p_{mn}^{k}\right)\right| \tag{15}$$

A BAS student does not have any focused approach for performance improvement. So its best described in Eq. (16).

$$p_{mn}^{k+1} = p_{\min,m} + \left[\text{rand} \times \left(p_{\max,m} - p_{\min,m}\right)\right] \tag{16}$$

where, p_{mn}^{k+1} and p_{mn}^{k}, is the performance of any student $\boldsymbol{m}$ for $\boldsymbol{n}$th subject in the class at $(k+1)$th and $\boldsymbol{k}$th iteration, respectively. The performance of the best student and any random student of the class for $\boldsymbol{n}$th subject in $\boldsymbol{k}$th iterations are represented by $p_{\text{best},mn}^{k}$ and p_{mn}^{k}, respectively. p_{avg}^{k} is the subjectwise average performance of the class for $\boldsymbol{k}$th iteration. $p_{\min,m}$ and $p_{\max,m}$ are the maximum and minimum bound of the decision variables, respectively. '$\boldsymbol{a}$' is a constant which can assume a value of 1 or 2 randomly.

4.2 Implementation of ISPBOA for ODA

The detailed pseudo code for ODA using the proposed method is shown in Table 1.

5 Results

In the present work, ODA is solved using an improved student psychology algorithm. A 33-bus test system [22] is considered to validate the proposed work by considering four scenarios encompassing four different load modeling such as constant power load (CPL), industrial load (IL), commercial load (CL) and residential load (RL), respectively. To minimize the statistical error, the best results out of 10 independent

Table 1 Pseudocode for ODA using ISPBOA

Step 1	Input the system data, i.e. line data and load data
Step 2	Set the control parameters of ISPBOA, i.e. class size = 40, maxiter = 100
Step 3	Randomly generate the initial class performance as $P = p_1, p_2, \ldots, p_{NS}$ where each $\boldsymbol{p}$ contains the location and size of DSTATCOM
Step 4	Evaluate the initial class performance using (5). This is done by performing load flow [5]
Step 5	Set the iteration counter $k = 1$
Step 6	Classify students into different group such as BS, GS, AS, BAS
Step 7	Update the class performance of each student belonging to different groups using (12–16) as applicable
Step 8	Evaluate the performance of the class for updated class using (5)
Step 9	If the present class performance is better than the previous class performance then replaces the previous class with present class
Step 10	If maximum iteration is reached then go to step 11 else increment the iteration counter $k = k + 1$ and go to step 6
Step 11	Print the best solution

trial runs of the algorithm are reported. A laptop having Intel(R) Core (TM) i3-6006U CPU @ 2.00 GHz, 4GB RAM is used to simulate all results in MATLAB environment.

5.1 Single Objective Optimization

At first, the optimal size and location for DSTATCOM is obtained for minimization of the RPL only. It can be seen from Table 2 that the performance of the DN in the absence of DSTATCOM is very poor as the RPL, minimum bus voltage and VSI are 202 kW, 0.9038 p.u. and 0.6951 p.u., respectively. However, with optimal DSTATCOM allocation, there is a significant improvement in RPL of 143.5 kW from 202 kW. Similarly, improvement in voltage profile and maximization of VSM

Table 2 Comparision of results for DSTATCOM allocation to minimize RPL

Methods	Location	Size, MVAr	Ploss, kW	Vmin (p.u.)	VSI (p.u.)
Base case	–	–	202.0	0.9038	0.6951
Proposed	30	1.3149	**143.5**	0.9256	0.7340
MoSCA [21]	30	1.3060	**143.5**	0.9255	0.7338
GA [9]	12	1114.2	173.9	–	–
IA [9]	12	0.9624	171.8	–	–
DE [11]	30	1.2527	**143.5**	0.9256	–

Table 3 Comparision of results for ODA for MOF considering different LM

Scenarios	Location	Size, MVAr	IRPL	IVD	IVSM
CPL	30	1.7101	0.7346	0.5088	0.9329
IL	7	1.8400	0.7188	0.4039	0.8821
CL	7	1.8400	0.6857	0.4035	0.8835
RL	7	1.7881	0.6567	0.4008	0.8829

is also apparent from 5th and 6th columns of Table 2. The results obtained by different approaches for ODA are also compared in Table 2. The optimal capacity of DSTATCOM obtained by the proposed method is 1.3149 MVAr which is marginally higher than that obtained by MoSCA. However, the proposed method reported the same RPL of 143.5 kW with significantly better results in terms of minimum bus voltage and VSI as obtained by the rest of the reported methods. Hence the proposed method is quite effective in solving ODA.

5.2 Multi-objective Optimization

This section presents the results of allocation of DSTATCOM for different load models such as CPL, IL, CL and RL when optimized using ISPBOA in a multi-objective framework. Table 3 compiles the results of optimal location, optimal size, IRPL, IVD and IVSM for above said loading scenarios. From Table 3, it is evident that the optimal size of the DSTATCOM is the highest for both IL and CL owing to larger reactive power demand for these scenarios. Performance of DN is significantly improved in the presence of optimally allocated DSTATCOM for CPL than the rest of the loading scenarios. However, in the presence of DSTATCOM, the performance of the DN is better than the base case for all loading scenarios. The convergence characteristic (CC) for ODA using the proposed method for MOF considering the above four loading scenarios is depicted in Fig. 4. It shows ISPBO is effective in solving ODA for all loading scenarios. The branch-wise power loss (BPL) and voltage profile (VP) for the base case as well as for all loading scenarios are shown in Figs. 5 and 6, respectively.

6 Conclusion

In this work, simultaneous optimal allocation (both location and size) of the DSTATCOM unit in a multi-objective framework for four different loading scenarios using the proposed ISPBOA has been investigated. A normal distribution based student classification scheme has been proposed to improvise the original SPBOA. The detailed analysis of results has shown that the performance of the DN in terms

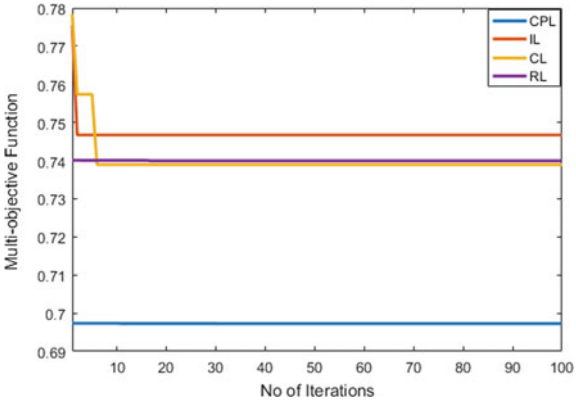

Fig. 4 Convergence characteristic for ODA using ISPBOA for different LM

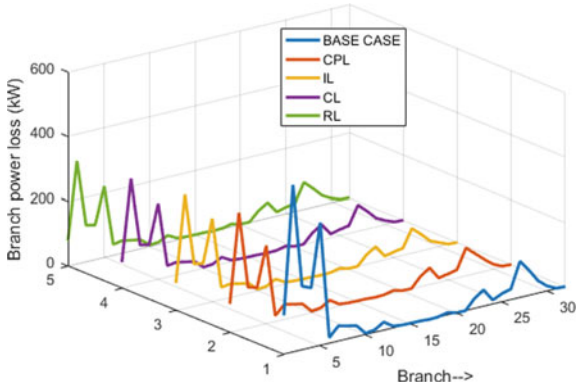

Fig. 5 Voltage profile of DN for ODA obtained by ISPBOA for different LM

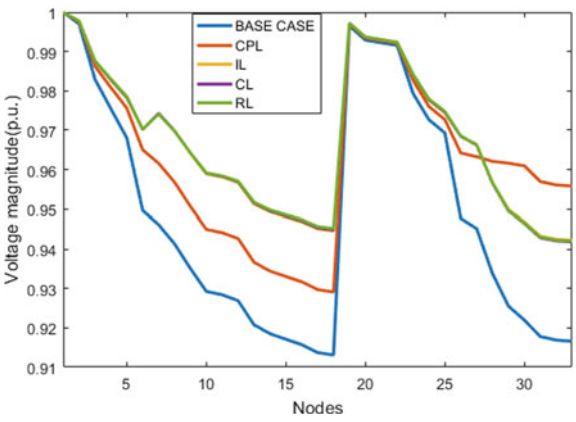

Fig. 6 Branch power loss of DN for ODA obtained by ISPBOA for different LM

of RPL minimization, enhancement in VSM and reduction in VD is better when DSTATCOM is optimally allocated. The proposed method, i.e. ISPBOA has been quite effective in solving ODA and also has performed better than other established approaches mentioned in the literature. Results also reveal that different load models have impacted differently to the optimal location as well as the size of the DSTATCOM. The optimal size of the DSTATCOM was found to be the highest for both IL and CL.

References

1. Hingorani, N. G: Introducing custom power. IEEE Spectrum. 32 (6) (2002). doi: https://doi.org/10.1109/6.387140.
2. Mehdi H, Ali SH, Mahmud F (2007) Modeling of D-STATCOM in distribution systems load flow. Journal of Zhejiang University - Science A: Applied Physics & Engineering. 8(10):1532–1542
3. S. Devi and M. Geethanjali: Electrical Power and Energy Systems Optimal location and sizing determination of Distributed Generation and DSTATCOM using Particle Swarm Optimization algorithm. Int. J. Electrical Power and Energy System. 62, 562–570 (2014).
4. Gupta AR, Kumar A (2015) Energy saving using D-STATCOM placement in radial distribution system under reconfigured network: Energy Procedia. 90:124–136
5. Yuvaraj T, Ravi K, Devabalaji KR (2017) DSTATCOM allocation in distribution networks considering load variations using bat algorithm. Ain Shams Engineering Journal. 8(3):391–403
6. A. R. Gupta and A. Kumar: Impact of various load models on D-STATCOM allocation in DNO operated distribution network. In 6th International Conference on Smart Computing and Communications, ICSCC. 862–870 (2018).
7. A. Amin and J. Yu: Developed Analytical Technique for Optimal Placement and Sizing of DG and DSTATCOM in Radial Distribution Systems. Twentieth. Int. Middle East Power System. Conference. 1087–1091(2018).
8. N. Kanwar, N. Gupta, K. R. Niazi, and A. Swarnkar: Improved Cat Swarm Optimization for Simultaneous Allocation of DSTATCOM and DGs in Distribution Systems. Journal of Renewable Energy. (2015).
9. S. A. Taher and S. A. Afsari: Electrical Power and Energy Systems Optimal location and sizing of DSTATCOM in distribution systems by immune algorithm. International Journal of Electrical. Power and Energy Systems.60, 34–44 (2014).
10. Yuvaraj T, Devabalaji KR, Ravi K (2015) Optimal placement and sizing of DSTATCOM using Harmony Search algorithm. Energy Procidia. 79:759–765
11. Sanam J (2020) Optimization of planning cost of radial distribution networks at different loads with the optimal placement of distribution STATCOM using differential evolution algorithm. Soft Comput 24:13269–13284
12. A. K. Arya and D. Á. G. S. A. Á. Loss: Analysis of Distribution System with D-STATCOM by Gravitational Search Algorithm (GSA). Journal of The Institution of Engineers (India) Series B. 100(1), (2019).
13. Bhadoriya J.S., Gupta A.R. (2021) Optimal Share of DG and DSTATCOM in Distribution Network Using Firefly Algorithm. In: Gupta O.H., Sood V.K. (eds) Recent Advances in Power Systems. Lecture Notes in Electrical Engineering, vol 699. Springer, Singapore.
14. Tejaswini V, Susitra D (2021) Optimal Location and Compensation Using D-STATCOM: A Hybrid Hunting Algorithm. J Control Autom Electr Syst 32:1002–1023
15. Castiblanco-Pérez, C. M., Toro-Rodríguez, D. E., https://sciprofiles.com/profile/1022389Giral-Ramírez, O. D. M. D. A.: Optimal Placement and Sizing of D-STATCOM in Radial and

Meshed Distribution Networks Using a Discrete-Continuous Version of the Genetic Algorithm. Electronics. 10(12), (2021).
16. Srijani R, Jordehi AR (2017) Optimal placement and sizing of distribution static compensator (D-STATCOM) in electric distribution network: A Review. Renewable and Sustainable Energy Review 77:688–694
17. Dash S.K., Mishra S., Pati L.R., Satpathy P.K. (2021) Optimal Allocation of Distributed Generators Using Metaheuristic Algorithms—An Up-to-Date Bibliographic Review. In: Sharma R., Mishra M., Nayak J., Naik B., Pelusi D. (eds) Green Technology for Smart City and Society. Lecture Notes in Networks and Systems, vol 151. Springer, Singapore. https://doi.org/10.1007/978-981-15-8218-9_45
18. Gupta AR, Kumar A (2018) Impact of various load moodels on D-STATCOM allocation in DNO operated distribution network. In International Conf ference on Smart Comp puting and Communications, ICSCC, pp 862–870
19. Thangaraj Y, Kuppan R (2017) Multi-objective simultaneous placement of DG and DSTATCOM using novel lightning search algorithm. Journal of Applied Research and Technology. 15(5):477–491
20. Das; Mukherjee, B.; Das, D.: Student psychology-based optimization algorithm: A new population-based optimization algorithm for solving optimization problems. Advances in Engineering Software. 146, 1–17 (2020).
21. Dash S.K., Mishra S. (2021) Simultaneous Optimal Placement and Sizing of D-STATCOMs Using a Modified Sine Cosine Algorithm. In: Das S., Mohanty M.N. (eds) Advances in Intelligent Computing and Communication. Lecture Notes in Networks and Systems, vol 202. Springer, Singapore. https://doi.org/10.1007/978-981-16-0695-3_41
22. Mishra S, Das D, Paul S (2017) A comprehensive review on power distribution network reconfiguration. Energy Syst 8(2):227–284

Symbiotic Organism Search (SOS) Algorithm Based Load Frequency Control for Hybrid Power System

Geetanjali Dei, Deepak Kumar Gupta, Sarita Samal, and Binod Kumar Sahu

Abstract This paper presents the optimal tuning of Proportional Integral and Derivative (PID) controller for maintaining the tie-line power exchange between the areas within the desired limits along with frequencies of both areas. Two intelligent optimization techniques named Particle Swarm Optimization (PSO) and Symbiotic Organism Search (SOS) have been used to find the optimal parameters of the PID controllers for hybrid power systems. For diversity, two unequal areas have been considered comprising of various power generation sources such as thermal power plant, hydro power plant, diesel power plant, and wind power plant. Area 1 includes wind, hydro, and thermal power plants, whereas in area 2, diesel power, thermal, and hydro power sources are used. Test system has been investigated by both optimization techniques by taking Integral Time multiplied by Absolute Error (ITAE) performance indices as objective function for different operating conditions. Comparison has been made for dynamic response of all the states variables in terms of settling time and overshoot / undershoot between the SOS and PSO based PID controllers.

Keywords Automatic generation control · Load frequency control · PID controller · Particle swarm optimization (PSO) · Symbiotic organism search (SOS)

G. Dei (✉) · D. K. Gupta · S. Samal
School of EE, KIIT Deemed to be University, Bhubaneswar, India
e-mail: geetanjali.deifel@kiit.ac.in

D. K. Gupta
e-mail: deepak.guptafel@kiit.ac.in

S. Samal
e-mail: ssamalfel@kiit.ac.in

B. K. Sahu
SOA Deemed to be University Bhubaneswar, Bhubaneswar, India

M. Mishra et al. (eds.), *Innovation in Electrical Power Engineering, Communication, and Computing Technology*, Lecture Notes in Electrical Engineering 814,
https://doi.org/10.1007/978-981-16-7076-3_35

1 Introduction

The flat frequency profile is the main objective in any power system. The prime intention of AGC is to furnish finer frequency control in the power system and to sustain the power of the tie-line at predefined level regardless of load demand in any area. An interconnected power system strives for generation, distribution, and transport of the power at base frequency and nominal voltage. The frequency of the power system will drift from the rated value if there is any difference between real power generated and the real power consumed [1, 2]. Because of unforeseen disturbances or any other causes if the load demand is more than the active power generation, the frequency decreases and there will be violation of the system frequency from its rated value. So it is the work of AGC to diminish the deviation in frequency as rapidly as possible and to retain the power in the interconnected tie-line at desired value. Controlling the deviation in power in the tie-line and deviation of the frequency are the sole objective of AGC system. A speed governor cannot provide constant frequency in an interconnected power system. Hence, an extra controller is needed to counteract the effects of the unexpected changes in load [3–5]. Different researchers in the world over have come up with different control as well as optimization techniques on AGC. K.P.S. Parmar et al. [6] described the concepts of optimal control theory. Different types of controller like Integral [7], Proportional-Integral [8], Proportional-Integral-Derivative [9], A tilt integral derivative controller is implemented using constrained nonlinear optimization [10]. Y. Arya et al. considered natural choice of power plants using optimal control theory in multi sources power system [11]. Khuntia et al. [12] proposed a new controller which is combination of a fuzzy controller and ANN. It shows a quick response. It is also adaptable to different situation. Pan et al. [13] proposed a controller implementing fuzzy technique to optimize a hybrid power system. In this paper, different generation systems like solar photovoltaic, diesel engine, aqua electrolyzer, wind turbine, and fuel-cells have been considered. Battery, ultra-capacitor, and flywheel have also been used as energy storage devices. Fuzzy control scheme is employed for controller tuning with PSO technique. Gheisarnejad et al. [14] proposed a fuzzy based fractional order PID controller with derivative filter. A new fuzzy based PID controller Mohapatra et al. [15] implemented FOPID Controller in a Power System with different generation area. It is a fuzzy based controller. SSA algorithm is used to optimize the controller gain. Lamba et al. [16] designed a FOPID Controller. The stability boundary locus method is used. The system parameters are varied by using the Kharitonov theorem. Arya et al. [17] designed a FOPID controller using fuzzy logy. Debbarma et al. [18] presented a robust cascaded combination of 2-DOF-PI controller with Double Derivative controller in a three unequal area thermal system. Nature-inspired firefly algorithm (FA) based optimization is implemented. Zhao et al. [19] proposed a two-degree-of-freedom PID controller based on predictive optimal control (PO-2-DOF-PID). He implemented a three area system to test the potency of the above mentioned controller. Tripathy et al. [20] presented a cascade controller in a hybrid system implementing Spider Monkey Optimization technique. He put forward a different controller. He has combined two

different controller, proportional–derivative controller with filter, and proportional–integral controller in cascade. Dash et al. [21] presented a different controller by cascading a PD controller with a PID controller which is optimized by Bat algorithm. He has made a maiden attempt to implement BA to optimize this cascade controller in AGC, considering generation rate constraints of 3%/min.

The proposed work presented the application of PSO and SOS optimization technique optimal tuning of PID controller for keeping the power flow in the interconnected tie-line between the two areas and frequency within the desired limits. Two intelligent optimization techniques named Symbiotic Organism Search and Particle Swarm Optimization have been implemented to find the best optimized gains of the PID controllers for hybrid system. Section 2 gives the information about PID controller whereas two area system with different generating sources is presented in Sect. 3. Section 4 gives the detail about intelligent optimization techniques. Section 5 shows result and discussion and Sect. 6 concludes the work. Appendix has been given in Sect. 7.

2 Proportional Integral and Derivative (PID) Controller

Equation for Proportional plus Integral Controller (PID) can be written as:

$$U(t) = K_{\text{pr}} e(t) + K_i \int e(t)\mathrm{d}t + K_d \frac{\mathrm{d}e(t)}{\mathrm{d}t} \tag{1}$$

where $u(t)$ is the output, $e(t)$ is error input to PID controller, K_i integral gain, K_{pr}.

3 Multi-area Hybrid Power System

For diversity two unequal areas have been considered comprising of various power generation such as thermal power plant, hydro power plant, gas, and wind power plant. Area 1 includes thermal plant, hydro plant, and wind power plant, whereas in area 2, thermal power plant, hydro plant, and diesel power plants are used. MATLAB/SIMULINK model of the hybrid test system including different energy resources have been shown in Fig. 1. For each power plant one PID controller has been used for load frequency control and maintaining the discrepancy in power flow in tie-line, frequency and Area Control Error within a desired limits. The output variation for each plants depend upon their participation factors which are different for each power plants with various operational shifts in the system such as load change.

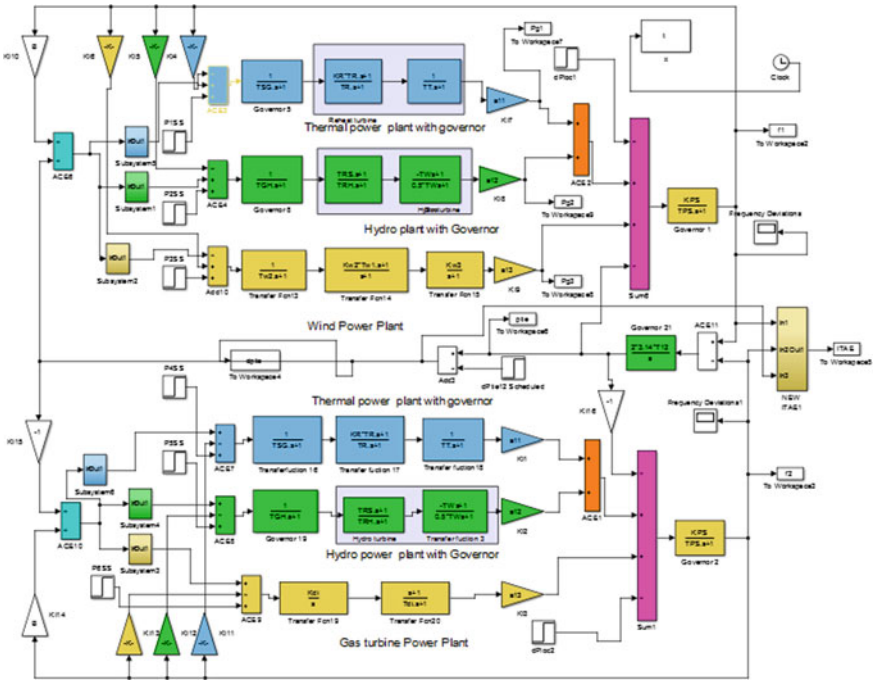

Fig. 1 Transfer function model of multi-source two area power system

3.1 Objective Function for Load Frequency Control

Optimal tuning of all parameters of PID controllers have been done by two intelligent optimization techniques. Tuning of the controllers includes robustness of model uncertainty, tracking of desired dynamic response of different variables and minimizing the oscillations. The PID feedback controller is a popular feedback controller used in various modern industries and is widely applicable in variety of control systems. Two intelligent optimization techniques named Symbiotic Organism Search (SOS) and PSO have been implemented to perceive the optimal gain constant of the controllers for the proposed test system.

Many researchers have reported the use of different performance indices such as Integral of Time multiplied Absolute Error (ITAE), Integral Absolute Error (IAE) and Integral Time weighted Squared Error (ITSE). However, ITAE has been found the best objective function for the use of Automatic Generation Control (AGC) problem in terms of overshoot/ undershoot and settling time. Therefore, ITAE has been considered in the proposed work as an objective function.

$$J = ITAE = \int_0^{t_{\text{sim}}} (|\Delta F_1| + |\Delta F_2| + |\Delta P_{\text{tie}}|).t.\text{d}t \tag{2}$$

ΔP_{tie} is the tie-line power variation, ΔF_1 and ΔF_2 are the change of frequency in area 1 and area 2, respectively. The objective function is being minimized by different intelligent optimization techniques for finding best solution for PID controllers.

Inequality Constraints:

$$K_{P_{\min}} < K_P < K_{P_{\max}}$$
$$K_{\text{I}_{\min}} < K_I < K_{\text{I}_{\max}}$$
$$K_{D_{\min}} < K_D < K_{D_{\max}}$$

The differential equation for PID controller has been shown in Eq. (2).

$$U_1 = K_{P_1} * \text{ACE}_1 + K_{I_1} * \int \text{ACE}_1 + K_{D_1} * \frac{\text{dACE}_1}{\text{d}t} \tag{3}$$

$$U_2 = K_{P_2} * \text{ACE}_2 + K_{I_2} * \int \text{ACE}_2 + K_{D2} * \frac{\text{dACE}_2}{\text{d}t} \tag{4}$$

where,

$$\text{ACE}_1 = \Delta P_{\text{tie}} + B_1 \Delta F_1 \tag{5}$$

$$\text{ACE}_2 = -\Delta P_{\text{tie}} + B_2 \Delta F_2 \tag{6}$$

4 Intelligent Optimization Technique

4.1 Particles Swarm Optimization (PSO) Technique

Particles swarm optimization is an intelligent algorithm based on social behavior of bird flocking [22]. Here, each individual variable is represented by a particle. All the particles moves with the velocity which updates accordance with the combination of own and others particles velocity. Meanwhile all the particles look at the best particles in their paths. Each particle should consider the current velocity, current position, and distance from *g*best and *p*best in order to update its position. Here, particles position is not in real number but in 0 and 1 form. Particles position and velocity can be updated by:

$$v_{id}^{t+1} = v_{id}^{t} + r1 * c1\left(p\text{best}^{t} - x_{id}^{t}\right) + r2 * c2\left(g\text{best}^{t} - x_{id}^{t}\right) \tag{7}$$

$$x_{id}^{t+1} = x_{id}^{t} + v_{id}^{t+1} \tag{8}$$

where, $p$best and $g$best are personal best and global best of particle, $c1$ and $c2$ are acceleration coefficient, $r1$ and $r2$ are random numbers, x_{id} is ith particle's position in dimension d and v_{id}^{t} is the ith particle's velocity in dimension d.

4.2 Symbiotic Organism Search (SOS) Algorithm

Implementation of Symbiotic Organism Search requires the three different stages.

Procedural algorithm:

Step 1: Set total no of organisms & Maximum number of iteration.Set iter = 1.
Step 2: Recognize the best organism from the fitness function.
Step 3: Select randomly one organism X_j so that $X_j \neq X_i$. Calculate the Fitness Value of the organism.
Step 4: Mutual relationship vector (Mutual_Vector) is determined using the equation given below.

$$\text{Mutual Vector} = (X_i + X_j)/2$$

Step 5: Determine the benefit factor (BF). It can be determined randomly either 1 or 2.
Step 6: Update organism X_i.

$$X_{i\text{new}} = X_i + \text{rand}(0, 1) \times (X_{\text{best}} - \text{Mutual Vector} \times \text{BF}_1)$$

Step 7: Update organism X_j using the mutual relationship

$$X_{j\text{new}} = X_j + \text{rand}(0, 1) \times (X_{\text{best}} - \text{Mutual Vector} \times \text{BF}_2)$$

Step 8: After updation of organisms, Calculate the Fitness of the newly modified organisms;
Step 9: If mutated organisms are superior than the older use the updated organisms X_i new and restore the previous organisms else reject modified organisms X_i new and keep the previous organisms.
Step 10: A organism X_j is randomly selected such that $X_j \neq X_i$.
Step 11: Create a Parasite Vector from the Organism X_i.
Step 12: Evaluate the Fitness Value of the newly chosen organism X_j & the corresponding fitness value of created Parasite vector.
Step 13: If *Parasite _Vector is better* than organism X_j, then organism X_j is replaced by the *Parasite _Vector.*
Step 14: If X_j *is better* than organism *Parasite_ Vector*, then delete *Parasite_Vector* & Keep organism X_j as it is.
Step 15: Check the stopping criterion. If yes then that is the optimal solution else iter = iter + 1 & repeat step 2.

The test model has been developed in MATLAB/SIMULINK while SOS algorithm is developed in MATLAB coding (.m files).

5 Result and Discussion

The reported work of optimal tuning of PID controller parameters for hybrid power system has been developed and tested in MATLAB (2016a) software with i5-6200 CPU@ 2.30 GHz with 8 GB RAM. MATLAB Simulink is used to develop hybrid multi source power system while optimization algorithms are developed in MATLAB coding (.m files). To demonstrate the effectiveness of the proposed concept for load frequency control various case study have been considered under dynamic change in system operating conditions. Perturbation response of have been compared for SOS optimization with PSO technique. Figure 1 reveals the simulation model of multi-source system with thermal plant, hydro plant and wind power plant connected in each area. ITAE performance has been used as the objective function to be minimize by the optimization techniques. To check the robustness of the algorithm various cases have been considered.

Case Study I: Step load change of 1 percentage in Area 1 has been considered and parameters of PID controllers are optimally tuned with PSO and recently developed SOS optimization technique. ITAE has been considered as objective function to be minimized and finding best possible parameters of PID controllers. Dynamic response of the state variables for both areas have been compared with optimization based controller. The comparison has been made in terms time domain performance indices. Figure 2 shows the dynamic response of Δf_1, Δf_2, and

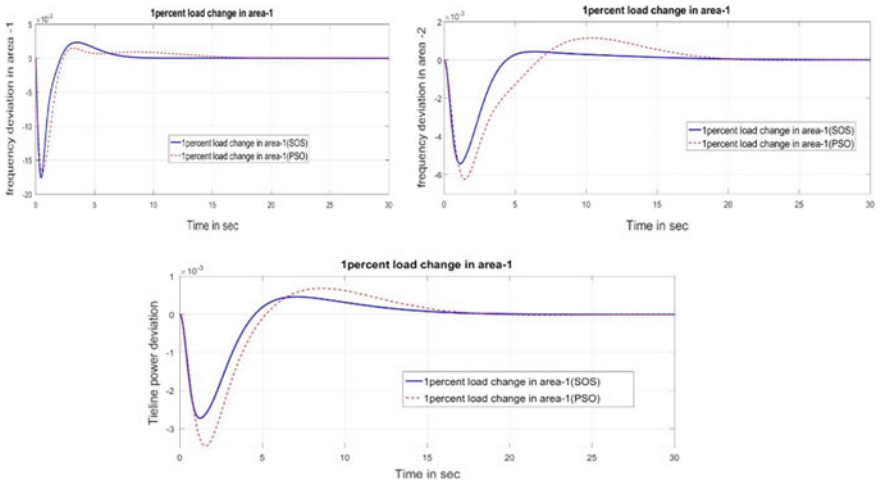

Fig. 2 Perturbation response of two area multi source system for Case I

Table 1 Optimally tuned Pid controller's parameter-Case Study I

Optimization technique		K_p	K_i	K_d	ITAE
SOS driven PID controller	PID1	1.4679	2.0000	2.0000	0.0003
	PID2	0.4644	0.4644	1.9951	
	PID3	1.9886	2.0000	1.9979	
	PID4	1.8839	0.4276	1.9984	
PSO driven PID controller	PID1	1.7063	1.6912	1.9801	0.0004
	PID2	0.4467	0.6304	0.4740	
	PID3	1.0349	0.3055	1.4497	
	PID4	1.0770	1.0180	0.9745	

Table 2 Overshoot and settling time for all the states variables-Case Study I

		Case Study I		
Optimization technique	States variables	Undershoot $U_{sh} \times 10^{-3}$ in Hz	Overshoot $O_{sh} \times 10^{-3}$ in Hz	Settling time T_s in s
SOS driven PID controller	Δf_1	−17.58	2.338	7.52
	Δf_2	−5.429	0.4349	9.781
	ΔP_{12}	−2.726	0.4598	11.61
PSO driven PID controller	Δf_1	−16.71	1.504	14.96
	Δf_2	−6.227	1.15	16.86
	ΔP_{12}	−3.459	0.6839	13.42

ΔP_{12} when 1 percentage change of load is considered in area 1. Table 1 shows optimally tuned PID parameters using both techniques whereas settling time and overshoot of dynamic response of state variables are given in Table 2. From Fig. 2 and Tables 1 and 2, it can be noticed that SOS based PID controller is yielding improved performance and shows better robustness as compared to PSO technique.

Case Study II: A Step load perturbation of 1 percentage in both area 1 and 2 has been considered to analyze the robustness of the algorithm. Time domain response of Δf_1, Δf_2, and ΔP_{12} for this case have been shown in Fig. 3 with the comparison of both technique. Optimal parameters of PID controllers using both PSO and SOS technique have been shown in Table 3, while Table 4 gives the settling time and overshoot of the state variables. From Fig. 3 and Tables 3 and 4, it is marked that SOS based PID controller is giving preferable performance and shows better robustness as compared to PSO technique.

Where, Pg1, Pg2, and Pg3 are thermal power plant, hydro power plant and wind power plant in area 1, while Pg4, Pg5, and Pg6 are thermal power plant, hydro power plant, and diesel power plant in area 2, respectively as shown from Fig. 4 and Fig. 5. From both the case studies, it can be states that the SOS optimization technique

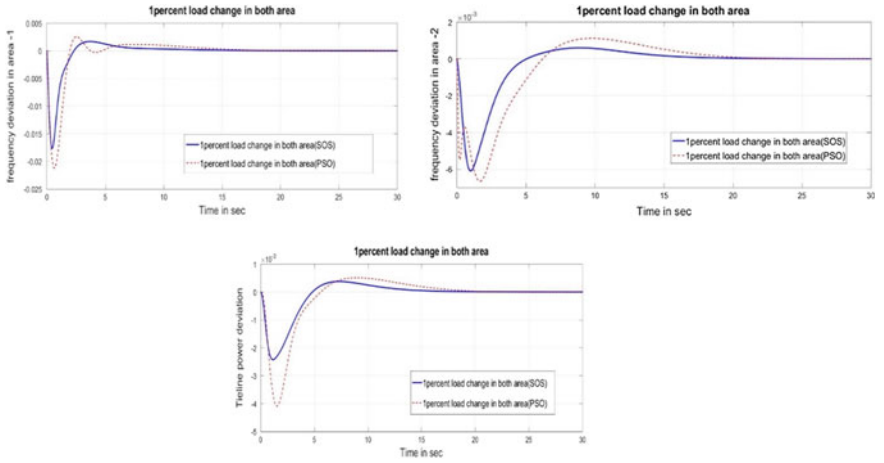

Fig. 3 Perturbation response of two area multi source system for Case II

Table 3 Optimally tuned Pid controller's parameter case study II

Optimization technique		K_{p}	K_i	K_{d}	ITAE
SOS driven PID controller	PID1	2.0000	1.9457	2.0000	0.0003
	PID2	0.8989	0.1061	2.0000	
	PID3	1.9896	1.7924	1.9829	
	PID4	1.9616	1.7303	2.0000	
PSO driven PID controller	PID1	0.7917	1.3940	2.0000	0.0005
	PID2	2.0000	0.3513	1.0525	
	PID3	1.1868	0.5454	0.6906	
	PID4	0.4438	2.0000	0.0100	

Table 4 Overshoot and settling time for all the states variables Case Study II

		Case Study II		
Optimization technique	States variables	Under-shoot $U_{\mathrm{sh}} \times 10^{-3}$ in Hz	Over-shoot $O_{\mathrm{sh}} \times 10^{-3}$ in Hz	Settling time T_{s} in s
SOS driven PID controller	Δf_1	−17.64	1.687	10.76
	Δf_2	−6.089	0.6047	13.19
	ΔP_{12}	−2.421	0.3808	9.284
PSO driven PID controller	Δf_1	−21.24	2.558	15.38
	Δf_2	−6.662	1.121	17.02
	ΔP_{12}	−4.09	0.5139	13.32

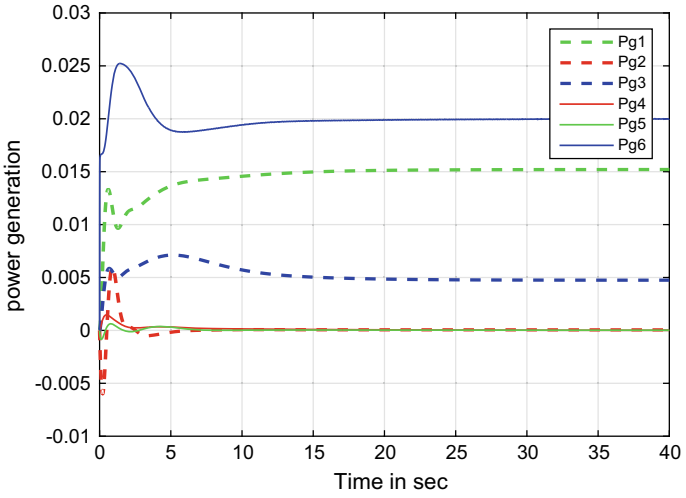

Fig. 4 Output power for all power plants for Case-II

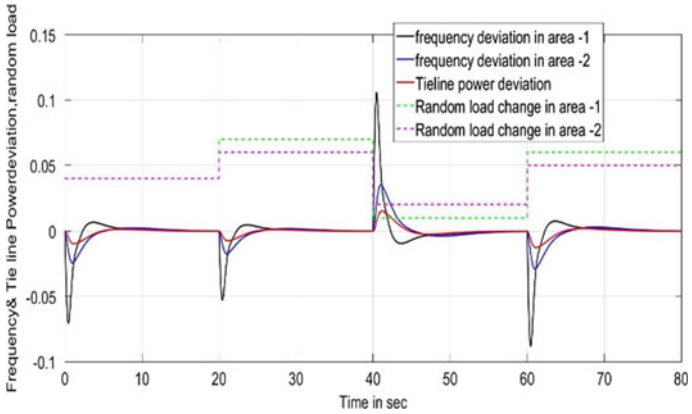

Fig. 5 Responses for random load in both areas

out performed well known PSO optimization technique in terms of time domain specification like settling time, overshoot, and undershoot by optimal tuning of PID controllers under various load change in both areas.

6 Conclusion

This paper addresses the different issues of load frequency control for multi-area multi-sources power system. Thermal power plant along with hydro, diesel, and

wind have been considered in both areas. A newly developed symbiotic organism search (SOS) has been applied for optimal tuning of PID controller parameters and comparison have been made with well known Particles Swarm Optimization (PSO) technique. ITAE has been considered as an objective function to tune the parameters for different operational shifts mSystem performance is examined considering perturbation step load change in both the areas. From the results, it can be states that the SOS optimization technique out performed well known PSO optimization technique in terms of settling time, and undershoot/overshoot by optimal tuning of PID controllers under various load change in both areas.

7 Appendix

Typical values for the system parameters are:

$P_R = 2000$ MW (rating); Frequency (f) = 50 Hz; $B_1 = 0.4312$ pu MW/Hz, $B_2 = 0.4312$ pu MW/Hz; $P_L = 1840$ MW; $T_t = 0.3$ s; $K_r = 0.3$; $T_r = 10$ s; $T_{sg} = 0.08$; $K_T = 0.543478$; $R_1 = R_2 = R_3 = 2.4$ Hz/pu MW; $T_{rh} = 28.75$ s; $T_{gh} = 0.2$ s; $K_G = 0.130438$; $K_H = 0.326084$; $Y_c = 1$ s; $X_c = 0.6$ s; $c_g = 1$; $b_g = 0.5$; $T_W = 1$ s; $T_{rs} = 5$ s; $T_{ps} = 11.49$ s; $T_{cd} = 0.2$ s; $T_{fc} = 0.23$ s; $T_{cr} = 0.01$ s; $K_{ps} = 68.9566$ Hz/pu MW; $T_{12} = 0.0433$ pu; $a_{12} = -1$.

Symbiotic organism search Optimization Technique: No. of Iteration: 50, No. of particles: 30. **PSO Parameters**: No. of Iteration: 50, No. of particles = 30.

References

1. Bevrani H (2009) Robust power system frequency control. Springer, pp 1–13
2. Nanda J, Mishra S, Saikia LC (2009) Maiden application of bacterial foraging-based optimization technique in multiarea automatic generation control. IEEE Trans Power Syst 24(2):602–609. 3
3. Guha D, Roy PK, Banerjee S (2018) Symbiotic organism search algorithm applied to load frequency control of multi-area power system. Energy Syst 9(2):439–468
4. Hassan MF, Abouelsoud AA, Soliman HM (2008) Constrained load-frequency control. Electric Power Compon Syst 36(3):266–279
5. Committee IEEE (1970) Standard definitions of terms for automatic generation control on electric power systems. IEEE Trans Elect Power Apparatus Syst 89:1358–1364
6. Abd-Elazim SM, Ali ES (2018) Load frequency controller design of a two-area system composing of PV grid and thermal generator via firefly algorithm. Neural Comput Appl 30(2):607–616
7. Debnath MK, Sinha S, Mallick RK (2018) Automatic generation control including solar thermal power generation with fuzzy-PID controller derivative filter. Int J Renew Energy Res (IJRER) 8(1):26–35
8. Patel NC, Debnath MK, Sahu BK, Dash SS, Bayindir R (2019) Application of invasive weed optimization algorithm to optimally design multistaged PID controller for LFC analysis. Int J Renew Energy Res (IJRER) 9(1):470–479

9. Mohanty PK, Sahu BK, Panda S (2014) Tuning and assessment of proportional-integral-derivative derivative controller for an automatic voltage regulator system employing local unimodal sampling algorithm. Electric Power Compon Syst 42(9):959–969
10. Mishra DK, Panigrahi TK, Mohanty A, Ray PK, Sahoo AK (2018) Robustness and stability analysis of renewable energy based two area automatic generation control. Int J Renew Energy Res (IJRER) 8(4):1951–1961
11. Arya Y, Kumar N (2017) Optimal control strategy-based AGC of electrical power systems: a comparative performance analysis. Optim Control Appl Methods 38(6):982–992
12. Khuntia SR, Panda S (2012) Simulation study for automatic generation control of a multi-area power system by ANFIS approach. Appl Soft Comput 12:333–341
13. Pan I, Das S (2016) Fractional order fuzzy control of hybrid power system with renewable generation using chaotic PSO. ISA Trans 62:19–29
14. Gheisarnejad, Meysam, Khooban MH (2019) Design an optimal fuzzy fractional proportional integral derivative controller with derivative filter for load frequency control in power systems. Trans Inst Measure Control 41(9):2563–2581
15. Mohapatra TK, Sahu BK (2020) Implementation of SSA-based fuzzy FOPID controller for AGC of multi-area interconnected power system with diverse source of generation. In: New paradigm in decision science and management. Springer, Singapore, pp 329–347
16. Lamba R, Singla SK, Sondhi S (2019) Design of fractional order PID controller for load frequency control in perturbed two area interconnected system. Electric Power Compon Syst, pp 1–14
17. Arya Y (2019) A new cascade fuzzy-FOPID controller for AGC performance enhancement of single and multi-area electric power systems. ISA Trans (article in press)
18. Debbarma S, Saikia LC, Sinha N (2014) Robust twodegree-of freedom controller for automatic generation control of multi-area system. Int J Electr Power Energy Syst 63:878–886
19. Zhao X, Lin Z, Fu B, He L, Fang N (2018) Research on automatic generation control with wind power participation based on predictive optimal 2-degree of-freedom PID strategy for multi-area interconnected power system. Energies 11(12):3325
20. Tripathy D, Sahu BK, Dev Choudhury NB, Dawn S (2018) Spider Monkey optimization based cascade controller for LFC of a hybrid power system. Int J Comput Intell IoT 2(4)
21. Dash P, Saikia LC, Sinha N (2015) Automatic generation control of multi area thermal system using Bat algorithm optimized PD–PID cascade controller. Int J Electr Power Energy Syst 68:364–372
22. Kennedy J, Eberhart R (1995) Particle swarm optimization. In: Proceedings of ICNN'95-international conference on neural networks, vol 4. IEEE

Simulink and FPAA Implementation of FSK Signals

Bikram Choudhury and Aruna Tripathy

Abstract Fundamental to all wireless communication is modulation, the process in which the message data is transmitted on a high frequency radio carrier. Most of the wireless transmissions today are digital as it has more advantages than analog; the effect of distortion, noise, interference is minimized through the use of ingenious digital signal processing as compared to analog communication system. In this paper, we have considered binary frequency shift keying (BFSK) as the modulation technique to send data over a wireless channel. The corresponding demodulator is responsible for retrieving the transmitted data from the noisy, faded signal as impacted by the channel. The metric usually used to evaluate a digital modulation scheme is its average probability of bit error. We have evaluated the bit error rate (BER) of BFSK signals in both the additive white Gaussian noise (AWGN) and flat Rayleigh fading channels. The evaluation has been carried out in both MATLAB and SIMULINK platforms which are subsequently validated by the corresponding theoretical values. After the simulated, BER values are verified and matched with their corresponding theoretical values, hardware realizations have been attempted. The contribution of this paper is (a) the BER evaluation of BFSK through MATLAB simulation and SIMULINK platform, followed by theoretical validations in two different channels and (b) investigation of a hardware platform called Field Programmable Analog Array (FPAA) to build and test a BFSK modulator demodulator (MODEM). Test results show promising outcomes as to the suitability of such MODEM. Indeed data is retrieved at the expense of a small delay.

Keywords FSK · BER · AWGN · Rayleigh flat fading · SIMULINK · FPAA

B. Choudhury (✉) · A. Tripathy
College of Engineering and Technology, Bhubaneswar, Odisha, India

A. Tripathy
e-mail: atripathy@cet.edu.in

M. Mishra et al. (eds.), *Innovation in Electrical Power Engineering, Communication, and Computing Technology*, Lecture Notes in Electrical Engineering 814,
https://doi.org/10.1007/978-981-16-7076-3_36

1 Introduction

Frequency Shift Keying (FSK) is a modulation scheme that is widely used in digital communication system due to the simple construction of both its modulator and demodulator (MODEM), the ease of generation of orthogonal carriers and simple envelope detection at the receiver. Here, the frequency of the carrier (which is usually a sinusoidal signal) is varied according to the amplitude of the message bearing or the baseband digital signal. For binary baseband signal, a higher carrier frequency (f_H) called mark frequency is produced for a binary '1', whereas for binary '0', a lower carrier frequency (f_L) called as space frequency is produced. Numerous efforts have been reported [1–10] that assess BFSK over different channels. The contribution of this paper is an attempt to assess the performance of a BFSK signal in both the additive white Gaussian noise (AWGN) as well as frequency flat Rayleigh fading channels using simulations carried out on MATLAB as well as SIMULINK. The simulated performances are validated with the corresponding theoretical values. The almost perfect match shown by the simulated results with their corresponding theoretical bounds motivated attempts to design a BFSK MODEM on a reconfigurable hardware platform. Hardware implementations of a number of analog functional blocks are reported on other platforms [11–17]. However, the suitability of an FPAA to construct and subsequently test it for information retrieval using BFSK is missing in literature. The novelty of this paper is one of the hardware implementation of a BFSK MODEM and to assess its suitability to detect data from the modulated waveform on a platform called Field Programmable Analog Array (FPAA) from Anadigm Designer 2. The MODEM shows promising results of information retrieval at the expense of a small delay. The necessary mathematical expressions used to evaluate a given MODEM are presented in Sect. 2. Section 3 discusses the system models developed in SIMULINK, followed by the FPAA implementation. Results are discussed in Sect. 4, followed by concluding remarks in Sect. 5.

2 Theoretical Bit Error Rate of BFSK in AWGN and Rayleigh Flat Fading Channels

A BFSK signal can be represented as

$$V_{fsk}(t) = V_c \cos\{2\pi[f_c + V_m(t)\Delta f]t\}, \quad 0 \le t \le T_b, \tag{1}$$

where $V_{fsk}(t)$ represents the binary FSK waveform, $V_m(t)$ is the digital message signal, Δf = frequency deviation from the carrier frequency, V_c = Peak analog carrier amplitude and T_b is the bit duration. So when $V_m(t) = +1$, we will get the frequency component as $f_c + \Delta f$ and $f_c - \Delta f$ when $V_m(t) = -1$. So in this sense, for binary '1', we are sending a higher carrier frequency (f_H) called as mark frequency, whereas for binary '0', lower carrier frequency (f_L) is called as space frequency.

We note from Eq. 1 that a multilevel base band signal changes the carrier frequency in multi steps instead of binary. The theoretical equation for probability of average BER in AWGN is,

$$P_e = Q\left(\sqrt{\frac{2E_b}{N_0}}\right) \tag{2}$$

E_b represents energy per bit while N_0 is the one-sided power spectral density of white noise in (2)**.** The simulated values are compared with Eq. 2. For Rayleigh flat fading channels, the average BER is expressed as [4]

$$P_{e,\text{Rayleigh}} = \left[\frac{1}{2}(1-\mu)\right]^L \sum_{k=0}^{L-1}\binom{L-1+k}{k}\left[\frac{1}{2}(1+\mu)\right]^k \tag{3}$$

In our work,

$$L = 1, \mu = \sqrt{\frac{\overline{\gamma_c}}{1+\overline{\gamma_c}}} \tag{4}$$

Further,

$$\overline{\gamma_c} = \frac{E_b}{N_0} \tag{5}$$

The expressions are simplified to the following in our work as,

$$P_{e,\text{Rayleigh}} = \frac{1}{2}(1-\mu) \tag{6}$$

For AWGN channels, the theoretical average BER is evaluated by (2), whereas for Rayleigh flat fading channels, use is made of Eq. 6 in the subsequent sections.

3 Simulink Models and Validation of Results

In this section, the SIMULINK models for a BFSK MODEM in both AWGN and Rayleigh flat fading channels are presented. A comparison is also made between the simulated BER with the theoretical ones using Eq. 2. The SIMULINK model of BFSK in AWGN is presented in Fig. 1.

The BER of BFSK in AWGN as obtained in Fig. 1 has been compared with the theoretical one using Eq. 2 in Fig. 2 and both show a good match.

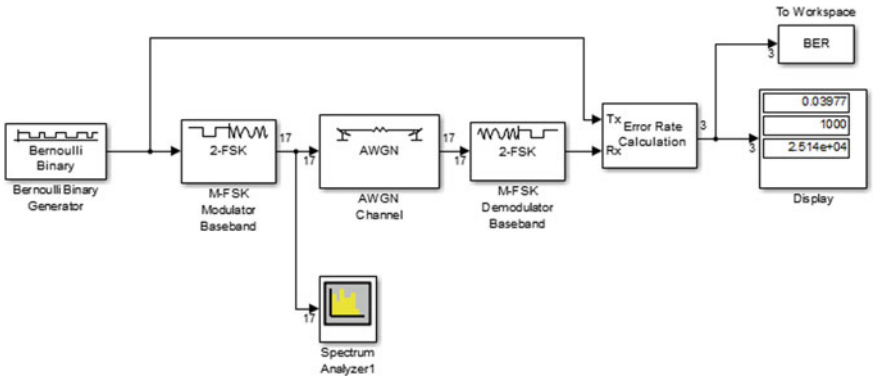

Fig. 1 BFSK SIMULINK Model in AWGN Channel

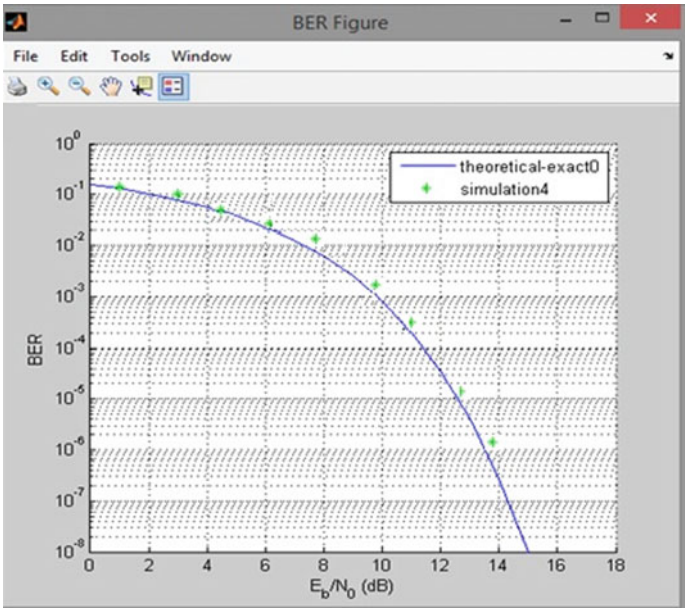

Fig. 2 BER curve of BFSK under AWGN Channel in SIMULINK Model

The model used to assess the BER of BFSK in flat Rayleigh fading is shown in Fig. 3. The Rayleigh fading block is used after the BFSK modulator block in order to determine the effect of Rayleigh fading effect in BFSK. The math function 1/u acts as a normalizing factor. The Spectrum Analyzer block accepts input signals with discrete sample times and displays frequency spectra of these signals. The Error Rate Calculation block compares input data from a transmitter with input data from a receiver and helps to obtain the BER curve.

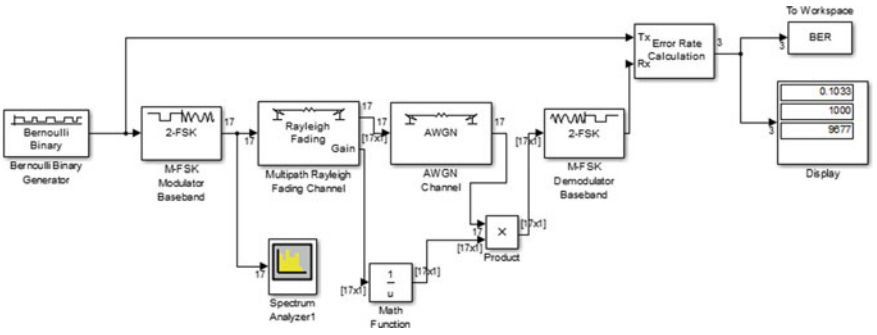

Fig. 3 BFSK SIMULINK model in Rayleigh fading

The BER of BFSK in flat Rayleigh fading as obtained in Fig. 3 has been compared with the theoretical one using Eq. 6 in Fig. 4 and both are in good agreement.

MATLAB 2014 version has been used to simulate the BFSK signal where binary data is taken as input. Two carrier signals $C_1(t)$and $C_2(t)$ are generated. According to two carriers, FSK signal is generated and demodulated.

The simulation for probability of bit error for BFSK over AWGN and Rayleigh Fading is done by using MATLAB 2014 and the parameters considered for this simulation are mentioned in Table 1.

Figure 5 shows the comparison of simulated BER curve which is simulated in MATLAB of BFSK in AWGN and Rayleigh fading channel. Here, SNR dB is taken from 0 to 12 dB. It is observed from this figure that the BER performance of BFSK

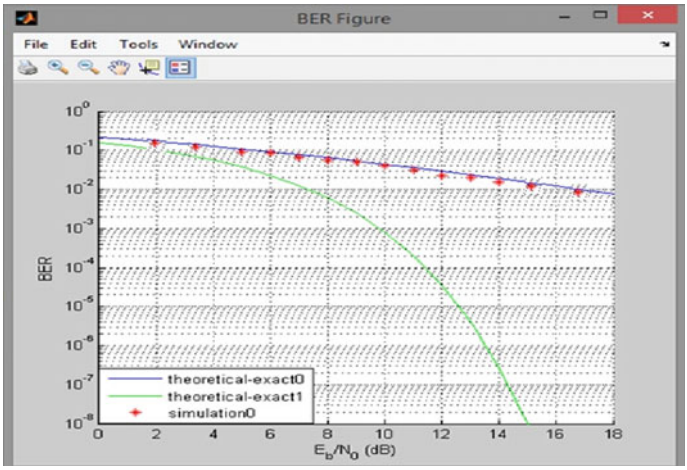

Fig. 4 BER curve of BFSK in Rayleigh fading in SIMULINK model compared with the corresponding AWGN curve

Table 1 Parameter table for simulation of bit error probability of BFSK over AWGN and Rayleigh fading

Modulation order (M)	2 (BFSK Coherent)
No. of Bits	1,000,000
Samples/bit	20
SNR	0:1:12 dB
Carrier frequencies	1 Hz, 2 Hz

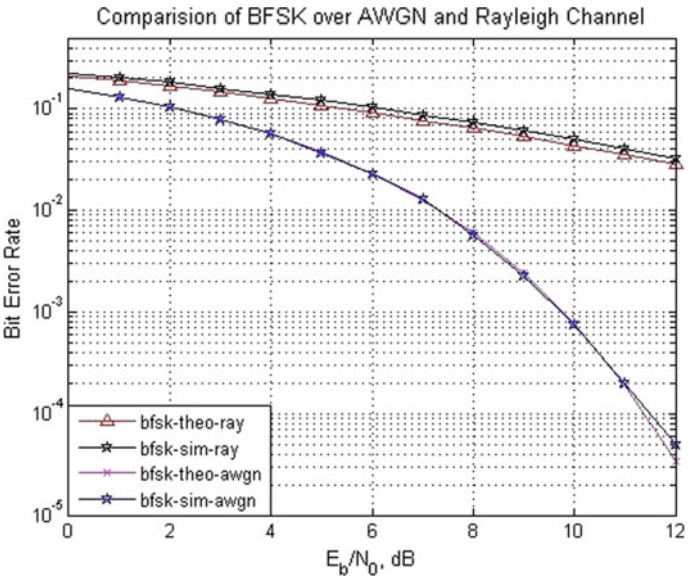

Fig. 5 Comparison of MATLAB Simulation of BER curves of BFSK in AWGN and Rayleigh fading channel

over AWGN is better than BER performance of BFSK over Rayleigh channel. This is for the sake of completeness.

From Figs. 2 and 3, the Spectrum analyzer is used after the BFSK modulator baseband block to obtain the Power spectral density of BFSK in Simulink model and to validate those results in MATLAB simulation, we have used FFT algorithm to obtain the Power Spectral Density in MATLAB 2014 version. The results for PSD of BFSK from SIMULINK and MATLAB simulation are mentioned in Figs. 6 and 7.

The PSD of BFSK signal is the superposition of PSD of two signals generated for 0 and 1. As we are computing PSD of BFSK, we observe two sharp peaks in Figs. 6 and 7. This is due to the two carrier frequencies used in BFSK. This is because of the orthogonal nature of the basic functions. From Figs. 7 and 8, two main lobes are generated exactly at the same distance from the center frequency. Two lobes from both the simulations correspond to the energy of the two symbols/frequencies.

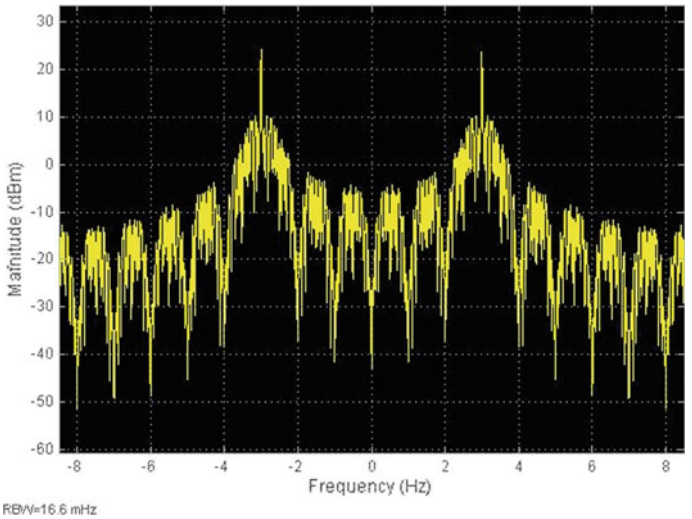

Fig.6 Simulated power spectral density of BFSK in SIMULINK Model

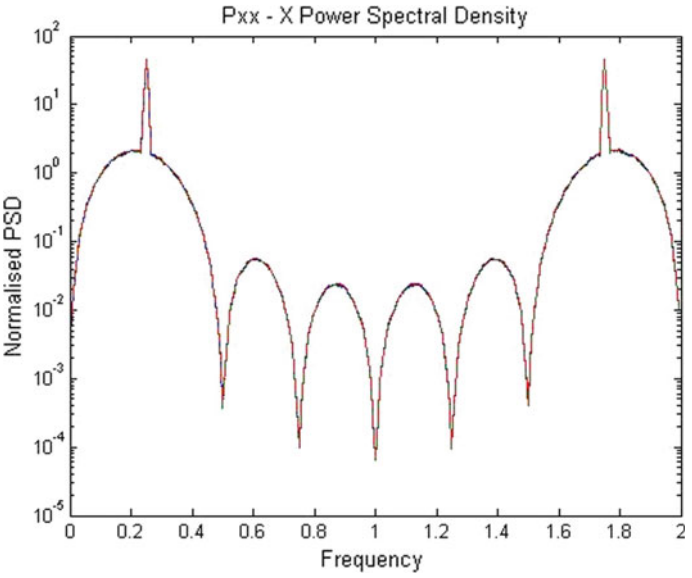

Fig.7 Simulated power spectral density of BFSK in MATLAB

The spike at center of each frequency lobe represents the carrier frequency of each symbol.

Next, we have shown one hardware implementation of a BFSK modem. Some of the readily available FPAA software sources are as follows: ANADIGM (CMOS

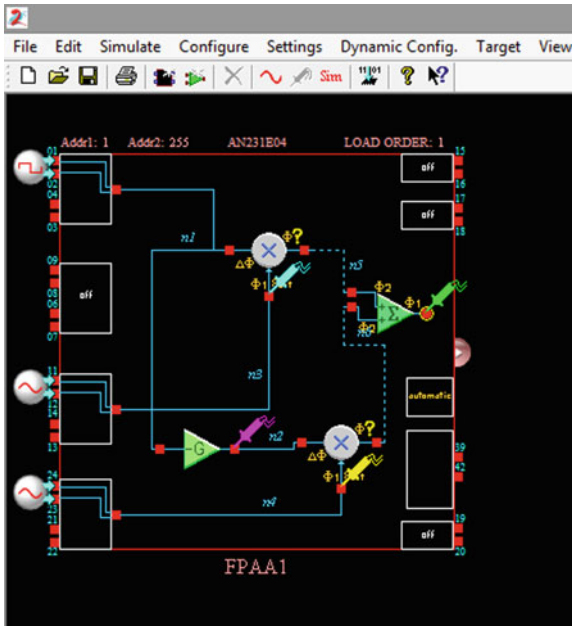

Fig. 8 Generation of BFSK Modulated signal using Anadigm Designer-2

Technology, 2 MHz BW), MOTOROLA (Discrete time Technology, 200 kHz BW), IMP Inc. (CMOS Technology, 125 kHz BW), FAST ANALOG SOLUTION (Bipolar Technology, 4 MHz BW), University of TORONTO (CMOS Technology, 100 kHz BW). But in this paper, the hardware realization has been carried out on ANADIGM-2 FPAA. FPAAs help in the algorithmic implementation of the analog circuit creation policies, provides a very convenient medium in which analog circuits and systems can be designed and implemented in a very short time frame. Anadigm Designer 2 software has designed all the functional codes and blocks as analog units and the programs that are inscribed in each block are suitable for analog modulation and demodulation scheme. However, some of the functional blocks like periodic wave generator, zero cross detector, etc., essential for a BFSK MODEM implementation are suitable and helpful in digital modulation schemes. Utilization has been made of these functional blocks to construct and test such a MODEM on this platform.

4 FPAA Implementation of BFSK Modulator

A hardware implementation of BFSK modulator has been carried out on a platform called ANADIGM DESIGNER 2. The message signal and two carrier signals are generated by the Signal Generator Controller and we set the frequency and amplitude of each signal used in this block. The message signal has 10 kHz frequency, and the 2 frequencies are 50 kHz and 20 kHz, respectively, and amplitude of 1 V. The

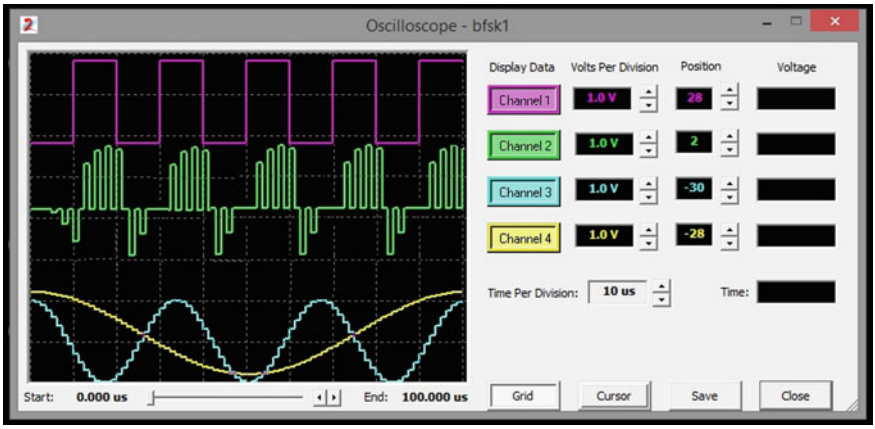

Fig. 9 Output of BFSK modulated signal

square wave message signal is passed through an inverter to produce 0 and 1 with equal probabilities. Then the message signal is multiplied with both the carriers with the help of two multipliers. Both multiplied signal passed to an adder to get the modulated signal. For the sum purpose, we have used the SumFilter. (It creates a full cycle summing stage with up to three inputs that includes a single pole low pass filter.) The inputs may be either inverting or non-inverting so that both sums and differences may be created in the transfer function. The modulator for BFSK signal in ANADIGM DESIGNER 2 is shown in Fig. 8, while its output is illustrated in Fig. 9.

From Fig. 9, we can observe that we are getting a high-frequency signal for + 1 of the binary wave and a low frequency signal for –1 of the binary wave. In this diagram, the purple color signal is the message signal, blue color signal indicates higher frequency signal, the yellow color signal is the lower frequency signal, and the green color signal indicates the modulated signal of BFSK technique. Next, we show one implementation of a BFSK demodulator using ANADIGM 2.

Figure 10 shows a realization of coherent demodulator. The modulated signal is multiplied with the same carriers as used in the modulator. Then these signals are passed through LPFs (Low pass filter) having cutoff frequency 25 kHz to get two output signals. Finally these signals are passed through a comparator to get the original message signal. The comparator will produce a digital output level of ± 2 V, based on the chip reference voltages. The output of this FPAA design is described in Fig. 11.

The Purple line indicates the message signal and the blue line indicates the demodulated signal. In this case, we are getting a delay in demodulated signal as compared to the message signal. This is attributable to the fact that all the functional blocks in an FPAA are designed to process analog signals leading to inherent delays between connecting blocks produced by the various functional blocks that process the analog signals.

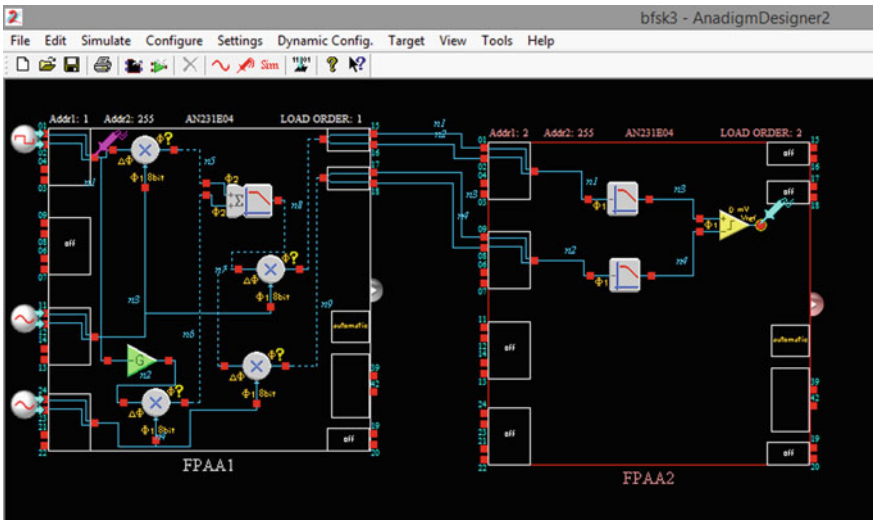

Fig. 10 BFSK demodulator on FPAA

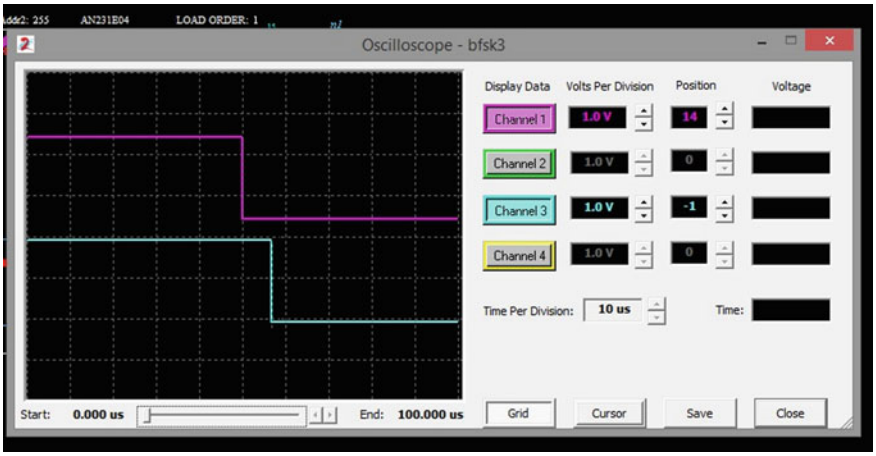

Fig. 11 Output of BFSK demodulated signal

5 Conclusion

The aim of this Simulink Model is to analyze the modulation/demodulation scheme BFSK using BER as a performance indicator. The BER characteristics as obtained through MATLAB simulation and SIMULINK models match their theoretical values both in the AWGN channel and Rayleigh fading for almost all the SNR values considered. The successful simulation of BFSK has motivated to construct and test a BFSK

MODEM. This has been carried out on a hardware platform called Anadigm Designer 2's FPAA. One of the possible implementations of a BFSK modem shown in this paper uses coherent detection in the absence of any real channel. During modulation process we are getting accurate outputs as desired but during demodulation process we observe some time shift at the outputs as Anadigm Designer 2 makes use of all analog signal processing blocks. Both the input signal and demodulated waveforms show a good match at the expense of a delay of about 15 μS.

References

1. Günay E, Altun K (2017) BER analysis and application in FPGA and FPAA based communication systems. In: 2017 international artificial intelligence and data processing symposium (IDAP), IEEE, pp 1–5. https://doi.org/10.1109/IDAP.2017.8090227
2. Almashhadani YS (2017) BER performance of M-ary FSK Modulation over AWGN and Rayleigh fading channels. Proc J Babylon Univ/Eng Sci 25(4)
3. Angkeaw K (2019) ISCIT 2019 invited talk 3. In: 2019 19th international symposium on communications and information technologies (ISCIT), IEEE, pp xxxviii-xxxviii. https://doi.org/10.1109/ISCIT.2019.8905132
4. Reddy BVR (2016) Field programmable analog array: A boon for analog world. In: 2016 3rd international conference on computing for sustainable global development (INDIACom). IEEE
5. George S et al (2016) A programmable and configurable mixed-mode FPAA System. IEEE Trans Very Large Scale Integr (VLSI) Systems 24(6):2253–2261
6. Sklar B (2014) Digital communications: fundamentals and applications. Pearson Education Limited
7. Haykin S, Wiley J (2005) Digital communications Systems. 1st edn
8. Proakis G, Salehi M (2013) Fundamentals of communication systems. Pearson Higher Ed
9. Proakis JG, Salehi M (2008) Digital communications, 5th edn. McGraw Hill Education Pvt. Ltd
10. Lathi BP, Ding Z (2009) Modern digital and analog communication systems. Oxford University Press
11. Anadigm® FPAA Solutions Training. Anadigm Apex on Line Customer Seminar series [online]. http://www.anadigm.com/_doc/trainingdocument2.pdf
12. AN220E04 Datasheet—Dynamically Reconfigurable FPAA [online]. http://www.anadigm.com/an220e04.asp
13. AN231E04 Datasheet—Dynamically Reconfigurable dpASP [online]. http://www.anadigm.com/an231e04.asp
14. Visan DA, Jurian M, Lita I, Cioc IB (2009) Reconfigurable platform for versatile generation of communication signals. In: 2009 32nd international spring seminar on electronics technology, Brno, pp 1–4
15. Pandiev IM (2012) Realization of low-frequency amplitude modulator and demodulator with FPAAs. In: ICEST 2012, 28–30 June, 2012, Veliko Tarnovo, Bulgaria, pp 517–520
16. Jammu BR, Botcha HK, Sowjanya AV, Bodasingi N (2017) FPGA implementation of BASK-BFSK-BPSK-DPSK digital modulators using system generator. In: 2017 international conference on circuit, power and computing technologies (ICCPCT), Kollam, pp 1–5
17. Zeynalov E, Bokov A (2019) Sawtooth voltage source based on field programmable analog array. In: 2019 ural symposium on biomedical engineering, radioelectronics and information technology (USBEREIT), Yekaterinburg, Russia, pp 348–351

Analysis of Lung Cancer by Using Deep Neural Network

Sourav Shandilya and Soumya Ranjan Nayak

Abstract Lung cancer is one of the world's deadliest cancers and one of the highest mortality rates. There has been a recent increase in the prevalence of lung cancer. The key aim of this research was to create a computer-aided diagnostic (CAD) method for classifying histopathological photographs of lung tissues. For the creation and validation of CAD, we used a publicly available dataset (15,000 samples) of histopathological photographs of lung adenocarcinoma, lung squamous cell carcinoma, and benign lung tissue from three different types. In order to extract image features, multi-scale processing was used. Finally, the comparison study has been made based upon seven pre-trained convolution neural network (CNN) models, including MobileNet, VGG-19, ResNet 101, DenseNet 121, DenseNet 169, Inception V3, InceptionResNet V2, and MobileNetV2 for classification of lung cancer. All pre-trained models are hyper-tuned by considering several factors such as batch size, learning rate, number of epochs, and model accuracy. Among all, ResNet 101 had the best accuracy of these CNN version, at 98.67%. This research will aid researchers in the development of more successful CNN-based lung cancer detection models.

Keywords Transfer learning · Lung cancer · Classification · CNN · Multi-scale processing

1 Introduction

Cancer is a term used to describe a group of diseases in which mutated cells form within the human body as a result of random mutations. When these cells are born, they differentiate rapidly and disperse across the body. Most cancers will lead to death if they are not treated in a timely manner. After coronary diseases, cancer is the leading cause of death worldwide. In 2020, there will be almost 228,820 new lung cancer patients in the United States alone. Lung cancer [1] is the primary cause of cancer-related deaths in the United States, accounting for about one-quarter of all

S. Shandilya · S. R. Nayak (✉)
Amity School of Engineering and Technology, Amity University Uttar Pradesh, Noida 201301, India

M. Mishra et al. (eds.), *Innovation in Electrical Power Engineering, Communication, and Computing Technology*, Lecture Notes in Electrical Engineering 814,
https://doi.org/10.1007/978-981-16-7076-3_37

cancer deaths. Based on information gathered between 2015 and 2017, at any point in their lives, two out of every five Americans will be diagnosed with cancer. Cancer cells can form in any part of the body, but the lungs, breast, brain, colon, rectum, stomach, scalp, and prostate are the most commonly affected organs. Lung and colon cancers are the most common cancers that cause mortality in both men and women. Cancer is caused by a variety of factors, including behavioral characteristics such as a high BMI, nicotine and alcohol use, as well as physical carcinogens such as ultraviolet rays and radiation, as well as some genetic and biological carcinogens. The source, on the other hand, can differ from one person to the next. Fractal feature [2] also plays a major role to analysis of cancer detection by using machine learning and deep learning.

Cancer staging refers to how far the disease has gone throughout the body and the way serious it is. Staging aids health care professionals and patients in determining the simplest course of therapy.

The most basic style of staging is as follows:

1. Localized, wherein the cancer is within a limited area
2. Regional, wherein the cancer has spread to nearby tissues or lymph nodes
3. Distant, wherein the cancer has spread to other parts of the body

Non-small cell carcinoma stages

The phases of non-small cell carcinoma are commonly described by health care experts using tumors size and spread, as follows:

Hidden or occult: On imaging scans, the cancer does not manifest, although malignant cells may emerge in phlegm or mucus.

Stage 0: Only the highest layers of cells lining the airways contain aberrant cells.

Stage 1: A tumor exists within the lung, but it is but four centimeters (cm) in diameter and has not migrated to other areas of the body.

Stage 2: The tumor has grown to a diameter of seven centimeters or less and has spread to adjacent tissues and lymph nodes.

Stage 3: The cancer has progressed to lymph nodes and other regions of the lung and its surroundings.

Stage 4: The cancer has progressed to other parts of the body, such as the bones or the brain, at this stage.

Carcinoma of small cells is divided into several categories. Limited and extended stages include the development of cancer within or outside the lungs. The cancer will only affect one side of the chest at this stage [3], but it will already be present in some nearby lymph nodes. Around a 3rd of persons with this type discover they need cancer when it is still in its early stages. Radiation treatment will be accustomed treat it as one region by health care specialists. At the advanced [4] stage, the cancer has spread over one side of the chest. In addition to other areas of the body, it has potential to influence the opposite lungs. Around two-thirds of individuals with small cell carcinoma discover that they need it when it is already within the extensive stage.

Fatigue, discomfort, respiratory problems, weight loss, and a variety of other symptoms are among the most frequent symptoms of cancer. As a result, detecting the presence of cancer without a screening test such as a computed tomography (CT) scan, magnetic resonance imaging [5] (MRI), positron emission tomography (PET) scan, ultrasound, or biopsy is usually difficult. In certain cases, the patients exhibit little or no symptom in the early stages, and by the time symptoms appear, it is usually too late [6]. In certain cases, a person inherits the cancer-causing gene from his or her parents. People who are at a higher risk of having hereditary cancers may have regular checkups. Lung cells that become cancerous as they mutate and expand uncontrollably form a cluster, which is referred to as a tumor. We can see from the knowledge that the carcinomas commonly reside in the flesh of smokers [3], but it can also appear face to face in non-smokers. The two prevalent forms of carcinoma are adenocarcinoma and epithelial cell carcinoma; however, other histological types include small and large cell carcinomas.

Adenocarcinoma of the carcinoma is most common in active or former smokers, although it may also occur in non-smokers. This form of cancer is most likely to strike young women and children, and it is usually located in the lungs' outer layers, before it gets out of hand. Smokers are more likely to develop epithelial cell carcinomas. On the other hand, small and large cells can form in any part of the lung and have a proclivity to expand and enroll quickly, making treatment more difficult.

CNN is often used to interpret medical imaging, such as CT scans or MRI, in order to track, diagnose, and improve patient-specific equipment [7, 8]. Medical imaging is currently completed by taking slices of the depth of the tissue to be examined, but since the body is made up of moving 3D objects, all of the images must be seen in context to be effective. Processes like identifying cancerous cells, evaluating arterial health, and structural imaging of brain tissue can be processed by a 3D CNN by integrating these static images with volume or spatial background, minimizing the time taken for individual assessment and allowing quicker patient treatment. First, the input image is improved for image contrast using histogram equalization, and then denoised using an adaptive bilateral filter (ABF) [2]. After preprocessing, the next step is to locate and remove the lung area. The artificial bee colony (ABC) segmentation technique is used to isolate the lung area. Inside the ABC segmented image, the holes in the lung region are filled using a mathematical morphology technique. Currently, feel functions are being extracted in order to locate cancerous lung nodules. After locating the cancerous lung nodules, the next step is to identify the lung disease name and incidence, which is aided by function extraction. In context to bio-medical image processing, most of the literature has shown the interest on various transfer model by hyper-tuning the model along with performing numerous kind of preprocessing and statistical techniques [2, 9, 10].

2 Proposed Work and Methodology

We propose a machine learning (ML) model for sub-classifying non-small cell lung cancer photographs into squamous cell carcinoma and adenocarcinoma in this article. In a wide variety of medical image processing systems, CNN [11] models have been shown to produce superior performance. In such situations, models based on the principle of transfer learning (TL) can be useful. In TL, the information obtained by a DL model trained on a big task is applied to a task with a smaller size. This reduces the need for a broad and lengthy learning period, which is required by DL methods that are taught from scratch. DenseNet 121, DenseNet 169, InceptionResNet V2, Inception V3, MobileNetV2, MobileNet, and ResNet101 were included in this analysis.

2.1 Dataset Used

There are 25,000 histopathological photographs [12] in the dataset, divided into five classes. Images have a resolution of 768 × 768 pixels and are saved as jpeg files.

The photographs were created using an inspired sample of HIPAA compliant and authenticated sources, consisting of 750 total images of lung tissue (250 benign lung tissue, 250 lung adenocarcinomas, and 250 lung epithelial cell carcinomas) and [9] 500 total images of colon tissue (250 benign colon tissue and 250 colon adenocarcinomas), which were then augmented to 25,000 using the Augmenter kit.

The dataset is divided into five classes, each with 5000 images: (i) lung tissue that is not cancerous, (ii) adenocarcinoma of the lungs, (iii) epithelial cell carcinoma of the lungs, (iv) adenocarcinoma of the colon, and (v) colon tissue that is benign.

The dataset can be downloaded as LC25000.zip, a 1.85 GB zip format. After removing the lung colon image set archive, which includes two subfolders, colon image sets and lung image sets. The colon image sets subfolder contains two secondary subfolders: colon aca, which contains approximately 5000 images of colon [12] adenocarcinomas, and colon n, which contains approximately 5000 images of healthy colonic tissues. Lung aca subfolder contains 5000 images of lung adenocarcinomas, lung_scc subfolder contains 5000 images of lung epithelial cell carcinomas, and lung n subfolder contains 5000 images of benign lung tissues in the subfolder lung image sets.

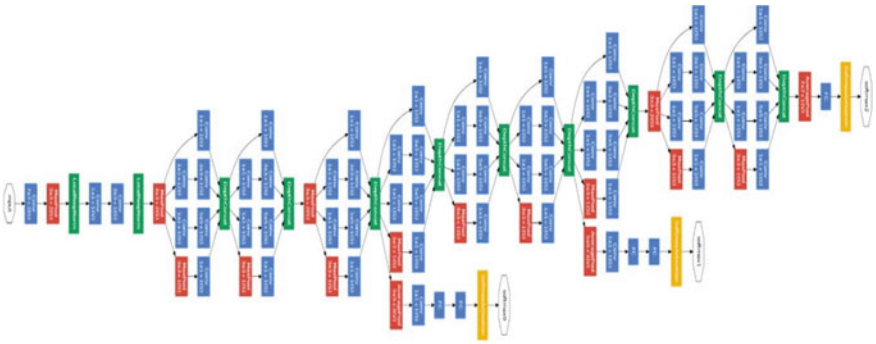

Fig. 1 Architecture of inception

2.2 Preprocessing

As we all know, when deeper networks begin to converge, a degradation problem arises; when the network complexity grows, precision becomes saturated and quickly degrades. The approach is to use direct mapping of a few stacked non-linear layers to solve the problem. To classify, we built a deep CNN with the following layers and parameters:

2.3 Proposed Models

The proposed approach uses a convolutional neural network [13] and several ML models combined to form an ensemble. For feature extraction, the CNN model is used, and machine learning algorithms are used for classification. The features extracted by the CNN model are clearly depicted in Fig. 1, and its detailed descriptions are described in following sub-sections:

Input Layer

The data is loaded and sent to the first convolution level by the input layer. The input in this case is a 150 × 150 pixel image [14] with three channels: red, blue, and green.

Convolution Layer

Convolution layer is used for inputting a filter image that can be learned for learning the spatial image structure [15]. This model has a total of three core layers of 3 × 3 filters in size. The first filters consist about 32 layers, and the two layers with 64 filters have Gaussian distribution initialized for this purpose. An extra ReLU [14] activation is added after all these layers to increase the general efficiency.

Pooling Layer

The pooling layer allows CNN to distinguish functionalities of different images regardless of the illuminated differences and the angle of view and of the images. For pictures outputing from a preceding layer which convolution layer [5] is used pooling. After any convolution layer with pooling size of 2, we have added a pooling layer that is kept true by design. Besides, all of the bundling layers have been maintained to use the most popular limit bundling.

Flatten Layer

The next move is to flatten the layers until the pooling process is complete and the pooled function map is received. In this procedure, the entire pooled functional map matrix is transformed into a single column [16], then fed into the completely connected sheet. We used it in this layer to transform a 1D tensor from the convolution layer for a very thick layer.

Fully connected layer

The flattened function map passes into a neural network after the flattening has been completed. This stage consists of a completely connected layer, input layer, and output layer [17]. The output layer is the layer we have the class we have foreseen. These are the layers that handle the input like a basic vector and provide us with a vector output. The model uses a total of two dense. First, the neurons are approximately 512, and second, the neurons are 3.

3 Experiment and Results

In this section, the findings of several studies are presented. About 10,500 photographs in 3 groups were found. And, 4500 pictures of three groups were found. We investigated the effects of many factors associated with these models and conducted a comparison of eight CNN model. Finally, the most effective model is discovered.

We have contrasted our findings to recent state-of-the-art methods. To ensure the classifiers generalize well, the data was divided into three groups, with 80–10–10 percent of the data going into preparation, checking, and validation sets, respectively. When it comes to medical image analysis [18], there are two approaches to assess it. The first is at the patient stage, which involves calculating the number of accurately identified photographs for each patient. Secondly, the number of images categorized correctly may be assessed in an image. Therefore, we agreed to proceed to a subsequent approach (Riquelme and Akhloufi 2020) [13] in LC25000 3 for assessing model success in no knowledge on patients.

4 Discussion

As from the above results, we can clearly see [19] that ResNet 101 got the highest percentage of accuracy with 98.67%, and with its first epoch, it started with 96.80%, and by Epoch 8, it went up to 98.67%. Similarly, the VGG-19 got the 97.78% at its Epoch 10, started with 95.73% at the Epoch 1. InceptionResNet V2 got the accuracy of only 46.04% at its Epoch 6, started with 66.44% at Epoch 1. DenseNet 121 accuracy kept getting increased by every epoch started with 41.78% at its first Epoch and it went up to 94.71% by Epoch 8. DenseNet 169 accuracy went up to 95.78% by Epoch 10. MobileNetV2 is not suitable for the model as it only goes up to 81.42%, and the accuracy of Inception V3 and InceptionResNet V2 is 85.02% and 46.04%, respectively. The detailed outcome of proposed scheme is tabulated in Table. 1. The following is derived from the above models' confusion matrix. The confusion matrix is a tool that is often used to assess the consistency of a designation. M(i,j) is proportional to the number of observations proven to be in group i and expected to be in group j, according to the concept of an uncertainty matrix an presented in Fig. 2. For testing memory, specificity, precision, and accuracy, an uncertainty matrix is very useful.

5 Conclusion

In this article, we carried out a series of experiments using a deep learning method on the LC25000 data collection. Various pre-trained CNN architectures used the transfer learning concept, many essential elements were assessed, and their findings were compared in LC25000 datasets. The results indicate that ResNet 101, with an accuracy of 98.67%, was able to operate against other competing networks and should also be considered a potential predictor of lung cancer. The radiologists will use or use this same CNN model to validate its scanning and reduce the cancer detection work. We have also managed in this analysis to further improve successful deep CNN models to detect lung cancer more precisely. For a multi-class classification query, the efficacy of the proposed model will be tested in further studies. In this field, we will discuss, along with the CNN models used in this analysis, the various optimization algorithms to produce a more accurate model.

Table 1 Training performance of all the proposed models

Model	Epoch	Valid accuracy (%)
DenseNet 121	1	41.78
	2	93.29
	3	94.49
	–	
	8	94.71
VGG-19	1	95.73
	2	96.73
	3	97.29
	–	
	10	97.78
ResNet 101	1	96.80
	2	96.49
	3	97.29
	–	
	8	98.67
MobileNetV2	1	89.91
	2	75.51
	3	88.53
	–	
	6	81.42
InceptionResNet V2	1	66.44
	2	36.49
	3	36.40
	–	
	8	46.04
DenseNet 169	1	90.71
	2	81.78
	3	95.78
	–	
	6	95.29
InceptionResNet V2	**1**	**79.16**
	2	**80.71**
	3	**83.69**
	–	
	10	**85.02**

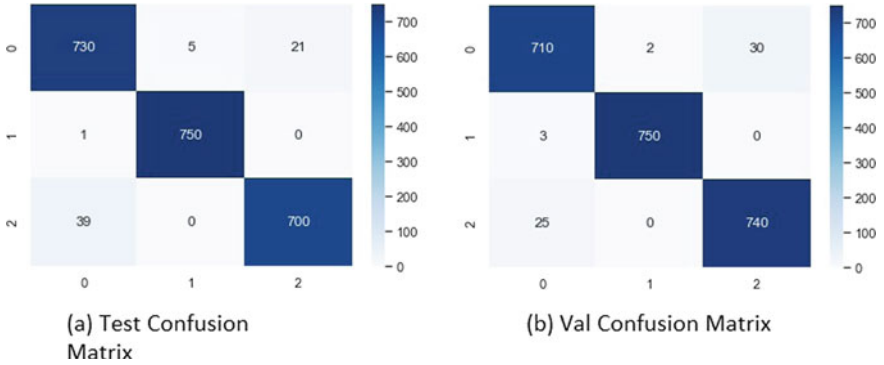

Fig. 2 Confusion matrix of ResNet 101

References

1. Da Silva GLF et al (2017) Lung nodules diagnosis based on evolutionary convolutional neural network. Multimedia Tools Appl 76(18):19039–19055
2. Nayak SR et al (2021) Application of deep learning techniques for detection of COVID-19 cases using chest X-ray images: a comprehensive study. Biomed Signal Process Control 64:102365
3. Sun W et al (2020) Attributable risk of all-cause mortality in hypertensive adults based on disease risk prediction model: a Chinese cohort study. J Infect Public Health 13(9):1290–1296
4. Mobiny A, Van Nguyen H (2018) Fast capsnet for lung cancer screening. In: International conference on medical image computing and computer-assisted intervention. Springer, Cham
5. Kalaivani N et al (2020) Deep learning based lung cancer detection and classification. In: IOP conference series: materials science and engineering, vol 994(1). IOP Publishing
6. Chang Y et al (2020) Effect of a computer network-based feedback program on antibiotic prescription rates of primary care physicians: a cluster randomized crossover-controlled trial. J Infect Public Health 13(9):1297–1303
7. Mohapatra S, Nayak J, Mishra M, Pati GK, Naik B, Swarnkar T (2021) Wavelet transform and deep convolutional neural network-based smart healthcare system for gastrointestinal disease detection. Interdisc Sci Comput Life Sci 1–17
8. Mohapatra S, Swarnkar T, Das J (2021) Deep convolutional neural network in medical image processing. In: Handbook of deep learning in biomedical engineering. Academic Press, pp 25–60
9. Nayak SR et al (2021) An automated lightweight deep neural network for diagnosis of COVID-19 from chest X-ray images. Arab J Sci Eng 1–18
10. Nayak SR et al (2021) A statistical analysis of COVID-19 using Gaussian and probabilistic model. J Interdisc Math 24(1):19–32
11. Patil R, Bellary S (2020) Machine learning approach in melanoma cancer stage detection. J King Saud Univ-Comput Inf Sci
12. Borkowski AA et al (2019) Lung and colon cancer histopathological image dataset (lc25000). arXiv preprint arXiv:1912.12142
13. Riquelme D, Akhloufi MA (2020) Deep learning for lung cancer nodules detection and classification in CT scans. AI 1(1):28–67
14. Kumar A et al (2019) Co-learning feature fusion maps from PET-CT images of lung cancer. IEEE Trans Med Imaging 39(1):204–217
15. Chao H et al (2021) Deep learning predicts cardiovascular disease risks from lung cancer screening low dose computed tomography. Nature Commun 12(1):1–10

16. Subramanian V, Do MN, Syeda-Mahmood T (2020) Multimodal fusion of imaging and genomics for lung cancer recurrence prediction. In: 2020 IEEE 17th international symposium on biomedical imaging (ISBI). IEEE
17. Coudray N et al (2018) Classification and mutation prediction from non–small cell lung cancer histopathology images using deep learning. Nature Med 24(10):1559–1567
18. Uzelaltinbulat S, Ugur B (2017) Lung tumor segmentation algorithm. Procedia Comput Sci 120:140–147
19. Nanglia P et al (2020) A hybrid algorithm for lung cancer classification using SVM and Neural Networks. ICT Express

A Novel 7-Level Switched-Capacitor Multilevel Inverter with Reduced Components for Renewable Energy Conversion Systems

Tapas Roy and Pradip Kumar Sadhu

Abstract A novel 7-level multilevel inverter (MLI) with inherent output voltage-boosting ability is proposed in this paper. The inverter uses the switched-capacitor voltage-boosting technique to step up the output voltage at the load-end. Further, the inverter can balance the capacitor voltages inherently. It requires lower switches, drivers, and capacitors compared to the recently proposed 7-level switched-capacitor MLIs. This lower component count leads to more cost-effectiveness of the proposed inverter and reduces conduction losses as compared to others. Detailed operating principles, voltage stress analysis, and high-frequency modulation strategy for the proposed inverter are presented in detail. Furthermore, the dynamic performance of the proposed inverter has been verified by closed-loop operation using the finite control set model predictive control (FCS-MPC) technique. An extensive open-loop and closed-loop simulation study of a 1 kW proposed inverter on the MATLAB/Simulink platform has been presented to validate the proposed inverter.

Keywords Boosting factor · Multilevel inverter · Switched capacitor · Total standing voltage · Voltage balance

1 Introduction

Nowadays, one of the viable DC to AC power converters is multilevel inverters (MLIs). The application of MLIs expands in different industrial fields such as electric vehicles, renewable energy conversion systems, UPS, FACTs, induction heating. MLIs can produce near sinusoidal output voltage waveform using switching devices and passive components from single or multiple DC sources [1]. Generally, the conventional MLIs are three types. They are cascaded H-bridge (CHB), neutral-point clamp (NPC), and flying capacitor (FC) MLIs. These MLIs have become viable MLIs for different industrial applications. However, for realizing high-level output voltage waveform, these MLIs suffer from a high component count. The CHBMLI needs

T. Roy (✉) · P. K. Sadhu
Department of Electrical Engineering, Indian Institute of Technology (ISM), Dhanbad, Jharkhand 826004, India

M. Mishra et al. (eds.), *Innovation in Electrical Power Engineering, Communication, and Computing Technology*, Lecture Notes in Electrical Engineering 814,
https://doi.org/10.1007/978-981-16-7076-3_38

many isolated DC supplies, whereas NPCMLI and FCMLI require several capacitors, switches, drivers, and diodes as the output voltage level enhances. Also, NPC and FC MLIs need separate circuits for keeping the capacitor voltages balanced. They make the inverter bulky, costly, and complex. Besides, the conventional MLIs do not have output voltage-boosting ability. This feature of MLIs is essential for converting the energy from renewable resources as the output voltages of these sources are low in magnitude [1, 2]. In recent years, researchers have developed several innovative MLIs with lower components [3]. However, they do not have boosting capability.

For incorporating the boosting feature with conventional MLIs, researchers have developed several innovative MLI structures. One of the prominent and emerging MLIs is switched-capacitor MLI (SCMLI). By charging and discharging the capacitors with respect to source, SCMLIs can balance the capacitor voltages and can boost-up the output voltage. They do not require extra circuits for capacitor balancing. This feature reduces the size and cost of the inverter. The first SCMLI was reported in the literature in 1998 by introducing a 31-level output voltage waveform from a single supply voltage [4]. However, the structure needs so many switches, drivers, and capacitors. Two numbers of cascaded SCMLIs using compact SC cells have been proposed in [5]. However, both the inverters require H-bridge circuits for voltage polarity generation. These H-bridge circuits increase the component count as well as switch voltage stress. The SCMLI proposed in [6] consists of a cascade configuration of SC cells and a back-end H-bridge circuit. The requirement of a large number of diodes hinders the reactive power flow capability of the inverter. The researchers of [7] have proposed an SCMLI with self-polarity generation capability. However, the necessity of higher switches and drivers increases the cost and complexity of the structure. The researchers of [8] have introduced a modified cascaded SCMLI with reduced TSV. The structure was developed from CHBMLI by changing the DC sources with capacitors. However, the high component count is the major drawback for the structure. The researchers of [9] have reported a 7-level SCMLI using a minimum number of capacitors. However, the inverter needs higher switches and corresponding drivers. The SCMLI proposed in [10] needs lower components for realizing the output voltage level. However, the switch voltage stress and TSV of the inverter are higher. The SCMLIs proposed in [11, 12] also require several components for realizing the higher output voltage level. The large component count and high TSV increase the rating, size, and cost of the inverters.

The high component count is one of the prime limitations of recently proposed SCMLIs. This paper proposes a novel 7-level SCMLI that needs reduced components. This lower component count improves the cost-effectiveness of the proposed inverter. Further, the inverter requires to conduct a lower number of switches for synthesizing the voltage levels at load. This feature reduces conduction losses and improves the efficiency of the inverter. The inverter has self-polarity generation capability.

The paper is organized as follows: Section 2 describes the proposed inverter, its operation, and voltage stress analysis. Implementation of a high-frequency switching strategy is illustrated in Sect. 3. Section 4 describes the comparative study. The description of closed-loop control of the proposed inverter using finite-set model

predictive control is presented in Sect. 5. Sections 6 and 7 present the simulation study of the proposed inverter in open-loop and closed-loop conditions. Finally, the conclusions and references are presented.

2 Proposed SCMLI Circuit

Figure 1 depicts the proposed 7-level SCMLI. It comprises six unidirectional switches (S_1, S_2, S_3, S_6, S_8, and S_9), three bidirectional switches (S_4, S_5, and S_7), two capacitors (C_1 and C_2), and a DC power supply (V_{in}). Switches S_1 and S_2 form a leg across the supply, whereas S_8 and S_9 form a leg across the capacitor bank. The capacitor bank is the series combination of the utilized capacitors C_1 and C_2 as depicted in Fig. 1. The switches S_3, S_4, S_5, and S_6 form a bridge that helps V_{in} to connect in series or parallel with the capacitors. Switch S_7 is connected between the mid-points of the capacitor bank, and the leg comprises S_1 and S_2 as depicted in Fig. 1.

In the proposed inverter, both capacitors can be charged to V_{in}. Considering the capacitors are fully charged by the source, the realization of different voltage steps is shown in Fig. 2. Further, Table 1 shows the ON switch list and capacitor states where the charging, not connected, and discharging states of the capacitor are depicted by C, N, and D. The inverter can realize the various voltage steps as follows:

(a) $\pm 0V_{in}$ *voltage step realization*: By short circuiting the load, the inverter synthesizes these voltage steps between the load terminals. When S_1, S_5, and S_8 conduct, the load gets short circuited and the $+0V_{in}$ voltage level is realized as depicted in Fig. 2a. Similarly, whenever S_4, S_2, and S_9 conduct, the load gets short circuited and the $-0V_{in}$ voltage level is synthesized as presented in Fig. 2b.

(b) $\pm 1V_{in}$ *voltage step realization*: The inverter can synthesis these voltage steps by directly connecting the source voltage between the load terminals. Further, the capacitors store charges from supply during these voltage steps as shown in Table 1. When S_2, S_5, S_7, and S_8 conduct, V_{in} is placed across the load and the capacitor C_1 as presented in Fig. 2c. Hence, $+1V_{in}$ is realized, and C_1

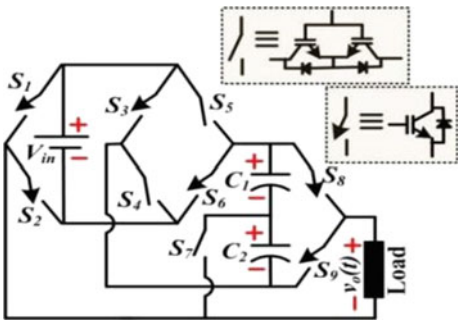

Fig. 1 Proposed 7-level SCMLI structure

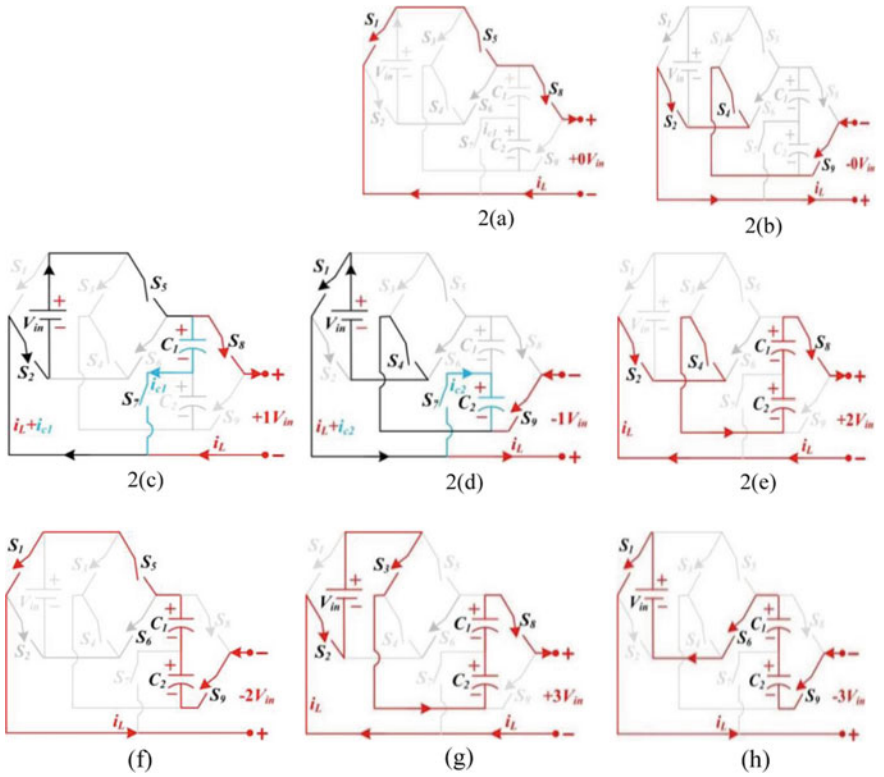

Fig. 2 Realization of various voltage steps in the developed SCMLI **a** $+0V_{in}$, **b** $-0V_{in}$, **c** $+1V_{in}$, **d** $-1V_{in}$, **e** $2V_{in}$, **f** $-2V_{in}$, **g** $+3V_{in}$, **h** $-3V_{in}$

Table 1 Switch and capacitor states for realizing different voltage steps

State no.	$v_o(t)$	ON switches	Capacitor state	
			C_1	C_2
1	$+3V_{in}$	S_2, S_3, S_8	D	D
2	$+2V_{in}$	S_2, S_4, S_8	D	D
3	$+1V_{in}$	S_2, S_5, S_8, S_7	C	N
4	+0	S_1, S_5, S_8	N	N
	–0	S_2, S_4, S_9	N	N
5	$-1V_{in}$	S_1, S_4, S_9, S_7	N	C
6	$-2V_{in}$	S_1, S_5, S_9	D	D
7	$-3V_{in}$	S_1, S_6, S_9	D	D

gets charged to V_{in} voltage level. During this circuit condition, C_2 remains in neither charging nor discharging state as shown in Table 1. Similarly, when S_1, S_4, S_7, and S_9 are ON, V_{in} becomes in parallel with C_2 and the load. The switch combination connects the source across the load in the opposite polarity as that for $+1V_{in}$ voltage level as presented in Fig. 2d. So, the load voltage becomes $-1V_{in}$, and C_2 gets charged to the V_{in} voltage level.

(c) $\pm 2V_{in}$ *voltage step realization*: These voltage steps can be synthesized by connecting the capacitor bank between the load terminals. When S_2, S_4, and S_8 conduct, connecting the capacitor bank between the load terminals, $+2V_{in}$ voltage step is realized as depicted in Fig. 2e. Similarly, when S_2, S_6, and S_9 are turned ON, the capacitor is placed between the load terminals and $-2V_{in}$ voltage step is synthesized by the inverter as depicted in Fig. 2f. During these voltage steps, the load is supplied by the capacitor bank only. Hence, the capacitors discharge their energy to the load.

(d) $\pm 3V_{in}$ *voltage step realization*: The highest positive and negative voltage steps, i.e., $+3V_{in}$ and $-3V_{in}$ are realized whenever the series combination of input source and capacitor bank appears between the load terminals. Figure 3g shows the current flow path and equivalent circuit for realizing $+3V_{in}$ voltage level. When S_2, S_3, and S_8 are turned ON, V_{in} becomes in series with the capacitor bank, and the whole series combination appears between the load terminals. Hence, the $+3V_{in}$ voltage step is realized. Similarly, when S_1, S_6, and S_9 are turned ON, placing the source in series with the capacitor bank and whole series combination appears between the load terminals as depicted in Fig. 2h. So, the $-3V_{in}$ voltage level is synthesized.

The proposed inverter can realize the peak amplitude of output voltage that is three times the input supply voltage. Hence, the inverter has a boosting factor (B) of 3. From Fig. 2, it can be observed that S_1 and S_2 are complementary to each other across V_{in}. So, the maximum voltage stress across them is V_{in}. Similar, S_8 and S_9 have a peak stress voltage of $2V_{in}$ each as they are connected across the capacitor bank. From Fig. 2a, it can be observed that when S_5 is ON, the capacitor bank appears across S_3. Hence, the voltage stress of S_3 is $2V_{in}$. Similarly, the peak stress voltage across S_6, S_5, and S_4 are $2V_{in}$, $3V_{in}$, $3V_{in}$, respectively. From Fig. 2e,f, the peak stress voltage across S_7 is $2V_{in}$. The inverter has a TSV of $19V_{in}$. The ratio of the TSV to the peak output voltage, known as per-unit TSV (TSV_{pu}), for the proposed inverter is 6.33.

3 Switching Strategy

This section describes the implementation of a high-frequency switching strategy for the developed inverter. Due to the symmetric nature of output voltage waveform, the implementation of switching strategy for positive half-cycle has been discussed in detail. Figure 3a depicts the carrier signals and reference signals in a positive

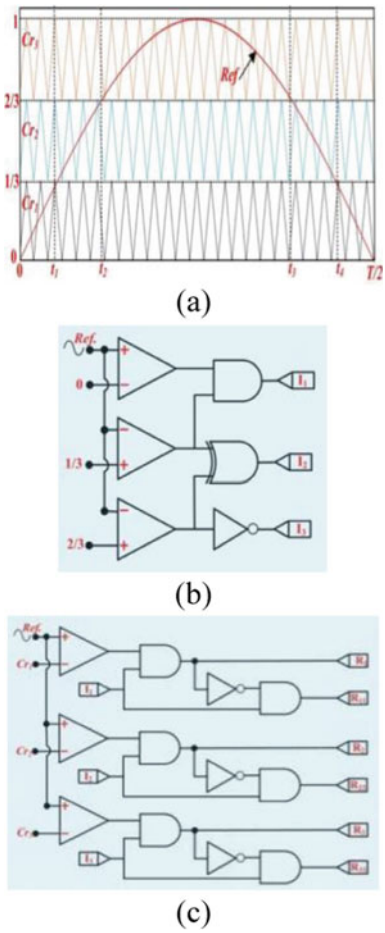

Fig. 3 Implementation of high-frequency modulation strategy in positive half-cycle **a** Carrier signals versus ref. signal. **b** Logic circuit 1. **c** Logic circuit 2

half-cycle. It has three high-frequency carrier signals (Cr_1, Cr_2, and Cr_3) and low-frequency sinusoidal reference signals (Ref.).

$$S_1 = R_{11} + RR_1 + RR_{22} + RR_2 + RR_{33} + RR_3 \tag{1}$$

$$S_3 = R_3, S_5 = R_{11} + R_1 + R_{22} + RR_2 + RR_{33} \tag{2}$$

$$S_7 = R_1 + R_{22} + RR_1 + RR_{22}, S_8 = R_{11} + R_1 + R_{22} + R_2 + R_{33} + R_3 \tag{3}$$

For implementing this modulation strategy, two logical circuits have been build up. Figure 3b shows the Logical circuit 1. In this circuit, the DC values 0, 1/3, and 2/3 have been compared with the reference sinusoidal signals, and I_1, I_2, I_3 are the output signals. In Logic circuit 2 as shown in Fig. 3c, the reference signal has been

compared with the carrier signals first. The produced logic signals are then logically AND with I_1, I_2, and I_3 as shown in Fig. 3c. After AND, the generated signals are R_1, R_2, and R_3. The complement of R_1, R_2, and R_3 are R_{11}, R_{22}, and R_{33}, respectively, as shown in Fig. 3c. In the positive half-cycle, the generated logical signals from Logic circuit 2 are (R_1, R_{11}), (R_2, R_{22}), and (R_3, R_{33}). Similarly, in the negative half-cycle, the generated logical signals are (RR_1, RR_{11}), (RR_2, RR_{22}), and (RR_3, RR_{33}). The switching pulses S_1, S_3, S_7, and S_8 for the proposed inverter can be derived by using the logical equations as shown in (1)–(3). Similarly, the pulses for other switches can be derived.

4 Comparative Study

The comparative study of the proposed inverter with others is presented in this section. The proposed inverter uses lower switches (N_{sw}) than the inverters developed in [7, 8, 11]. It requires the same N_{sw} as that for the inverters developed in [9, 12]. However, it requires a higher N_{sw} than the inverter reported in [10].

As compared to the required drivers (N_{dr}), the proposed inverter needs the lowest drivers than all the suggested inverters. Furthermore, it does not require power diodes (N_{di}). For the required capacitors (N_c), the proposed inverter utilizes lower capacitors than the inverters presented in [8, 12]. However, it has the highest per-unit TSV. For a fair comparison, the overall costs of the structures per boosting factor per level (CF/B/N_L) have been evaluated for all the inverters as per a standard cost-effective function (CF) as depicted in (4).

$$\mathrm{CF} = (n_{sw} + n_{dr} + n_{di} + n_{ca}) + \beta \times (\mathrm{TSV} + \mathrm{PIV})_{pu} \tag{4}$$

As per Table 2, the developed inverter has the lowest value of CF/B/N_L than all the suggested inverters. This feature validates that the developed inverter is a more cost-effective solution than others for realizing the same output voltage levels.

Table 2 Comparative table of developed SCMLI with others

Topology	N_{sw}	N_{dr}	N_{di}	N_c	N_{path}	$(\mathrm{TSV})_{pu}$	B	CF/($B \times N_L$)		Negative level
								$\beta = 0.5$	$\beta = 1.5$	
[7]	14	14	2	2	6	4.67	3.0	1.63	1.85	Inherent
[8]	13	13	3	3	6	5.00	3.0	1.64	1.88	Inherent
[9]	12	11	0	2	6	5.33	3.0	1.32	1.57	Inherent
[10]	10	10	4	2	3	6.00	3.0	1.38	1.67	Inherent
[11]	16	14	0	2	6	4.67	3.0	1.63	1.85	Inherent
[12]	12	12	4	4	6	5.33	3.0	1.65	1.90	Inherent
Proposed	12	9	0	2	3	6.33	3.0	1.24	1.54	Inherent

Furthermore, the developed inverter conducts lower switches for realizing the highest voltage step, i.e., N_{path} than the inverters reported in [7–9, 11, 12]. This feature reduces the conduction losses of it than others. Lastly, it has inherent negative voltage-level generation capability as suggested inverters. This means, it does not require an H-bridge circuit that reduces the switch count as well as the voltage stress across the switches.

5 Model Predictive Control (MPC) of Proposed Inverter

To evaluate the performances of the proposed inverter under closed-loop conditions, the popular finite control set model predictive control (FCS-MPC) technique is described here. In FCS-MPC, the load current (i_{L}) tracks the reference current (i_{ref}) based on a predictive model of the system. It predicts the load current for the next sample instant ($k + 1$) based on the sample at the present instant k. After that, the optimum switching state will be selected by ensuring the minimization of the cost function [13]. The block diagram for MPC control of the proposed inverter is shown in Fig. 4.

The predicted load current ($i_{\text{L}(k+1)}$) can be expressed by (5) by using Euler's forward method. Similarly, the predicted reference current ($i_{\text{ref}(k+1)}$) can be evaluated by Lagrange extrapolation by (6). The cost function ($g(n)$) expresses the absolute error between the predicted reference current and the load current as shown in (7). In an iteration, the predicted current needs to evaluate for all the possible voltage levels ($n = 1$ to 7) (as per Table 1). For each predicted load current, the cost function $g(n)$ needs to be evaluated. The minimum $g(n)$ provides the optimum switching state. After that, the optimum switching state is selected and applied to the inverter.

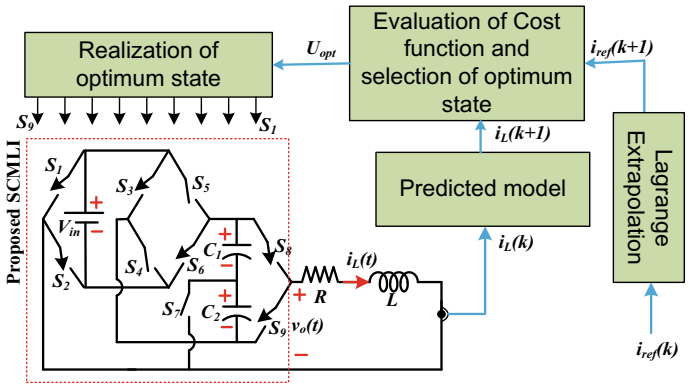

Fig. 4 FCS-MPC for the proposed 7-level inverter

$$i_{\mathrm{L}}(k+1) = \left(1 - \frac{RT_{\mathrm{s}}}{L}\right) i_{\mathrm{L}}(k) + \frac{T_{\mathrm{s}}}{L} v_{\mathrm{o}}(n) \tag{5}$$

$$i_{\mathrm{ref}}(k+1) = 3i_{\mathrm{ref}}(k) - 3i_{\mathrm{ref}}(k-1) + i_{\mathrm{ref}}(k-2) \tag{6}$$

$$g(n) = |i_{\mathrm{ref}}(k+1) - i_{\mathrm{L}}(k+1)| \tag{7}$$

6 Simulation Study: Open Loop

To evaluate the performances of the developed inverter, an extensive simulation study was conducted on the MATLAB/Simulink platform on a 1 kW inverter. The selected DC source voltage is 120 V. Based on 1 kW output power and 50 Hz output frequency, the selected capacitance values for SCs are $C_1 = C_2 = 1880\ \mu$F [9, 11]. To carry out the simulation study, MOSFETs with on-state resistance of 0.18 Ω have been selected as switching devices. Further, the equivalent series resistance (ESR) of each capacitor is considered as 0.1 Ω. The simulated results under different load conditions are presented as follows.

With considering a resistive load of 54 Ω, the simulated output current ($i_{\mathrm{L}}(t)$) and output voltage ($v_{\mathrm{o}}(t)$ are depicted in Fig. 5a. The $v_{\mathrm{o}}(t)$ has seven output voltage steps with a peak amplitude of 320 V. Further, $i_{\mathrm{L}}(t)$ has also seven steps with a peak amplitude of 6 A and in phase with $v_{\mathrm{o}}(t)$. *C*onsidering the same load condition, the simulated steady-state voltages for capacitors are depicted in Fig. 5b. As per this figure, the voltages are stable and well-balanced by the utilized switching technique.

The average magnitude of steady-state capacitor voltages is 110 V each. Considering the same load, Fig. 6a presents the profiles of stress voltages profiles for S_4, S_5, and S_7. Figure 6b depicts the simulated waveform of $i_{\mathrm{L}}(t)$ and $v_{\mathrm{o}}(t)$ for the resistive-inductive load ($L = 50$ mH, $R_{\mathrm{L}} = 54\ \Omega$). As per this figure, $i_{\mathrm{L}}(t)$ is sinusoidal in

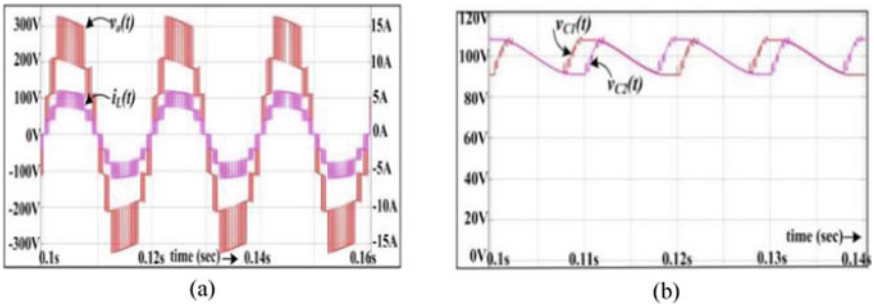

Fig. 5 Simulated waveform of **a** Load current ($i_{\mathrm{L}}(t)$) and output voltage ($v_{\mathrm{o}}(t)$). **b** Steady-state voltages across capacitors for resistive load ($R_{\mathrm{L}} = 54\ \Omega$)

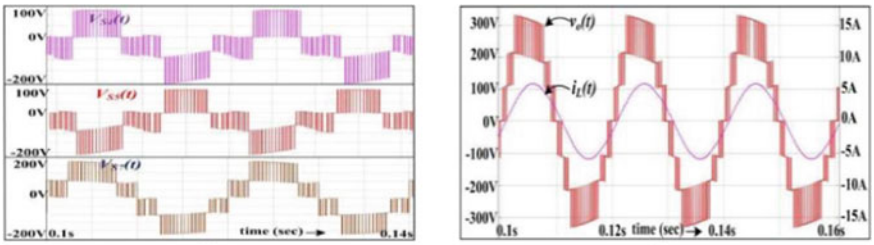

Fig. 6 Simulated waveform for **a** Voltage stress across S_4, S_5, and S_7 under resistive load ($R_L = 54\ \Omega$). **b** Output voltage and current under resistive-inductive load ($R_L = 54\ \Omega$, $L = 50$ mH)

nature and lags $v_o(t)$. Furthermore, Fig. 7a depicts the simulated waveform of $v_o(t)$ and $i_L(t)$ for $L = 175$ mH. As per this figure, $i_L(t)$ is sinusoidal in nature and lags $v_o(t)$ *by* 90°.

To validate the dynamic performances of the developed inverter in an open-loop condition, the inverter has been initially loaded with a resistive-inductive load of ($R_L = 108\ \Omega$, $L = 50$ mH). After some time (Load change point 1 in Fig. 7b), the inverter is loaded with ($R_L = 54\ \Omega$, $L = 50$ mH). Because of the sudden decrement of load resistance, the load current has been increased as well as the capacitor ripple voltage has been increased as presented in Fig. 7b. However, after Load change point 1, output current, and capacitor voltages remain stable. The same can be observed whenever the load resistance has been increased to its initial value after Load change point 2. Hence, the inverter is stable and performs well under sudden load change conditions.

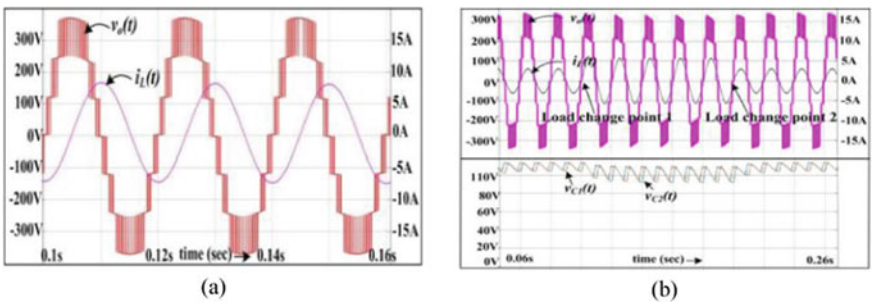

Fig. 7 Simulated waveform for **a** Output voltage and current under inductive load ($L = 175$ mH). **b** Output voltage, load current, and voltages across capacitors for dynamic/sudden load condition

7 Simulation Study: Closed Loop

To evaluate the closed loop and dynamic performances of the proposed inverter, the FCS-MPC was implemented in the MATLAB/Simulink platform. The DC link voltage and capacitance for capacitors are the same as in the open-loop study. The selected sample time (T_s) for close loop study is 50 μs. The study was performed considering resistive-inductive load ($L = 50$ mH, $R_L = 54\ \Omega$). Figure 8a shows the inverter voltage and inverter current waveform. Initially, i_{ref} is set at 3A; hence, the output voltage is 5 level. At time $t = 0.7$ s, the i_{ref} is suddenly increased to 5.5 A. So, the output voltage becomes 7 level. Similarly, after $t = 0.17$ s, the i_{ref} is suddenly decreased to the 3 A; hence, the output voltage again becomes 5 level. Figure 8b depicts the tracking of load current (i_L) to the reference current (i_{ref}). As per this figure, the load current or the inverter current tracks the reference current in well manner. Further, Fig. 8c shows the zoom version of the sudden change portion of the reference current waveform.

Figure 8d shows the voltage profiles of switched capacitors during the FCS-MPC operation with the sudden reference current change condition. As per this figure, the voltages across the capacitors are near about 120 V and well-balanced throughout

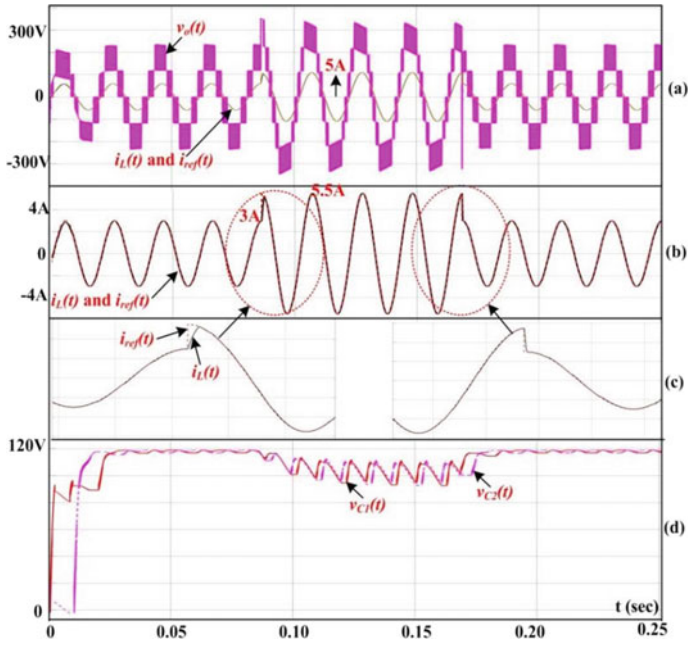

Fig. 8 Simulated waveform for **a** Inverter output voltage (100 V/div) and output current (5A/div). **b** Reference current and load current. **c** Zoomed reference and load currents during sudden changes condition. **d** Capacitor voltages under closed-loop operation of proposed inverter using FCS-MPC technique

the operation. However, the voltage ripple depends upon the magnitude of the load current. With the increment of the load current, the capacitor voltage ripple increases as depicted Fig. 8d.

This study shows that the proposed inverter can perform well under closed loop and dynamic load conditions. The inverter performance is stable and balanced with the specified operating condition.

8 Efficiency Comparison and THD

The efficiency, conduction losses, and switching losses of the developed inverter were evaluated and compared with the inverters presented in [9, 11, 12]. For this study, the conduction and switching losses were evaluated based on the process described in [14]. Figure 9a depicts the comparison of conduction losses for different power levels. As per this figure, the developed inverter has the lowest conduction losses for all power levels. However, it has the highest switching losses as shown Fig. 9b. The efficiency comparison of the inverters is shown in Fig. 9c. The proposed inverter has a higher efficiency than others for all the power levels.

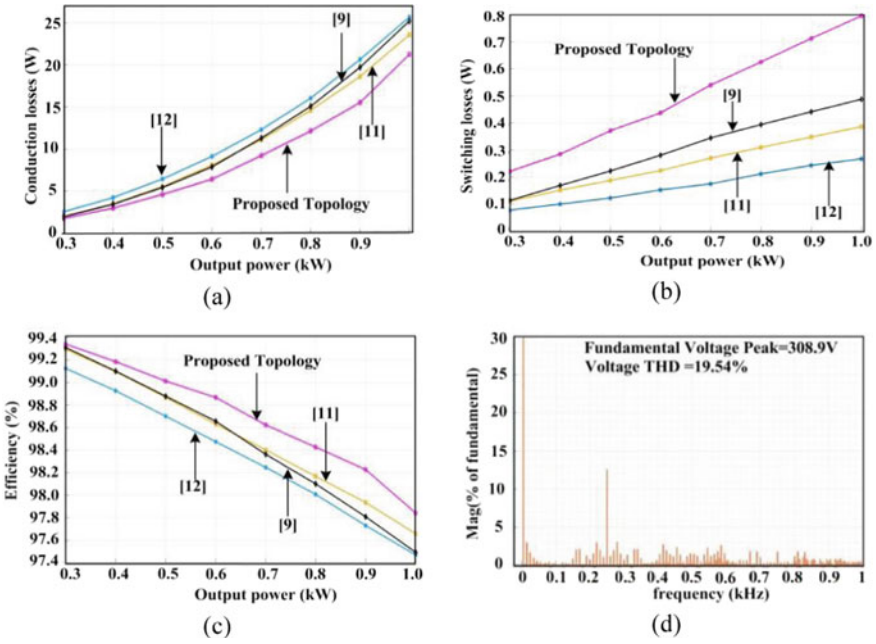

Fig. 9 Comparison of **a** Conduction losses. **b** Switching losses. **c** Efficiency of proposed topology with other inverters for different power levels. **d** FFT analysis of output voltage for resistive load of 54 Ω

Furthermore, considering resistive load (54 Ω) and high-frequency switching strategy (carrier frequency = 2.5 kHz), the output voltage's FFT profile is presented in Fig. 9d. As per this figure, the output voltage waveform has high-frequency components and a THD of 19.54%. This THD is measured without any filtering operation.

9 Conclusions

A novel inverter with boosting ability was developed and analyzed in this paper. The inverter can synthesize seven output voltage steps and can boost the output voltage three times the input supply voltage. The operating principle, stress voltage analysis, and high-frequency switching strategy for the inverter were discussed in detail. A comparative study based on the component count, TSV, boosting factor, the number of conducting switches, and cost function were presented. The developed inverter uses a lower component than others. Further, the inverter has a lower cost function than others at the same boosting factor and level. The closed-loop operation of the developed inverter using FCS-MPC was presented. The inverter shows a well dynamic performance in respect of reference current tracking and capacitor voltage balancing. The structure has significantly lower conduction losses than others. As the inverter has the inherent boosting ability, it applies to photovoltaic (PV) applications.

References

1. Franquelo LG, Rodriguez J, Leon JI, Kouro S, Portillo R, Prats MAM (2008) The age of multilevel converters arrives. IEEE Ind Electron Mag 2(2):28–39
2. Malinowski M, Gopakumar K, Rodriguez J, Perez MA (2010) A survey on cascaded multilevel inverters. IEEE Trans Ind Electron 57(7):2197–2206
3. Gupta KK, Ranjan A, Bhatnagar P, Sahu LK, Jain S (2016) Multilevel inverter topologies with reduced device count: a review. IEEE Trans Power Electron 31(1):135–151
4. Mak OC, Ioinovici A (1998) Switched-capacitor inverter with high power density and enhanced regulation capability. IEEE Trans Circuits Syst I Fundam Theory Appl 45(4):336–347
5. Babaei E, Gowgani SS (2014) Hybrid multilevel inverter using switched capacitor units. IEEE Trans Ind Electron 61(9):4614–4621
6. Ye Y, Cheng KWE, Liu J, Ding K (2014) A step-up switched-capacitor multilevel inverter with self-voltage balancing. IEEE Trans Ind Electron 61(12):6672–6680
7. Taghvaie A, Adabi J, Rezanejad M (2018) A self-balanced step-up multilevel inverter based on switched-capacitor structure. IEEE Trans Power Electron 33(1):199–209
8. Jahan HK, Abapour M, Zare K (2019) Switched-capacitor-based single-source cascaded h-bridge multilevel inverter featuring boosting ability. IEEE Trans Power Electron 34(2):1113–1124
9. Siddique MD, Mekhilef S, Shah NM, Ali JSM, Blaabjerg F (2020) A new switched capacitor 7L inverter with triple voltage gain and low voltage stress. IEEE Trans Circuits Syst II Express Briefs 67(7):1294–1298

10. Siddique MD, Ali JSM, Mekhilef S, Mustafa A, Sandeep N, Almakhles D (2020) Reduced switch count based single source 7L boost inverter topology. IEEE Trans Circuits Syst II Express Briefs 67(12):3252–3256
11. Lee SS (2018) A single-phase single-source 7-level inverter with triple voltage boosting gain. IEEE Access 6:30005–30011
12. Fong YC, Cheng KWE, Raghu Raman S (2020) A modular concept development for resonant soft-charging step-up switched-capacitor multilevel inverter for high-frequency AC distribution and applications. IEEE J Emerging Selected Topics Power Electron. https://doi.org/10.1109/JESTPE.2020.3043126
13. Harbi I, Abdelrahem M, Ahmed M, Kennel R (2020) Reduced-complexity model predictive control with online parameter assessment for a grid-connected single-phase multilevel inverter. Sustainability 12:7997–8020
14. Hinago Y, Koizumi H (2012) A switched-capacitor inverter using series/parallel conversion with inductive load. IEEE Trans Ind Electron 59(2):878–887

Design of Variational Autoencoder for Generation of Odia Handwritten Numerals in CNN Model

Abhishek Das, Saumendra Kumar Mohapatra, and Mihir Narayan Mohanty

Abstract Generative models have fascinated attention of researchers as it learns the important features from the trained data to generate the structures similar to the data provided for training. Autoencoders are the basic building components of generative models. In this work, we have designed a variational autoencoder to generate a large number of data to support the generative adversarial network model. The encoder, as well as the decoder of the proposed model, is designed using convolutional layers. The proposed method is verified on IIT Bhubaneswar Odia handwritten database. The encoder generates the feature vectors with the probability distribution of each category in latent space that follows the Gaussian distribution. It is verified that the decoder recognizes the features due to proper training. The generated images are quite similar to original data that validate the proposed VAE is well-generative. To measure the performance of the model, loss is calculated using binary cross-entropy along with Kullback–Leibler divergence loss. The proposed model is trained with Adam optimizer.

Keywords Generative models · Autoencoder · Variational autoencoder · Convolutional neural network · Odia handwritten recognition

1 Introduction

In opposition to an ordinary autoencoder, which figures out how to encode some contribution to a point in latent space, variational autoencoders (VAEs) figure out how to encode likelihood distributions of trained data into latent space, given their setup typically Gaussian ones. Rather than the more standard employments of neural

A. Das · M. N. Mohanty (✉)
ITER, Siksha 'O' Anusandhan (Deemed To Be University), Bhubaneswar 751030, India
e-mail: mihirmohanty@soa.ac.in

S. K. Mohapatra
Department of Computer Science and Engineering, Saveetha School of Engineering, Saveetha Institutes of Medical and Technical Sciences, Chennai, India
e-mail: saumendrakumam.sse@saveetha.com

M. Mishra et al. (eds.), *Innovation in Electrical Power Engineering, Communication, and Computing Technology*, Lecture Notes in Electrical Engineering 814,
https://doi.org/10.1007/978-981-16-7076-3_39

networks as regressors or classifiers, VAEs are ground-breaking generative models, presently having applications as different as creating fake human-like faces [1–3], to deliver simply synthetic music [4, 5]. The VAEs are also used to generate the labels for the image as well in generating captions by studying the features of the image. Pu et al. [6] have used a Bayesian support vector machine for labels generation and a recurrent neural network for caption generation. In the field of anomaly detection, An et al. [7] used a probabilistic variational autoencoder which uses the variational difference among the variables as a reconstruction probability measure. Direct optimization of loss function using the *arg max* function to the discrete latent variable model is done where no other optimization techniques such as the use of the softmax activation function or Adam optimizer are used in case of a variational autoencoder [8].

Some works have been proposed on Odia handwritten character recognition. Dash et al. have given a summarized study [9] on different methods used in both Odia printed and handwritten alphanumeric recognition where no work has been found to implement VAE. For Odia handwritten numeral recognition, a study has been conducted, a combined CNN-RNN model has been proposed in [10], and recurrent networks such as long short-term memory (LSTM) have been used by Das et al. [11] and the accuracy in recognition in these approaches are found to be 99.99% and 97.93%, respectively. Application of support vector machine in Odia handwritten recognition has been found in the work of Sanjibani Sudha [12] where the model provided 85% accuracy. The linear discriminant analysis (LDA) model was used to recognize Odia handwritten numerals. In that work, Jena et al. [13] have given a comparison study of LDA with principal component analysis (PCA) and found that LDA performs better in comparison with PCA. Dash et al. [14] have proposed a hybrid model that used Krisch gradient-based operator and curvature details of handwritten Odia numerals features for recognition. Authors have also used PCA for feature reduction in dimension to minimize the computational constraint. Dash et al. [15] have proposed the use of Stockwell transform, a non-redundant method of transformation, and also optimal zoning method based on bio-inspired algorithms for classifying handwritten Odia numerals. Various forms of zone extraction are proposed for the development of features. For Odia handwritten character recognition, Rushiraj et al. [16] have taken 48 geometrical features including distance-based features, shadow features, and centroid features to train the model. Euclidean distance was considered as a distance feature in their approach. An artificial neural network with two stages has been used based on features like zonal centroid distance and standard deviation for Odia handwritten recognition [17].

The encoder generates the feature vectors with a probability distribution of each category in latent space which follows the Gaussian distribution. The decoder recognizes the features due to proper training and generates images similar to original data from those extracted features which make VAEs generative. In this work, we have designed a variational autoencoder for handwritten Odia numerals.

The rest of the paper is organized as follows. Section 2 describes the method adopted for designing VAE. In Sect. 3, the results are given and the discussion is done. Section 4 concludes the work.

2 Methodology

The proposed variational autoencoder is designed with the convolutional layer activated by ReLU activation function followed by batch normalization, flatten layer, and dense layer in the encoder, and the reconstruction is done in the decoder for which the dense layer followed by transpose_convolutional layers and batch normalization are used. The reconstruction loss is calculated by applying binary cross-entropy along with Kullback–Leibler (KL) divergence loss to ensure that the latent space created in between encoder and decoder is continuous and complete.

Instead of mapping the input image to a fixed point vector in the case of normal autoencoders, in the proposed VAE, we have mapped the latent space as a continuous Gaussian distribution (p_θ), parameterized in terms of θ. If the input data is represented by x and the latent space information as l, then the following distributions are possible, i.e., (a) prior $p_\theta(l)$, (b) likelihood $p_\theta(x|l)$, and (c) posterior $p_\theta(l|x)$. To generate real-like data, two steps are followed such as:

(i) A sample l^i is extracted from the prior distribution $p_{\theta^*}(l)$
(ii) Real-like image data x^i is then generated from the conditional distribution $p_{\theta^*}(x|l = l^i)$, where θ^* is the known parameter which is given by

$$\theta^* = \arg\max_\theta \prod_{i=1}^{n} p_\theta(x^i) \tag{1}$$

The function used to approximate the function representing the input x is introduced as $q_\varphi(l|x)$ parameterized in terms of φ. The graphical representation of the variational autoencoder is given in Fig. 1.

The dotted lines in the above figure represent $q_\varphi(l|x)$ an approximation to the posterior distribution $p_\theta(l|x)$, and the solid lines represent the generative function $p_\theta(\bullet)$.

The loss function to be minimized is the combination of binary cross-entropy and the KL loss. The KL divergence between approximation function $q_\varphi(l|x)$ and $p_\theta(l|x)$ is given by Eq. (2) as:

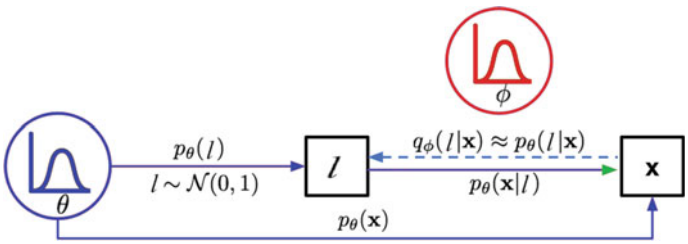

Fig. 1 Graphical representation of VAE

$$D_{KL}(q_\varphi(l|x)||p_\theta(l|x)) = \log p_\theta(x) + D_{KL}(q_\varphi(l|x)||p_\theta(l)) - E_{l\sim q_\varphi(l|x)} \log p_\theta(x|l) \tag{2}$$

The total loss calculated in our approach is given by Eq. (3) as:

$$L_{\text{VAE}} = \text{Binary Cross Entropy} + D_{KL}(q_\varphi(l|x)||p_\theta(l|x)) \tag{3}$$

The objective of the model is to minimize the above loss, and the network is optimized using Adam optimizer to train the model properly for better results.

3 Results and Discussion

The proposed VAE model is verified with the Odia numeral database collected from IIT Bhubaneswar [15]. It is having 5165 total images. To reduce the computation time, the dataset is resized to 28 × 28 pixel images and converted to binary form. These samples of each category starting from "Suna" to "Na" are shown in Fig. 2.

The method of VAE described above is implemented using Jupyter Notebook with Python 3 environment. The number of epochs used to get the result from this model is 100. TensorFlow with GPU environment is used in Google Colaboratory for faster implementation. The latent space generated after the encoder is shown in the two-dimensional scatter plot in Fig. 3. In the scatter plot, different colors are representing the location of the distribution of the ten numbers starting from zero to nine. From this scatter plot, it can be observed that at (0,0), the density of the points is high, and it decreases as we move away from (0,0) which can be represented as a Gaussian distribution.

The numerals generated after 100 epochs with variational distribution are shown in Fig. 4. The numbers with less distance among them are shown nearer to each other. This relation is also observed in latent space representation in terms of the scatter plot above.

The whole dataset is divided into training and validation sets with an 8:2 ratio. The loss calculated in this approach is shown in Fig. 5. The training loss and the validation loss after 100 epochs are found to be 149.4915 and 147.9843, respectively.

Fig. 2 Sample of input images to the VAE model

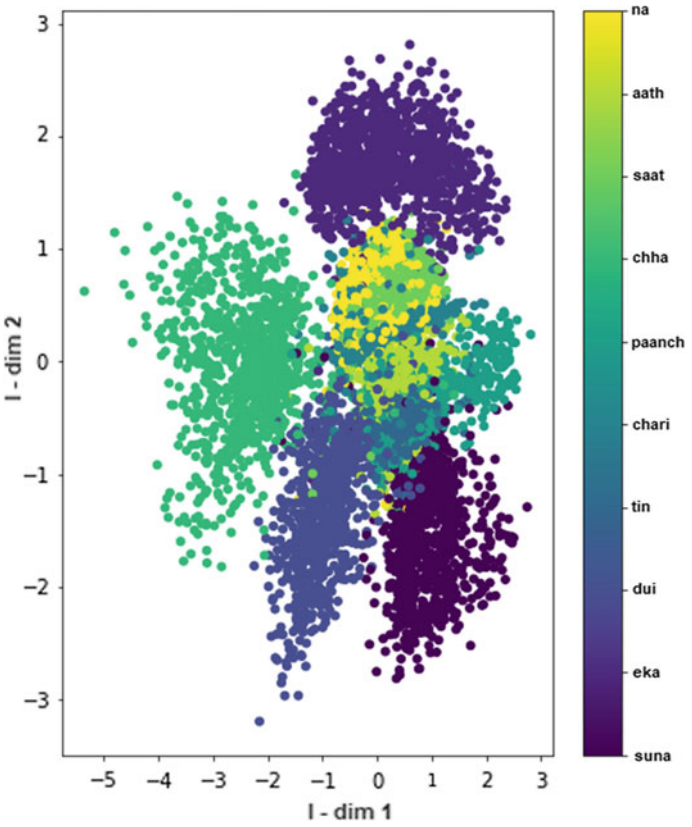

Fig. 3 Scatter plot of latent space

4 Conclusion

In the field of image processing, different methods are developed, and scopes to develop new methods are also there. In this work, we have designed a variational autoencoder using convolutional neural networks and used the KL divergence as a loss function along with binary cross-entropy to recognize and generate Odia handwritten numerals. Training loss and validation loss obtained in our proposed work are 149.4915 and 147.9843, respectively, which is a remarkable achievement in handwritten numeral processing. Variational autoencoder is found to be a better generative model in image processing which needs to be explored more with less loss in the future. We are also thankful to Google Colaboratory for providing an online GPU that efficiently decreased the runtime for 100 epochs.

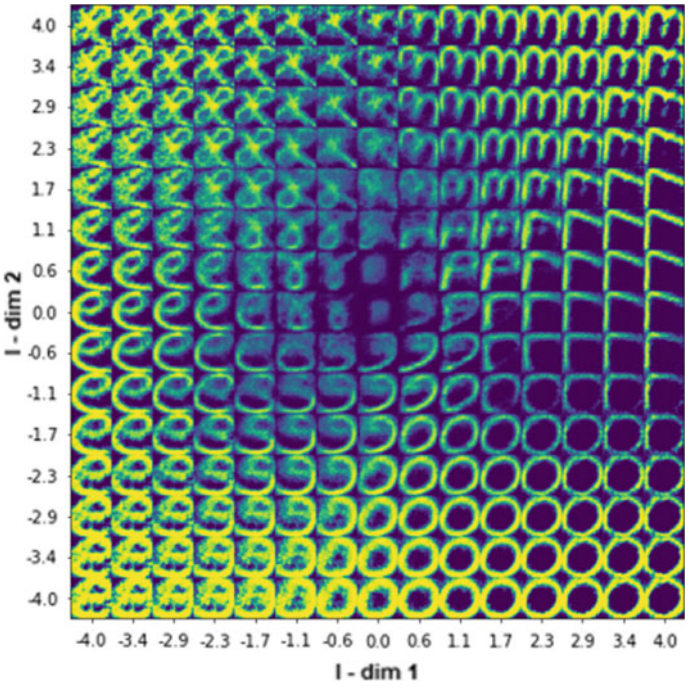

Fig. 4 Numeral outputs from the proposed VAE model after 100 epochs

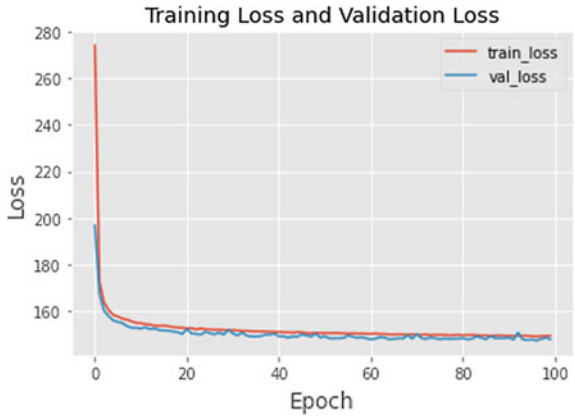

Fig. 5 Loss plot of the proposed VAE model after 100 epochs

References

1. Hou X, Shen L, Sun K, Qiu G (2017) Deep feature consistent variational autoencoder. In: 2017 IEEE winter conference on applications of computer vision (WACV), pp. 1133–1141. IEEE
2. Guo Qi, Zhu C, Xia Z, Wang Z, Liu Y (2017) Attribute-controlled face photo synthesis from simple line drawing. In: 2017 IEEE international conference on image processing (ICIP),

pp. 2946–2950. IEEE
3. Lombardi S, Saragih J, Simon T, Sheikh Y (2018) Deep appearance models for face rendering. ACM Trans Graphics (TOG) 37(4):1–13
4. Roche F, Hueber T, Limier S, Girin L (2018) Autoencoders for music sound modeling: a comparison of linear, shallow, deep, recurrent and variational models. arXiv preprint arXiv:1806.04096
5. Mor N, Wolf L, Polyak A, Taigman Y (2018) A universal music translation network. arXiv preprint arXiv:1805.07848
6. Pu Y, Gan Z, Henao R, Yuan X, Li C, Stevens A, Carin L (2016) Variational autoencoder for deep learning of images, labels and captions. In: Advances in neural information processing systems, pp 2352–2360
7. An J, Cho S (2015) Variational autoencoder based anomaly detection using reconstruction probability. Special Lecture on IE 2, no. 1
8. Lorberbom G, Gane A, Jaakkola T, Hazan T (2019) Direct Optimization through arg max for Discrete Variational Auto-Encoder. In: Advances in neural information processing systems, pp 6200–6211
9. Dash KS, Puhan NB, Panda G (2017) Odia character recognition: a directional review. Artif Intell Rev 48(4):473–497
10. Das A, Mohanty MN (2021) An useful review on optical character recognition for smart era generation. In: Multimedia and sensory input for augmented, mixed, and virtual reality, pp 1–41. IGI Global
11. Das A, Patra GR, Mohanty MN (2020) LSTM based Odia handwritten numeral recognition. In: 2020 international conference on communication and signal processing (ICCSP), pp 0538–0541. IEEE
12. Pattanayak SS (2017) Recognizing ODIA handwritten scripts. In: 2017 second international conference on electrical, computer and communication technologies (ICECCT), pp 1–4. IEEE
13. Jena OP, Pradhan SK, Biswal PK, Nayak S (2018) Implementation of linear discriminant analysis for Odia numeral recognition. In: 2018 international conference on information technology (ICIT), pp 166–171. IEEE
14. Dash KS, Puhan NB, Panda G (2014) A hybrid feature and discriminant classifier for high accuracy handwritten Odia numeral recognition. In: 2014 IEEE region 10 symposium, pp 531–535. IEEE
15. Dash KS, Puhan NB, Panda G (2015) Handwritten numeral recognition using non-redundant Stockwell transform and bio-inspired optimal zoning. IET Image Proc 9(10):874–882
16. Rushiraj I, Kundu S, Ray B (2016) Handwritten character recognition of Odia script. In: 2016 international conference on signal processing, communication, power and embedded system (SCOPES), pp 764–767. IEEE
17. Padhi D, Senapati D (2013) Zone centroid distance and standard deviation based feature matrix for Odia handwritten character recognition. In: Proceedings of the international conference on frontiers of intelligent computing: theory and applications (FICTA), pp 649–658. Springer, Berlin, Heidelberg

Classification of Skin Lesions Using Deep Convolutional Neural Network

Bhanja Kishor Swain, Susanta Kumar Rout, Mrutyunjaya Sahani, Upasana Muduli, and Renu Sharma

Abstract The melanoma is a type of skin cancer which develops from melanocytes, responsible to provide the skin color. The severity of melanoma cancer is defined on the basis of different stages which depends upon the depth of penetration and the early detection of melanoma at its prodromal stage is very crucial to stop its advancement. In this work, a novel variant of deep convolutional neural network (DCNN) is developed to perform a binary classification of normal nevus and melanoma by using the dermoscopic images of the PH^2 dataset. Finally, the classification accuracy of the proposed DCNN emerged as the best method to categorize the normal nevus and melanoma with competitive classification accuracy.

Keywords Deep convolutional neural network (DCNN) · Dermoscopic images · Binary classification · Melanoma · Normal nevus

1 Introduction

It has been found that melanoma has now become the most common type of cancer, and it is mostly seen in the white population. There is a huge number of the population which have been affected by this disease. It has been found that it can be cured by performing surgical excision, but there is a condition that it must be detected before it spreads to other organs. The research found that a huge number of people get to know about melanoma disease in their ending stage, and due to this, we receive a high mortality rate. People should know to make difference between the normal nevus and melanoma so that the recovery rate can be increased.

However, the latest technologies had made this possible, by the use of machine learning and computer vision. Now, these diseases can be classified just by looking at an image, and this process has made the detection easier, cheaper, and quicker than using biopsy. Even it will make the therapy easier. In 2019, an experiment

B. K. Swain · S. K. Rout (✉) · M. Sahani · U. Muduli · R. Sharma
Shiksa 'O' Anusandhan Deemed To Be University, Bhubaneswar, India

M. Mishra et al. (eds.), *Innovation in Electrical Power Engineering, Communication, and Computing Technology*, Lecture Notes in Electrical Engineering 814,
https://doi.org/10.1007/978-981-16-7076-3_40

was performed to detect melanoma disease by an image, between different dermatologists having various experiences and an application called convolutional neural network (CNN) algorithm [1]. It was found that the CNN has better performance in comparison with the performance of dermatologists. CNN algorithms work by machine learning and data analysis. The result was found that in terms of sensitivity and specificity the performance of CNN is superior to that of dermatologists. This experiment showed that the CNN algorithm is highly designed so that it can capture the disease by just looking into the picture. There are different layers used to form a convolutional neural network (CNN) like convolutional layer, pooling layer, rectified linear unit (ReLU) layer, and fully connected layer. CNN algorithms had been updated by using max pooling. The filters are given some more weight by updating backpropagation, as this is the reason for CNN to recognize a picture. In [2], about 122 features were taken from segmented skin lesions and are fed to CNN for the classification into different classes. Yuan, et al. applied Gabor filter to extract the distinguished features from the dermoscopic images and fed them to support vector machine (SVM) to classify the melanoma from other skin lesions [3]. The testing was performed on 22 images of skin lesions, and the result found the accuracy was 70%. In [4], the skin lesions are divided into different parts, and then, their extracted size, color, and shape were frd to the classifier to categorize different classes, and this process was done by using automatic region growing [4]. This was performed on 60 melanoma images, and this gave an accuracy of 83.3%, sensitivity of 80.0%, and specificity of 86.7%. The research showed a positive result, while two things that were used to make the classification performance better are conventional machine learning and the computer vision method. In this paper, the classification of skin lesions into common nevus and melanoma is performed on a publicly available dataset. A novel architecture of a deep convolutional neural network (DCNN) is proposed to perform a binary classification of the dermoscopic images. The resized images of PH^2 dataset are used as input to the proposed classifier. Finally, the classification accuracy of the proposed DCNN emerged as the best method to categorize the normal nevus and melanoma with competitive classification accuracy.

2 Related Research and Methodology

In the literature, various types of convolutional neural networks classifiers are proposed for the detection of melanoma [5–9]. For instance, Dorj et al. have tried to address the requirements of an intelligent as well as fast classification system [10]. To extract the distinguished features from the dermoscopic images, the AlexNet pre-trained DCNN is applied. Then, the skin cancer images are classified by using error-correcting output codes support vector machine (ECOC-SVM). The accuracy, sensitivity, and specificity of the method are found to be very competitive. In [11], the problem of data imbalance is addressed. An augmented dataset and a non-augmented dataset are prepared, and both the datasets are fed to a CNN classifier. Applying the same classifier for two different datasets resulted in a conclusion that the augmented

dataset can achieve a better accuracy than the non-augmented dataset. A multi-tract CNN is proposed by Kawahara et al. to classify the skin lesion [12]. This method provides an accuracy of 77.3% with auxiliary loss and 75.5% without auxiliary loss. Then, for further improvement, the data augmentation method is used to achieve an accuracy of 79.5%. Codella et al. [13] proposed a method consisting of parallel paths; one path uses CNN with transfer learning, and the other one uses sparse coding. The maximum accuracy achieved is 93.1% by using nonlinear SVM with histogram intersection kernel. The accuracy for classification of melanoma and non-melanoma is 93.1%, and melanoma and atypical nevus is 73.9%. Neol et al. [14] proposed a segmentation method using fully convolutional neural network, and the nonlinear SVM is applied for classification purpose. This method produced a precision of 0.649 by combining some specific features like sparse coding, edge histogram, color histogram, etc.

3 Dataset

For the binary classification of melanoma and normal nevus, in this proposed work, the publicly available PH^2 dataset is employed. This dataset contains high-quality digital images acquired at the Dermatology Service of Hospital Pedro Hispano, Matosinhos, Portugal. The RGB color space is used represent the images in the dataset, and each RGB image is represented in 8-bits with a resolution of 768 × 560.The dataset contains a total of 200 8-bit RGB images out of which 80 images are for normal nevus, 40 images are for melanoma and remaining 80 images are for atypical nevus. Figure 1 shows some selected samples of dermoscopy images collected from PH^2 dataset.

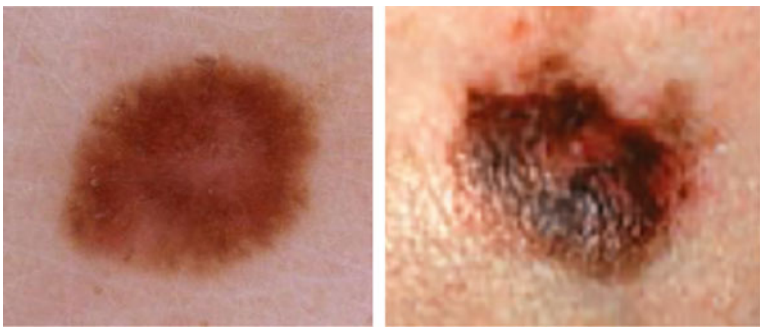

(a) Common nevus (b) Melanoma

Fig. 1 Selected samples from PH^2 database

4 The Deep Convolutional Neural Network (DCNN)

In the field of deep learning, the convolutional neural network similar to the artificial neural network (ANN) has been a very effective machine learning technique. With the application of a greater number of convolutional layers, the network gets deeper, and hence, it is called as a deep convolutional neural network (DCNN). Generally, the DCNN has four main blocks to construct its architecture; they are convolutional layer, rectified linear unit (ReLU) layer, pooling layer, and fully-connected (FC) layer [15–17]. Finally, after all the layers, the softmax layer does the classification of various classes.

4.1 Convolutional Layer

The main part of the DCNN is the convolutional layer. The output of the convolutional layer is represented in Eq. (1), which is obtained by applying pre-defined filters of certain sizes. The filters are allowed to slide over the input images to produce the output either in the form of cubic or in the form of rectangular blocks of neurons.

$$C_m = \sum_{n=0}^{N-1} f_n k_{m-n} \tag{1}$$

where k and f are the input signal and the filter selected for convolution operation respectively. C_m is the mth output element, and the total number of data points are represented by N.

4.2 Rectified Liner Unit (ReLU) Layer

The activation function of ReLU layer produces dead neurons that means if the input is positive; it outputs the input directly otherwise, and it outputs zero. The ReLU activation function is given as follows.

$$f(m) = \begin{cases} M; & m \geq 0 \\ 0; & \text{Otherwise} \end{cases} \tag{2}$$

Batch normalization operation is used to normalize the input of a layer by the method of subtracting the mean of mini-batch and dividing it by the standard deviation of the mini-batch.

4.3 Pooling Layer

The max pooling operation is applied to select the maximum number of elements of the feature map covered by a pre-selected filter. As a result, the new feature map obtained after the max pooling operation contains the most prominent features of the previous feature map.

4.4 Fully-Connected Layer

Fully connected (FC) layer is an example of the very common feedforward neural network. The output of the last convolutional layer is flattened and given as the input to the FC layer. In FC layer, all the inputs from one layer are connected to every activation unit of next layer. The output of fully connected layer is the sum of the product of input with the weights w and bias b and is represented in Eq. 3.

$$x_i = \sum_j w_{ji} y_j + b_i \tag{3}$$

where x represents the output of current layer and y represents the output of previous layer.

4.5 Softmax Layer

The softmax layer employs the concept of probability distribution where the sum of the probability of the occurrence of all the classes is one. The softmax activation function is given as

$$P_i = \frac{e^{x_i}}{\sum_m^k e^{x_i}} \tag{4}$$

where $P(x_i)$ belongs to the class of x_i and represents its probability within a range of 0 to 1. Figure 2 shows the complete architecture of the proposed DCNN.

5 Result and Discussion

In this work, the dermoscopic images of PH^2 dataset is used. The proposed DCNN for the binary classification of melanoma and normal nevus has 14 individual layers

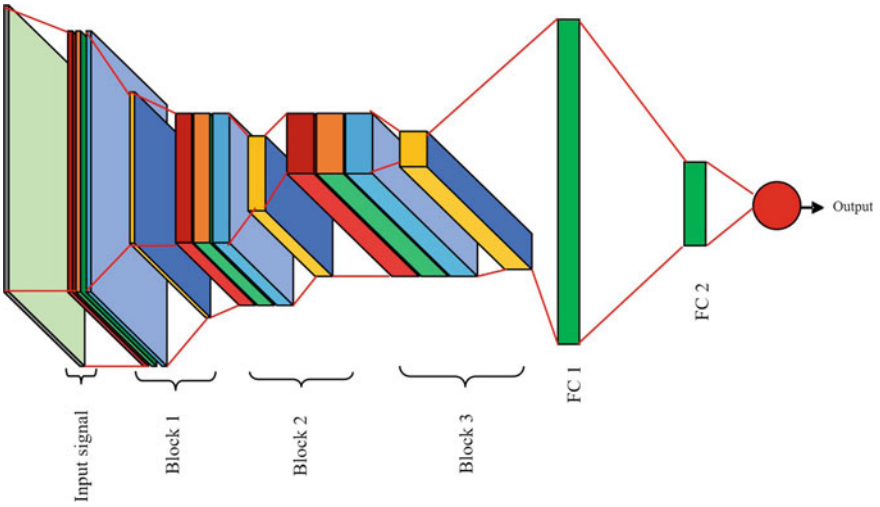

Fig. 2 Architecture of the proposed deep convolutional neural network (DCNN)

including the FC layer, and the softmax is used for classification at the end of the last FC layer. The architecture has three blocks each containing a set of convolutional, ReLU, batch normalization, and max pooling layers, respectively. After three main blocks, the feature map is flattened and represented by two FC layers. Finally, the output of last fully connected layer is given to the softmax layer to classify the melanoma and normal nevus images. As shown in Table 1, the filter size of the first

Table 1 Architecture of fast deep convolutional neural network (fast-DCNN)

Layer	Name	Output nodes	Filter size	Stride
0–1	Convolution	[598 × 798 × 3] × 8	3	1
1–2	ReLU	[598 × 798 × 3] × 8	1	1
2–3	BN	[598 × 798 × 3] × 8	10	10
3–4	MP	[299 × 399 × 3] × 8	2	2
4–5	Convolution	[295 × 395 × 3] × 5	5	1
5–6	ReLU	[295 × 395 × 3] × 5	1	1
6–7	BN	[295 × 395 × 3] × 5	10	10
7–8	Max pooling	[147 × 197 × 3] × 5	2	2
8–9	Convolution	[138 × 188 × 3] × 5	10	1
9–10	ReLU	[138 × 188 × 3] × 5	1	1
10–11	BN	[138 × 188 × 3] × 5	10	10
11–12	MP	[69 × 94 × 3] × 5	2	2
12–13	FC	100 × 1	0	0
13–14	FC	2 × 1	0	0

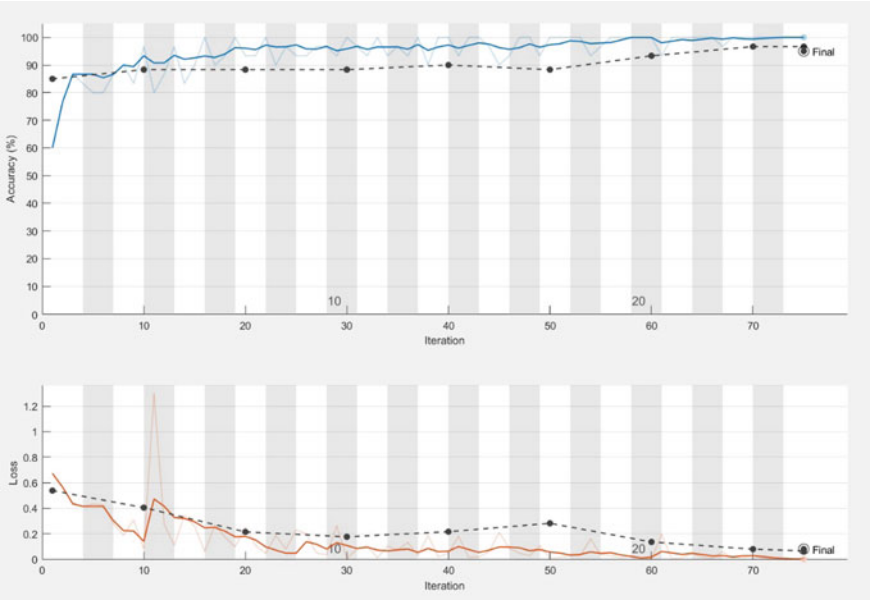

Fig. 3 Performance of the proposed fast-DCNN classifier

convolutional layer is 3×3 and with a stride of 1 and the debt of the first convolutional layer is 8. Similarly, for the second block, the filter size chosen is 5×5 and with a stride of 1, and the debt of the second convolutional layer is 5. Again, for the third block, the filter size chosen is 10×10 and with a stride of 1, and the debt of the third convolutional layer is 5. In this proposed method, the debt of each convolutional layer is increased gradually. Many combinations of filter size, stride, and debt are tried and after numerous simulations with several combinations of filter size, stride, and debt the best performance in terms of classification accuracy is achieved with the proposed architecture. The last feature map from the third convolutional layer is flattened to a size of 100×1 to form the first FC, and later, it is reduced to a size of 2×1 at the last FC as it is a case of binary classification of melanoma and normal nevus. The digital images obtained from the dataset is of different sizes; hence, all the images are resized to a size of $600 \times 800 \times 3$; then, the resized images are fed as input to the DCNN. The maximum classification accuracy with minimum training loss as shown in Fig. 3 is achieved by the proposed DCNN.

6 Conclusion

The binary classification of normal nevus and melanoma are performed by using the resized dermoscopic images of PH^2 dataset. A novel deep convolutional neural

network (DCNN), consisting of three sets of convolutional layers, two fully connected layers, and the probability density function-based softmax layer is proposed and developed to perform a binary classification of normal nevus and melanoma by using the dermoscopic images of the PH^2 dataset. Finally, the classification accuracy of the proposed DCNN emerged as the best method to categorize the normal nevus and melanoma with competitive classification accuracy.

References

1. Brinker TJ, Hekler A, Enk AH, Klode J, Hauschild A, Berking C, Schilling B et al (2019) Deep learning outperformed 136 of 157 dermatologists in a head-to-head dermoscopic melanoma image classification task. Euro J Cancer 113:47–54
2. Ganster H, Pinz P, Rohrer R, Wildling E, Binder M, Kittler H (2001) Automated melanoma recognition. IEEE Trans Med Imaging 20(3):233–239
3. Yuan X, Yang Z, Zouridakis G, Mullani N (2006) SVM-based texture classification and application to early melanoma detection. In: 2006 international conference of the IEEE engineering in medicine and biology society, pp 4775–4778. IEEE
4. Rokhana R, Herulambang W, Indraswari R (2020) Deep convolutional neural network for melanoma image classification. In: 2020 International electronics symposium (IES), pp 481–486. IEEE
5. Maglogiannis I, Doukas CN (2009) Overview of advanced computer vision systems for skin lesions characterization. IEEE Trans Inf Technol Biomed 13(5):721–733
6. Yang J, Xie F, Fan H, Jiang Z, Liu J (2018) Classification for dermoscopy images using convolutional neural networks based on region average pooling. IEEE Access 6:65130–65138
7. Soudani A, Barhoumi W (2019) An image-based segmentation recommender using crowdsourcing and transfer learning for skin lesion extraction. Expert Syst Appl 118:400–410
8. Khan MA, Sharif MI, Raza M, Anjum A, Saba T, Shad SA (2019) Skin lesion segmentation and classification: a unified framework of deep neural network features fusion and selection. Expert Syst. Art. no. e12497
9. El-Khatib H, Popescu D, Ichim L (2020) Deep learning_based methods for automatic diagnosis of skin lesions. Sensors 20(6):1753
10. Dorj U-O, Lee K-K, Choi J-Y, Lee M (2018) The skin cancer classification using deep convolutional neural network. Multimedia Tools Appl 77(8):9909–9924
11. Ayan E, Ünver HM (2018) Data augmentation importance for classification of skin lesions via deep learning. In: 2018 Electric electronics, computer science, biomedical engineerings' meeting (EBBT), pp 1–4. IEEE
12. Kawahara J, Hamarneh G (2016) Multi-resolution-tract CNN with hybrid pretrained and skin-lesion trained layers. In: Wang L, Adeli E, Wang Q, Shi Y, Suk H-I (eds) MLMI 2016, vol 10019. LNCS. Springer, Cham, pp 164–171
13. Codella N, Cai J, Abedini M, Garnavi R, Halpern A, Smith JR (2015) Deep learning, sparse coding, and SVM for melanoma recognition in dermoscopy images. In: Zhou L, Wang L, Wang Q, Shi Y (eds) MLMI 2015, vol 9352. LNCS. Springer, Cham, pp 118–126
14. Codella NC, Nguyen QB, Pankanti S, Gutman D, Helba B, Halpern A, Smith JR (2017) Deep learning ensembles for melanoma recognition in dermoscopy images. IBM J Res Dev 61(4):1–5
15. Mohapatra S, Swarnkar T, Das J (2021) Deep convolutional neural network in medical image processing. In: Handbook of deep learning in biomedical engineering. Academic Press, pp 25–60

16. Mohapatra S, Swarnkar T, Mishra M, Al-Dabass D, Mascella R (2021) Deep learning in gastroenterology: a brief review. In: Handbook of computational intelligence in biomedical engineering and healthcare, pp 121–149
17. Mohapatra S, Nayak J, Mishra M, Pati GK, Naik B, Swarnkar T (2021) Wavelet transform and deep convolutional neural network-based smart healthcare system for gastrointestinal disease detection. Interdisc Sci: Comput Life Sci 1–17

A Genetic Algorithm-Based Demand Side Management Program for Implementation of Virtual Power Plant Integrating Distributed Energy Resources

Sarthak Mohanty, Subhasis Panda, Binod Kumar Sahu, and Pravat Kumar Rout

Abstract The concept of Virtual Power Plant (VPP) provides flexibility in the operation of current Smart Grid (SG) based electric power systems. Demand Side Management (DSM) programs present a lot of scope in the optimization of the load consumption and curtailing of loads during peak usage periods. VPP and DSM together enable communication-based dispatching of loads depending upon the consumption pattern of consumers and generation capacity of Distributed Energy Resources (DER). Various optimization techniques have been proposed for efficient and cost-effective dispatch schedules within the intended power networks. In this paper, a Genetic Algorithm (GA) based optimization approach is presented to allow for reduction of the overall cost of the market price of electricity and reduction of burden during peak periods of use after integration of DERs and Demand Response (DR) strategy.

Keywords Genetic algorithm · Virtual power plant · Demand side management · Demand response

1 Introduction

The present power system scenario has seen a transition from centralized generation and distribution to the setting up of a smaller-scale interconnected microgrid (MG) system [1, 2]. Individual MGs allow for localized setup of power generation and supply systems based upon the load requirement and usage patterns. MGs also allow for a more flexible, local, and independent operation without compromising on security, quality, resiliency, and reliability [3]. To facilitate their operation in handling

S. Mohanty (✉) · S. Panda · B. K. Sahu
Department of Electrical Engineering, Siksha 'O' Anusandhan University, Bhubaneswar 751030, India

P. K. Rout
Department of Electrical and Electronics Engineering, Siksha 'O' Anusandhan University, Bhubaneswar 751030, India

M. Mishra et al. (eds.), *Innovation in Electrical Power Engineering, Communication, and Computing Technology*, Lecture Notes in Electrical Engineering 814,
https://doi.org/10.1007/978-981-16-7076-3_41

various power demands, Distributed Energy Resources (DERs) are often integrated with MGs.

These DERs may either be based on conventional energy sources or renewables. Renewable source-based DERs have increasingly sparked the interest in setting up demand for greener sources of energy, mainly due to the current energy crisis, their abundance of generating sources, and for being highly reproducible. DER operation allows for the utility to compensate for various shortfalls in the meeting of load demands during peak periods of operation. This brings down the burden on electrical utility and allows for a less stressed network to function, thereby increasing the reliability of the Distribution Network (DN). These small-scale power generation units are eventually replacing conventional generation sources due to lower carbon footprints and government incentivized installation schemes. With the current trend of the shift from conventional grid systems to smart grid systems, greater emphasis has been put on the development of communication and dispatch capabilities of these DER units within MG systems. DER units coupled with Information and Communication Technologies (ICTs) have enabled faster and more efficient dispatch of power when and wherever it is required.

The interconnection of these MGs and DERs have allowed for the development of the Virtual Power Plant (VPP) concept in recent years [4], with optimized integration of DERs and focus on improvement of ICT and dealing with the intermittent nature of most of the Renewable Energy Sources (RES). This concept allows for smaller DERs to participate in coordination with the controllable loads and Energy Storage Systems (ESSs). It integrates the ICT infrastructure either through a cloud or a stand-alone set up to connect, monitor, and coordinate the operation of various controllable loads and operating schedule of loads using Demand Side Management (DSM) techniques [5, 6] through the Internet of Things (IoT) connected loads and devices at the consumer premises.

Proper scheduling of these DER sources allows for better and lower energy production costs and curtailment of emission of greenhouse gases, thus maximizing profits and making the whole supply and distribution network sustainable. VPP with its ICT features allows for a more market-centric generation of power with the generating units playing an important part in the regulation of electricity prices in the market.

Excess power generation can thus be sold in electricity markets, thereby making the whole system more profitable in operation during times of peak generation and low demand for power. It also allows for various features to be implemented in the current conventional MG set up segregating it from the former as in structural and operational differences as well as the services offered by it. Some of these features are discussed below:

- Along with the integration of various DERs, ESSs, VPP allows for control over controllable loads and dispatching of RES to account for unpredictability in the operation of the MG system [7].
- It gives greater scope for the participation and conglomeration of DERs, ESSs, and IoT-connected devices in the SG setup.

- They can be coupled with other nearby grid setups using open communication protocols to allow for the various constituent units to participate in electricity wholesale markets.
- They can facilitate intercommunication over a larger geographical area and diverse MG setups by using newer communication protocols and technologies [7].
- They can not only manage the basic operations undertaken by MGs but also make the overall system offer a higher degree of control and operation by offering ancillary services [8] like frequency regulation, contingency protocols, Demand Response (DR) programs [9, 10] like peak load shaving, and load shifting as well as price regulation of electricity market prices.

In this paper, a VPP setup is implemented for the DSM-based DR program using Genetic Algorithm (GA) to allow for Load Shifting and Peak Load Shaving along with the integration of DERs.

2 Genetic Algorithm

The Genetic Algorithm is a search-based algorithm incorporating natural selection and gene-based heredity. It forms a subdivision of a large area of a computational process called Evolutionary Computation. It is a probability-based evaluation process in nature, but on the contrary, they are effective in local random search to identify the best possible solutions, as historic data makes it more complex and intricate. The solutions obtained after initialization of the population go through a process of recombination as well as mutation of genes. This results in the offspring having different characteristic values as that of the parents and this process continue for multiple generations. Each chromosome is evaluated using a distinct fitness value which is calculated using a predefined objective function. The individuals who are more fit have a greater probability of mating to reproduce more fit individuals. This entire process results in the creation of fitter individuals having better solutions in each succeeding generation and the process is continued till the final stopping criterion is fulfilled.

2.1 Operations Involved in GA

Generally, GA comprises three main operations for obtaining fitness values:

- Selection
- Crossover
- Mutation

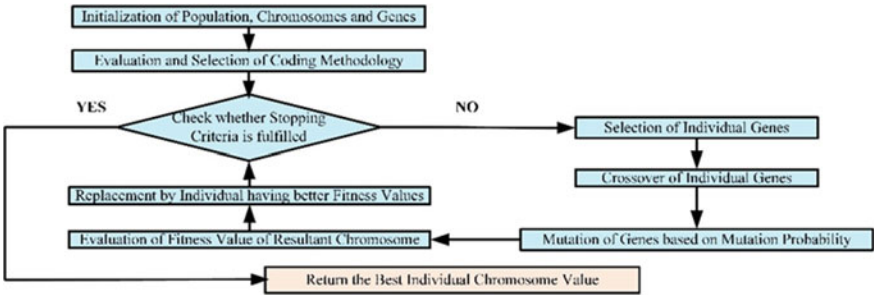

Fig. 1 Genetic algorithm flow chart

The whole process is illustrated in Fig. 1, which starts with the population initialization with chromosomes and genes being encoded. After that, the fitness value of all the chromosomal genes is evaluated by applying the fitness function.

After the initialization process, the selection of chromosomes having larger fitness values are selected and then processed through crossover and mutation operations based on crossover and mutation factor and process. When the iterative process is completed, better fitness value individuals replace the parent chromosomes and the whole cycle is repeated until the stopping criterion is fulfilled. The chromosomes referring to solutions have been processed through the entire process in GA, and the best individuals having optimal chromosomal values are returned. The whole process is continued till the solution has been satisfactorily obtained satisfying the allowable tolerance value.

3 Problem Setup

The problem setup has been based on the scheduling of loads during 24 h's time period. The load has been studied before Photovoltaic (PV) Arrays and Wind Turbines (WT) have been integrated and optimized using single-objective GA to present lower electricity consumption costs for the consumer and also to reduce peak loads during DER generation periods.

The developed model presents a VPP comprising three-generation sources: PV.

Arrays, Wind Turbine Power Plants (WTPP), and Conventional Power Plant (CPP) represented by the electricity grid supply. The power output of the PV and WT-based sources is simulated using models in SIMULINK and the power output is logged accordingly. The total electrical power consumption load logged by the PV inverter system at the premises over 24 h is taken into consideration after averaging out daily load consumption over a week.

The VPP is responsible for the timely dispatch of DER generation to deliver contracted energy to customers in hourly blocks and to minimize the power consumed from the electric grid supply.

4 Problem Formulation

The VPP optimization problem is based on the minimization of the operation cost of VPP by a reduction in consumption of power from the CPP and ensuring maximum dispatch possible from DERs. A modified version of the objective function used in is incorporated as the objective function in this paper.

Objective function

$$\text{Profit} = \sum_{i=1}^{N}\sum_{t=1}^{T}(C_u.P_{ub}) - \sum_{i=1}^{N}\sum_{t=1}^{T}\left(C_u.P_u + C_{dr}.P_{dr} + C_{pv}.P_{pv} + C_w.P_w\right) \quad (1)$$

where profit is in Rs/KWh, C_u is the cost of each kWh of utility generation in Rs/kWh, P_{ub} is the number of units of energy consumed from the utility grid before application of DSM in kWh, P_u is the number of units consumed from the utility grid after DSM and GA application in kWh, C_{dr} is the cost of each kWh of DR-based generation in Rs/kWh, P_{dr} is the number of units consumed from the utility grid through DR reduction in kWh, C_{pv} is the cost of each kWh of PV-based generation in Rs/kWh, P_{pv} is the number of units consumed from PV plant generation in kWh, C_w is the cost of each kWh of WT-based generation in Rs/kWh and P_w is the number of units consumed from WT plant generation in kWh.

Subject to:

Constraints

The utility, PV, and WT power consumption must remain between their minimum and maximum limits.

$$P_u^{\min} \le P_u \le P_u^{\max}; \quad \forall t \in T \quad (2)$$

$$P_{pv}^{\min} \le P_{pv} \le P_{pv}^{\max}; \quad \forall t \in T \quad (3)$$

$$P_w^{\min} \le P_w \le P_w^{\max}; \quad \forall t \in T \quad (4)$$

$$P_{dr} \le P_u; \quad \forall t \in T \quad (5)$$

Equalities

$$P_{FG} = P_u + P_{dr} - P_{pv} - P_w \quad (6)$$

where, $P_u^{\min}$ and $P_u^{\max}$ are the minimum and maximum values of power consumption from the utility in kWh, $P_{pv}^{\min}$ and $P_{pv}^{\max}$ are the minimum and maximum values of PV

power generation in kWh, $P_w^{\min}$ and $P_w^{\max}$ are the minimum and maximum values of WPP power generation in kWh, and P_{FG} is the final net generation from the utility grid and through reduction of peak load using DR, PV, and WPP generation sources in kWh.

5 Case Study

The VPP considered in this case study consists of WPP with an installed capacity of 61.8 kW, and PV with an installed capacity of 176.6 kW. Here the PV case study is done on a grid-tied PV plant installed at OUAT (Odisha University of Agriculture and Technology), Bhubaneswar, Odisha.

The installed PV system selected for the case study is installed on the building rooftop of the OUAT premises, Bhubaneswar, Odisha, India. The arrangement comprises 570 PV modules over a total area of 1760 m^2. The total power generation capacity is 176.6 kWp based on the campus load requirements. The WAREE WS-310 multi-crystalline Silicon modules of 310 Wp capacity and conversion efficiency of 15.97% under standard test conditions (STC) are used. The PV modules are installed with the base at an angle of 10° tilt angle. Table 1 illustrates the technical specifications of the PV plant and the PV module specifications carried out in this case study. Figure 2 shows the SIMULINK PV array model implemented in this paper.

For the WT plant source, a SIMULINK/MATLAB model is implemented using as reference documentation comprising three individual wind turbine generators of 20 kW each. The maximum aggregated power output from the WPP is 60 kW. For the choice of simulation, RyseEnergy E-20 HAWT is chosen as a test case model. The technical specifications of the chosen WT system are given in Table 2. The SIMULINK model of E-20 HAWT is shown in Fig. 3.

The VPP is on a bilateral contract with customers on the electricity market and is contracted to deliver energy at a preset market price after the integration of DER energy production. The power delivery is on a contractual basis of an hourly period. The RES sources produce maximum power as they can deliver at any given time and the remaining is covered by the CPP if required. Figure 4 shows the hourly electricity consumption of the case study logged by the PV inverter system before integration of DSM principles, PV, and WPP sources.

The hourly market prices for the utility are obtained using the Indian Energy Exchange's (IEX) Day-Ahead Market Data Tool available on IEX website with the average data chosen according to the time frame taken for the load consumption data. The hourly market prices at Market Clearing Price (MCP) is applied in the utility contract power delivery is illustrated in Fig. 5.

Table 1 Technical specifications of 176.6 kW PV plant and PV module specifications

Parameters	Specifications
No. of connected PV modules	570
PV panel technology	Multi-crystalline Si
Manufacturer of PV module	WAREE
No. of series strings	19
No. of parallel strings	30
Rated power of PV Plant	176.7 kWp
Tilt angle	10°
Total area span	1760 m^2
Tracking system	Perturb and Observe
Installed number of inverter units	3
Manufacturer of inverter	SUNGROW
V_{OC}	45.20 V
I_{SC}	9.14 A
V_{MP}	36.70 V
I_{MP}	8.45 A
Power thermal coefficient (γ)	–0.3845
Efficiency % of the module	15.97%
Fill factor	0.75
Dimension of each PV module	1960 mm × 990 mm × 40 mm
Solar cells per module	72 (12 × 6)
Nominal maximum module Power	310 Wp
Operating temperature	–40 to 85 °C

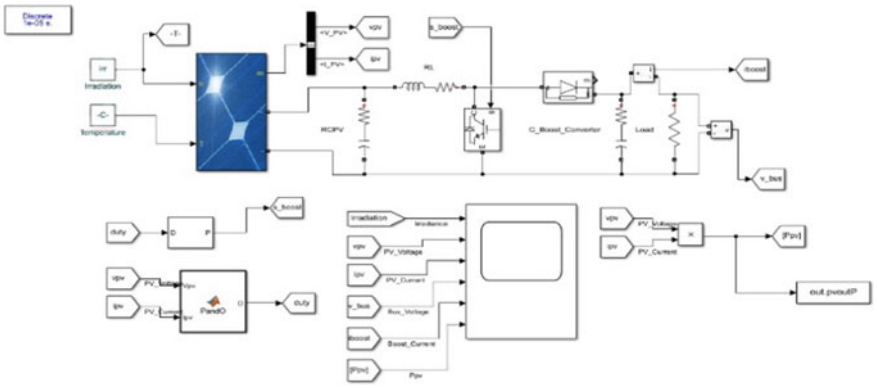

Fig. 2 PV system model in SIMULINK

Table 2 Technical specifications of 20 kW WT system

Parameters	Specifications
Generator type	Permanent magnet
Configuration	Horizontal axis
Manufacturer of WT	RyseEnergy
No of blades	3
Blade length	4.5 m
Rotor diameter	9.8 m
Swept area	75.4m^2
Nominal rotor speed	120 rpm
Cut-In speed	2 m/s
Rated wind speed	9 m/s
Cut-Out speed	30 m/s
Survival speed	70 m/s
Weight of rotor	1000 kg
Pitch	Downward active pitch
Yaw	Assisted yaw
Turbine design class	IEC 61400-2 Class I
Operating temperature	–20 to 50 °C
Lattice	15–36 m
Monopole	18–27 m
Tilt-Up	18–27 m
Rated power	18 kW
Maximum power	20 kW

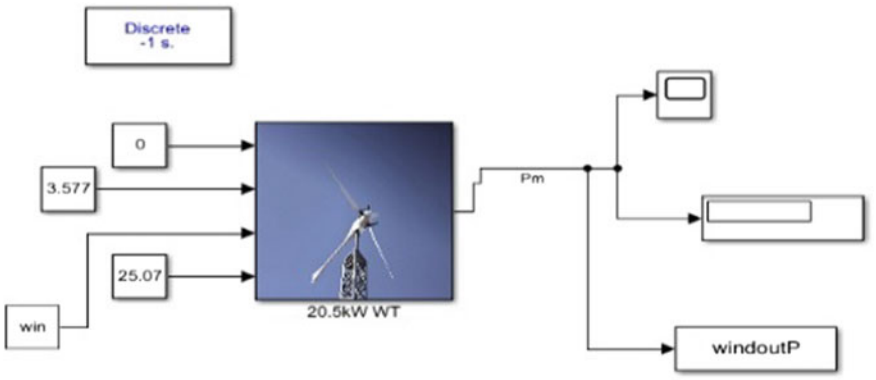

Fig. 3 WT system model in SIMULINK

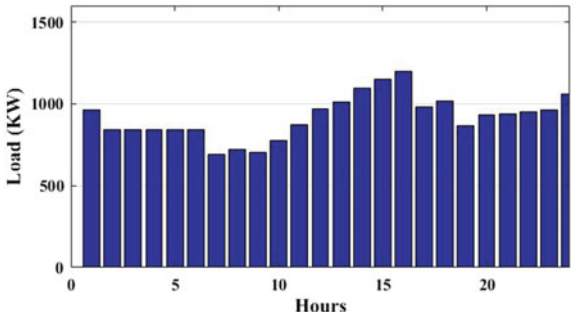

Fig. 4 Total power consumption before integration of PV, WPP, and DSM techniques

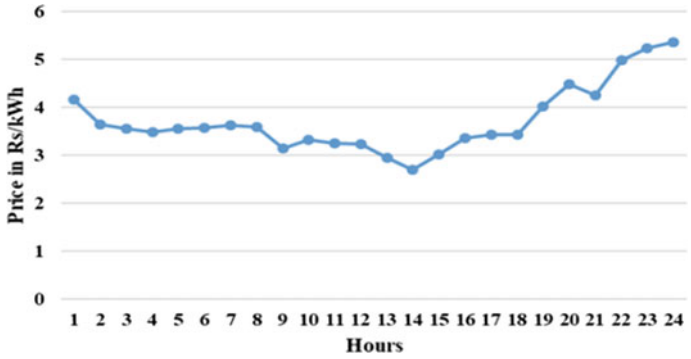

Fig. 5 Hourly utility market prices

6 Results of Simulation and Discussion

Simulation of PV and WPP is carried out for an entire day time frame based on the meteorological data supplied by SolCast Database and National Renewable Energy Laboratory (NREL) datasets. The same is simulated using MATLAB/SIMULINK and the PV and WPP output are obtained. The power generated from PV and WPP sources are illustrated in Fig. 6.

Next, GA constraints are defined and the parameters used in the GA are represented by a function as follows [11]:

$$\text{GA} = \left(p^i, I, \lambda, \text{length}, \text{FF}, N_G, e, c, m, S, \text{eqc}\right) \tag{7}$$

where, p^i = Initial population size; I = Encoding of chromosomes; λ = Size of population; length = Chromosome length; FF = Fitness function; N_G = Generation number; e = Elitism function; c = Crossover function; m = Mutation function;

S = Stopping criterion; and eqc = Equality constraints.

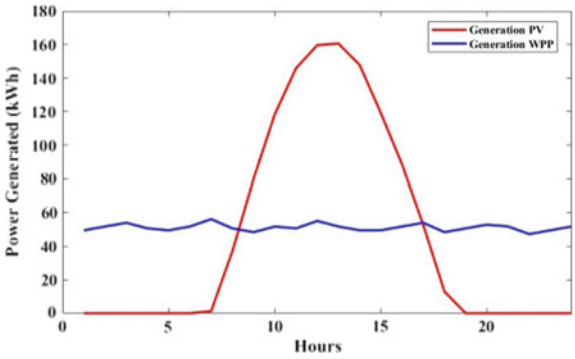

Fig. 6 PV and WPP generated output power

In the optimization method, the following parameters are assigned to solve the GA problem: (1) Number of Generations: 400, (2) Population Size: 50, (3) Crossover Rate: 0.7, (4) Mutation Rate: 0.03, and (5) Elitism Rate: 0.25.

The execution of GA on forecasted hourly values of load resulted in peak shifting of loads from peak usage periods to a more levelized usage pattern before the integration of RES. This eventually results in lower utility power purchase costs. The resultant optimized load pattern through GA is illustrated in Fig. 7.

After completion of the GA optimization, the optimized load values are integrated with the power generated from PV and WPP, and the units of consumption of utility are calculated. The final power consumed from the utility is then used to calculate the final cost of the utility consumption. The reduction in peak load shaving and peak load shifting operations is calculated using Load Demand Response (LDR). The comparative graph between final utility consumption and the consumption after LDR techniques is illustrated in Fig. 8.

The final objective of the optimization is to maximize VPP profits [12]. This has been achieved by the reduction in the cost of power consumption from CPP and by supplementation of different pricing mechanisms of RES and DR-based sources.

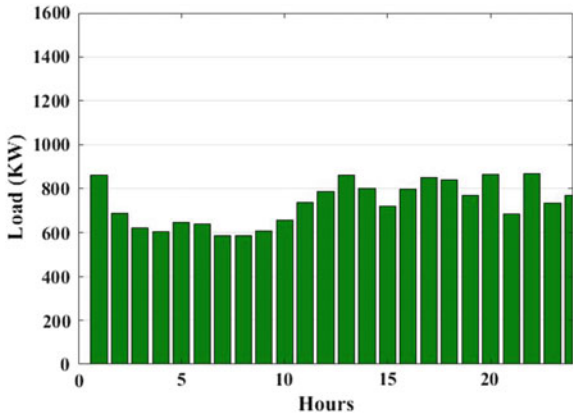

Fig. 7 Load after application of DSM principles using GA algorithm

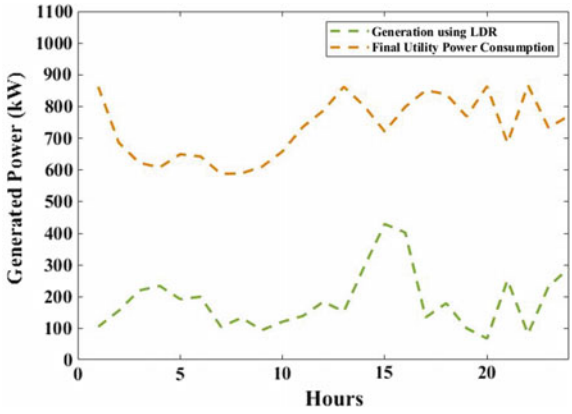

Fig. 8 Final utility power consumption and generation using LDR

The final difference in the cost of hourly power consumption for the system as a whole has been illustrated in Figs. 9 and 10 indicate the before-after cost reduction

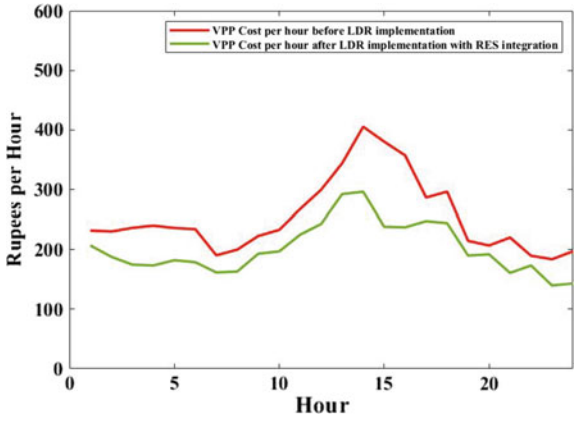

Fig. 9 VPP cost before and after GA algorithm and DER integration

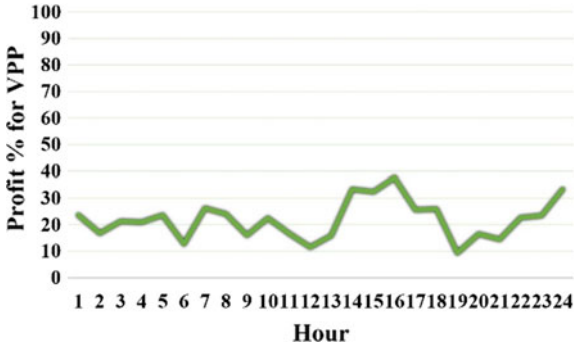

Fig. 10 VPP profit over unoptimized scheduling

policies of the system as a whole with integrated DER components and the VPP profit maximization percentage chart respectively.

7 Conclusion

The objective of this research paper is to provide a profit-maximizing framework for VPP optimal operation. The main importance to achieve profit maximization is to influence the shift from CPP-based generation towards non-conventional generation sources which provide cheaper energy consumption tariff rates and cleaner less carbon-emitting sources [13]. Based on the provided results, it is observed that.

optimization techniques like GA present convenient algorithms in DSM and DR-based programs. Other Artificial Intelligence (AI) and Nature-inspired techniques can induce similar optimization results due to their suitability in dealing with forecasted market data without distortion of data falling into either local maxima or minima.

Future work will be oriented towards the improvement of the presented optimization model by the inclusion of dynamic pricing of CPP and DR reduction price of utility based on PV and WPP production. Further work can be focused upon the inclusion of ESS and uncertainty modeling. Universal interaction scheme modeling of VPP with other market entities can provide greater scope for participation in the market framework to improve profit maximization/cost reduction policies.

References

1. Pudjianto D, Ramsay C, Strbac G (2005) Microgrids and virtual power plants: concepts to support the integration of distributed energy resources. Proc Inst Mech Eng Part A: J Power Energy 222(7):731–741
2. Dulau LI, Abrudean M, Bica D (2014) Applications of virtual power plants approaches. In: 2014 international conference and exposition on electrical and power engineering (EPE). IEEE
3. Pasetti M, Rinaldi S, Manerba D (2018) A virtual power plant architecture for the demand-side management of smart prosumers. Appl Sci 8(3):432
4. Nikonowicz, ŁB, Milewski J (2012) Virtual power plants-general review: structure, application and optimization. J Power Technol 92(3):135–149
5. Nosratabadi SM, Hooshmand RA, Gholipour E (2017) A comprehensive review on microgrid and virtual power plant concepts employed for distributed energy resources scheduling in power systems. Renew Sustain Energy Rev 67:341–363
6. Esther BP, Sathish Kumar K (2016) A survey on residential demand side management architecture, approaches, optimization models and methods. Renew Sustain Energy Rev 59:342–351
7. Behrangrad M (2015) A review of demand side management business models in the electricity market. Renew Sustain Energy Rev 47:270–283
8. Macedo MNQ et al (2015) Demand side management using artificial neural networks in a smart grid environment. Renew Sustain Energy Rev 41:128–133
9. Mesarić P, Krajcar S (2015) Home demand-side management integrated with electric vehicles and renewable energy sources. Energy Build 108:1–9

10. Aghajani GR, Shayanfar HA, Shayeghi H (2017) Demand side management in a smart micro-grid in the presence of renewable generation and demand response. Energy 126:622–637
11. Shukla A, Pandey HM, Mehrotra D (2015) Comparative review of selection techniques in genetic algorithm. In: 2015 international conference on futuristic trends on computational analysis and knowledge management (ABLAZE). IEEE
12. Narkhede MS, Chatterji S, Ghosh S (2013) Multi objective optimal dispatch in a virtual power plant using genetic algorithm. In: 2013 international conference on renewable energy and sustainable energy (ICRESE). IEEE
13. Kuzle I, Zdrilić M, Pandžić H (2011) Virtual power plant dispatch optimization using linear programming. In: 2011 10th international conference on environment and electrical engineering. IEEE

Analysis of Evaporation Rate Based Water Cycle Algorithm Tuned 2-DOF PIDF Controller for Automatic Generation Control of Power System

Gauri Sahoo, Rabindra Kumar Sahu, and Sidhartha Panda

Abstract This study addresses Automatic Generation Control of Two Equal Area Interconnected Reheat Thermal Power System Including Non-Linearity. The 2-DOF PIDF controller leads to faster disturbance rejection with minimum peak values in set point tracking and also mitigates the effects due to any changes in the reference signal, as compared to PID controller. Hence, 2-DOF PIDF controller is implemented in this paper. Evaporation Rate Based Water Cycle Algorithm (ERWCA) is an optimization technique that demonstrates smooth coordination between exploration and exploitation due to which it gives a high probability of finding global optima with faster convergence. In this constrained optimization problem, controller gain parameters are tuned using Evaporation Base Water Cycle Algorithm till the Objective Function (ITAE) reaches a minimum value. Initially, ITAE values were computed using ERWCA, Firefly Algorithm, and Particle Swarm Optimization techniques for the power system model with PID controller and it was observed that ERWCA optimization technique yields least ITAE. Further, 2-DOF PIDF controller tuned by ERWCA was implemented in the model and it was found that the ITAE value is further reduced as compared to the PID controller. Time domain system dynamic characteristics of the power system model are analyzed.

Keywords Evaporation rate water cycle algorithm · 2DOF PIDF · Automatic generation control

1 Introduction

Frequency deviation in an interconnected power system adversely affects the power system operation and reliability. Frequency deviation is a useful index that indicates

G. Sahoo (✉) · R. K. Sahu · S. Panda
Department of Electrical Engineering, Veer Surendra Sai University of Technology Odisha, Burla, Odisha 768018, India
e-mail: gauri.sahoo@ves.ac.in

R. K. Sahu
e-mail: rksahu_ee@vssut.ac.in

M. Mishra et al. (eds.), *Innovation in Electrical Power Engineering, Communication, and Computing Technology*, Lecture Notes in Electrical Engineering 814,
https://doi.org/10.1007/978-981-16-7076-3_42

the imbalance between the generation and electrical load. Automatic Generation Controller (AGC) is responsible for frequency control and power interchange, as well as economic dispatch. Frequency control is one of the most important issues in power system control. An intelligent AGC simultaneously minimizes the system frequency deviations and regulates tie-line power flows to match total generation and load demand using intelligent control methodologies. In modern thermal power plant, exit steam from the high-pressure turbine is reheated by a super heater, and the reheat steam is again passed through an intermediate and low-pressure turbine to optimize the thermal efficiency. In a practical thermal power plant, due to the limitations of thermal and mechanical stresses, the rate of change of power generation is physically constrained by Generation Rate Constraint (GRC). Also, speed governor may not immediately react to change the valve position for mismatch in generation and electrical load until the input signal reaches a threshold value. For large steam turbines, Governor Dead Band (GDB) is set for 0.06% (0.036 Hz). Hence, for a realistic approach of a thermal power plant, such non-linearity needs to be addressed while modeling the power system [1–3].

In recent times, several natures inspired intelligent computational methods based on swarm and evolutionary optimization algorithms have been proposed for AGC studies. Researchers around the world have applied these approaches for improvements in performance of AGC. Computational methods like Firefly Algorithm (FA) [4], Particle Swarm Optimization Technique (PSO) [5], Hybrid BFOA–PSO [6], Teaching Learning Based Optimization (TLBO) Algorithm, and Genetic Algorithms (GA) has been used for study of AGCs. From these literature reviews, it is understood that for achieving accurate and reliable AGC performance heuristic-based optimization techniques are preferred for research studies. A 2-DOF PIDF controller is preferred over the classical PID controllers in view of achieving better tracking of set-points and regulation against the disturbance input signals [7]. ERWCA demonstrates smooth coordination between exploration and exploitation due to which it gives a high probability of finding global optima with a faster convergence [8].

In this paper, automatic generation control using 2-DOF PIDF controller optimally tuned by ERWCA has been demonstrated. For a realistic approach, non-linearity like GRC and GDB has been included in this power system model. In this constrained optimization problem, the controller gain parameters are tuned till the Objective Function (ITAE) reaches a minimum value. Time domain system dynamic performances are verified under normal and abnormal load conditions. Further, robustness of the controller is investigated by sensitivity analysis. The supremacy of control strategy is compared with other techniques based on the computed ITAE values and time domain system dynamic characteristics.

2 Power System Under Study

The power system considered for investigation consists of two interconnected control areas with reheat thermal power units shown in Fig. 1. Each area is operating at 50%

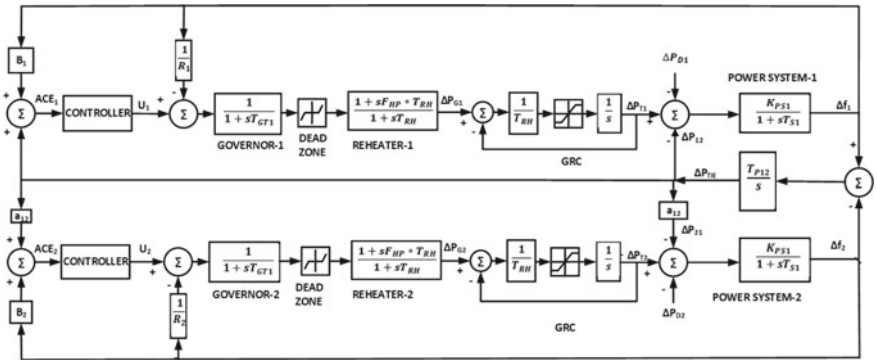

Fig. 1 Power system model

of its rated capacity and has a rated generation capacity of 2000 MW. The nominal system frequency of each generator is 60 Hz. In a practical power plant, the speed governor does not change the valve position immediately for control of mismatch between the generation and load demand until the input signal reaches a threshold value. Due to the limitations of thermal and mechanical stresses, the rate of change of power generation is physically constrained by Generation Rate Constraint (GRC) which increases oscillations in the system dynamics. For large thermal power plants, typical values of GRC are selected in the range of 2–10% per minute, and GDB is typically specified as 0.06% (0.036 Hz). For reheat thermal power plants, the power fraction for HP turbine is specified to 31%. The power system model parameters are defined and typical values used in this paper are given in Appendix. The mismatch in power (ΔP_{Tie}), deviation in system frequency (Δf), and frequency biasing factor (B) for each area are given by Area Control Error (ACE) in Eq. (1),

$$\left.\begin{aligned} \text{ACE}_1 &= \Delta P_{\text{Tie12}} + B_1.\Delta f_1 \\ \text{ACE}_2 &= \Delta P_{\text{Tie12}} + B_2.\Delta f_2 \end{aligned}\right\} \tag{1}$$

ACE1 and ACE2 are used as input signals to the controllers.

3 The Proposed Approach

The 2-DOF PIDF controller includes set point weightages on the proportional and derivative terms. The 2DOF-PIDF controller can lead to fast disturbance rejection without any significant increase in peak values in set point tracking and is also useful for mitigating the influence on the control signal due to any changes in the reference signal. The 2-DOF PIDF controller structure is shown in Fig. 2. $C(s)$ is 1-DOF controller, $D(s)$ is applied load disturbance and $F(s)$ is a pre filter for $R(s)$ as shown in Fig. 3.

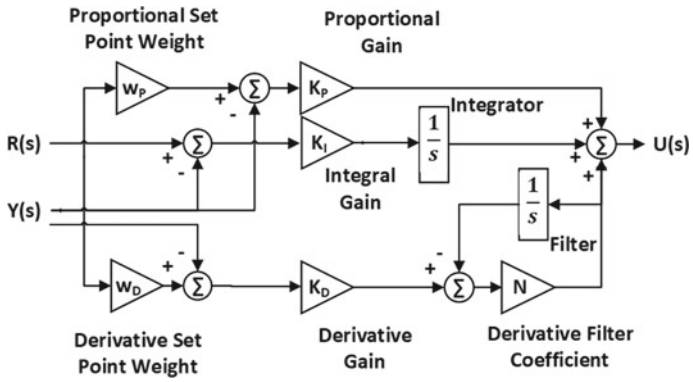

Fig. 2 2-DOF PIDF controller structure

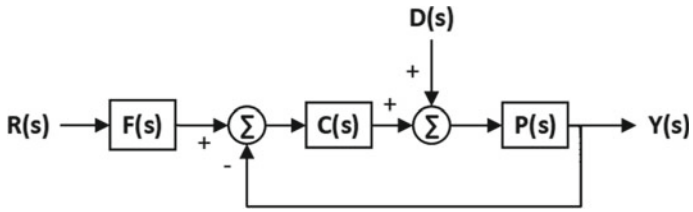

Fig. 3 2-DOF PIDF control system

4 Modeling of Objective Function and Constraints

In this constrained optimization problem, controller gain parameters are adjusted till the Objective Function is computed for its minimum value. ITAE is the performance index that produces smaller overshoots and oscillations than other control system performance indices. In this paper, ITAE is the objective function. General expression for ITAE is given in Eq. (2).

$$\text{ITAE} = \int_0^{t_{\text{sim}}} t.\left[\sum_{i=1}^{2}|\Delta f_i| + \sum_{j=1}^{1}|\Delta P_{\text{Tie}}|\right].\text{d}t \tag{2}$$

The controller gain parameters are tuned within their allowable limits so as to compute the minimum value of Objective Function ITAE using the ERWCA optimization technique. The problem constraints are given in Eq. (3).

$$\begin{aligned} -2 \leq K_P^n \leq 2 \\ -2 \leq K_I^n \leq 2 \\ -2 \leq K_D^n \leq 2 \\ 0 \leq w_P \leq 5 \\ 0 \leq w_D \leq 5 \\ 0 \leq N \leq 500 \end{aligned} \tag{3}$$

5 Simulation Results, Demonstration, and Discussions

In this paper, AGC for the power system model is implemented using MATLAB/SIMULINK version: 9.0.0.341360 (R2016a), 64-bit on an Intel(R) Core™ i5-7300HQ CPU @ 2.50 GHz, 8.00 GB RAM, 64-bit Operating System LAPTOP-50GFA3PT. The viability of the proposed ERWCA-based AGC is investigated and demonstrated. The AGC of power system model is verified in SIMULINK environment, whereas the computational code is written in MATLAB files. In this paper, power system model with non-linearity (GRC ±0.001pu/s and GDB 0.036 Hz) is considered for investigation. The reheat thermal power plant power fraction for high-pressure turbines is considered 0.31. The typical values of system parameters are given in Appendix A. ITAE values were computed for the power system model with PID controller using ERWCA, Firefly Algorithm (FA), and Particle Swarm Optimization (PSO) techniques and it was observed that ERWCA optimization technique yields the least ITAE. The convergence graphs shown in Fig. 4 justify that ERWCA gives faster convergence than FA and PSO.

In the power system model, Area-1 was given with a step load disturbance of +1%. Time domain simulations were demonstrated. The optimal tuned parameters of controllers were generated by estimating the objective function using FA, PSO, and ERWCA. The corresponding system performance index is measured using

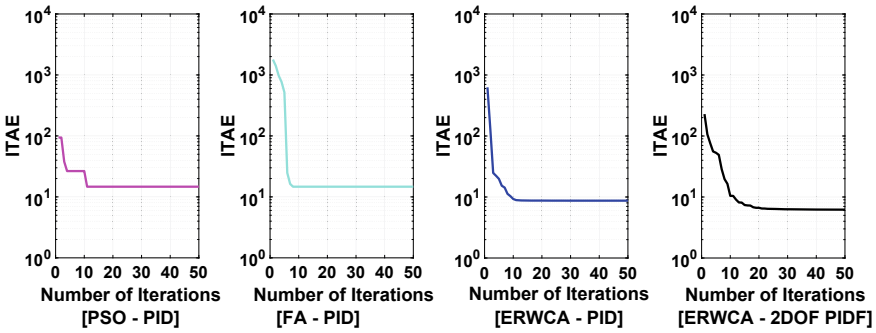

Fig. 4 Convergence of ITAE by FA, PSO, and ERWCA

the optimized controller gain parameters. From Table 1, it can be observed that PID controller tuned by ERWCA technique gives better performance than tuned by PSO and FA which establishes that ERWCA is a better optimization technique for AGC studies. Tuning of 2-DOF PIDF controller gain parameters is carried out using ERWCA technique which gives the best performance among all the controller strategies mentioned in this paper. The least ITAE value is 6.3729 for ERWCA tuned 2-DOF PIDF controller. The minimum damping ratio is found to be 0.1624 and peak values (overshoot) for Δf_1, Δf_2, and ΔP_{Tie} are found to be 0.0115 Hz, 0.0099 Hz, and 0.0012puMW respectively. The optimal tuned gains of 2-DOF PIDF controllers are given in Table 2. The time domain system dynamic responses of the power system model with the optimally tuned gains of 2-DOF PIDF controllers is shown in Fig. 5.

Further, Eigen values were computed for each of the controller strategies and shown in Table 3, where it can be observed that for all controller strategies these values are found to be in the left half of *s*-plane. Hence, the closed loop system is inherently stable for uncertainties in system parameter variation. Sensitivity analysis is done to examine the robustness of the control system. Uncertainties of ±50%, ±25% in Frequency Biasing Coefficient (B), Synchronizing Torque Coefficient (T_{P12}), Steam Turbine Time Constant of Steam Chest (T_{CH}), and Steam Governor Time Constant (T_{GT}) are applied and the system dynamic characteristics in terms of ITAE, MDR, Peak values and settling time is computed. It can be observed that for uncertainties in all system parameter variations, the values of ITAE, MDR. Peak value and Settling Time are very close to each other. Hence, it can be concluded that the control strategy for AGC of the power system model optimized by ERWCA is robust and stable for the above uncertainties in system parameters. Again, the tuned values of controller

Table 1 System dynamic characteristics comparison to other competing methods

Optimization technique	ITAE	MDR (ζ)	Peak values (overshoot)			Settling time, *Ts* (seconds) (±2% band)		
			Δf_1 (Hz)	Δf_2 (Hz)	ΔP_{Tie12} (puMW)	Δf_1	Δf_2	ΔP_{Tie12}
ERWCA-PID	8.2779	0.2894	0.0243	0.0225	0.0009	24.3668	23.9779	25.9726
ERWCA-PIDF	6.9155	0.3543	0.0172	0.0149	0.0009	20.8949	19.9410	25.5942
ERWCA-2DOFPIDF	**6.3729**	**0.1624**	**0.0115**	**0.0099**	**0.0012**	**19.9099**	**20.7617**	**20.7823**
FA-PID	12.8681	0.2276	0.0442	0.0423	0.0003	25.3204	25.3837	27.6216
PSO-PID	17.8587	0.4385	0.0591	0.0562	-0.0010	27.5075	27.4845	27.4531

Bold represents supremacy of 2DOFPIDF Controller using ERWCA over other optimization techniques and controllers

Table 2 Optimal tuned gains of 2DOF-PIDF controllers

2-DOF PIDF	K_P	K_I	K_D	N	w_P	w_D
(1)	1.0622	−0.0000	0.8157	254.0180	0.0000	3.0083
(2)	−1.9440	−0.0026	1.9990	0.0509	0.0061	0.4040

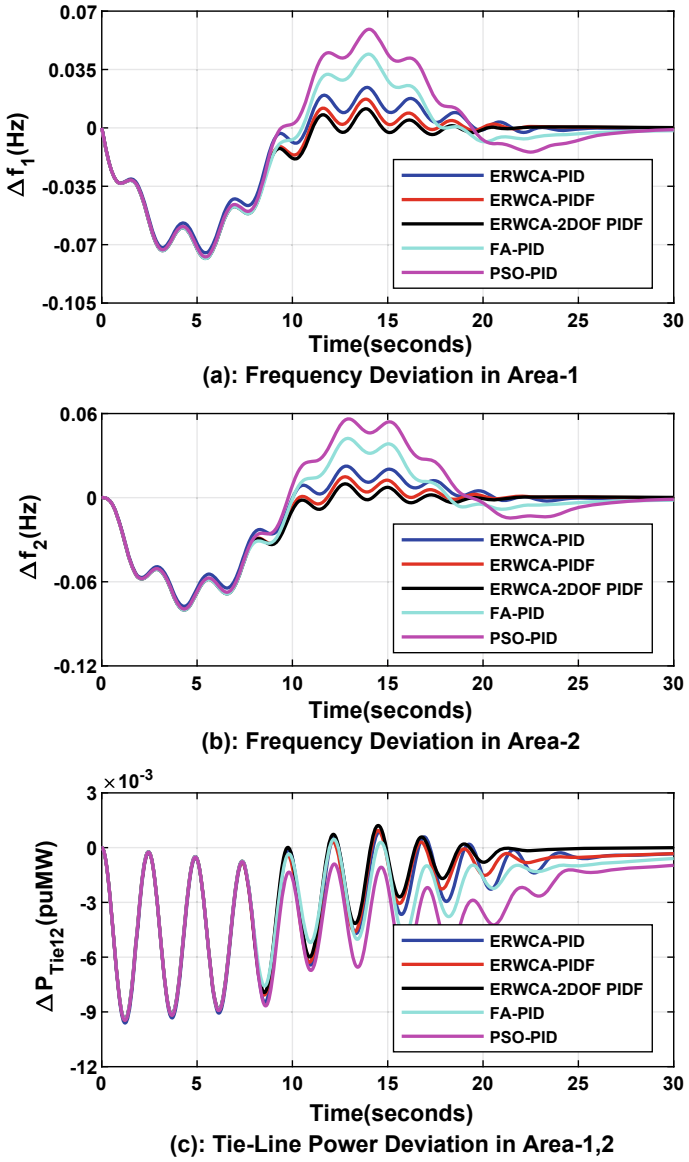

Fig. 5 System dynamic responses of the power system model

gain parameters need not be re-evaluated for such variations. Table 4 summarizes the computed values of ITAE, MDR, Peak Values, and Settling Time under variations in system parameters.

The system Eigen values were computed for the uncertainties in system parameter variations using the tuned parameters of 2-DOF PIDF controller and shown in Table

Table 3 Comparison of system Eigen values for different techniques and controllers

ERWCA PID	ERWCA PIDF	ERWCA 2DOF PIDF	FA-PID	PSO-PID
−101.05	−22.6173	−268.75	−100.19	−100.98
−99.90	−16.8272	−1.85 ± 11.25i	−100.13	−100.06
−17.42	−4.3442 ± 6.8089i	−14.04	−15.47	−16.36
−8.58 ± 6.11i	−2.7628	−5.42	−15.92	−8.58 ± 5.39i
−2.75	−0.9257 ± 2.4437i	−0.83 ± 2.09i	−3.73	−2.85
−0.68 ± 2.25i	−0.1552	−0.10	−0.64 ± 2.72i	−1.10 ± 2.26i
−0.28 ± 0.20i	−0.3399 ± 0.1294i	−0.32 ± 0.15i	−0.32 ± 0.25i	−0.28 ± 0.21i
−0.06 ± 0.03i	−0.0503 ± 0.0243i		−0.05 ± 0.02i	−0.05 ± 0.07i

Table 4 Sensitivity analysis

Uncertainties		ITAE	MDR (ζ)	Peak values			Settling time, *Ts* (seconds) (±2% band)		
				Δf_1 (Hz)	Δf_2 (Hz)	ΔP_{Tie12} (puMW)	Δf_1	Δf_2	ΔP_{Tie12}
B	Nominal	6.5286	0.1624	0.0784	0.0802	0.0094	19.8886	20.6615	20.7884
	+25%	6.6909	0.1537	0.0784	0.0802	0.0094	19.6623	19.1125	23.1496
	−25%	6.8775	0.1690	0.0784	0.0802	0.0094	21.8683	21.0669	22.7335
	+50%	7.1430	0.1449	0.0783	0.0802	0.0094	19.5002	19.3670	24.3127
	−50%	8.9251	0.1659	0.0800	0.0813	0.0094	29.2548	28.4249	28.1981
T_{P12}	Nominal	6.5286	0.1624	0.0784	0.0802	0.0094	19.8886	20.6615	20.7884
	+25%	6.9368	0.1493	0.0789	0.0774	0.0095	21.9340	21.3933	22.6098
	−25%	7.5018	0.1752	0.0792	0.0823	0.0093	22.5943	22.2710	20.9664
	+50%	7.0580	0.1360	0.0799	0.0782	0.0095	21.7445	21.1819	22.5130
	−50%	6.9254	0.1876	0.0856	0.0808	0.0092	18.1669	20.1967	22.7863
T_{CH}	Nominal	6.5286	0.1624	0.0784	0.0802	0.0094	19.8886	20.6615	20.7884
	+25%	6.6108	0.2859	0.0786	0.0804	0.0094	19.9699	20.9421	22.7109
	−25%	6.4475	0.0122	0.0781	0.0800	0.0094	19.8104	18.9579	20.8058
	+50%	6.6991	0.3892	0.0788	0.0806	0.0094	20.0431	21.0868	22.8353
	−50%	6.3694	0.1914	0.0779	0.0798	0.0094	19.7057	18.8893	20.8444
T_{GT}	Nominal	6.5286	0.1624	0.0784	0.0802	0.0094	19.8886	20.6615	20.7884
	+25%	6.6399	0.1612	0.0785	0.0803	0.0094	19.9976	20.9837	22.7397
	−25%	6.4271	0.1662	0.0782	0.0801	0.0094	19.7628	18.9547	20.8433
	+50%	6.7826	0.1611	0.0787	0.0805	0.0094	21.7960	21.1363	22.7335
	−50%	6.3506	0.1760	0.0781	0.0800	0.0094	19.4862	18.8684	20.9264

Table 5 Comparative system Eigen values for uncertainties

Uncertainties	Nominal	+ 25%	−25%	+ 50%	− 50%
B	−268.75 −1.85 ± 11.25i −14.04 −5.42 −0.83 ± 2.09i −0.32 ± 0.15i	−268.85 −1.92 ± 12.35i −14.04 −5.41 −0.73 ± 2.08i −0.31 ± 0.14i	−268.65 −1.72 ± 10.02i −14.03 −5.43 −0.98 ± 2.09i −0.34 ± 0.17i	−268.94 −1.96 ± 13.36i −14.04 −5.40 −0.66 ± 2.07i −0.30 ± 0.13i	−268.56 −14.03 −5.45 −1.45 ± 8.63i −1.26 ± 2.05i −0.38 ± 0.18i
T_{P12}	−268.75 −1.85 ± 11.25i −14.04 −5.42 −0.83 ± 2.09i −0.32 ± 0.15i	−268.75 −1.70 ± 11.27i −14.03 −5.45 −0.96 ± 2.31i −0.32 ± 0.15i	−268.75 −2.00 ± 11.24i −14.04 −5.39 −0.70 ± 1.83i −0.32 ± 0.15i	−268.75 −1.55 ± 11.29i −14.03 −5.48 −1.10 ± 2.49i −0.32 ± 0.15i	−268.75 −2.14 ± 11.23i −14.04 −5.35 −0.57 ± 1.50i −0.32 ± 0.15i
T_{CH}	−268.75 −1.85 ± 11.25i −14.04 −5.42 −0.83 ± 2.09i −0.32 ± 0.15i	−265.91 −2.86 ± 9.59i −14.80 −4.05 −0.87 ± 2.13i −0.33 ± 0.15i	−273.38 −0.16 ± 13.30i −11.46 −9.07 −0.78 ± 2.05i −0.32 ± 0.15i	−263.99 −15.21 −3.51 ± 8.17i −3.28 −0.92 ± 2.17i −0.33 ± 0.15i	−282.27 −3.12 ± 15.98i −11.37 ± 5.60i −0.74 ± 2.02i −0.32 ± 0.15i
T_{GT}	−268.75 −1.85 ± 11.25i −14.04 −5.42 −0.83 ± 2.09i −0.32 ± 0.15i	−265.79 −1.65 ± 10.11i −10.20 −5.92 −0.84 ± 2.09i −0.32 ± 0.15i	−273.70 −2.17 ± 12.87i −19.87 −5.14 −0.82 ± 2.08i −0.32 ± 0.15i	−263.82 −1.51 ± 92.6i −6.95 ± 1.29i −0.85 ± 2.09i −0.32 ± 0.15i	−283.64 −31.17 −2.77 ± 15.47i −4.95 −0.81 ± 2.08i −0.32 ± 0.15i

5, where it can be observed that for all mentioned uncertainties, these values are found to be in the left half of s-plane. Hence, the closed loop system is inherently stable for system parameters variations. The system dynamic response for uncertainties in Frequency Biasing Coefficient (B), Synchronizing Torque Coefficient (T_{P12}), Steam Turbine Time Constant of Steam Chest (T_{CH}), and Steam Governor Time Constant (T_{GT}) are shown in Figs. 6, 7, 8 and 9 respectively. Further, robustness is demonstrated by applying random step load disturbances varying between −0.1 to +0.2% with a sample time of 100 s and applied in area-1. The random step load disturbance and oscillations of system dynamic response profiles are shown in Fig. 10. Hence, AGC of the power system using 2-DOF PIDF controller gain parameters optimized by ERWCA is capable to deal with random step load disturbances efficiently and also stabilizes the system.

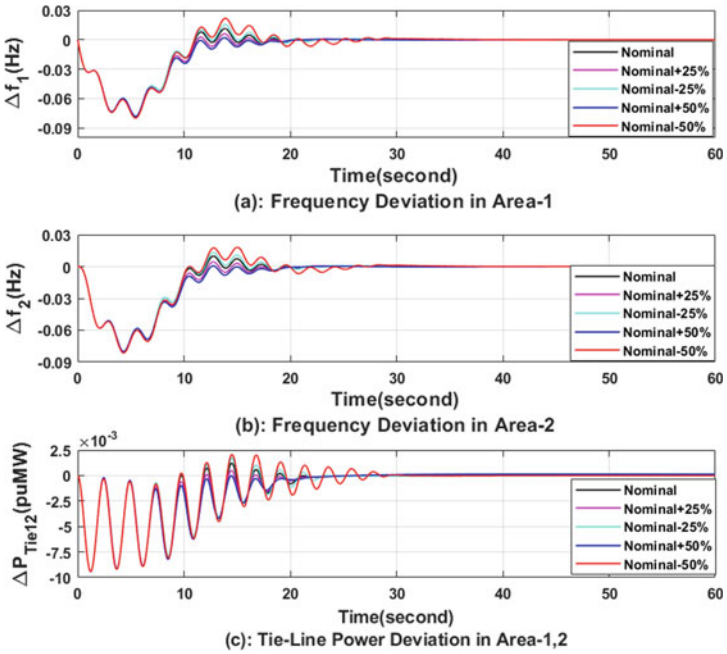

Fig. 6 System dynamic response for uncertainties in frequency biasing coefficient (B)

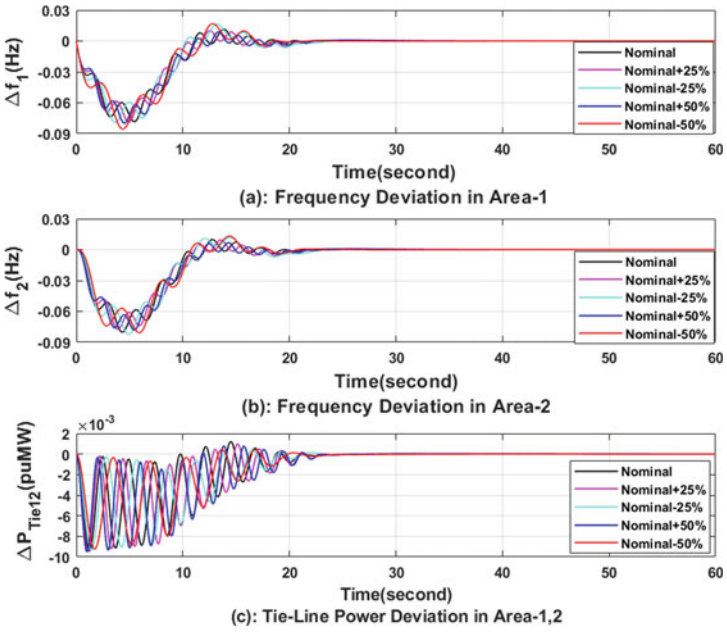

Fig. 7 System dynamic response for uncertainties in synchronizing torque coefficient (T_{P12})

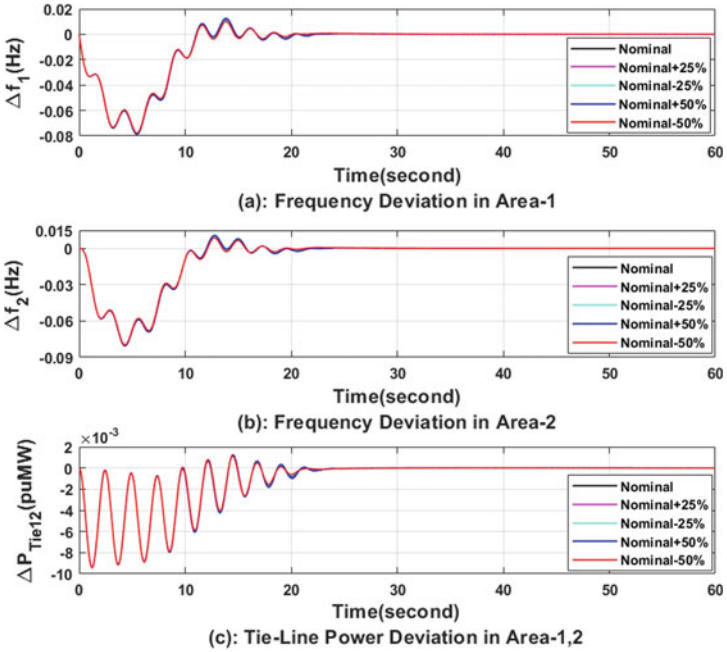

Fig. 8 System dynamic response for uncertainties in steam turbine time constant of steam chest (T_{CH})

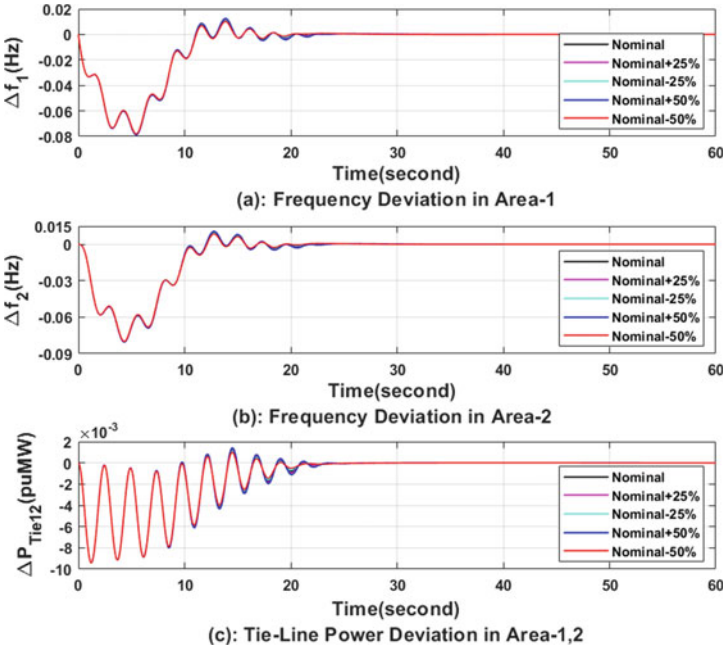

Fig. 9 System dynamic response for uncertainties in steam governor time constant (T_{GT})

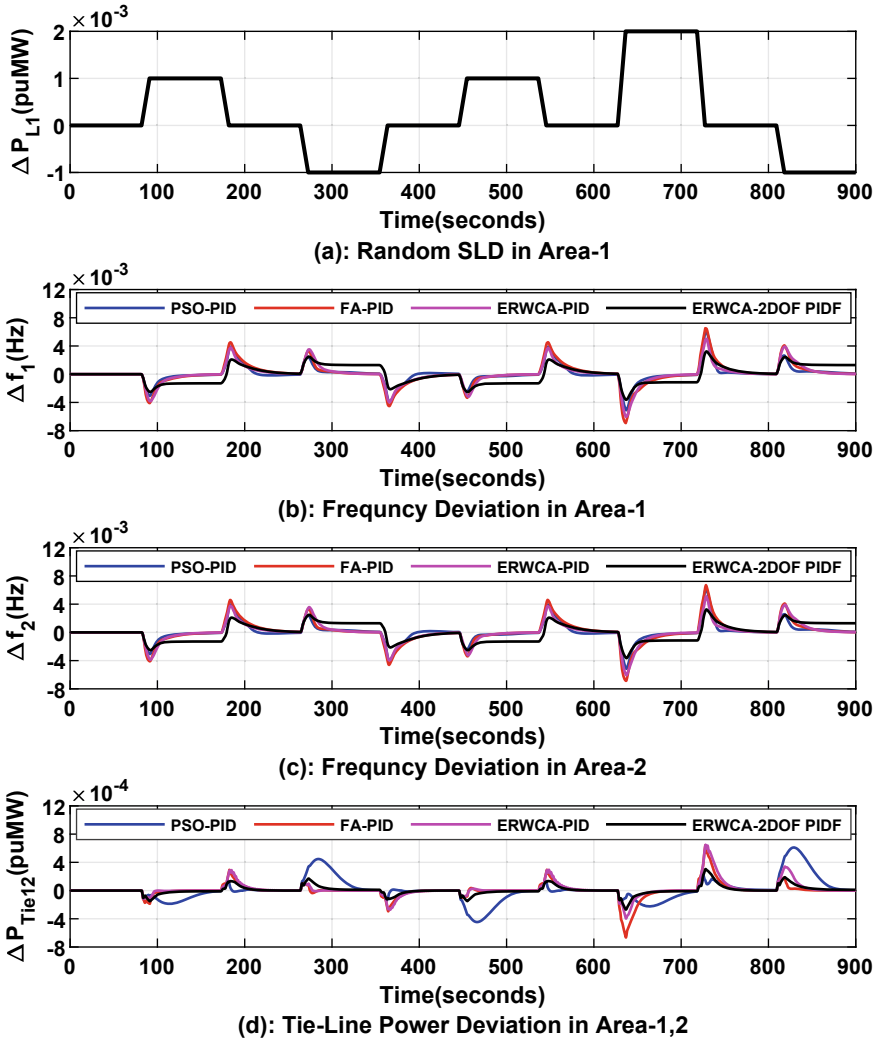

Fig. 10 System dynamic response for uncertainties in random step load disturbances

6 Conclusion

Automatic Generation Control for a realistic power system model with non-linearity was developed and investigated. It was observed that ERWCA optimization technique gives faster convergence than FA and PSO. PID controller tuned by ERWCA technique gives better performance than tuned by PSO and FA which establishes that ERWCA is a better optimization technique for AGC studies. Time domain system dynamic characteristics are analyzed. From the simulation result, it is observed that using 2-DOF PIDF controller optimized by ERWCA, computes the least ITAE value and gives better quality measures as compared to classical PID controllers. The control strategy is robust, performs efficiently under the effect of uncertainties and random load disturbances.

Appendix

System Parameters used for investigation are:

$f_0 = 60$ Hz; $B_1, B_2 = 0.425$ puMW/Hz; $R_1, R_2 = 2.4$ Hz/puMW; $T_{GT1}, T_{GT2} = 0.06$ s; $F_{HP1}, F_{HP2} = 0.31$; $T_{RH1}, T_{RH2} = 10.0$ s; $T_{CH1}, T_{CH2} = 0.3$ s; $K_{PS1}, K_{PS2} = 120$ Hz/puMW; $D = 1/120$puMW/Hz; $T_{PS1}, T_{PS2} = 20$ s; GDB $= 0.036$ Hz; GRC $= 0.001$pu/s; $a_{12} = -1$; $T_{P12} = 0.0866$pu; $A_1 = 0.01$puMW; $A_2 = 0.00$puMW.

The adapted parameters of ERWCA are: $\text{Max}_{\text{iter}} = 50$, $N_{\text{pop}} = 500$, $N_{\text{sr}} = 8$ and $d_{\max} = 10^{-16}$.

References

1. Elgerd OI (2007) Electric energy systems theory. An introduction, 2nd edn. Tata McGraw-Hill, New Delhi
2. Kundur P (2009) Power system stability and control; 8th reprint. Tata McGraw-Hill, New Delhi
3. Bevrani H (2014) Robust power system frequency control, 2nd edn (chapter 1). Springer, New York, pp 19–41. ISBN 978–3–319–07278–4
4. Sahu RK, Panda S, Padhan S (2015) A hybrid firefly algorithm and pattern search technique for automatic generation control of multi-area power systems. Int J Electr Power Energy Syst 64:9–23. https://doi.org/10.1016/j.ijepes.2014.07.013
5. Sahu RK, Panda S, Chandra GT (2015) A novel hybrid PSO-PS optimized fuzzy PI controller for AGC in multi area interconnected power systems. Int J Electr Power Energy Syst 64:880–893. https://doi.org/10.1016/j.ijepes.2014.08.021
6. Panda S, Mohanty B, Hota PK (2013) Hybrid BFOA–PSO algorithm for automatic generation control of linear and nonlinear interconnected power systems. Appl Soft Comput 13(12):4718–4730. https://doi.org/10.1016/j.asoc.2013.07.021
7. Sahu RK, Panda S, Rout UK, Sahoo DK (2016) Teaching learning-based optimization algorithm for automatic generation control of power system using 2-DOF PID controller. Int J Electr Power Energy Syst 77:287–301. https://doi.org/10.1016/j.ijepes.2015.11.082

8. El-Hameed MA, El-Fergany AA (2016) Water cycle algorithm-based load frequency controller for interconnected power systems comprising non-linearity. IET Gener Trans Distrib 10(15):3950–3961

A Critical Assessment of IoT Based Landslide Prediction Systems Using AHP

Abhipsa Kar and Manas Ranjan Das

Abstract Worldwide landslide is a serious hazard that causes great damage not only to the economic and societal development but also to precious human lives. Therefore, there is an urgent need for a good landslide prediction system. Recently, Internet of Things (IoT) has emerged as a popular technology that has a quick response to rapid changes in data. Hence, it has been widely used for landslide monitoring and prediction. Present study focuses on a review of existing IoT based landslide prediction systems. Ten most widely referred systems developed by various researchers have been reviewed. A comparative analysis of their key features has been performed. Prioritization of these ten systems has been done using Analytical Hierarchy Process (AHP) based on three factors, i.e., Cost, number of parameters sensed, and technology. The most suitable IoT based landslide prediction system as obtained from AHP based prioritization is recommended for implementation.

Keywords Landslide · IoT · Prediction · AHP

1 Introduction

Landslide is a geological phenomenon caused due to perceptible downward and outward movement of soil, rock, and vegetation under the influence of gravity. Landslides can be classified according to geotechnical properties of rocks, movement of materials, etc. Landslide movement can be of various types viz., fall, slide, topple, spread or flow. The velocity can vary from very slow to rapid [1]. Mountainous regions are generally considered landslide prone areas. In low-relief areas like roadway and relief excavations, landslides occur as cut and fill failures, river bluff failures, lateral spreading landslides, collapse of mine-waste piles (especially

A. Kar (✉) · M. R. Das
Siksha 'O' Anusandhan (Deemed to be University), Jagamara, Khandagiri, Bhubaneswar, India
e-mail: abhipsakar@soa.ac.in

M. R. Das
e-mail: manasdas@soa.ac.in

M. Mishra et al. (eds.), *Innovation in Electrical Power Engineering, Communication, and Computing Technology*, Lecture Notes in Electrical Engineering 814,
https://doi.org/10.1007/978-981-16-7076-3_43

coal), and a wide variety of slope failures associated with quarries and open pit mining. Landslides may be natural or anthropogenic. There are various morphological, geological, and environmental causes that trigger the occurrence of landslides. Furthermore, anthropogenic activities like construction, farming, deforestation and removal of vegetative cover, etc. are responsible for triggering landslides. These activities cause significant changes in groundwater table and increase the slope gradient resulting in unstable slopes. Landslides result in severe economic losses and casualties. Moreover, these catastrophes cause significant loss of infrastructure by damaging road networks, railways, electrical supply lines, bridges, etc. It also affects the emotional well-being of people by destroying their personal belongings and causing death of their near and dear ones as well as increasing their psychological stress. The Himalayan region, Eastern and Western Ghats, Vindhya range, Nilgiris, and Indo-Burmese range are some of the major landslide prone areas of India [2]. It is very important to identify the parameters which control the occurrence of landslides and develop an early warning system for minimizing these tremendous losses [3]. Protection of infrastructure and population is the major purpose of landslide monitoring. There is a necessity for a real time monitoring system to follow the changes in driving factors for proper forecasting and rapid detection of instantaneous landslides [4, 5]. Various researches have been conducted on prediction, detection, and monitoring of landslides done using various technologies like satellite remote sensing, machine learning algorithms, wireless sensor networks, etc. Furthermore, various follow-up methods viz., LIDAR, electrical resistivity measurements, GPS, electrical resistivity tomography (ERT), etc. have been effectively used for landslide monitoring.

Internet of things (IoT) has emerged as a popular technology that has a quick response to rapid changes in data and transfer of these data to analysis centers [6]. It connects the physical world and virtual things. It has been applied in various fields like smart houses, personal healthcare, water quality analysis, smart traffic management, spatio-temporal prediction, etc. [7]. IoT consists of embedded sensors and controllers which have the capability of communicating with the internet world resulting in modeling of new and innovative processes which help in reducing the associated risks and costs of the existing processes. Along with an increase in yields, they also help in decision making process of the end users. It relates the physical world to the internet through organization of data and exchange of information. The main objective of IoT is to establish a connection between devices viz., vehicles, smartphones, office connected devices, etc. where each device provides information. IoT is a data driven approach that has been effectively used in landslide detection and early warning. Present study attempts a comparative analysis and prioritization of IoTs developed by various researchers for most effective landslide prediction.

2 Causes and Impacts of Major Landslides

Landslides are complex phenomena that have several types of movements based on types of materials. Some of the major landslides which occurred around the globe are mentioned in Table 1 [8].

On 7th August 2010, heavy rainfall triggered a devastating landslide in Zhouqu County of Gannan Tibetan Autonomous Prefecture. Debris flow started flowing towards south county from north county destroying multiple houses along the road killing around 1287 people. By 18th August 2010, 457 people were reported to be missing.

A mid-day cloudburst led to a devastating landslide in Uttarakhand, India in June 2013 which became the worst natural disaster after the Tsunami which took place in 2004. The landslide resulted in heavy flooding of the area. Major overflow was caused due to the blockage of rivers by debris. Heavy rainfall occurred in Haryana, Uttar Pradesh, Delhi, Himachal Pradesh, some parts of western Tibet, and Nepal. The water drained through river system inundating Uttarakhand leading to 89% of casualty killing around more than 5000 people. The floods affected more than 4200 villages.

A landslide hit Malin village of Pune district, Maharashtra, India on 30th July 2014. The major cause of the landslide was intensive rainfall, practice of deforestation in that area, and changing agricultural practices. The landslide killed at least 151 people and 300 cattle.

On 22nd March 2014, a devastating landslide occurred in Washington, USA. Mud and debris flow occurred due to the collapse of a portion of an unstable slope. The

Table 1 Major landslides and their causes

S.no	Event (year of occurrence)	Cause	Nature of cause
1	Landslide in Zhouqu county (2010)	Heavy rainfall	Natural
2	Uttarakhand landslide (2013)	Mid-day cloud burst	Natural
3	Malin landslide, Pune (2014)	Intensive rainfall triggered due to anthropogenic activities like agricultural practices and deforestation	Anthropogenic
4	Washington landslide (2014)	Debris flow due to failure of unstable slope	Natural
5	Debris flow in Columbian town, Mocoa (2017)	Extreme rainfall	Natural
6	Hiroshima landslide (2018)	Dreadful rains	Natural
7	Landslide in Gajapati district, Odisha (2018)	Rainfall due to cyclonic storm Titli	Natural
8	Landslide in Gajapati district, Odisha (2019)	Heavy rains	Natural

landslide engulfed a rural area killing 43 people and destroying 49 homes. It was found that loosening of debris occurred due to previously weakened slope material which was disturbed by the slide which occurred in 2006.

A powerful debris flow hit the Colombian town of Mocoa on 1st April 2017 which resulted in an overflow of rivers. The flood along with vast amounts of rocks and soil, swept through the town causing around 329 deaths, injuring 332 people while 70 were reported as missing.

Hiroshima, Japan suffered extensive damage in July 2018 due to landslides caused due to dreadful rains. The catastrophe killed at least 108 people and the flood induced due to the landslide increased the fatality count by over 120.

In October 2018, the cyclonic storm Titli caused incessant rainfall in Barghara village, Gajapati district, Odisha. The rainfall triggered a landslide that killed around 16 people, including five children.

A landslide that occurred on 24th October 2019 in Gajapati district, Odisha state, damaged around 20 houses. Heavy rainfall triggered the landslide.

Impact of these catastrophes could have been reduced much by an effective early warning system based on advanced technology. Present study projects IoT as a solution in this direction.

3 Comparative Analysis of Key Features of IoT Based Landslide Prediction Systems

IoT has the capability of providing accurate real time monitoring and proper forecasting of landslides by generating alerts well beforehand which will help in evacuation of lives under potential risk and danger. In this section, the key features of ten no's of IoT based landslide prediction systems have been reviewed and comparative analysis among them has been presented.

Moulat et al. [1] modeled a ground-based monitoring system for mountainous zone of North-Western RIF of Morocco. It consisted of multiple sensors in which data acquisition units were installed for recording sensor measurements. The triggering of landslides may occur due to reactivation of the tectonic layering which may lead to huge damage and casualties. They identified the areas susceptible to landslides using two methods viz., Weights of Evidence (WofE) and Logistic Regression (LR) in their previous researches. They developed a robust ground monitoring system with an early warning mechanism for timely and proper evacuation. The real time-monitoring system was employed with automated data processing unit and communication was done via IoT.

Sruthi et al. [2] proposed a system based on IoT viz., Input, data processing, and decision making. Data input was generally done through two sensors viz., flex sensor (to sense angle of bending) and moisture sensor (to measure water content and humidity). After the data acquisition process, the transmission of sensor values was done to the server for comparing them with a threshold value. The decision making

process was done using a Fuzzy logic multi attribute algorithm. The end user was considered as admin in the disaster management center. A notification regarding landslide prediction was sent to the registered user via internet applications after the decision was made.

Mala et al. [7] introduced a ground-based landslide tracking framework using IoT technologies. The IoT based system consisted of autonomous ground sensors like rain gauge sensor (measuring effect of rainfall on slope and pore water pressure), accelerometer (for sensing sudden movements), dielectric moisture sensor (for measuring water content), humidity and temperature sensor (for sensing changes in soil and water with a change in temperature). The wireless and low cost Lora network was used for data transmission to cloud servers. A mechanism of early warning system was designed which had the ability to activate when the sensor values exceeded the threshold value. After collecting data from Lora network, a graph was plotted between sensor results and date using ThingsSpeak which helped in evaluation and real time monitoring.

Singh et al. [4] developed an intelligent monitoring system based on machine learning and IoT. They also studied topographic and hydro-meteorological factors which led to slope failure. A statistical model was established with the employment of standard deviation to an intelligent algorithm. Accurate results were collected from the data collected through a back end developed software that was integrated with IoT for early warning. The early warning system was capable of working separately for zones having different vulnerabilities. The calibration was done with the help of an optimization algorithm.

Chaturbedi et al. [3] designed an IoT based landslide monitoring framework which consisted of sensing units in which accelerometers measured ground accelerations and moistures sensor sensed soil moisture; data logging and thresholding unit and an alert generating unit. In this section, a detailed description of each of these components is provided. GSM is used for transmission of data for better strength in signal. The alert generating unit generates alerts through SMS when the threshold values/critical values were breached. The preregistration of mobile numbers was also provided for sending SMS alerts.

Butler et al. [9] developed an IoT system for efficient monitoring of landslides for Bournemouth Borough Council (UK). The system consisted of sensing devices that were custom-made. The sensing devices transmitted data through wireless network connections like SigFox network to MQTT broker and ELK stack for visualization of data. The system was easily deployed, cost efficient, provided high precision data, and was user friendly.

Bhatt and Papola [10] developed a landslide prediction model for Uttarakhand, India using WEKA tool. The model was developed with the help of landslide data of Uttarakhand. They used two techniques namely J48 and LMT for categorizing the subjects into four classes viz., Non-susceptible, Less-susceptible, Moderately-susceptible, and High-susceptible. The analysis of classifiers was done on WEKA tool and the landslide prediction model was implemented in MATLAB. The landslide prediction models were developed using landslide data of Uttarakhand. They found

that J48 classifier performed better than LMT and also concluded that WEKA tool may be used for landslide prediction in mining areas.

Pitambar et al. [11] proposed a system capable of detecting the conditions responsible for landslides and providing an early warning so that necessary preventive measures could be taken well before the occurrence time. Soil moisture and accelerometer sensors were used for measuring sensing parameters. Transmission of sensed data occurred to Raspberry Pi (Rpi) in the control room via MQTT protocol. The Raspberry Pi was capable of displaying the entire data range as SAFE, MIDDLE and DANGER. When the sensed value exceeded the threshold value, alert was given for MIDDLE and DANGER zone. The pattern and purpose of alert varied according to the zone. First alert was given when the sensed data lied in MIDDLE Zone and final alert was given when the sensed value belonged to DANGER zone.

Abraham et al. [12] determined the threshold values of rainfall which proved to be effective in predicting the occurrence of landslides in the Himalayan regions using IoT. They used multiple false alarms as warning systems which were observed as a major drawback. For a LEWS (landslide early warning system) to be successfully operational, it is obligatory to reduce the number of false alarms using physical monitoring. The active landslide prone slopes of Chibo, Darjeeling Himalayas were monitored using a network of sensors viz., volumetric water content sensors, and MEMS based tilt sensors to enhance the efficiency of the early warning system. Real time monitoring of the slopes was done during the monsoon for three consecutive years (2017–2019). Then, a comparison of data was done with the rainfall data and field observations.

Huang et al. [13] modeled a Series of system along the three Gorges and cases from the literature. Furthermore, they proposed a theoretical model to analyze the impact of deformations in landslide based on the monitoring data from Bazimen landslide, Zigui County; rainfall data of Shahzen and Guizhou, water level change data of the Three Gorges dam. Regression analysis was used to establish correlation and hysteresis of lands. They used BP neural network model for predicting Bezimen landslide and concluded that there needs further improvement in the model accuracy for short term forecasting.

There are various literatures available on IoT based landslide monitoring and prediction systems. But in the present study ten most widely referred IoTs have been considered for analysis based on an opinion from experts. These IoT based landslide prediction systems have been designated as mentioned in Table 2.

Table 3 presents a comparative review of IoT based landslide prediction systems.

4 Critical Evaluation of IoT Based Landslide Prediction Systems by Prioritization Using AHP

Present section focuses on prioritization of IoT based landslide monitoring systems based on performance. Again, performance is assessed considering three selected

Table 2 Designations of various IoT based landslide prediction systems

Developers	Designations of various IoT based landslide prediction systems
Butler et al. [9]	IoT1
Mala et al. [7]	IoT2
Chaturbedi et al. [3]	IoT3
Pitamber et al. [11]	IoT4
Sruthi et al. [2]	IoT5
Bhatt and Papola [10]	IoT6
Huang et al. [13]	IoT7
Singh et al. [4]	IoT8
Abraham et al. [12]	IoT9
Moulat et al. [1]	IoT10

factors. AHP is used to find the relative effectiveness and priority of different IoT based monitoring systems. This method has also been widely used in determining the susceptibility of landslides [14]. The whole process of AHP is implemented in a step-by-step procedure as shown in Fig. 1.

The AHP model is conventionally based on a rating system provided by opinions and judgments of various experts. Three influencing factors have been chosen for the assignment of weights based on an intensive review of the literature and judgments from a panel of technical experts which consisted of three field experts viz., a geotechnical consultant, an IoT engineer, and an environmentalist; three academicians viz., Professor of electronics and communication engineering, Professor of computer science and engineering and Professor of electrical engineering. The selected factors include: cost; number of parameters sensed and technology. The IoT based landslide prediction system have been compared based on these factors on the basis of past literature and experts' feedback. Further calibration was done on a numerical pair-wise comparison scale (Saaty's scale) starting from 1 to 9 [15]. The maximum Eigen value, consistency ratio CR, consistency index CI were computed to check the consistency of the assigned ranks. The matrix with the lowest value of CR (<10%) was taken into consideration for computation of priority vectors.

Cost: The performance of an IoT based monitoring system is directly dependent on the costs of the components used [16]. Hence, before deployment of solution, the solution developer must be conscious regarding the budget. The cost incurred for computational aspects, memory, and privacy aspects may vary accordingly. Budget constraints play a very significant role in selecting the components of IoT. Therefore, this factor has been considered significant in the present study.

Number of parameters sensed: Sensor is a physical device that is responsible for detecting change in the physical system and then converting it into quantifiable data which can be measured by a data acquisition system. The life on earth and the changes in its surroundings are dependent on each other. There have been tremendous advancements in wireless sensor networks in recent years because of small size, low

Table 3 Review of IoT based landslide prediction systems

IoT	Key features	Advantages
IoT 1	Wireless SigFox network MQTT broker and ELK stack	High reliability Low cost User friendly
IoT 2	Autonomous sensing devices fitted with specially tailored suit LORA network powered by Cloud Server Soil moisture sensor, temperature & humidity sensor, rain gauge sensor, accelerometer sensor	Robustness and flexibility Low cost
IoT 3	IoT framework (sensing unit, data logging, and thresholding unit, alert generating unit) MEMS based accelerometers & moisture sensors GSM module	Low cost
IoT 4	Soil moisture and accelerometer sensors MQTT Protocol & Raspberry Pi Cloud Server ThingSpeak	Low power Consumption
IoT 5	Moisture sensor and flex sensor Fuzzy logic algorithm for decision making	Early prediction
IoT 6	WEKA Tool MATLAB	High accuracy and capability
IoT 7	Linear regression BP Neural network model	Accuracy of training network
IoT 8	IoT and machine learning based intelligent monitoring system Standard deviation and intelligent algorithm	Intelligent technique Top-notch sensors
IoT 9	LEWS (landslide early warning system) MEMS based tilt sensors Volumetric water content sensors WSN	Detection of very slow ground movements
IoT 10	Weights of evidence Logistic regression Ground-based monitoring system via IoT	Robust Improved storage efficiency

cost, and capability of powerful data processing and communication [17, 18]. More the no. of parameters that the monitoring system can sense, more robust will be the prediction of ground movements indicating landslides. Hence, this significant factor has been considered in the present analysis.

Technology: The unique platform of IoT is gaining huge popularity with time because of its capability of getting linked to everything. The objective of the present work is to identify the depth and diversities of various technologies used in IoT. In IoT, data is transmitted from the physical system to the world of internet. Hence,

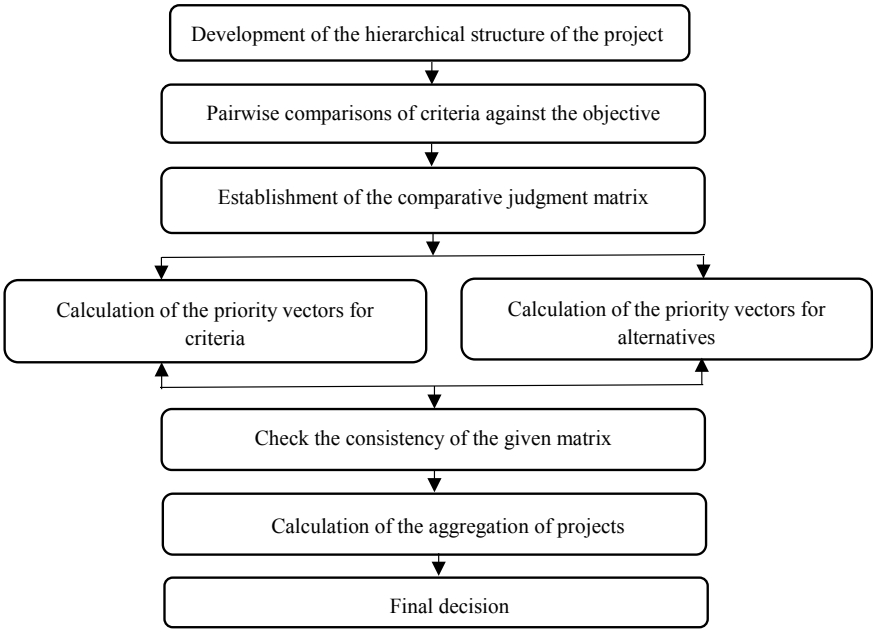

Fig. 1 Flowchart of the step-by-step procedure of AHP

coverage and connectivity are challenging tasks for an IoT application. The system developers always opt for enhancement of their solution by different data processing techniques [19]. Therefore, technology is considered a significant factor in the present work.

Pair-wise comparisons of the ten IoT based landslide systems along with class ranking and weights of influencing factors have been mentioned in Table 4.

The prioritization of three criteria after pair-wise comparison has been given in Table 5.

After the implementation of AHP, the acquired weights of the influencing factors (cost, no. of parameters sensed and technology) and the ranks of different classes (various literature considered in the study), the consistency of the ranks were checked after calculating the Eigen value of these pair-wise comparison matrices. The ranks were accepted as the consistency ratio was less than 0.1. The priorities of the prediction systems based on influencing factors are shown in Table 6.

The matrix of priority vector of different alternatives (10*3) is multiplied with the priority vector of criteria (3*1) to obtain the global rating as shown in Table 7.

After AHP analysis, it has been found that on the basis of cost, the priority of the IoT based landslide prediction system developed by Mathew Butler et al. is highest with a priority of 0.281. On the basis of a number of parameters sensed by the system, IoT based landslide prediction system developed by Mathew Butler et al. is again found to be most suitable with a priority of 0.281. The system developed by Vinay Kumar Singh et al. has been found to be the best on the basis of technology with a

Table 4 Pair-wise comparison matrix with class rankings and weights of influencing factors

Pair-wise comparisons										
Factor	Cost									
	IoT1	IoT2	IoT3	IoT4	IoT5	IoT6	IoT7	IoT8	IoT9	IoT10
IoT1	1.000	2.000	3.000	4.000	5.000	5.000	8.000	9.000	9.000	4.000
IoT2	0.500	1.000	1.500	2.000	2.500	3.500	7.000	8.000	9.000	2.000
IoT3	0.333	0.667	1.000	1.330	1.500	2.000	5.000	7.000	9.000	1.500
IoT4	0.250	0.500	0.752	1.000	2.500	3.500	7.000	9.000	9.000	2.000
IoT5	0.200	0.400	0.667	0.400	1.000	1.500	2.500	5.000	7.000	0.667
IoT6	0.200	0.286	0.500	0.286	0.667	1.000	2.000	3.000	5.000	0.500
IoT7	0.125	0.143	0.200	0.143	0.400	0.500	1.000	1.500	2.000	0.333
IoT8	0.111	0.125	0.143	0.125	0.200	0.333	0.667	1.000	2.000	0.200
IoT9	0.111	0.111	0.111	0.111	0.143	0.200	0.500	0.500	1.000	0.143
IoT10	0.250	0.500	0.667	0.500	1.500	2.000	3.000	5.000	7.000	1.000
Factor	No. of Parameters Sensed									
	IoT1	IoT2	IoT3	IoT4	IoT5	IoT6	IoT7	IoT8	IoT9	IoT10
IoT1	1.000	2.000	3.000	5.000	5.000	7.000	7.000	9.000	3.000	5.000
IoT2	0.500	1.000	1.500	3.000	5.000	8.000	7.000	8.000	5.000	5.000
IoT3	0.333	0.667	1.000	3.000	3.000	5.000	5.000	7.000	0.500	3.000
IoT4	0.200	0.333	0.333	1.000	1.500	5.000	7.000	9.000	0.330	1.500
IoT5	0.200	0.200	0.333	0.667	1.000	3.000	4.000	5.000	0.200	0.667
IoT6	0.143	0.125	0.200	0.200	0.333	1.000	0.333	0.330	0.143	0.333
IoT7	0.143	0.143	0.200	0.143	0.250	3.000	1.000	0.333	0.200	0.250
IoT8	0.111	0.125	0.111	0.143	0.200	3.000	3.000	1.000	0.330	0.200
IoT9	0.333	0.200	2.000	3.000	5.000	7.000	0.500	3.000	1.000	5.000
IoT10	0.200	0.200	0.333	0.667	1.500	3.000	4.000	5.000	0.200	1.000
Factor	Technology									
	IoT1	IoT2	IoT3	IoT4	IoT5	IoT6	IoT7	IoT8	IoT9	IoT10
IoT1	1.000	3.000	3.000	1.500	5.000	7.000	3.000	0.500	5.000	4.000
IoT2	0.333	1.000	2.000	0.500	5.000	7.000	2.000	0.330	5.000	5.000
IoT3	0.333	0.500	1.000	0.333	2.000	8.000	3.000	0.667	5.000	2.000
IoT4	0.667	2.000	3.000	1.000	2.000	9.000	5.000	0.330	5.000	1.500
IoT5	0.200	0.200	0.500	0.500	1.000	5.000	0.330	0.143	0.333	0.667
IoT6	0.143	0.143	0.125	0.111	0.200	1.000	0.200	0.111	0.200	0.500
IoT7	0.333	0.500	0.333	0.200	3.000	5.000	1.000	0.333	2.000	2.500
IoT8	2.000	3.030	1.500	3.000	7.000	9.000	3.000	1.000	7.000	7.000
IoT9	0.200	0.200	0.200	0.200	3.000	5.000	0.500	0.143	1.000	3.000
IoT10	0.250	0.200	0.500	0.667	1.500	5.000	0.400	0.143	0.333	1.000

Table 5 Pair-wise comparison of the influencing factors

Factors	Cost	Number of parameters sensed	Technology	Priority vector
Cost	1	3	5	0.648
Number of parameters sensed	0.333	1	2	0.230
Technology	0.2	0.5	1	0.122

Table 6 Priority vectors of different IoT based landslide prediction systems based on influencing factors

IoT	Priority vector based on cost	Priority vector based on no. of parameters sensed	Priority vector based on technology
IoT1	0.281	0.281	0.192
IoT2	0.179	0.223	0.116
IoT3	0.126	0.128	0.099
IoT4	0.133	0.083	0.157
IoT5	0.075	0.056	0.035
IoT6	0.055	0.018	0.014
IoT7	0.027	0.023	0.061
IoT8	0.020	0.027	0.248
IoT9	0.015	0.102	0.038
IoT10	0.089	0.059	0.040

Table 7 Global priority vector representing the final ranking of the IoT based landslide prediction systems

IoT	Global priority vector
IoT1	0.270
IoT2	0.181
IoT3	0.123
IoT4	0.124
IoT5	0.065
IoT6	0.056
IoT7	0.030
IoT8	0.050
IoT9	0.037
IoT10	0.076

priority of 0.248. Overall, in all the three aspects of cost, no. of parameters sensed and technology, the IoT based landslide prediction system developed by Mathew Butler et al. with a priority of 0.270 is found to be the best among all the ten IoT based prediction systems considered in the present study.

5 Conclusion

The prediction of uncertainty in soil parameters is a complex and tedious process as a slight change in these parameters will affect the strength and deformation behavior of land on a slope. Change detection cannot be done by field observations at the time of occurrence. Therefore, there is a necessity for a real time monitoring system to identify the landslide susceptibility of a slope/ground.

In this context, IoT based early warning system is believed to provide a good solution for effective real time monitoring of slopes. In the present study, an attempt has been made to critically review existing IoT based landslide prediction systems developed by various researchers. Ten numbers of most widely referred IoT based landslide prediction systems have been considered out of a lot for analysis based on expert opinion. AHP based prioritization of these systems has been done which will help policy planners. Following conclusions on the most preferred IoT based landslide prediction system have been drawn.

1. Considering the cost aspect, IoT based landslide prediction system developed by Mathew Butler et al. is found to be most suitable.
2. Considering most critical parameters that a system can sense for better prediction, IoT based landslide prediction system developed by Mathew Butler et al. is again found to be most suitable.
3. If technology advancement will be considered, then the system developed by Vinay Kumar Singh et al. is observed to be most suitable.
4. In overall, considering all three aspects, the IoT based landslide prediction system developed by Mathew Butler et al. is found to be most suitable and hence, recommended for implementation by policy planners.

Present work is a state-of-the-art demonstration of AHP based prioritization of IoT based landslide monitoring systems. More numbers of criteria could be considered for a robust analysis.

References

1. Moulat ME, Debauche O, Mahmoudi S, Brahim LA, Manneback P, Lebeau F (2018) Monitoring system using internet of things for potential landslides. In: The 15th international conference on mobile systems and pervasive computing (MobiSPC 2018), https://doi.org/10.1016/j.procs.2018.07.140
2. Sruthi, Varshini, Balaji (2018) IoT based landslide prediction system. Int J Curr Eng Sci Res (IJCESR) 5(4):2394–0697. ISSN (Print): 2393-8374, (Online)
3. Chaturbedi P, Thakur KK, Mali N, Kala VK, Kumar S, Yadav S, Dutt V (2018) A low-cost IoT framework for landslide prediction and risk communication. https://www.researchgate.net/publication/320719673. https://doi.org/10.1002/9781119456735.ch21
4. Singh VK, Vishal V, Angara PK, Singh TN (2019) Shallow landslides monitoring using the internet of things and machine learning technique. In: Second international conference on smart systems and inventive technology (ICSSIT), IEEE Xplore Part Number: CFP19P17-ART; ISBN: 978-1-7281-2119-2

5. Bai D, Tang J, Lu G, Zhu Z, Liu T, Fang J (2020) The design and application of landslide monitoring and early warning system based on microservice architecture. Geomat Nat Haz Risk 11(1):928–948. https://doi.org/10.1080/19475705.2020.1766580
6. Nayak J, Vakula K, Dinesh P, Naik B, Mohapatra S, Swarnkar T, Mishra M (2021) Intelligent computing in IoT-enabled smart cities: a systematic review. Green Technol Smart City Soc 1–21
7. Mala P, Khan I, Rijal S, Pillai S, Kandel U (2020) Robust early detection mechanism for IoT enabled landslide monitoring using Lora technology. Int J Innov Res Sci Eng Technol (IJIRSET) 9(7):2320–6710. e-ISSN: 2319-8753, p-ISSN: 2320-6710
8. List of landslides-Wikipedia (2021) https://en.m.wikipedia.org>wiki. Accessed date 01 Jul 2021
9. Butler M, Angelopoulas M, Mahy D (2019) Efficient IoT-enabled landslide monitoring. IEEE 978-1-5386-4980-0/19
10. Bhatt C, Papola A (2014) Analysis and prediction of landslides in Uttarakhand using Weka tool. Int J Eng Tech Res (IJETR) 2(8). ISSN: 2321-0869
11. Pitamber P, Patil A, Hardik R, Ravi H, Shubhangi R (2019) IoT based landslide detection and monitoring, 6(2). E-ISSN 2348-1269, P-ISSN 2349-5138
12. Abraham MT, Satyam N, Pradhan B, Alamri AM (2020) IoT-based geotechnical monitoring of unstable slopes for landslide early warning in the Darjeeling Himalayas. Sensors 20:2611. https://doi.org/10.3390/s20092611
13. Huang J, Liu Z, Li N (2014) Study on displacement prediction of landslide based on neural network. J Chem Pharm Res 6(6):1315–1322. ISSN: 0975-7384 (CODEN(USA): JCPRC5)
14. Meghuzi TH, Akhir JM, Rafek AG, Abdullah I (2012) Analytical hierarchy process method for mapping landslide susceptibility to an area along the E-W highway (Gerik-Jeli), Malaysia. Asian J Earth Sci 5(1):13–24. https://doi.org/10.3923/ajes.2012.13.24@2012. ISSN 1819-1886 (Academic Journals Inc)
15. Saaty TL (2008) Decision making with the analytical hierarchy process. Int J Serv Sci 1(1)
16. Chakraborty B, Divakaran DM, Nevat I, Peters GW, Gurusamy M (2021) Cost-aware feature selection for IoT device classification. arXiv:2009.01368v3 [cs.NI] 21 Apr 2021
17. Ramachandran R (2018) The analysis of different types of IoT sensors and security trend as quantum chip for smart city management. https://doi.org/10.9790/487X-2001045560
18. Carri A, Valletta A, Cavalca E, Savi R, Segalini A (2021) Advantages of IoT-based geotechnical monitoring systems integrating automatic procedures for data acquisition and elaboration. Sensors 21:2249. https://doi.org/10.3390/s21062249
19. Balaji S, Nathani K, Santhakumar R (2019) IoT technology, applications and challenges: a contemporary survey. Wireless Pers Commun. https://doi.org/10.1007/s11277-019-06407-w

Design and Analysis of Memductor Based PID Controller for AVR

Sunita S. Biswal, Dipak R. Swain, and Pravat Kumar Rout

Abstract In this work, a design of the PID controller constructed on the memductor model concept and its performance is evaluated further by applying it to an automatic voltage regulator (AVR). The idea is to adjust the PID controller gain settings online through the variation of memconductance during abnormal or transient conditions. The current-feedback operational amplifier (CFOA) is used to regulate the transient response. Further, a charge-controlled grounded emulator (CCGE) circuit is employed for the memductor PID controller (MPID). The proposed approach results in a varying optimum gain parameter of the PID controller instead of constant gain parameter operation in the case of conventional PID controllers. To support the controller's performance, the challenges generally occurred to regulate output voltage automatically by the excitation voltage control in case of synchronous generators under various conditions are taken for investigation and to provide a solution to it. In the end, the superiority and robustness of the memductor based PID controller in comparison to the conventional PID controller are presented and verified with stability analysis in both time and frequency domain form. The comparative simulation results are demonstrated to justify the possibility of real-time application of the proposed approach due to its better performance for numerous power system control applications.

Keywords AVR · PID controller · Memductor PID controller (MPID) · CFOA · CCGE

S. S. Biswal (✉) · P. K. Rout
Department of Electrical and Electronics Engineering, Siksha 'O' Anusandhan University, Bhubaneswar 751030, India

P. K. Rout
e-mail: pravatrout@soa.ac.in

D. R. Swain
Department of Electrical Engineering, CET, Bhubaneswar 751029, India

M. Mishra et al. (eds.), *Innovation in Electrical Power Engineering, Communication, and Computing Technology*, Lecture Notes in Electrical Engineering 814,
https://doi.org/10.1007/978-981-16-7076-3_44

1 Introduction

In general, the AVR is used in power system engineering and is categorized by its dynamic performance [1]. The major objective is to regulate and control the output voltage of an alternator at a precise level through calibrating the generator exciter voltage. Due to the variation in the load of the alternator, the terminal voltage produces a slow and unstable response due to the associated nonlinearity and complex dynamics of the power system and the machine itself. To avoid this situation and to provide the desired level of stability for the AVR [2], it is necessary to add an optimal controller. Therefore, it is required to design a proper control scheme for the AVR which not only enhances the performance of AVR operation but also contributes significantly to the overall stability of the power system [3].

Rapid industrialization and automation industries need to upgrade the process control applications for a stable, smooth, and higher performance in operation. To make it a reality, the system needs a robust and adaptive closed-loop control to obtain an ideal and automatic response. Even with wide progress in digital systems, to date the industrial process extensively used conventional proportional-integral-derivative (PID) controllers [4] with constant gain control parameters. The major attraction for its wide acceptance is its simplicity in design, cost-effectiveness, trouble-free maintenance, and moderate efficiency. The PID-based controller consists of three major parameters (K_p, K_i, and K_d) and these parameter values are needed to be set at their optimal values to achieve accurate and better performance during real-time applications. However, it is found at reduced performance under widely and rapidly varying nonlinear and complex dynamic conditions. In many cases, a steady-state error is accompanied by the conventional PID controller applications. So, it is a formidable task and an open issue for research to develop a superior control strategy-based controller, which varies adaptively online in proportionate to the system variation and associated error occurrence. This paper initiates this issue with an objective to build a new online adaptive PID controller based on the idea model of a memductor. The memductor is employed, when the current flow to the memductor is halted by its memductance, and thus this characteristic states that it is feasible to upgrade the gains of PID controllers online.

Among many suggested methods, the gain parameter estimation through Ziegler–Nichols (ZN) [5] is the oldest and simplest one. However, this approach to set the PID controller's gain subject to complex and large nonlinear systems does not result in improved performance. Apart from that this approach provides undesirable large overshoot and settling time. Later, as an up-gradation to the limitations of the above approach, a better technique is suggested by Cohen and Coon [6] for tuning the PID gain parameters. But, enhanced performance in restricted plant cases did not make the method to be so attractive. The limitation still exists due to constant gain parameters and not easy to implement for adaptive gain computation. Ultimately, this results in poor dynamic response. Afterward, many innovative methods are suggested as a solution to these limitations based on fuzzy logic [7], robust control technology [8], neural network [9], evolutionary optimization [10], and adaptive control method

[11], etc. These methods are not independent of the system parameters and need to change their strategy to make the system adaptive under the change in conditions. The unresolved issue and challenge with regards to controller design to up-date parameters online as a continuous process till an open field of research to focus further.

In this study, an innovative control approach based on the memresistor [12] concept is recommended to improve controller performance. Memristor is a two-terminal element with flux or charge regulated functioning. In the current year, the memristor is applied in the classical control method to resolve the difficulty that the gains of controllers cannot be tuned conveniently. This is because of memresistance. The memristor resistance can be tuned spontaneously in on changing of voltage. Hence a memristor [13] can be accepted as an adjustable gain. In this work, the resistor employed in the PID controller circuit schematic has been replaced by the memristors, and then the impulse voltage is applied to the memristor within the PID [14] controller and then the performance of an MPID controller is analyzed. Memristor [15] is relatively appropriate for control applications because of its compact structure and energy-saving ability. The effective execution of the MPID controller [16] is estimated with its transient response characteristics (peak time, maximum overshoot, etc.) and also compared with the conventional PID controller. The result of MPID controllers demonstrates its peripheral attributes, energy efficiency, quick convergence characteristics, and proficiency over the PID controller. Additionally, the robustness of the MPID has also been investigated by allowing 50% uncertainty in the AVR model. In this study, a charge-controlled incremental type grounded memductor emulator circuit (GMEC) is employed, whose behavioral model has been experimentally confirmed in [13]. An interested reader can obtain a complete theory related to memresistor or memductor in L. Chua, 1971 [17].

The following parts are the organization of this paper. Section 2 describes the basic components of the AVR and its transfer function. Section 3 discusses the design of the conventional PID controller. Section 4 introduces the MPID controller. In Sect. 5 the corresponding comparative simulation results of the proposed approach in contrast to the conventional PID controller for the AVR application are presented. At last, the paper concludes with the findings of the study and future possibilities of research in this direction.

2 AVR Modeling

AVR is regarded as one of the most important power system control schemes, as it operates locally in a synchronous generator. The simple AVR model has four major mechanisms: an amplifier, an exciter, a synchronous generator, and a feedback sensor. The objective of the AVR operation is to retain the terminal voltage $\Delta V_t(s)$ of a generator at a fixed value. This terminal voltage can be regulated at its desired or reference value by the excitation control of the generator even under abnormal and changed conditions. A feedback sensor receives the terminal voltage. The voltage at

the reference terminal is set to $\Delta V_r(s)$. The difference between $\Delta V_r(s)$ and $\Delta V_t(s)$ is used to calculate the error voltage $\Delta V_e(s)$. After that $\Delta V_e(s)$ is amplified and used to control the generator's excitation. The configuration of the AVR design and the dynamic response in the absence of a controller is illustrated in Fig. 1a, b respectively.

The standard parameter ranges for a stable AVR model and time constants are shown in Table 1.

From Fig. 1, the equation for the transfer function of the AVR can be modeled as follows:

$$\frac{\Delta V_t(s)}{\Delta V_r(s)} = \frac{0.1 \times s + 10}{0.0004 \times s^4 + 0.045 \times s^3 + 0.555 \times s^2 + 1.51 \times s + 11} \tag{1}$$

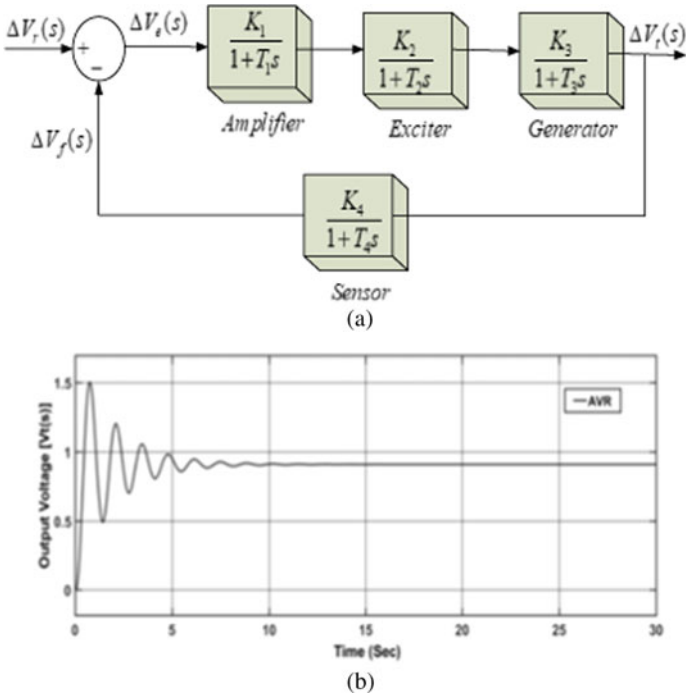

Fig. 1 **a** Block diagram illustration of AVR and **b** dynamic response (not using a controller)

Table 1 Transfer function with AVR model parameter values

Models	Transfer function	Parameter ranges	Values of parameters
Amplifier	$K_1/(1+sT_1)$	$10 \le K_1 \le 400, 0.02 \le T_1 \le 0.1s$	$K_1 = 10, T_1 = 0.1$
Exciter	$K_2/(1+sT_2)$	$1 \le K_2 \le 200, 0.4 \le T_2 \le 1s$	$K_2 = 1, T_2 = 0.4$
Generator	$K_3/(1+sT_3)$	$0.7 \le K_3 \le 1, 1 \le T_3 \le 2s$	$K_3 = 1, T_3 = 1$
Feedback Sensor	$K_4/(1+sT_4)$	$K_4 = 1, 0.01 \le T_4 \le 0.06s$	$K_4 = 1, T_4 = 0.1$

Table 2 Response of the AVR model

Parameters	Values of parameters
Rise time (s)	0.2504
Peak time (s)	0.748
Settling time (s)	6.9823
Maximum overshoot (%)	64.5283

From Fig. 1b, it can be observed that the AVR output voltage $V_t(s)$ is not giving the required performance in terms of large settling time and peak overshoot. Table 2 shows all the parameters values of AVR.

Using the numerical expression given in (1), the pole-zero, and bode plots are illustrated in Fig. 2a, b. These plots indicate that the closed-loop response of AVR is not stable and has poor transient response specifications.

The AVR gain and time constant have been reviewed in numerous research papers. For ease of use, a linearized AVR is analyzed here concerning the huge time constant while escaping saturation and extra non-linearities. Several control strategies have been employed and tested in the present study to a better realization of the AVR along with an upgraded dynamic response.

3 Design of Conventional PID Controllers

The most utilized industrial application controllers are PID. Because of their simplicity, dependability, and adequate performance, these are excellently applied for the design of an efficient AVR system. Figure 3 illustrates the basic structure of the AVR model with a conventional PID controller.

Basically, this conventional controller has three parameters: proportional (P), integral (I), and derivative (D). Each one of these parameters is adjusted to obtain the best possible outcome. The transfer function of the controller can be represented as:

$$T(s) = K_{p.} + K_{d.} \times s + K_{i.} \times \frac{1}{s} \tag{2}$$

The above equation can be incorporated with CFOA as illustrated in Fig. 4. The transfer function of this circuit is as follows:

$$T(s) = \frac{A_{v1}A_{v2}}{A_i}\{(R_1/R_2) + (C_2/C_1) + R_1C_2s + (1/R_2C_1s)\} \tag{3}$$

where $A_{v1,2}$ and A_i denotes the voltage and current gains of the voltage and current followers with values ≈ 0.98 and are placed between Y-X, Z-W, and X-Z terminal respectively. The values of resistances and capacitances are $R_1 \approx 2K\Omega$, $R_2 \approx 6.8K\Omega$, and $C_1 = C_2 \approx 5n$F. From Eqs. (2) and (3), the three controller gains have

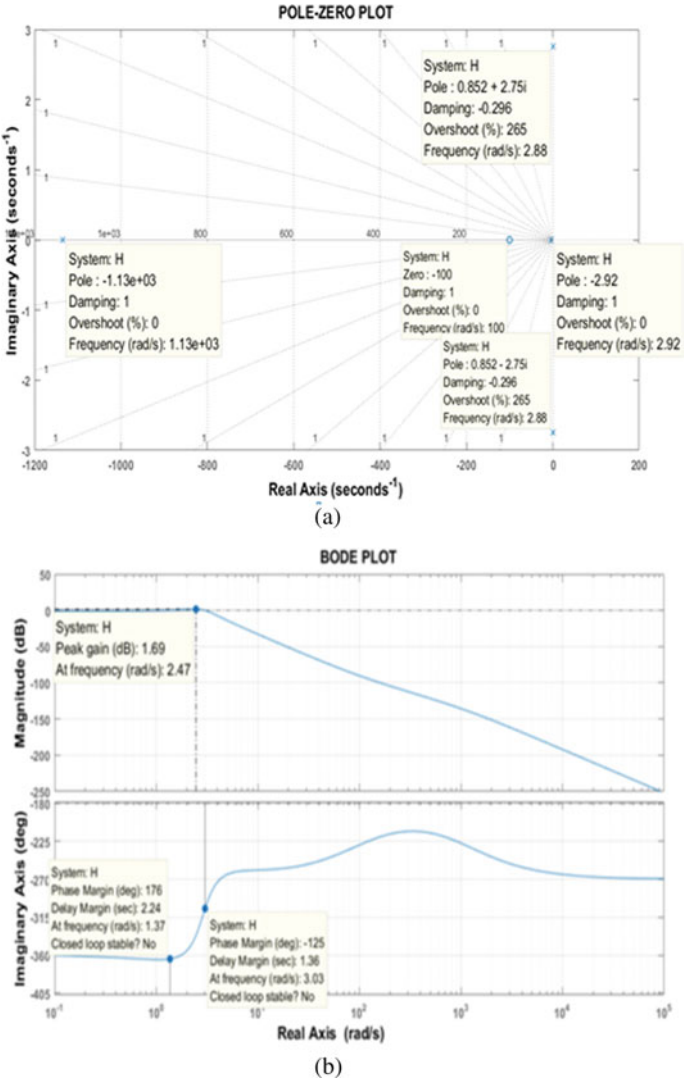

Fig. 2 **a** Pole-zero, **b** bode representation of AVR (not using a controller)

the form:

$$K_p = \frac{A_{v1}A_{v2}}{A_i}\{(R_1/R_2) + (C_2/C_1)\}$$
$$K_d = \frac{A_{v1}A_{v2}}{A_i}(R_1C_2)$$
$$K_i = \frac{A_{v1}A_{v2}}{A_i}(1/R_2C_1) \quad (4)$$

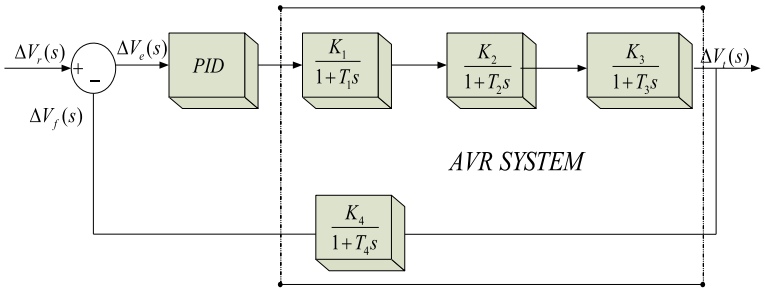

Fig. 3 AVR system with conventional PID controller

Fig. 4 Conventional PID controller in using CFOA

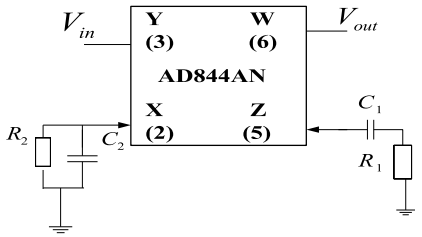

The required dynamic response of AVR through the PID controller depends on the controller gains. However, it is not easy to adjust the settings of the PID controller. Once these parameters are adjusted, they remain fixed throughout the control processes. Therefore, an appropriate tuning of controller gains needs to be used to achieve proper control and the ideal response of AVR. For this reason, a new control strategy has been designed based on the concept of memresistor, which is applied in support of automatic tuning of the controller parameters and is described in the next section.

4 Memductor PID Controller (MPID)

The concept of memductor PID is based on charge-controlled memresistor emulator circuits. The design of memristor emulator circuits and performance is further exploited in this study. There are two versions of this circuit: floating and grounded. Grounded memristor circuits are fabricated using analog multipliers and operational amplifiers. Nevertheless, the connection of these emulator circuits to other circuit parts, whether serial or parallel, is restricted. Furthermore, a floating memristor circuit has been used; however, it needs numerous integrated circuits, making them complicated and massive, with limitation of the low frequency pinched hysteresis loop. In this study, a grounded memductor emulator circuit has been selected. It is simple in design as shown in Fig. 5. According to [15], the memductance has the form:

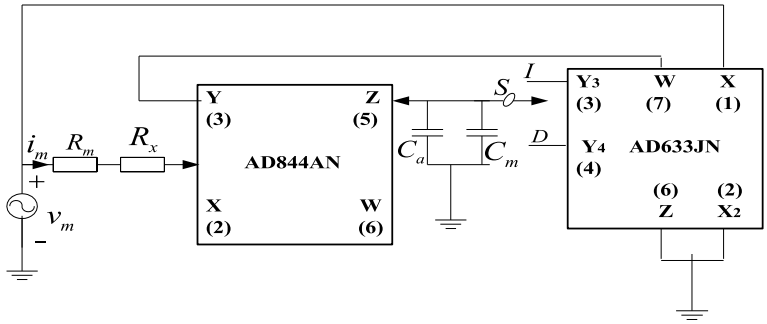

Fig. 5 Circuit of CCGE referred from [6]

$$\frac{i_m(t)}{v_m(t)} = \frac{1}{R_m + R_x} \pm \frac{A_v A_i}{10(R_m + R_x)(C_1 + C_a)} \int_0^t i_m(\tau) d\tau \tag{5}$$

where $R_m \approx 5.8k\Omega$, $R_x \approx 75\Omega$ are the parasitic resistance and the parasitic capacitance $C_a \approx 5.5$pF are linked correspondingly at the terminal X and Z. $A_{v,i} \approx 0.98$, similar as denoted in Eq. (3) and of limited bandwidth. These gains are considered frequency-dependent. Therefore, the MPID controller operating frequency is chosen less than its corner frequency. When the operating frequency is infinite, time 't' becomes zero and the linear time-varying memductor element is also zero. Therefore Eq. (5) has the form:

$$i_m(t) = \frac{v_m(t)}{R_m + R_x} \tag{6}$$

In Fig. 5 when switch 'S' is coupled to terminal 'I' and denoted as (+ve) sign in Eq. (5) an incremental action is acquired and a decremental action is obtained when that switch is coupled to 'D' and denoted as (−ve) sign as given in Eq. (5). In this study, incremental type is used. Using Eqs. (5) and (6), a MATLAB SIMULINK model of the CCGE circuit can be built which is shown in Fig. 6.

The memductor has been developed for 300 Hz operation [15] with $C_m \approx 2.2n$F. As the GMEC circuit has been applied therefore in Fig. 4, R1 and R2 are considered as grounded resistors. As previously discussed memresistor resistance can vary adaptively with its voltage changes. So, any one of the resistors can be replaced by the memductor in the parallel capacitor. In this study, only R2 is chosen to be replaced by the tuneable resistor or memductor M_2 of Fig. 5 to redesign the rise time, peak time and also reduce the overshoot, error [13]. Using Eq. (5), in Eq. (3) the transfer function of an MPID controller has the form:

$$T_m(s) = \frac{A_{v1} A_{v2}}{A_i} \{(R_1 M_2) + (C_2/C_1) + R_1 C_2 s + (M_2/C_1 s)\} \tag{7}$$

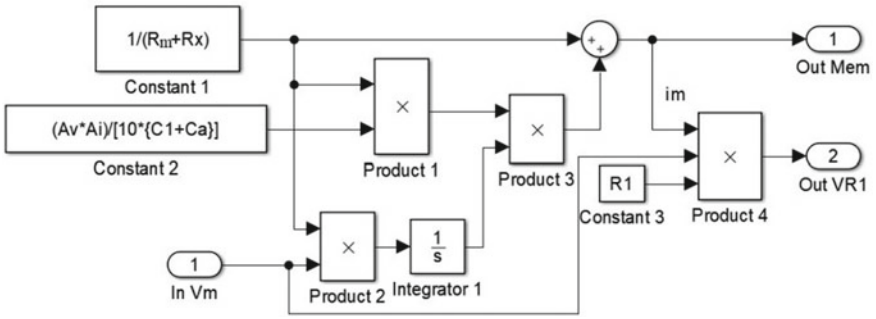

Fig. 6 MATLAB SIMULINK model of CCGE circuit

where $R_2 = \frac{1}{M_2}$. Based on the references [13] and [14] memductance can be increased or decreased and the corresponding mathematical simulations can be done. The MPID controller provides more robustness with additional gain margin and phase margin. MPID can improve system stability in comparison to the PID. MPID controller responds more quickly and stoutly, and in addition to that few parameters of this controller adjust adaptively with the input.

5 Simulation Outcomes and Discussion

This segment scrutinizes the efficacy of the MPID controller applying for the AVR model. This study has been done with the execution in MATLAB (Simulink). The results based on the memresistor technique-based MPID are compared with the conventional PID controllers tuned by the ZN method. Figure 7 represents the

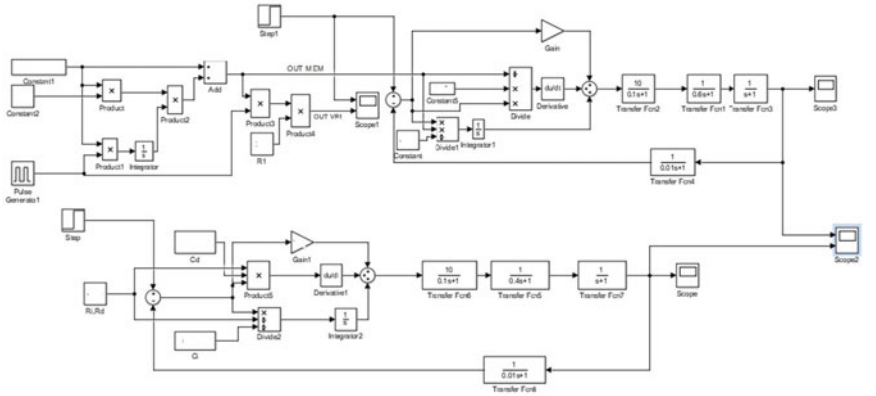

Fig. 7 MATLAB Simulink model of AVR with MPID controller

MATLAB Simulink model of the AVR using the MPID controller. The discussed technique is applied to the accurate and ideal design of MPID to upgrade the dynamic response of the system. The following subsections present the study's significant observations and analysis.

5.1 Transient Response Based Analysis

The classical parameters of PID were first approximated using the ZN method [4]. R, C components, and active devices are employed as integral and differential parts of the conventional PID controller [15], therefore the values are $R_i = R_d = 4K\Omega$, $C_i = 0.05\mu$F and $C_d = 0.4\mu$F. The result shows that the MPID controller with AVR system has an improved response than the conventional controller. Table 3 shows the finest probable values of the parameters PID and MPID controller determined by using MATLAB (Simulation) to the equations given in Sects. 3 and 4.

The above-mentioned table clearly shows that MPID provides a better response than ZN-PID. This is due to the memductor's inherent arbitrariness. This is not possible with the ZN technique. As a result, memconductor PID can be used as a viable solution for complex problems. From Fig. 8, it is obvious that the transient behavior for step response of the MPID approach gives improved results than the PID approach.

Table 3 Performance indices comparison between PID and MPID controllers

Controllers	Maximum overshoot (%)	Peak time (s)	Rise time (s)	Settling time (s)
PID	29	0.620	0.413	2.572
MPID	18	0.6	0. 442	1.847

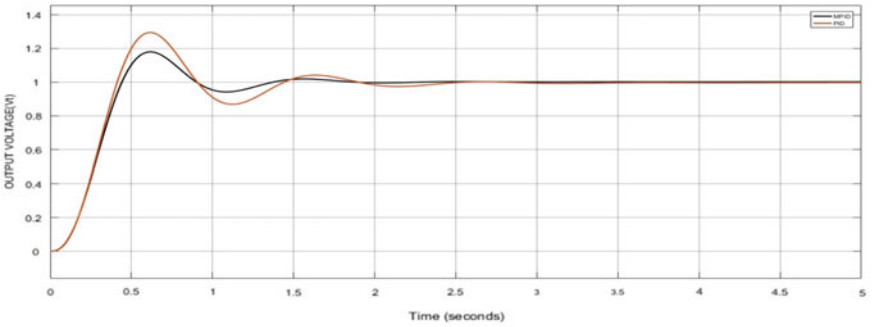

Fig. 8 Transient response of AVR using MPID and PID controllers

5.2 Robustness Based Analysis

This section analyzes the robustness of the MPID controller by varying time constants of the four major parts of the AVR in the range of −50% to +50% within steps of 25% and outcomes are studied. Figure 9 and Table 4 analyze the transient response under these different intervals. As can be observed from this table, all of the deviations for

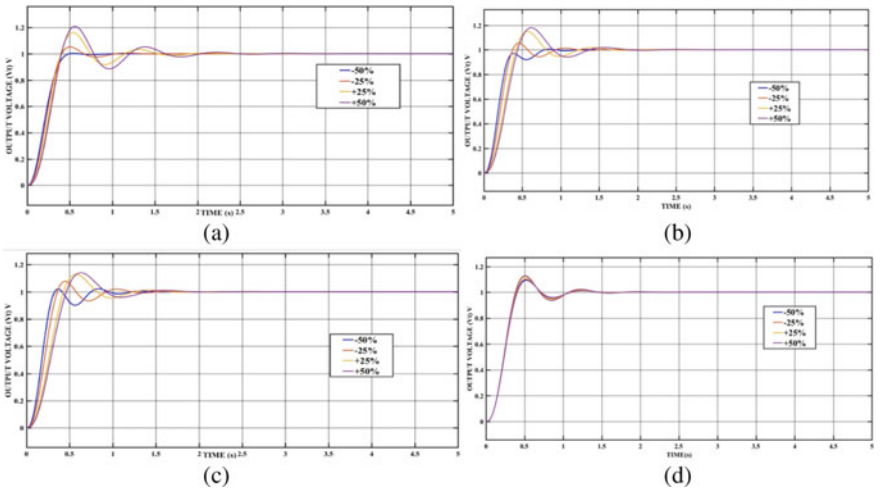

Fig. 9 Output voltage responses line up (−50% to + 50%) for **a** T_1, **b** T_2, **c** T_3, and **d** T_4

Table 4 Robustness study of AVR step response parameters by MPID

Parameter	Rate of change	Peak overshoot (pu)	Rise time (s)	Settling time (s)	Peak time (s)
T_1	−50%	1.004	0.489	1.005	0.540
	−25%	1.053	0.404	1.258	0.502
	+25%	1.163	0.394	2.147	0.540
	+50%	1.210	0.404	2.452	0.560
T_2	−50%	1.006	0.781	1.234	0.848
	−25%	1.055	0.375	1.297	0.460
	+25%	1.150	0.418	1.722	0.568
	+50%	1.180	0.442	1.965	0.620
T_3	−50%	1.021	0.322	1.769	0.366
	−25%	1.079	0. 356	1. 846	0.446
	+25%	1.129	0.432	1.803	0.580
	+50%	1.141	0.466	1.941	0.628
T_4	−50%	1.095	0.408	1.507	0.522
	−25%	1.102	0.399	1.674	0.520
	+25%	1.119	0. 384	1.583	0.518
	+50%	1.128	0. 389	1.801	0.508

the specified condition are equal. In general, system parameters are in tiny ranges. For the time constant T_4, there are essentially no variations. Changes in gains are influenced by larger deviations than changes in time constants. It is proved that the MPID controller provides more robustness besides uncertainties in the AVR model.

5.3 Stability Based Analysis

The analysis of the MPID-AVR performance is also evaluated using two stability criteria (pole/zero and bode plot) and is illustrated in Fig. 10a, b. The findings of the stability study reveal that all the closed-loop poles are on the left side of the s-plane. In addition, the peak gain, gain margin, and phase margin obtained from Bode Plot analysis are shown in Fig. 10b. As a consequence, a stable system and a good frequency response may be achieved.

All two plots obtained from Fig. 10 of the MPID-controlled AVR model are compared to the AVR model shown in Fig. 2. All plots of the above figure yield the necessary information regarding the stability of the AVR model. As a result, it is clear that the MPID-AVR system is considered to be more stable than the AVR without the controller. Hence, the efficiency of the MPID controller for the AVR is confirmed by differentiating its performance from that of the conventional controller for the same model.

6 Conclusion

In this paper, the MPID controller has been demonstrated for the analysis while implemented for controlling the AVR executed for maintaining the output voltage of the alternator in real-time applications. It is found that the simulation and results have fewer oscillations, favorable damping ability, and more stable transient response in comparison to the traditional PID controller. The memristor can vary the time to intelligently control the electrical circuits. As a result, the MPID controller can deal with the nonlinear behaviors and system disruption adaptively. The controller's robustness is proven with the change in AVR model parameters. At the end of this study, the stability of the MPID controller is investigated through pole-zero and bode plots. It is also revealed that the MPID controller in AVR increases dynamic performance. Therefore, because of these qualities of MPID with the AVR model, it can be devoted to the power system application.

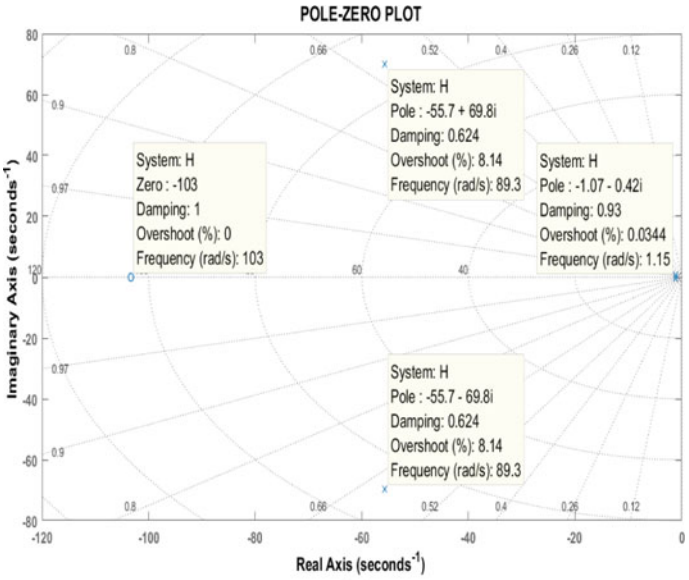

(a)

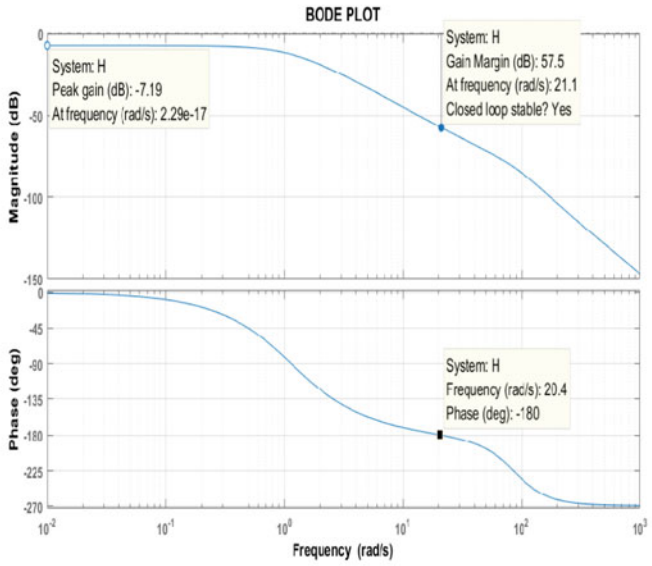

(b)

Fig. 10 **a** Pole-zero, **b** bode representation of AVR with MPID controller

References

1. Kundur PS (2017) Power system stability. In: Power system stability and control. CRC Press, pp 8-1
2. Khalid A, Shahid AH, Zeb K, Ali A, Haider A (2016) Comparative assessment of classical and adaptive controllers for automatic voltage regulator. In: 2016 International conference on advanced mechatronic systems (ICAMechS). IEEE, pp 538–543
3. Biswal SS, Swain DR, Rout PK (2020) Improving the performance of AVR system using grasshopper evolutionary. In: Proceedings of GTSCS (Green technology for smart city and society), vol 151, pp 401
4. Basilio JC, Matos SR (2002) Design of PI and PID controllers with transient performance specification. IEEE Trans Educ 45(4):364–370
5. Hang CC, Åström KJ, Ho WK (1991) Refinements of the Ziegler–Nichols tuning formula. In: IEEE Proceedings D on control theory and applications, March 1991, vol 138, no. 2. IET Digital Library, pp 111–118
6. Azman AA, Rahiman MHF, Mohammad NN, Marzaki MH, Taib MN, Ali MF (2017) Modeling and comparative study of PID Ziegler Nichols (ZN) and Cohen-Coon (CC) tuning method for multi-tube aluminum sulphate water filter (MTAS). In: 2017 IEEE 2nd international conference on automatic control and intelligent systems (I2CACIS), October 2017. IEEE, pp 25–30
7. Modabbernia M, Alizadeh B, Sahab A, Mirhosseini Moghaddam M (2020) Designing the robust fuzzy PI and fuzzy type-2 PI controllers by metaheuristic optimizing algorithms for AVR system. IETE J Res 1–15
8. Gozde H (2020) Robust 2DOF state-feedback PI-controller based on meta-heuristic optimization for automatic voltage regulation system. ISA Trans 98:26–36
9. Salih AM, Humod AT, Hasan FA (2019) Optimum design for PID-ANN controller for automatic voltage regulator of synchronous generator. In: 2019 4th scientific international conference Najaf (SICN), April 2019. IEEE, pp 74–79
10. Köse E (2020) Optimal control of AVR system with tree seed algorithm-based PID controller. IEEE Access
11. Batmani Y, Golpîra H (2019) Automatic voltage regulator design using a modified adaptive optimal approach. Int J Electr Power Energy Syst 104:349–357
12. Kim H, Sah MP, Yang C, Cho S, Chua LO (2012) Memristor emulator for memristor circuit applications. IEEE Trans Circuits Syst I Regul Pap 59(10):2422–2431
13. Sánchez-López C, Aguila-Cuapio LE (2017) A 860 kHz grounded memristor emulator circuit. AEU-Int J Electron Commun 73:23–33
14. Lu Y, Liang Q, Huang X (2018) Parameters self-tuning PID controller circuit with memristors. Int J Circuit Theory Appl 46(1):138–154
15. Wang X, Zhao Y, Liao Y (2011) Dynamic performance analysis of PID controller with one memristor. In: International conference on information science and technology, March 2011. IEEE, pp 1234–1237
16. Sánchez-López C, Morales-López FE, Carrasco-Aguilar MA (2016) High-level simulation of a PID controller based on memristor. In 2016 14th IEEE international new circuits and systems conference (NEWCAS), June 2016. IEEE, pp 1–4
17. Chua L (1971) Memristor-the missing circuit element. IEEE Trans Circuit Theory 18(5):507–519

Solar Photo Voltaic Renewal Energy: Analyzing the Effectiveness of Marketing Mix Strategies

Saumendra Das, Janmenjoy Nayak, Manohar Mishra, and Bighnaraj Naik

Abstract Over the years, fossils fuel is massively used for the purpose of energy. It is the decomposition of dead organisms which releases energy combustion containing more percentages of carbon. In the form of petroleum, coal, kerosene and natural gas fossil fuel have enlarged its usage across the world. Particularly the renewable energy has wider potential in developing countries that balance economy and stability. The renewable energy facilitates the balance in both economic-technical systems and the environment in the world. Now the adoptions of renewable energy technologies are very negligible. The public awareness of its advantages should penetrate the public through a proper marketing mix program that will definitely increase the market share of renewable energy technology. Solar photovoltaic technology is the ultimate development in renewable technology for household purposes which could reduce the greenhouse effect and balance the ecosystem when widely adopted. So a strong adoption theory and a proper marketing strategy will definitely enlarge the scope of solar PV market. This paper is systematic review of selected papers on solar energy adoption and marketing. Here the researcher analyzed that a proper promotional message and product adoption will create a distinct place in solar energy sector.

Keywords Renewable energy · Solar photovoltaic · Marketing strategy · Product · Promotion · Marketing mix

S. Das
Department of MBA, Aditya Institute of Technology & Management, Tekkali 532201, India

J. Nayak (✉)
Department of CSE, Aditya Institute of Technology & Management, Tekkali 532201, India

M. Mishra
Department of EEE, SOA University, Bhubaneswar, Odisha, India

B. Naik
Department of Computer Application, Veer Surendra Sai University of Technology, Burla 768018, India

M. Mishra et al. (eds.), *Innovation in Electrical Power Engineering, Communication, and Computing Technology*, Lecture Notes in Electrical Engineering 814,
https://doi.org/10.1007/978-981-16-7076-3_45

1 Introduction

Over the years, fossils fuel is massively used for the purpose of energy. It is the decomposition of dead organisms that releases energy combustion containing more percentages of carbon. In the form of petroleum, coal, kerosene and natural gas fossil fuel have enlarged its usage across the world. People living in the rural villages have the common practice to use cow dunk in the form of fossil fuel. The proportion of use of fossil fuel created many problems for the earth and also imbalanced the ecosystem. The severity of environmental effect is considering climate change and probability of natural disaster emphasizing the future of fossil fuel demand. Looking at this difficulty, sustainable development and the impact of energy on environment in the world, we must adopt renewable energy to balance the ecosystem. Today, renewable energy such as solar, wind, and geothermal are ready to satisfy the needs for energy across the world. Particularly the renewable energy has wider potential in developing countries that balance economy and stability. The renewable energy facilitates the balance in both economic-technical systems and the environment in the world. We can observe many advantages of renewable energy in the form of security features, fewer dependencies on fossil fuel, conservation of natural resources, pollution, quality energy, and less cost. However, the market share of renewable energy is very less compared to non-renewable energy. People still do not have trust in renewable energy technologies. The adoptions of renewable energy technologies are highly negligible which needs greater awareness among the public to sustain this technology. The public awareness of its advantages should penetrate to the public through a proper marketing mix program will definitely increase the market share of the renewable energy technology and could also bring trust among the public [1].

Considering the factors affecting the adoption of renewable energy technology, a proper policy or guideline by the government should also help to increase the further adoption of renewable energy. There must have a proper strategy on the product quality, price, promotion, and supply chain to market renewable energy. Since the various forms of fossil fuel or conventional technologies for electricity production have captured the market share, it may be a complex task for the marketer or the government to create a specific identity of renewable energy technologies. Among various renewable technologies, solar energy has a long history. Earlier the solar energy was used for water heating, to run engines, or for irrigation purposes. But now there are massive developments in solar energy technologies observed since 1954 when solar photovoltaic (PV) cells were invented at Bell Labs in the United States. The decline in oil price had a phenomenal growth of solar photovoltaic (PV) in 1980. Further, the solar energy market regained its market share in early 2000. The solar-based installation capacity has increased its phenomenal growth of electricity generation to 40 GW in 2010. It also observed that there is an impressive technological shift in solar energy technologies which consists of small-scale photovoltaic (PV) cells to large-scale PV systems that feed into electricity grids. But in recent days there was a drop in solar energy market which is absolutely due to improper policy to control the use of fossil fuel [2]. In their article de Sousa Stilpen et al. (2015),

articulated that Brazil was facing difficulties to provide conventional energy to its public. With the initiation of the government of Brazil, they were able to replace solar energy instead of convention energy and also provided solar photovoltaic techniques on large scale. The government declared auction of solar photovoltaic to all communities [3]. In this connection, we can extend the interest of customers with a proper marketing mix program to market and adopt solar photovoltaic across the world.

In this paper, a brief review is conducted on the usage level of Solar Photo Voltaic Renewal Energy and effect of marketing mix strategies. The paper is classified into six sections. Section 2 is dealing with the background of the study. Section 3 is extending the review of literature, Sect. 4 is conceptual framework, Sect. 5 is critical analysis and finally, Sect. 6 has expanded the discussion and conclusion.

2 Background Study

Solar photovoltaic technology is the ultimate development in renewable technology for household purposes which could reduce the greenhouse effect and balance the ecosystem when widely adopted. Solar PV technology is a cost effective tool suitable for any roof space for solar to subside the nation's electricity demand. [4, 5] The US official reduced the residential PV prices in 2010 and also reduced the installation cost. Despite the suitable efforts of the government, the process of selling solar to consumers needs strong market growth. Several studies revealed that the adoption of PV technologies is absolutely depending on the advantages of cost, awareness about the product, adequate promotion, and third party installation widely adopted [6]. In this connection, the PV installation could attract the perceived risk of consumers vividly where they can compare it with the conventional energy. In their article Lan, Haifeng, et al. (2020) proposed that solar feed in tariff (FiT) policy works as electricity generation through PV system and could promote household solar panel adoption in Australia. The results showed that the installation of household solar panels was correlated with the change of FiT policies. In this paper, the author revealed that installation of PV panels is not only a rational decision making on investment perspective but is influenced by neighborhood peer effect and market speculation [7]. According to Peter Raja et al. (2002), renewable energy has an important role in providing needed power in the context of growing global concern about sustainable energy supplies and protecting the environment from the poor effects of fossil fuel utilization. In their paper, they identified the factors which influenced the adoption of solar-based technology. They suggested that innovation and diffusion of technologies are basic requirements to market solar PV in the global market [8]. So in this competitive world, there must have proper policies structure and marketing plan to sell solar PV.

3 Classification of Marketing Mix Strategies of Solar Power

In this section, various classifications marketing mix such as product, distribution, price, and promotion mix of solar power have been explained. In his article Singh (2016) examined the innovation and diffusion of off-grid power supply, i.e., solar energy in the area without grid. He found that with more than 300 million populations in India innovation and diffusion of recent technology like off-grid solar power will have insignificant adoption due to several reasons. The reasons may be the cost, government policies like subsidies, or proper promotion. It has been seen that most of the companies are not offering proper service to the consumers where they are living without grid power. The likelihood of these firms is slowly defamed due to imbalanced market conditions. The author suggests that without a proper marketing strategy the survival of off-grid technology could not possible. He conducted an extensive field survey about off-grid solar technologies and found that most off-grid solar energy enterprises in India are not functioning in the government subsidy market and more than half are not offering any form of financial benefits to their customers. Hence the firm should take all kinds of necessary measures to secure the position in energy market and also capture the attention of the customers [9]. In their article, Faiers and Charles (2006) studied the consumer attitude towards household solar energy in the UK. They found that the diffusion of innovation model is the most important concept to understand the customer psychology towards household solar energy. From the article, it observed that the attributes of customers towards solar energy is having two characteristics such as early majority and early adopters. Among these two conceptions, early majority have positive perception of environmental characteristics of solar power, its financial and economic, and aesthetic characteristics are limiting adoption. However, the other factors like relative advantage of solar power energy, cost, and its availability also increase the adoption [10].

The adoption of solar PV in US residential was growing quickly because of several reasons such as economic, likelihood, or attitude of the individual customers. In spite of providing several incentive plans by the government, the customers are not ready to adopt the technology. So a proper marketing plan, door to door canvassing, trusted contacts from social networks, third party guarantee could be helpful to increase the market share of solar photovoltaic [11]. In their paper, Kumar et al. (2020) stated that the customer attitude towards solar power energy is influenced by green purchase behavior and government initiatives rather than the promotion or advertisement [12]. There is a growing demand for restructuring electricity power and replacement of renewable energy for a decade. The marketing approaches like advertising or promotion may not be sufficient to attract the customer towards renewable energy because the customer may think of price or other related factors. Now, the customers are demanding environmentally friendly electricity like green power which could act as the voluntary provision of public goods. Therefore the green marketing of renewable energy could able to attract the customer's attention and market the product across the globe [13]. The review of literature is classified according to the marketing mix

Table 1 Different contributions on product mix of solar energy

Sl. No	Contributions	Suggested outcomes	Reference
1	Techno-economic analysis of CSP	• Hybrid technologies PTC with biogas, solar PV, and biomass	[17]
2	Optimal placement and sizing of solar	• Non-polluting and sustainable • Intermittent generation	[18]
3	Natural convection mix-mode solar dryer (NCMMSD) for drying agricultural products	• Drying air • Reduce moisture • Dry agri-products	[19]
4	Life time assessment of solar plant	• Clean electricity	[20]
5	Economic growth of solar energy	• Improving quality of work life	[21]

decision of solar photovoltaic viz. product mix, distribution mix, price mix, and promotion mix decision.

3.1 Product Mix of Solar Power

Marketing of any product will be easy and quick when the quality of product, its effectiveness, consistency, performance, etc. are remarkable. The authors studied that in rural Cambodia, the customers believe in the quality and performance of the solar PV than other attributes. So in order to satisfy the customer, we have to prepare the product according to the customer satisfaction and preferences [14]. Solar photovoltaic is having various features which provide a clean energy source from the sun. It does not release any pollutants or hazardous waste. We can find the solar panels markets in Europe (Germany, Spain, Italy, Greece, France, and Portugal) and also the USA, China, Japan, South Korea, India. Solar photovoltaic is providing uninterrupted service on rural electrification, water pumping, small consumers of electricity, etc. [15]. Hence the solar photovoltaic is highly incredible for smart villages to smart cities. Solar energy can be marketed through CSR model where SHG will support all kinds of technical and managerial support to the customers [16]. Table 1 illustrates various important contributions to product mix of solar energy.

3.2 Distribution Mix of Solar Power

Solar energy supply is an important area of demand and supply of a commodity. The supply or distribution of solar energy in the world is leading to the availability of energy sources. The renewable energy sources in the world have wide demand than the fossil fuel because it produces green energy without pollution. The approximate value of solar energy is about 1.5 $\times$ 1018 kW h/year. So we can appreciate establishing solar energy in different parts of the world to replace conventional energy

Table 2 Different contributions on distribution mix of solar energy

Sl. No	Contributions	Suggested outcomes	Reference
1	Optimal mix of solar PV	• It can minimize the classical power generation • Wide distribution	[26]
2	Minimize annual energy loss	• Rural distribution is strong • Expansion of distributed generation (DG) units	[26]

[22]. The change in weather conditions is also depending on the distribution of solar PV market. Due to climate change variable renewable energy (VRE) will help to wide distribution of the solar energy among the common customer [23]. Therefore marketing and distributing solar energy is significantly affected by climatic conditions [24]. In order to strengthen the market situation, the Thailand government made two different models of solar energy distribution, i.e., Stand Alone System (SAS) and Grid Connected System (GCS). The SAS is used for DC current while GCS is for AC. The SAS is very cheap and has wide acceptance while GCS recharges the battery for water pump, lighting, etc. However, the distribution of solar PV and others requires a proper distribution system to connect all kinds of customers [25]. Table 2 views the distribution mix of solar energy such as an optimal mix of solar PV and minimization of energy loss.

3.3 Price Mix of Solar Power

According to the experts, price is a deterministic factor to expand the market. In case of solar PV market in developing countries, it is observed that the price of the solar PV and its equipment are significantly expanding the market. Today the demand of auction sales is also balancing the price to stimulate the demand for solar PV [27]. The price of VRE is an alternative decision to capture the attention of consumers. The author explained that reduction of price in the solar energy segment improves almost 15% market penetration [28]. So a proper pricing mix decision like discounts, rebates, benefits, off, and other relative concessions should be provided to attract the customer towards the solar PV. Various other contributions on price mix of solar energy are represented in Table 3.

3.4 Promotion Mix of Solar Power

Next to the pricing decision, the marketing of a solar PV is hugely dependent on the awareness of renewable energy. The combustion of fossil fuel effect and carbon emission greatly affected the air which converted the climate change and also greenhouse

Table 3 Different contributions on price mix of solar energy

Sl. No	Contributions	Suggested outcomes	Reference
1	Price of PV installation and a battery	• Increase the electricity price than the demand for battery increases	[29]
2	Incentive program to encourage solar power	• Early adopters will get more incentives than late adopters	[30]
3	Economic developments of solar energy	• Less subsidy • Lack of awareness • Institutional support is less	[31]
4	Price reduction in solar PV	• More supply reduction in price	[3]
5	Cost reduction and government policies on solar energy	• Solar energy benefits from tariff rates, taxes, or other incentives provided by the government	[2]
6	Solar portfolio management	• Cost reduction and tax incentives to customers	[32]

effect. Therefore a proper and institutional promotional program like advertising, publicity, public relations, sales promotion, etc. has to extend its service to enlarge the solar energy market. Perception of buyers towards solar PV is incredible with various benefits posed by the public like financial, environmental, technical, social, aesthetic, etc. Most people believe that the roof top solar PV is wastage of investment. In this regard, a better promotional message should reach the individuals to attract attention and create awareness on the solar PV [33]. The awareness of solar energy can also be brought through public preferences. In the Italian market, the public pays 3.5 times more attention to solar energy. So some kind of incentives or other benefits should be provided to attract the customers [34]. In some countries such as the USA, Germany, the UK, and China the government has taken initiations to promote solar energy for sustainable development of renewable energy [35]. In the same way, the government of Srilanka has taken the initiative of green power investment rather than the conventional source of energy. In this article, the author tried to emphasize 110 households and 25 marketing experts on the adoption of public solar energy. The study revealed that systematic strategies such as cause-related, community-based, and personal selling could promote solar power in Srilanka [36]. Basically, solar energy contributes to replace solar energy which could protect the environment and provide economic benefits. In his article, the author asked 20 in-depth questionnaires to the public of Ho Chi Minh City, Vietnam on the environmental and economic benefits of solar energy. He found that there was no proper integrated marketing communication (IMC) to promote solar energy and also no awareness created on environmental and economic benefits of solar energy [37]. Different proposed promotion mix strategies such as solar energy policies, Government policy, and other hybrid technologies with their benefits are illustrated in Table 4.

Table 4 Different contributions on promotion mix of solar energy

Sl. No	Contributions	Suggested outcomes	Reference
1	Promote solar energy policies	• FIT, RPS, and incentives are to be promoted • Environment friendly energy	[38]
2	Promote Government policy on cost reduction	• Incentives • Technical features • Economic benefits	[2]
3	Promotion of solar PV in Malaysia in Covid-19 era	• Govt. announced US$ 2.9 billion • Installation of solar PV in roof top • Enhance the solar energy usage	[39]
4	Motivations and extensive development of solar energy conversion	• Rural dwellers	[40]
5	Sustainable tourism development through solar PV	• ICS solar water heaters • The colored flat plate-collectors, the CPC collectors • Hybrid PV/T collectors	[41]
6	Promoting hybrid technologies	• PV panel with battery storage unit • Diesel back-up provides 17% of load demand	[42]

4 Conceptual Framework

Among all types of renewable energies solar photovoltaic is an important tool that provides energy to all kinds of households. In common solar cells (solar PV) convert sunlight directly into electricity. The solar PV is also efficient to provide energy for various purposes such as households, agriculture, or business. Therefore it has more importance than conventional or classical energy. However, a proper marketing mix strategy is required to sustain and develop solar energy in this twenty-first century. The massive use of fossil fuel and high combustion of carbon damaged the ecosystem throughout the world. With this effect, climate change and greenhouse effect are also happing. In order to observe this kind of situation, the adoption of renewable energy with systematic marketing mix is necessary. Now the social marketing could be the best option to integrate with marketing mix for the state, organizations, businesses, and consumers where separate policy will help to market the solar energy [43]. Therefore, the policymaker or government should provide the products according to the customer preferences and willingness.

In EU member states, it has been observed that solar thermal technologies (STT) are mature enough. However in some EU states the solar heating, solar households, etc. are in primary conditions. Thereby it needs a lot of developments in marketing mix strategy where major strengths and weaknesses of STT were examined to remove the barriers opposed to RTD (Research and technology development). Further, the policy should be adopted to create awareness, and also government should take

necessary steps [44]. So in order to establish a marketing strategy for solar photovoltaic and its adoption, the marketing mix decision such as product, place, price, and promotion (4p's) have to implement through different stakeholders.

Figure 1 exhibited the marketing mix strategy which will be applicable to develop the product quality, variety, design, features, brand name, packaging, size, warranty, returns of a product. These tools could perceive the expectation of the consumers in different aspects. Solar photovoltaic market across the world is also depending on the product preferences of consumers. Most of the consumers feel that the product is not fulfilling the expectation and also not providing sufficient energy. Hence the product quality, design, features should be changed to adopt the solar photovoltaic panel installed on the top of the roof. In this context least price, discounts, allowance, payment periods, credit terms, etc. are also the marketing tool to motivate the customers to adopt the solar photovoltaic. Most of the developing countries have initiated to provide a subsidy, allowance for installation, and credit facilities for the solar photovoltaic. Place or distribution of the solar energy is also an important tool to attract the customer. We can observe that some of the countries are distributing solar energy through standalone systems and grid generated systems also. It has more demand in the developing countries where they distribute solar energy through solar transmission with the help of renewable energy. Final stage of marketing mix is promotion. In this segment, the components such as advertisement, public relations, sales promotion, etc. are the tools to develop the marketing strategy. Solar photovoltaic is also promoted through greater awareness among the public and through government initiatives. Hence a proper marketing mix strategy could help the system for adoption and distribution of solar photovoltaic across the world.

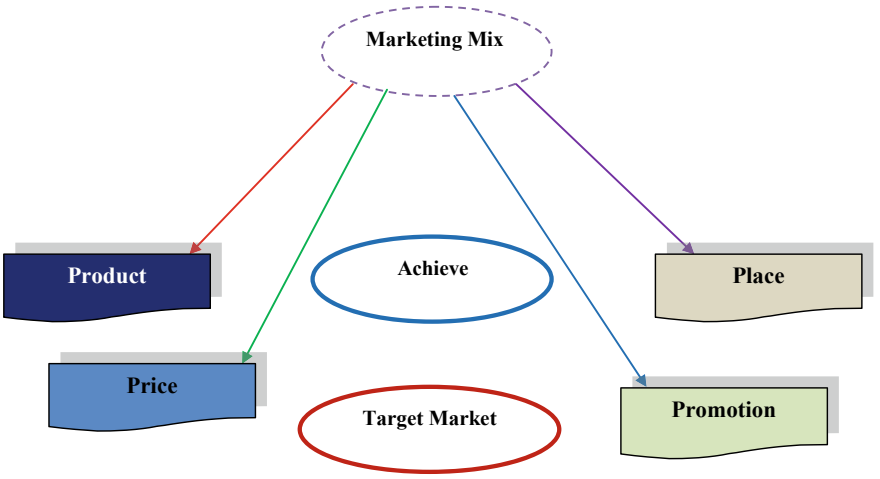

Fig. 1 4p's of marketing mix

5 Critical Analysis

In this section, the analysis is made on the basis of adoption of solar photovoltaic and implementation of marketing mix strategies to ensure adoptability. After a thorough revision of the literatures, it has been observed that the adoption rate of solar energy is very less as compared to conventional forms of energy. Till now people are addicted to alternate current. Hence it requires a proper analysis to accept the solar photovoltaic for household use.

5.1 Adoption of Solar Photovoltaic

The commercialization of PV has conceptually accepted the classical adoption theory. This process will reveal whether to accept or reject the product. The classical method concentrated on the process of awareness, interest, evaluation, trial, and adoption. Some of the theories said that existing knowledge is also important to select or reject the product. The knowledge of the person creates an attitude to persuade the product either for selection or rejection. So knowledge, persuasion, decision, implementation, and confirmation may help to make the decision before adopting the product. Particularly, the adoption of solar photovoltaic is depending on innovation and diffusion where the mindsets of the customer need to be changed. The adoption and acceptance of solar PV systems depend on a variety of socio-techno-economic factors. Figure 2 exhibited that motivation and role of government are very important areas where subsidy, enhancement of electricity charge or incentives could turn the customer expectation largely. Next to it, the role of supplier or distributor is also important because the supplier could identify the areas, where till now no electric power is supplied. Particularly in the rural areas where the alternative current is not available, solar photovoltaic could be the major form of adoption. The context and demonstration sites are also viable factors for the adoption of solar energy. The context of the policy and exhibition are also important factors to penetrate the message among the customers. In this connection finance, experience, and existing knowledge will help to promote the solar photovoltaic.

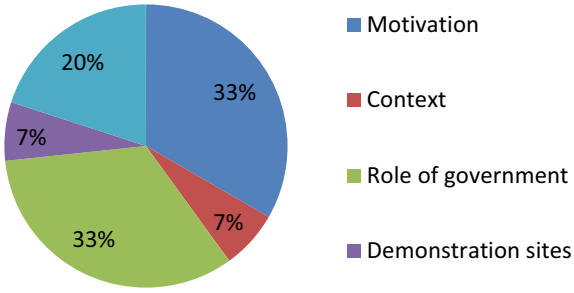

Fig. 2 Adoption of solar PV

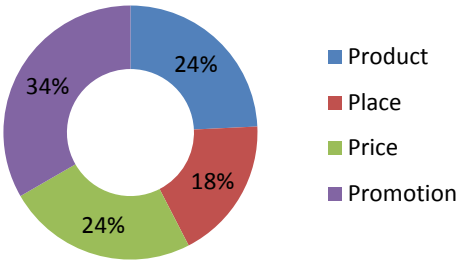

Fig. 3 Marketing mix strategy

5.2 Implementation of Marketing Mix Strategy

Without proper marketing and advertising, solar PV will not be accepted by the public at large. In this connection, there is wide diversification of marketing strategy tool should be applicable to expand the market and motivate the customer. Figure 3 depicted the role of marketing strategy for solar PV market. The figure exhibited that most of the authors suggested the need for promotional tools to attract customers. In this connection, the government or the supplier should plan proper promotional strategies like advertising, sales promotion, publicity, or public relation to differentiating the use of conventional forms of energy from renewable energy. The people should also understand the benefits of renewable energy and adopt it across the world. The figure is also exhibiting about the product and price. Most of the developing countries are now providing incentives or other allowance to attract the customer towards the solar energy. Some of the countries developed the product quality, size, design, or other features of solar energy. They used to provide wide varieties of facilities which could attract the customer on solar PV.

By observing the various aspects of marketing strategy, the policymaker or the government should decide the use of solar PV in rural and urban areas and should motivate the customers. The adoption of this equipment will definitely penetrate due to shortage of fossil fuel and high combustion of carbon. In response to the safety measures, the solar PV will be used as an important household item like others.

6 Discussion and Conclusion

Solar photovoltaic is the ultimate development in renewable technology for household purposes which could reduce the greenhouse effect and balance the ecosystem when widely adopted across the world. Solar PV technology is a cost effective tool suitable for any roof space for solar to subside the nation's electricity demand. It can also replace the conventional form of energy. The high consumption of electricity, petroleum products have already polluted the environment and greatly affected the ecosystem. In this regard, the present study reviewed the prospects and challenges of renewable energy in general and solar PV in particular. The rise in the adoption of

these technologies could balance nature and maintain harmony in society. To review the prospects of these technologies, the study has been divided into six different sections. Section 2 pointed out the background of the study with a special emphasis on various cost effective policies for PV power usages. In this section, the adoption and marketing strategies of solar PV are enlarged. Section 3 brought the literature gap on adoption and marketing strategies of solar PV. Section 4 is dealing with the conceptual framework of marketing mix where 4p's of marketing mix has been elaborated. Section 5 is about critical analysis where it observed that innovation and diffusion of these technologies and a proper marketing mix strategy could be helpful to sell solar PV. So motivation, persuasion, and presentation of the technology are important to sell the solar PV.

Further, it is apt to say that being a developing country, effective planning on the usage of photovoltaic power is required for societal growth as well as industrial progress. More importantly, researchers should focus on the hybridization of different renewable energy sources for the reduction of heavy dependency on conventional energy sources. From the study, it can be realized that to meet the future power needs of India (with steady growth in industrialization), usage of renewable energy may provide a sustainable solution for new green and pollution free country. Also, the exact use of existing resources and infrastructure plays an important role in generation of power at different levels. The major concern of India is to analyze the proper impediments of implementation of solar power systems through efficient intelligent computing tools. These tools are useful for capitalizing the analysis of solar generation systems as well as the requisite size of photovoltaic system. So, the use of advanced software packages may overcome the limitations of traditional simulation packages and make an efficient authentication of advanced models. Hope with a variety of advanced energy based tools and solutions, proper adoption of various marketing mix strategies, advertisements with promotional activities on renewable energy, and other important planning strategies, the goal of the Prime Minister of India is to reach 100 GW solar power installation by 2022 will be on a leading path towards the next level development of the country.

References

1. Sharifi M et al (2019) Forecasting of advertising effectiveness for renewable energy technologies: a neural network analysis. Technol Forecast Soc Change 143:154–161. https://doi.org/10.1016/j.techfore.2019.04.009
2. Timilsina GR, Kurdgelashvili L, Narbel PA (2012) Solar energy: markets, economics and policies. Renew Sustain Energy Rev 16(1):449–465. https://doi.org/10.1016/j.rser.2011.08.009
3. de Sousa Stilpen DV, Cheng V (2015) Solar photovoltaics in Brazil: a promising renewable energy market. In: 2015 3rd International renewable and sustainable energy conference (IRSEC). IEEE. https://doi.org/10.1109/IRSEC.2015.7455077
4. Mishra M, Dash PB, Nayak J, Naik B, Swain SK (2020) Deep learning and wavelet transform integrated approach for short-term solar PV power prediction. Measurement 166:108250
5. Swain MK, Mishra M, Bansal RC, Hasan S (2021) A self-powered solar panel automated cleaning system: design and testing analysis. Electr Power Compon Syst 1–13

6. Wolske KS et al (2018) Accelerating demand for residential solar photovoltaics: Can simple framing strategies increase consumer interest?. Glob Environ Change 53:68–77. https://doi.org/10.1016/j.gloenvcha.2018.08.005
7. Lan H et al (2020) An evaluation of feed-in tariffs for promoting household solar energy adoption in Southeast Queensland, Australia. Sustain Cities Soc 53:101942. https://doi.org/10.1016/j.scs.2019.101942
8. Peter R, Ramaseshan B, Nayar CV (2002) Conceptual model for marketing solar-based technology to developing countries." Renew Energy 25.4:511–524. https://doi.org/10.1016/S0960-1481(01)00080-5
9. Singh K (2016) Business innovation and diffusion of off-grid solar technologies in India. Energy Sustain Dev 30:1–13. https://doi.org/10.1016/j.esd.2015.10.011
10. Faiers A, Neame C (2006) Consumer attitudes towards domestic solar power systems. Energy Policy 34(14):1797–1806. https://doi.org/10.1016/j.enpol.2005.01.001
11. Sigrin B, Pless J, Drury E (2015) Diffusion into new markets: evolving customer segments in the solar photovoltaics market. Environ Res Lett 10.8:084001. https://doi.org/10.1088/1748-9326/10/8/084001
12. Kumar V, Hundal BS, Syan AS (2020) Factors affecting customers' attitude towards solar energy products. Int J Bus Innov Res 21(2):271–293. https://doi.org/10.1504/IJBIR.2020.104819
13. Wiser RH (1998) Green power marketing: increasing customer demand for renewable energy. Utilities Policy 7(2):107–119. https://doi.org/10.1016/S0957-1787(98)00005-8
14. Rijke KC, Diehl JC, Schoormans JPL (2009) Introducing solar products in rural Cambodia: a quest for the right marketing mix in base of pyramid markets. Online. Accessed 13 June 2015
15. Cristian CD (2008) A marketing strategy on photovoltaic market. ANALELE UNIVERSITĂŢII DIN ORADEA, p 824
16. Das SS Marketing models for solar products in rural areas of Odisha
17. Islam MT, Huda N, Saidur R (2019) Current energy mix and techno-economic analysis of concentrating solar power (CSP) technologies in Malaysia. Renew Energy 140:789–806. https://doi.org/10.1016/j.renene.2019.03.107
18. Kayal P, Chanda CK (2015) Optimal mix of solar and wind distributed generations considering performance improvement of electrical distribution network. Renew Energy 75:173–186. https://doi.org/10.1016/j.renene.2014.10.003
19. Simo-Tagne M et al (2020) Numerical analysis and validation of a natural convection mix-mode solar dryer for drying red chilli under variable conditions. Renew Energy 151:659–673. https://doi.org/10.1016/j.renene.2019.11.055
20. Piemonte V et al (2011) Life cycle assessment of a high temperature molten salt concentrated solar power plant. Solar Energy 85(5):1101–1108. https://doi.org/10.1016/j.solener.2011.03.002
21. Sharma A (2011) A comprehensive study of solar power in India and World. Renew Sustain Energy Rev 15(4):1767–1776. https://doi.org/10.1016/j.rser.2010.12.017
22. Mohanty S et al (2017) Forecasting of solar energy with application for a growing economy like India: survey and implication. Renew Sustain Energy Rev 78:539–553. https://doi.org/10.1016/j.rser.2017.04.107
23. Eising M, Hobbie H, Möst D (2020) Future wind and solar power market values in Germany—evidence of spatial and technological dependencies?. Energy Econ 86:104638. https://doi.org/10.1016/j.eneco.2019.104638
24. Book T (1999) Marketing and selling solar energy equipment. Renew Energy 16(1–4):800–804. https://doi.org/10.1016/S0960-1481(98)00285-7
25. Pattara premcharoen M et al (2007) Marketing model for solar energy in Thailand. J Renew Energy Smart Grid Technol 2(1):56–64
26. Atwa YM et al (2009) Optimal renewable resources mix for distribution system energy loss minimization. IEEE Trans Power Syst 25(1):360–370. https://doi.org/10.1016/j.renene.2015.06.010

27. Dobrotkova Z, Surana K, Audinet P (2018) The price of solar energy: comparing competitive auctions for utility-scale solar PV in developing countries. Energy Policy 118:133–148. https://doi.org/10.1016/j.enpol.2018.03.036
28. Hirth L (2013) The market value of variable renewables: the effect of solar wind power variability on their relative price. Energy economics 38:218–236. https://doi.org/10.1016/j.eneco.2013.02.004
29. Mulder G et al (2013) The dimensioning of PV-battery systems depending on the incentive and selling price conditions. Appl Energy 111:1126–1135. https://doi.org/10.1016/j.apenergy.2013.03.059
30. Swezey B, Bird L, Herig C (2002) Supporting solar energy development through green power market. IEEE Trans Power Syst 1–5
31. Wang Z et al (2015) Solar water heating: from theory, application, marketing and research. Renew Sustain Energy Rev 41:68–84. https://doi.org/10.1016/j.rser.2014.08.026
32. Herche W (2017) Solar energy strategies in the US utility market. Renew Sustain Energy Rev 77:590–595. https://doi.org/10.1016/j.rser.2017.04.028
33. Kratschmann M, Dütschke E (2021) Selling the sun: a critical review of the sustainability of solar energy marketing and advertising in Germany. Energy Res Soc Sci 73:101919. https://doi.org/10.1016/j.erss.2021.101919
34. Vecchiato D, Tempesta T (2015) Public preferences for electricity contracts including renewable energy: a marketing analysis with choice experiments. Energy 88:168–179
35. Lu Y et al (2020) A critical review of sustainable energy policies for the promotion of renewable energy sources. Sustainability 12(12):5078. https://doi.org/10.3390/su12125078
36. Ambepitiya K (2018) Possible green power marketing strategies to promote solar power in Sri Lanka. J Entrepreneurship Bus Econ 6(1):166–204
37. Mai NH (2020) Integrated marketing communication in promoting solar energy in Vietnam. Int J Recent Trends Bus Tourism (IJRTBT) 4(3):7–13
38. Solangi KH et al (2011) A review on global solar energy policy. Renew Sustain Energy Rev 15(4):2149–2163. https://doi.org/10.1016/j.rser.2011.01.007
39. Vaka M et al (2020) A review on Malaysia's solar energy pathway towards carbon-neutral Malaysia beyond Covid'19 pandemic. J Clean Prod 122834. https://doi.org/10.1016/j.jclepro.2020.122834
40. Ohunakin OS et al (2014) Solar energy applications and development in Nigeria: drivers and barriers. Renew Sustain Energy Rev 32:294–301. https://doi.org/10.1016/j.rser.2014.01.014
41. Michalena E, Tripanagnostopoulos Y (2010) Contribution of the solar energy in the sustainable tourism development of the Mediterranean islands. Renew Energy 35(3):667–673. https://doi.org/10.1016/j.renene.2009.08.016
42. Elhadidy MA, Shaahid SM (2004) Promoting applications of hybrid (wind+ photovoltaic+ diesel+ battery) power systems in hot regions. Renew Energy 29(4):517–528. https://doi.org/10.1016/j.renene.2003.08.001
43. Menegaki AN (2012) A social marketing mix for renewable energy in Europe based on consumer stated preference surveys. Renew Energy 39(1):30–39. https://doi.org/10.1016/j.renene.2011.08.042
44. Tsoutsos TD (2002) Marketing solar thermal technologies: strategies in Europe, experience in Greece. Renew Energy 26(1):33–46. https://doi.org/10.1016/S0960-1481(01)00096-9

A Brief Analysis on Microgrid Control

Sheetal Chandak, Buddhadeva Sahoo, Pravat Kumar Rout, Sthitaprajna Mishra, and Manohar Mishra

Abstract Microgrids have been an innovative enhancement in the power sector to integrate distributed power sources. Having the capability to operate in two modes, the control of microgrid is an important aspect to be studied. The paper discusses the operational concept and challenges faced by microgrids in different modes of operation to achieve optimum stability. The study on microgrid's control hierarchy has been analyzed in this paper. A brief analysis of several challenges faced by microgrid control strategy till-date has been discussed. Several power sharing strategies, energy management, and load balancing strategies have been studied. Along with the challenges faced, the paper explores future aspects of research in the field of microgrid control.

Keywords Microgrid · Microgrid control · Power sharing · Energy-management

1 Introduction

The shifting power demand and environmental combat have been a constant source of change and development in the growth of power sector. Integration of distributed power sources earlier was restricted to medium and high voltage levels of power systems. However, the innovations, developments, and improvements in the miniaturized scale of power generation and distribution have promoted the use of distributed power sources at low voltage levels. This idea of integrating distributed sources in distribution networks has prompted the setup of microgrids addressing the demand

S. Chandak · B. Sahoo (✉)
Department of Electrical Engineering, Siksha 'O' Anusandhan University, Bhubaneswar, Odisha, India

P. K. Rout · M. Mishra
Department of Electrical and Electronics Engineering, Siksha 'O' Anusandhan University, Bhubaneswar, Odisha, India

S. Mishra
Department of Electrical and Electronics Engineering, GMR Institute of Technology, Rajam, India
e-mail: sthitaprajan.m@gmrit.edu.in

M. Mishra et al. (eds.), *Innovation in Electrical Power Engineering, Communication, and Computing Technology*, Lecture Notes in Electrical Engineering 814,
https://doi.org/10.1007/978-981-16-7076-3_46

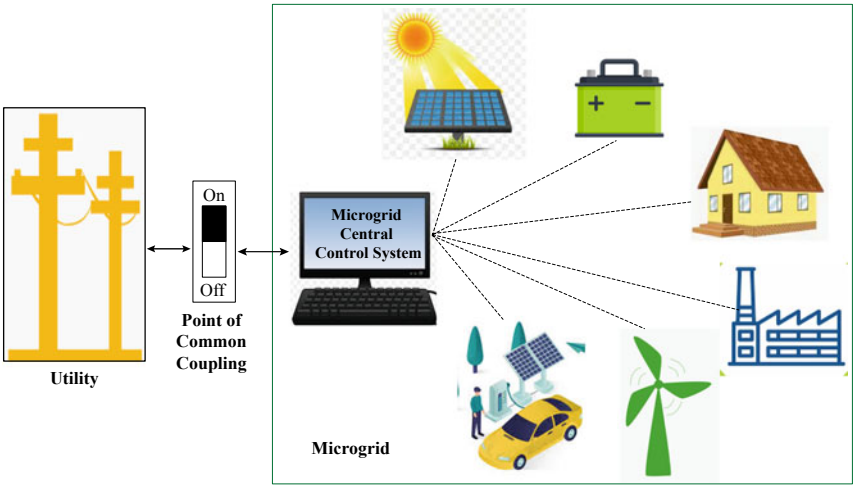

Fig. 1 The utility integrated microgrid

for reliable and eco-friendly power supply [1–3]. Microgrids can be defined as an interconnection of distributed power sources, loads, and storage devices with considered electric restrictions that act as an isolated controllable unit with reference to the main distribution grid as shown in Fig. 1 [4]. Further, microgrid characterizes a major feature that allows itself to autonomously control during the grid-connected or isolated mode of operation. As the microgrid controls the entire process of generation, distribution, and consumption of power. At times it has been used as supportive backup system to the end user when the main grid breaks down [5].

Several unacceptable abnormal conditions occur due to the faults in the power system, which leads to significant fluctuation in system voltage and frequency resulting in power breakdown. Under such a scenario, implementation of microgrid technology can perform as a backup system to retain the power in the utilities. This supports in powering the critical load even while operating in an isolated mode of operation. However, the major issue that arises while operating in standalone mode is the power imbalance between the generation and demand. To address this issue, microgrid central control unit must execute an efficient power sharing and load shedding strategy [6]. The paper reviews several widely practiced control strategies in the microgrid operation to ensure a reliable energy flow between the source and load.

Motivation for this survey:

- The study on microgrids is significantly important as they are shifting from laboratory to real-time deployment.
- Microgrids have been analyzed to be flexible solutions for broad diversified sources of power generation which demands accurate control strategy.

- Microgrids require precise control to support the integration of renewable sources, storage devices, and electric vehicles into the system.
- Microgrids with the feature of operating in autonomous and grid-connected mode face several legal and regulatory uncertainties.

2 Mode of Operation

Microgrid's control unit is designed to efficiently perform in two modes of operation, i.e., grid-connected mode and isolated/islanded mode of operation. In grid-connected mode of operation, the microgrid exchanges power with the utility grid as required. Microgrid draws power from the utility when the local load demand increases and feeds power to the utility when the power generated is more than the demand [7]. However, in emergency situations, the microgrid disconnects itself from the utility grid and operates autonomously in an islanded mode of operation. In both the modes of operation, the control units of microgrid perform to maintain the power quality and system stability [8].

The operation of microgrids becomes critical during emergencies, as the point of interconnection between the utility and microgrid has to split and subsequently switch the control mode of power sources to ensure uninterrupted power supply to the critical load. The power management between the sources and loads in the low voltage isolated mode has to be handled differently and carefully [9].

Challenges: Microgrid, an enhanced and improvised operating system with many significant advantages is installed and integrated into a low voltage (LV) distribution system. As a consequence, the conventional (i.e., present-day) distribution system undergoes variations in its operational characteristics. The variations or the difference in the characteristics significantly increases with the increase in the number of microgrids. This challenges the designing of a feasible controller which anticipates the variation in LV system [10]. The operation control of microgrids also aims to optimize the production and consumption of energy to increase efficiency. The microgrids also inherit certain characteristics of controlling high degree of imbalance and diversified distributed power units. Besides, the lost input parameters while controlling the microgrid in either centralized or decentralized mode is another challenging task [11].

Further, the microgrid controllers accommodate two modes of operation: autonomous (i.e., islanded or grid-forming) mode of operation and grid-connected (i.e., grid-following) mode of operation. The microgrid operation requires a transition between the two modes. Further, the transition between the modes causes a large mismatch in generation and load [12]. This results in severe fluctuations in the system voltage and frequency, along with the increased complexity of the control system. Furthermore, the ability of the microgrid to plug and play creates a serious issue if there are large numbers of distributed micro sources in the microgrid [13].

The presence of electronic control units in microgrid, has a considerable impact on the fault transients, which significantly affects the control and protectional aspect

of the microgrid. A basic step to attain efficient control in the microgrid is to identify the mode of operation. The control operation of the microgrid in different modes is controlled by the local controllers and a central or supervisory controller of the microgrid.

The microgrids operate in two different modes and they are as follows:

A. *Grid-connected mode of operation*

In this mode of operation, the microgrid comprising of localized power sources and loads operates according to the measured parameter values at the utility side. The operation of entire microgrid is mainly controlled according to the system utility. The supervisory control of the microgrid receives signals and information from the utility, to control the internal operation of the microgrid. The controllers in microgrid operate in current control mode, controlling the active power and the reactive power injected by each power source. This mode is also known as *grid-following* mode of operation.

B. *Islanded mode of operation*

In this mode of operation, the local controllers and the supervisory control unit of the microgrid are solely responsible for a smooth operation of a microgrid. The controller in microgrid operates in voltage control mode, controlling the microgrids voltage and frequency in the operating limits. This mode is also known as grid-forming mode of operation (The control strategy of the controller, follows either of the two modes: Centralized control and Decentralized control of the microgrid).

3 Microgrid Control Hierarchy

A planned configuration of a microgrid requires various technical and non-technical aspects under consideration to explicitly classify the system functions and controls. The microgrid central control system (MCCS) is a computer-based interfacing system. The software used holds control over almost every operational aspect of microgrid. It uses interfacing of human machines and supervisory control and data acquisition (SCADA) to analyze, monitor, and control the system data. It implements a forecasting technique to monitor the power demand, generation, and electricity market prices. It also executes unit commitment and economic dispatch to attain an optimal power supply with the minimum cost [14]. MCCS operates to deal with both centralized and decentralized information. While dealing with centralized processing, the MCCS handles all the information of a microgrid. Whereas, in decentralized processing, the MCCS only handles a few of the information obtained from the real-time operation [15].

The central controller coordinates with each of the components present in the microgrid system to ensure a secure, reliable, and economic operation. MCCS performs a significant role in the integration and control of distributed power sources (especially renewable sources) in an optimal way, indifferent to the microgrid's mode of operation. As the control of the microgrid becomes a key aspect, the design of

the control strategy is such that it presents a microgrid as a self-governed unit from grid's viewpoint. The hierarchy of the control approach is set into three levels:

A. *Level-I: Primary control*

The first level of the hierarchy is designed to perform a basic function of maintaining the system operating parameters (i.e., voltage and frequency) in their operation limit while operating in both islanded and grid-connected mode. Along with that, the primary level provides a plug-and-play feature for the distributed power sources, with an efficient active and reactive power share among themselves. The level helps in mitigation of circulating current to avoid the over-current in the power-electronic devices and damage in the DC link capacitors present in the microgrid [16, 17].

B. *Level-II: Secondary control*

It has been discussed that the frequency deviation during the steady state is actively controlled by the primary control. Moreover, the storage devices present in the microgrid support to compensate for the deviation. But the storage devices may fail to compensate and control the load frequency for a considerably longer term because of their smaller energy capacity.

Therefore, the secondary control is designed as a centralized controller to control and restore the deviations in system parameters caused by the primary controller. The level-II of the control structure has a characteristic of slower dynamic response compared to the level-I, thus justifying the de-coupled operational dynamics between the primary and secondary levels of control [18]. Thus, the individual levels are designed, operated, and controlled with ease.

C. *Level-III: Tertiary control*

The last level of the control hierarchy, named tertiary control is the slowest among all the three levels of the control structure. This level functions to attain an optimal operation of the microgrid with all the economic concerns and maintains the power flow between the microgrid and the utility grid [17]. Further, while operating in grid-connected mode of operation the power flow between the microgrid and the utility grid is controlled by regulating the frequency and voltage of distributed power sources [19].

Challenges: The execution of all three levels, suffers from a computational burden, significant cost, and reduced reliability, as a failure at any point in the microgrid sends signal to each distribution generator (DG) unit by means of low-bandwidth communication lines. To overcome the reliability issues, several advanced control approaches present the concept of executing the primary and secondary levels in a decentralized way [20]. Furthermore, to mitigate the communication cost, the primary level executes the concept of droop control and the secondary level executes the multi-agent system (MAS) in a distributed manner to maintain the stability in system parameters [21, 22]. An extensive review of the MAS strategy implemented in microgrid is presented in [23, 24]. The MAS technologies can be successfully operated in grid-connected microgrid but may fail while operated in an islanded mode of operation of the microgrid.

Though the primary and the secondary level of the MCCS prefers to operate in a decentralized manner to improve the microgrid's reliability the tertiary level needs to operate in a centralized manner. The level majorly operates to coordinate the microgrids with each other and with the grid utility. It also provides optimal energy management of the DPGs present in the microgrid [25]. The central control system senses the fluctuations and variations at the point of common coupling (PCC) to determine the microgrid's operating mode (i.e., either autonomous or grid-connected). The MCCS also plays a major role in re-synchronizing the islanded microgrid with the utility, once the utility and the microgrid restore the power quality [26].

The microgrid comprises various power sources having different features and operation characteristics along with fluctuating power levels. This challenges the operation of MCCS to attain an efficient power balance in the system. To overcome the challenges, several control strategies have been proposed in literature [27–30]. Power balancing has been majorly focused to evade the fluctuations in system parameters to achieve a safe and reliable operation. Various algorithms have been stated to optimize the power generation and power exchange with the utility in [31]. Further, several load shedding algorithms have been proposed to balance the power difference between the demand and supply in [32, 33]. Since the storages devices play a significant role in controlling the voltage and frequency variations of autonomous microgrids, MCCS strategy operates within its limits to prevent their degradation [20]. The MCCS strategy prevents the storage devices from overcharging by reducing their generated active power, avoids deep discharge by load shedding, and evades the degradation caused by the unequal charge by executing the charge equalization strategy among the units [34, 35].

4 Control Aspects of Microgrid

Microgrids with the unique characteristic of operating in both grid-connected and standalone modes require proper control in both modes to attain a stable and efficient operation [36]. The microgrid control structure requires a hierarchical control, addressing all the above control requirements in each different level of hierarchy [37]. The stratified control strategy of the microgrid comprises three significant levels of primary control, secondary control, and tertiary control, and the coordinated operation of all three levels is shown in Fig. 2 [38]. Analysis of system stability after any type of fault event has always been a major focus. The control strategy for microgrid stability has to be designed addressing its voltage and frequency stability for both the islanded and grid-connected mode of operation by differentiating the system disturbances into small disturbance and large disturbance.

A. Power sharing control among the DGs
   The microgrid comprises several types of power generating and storage units. The microgrid requires a control strategy to ensure reliable, stable, and economic operation of the system. The active and reactive power generated

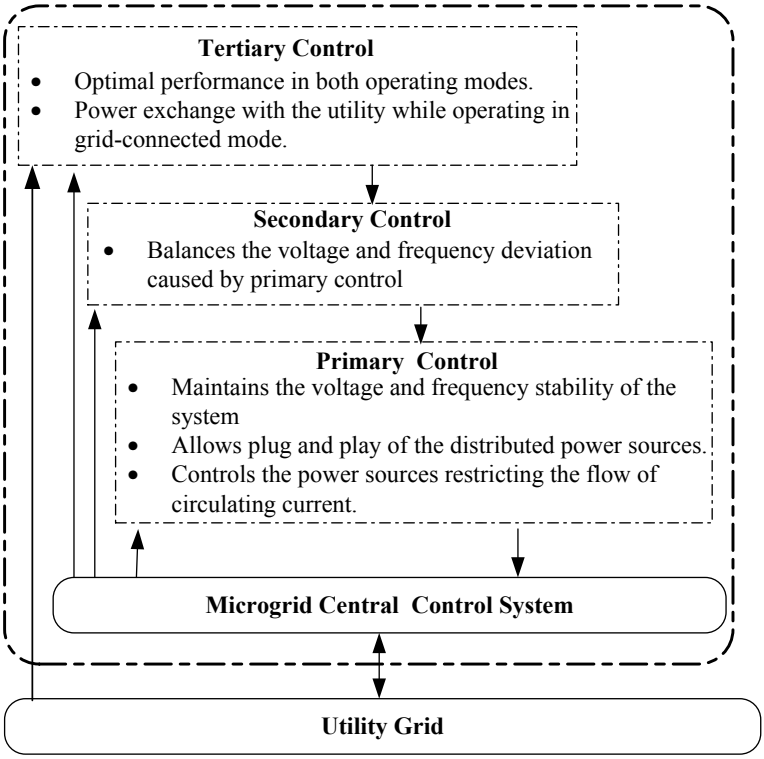

Fig. 2 The control hierarchy of microgrid

and stored by the power sources has to be shared efficiently. The simultaneous control and accurate sharing with the varying loads majorly depend on the type of power sources, feeders, and non-linear loads. Further, the sharing of power has been a tough task with the integration of unpredictable renewable power sources and resistive nature of the microgrid system [39]. The efficient sharing of power can be attained either by a communication based or by a communication-less channel. Table 1 discusses some of the well-known power sharing strategies.

The communication-based control strategies execute to control the active power sharing along with voltage regulation but at a higher installation cost. The communication-based control also includes centralized control, master–slave control, peak load sharing control, peak current sharing control, etc. [40]. Among the several control scheme, master–slave has been extensively implemented [41, 42]. In master–slave control strategy, the master DG takes complete charge of power sharing control operation depending on the microgrid's mode of operation. During standalone mode, the master operates as voltage source controller and regulates the voltage and frequency of the system. On the other hand, the slave units operate as current source controllers and abide by the

Table 1 Certain well-known power sharing strategies

Control strategies	Benefits	Drawbacks
Communication based	• Precise and efficient sharing • Eliminates circular current • Faster transient response	• Higher installation cost • Limits DGs incorporated • Reliability issues
P-f droop	• Plug and play of DGs • Eliminates channel • Apply for high and medium voltage lines	• Responsive to physical components • Slow transient response • Weak reactive power control
P-V droop	• Allows plug and play for DGs • Eliminates communication channels • Apt for low voltage line	• Responsive to physical components • Slow transient response • Weak active power control
V-I droop	• Faster transient response • Controls active and reactive power • Feasible for DGs with small inertia	• Oscillations for small droop coefficients • Voltage issue under heavy load condition
Virtual flux	• Controller configurations are simple • Enhanced control over frequency	• Not applicable for large systems • Sluggish transient response
Voltage based	• Applicable for resistive network • Supports renewable power generation • Effortless power balancing	• Practical implementation is challenging • With load variation, the voltage varies

current pattern directed by the master unit [43]. An efficient power sharing with easy installation can be achieved, however, the failures or the delays in communication channel hampers the reliability of the microgrid system. The strategy also limits the number of DGs integrated [40].

Power sharing without any communication has been accomplished based on the droop characteristics. The droop control increases the system reliability and reduced the installation cost as required by the communication channels.

The strategy significantly helps in connecting the remote DGs and allows plug-and-play features for the DGs without disturbing the operating system [44]. The droop control is performed by the steady state characteristics of the DG units. The strategy enhances the system reliability but has a major challenge of controlling the coupling power. Further, the strategy encounters several challenges due to the dependency on network impedance, operation of non-linear loads, and deviations in voltage and frequency [40]. Several control approaches with strengths and weaknesses have been discussed.

B. *Energy management*

The management of power is a vital task to achieve optimal scheduling to manage an efficient generation dispatch, reduce distribution and system losses, support reactive power balancing and energy shaving, mitigate the emission of greenhouse gasses, reducing the operational cost with improved efficiency and reliability of microgrid [45]. With the increased integration of renewable power sources, energy storage devices, and electric vehicles in the existing network, the complexity of energy management increases. The energy management in microgrids can either be performed from generator side or the load side. Traditionally, the former has been generally implemented for energy management, but with the fluctuating power generation and demand in microgrid, the requirement of power balancing with every second turns the generation side management to be a challenging task. Therefore, load side management in microgrids has been implemented, addressing the maximum use of power generated and supplied to the demand. The management strategy is designed undertaking several important constraints like system voltage, frequency, power generated, power storage, and logistics, so as to support a sustainable, consistent, and economic operation of microgrid [46]. The strategy also needs to take into account the cost of operation, maintenance, and degradation of several system components and batteries in the microgrid [47]. Numerous computational algorithms have been proposed, like linear programming, non-linear programming, genetic algorithm, fuzzy based programming, neural networks, and, etc. to attain a faster convergence in load management. The algorithm reduces the computational complexity along with increased efficiency and reliable operation in microgrids.

The linear computation minimizes the load consumption with balanced supply and demand of power in [48]. Addressing minimization of cost, the article [49] attains optimal management of energy in a grid-connected microgrid that has a charging spot for vehicle to grid system. The cost minimization strategy, includes the energy trading cost, the draining cost of electric vehicles, and also the penalty of load shedding. Further, in [50], renewable power sources and storage devices have been considered for energy management. The study addresses the incorporation of photovoltaic sources to achieve efficient peak shaving using the predictive control strategy based dynamic programming to attain an optimal power flow. In [51], the power management of batteries along with the optimal use of renewable sources like wind and photovoltaic has been analyzed. In [52], multi-objective optimization algorithm

has been implemented on microgrid system, to accomplish a reliable and efficient operation at minimal operational cost. Local computation and sparse communication networks have been studied in [53], performing the real-time distributed algorithms to converge at an optimal solution with ultimate operational benefits to the loads. Further in [54], the power flow and the operational constraints of microgrid have been analyzed by online power management strategy. An extensive research can be carried out in the field of energy management by improving several adaptive management algorithms or by conducting several optimization algorithms with different combinations of objective functions with an aim to reduce the computational time as well as operational complexity [55].

5 Future Aspects

An efficient control strategy is required to maintain the system parameters, as the operating elements of the microgrid have diversified characteristics. Some of the future aspects of research on microgrids can be stated as:

- A robust, reliable, and coordinated power allocation and sharing strategy are required between the diversified multiple DGs and storage devices in the microgrid.
- Efficient active and reactive power sharing for these composite loads like dynamic loads, constant loads, inductor motor, pulsed loads, and electric vehicles.
- The control strategy designed with the maximization of reliability and controllability must also address the minimization of operation cost.
- In a network with diversified, the power sharing strategy must consider the communication delay may it be constant, bounded, or random delay.
- The strategy requires timely control and communication with all the DGs with variable inertia integrated into the microgrid.
- A microgrid requires an efficient load shedding strategy that addresses the voltage stability and frequency stability simultaneously to overcome any form of instabilities.
- An extensive study is required for voltage stability index and frequency stability index in load shedding, particularly to study an isolated microgrid system.
- Moreover, a wide ranging study is required on the existing load shedding strategy while implemented for an isolated system.
- The load restoration approach needs the participation of energy storage devices to attain a faster and reliable restoration.
- The microgrid with multiple DGs and their variable inertia must be analyzed to extend the study on restoration characteristics index.
- Establishment of an efficient signaling and communication setup to coordinate and co-operate the microgrids closely installed. This will help the microgrids to attain a harmonious operation and uninterrupted supply to the loads.

- Incorporation of storage devices with various characteristics, so as to maintain the inertia of the microgrid.
- With significant growth in electric vehicles, their incorporation within the microgrid will play a significant role in the growth of the developing power system.

6 Conclusion

Stable and controlled operation of power systems has always been a vital aspect. The paper analyzed the microgrid control strategy for efficient performance. Smooth control of microgrids in two different modes of operation is an important viewpoint for the implementation and execution of a microgrid concept. The stability in microgrid requires frequency and voltage to be constant within the operating limits with minimal difference between the generation and load. The primary, secondary and tertiary control stages in microgrid control hierarchy have been briefly analyzed. Further, the paper discusses several well-known power balancing and energy management strategies with respect to the microgrid's control hierarchy.

Acknowledgements The authors acknowledge the financial support provided by the Council of Scientific and Industrial Research (CSIR), Government of India.

References

1. Lasseter RH, Paigi P (2004) Microgrid: a conceptual solution. In: 2004 IEEE 35th annual power electronics specialists conference (IEEE Cat. No. 04CH37551), vol 6. IEEE, pp 4285–4290
2. Patnaik B, Mishra M, Bansal RC, Jena RK (2021) MODWT-XGBoost based smart energy solution for fault detection and classification in a smart microgrid. Appl Energy 285:116457
3. Mishra M, Panigrahi RR, Rout PK (2019) A combined mathematical morphology and extreme learning machine techniques based approach to micro-grid protection. Ain Shams Eng J 10(2):307–318
4. Patnaik B, Mishra M, Bansal RC, Jena RK (2020) AC microgrid protection—a review: current and future prospective. Appl Energy 271:115210
5. Farrokhabadi M, Cañizares CA, Simpson-Porco JW, Nasr E, Fan L, Mendoza-Araya PA, Tonkoski R et al (2019) Microgrid stability definitions, analysis, and examples. IEEE Trans Power Syst 35(1):13–29
6. Olivares DE, Mehrizi-Sani A, Etemadi AH, Cañizares CA, Iravani R, Kazerani M, Hajimiragha AH et al (2014) Trends in microgrid control. IEEE Trans Smart Grid 5(4):1905–1919
7. Chandak S, Rout PK (2020) Optimal performance of a self-healing microgrid. IET Smart Grid 3(1):51–59
8. Basak P, Chowdhury S, nee Dey SH, Chowdhury SP (2012) A literature review on integration of distributed energy resources in the perspective of control, protection and stability of microgrid. Renew Sustain Energy Rev 16(8):5545–5556
9. Chandak S, Bhowmik P, Rout PK (2019) Robust power balancing scheme for the grid-forming microgrid. IET Renew Power Gener 14(1):154–163
10. Cagnano A, Tuglie ED, Mancarella P (2020) Microgrids: overview and guidelines for practical implementations and operation. Appl Energy 258:114039

11. Anestis A, Georgios V (2019) Economic benefits of smart microgrids with penetration of DER and mCHP units for non-interconnected islands. Renew Energy 142:478–486
12. Zamora R, Srivastava AK (2010) Controls for microgrids with storage: review, challenges, and research needs. Renew Sustain Energy Rev 14(7):2009–2018
13. Nikkhajoei H, Lasseter RH (2007) Microgrid protection. In: 2007 IEEE power engineering society general meeting. IEEE, pp 1–6
14. Imes K, Hollister J (2011) Energy management system. U.S. patent 8,024,073, issued 20 Sept 2011
15. Zia MF, Elbouchikhi E, Benbouzid M (2018) Microgrids energy management systems: a critical review on methods, solutions, and prospects. Appl Energy 222:1033–1055
16. Mohamed YAI, Radwan AA (2011) Hierarchical control system for robust microgrid operation and seamless mode transfer in active distribution systems. IEEE Trans Smart Grid 2(2):352–362. https://doi.org/10.1109/TSG.2011.2136362
17. Chandak S, Bhowmik P, Mishra M, Rout PK (2018) Autonomous microgrid operation subsequent to an anti-islanding scheme. Sustain Cities Soc 39:430–448
18. Karaarslan A, Seker ME (2020) Distributed control of microgrids. In: Microgrid architectures, control and protection methods. Springer, Cham, pp 403–422
19. Chandak S, Bhowmik P, Rout PK (2019) Dual-stage cascaded control to resynchronise an isolated microgrid with the utility. IET Renew Power Generation 14(5):871–880
20. Roslan MF, Hannan MA, Ker PJ, Uddin MN (2019) Microgrid control methods toward achieving sustainable energy management. Appl Energy 240:583–607
21. Rahman MS, Oo AMT (2017) Distributed multi-agent based coordinated power management and control strategy for microgrids with distributed energy resources. Energy Convers Manage 139:20–32
22. Vandoorn TL, Guerrero JM, De Kooning JDM, Vásquez J, Vandevelde L (2013) Decentralized and centralized control of islanded microgrids including reserve management. IEEE Ind Electron Mag 1–14
23. Khan MW, Wang J (2017) The research on multi-agent system for microgrid control and optimization. Renew Sustain Energy Rev 80:1399–1411
24. Anvari-Moghaddam A, Rahimi-Kian A, Mirian MS, Guerrero JM (2017) A multi-agent based energy management solution for integrated buildings and microgrid system. Appl Energy 203:41–56
25. Olatomiwa L, Mekhilef S, Ismail MS, Moghavvemi M (2016) Energy management strategies in hybrid renewable energy systems: a review. Renew Sustain Energy Rev 62:821–835
26. Almada JB, Leão RPS, Sampaio RF, Barroso GC (2016) A centralized and heuristic approach for energy management of an AC microgrid. Renew Sustain Energy Rev 60:1396–1404
27. Yusof NAM, Ali Z (2019) Review of active synchronization for renewable powered microgrid. Int J Eng Technol 8(1.7):14–21
28. Abdi H, Beigvand SD, La Scala M (2017) A review of optimal power flow studies applied to smart grids and microgrids. Renew Sustain Energy Rev 71:742–766
29. Badal FR, Das P, Sarker SK, Das SK (2019) A survey on control issues in renewable energy integration and microgrid. Protect Control Modern Power Syst 4(1):8
30. Diaz NL, Luna AC, Vasquez JC, Guerrero JM (2016) Centralized control architecture for coordination of distributed renewable generation and energy storage in islanded AC microgrids. IEEE Trans Power Electron 32(7):5202–5213
31. Han Y, Li H, Shen P, Coelho EAA, Guerrero JM (2016) Review of active and reactive power sharing strategies in hierarchical controlled microgrids. IEEE Trans Power Electron 32(3):2427–2451
32. Bakar NNA, Hassan MY, Sulaima MF, Na'im Mohd Nasir M, Khamis A (2017) Microgrid and load shedding scheme during islanded mode: a review. Renew Sustain Energy Rev 71:161–169
33. Chandak S, Bhowmik P, Rout PK (2019) Load shedding strategy coordinated with storage device and D-STATCOM to enhance the microgrid stability. Protection Control Modern Power Syst 4(1):22

34. Arani AAK, Gharehpetian GB, Abedi M (2019) Review on energy storage systems control methods in microgrids. Int J Electr Power Energy Syst 107:745–757
35. Shayeghi H, Shahryari E, Moradzadeh M, Siano P (2019) A survey on microgrid energy management considering flexible energy sources. Energies 12(11):2156
36. Lasseter RH (2002) Microgrids. In: 2002 Proceedings of conference on IEEE Power engineering society winter meeting (Cat. No. 02CH37309), vol 1. IEEE, pp 305–308
37. Guerrero JM, Vasquez JC, Matas J, De Vicuña LG, Castilla M (2010) Hierarchical control of droop-controlled AC and DC microgrids—a general approach toward standardization. IEEE Trans Ind Electron 58(1):158–172
38. Palizban O, Kauhaniemi K (2015) Hierarchical control structure in microgrids with distributed generation: Island and grid-connected mode. Renew Sustain Energy Rev 44:797–813
39. Sen S, Kumar V (2018) Microgrid control: a comprehensive survey. Annu Rev Control 45:118–151
40. Hossain MA, Pota HR, Issa W, Hossain MJ (2017) Overview of AC microgrid controls with inverter-interfaced generations. Energies 10(9):1300
41. Caldognetto T, Tenti P (2014) Microgrids operation based on master–slave cooperative control. IEEE J Emerg Select Topics Power Electron 2(4):1081–1088
42. Chen JF, Chu CL (1995) Combination voltage-controlled and current-controlled PWM inverters for UPS parallel operation. IEEE Trans Power Electron 10(5):547–558
43. Vandoorn TL, De Kooning JDM, Meersman B, Vandevelde L (2013) Review of primary control strategies for islanded microgrids with power-electronic interfaces. Renew Sustain Energy Rev 19:613–628
44. Pham XHT (2020) Power sharing strategy in islanded microgrids using improved droop control. Electr Power Syst Res 180:106164
45. Mbungu NT, Naidoo RM, Bansal RC, Vahidinasab V (2019) Overview of the optimal smart energy coordination for microgrid applications. IEEE Access 7:163063–163084
46. Sahoo B, Routray SK, Rout PK (2021) AC, DC, and hybrid control strategies for smart microgrid application: A review. Int Trans Electr Energy Syst 31(1):e12683
47. Bidram A, Davoudi A (2012) Hierarchical structure of microgrids control system. IEEE Trans Smart Grid 3(4):1963–1976
48. Riffonneau Y, Bacha S, Barruel F, Ploix S (2011) Optimal power flow management for grid connected PV systems with batteries. IEEE Trans Sustain Energy 2(3):309–320
49. Wei Q, Shi G, Song R, Liu Y (2017) Adaptive dynamic programming-based optimal control scheme for energy storage systems with solar renewable energy. IEEE Trans Industr Electron 64(7):5468–5478
50. Shi G, Wei Q, Liu D (2017) Optimization of electricity consumption in office buildings based on adaptive dynamic programming. Soft Comput 21(21):6369–6379
51. Squartini S, Fuselli D, Boaro M, De Angelis F, Piazza F (2013) Home energy resource scheduling algorithms and their dependency on the battery model. In: 2013 IEEE computational intelligence applications in smart grid (CIASG). IEEE, pp 122–129
52. Kirschen DS, Strbac G (2018) Fundamentals of power system economics. Wiley
53. Xu Y, Yang Z, Gu W, Li M, Deng Z (2015) Robust real-time distributed optimal control based energy management in a smart grid. IEEE Trans Smart Grid 8(4):1568–1579
54. da Silva HB, Santiago LP (2018) On the trade-off between real-time pricing and the social acceptability costs of demand response. Renew Sustain Energy Rev 81:1513–1521
55. Hossain MA, Pota HR, Hossain MJ, Blaabjerg F (2019) Evolution of microgrids with converter-interfaced generations: challenges and opportunities. Int J Electr Power Energy Syst 109:160–186

An Overview of Power System Resilience: Causes, Planning and Restoration Processes

Fanidhar Dewangan, Monalisa Biswal, and Manohar Mishra

Abstract In the present scenario, fast and effective restoration of power is a big challenge for any outage caused by a natural disaster. Natural disasters may term for heavy storms, floods, earthquakes, cyclones, Tsunami, etc. These events may cause a complete blackout of a region and many times to the regional grids. Various such events across the globe are the key witness which caused outages for many days or weeks also. Taking the consideration of events like various natural disasters occurred in India, the enhancement of power system resilience has been always challenging to the government and individuals. In this paper, the planning and action related steps are described which may lead to enhancement in the restoration of power system. Focusing on the past disasters and current disasters that occurred in India, some of the findings and their preparedness are elaborated in the below sections. The strengthening and controlling of electrical parameters at the time of event have been considered irrespective of power system resilience.

Keywords Power system resilience · Power system protection · Power grid · Microgrid · Blackout · Power management system · Energy management system · SCADA

1 Introduction

Power system stability is one of the biggest challenges in the present era especially in case of disturbances that are caused by naturally, man-made or system related activities [1, 2]. Among all three, natural disasters are very dangerous for power systems. The unpredictable storms, unstoppable floods, heavy dense cyclonic clouds, breath-taking earthquakes, and many other such events had been categorized under

F. Dewangan · M. Biswal
National Institute of Technology, Raipur, Chhattisgarh 492010, India

M. Mishra (✉)
Department of Electrical and Electronics Engineering, Siksha 'O' Aunusandhan University, Bhubaneswar, India

M. Mishra et al. (eds.), *Innovation in Electrical Power Engineering, Communication, and Computing Technology*, Lecture Notes in Electrical Engineering 814,
https://doi.org/10.1007/978-981-16-7076-3_47

natural disaster. Talking about man made and system related occurrences, they are not natural. Therefore, all three are the main causes of the power system outages.

This loss of power may impact the following:

- Production loss in industrial sector,
- Loss of human lives,
- Loss of houses, lands, business parks, apartments, etc. in the society,
- Social, ecological and educational loss to some extent [3, 4],
- Economical loss of the respective state later to the country [5],
- Loss of health system in the affected region [6],
- Loss of electricity to critical loads like hospitals, railways, airports, etc.

Hence the process of resilience enhancement in the system is carried out. As termed by the various researchers, resilience may be described by the planning, preparedness, emergency response, and restoration of the power system before and after the high impact caused by disasters [4, 7, 8]. The high impact may lead to various damages like collapse of 132 kV and above high voltage transmission line towers along with the lines, distribution transformers, rotating blades of wind energy turbine, solar panels, and many other electrical related equipment at large.

2 Planning and Execution for Resilience Activity

The natural disaster may cause a high impact and low probability in the power system [9]. This impact is unpredictable for any organization. Hence proper planning is needed and according to that execution steps are required for restoration. The planning and execution may be categorized into three parts: Preplanning, emergency handling, and post event execution. The timing of event occurrence in any region according to three parts of planning and execution is shown (see Fig. 1).

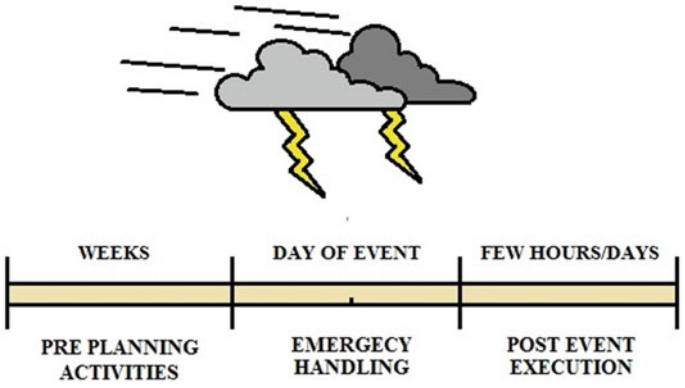

Fig. 1 Timing of pre-planning, emergency handling, and post event execution

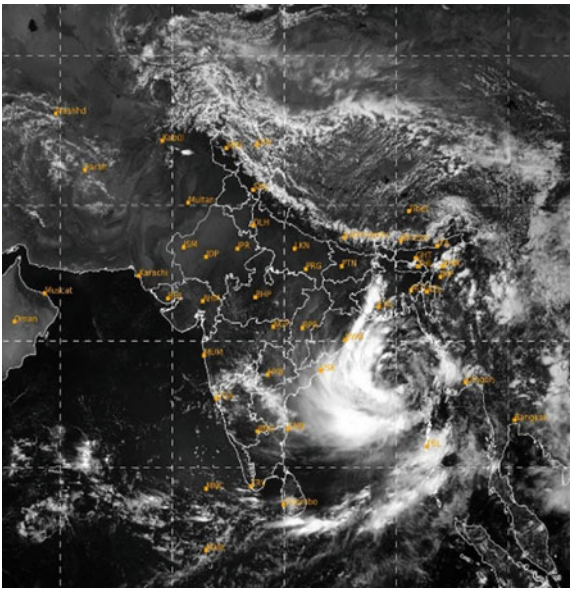

Fig. 2 Satellite image of cyclone Yaas in Bay of Bengal region

2.1 Pre-planning Activities

Pre-planning under resilience is very much necessary. Pre-preparedness of all the hardware and software related spares, availability of alternate inventory, back-up of all highly rated equipment, spares of conveyors and transportations, manpower availability, etc.

2.1.1 Forecasting

Indian Meteorological Department (IMD) directs the information to its official website which is collected from satellite. Also, there are various applications on PCs and mobile phones, which can help to determine the position of such events, so that local authorities may get prepared for the disaster before it gets a strike. Shows the satellite and track view of cyclone Yaas in Bay of Bengal of India in the month of May 2021 is shown in the figure (see Figs. 2 and 3). All the images have been taken from IMD website.

2.1.2 Alertness

Various modes of communication are available nowadays for alerting the operators weeks ago about the event. Also, day by day, hour by hour information is been flashed

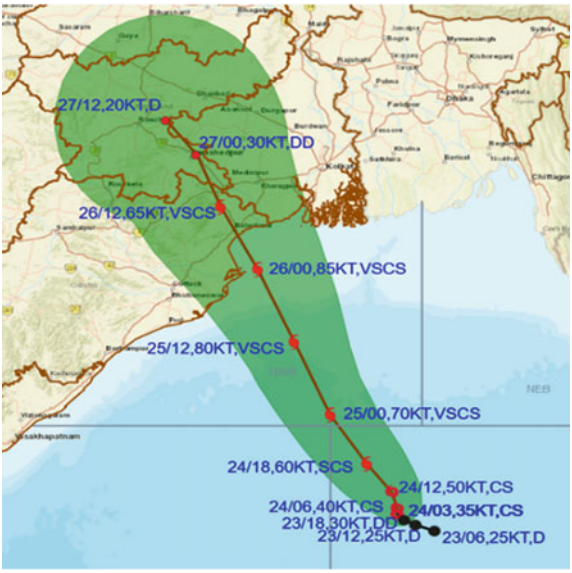

Fig. 3 Track view of cyclone Yaas in Bay of Bengal region

on the television and information has been shared on radio. Hence with the help of all these modes, preparedness can be done.

2.1.3 Strengthening of Infrastructure

The scheduled survey for checking the strength of infrastructures like electric tower/poles, concrete structures, outdoor and indoor equipment and overhead conductor to be carried out in a fixed period of time or before the occurrence of event [10, 11]. If needed then work related to the strengthening of such infrastructures to be carried time being. This would help in the reduction of mean time to repair (MTTR).

2.1.4 Availability of Fuels

The availability and storage of sufficient number of fuels to the generating stations should be there so that after the event, the small captive power generation stations can get light up easily. The availability of other raw materials should also be made for the smooth operation.

2.1.5 Availability of Mobile DG Sets and Dewatering Pumps

The most usable and highly demanded mobile DG sets are to be called for availability at their concerned vendors. These DG sets are to be pre located at a distance from the area that would be affected [12]. Keeping these mobile DGs apart is necessary so as to rush immediately after the impact to most critical region.

The same is also considered for the dewatering pumps. The pre planning of inventory and its spares are to be made so that in case of flood, water can be removed quickly from the drainages, cable trenches, cellar rooms, underground control station, etc. Sometimes due to choking of drainage system in the substation the water gets logged in the working area, which may cause electrocution at site. Hence in such a case, the dewatering becomes necessary.

2.1.6 Redundancy of System

The system redundancy is to be checked by the operator whether it is hardware related or software related. The working of all OFF load and ON load equipment are also checked during redundancy check. For the software related redundancy check, the main operating server is to be switched from main server to redundant server and again to main. Various types of drills can also be performed so as to train the operators, how to react in emergency situations.

2.2 Emergency Handling

Once the natural event has occurred, then the handling of power system and its failure becomes quite important for the recovery purpose. Also, it is very chronic, physically as well as mentally to the people who are affected due to this event. Hence emergency handling becomes challenging during natural disasters. Many other points are described below for emergency handling which is as follows.

For the generating station load, shedding scheme must work precisely. The shedding of loads must be there in appropriate defined timing. The relay coordination, load shedding, and sharing logics are to be verified by the operators. At the time of the occurrence, this system may work accurately for proper guarding of power system.

2.2.1 Smart Islanding and Load Shedding

At the time of occurrence, the operators must perform the islanding process depending upon the load requirement and area criticality [13]. The grid contains

paralleling of lines, so the already identified line is then diagnosed, and based on the parameters its isolator can be made open protecting other lines. The islanding phenomenon is being done manually as well as automatically. Also, the protection system should be so arranged that in case of any mishappening, it will directly command to respective faulty line breaker or isolator to react fast. It must be also kept in mind that in the cascaded system, congestion can occur due to islanding of system [14]. So, this will directly impact in huge switching of other lines.

2.2.2 Effective Operation

All the operators and co-workers are trained regularly those who are placed at the power control station in coastal areas. These operators should be able to handle during such events. Sequence of events about the switching ON and OFF of panels, transformers, grid isolators, circuit breakers, and, etc. to be given to them for effective optimization of power system.

2.2.3 Battery Backup System

The battery banks at different locations of substations and switchyards are to be checked and charged fully so that in case of completed black out DC back up power supply to be fed to UPS (Uninterrupted Power Supply) system. This backup power is very meaningful for restart and restoration purposes.

2.3 Post Event Restoration

These DG sets will perform mainly two functions, first to supply black start power to generating stations. And second, to provide lighting loads to domestic and commercial users.

2.3.1 Clearance of Road Ways

Due to huge storms and high wind velocity, there is blockage of roadways. The fallen trees, light poles, transmission towers, building blocks, and many other infrastructures are to be removed rapidly. A special team to be divided into all the affected areas so that they perform clearance of roadways activities. The government organization may also provide proper tools to these teams.

2.3.2 Allotment of Mobile DG Sets

As the disaster get over, soon there would be allotment of tire mounted DG sets from safer area to affected area. The DG sets are so commanded that there should not be any congestion and no set other than allotted one reach to the same site. Hence proper planning should be done with each set.

2.3.3 Prioritizing the Loads

As the backup supply is reached to different locations, it should be prioritized for power availability. The priority should be so made that the power to be given to hospitals, care centers, rescue centers, government offices, etc., firstly [12]. After this, the distribution is to be done for domestic purposes.

2.3.4 Start-up of Non-conventional Energy Sources

The area where non-conventional energy sources are installed can be made ready for their start-up and operation. It is obvious that in such a heavy disaster there is infrastructural loss of all types of generation sources. Blown away of solar cell panels and damage of wind turbine blades may be the effect of such storms. Focusing on that, a separate specialized team is to be diverted for their readiness. As soon as, the system gets ready than it should be started for its operation so that some power may get delivered to the grid or to small sector. This can also be used under the concept of smart grid or micro grid. In smart grid, a combination of conventional, non-conventional and grid system are present [15–18]. The benefit of such system is that in case of complete blackout, power can be restored by non- conventional energy sources. And further can contribute to the light up of conventional sectors.

2.3.5 Underground Cable Arrangement

Since no support structures are available after the disaster, the temporary cable laying process takes place underground only. This may provide less infrastructural cost, easy and fast recovery of power. An arrangement of cables is to be made early before the event strikes the area. So, after the event, this cable is to be directly laid from source station to load end.

2.3.6 Healthiness of Protection System

As there is a huge loss in the electrical power system of affected area, the protection system also got disturbed. Hence for temporary lighting up of critical loads and distribution transformers, there may be a chance to temporarily change the relay setting also to bypass some of the settings. Sometimes back charging may also need to change the relay setting many a time in the power system. Hence for doing all these activities it needs to have a well-protected system and healthiness of system including the relays configuration, relay operation, circuit breaker operation, relay coordination with all the connected sources and loads, etc.

3 Technical Approach for Resilience

The above discussions on resilience show a conventional approach focusing on the planning and execution in various ways. But looking at the technical part there are various parameters that need to be identified and pre-post action to be needed. Encouraging the electrical parameters we need to strengthen them for their best operation. At the time of natural disturbances, operators must be in contact with the regional control centers so that preventive action may be taken before the disturbances. These operators must be trained to handle critical situations like power swing, change in voltage, reactive power variations, frequency fluctuations, and power factor control.

Figure 4 shows that there are various consequences of natural disturbances. These consequences may cause system outage or equipment failure which later results in

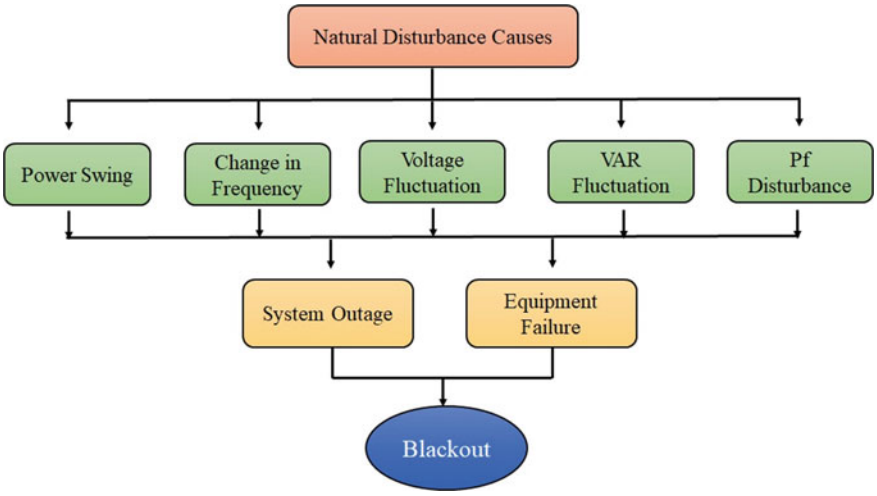

Fig. 4 Flow diagram showing the causes of natural disturbances on power system

blackout of the system. Also, it is equally necessary to strengthen these parameters for early recovery. Some of them can be quickly recovered which escapes the power system from turbulence while some may not, which may lead to outages. Some of the ideas and practices are discussed here below for strengthening the parameters which may strengthen the power system.

3.1 Active Power (W) and Reactive Power (VAR) Strengthening

For the active power control, load management system would be there which may be controlled by local operator. Now a days automated load controlling stations are available which control the active power (W) in auto mode depending upon various conditions. One of the best ways to strengthen power is implementation of load shedding scheme. This is considered as the best method for Power Management System (PMS). Under this, the load may be sheded in emergency conditions like during outage of any critical circuit breaker or any major equipment failure, protecting the source generator. These loads are shed on the basis of their priorities. The priority is so decided that the non-critical heavy loads are shed prior to any other load. For load shedding scheme under PMS, automation is so done that status of each source breaker, transformer breakers, load breakers, and grid breakers are taken as input to logic gate blocks which are formed by combination of various gates. Also during emergency conditions, at the time of communication failure, the hardware interlocking and tripping system are given to the operator's control room so as to shed the load quickly, protecting the source breaker or generator.

Load shedding scheme is best seen in microgrid (MG). MGs are so designed that generation, distribution, load, grid power, and renewable sources together form a power system. Hence, in this, islanding and load shedding are handled very smoothly in case of any miss happening occurred either naturally or manually [19].

Just like active power, reactive power strengthening is also important for any power system in case of system disturbance. The scarcity or over demand of VAR may lead to outages and sometimes blackouts. The malfunctioning of system voltage is the main cause of VAR malfunctioning. This fluctuation of voltage is caused by voltage unbalance in grid, under/overexcitation of generator, unplanned operation of capacitor banks, etc. Hence to strengthen reactive power the respective power system should have the following installations:

3.1.1 Capacitor Banks

Capacitor banks are mainly installed at the load end. Basically, reactive power demand will be more at load side of the power system, hence capacitors should be placed as close as possible to load. In specific, capacitor banks should be placed

where low voltage problem occurs. There are two ways in which these capacitors are installed in system that is in series and in shunt. Both of these installations are used to generate reactive power for improving power factor and voltage.

In series capacitors, the generation of reactive power is proportional to square of load current whereas, in shut capacitors, reactive power generation is proportional to square of voltage. Hence after any disturbance, the primary voltage improvement is done by these capacitor banks only. So the readiness of these capacitors is the most important activity after any event for resilience.

3.1.2 Application of STATCOM

STATCOM is an electronic device that can be used to feed reactive power in the transmission line. Whenever there is scarcity of reactive power in the line, STATCOM increases its end voltage to balance the line voltage. Also in case of sudden load throw off, the STATCOM immediately absorb reactive power to stabilize the voltage to normal value.

3.1.3 Excitation Control by Generator

For any fluctuation of reactive power in the system, the excitation control can be done at the generation end. As there is any change in reactive power, respectively voltage gets change. This voltage is then maintained by comparator unit in voltage regulator system (see Fig. 5). The change in voltage is compared with set value and

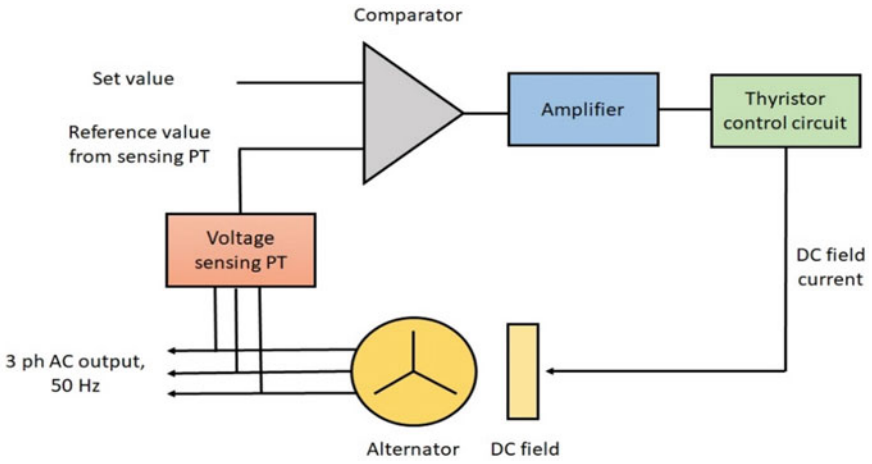

Fig. 5 Excitation control in AVR

based on the difference, the excitation current is regulated which in turn controls the field current of generator as later contributes to reactive power and voltage balance. Though voltage regulation is done automatically but in case of emergency, voltage can be maintained manually through AVR panel.

3.1.4 Tap Changing of Power Transformer

For any power system containing its own generation and grid, whenever voltage fluctuation occurs due to disturbance in grid side, the interconnecting power transformer's tap can be changed so as to maintain the voltage in existing system. This contributes to the reactive power balance in system. The tap can be regulated by On load tap changer, which automatically changes the voltage level while in load. And after the clearance of disturbance in the grid when grid voltage comes to normal state, these taps can be re-switched to its normal tap position.

3.1.5 Availability of Renewable Energy Sources

In the present scenario, availability of renewable energy sources are necessary for protection of fuels and to utilize maximum of natural resource for green energy. Easily available source which is available in abundant is solar energy, hence utilization of this source is easy and efficient. Installation and commissioning of solar energy systems are also easy now a days. Similarly, other sources like wind energy, biomass, hydro energy can also be installed in micro grid systems. These energies can be stored in battery banks which can supply the power later on. These power sources are better sources of reactive power that can efficiently fulfill the demand of VAR to the system.

3.2 Frequency Control and Strengthening

Many a time it has been seen that under frequency and over frequency may lead to disturbance in system or sometimes results in a complete blackout. Whenever natural disturbance occurs, most of the power system faces the problem of frequency swing. This frequency swing occurs due to sudden throw of heavy loads. As the load throw takes place, there is sudden jerk in generator turbine. Also, the frequency swing can lead to more load throw due to its unbalancing nature. Hence it gets mandatory to control and improve the frequency. Following are the methods by which frequency can be maintained in a power system.

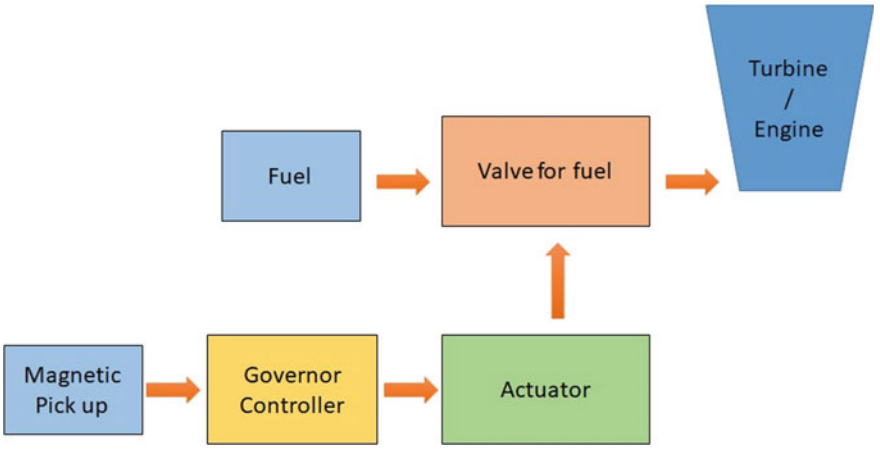

Fig. 6 Flow diagram showing the steps of Governor control

3.2.1 Governor Control

Governor is a speed control unit of turbine. It controls the speed by controlling and regulating the flow of steam or other sources. It has an actuator, which operates electrically when commanded. After getting a command it opens or closes the valve position for steam or water. Due to this, flow can be controlled maintaining the constant pressure at the turbine inlet end. As the flow is regulated, the output mechanical torque is regulated to achieve a set value and thus frequency is controlled. All the controlling takes place in governor control panel which is installed at the operator's end. Operator can control this change in frequency either in auto mode or manual mode. The whole process of controlling the output torque and thus frequency takes place within fraction of seconds. The governing control for any engine is shown in figure below (see Fig. 6).

3.2.2 Fast Load Shedding

At the time of occurrence of natural disasters, due to swing of voltage or frequency, the sudden load variation takes place in power system. This variation of loads may lead to an outage of generator and also causes a blackout. Hence, shedding of non-critical loads is the solution to overcome the chances of complete blackout. These load shedding can be done on the basis of:

- Outage of any critical equipment from circuit,
- Change of frequency (df/dt),
- Difference between the total generation and load consumption (Unbalance of power),

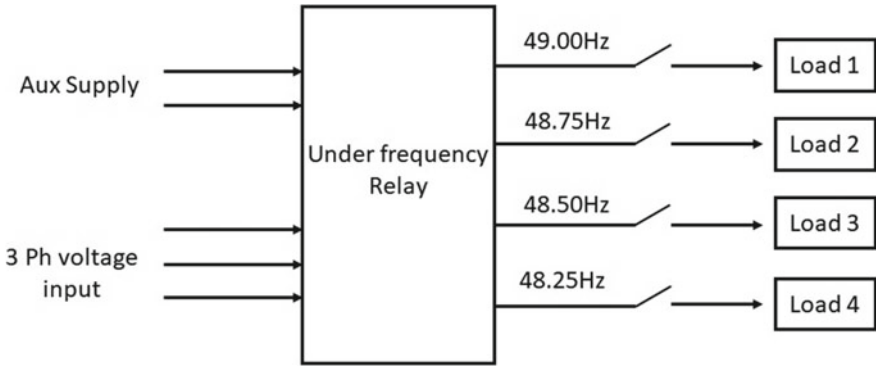

Fig. 7 Connection diagram of under- frequency relay and output connecting loads at four stages

- Low pressure at turbine inlet.

Depending on the various types of loads and mode of operation, different logics are prepared for effective load shedding. These schemes are so designed that in case any turbulence, system may not affect completely and doesn't result in blackout. While designing the load shedding schemes, the designer may also consider the behavior of atmospheric change while considering renewable energy sources of generation. Because, sudden change in atmospheric behavior may cause sudden impact on generation so this may mislead the shedding operation.

Sometimes it happens that due to heavy storms or disturbances, the communication medium of PMS may get fail. At this condition, no load shedding command is released by the installed SCADA system. Hence to overcome this problem, it needs to have a hard wiring interlocking of critical load breaker with under frequency relay, irrespective of frequency. It may be configured into three to four stages like starting from 49.0, 48.75, 48.50, and 47.25 Hz. Depending upon the priority, the tripping command can be given through relay directly to the loads (see Fig. 7).

4 Cyber Physical Security System

In the cyber physical system, resilience enhancement methods based on information technology are used to improve the resilience of the power system in extreme disasters. During the natural disaster attack at any area, as the loss of transmission system takes place, similarly the communication loss also takes place. This loss of communication may then proceed for huge outage of system due to malfunctioning of software logics. Though it takes less time to recover the communication failure as compared to main phase line. As we are moving into the world of Internet of things technology, the monitoring system for the equipment of power system should be

perfect [20]. But beyond all this, cyber-attacks are more to the power system which can be done in the following forms:

4.1 Wiretapping of Telecommunications/LAN/WAN

They can wiretap the telecommunications and attack the master server of information technology. They can easily access the door of EMS/ DMS/PMS and back feed the error signals into the server.

4.2 Access to Control Access Point of SCADA

The attackers may easily access the control center access point and may insert the malware parameters of running system. These parameters can be in terms of magnitude of current and voltage, angle of current or voltage, and harmonics to the system [20].

4.3 Knowledge of Architecture and Topology of Network

The hackers are experts in the geological, topological, and architectural approach of the installed system. Hence this knowledge may definitely make them easy approach to system and may cause the theft of electricity.

4.4 Insertion of Malware Algorithm to Existing Software

Once the attacker gets the access to operate the system architecture, then extracting out the logic and server details is the easy step for them. Hence they insert malware algorithms into an existing system.

4.5 Load Redistribution Attack to Overload Designated Lines

Sometimes the attackers may manipulate the electrical parameters of a certain line, due to this other lines may get under loaded or overloaded. Hence this may miss guiding the system and cause the collapse of system [21].

4.6 Attack to EMS, DMS, and Injection of Fault Meter Data Through Cyber Attack

The attackers may track the remote energy meters and collect the data from it. Hence false meter data is then injected into the reporting system or server which then miss leading the agency and further cause the wrong billing and pre estimation in open grid [22].

4.7 Energy Theft in Smart Grid

Sometimes the third party hackers take illegal entry into the SCADA system. This may then draw a certain amount of power unknowingly and feed to some other independent system [23, 24]. This theft can be seen in a very large manner. Some thefts are also done at the distribution end but that is for domestic purposes.

In order to improve the resilience of the power grid against unpredicted attacks and cyber intrusions, advancements should be done in detection techniques, protection systems, and mitigation plans in generation, transmission, and distribution sectors. There are various security based new algorithms present, which may early detect the malware if attacks to the system. Artificial intelligence and neural network can also lead to fast detection of cyber attacks on the system [25]. The machine language is so defined that it can detect any type of attacker and malware.

5 Conclusion

Natural disasters can occur at any time, anywhere especially in the peninsular regions. Hence in this condition, it is necessary to have proper pre and post planning to fight against such events. The power system resilience mainly depends on planning, emergency handling, and post restoration of the system. In this paper, it has been clearly explained that what are the ways and how resiliency can be achieved by pre-post activities and during actual emergency conditions. During the disaster event, as there is huge damage of infrastructures like high tension towers, electric poles,

transmission lines, and communication network lines, which causes high impact on electrical parameters. Strengthening of voltage and current magnitude, active power, and reactive power are to be done in various ways to control the swing in the system. Similarly the under and over frequency control and its strengthening are to be done for fast recovery of the system. Resilience of cyber physical system is very much necessary as there are huge chances of theft, parameters tempering, false feeding of data into SCADA, wrong billing due to hacking of meter data, etc.

References

1. Smith AB, Katz RW (2013) US billion-dollar weather and climate disasters: data sources, trends, accuracy and biases. Nat Hazards 67(2):387–410
2. Staudt A, Curry R (2011) More extreme weather and the US energy infrastructure. Nat Wildlife Federation Report, Reston, VA, USA, Rep. 16
3. Neil Adger W (2000) Social and ecological resilience: are they related? Prog Hum Geogr 24:347–364
4. Holling CS (1973) Resilience and stability of ecological systems. Annu Rev Ecol Syst 4:1–23
5. Rose A (2007) Economic resilience to natural and man-made disasters: multidisciplinary origins and contextual dimensions. Environ Hazards 7(4):383–398
6. Lembani M, Mohammed A, Abdulwahab A, Garba A, Pinho HD, Delobelle P (2014) Health systems resilience: a systems analysis
7. Panteli M, Mancarella P (2015) Influence of extreme weather and climate change on the resilience of power systems: impacts and possible mitigation strategies. Electr Power Syst Res 127:259–270
8. Kahan JH, Allen AC, George JK (2009) An operational framework for resilience. J Homeland Secur Emerg Manag 6(1):1547–7355
9. Panteli M, Pickering C, Wilkinson S, Dawson R, Mancarella P (2017) Power system resilience to extreme weather: fragility modelling, probabilistic impact assessment, and adaptation measures. IEEE Trans Power Syst 32(5):3747–3757
10. Panteli M, Mancarella P (2017) Modeling and evaluating the resilience of critical electrical power infrastructure to extreme weather events. IEEE Syst J 11(3):1733–1742
11. Xu Y, Liu C-C, Schneider KP, Ton DT (2015) Toward a resilient distribution system. In: IEEE Power and energy society general meeting, pp 1–5
12. Lei S, Wang J, Chen C, Hou Y (2018) Mobile emergency generator pre-positioning and real-time allocation for resilient response to natural disasters. IEEE Trans Smart Grid
13. Panteli M, Trakas DN, Mancarella P, Hatziargyriou ND (2016) Boosting the power grid resilience to extreme weather events using defensive islanding. IEEE Trans Smart Grid 7(10):2913–2922
14. Panteli M, Mancarella P, Trakas DN, Kyriakides E, Hatziargyriou ND (2017) Metrics and quantification of operational and infrastructure resilience in power systems. IEEE Trans Power Syst
15. Ma S, Chen B, Wang Z (2018) Resilience enhancement strategy for distribution systems under extreme weather events. IEEE Trans Smart Grid (to be published)
16. Shahidehpour M, Clair J (2012) A functional microgrid for enhancing reliability, sustainability, and energy efficiency. Electrical J 25(8):21–28
17. Liu X, Shahidehpour M, Li Z, Liu X, Cao Y, Bie Z (2017) Microgrids for enhancing the power grid resilience in extreme conditions. IEEE Trans Smart Grid 8(2):589–597
18. Patnaik B, Mishra M, Bansal RC, Jena RK (2020) AC microgrid protection—a review: current and future prospective. Appl Energy 271:115210

19. Zhang J, Guan L, Wang X (2016) Impacts of island load shedding and restoration strategies on reliability of microgrid in distribution system. In: IEEE PES Asia-Pacific power and energy conference, Xi'an, China
20. Ten C-W, Liu C-C, Manimaran G (2008) Vulnerability assessment of cyber security for SCADA systems. IEEE Trans Power Syst 23(4):1836–1846
21. Liang G, Zhao J, Luo F, Weller SR, Dong ZY (2017) A review of false data injection attacks against modern power systems. IEEE Trans Smart Grid 8(4):1630–1638
22. Kezunovic M, Dehghanian P, Sztipanovits J (2016) An incremental system-of-systems integration modelling of cyber-physical electric power systems. In: Proceedings of grid future symposium, CIGRE US Nat. Committee, pp 1–6
23. Jokar P, Arianpoo N, Leung VCM (2016) Electricity theft detection in AMI using customers' consumption patterns. IEEE Trans Smart Grid 7(1):216–226
24. Analysis of the cyber attack on the Ukrainian power grid, defense use case (2016) Electricity Information Sharing and Analysis Center, Washington, DC, USA, March 2016
25. Borges Hink RC, Beaver JM, Buckner MA, Morris T, Adhikari U, Pan S (2014) Machine learning for power system disturbance and cyberattack discrimination. In: Proceedings of 7th international symposium resilient control system (ISRCS), August 2014, pp 1–8

Author Index

M. Mishra et al. (eds.), *Innovation in Electrical Power Engineering, Communication, and Computing Technology*, Lecture Notes in Electrical Engineering 814,
https://doi.org/10.1007/978-981-16-7076-3